



HAL
open science

Conditions of formation and agglomeration of dust in the early solar system

Gabriel Pinto

► **To cite this version:**

Gabriel Pinto. Conditions of formation and agglomeration of dust in the early solar system. Cosmology and Extra-Galactic Astrophysics [astro-ph.CO]. Université de Lorraine; Universidad de Atacama (Copiapó, Chile), 2023. English. NNT : 2023LORR0033 . tel-04472169

HAL Id: tel-04472169

<https://theses.hal.science/tel-04472169v1>

Submitted on 22 Feb 2024

HAL is a multi-disciplinary open access archive for the deposit and dissemination of scientific research documents, whether they are published or not. The documents may come from teaching and research institutions in France or abroad, or from public or private research centers.

L'archive ouverte pluridisciplinaire **HAL**, est destinée au dépôt et à la diffusion de documents scientifiques de niveau recherche, publiés ou non, émanant des établissements d'enseignement et de recherche français ou étrangers, des laboratoires publics ou privés.



**UNIVERSITÉ
DE LORRAINE**

**BIBLIOTHÈQUES
UNIVERSITAIRES**

AVERTISSEMENT

Ce document est le fruit d'un long travail approuvé par le jury de soutenance et mis à disposition de l'ensemble de la communauté universitaire élargie.

Il est soumis à la propriété intellectuelle de l'auteur. Ceci implique une obligation de citation et de référencement lors de l'utilisation de ce document.

D'autre part, toute contrefaçon, plagiat, reproduction illicite encourt une poursuite pénale.

Contact bibliothèque : ddoc-theses-contact@univ-lorraine.fr
(Cette adresse ne permet pas de contacter les auteurs)

LIENS

Code de la Propriété Intellectuelle. articles L 122. 4

Code de la Propriété Intellectuelle. articles L 335.2- L 335.10

http://www.cfcopies.com/V2/leg/leg_droi.php

<http://www.culture.gouv.fr/culture/infos-pratiques/droits/protection.htm>



UNIVERSITÉ
DE LORRAINE

SIReNa



CRPG



UNIVERSIDAD
DE ATACAMA



Thèse

présentée et soutenue publiquement pour l'obtention du grade de
Docteur de l'Université de Lorraine en Géosciences

Conditions of formation and agglomeration of dust in the early solar system

Conditions de formation et d'agglomération des poussières
dans le système solaire primitif

Par GABRIEL ANGEL PINTO MORALES

Soutenance publique le 17 mars 2023

Membres du Jury :

Directeur(s) de thèse :	Yves MARROCCHI Felipe OLIVARES Béatrice LUAIS	Directeur de recherche, CRPG, Université de Lorraine, Nancy Assistant Professor, INCT, Universidad de Atacama, Copiapó Chargée de Recherches, CRPG, Université de Lorraine, Nancy (Co-directeur de thèse)
Président du jury :	Jérôme GATTACCECA	Directeur de recherche, CEREGE, Université de Aix-Marseille, Aix-en-provence
Rapporteurs :	Rhian JONES	Directrice de recherche émérite, Department of Earth and Environmental Sciences, University of Manchester, Manchester
Examineurs :	María E. VARELA Johan VILLENEUVE Lorenzo MORELLI	Directrice de recherche, ICATE, Universidad Nacional de San Juan, San Juan Ingénieur de recherche, CRPG, Université de Lorraine, Nancy Assistant Professor, INCT, Universidad de Atacama, Copiapó
Invités :	Christophe MORLOT	Ingénieur d'études, GeoRessources, Université de Lorraine, Nancy

“Our eyes open today to new horizons”

– Ernesto Guevara –

To my grandmother

Foreword

This doctoral thesis was carried out within the framework of a collaboration agreement between the University of Lorraine (Nancy, France) and the University of Atacama (Copiapó, Chile) promoted by Campus France and the Eiffel scholarship program. The director was Dr. Yves Marrocchi, a French specialist in meteoritics and cosmochemistry, and Dr. Felipe Olivares, a Chilean specialist in astrophysics. The manuscript is entirely in English. Cover images in each chapter were created using MidJourney artificial intelligence software.

Avant-propos

Cette thèse de doctorat a été réalisée dans le cadre d'un accord de collaboration entre l'Université de Lorraine (Nancy, France) et l'Université d'Atacama (Copiapó, Chili) promu par Campus France et le programme de bourses Eiffel. Le directeur était le Dr. Yves Marrocchi, un spécialiste français en météoritique et cosmochimie, et le Dr. Felipe Olivares, un spécialiste chilien en astrophysique. De plus, le manuscrit est entièrement rédigé en anglais avec un résumé en français du travail accompli. Les images de couverture de chaque chapitre ont été créées à l'aide du logiciel d'intelligence artificielle MidJourney.

Acknowledgments

When I started studying meteorites five years ago, I never thought about the moment I am now: finishing my Ph.D. studying meteorites. It has been a journey full of both academic and life learning. A change from discipline to astronomy, a global pandemic, a new life in another country, living alone, the loss and appearance of new people, a range of new analytical tools and research, and endless conversations with a café in languages I never spoke. All this has made this Ph.D. trip, a surreal landscape framed in a context where I performed what I wanted to do five years ago: research in meteorites. I am sure this work has been possible thanks to the support and confidence of many people in my walk-in science and life. I hope to be able to thank most of them in the following paragraphs.

To my supervisor Yves, with whom we met completely randomly and somehow matched our attitudes and aptitudes for research. Much of my research growth is reflected in the advice you gave me. Thank you for trusting in me and my ideas; you always knew how to channel them into success. I want to improve every day on that special skill you have to see correlations! Thanks To my supervisor Felipe, for the endless support over these three years. This work results thanks to your particular point of view; you always gave me accurate advice that substantially improved the final results. Thanks to all your support in my personal life, sometimes our weekly meeting via zoom during the pandemic was a great rescue from the cold winter in France.

Many thanks to my collaborator and friend Rodrigo Martínez de los Ríos. Thank you for giving me the confidence and opportunity of my first meteorite job and thesis. I will always admire your passion for adventure! You are the real explorer of the 21st century! Thanks to María Eugenia Varela, who always offered me her time to talk and discuss meteorites topics; thanks for receiving me in Argentina for two months. We laugh a lot in that microscope! There I learned how meteoritics science is done in South America. To Millarca Valenzuela, always give me your support whenever necessary. Thank you for your sympathy and passion for the meteorites from the Atacama Desert. I trust that better times will come for the conservation of meteorites in Chile. Also, thanks to my daily colleagues and collaborators who were always there to discuss scientific and non-scientific issues, Laurette Piani, Camille Cartier, Johan Villeneuve, Beatrice Luais, David Beckaert, Michael Broadley and Emmanuel Jacquet.

To my friends and colleagues who have accompanied me on this doctoral adventure! Janaina, Mario, Adrien, Daniela, Shanguita and Venkat. ¡ So many adventures inside and outside the INCT! To my friends and colleagues of the CRPG Marius, Maxime, Nicola, Aswin, Dorian, Carolina, Leaf, Simon,

Mathieu, Nicola, Ettiene, Belen, and many more! Thank you very much for sharing laughter, moments, and sympathy in a city full of rain and adventures.

My greatest gratitude to my family, who has given me the strength to live under the flag of my dreams. To my grandmother Janet Cortes who taught me to live with passion and love for what I do and to respect and love daily the people who accompany our life. If I say I am human, it is thanks to your wisdom. To my father, Dario Pinto, for every support and teaching of life. Thank you for backup me in any idea or adventure I want to perform. Thanks to my mother Yuvitza Morales, who allowed me to exist. Only beautiful memories I keep of your sympathy and extravagance. Many thanks to my uncles, aunts, sisters, and brothers. They have been omnipresent in my life, and as more mature, I admire them more and more for their teachings, support and love.

Abstract

The conditions of formation and agglomeration of solids in the early solar system are still relatively poorly understood. Today, we can analyze chondritic meteorites to evaluate these events. Chondrites are fragments of asteroids that were never sufficiently heated to melt their constituent and thus preserve primitive grains of the materials from which they agglomerated. These meteorites are constituted mainly by chondrules, refractory inclusions and metal beads, all cemented together by a fine-grained material. This thesis brings together a suite of petrographic observations, chemical, and isotopic analysis, as well as astrophysical modeling of chondrite accretion to address the complex nature of formation and agglomeration of solids in the early solar system. The ultimate goal of this thesis is to provide a comprehensive study of several aspects of chondrites properties that are associated with the recycling and accretion events in the evolution of our solar system. The work is based on some of the most pristine chondrites from the Atacama Desert collection.

In this thesis, we focus on three different features of chondritic material formation and agglomeration to (i) determine dust recycling through Mg-rich relicts in Fe-rich chondrules, (ii) decipher the origin and relationship between the rimmed bearing chondrules and fine-grained matrix, and (iii) constrain the aerodynamic sorting processes of chondrules during their accretion into planetesimals. The main results and conclusions for each goal are: I. Mg-rich relicts in type II chondrules generally display $\Delta^{17}\text{O}$ values of -5‰ , -2.5‰ , and 2‰ for CO, CR and ordinary chondrites. These values are similar to the host olivines in type I chondrules. Minor element composition of Mg-rich relicts tends to be MnO-poor and slightly CaO-rich, similar to the ranges of host grains in type I chondrules. We conclude that most Mg-rich relicts in type II chondrules were originate from a previous generation of type I chondrules before their accretion into planetesimals. II. The fine-grained rims around chondrules in CO, CM, CR, and CV carbonaceous chondrites revealed a positive correlation between (i) rim thickness and host chondrule radius and (ii) the abundance of rimmed chondrules and that of other fine-grained matrix material. Our data suggest that rims did not form during parent-body evolution but rather resulted from nebular processes, with the frequency and thickness of fine-grained rims directly related to the abundance of available dust in their respective chondrule formation regions. III. The particle-size distributions in various CO carbonaceous chondrites revealed that the mean spherical diameters of chondrules increase with increasing metamorphic degree. Combining our results with literature data, we show that this relationship was not established during post-

accretion thermal metamorphism, but instead it records aerodynamic size-sorting of particles during the accretion of the CO parent body(ies). By modeling the self-gravitating contraction of clumps of chondrules, we show that the accretion processes generated a gradual change in chondrule size, with larger chondrules being more centrally concentrated in the parent body(ies) than smaller ones.

Table of Contents

Résumé des travaux	– xxix –
I. Introduction	– xxxi –
II. Échantillons et méthodes analytiques	– xxxiii –
III. Principaux résultats	– xxxv –

CHAPTER 1. Introduction	– 1 –
I. Solar System and planetesimal formation	– 2 –
1.1. Molecular cloud and solar nebula	– 2 –
1.2. Protoplanetary disk evolution	– 3 –
1.3. Accretion processes of planetesimals and planets	– 5 –
1.3.1. Streaming instability	– 6 –
1.3.2. Pebble accretion	– 8 –
II. Cosmochemistry and meteorites	– 10 –
1.4. Meteorite classification	– 10 –
1.5. The solar system dichotomy	– 11 –
1.6. Chondritic meteorites properties	– 16 –
1.7. Secondary processes in chondritic asteroids	– 20 –
1.7.1. Petrologic type	– 21 –
1.7.2. Shock metamorphism	– 24 –
1.7.3. Terrestrial alteration	– 24 –
1.8. Components in chondrites	– 26 –
1.8.1. Refractory inclusions	– 27 –
1.8.2. Chondrules	– 30 –
1.8.3. Relicts and precursor material of chondrules	– 34 –
1.8.4. Oxygen isotopic composition of chondrite components	– 36 –
III. Thesis goals and layout.	– 38 –

CHAPTER 2. Samples and analytical techniques – 41 –

I.	Meteorite background and sample preparation	– 42 –
2.1.	Sample sources	– 42 –
2.2.	Section preparation	– 44 –
II.	Analytical techniques	– 45 –
2.3.	Optical and electron microscope	– 46 –
2.4.	Electron probe microanalysis	– 48 –
2.4.1.	Technical description	– 48 –
2.4.2.	Chemical composition of chondrules and subtype classification	– 48 –
2.5.	Secondary ion mass spectroscopy	– 50 –
2.5.1.	Secondary ion generation	– 51 –
2.5.2.	Secondary ion measurement	– 53 –
2.5.3.	Evaluation of isotopic analysis	– 55 –
2.5.4.	Oxygen isotope composition	– 57 –
2.6.	X-ray microtomography	– 60 –
2.6.1.	Technical description	– 60 –
2.6.2.	Chondrule analysis	– 61 –
2.7.	Particle size analysis	– 63 –

CHAPTER 3. Deciphering recycling processes during solar system evolution from relict olivine grains in type II chondrules – 65 –

3.1.	Introduction	– 66 –
3.2.	Material and methods	– 69 –
3.3.	Results	– 71 –
3.3.1.	Petrography and chemistry	– 71 –
3.3.2.	Oxygen isotopes	– 77 –
3.4.	Discussion	– 84 –
3.4.1.	The source of forsteritic relict grains in type II chondrules	– 84 –
3.4.2.	Comparison between type I and type II chondrule precursors	– 87 –

CHAPTER 4. Formation of chondrule fine-grained rims from local nebular reservoir – 92 –

4.1. Introduction	– 94 –
4.2. Samples and analytical methods	– 95 –
4.3. Results	– 96 –
4.3.1. Petrography characteristics of fine-grained rims around chondrules	–96 –
4.3.2. Fine-grained rim statistics: frequency and thickness	– 96 –
4.3.3. Microchondrules in fine-grained rims and the intercomponent matrix	– 99 –
4.4. Discussion	– 101 –
4.4.1. A nebular formation of fine-grained rims	– 101 –
4.4.2. Fine-grained rims and chondrule formation	– 102 –
4.5. Concluding remarks	– 104 –

CHAPTER 5. Constraints on planetesimal accretion inferred from particle-size distribution in CO chondrites – 108 –

5.1. Introduction	– 110 –
5.2. Material and methods	– 111 –
5.3. Results	– 111 –
5.4. Discussion	– 111 –
5.4.1. Correlation between chondrule-size distribution and degree of metamorphism	–111 –
5.4.2. Size-sorting during planetesimal formation	– 115 –
5.5. Conclusions	– 118 –

CHAPTER 6. Distribution and alteration of meteorite in the dense collection areas of the Atacama Desert, northern Chile	– 120 –
6.1. Introduction	– 121 –
6.2. Distribution of meteorites in the Atacama Desert	– 123 –
6.2.1. Non-chondritic meteorites	–125 –
6.2.2 Chondritic meteorites	– 143 –
6.3. Climatic and geomorphology conditions of Atacama DCAs	– 133 –
6.4 Terrestrial weathering of Atacama meteorites	– 136 –
6.4.1. Meteorites in Atacama and other collections	– 136 –
6.4.2 Suitable areas in the Atacama Desert for meteorite preservation	– 140 –
6.5. Final consideration and perspectives	– 146 –
CHAPTER 7. Conclusions and perspective	– 147 –
7.1. Conclusions	– 148 –
7.2. Perspectives and ongoing works	– 150 –
Bibliography	– 152 –
Appendix A Supplementary Material Chapter 3	– 174 –
Appendix C Supplementary Material Chapter 4	– 233 –

List of Figures

Résumé des travaux

Figure 1 : Schéma de classification des météorites selon leur source de corps parent. À gauche, les météorites indifférenciées (c'est-à-dire les chondrites) n'ont jamais été suffisamment chauffées pour faire fondre leurs constituants et ainsi préserver les grains primitifs des matériaux à partir desquels elles se sont agglomérées. À droite, les météorites différenciées proviennent de planétésimaux ou de planètes entièrement fondus. Elles ont réparti leurs éléments chimiques entre différentes couches, comme le noyau, le manteau et la croûte. Pas à l'échelle. – xxxi –

Figure 2 : Image électronique rétrodiffusée de la chondrite carbonée Catalina 008 (CO3). Les composants primaires sont indiqués par des lignes orange et décrits dans le texte principal. – xxxii –

Figure 3 : Toutes les chondrites étudiées dans cette thèse. Elles sont classées par classe de chondrite. Le type pétrologique estimé est indiqué pour chaque chondrite. – xxxiv –

Figure 4 : Diagramme des cinq techniques analytiques utilisées dans cette thèse, axées sur trois échelles différentes pour caractériser cinq paramètres différents : composition isotopique et élémentaire, minéralogie, pétrographie et analyse des particules. – xxxv –

Figure 5 : Représentation schématique des résultats de cette thèse de doctorat. Le chapitre 3 décrit les conditions de formation des chondres riches en Fe par recyclage des chondres pauvres en Fe. Le chapitre 4 a déterminé l'abondance des chondres bordés parmi les différents réservoirs de chondrites carbonées et leur relation avec l'abondance des matériaux à grains fins. Dans le chapitre 5, nous limitons la distribution granulométrique combinée de la formation du corps parent CO et le modèle théorique d'accrétion des planétésimaux par l'effondrement d'un amas de chondres. Le chapitre 6 récapitule et compare la distribution et la préservation des météorites dans les 32 zones de collecte dense du désert d'Atacama (nord du Chili). – xxxix –

Chapter 1

Figure 1.1: Sketch illustrating the protostellar and stellar phases of formation. Modified from Feigelson & Montmerle (1999). AU: Astronomical unit. – 2 –

Figure 1.2: The distribution of common elements in dust and gas in molecular clouds. From Taylor (2001). – 3 –

Figure 1.3: (a) circumstellar disk HL Tauri observed by ALMA telescope at the Atacama Desert (Chile). The dark, narrow gaps between the broad red rings have low dust densities. Planets that formed from agglomerating dust likely have formed the gaps. (b) Fraction of stars with near-infrared disk emission as a function of the age of the stellar group. The negative linear correlation (blue dotted line) between disk frequency and age of stellar clusters suggested an almost linear dissipation of the circumstellar disk over time. (b) modified from Hernandez et al. (2007). – 4 –

Figure 1.4: Scaling the size ladder from dust to planets. The physical processes are divided into growth (white circles) or concentrate solids (yellow). Numbers advance from the earliest to the latest stages of planet formation. The relevance of a given mechanism tends to be restricted to a certain range of particle sizes, indicated crudely by the bars on the ladder. The ranges shown are subject to debate and actively researched. Dimensionless stopping times associated with particle sizes are shown as τ_s and are defined for 1 AU. From Chiang and Youdin (2010).

– 5 –

Figure 1.5: Illustration of some processes that can lead to streaming instability in the aerodynamically coupled particle-gas system. The vertical settling and radial drift, operating on particles that have grown big enough to be imperfectly coupled to the gas, act to enhance the local metallicity toward the values where the streaming instability would operate. Simulations of the streaming stability and gravitational collapse by Simon et al. (2016). From Armitage (2019).

– 8 –

Figure 1.6: The mass growth of two planetesimals in the outer disc (red) and inner disc (green). Initially both planetesimals have 0.5 of the Lunar mass; the one in the outer disc accretes cm-size pebbles, whereas the one in the inner disc accretes mm-size pebbles, with 0.5 of the total mass flux (due to the sublimation of ice at the snowline). Thus, the planetesimal in the outer disc grows to 20 Earth masses in the time when the planetesimal in the inner disc reaches only one mass of Mars. From Morbidelli et al. (2015).

– 9 –

Figure 1.7: Classification scheme of meteorites by their parent bodies source. On the left side, undifferentiated meteorites (i.e., chondrites) that were never sufficiently heated to melt their constituents and thus preserve primitive grains of the materials from which they agglomerated. On the right side, differentiated meteorites that were full melted to segregate their elements and minerals among different layers such as the core, mantle and crust. Not to scale.

– 11 –

Figure 1.8: Oxygen isotopic composition to classified chondrites (a) and achondrites (b). Ordinary chondrites (H, L, LL) are enriched in $\delta^{17}\text{O}$, $\delta^{18}\text{O}$. R chondrites have the highest $\Delta^{17}\text{O}$ of any of the chondrite groups, while Enstatite chondrites are not resolved from terrestrial. Carbonaceous chondrite compositions appear to be derived from a mixture of mass dependently fractionated oxygen (e.g. CI chondrites), and a ^{16}O -rich reservoir located on the CCAM mixing line. In (b) the colored boxes display $\pm 2\sigma$ variation of group mean values (see Greenwood et al. 2012 for further details). Abbreviations: MGP: main group pallasites, HEDs: Howardite-Eucrite-Diogenite suite, TFL: Terrestrial Fractionation Line, CCAM: Carbonaceous Chondrite Anhydrous Minerals line, slope = 0.95 (Clayton et al. 1977; Clayton and Mayeda 1999), Y&R: The ^{16}O fractionation line with slope = 1 (Young and Russell 1998). From Ireland et al. (2020).

– 12 –

Figure 1.9: NC-CC dichotomy inferred from isotopic signatures of bulk samples: (a) ^{50}Ti vs. ^{54}Cr and (b) ^{17}O vs. ^{54}Cr . Error bars denote uncertainties ($\pm 2\sigma$). Labels depict ordinary chondrites (OC), enstatite chondrites (EC), rumuruti chondrites (RC), howardites-eucrites-diogenites (HED), and pallasite main group (MG). (c) schematic formation scenario of the NC-CC dichotomy: I. Rapid expansion of early infalling material; II. Infalling material dominates the composition of the inner disk resulting in a NC composition, i.e., depleted in neutron-rich nuclides; and III. Mixing within the disk should have reduced the initial isotopic difference between solids from the inner and outer disk, however the rapid formation of Jupiter’s core

prevented a complete homogenization. (a-b) from Kruijjer et al. (2020) and (c) from Nanne et al. (2019). – 13 –

Figure 1.10: S-process mixing lines using $\epsilon^{95}\text{Mo}$ versus $\epsilon^{94}\text{Mo}$ for bulk NC and CC meteorites. The Mo isotope variability along the NC- and CC-lines is predominantly governed by s-process variations, in good agreement with the calculated slope from presolar SiC grain, whereas the offset between the two lines reflects an approximately constant r-process excess in the CC over the NC reservoir. From Kleine et al. (2020). – 15 –

Figure 1.11: Backscattered electron maps of two unequilibrated chondrites found at Los Vientos (hereafter LoV) dense collection area in the Atacama Desert. LoV 123 (a) and LoV 098 (b) are classified as CC CO-type and OC L group, respectively. According to the MnO content in Fe-rich olivines, LoV 123 and 098 are classified as petrologic type 3.05 and 3.15, respectively. – 18 –

Figure 1.12: Bulk composition of chondrite groups normalized to CI composition. Major elements are represented by their “cosmochemical character” as refractory (square), main (diamond), moderately volatile (triangle), and highly volatile (circle). Data from Lodders & Fegley (1998). – 20 –

Figure 1.13: Average of Tellurium concentration of carbonaceous chondrite groups versus volume fraction of matrix. Matrix volume fractions taken from summary in Alexander (2019). Uncertainties are two times the standard deviation and dashed lines represent. TL: Tagish Lake chondrites. From Hellmann et al. (2020). – 21 –

Figure 1.14: Classification system for petrologic type of chondrites by thermal and aqueous alteration. The type of secondary processes and approximate temperatures are shown at the top. The different chondrite groups are shown in the bottom. Modified from Van Schmus and Wood (1967); Sears et al. (1980) and McSween and Huss (2022). – 22 –

Figure 1.15: Distribution of CO3 chondrites with petrologic subtype ≤ 3.2 on the basis of $\sigma\text{-Cr}_2\text{O}_3$ vs. mean Cr_2O_3 in ferroan olivine grains. Three trends are shown: the middle trend is the original one from Grossman and Brearley (2005), the top trend is from Grossman and Rubin (2006), and the bottom trend is from Davidson et al. (2014). Diamonds are from Rubin and Li (2019) and filled circles are from Grossman and Brearley (2005); Grossman and Rubin (2006); Davidson et al. (2014). Approximate boundaries between adjacent subtypes are marked by dashed lines. – 23 –

Figure 1.16: Sketches of the internal structure of chondritic parent bodies as onion shell (a) and rubble pile (b) asteroids. The numbers identify petrologic type. Modified from McSween & Huss (2022). – 24 –

Figure 1.17: Hf-W isochron ages of ordinary chondrites. For a given petrologic type, there are no systematic Hf-W age differences between H, L and LL chondrites, and in general, the ages become younger with increasing petrologic type. From Hellmann et al. (2019). – 25 –

Figure 1.18: Back-scatter electron image of the carbonaceous chondrite Catalina 008 (CO3). The primary components are remarked by orange lines and described in the main text. – 27 –

Figure 1.19: Condensation of major rock-forming phases from a gas of solar composition (Anders and Grevesse, 1989) at a total pressure of 10^3 atm. This calculation was done with the best currently available internally consistent thermodynamic data for solid and gaseous phases and includes nonideal solid solution models for melilite, Ca-rich pyroxene, feldspar, and metal. From Davis and Richter (2014). – 28 –

Figure 1.20: Backscattered electron images and x-ray map of refractory inclusions in the CO chondrite Catalina (Cat) 008. Fluffy Type A (FTA) CAI (a-b) composed by melilite (mel), spinel (sp), perovskite (pv), Al-diopside (cpx) and the porosity display gypsum (gyp) results of terrestrial alteration. “Compound” Type B CAI and AOA (c-d). The Type B CAI displays a forsterite (fo) rim, probably formed from the relatively melted AOA. – 29 –

Figure 1.21: Backscattered electron image of chondrule classified by texture and chemical composition. Porphyritic chondrules (a-c) have bigger crystals well developed (euhedral to subhedral); they can have relict grains (arrows in c). On the contrary, nonporphyritic chondrules (b-d) do not develop proper crystalline structures; they are frequently composed of small grains with skeletal and/or anhedral textures. The pictures in the upper and lower part represent FeO-rich and Fe-poor (Mg-rich) chondrules. – 31 –

Figure 1.22: Summary of chondrule thermal history from experimental conditions. The maximum peak temperature is relative to liquidus for three different textural types, range between 1400 to 1700 °C (Radomsky & Hewins, 1990). The sketch assumes heterogeneous nucleation (solid precursor) and short exposition time to the peak temperature (maximum 2 hrs.). The cooling rates are a range from different results of dynamics crystallization experiments. Modified from Jones et al. (2018). – 32 –

Figure 1.23: Backscattered electron image of Fe-poor relicts in type II chondrules (blue arrow) in CO3 carbonaceous chondrites: (a-d) Los Vientos 123 (CO3.1) and (e-f) El Médano 465 (CO3.2). Some chondrules display gypsum filled porosity and fractures as massive overgrowth (e-f). This secondary mineralogy is the result of terrestrial alteration in the Atacama Desert. Tro = Troilite; Kam = Kamacite; Gyp = gypsum; Fa = Fayalite; Fo = forsterite; Meso = mesostasis. – 35 –

Figure 1.24: Three isotopes oxygen diagram showing representative compositions of major primary components of solar system matter, the solar wind (SW), and our preferred value for the Sun. All data fall predominantly on a single mixing line characterized by excesses (lower left) or depletions (upper right) of ^{16}O relative to all samples of the Earth and Moon. Plotted are the most ^{16}O -enriched solar system samples: an unusual chondrule (K. Kobayashi, H. Imai, H. Yurimoto, 2003); individual platy hibonite grains (Li et al., 2009), which are ultrarefractory oxides from carbonaceous chondrites (CC); water inferred to have oxidized metal to magnetite (Choi et al., 1998) ordinary chondrites (OC); very ^{16}O -depleted water from the CC Acfer 094 (Sakamoto et al., 2007), and whole CAIs from CC (Clayton, 1993); and chondrules from CC and OC (Clayton, 1993), bulk Earth (mantle), and Mars (SNC meteorites). The mass-dependent fractionation trajectory of primary minerals in FUN inclusions and the pure ^{16}O (slope 1.0) line (Young & Russell, 1998) are also shown. From McKeegan et al. (2011). – 37 –

Chapter 2

Figure 2.1: Name and abundance of meteorites found in all dense collection areas in the Atacama Desert. The dense collection areas with a major abundance of meteorites are El Médano (EM), Los Vientos (LoV) and Catalina (Cat). – 42 –

Figure 2.2: All chondrites studied in this thesis. They are classified by chondrite class. The estimated petrologic type is shown for the eight samples found in the Atacama Desert and donated by the Museo del Meteorito (Chile) collection. – 43 –

Figure 2.3: Schematic of the meteorite section preparation. After cutting the sample slice with the diamond saw, the slice is placed in (a) a resin block or (b) resin with an aluminum ring. In this study, both section types were used. – 44 –

Figure 2.4: Diagram of the five analytical techniques used in this thesis focused on three different scales to characterize five different parameters: isotopic and elemental composition, mineralogy, petrography, and particle analysis. – 45 –

Figure 2.5: SEM components (a) and the interactions between accelerated electrons and atoms of the sample (b). – 46 –

Figure 2.6: Trends of low petrologic subtype basis on $\sigma\text{-Cr}_2\text{O}_3$ vs. mean Cr_2O_3 in ferroan olivine grains for CO (a) and ordinary chondrites (b). CO chondrites displays two trends: the bottom one proposed by Grossman and Brearley (2005), and the top trend from Grossman & Rubin (2006). The approximate boundaries between adjacent subtypes (dashed lines) were modified from Rubin and Li (2019). The trend of ordinary chondrites was proposed by Grossman and Brearley (2005). LoV 098 plot above the trend defined by the other ordinary chondrites, similar to Ngawi, a breccia of type 3.1 and 3.6/3.7 material. CO chondrites analyzed in this thesis are shown as blue diamonds. LoV 098 is shown as a blue circle. Literature data (filled gray circles) are from Grossman and Brearley (2005); Grossman and Rubin (2006); Davidson et al. (2014); Rubin and Li (2019); Yamanobe et al. (2018); and Ushikubo & Kimura, (2021). – 49 –

Figure 2.7: Sketch of the ionization of the surface's sample by the bombarding of ions from the primary source. – 50 –

Figure 2.8: Schematic of instrument localization in the SIMS: 1. Cesium ion source; 2. Duoplasmatron ion source; 3. Primary beam mass filter; 4. Immersion lens; 5. Sample; 6. Electron gun; 7. Transfer optical system; 8. Entrance slit; 9. Electrostatic sector; 10. Energy slit; 11. Spectrometer lens; 12. Magnetic sector; 13. Exit slit; 14. Projection lenses; 15. Deflector; 16. Channel-plate; 17. Fluorescent screen; 18. Deflector; 19. Faraday cup; and 20. Electron multiplier. Adapted from Joo & Liang (2013). – 52 –

Figure 2.9: Schematic representation of spectrometer modification setting as input and output. The mass resolution setting improves the difference between the two peaks M_1 and M_2 measurements and permits overcoming isobaric and molecular interferences. Modified from Chaussidon (1998); Rollion-Bard (2001); and Villeneuve (2010). – 55 –

Figure 2.10: Graph of the scan of the three oxygen isotopes in the measured signal of the analysis. The separation of the ^{17}O peak from the ^{16}OH hydride was using an MRP of ~ 7000 .
– 58 –

Figure 2.11: Triple oxygen isotope plot of the standards San Carlos olivine (SCOL-B), CAF and JV1 diopside (JV1-B). These terrestrial standards are analyzed to calibrate the TFL of the measured samples.
– 58 –

Figure 2.12: The Oxygen three-isotope diagram. Oxygen isotope ratios are referenced to deviations from Vienna Standard Mean Ocean Water (V-SMOW) to generate the delta scale. Mass dependent fractionation related to kinetic isotope mass fractionation lies on the Terrestrial Fractionation Line of slope of approximate $\frac{1}{2}$ (i.e., $\delta^{17}\text{O} = 0.5 * \delta^{18}\text{O}$). The $\Delta^{17}\text{O}$ refers to the deviation of a composition from the mass dependent fractionation line and is expressed as the distance to the Terrestrial Fractionation Line at the given $\delta^{18}\text{O}$ (i.e., $\Delta^{17}\text{O} = \delta^{17}\text{O} - 0.52 * \delta^{18}\text{O}$). For instance, the green triangle at $\delta^{18}\text{O} = -40\text{‰}$ on the slope 1 reference line, the $\Delta^{17}\text{O}$ is -19.2‰ .
– 59 –

Figure 2.13: Sketch of micro CT acquisition and reconstruction data processes. A series of X-ray projection images are acquired and mathematically reconstructed to produce a 3D map of X-ray absorption in the sample volume. 3D image is commonly represented as a series of 2D slice images (virtual images). From Landis and Keane (2010).
– 60 –

Figure 2.14: Figure 2.13. X-ray microtomography images of the relict-bearing type II chondrule in LoV 123 (CO3). Both images show a 2D slides of the chondrule Ch_20 in the xy axis (a) and the xz axis (b). The Mg-rich relict is indicated with a orange circle.
– 61 –

Figure 2.15: X-ray microtomography of relicts in the Ch_01 type II chondrule from LoV 123 (CO3). The sphericity (a) and volume (b) are shown for each relict in the chondrule. The relict selection starts with a black and white threshold to delimitate the Mg-rich borders, which are subsequently corrected by hand selection in each virtual image.
– 62 –

Figure 2.16: Particle analysis processes. A) X-ray compositional map of EM 463, with Mg, Al, Ca and Fe as red, blue, green and white. B) compositional map using a mean filter and enhanced contrast function in Fiji/ImageJ software. C) Mask layer of free-hand selected particles showing the colored outlines.
– 63 –

Figure 2.17: Sketch of methodology applied to determine the particle diameter and the fine-grained rim (FGR) thickness of rim-bearing chondrules.
– 64 –

Figure 2.18: Probability density function of three physical parameters in chondrules: Aspect ratio (a); Roundness (b); and circularity (c).
– 64 –

Chapter 3

Figure 3.1: Backscattered electron images of relict-bearing type II chondrules from (a-b) LoV 123 (CO3.05), (c-d) LoV98 (L3.05) and (e-f) Renazzo (CR2.4). LoV123_Ch02 (a) is a relict-bearing chondrule with at least ~ 12 relict grains showing Mg diffusion and sharper border inside

either larger or smaller Fe-rich olivine grains. LoV123_Ch10 (b) show abundant metal beads in the mesostasis and inside host as well as relict olivines. The central Mg-rich relict crystal contains three metal beads with a roundness shape probably related to their reduced condition of formation. LoV98_Ch05 and LoV98_Ch02 (c-d) are classic agglomerated Fe-rich chondrules in ordinary chondrites. Both are surrounded by a relatively thin layer (~20 μm) of sulfides and metals. (e) Ren_Ch03 is a relatively large porphyritic chondrule with the most ^{16}O -rich relict grain at $\Delta^{17}\text{O} = -7.5$ ‰. (f) Ren_Ch02 display a clusters of Mg-rich olivine phenocrysts whereas each one is surrounded by thin layer of Fe diffusion. Spot analysis in SIMS is indicated as orange and blue circles for relict and host olivines. Tro = Troilite; Kam = Kamacite; Chr = Chromite; Gyp = gypsum. – 72 –

Figure 3.2: Frequency plot of olivine Fo content ($=100 \times \text{Mg}/[\text{Mg} + \text{Fe}]$) for CO carbonaceous (a) and ordinary (b) chondrites. The mean Fo composition of relict and host olivine grains is shown as dotted orange and blue lines, respectively. One sigma of each mean value is shown for reference. – 73 –

Figure 3.3: Difference trends of relicts and host olivine grains in CO, CR, and ordinary type II chondrules by FeO/MgO versus FeO/MnO ratios (b). The mean composition of host grains (\pm one sigma) in ordinary and carbonaceous chondrites is indicated by an orange and blue lines, respectively. – 74 –

Figure 3.4: Elemental compositions of the studied olivine grains. The plots show $\Delta^{17}\text{O}$ values vs. MnO (a), CaO (b), Cr_2O_3 (c), and Al_2O_3 (d). The circle and square symbols indicate relict and host olivine grains in the type II chondrules. Reference lines are Terrestrial Fractionation (TFL; Clayton et al., 1991). – 77 –

Figure 3.5: (a) Triple oxygen isotope plot of the olivine crystals in the twenty analyzed Fe-rich chondrules. Relict grains show mass-independent variations plotting along the Primary Chondrule Mineral (PCM) line. The host olivine grains in Cat08_Ch02 (CO chondrites) show mass-dependent variation indicated by a parallel slope to the Terrestrial Fractionation Line (TFL; Clayton et al., 1991). (b) Olivine Fa content ($=100 \times \text{Fe}/[\text{Mg} + \text{Fe}]$) is plotted in log scale against $\Delta^{17}\text{O}$ values ($= \delta^{17}\text{O} - 0.52 \times \delta^{18}\text{O}$). The estimated composition of type I and type II chondrules is shown for reference. – 79 –

Figure 3.6: Oxygen three-isotope diagrams for type II chondrules from (a–i) CO, (j–o) ordinary, and (p–t) CR chondrites. Reference lines are Terrestrial Fractionation (TFL; Clayton et al., 1991), and the Primitive Chondrule Minerals (PCM; Ushikubo et al., 2012). The error bars are smaller than marker size. – 82 –

Figure 3.7: The Mg# - $\Delta^{17}\text{O}$ value of relict and host olivines in type I and type II chondrules from CO (a), CR (b), and ordinary (c) chondrites. The TFL is shown as blue line for reference. Fa content ($=100 \times \text{Fe}/[\text{Mg} + \text{Fe}]$) is plotted in log scale revealing a transition and overlapping between olivine grains in type I chondrules and relict grains in type II chondrules for carbonaceous chondrites. Opposite to the constant $\Delta^{17}\text{O}$ values in a wide range of Fa content in ordinary chondrites. The probability density function of relict and host grains in type I and II chondrules are show to the right of each chondrite class. Errors are 2σ . Data of type I chondrules in carbonaceous and ordinary chondrites are from Hertwig et al. (2016); Chaumard et al. (2018); Marrochi et al. (2018, 2019, 2022); and Piralla et al. (2021). – 83 –

Figure 3.8: Relict bearing chondrule Ch_18 in LoV 123 (CO3.1). (a) Chondrule constituted by various small relicts in the borders and one larger Mg-rich relict chondrule in the center. (b) Zoom to the rectangle in (a) showing the larger Mg-rich relict. (c-d) Compositional maps of Mg-Si and Fe-S indicate Fe-rich olivine crystals inside the relict chondrule which is mainly constituted by Ca-poor pyroxene. – 85 –

Figure 3.9: The $\Delta^{17}\text{O}$ value plotted against MnO (a), CaO (b), Cr_2O_3 (c), and Al_2O_3 (d) for relict and host olivines in type I and II chondrules from CO, CV, CM and C2 ungrouped carbonaceous chondrites. The TFL is shown as blue line for reference. Detection limit of minor elements in type II chondrules are show as gray dashed line. Errors are 2σ . Data of type I chondrules in CV, CM and C2-an carbonaceous chondrites from Hertwig et al. (2016); Chaumard et al. (2018); Marrochi et al. (2018, 2019). – 86 –

Figure 3.10: The $\Delta^{17}\text{O}$ value plotted against MnO (a), CaO (b), Cr_2O_3 (c), and Al_2O_3 (d) for relict and host olivines in type I and II chondrules from CR chondrites. The TFL is shown as blue line for reference. Errors are 2σ . Detection limit of minor elements in type II chondrules are show as gray dashed line. Data of type I chondrules from Marrocchi et al. (2022). – 87 –

Chapter 4

Figure 4.1: Representative examples of rimmed chondrules in back-scattered electron images of (a, b) EM 397, (c, d) Paris, (e, f) Renazzo and (g, h) Vigarano; CO, CM, CR and CV carbonaceous chondrites, respectively. Dashed white lines mark chondrule borders and dashed yellow lines the FGR–matrix interface. (b) and (d) show details of FGR–matrix boundary. (b) shows a discontinuous thin film ($\sim 3\ \mu\text{m}$) of iron oxide. (c) The FGRs are narrower at the contact between the two rimmed type II chondrules, which may have collided and agglomerated before the end of dust accretion onto chondrules (so that the thickness at the contact was deprived of further increase). Collision of the two rimmed type II chondrules shortly after their formation is statistically more likely than later coagulation given the rarity of type II chondrules in carbonaceous chondrites. (d) Multilayered structures observed in the FGRs; Dashed orange lines mark compacted material at the chondrule–FGR interface and dashed red line the porous outer layer containing imbricated minerals and metal beads oriented parallel to the chondrule perimeter. The white arrows indicate TCI. – 97 –

Figure 4.2: Broken chondrules in (a, b) CO and (c, d) CV chondrites have FGRs mantling only their intact edges. In (d), the white arrows mark a discontinuous radial crack in the FGR of the broken CV chondrule that does not affect the matrix, and the yellow arrow indicates a microchondrule within the FGR. Dashed white lines mark the exterior borders of chondrules and dashed yellow lines the FGR–matrix interface. – 98 –

Figure 4.3: Positive correlations between apparent chondrule radius and apparent FGR thickness among the studied (a) CO, (b) CM, (c) CR, and (d) CV carbonaceous chondrites. Colored solid lines and black dashed lines represent weighted (Thirumalai et al., 2011) and simple regressions, respectively (Thirumalai et al., 2011); fitting parameters are shown for the weighted regressions only. – 99 –

Figure 4.4: Back-scattered electron images and compositional maps of two microchondrules within rimmed type I chondrules in (a–c) CO and (d–f) CV chondrites. The CO chondrite microchondrule shows sharp contact with the fine-grained material and is composed of an olivine core surrounded by Ca-poor pyroxene (c) as well as a small metal bead inside (b). These petrographic features are similar to their host chondrule. The CV chondrite microchondrule shows sharp contact with the fine-grained material and is Ca- and Al-rich (f, Mg-Al-Ca compositional map), different from their host chondrule (Mg-rich). It could represent melted mesostasis expelled from some parent chondrule. Yellow arrows mark the microchondrules, and red boxes indicate the areas shown in the compositional maps. Dashed white lines mark chondrule borders and dashed yellow lines the FGR–matrix interface. – 100 –

Figure 4.5: Correlation between the modal abundance of ICM+FGR and the percentage of rimmed chondrules in CO, CM, CR, and CV chondrites. The black solid line represents the simple linear regression for all measurements, and the fit parameters are reported at top left. Reference data do not report errors associated with the modal abundance or percentage of rimmed chondrule. Error bars are smaller than symbol sizes in most cases of our reported data. – 101 –

Figure 4.6: Positive correlations between apparent chondrule radius and apparent FGR thickness between type I and type II chondrules in (a) CO, (b) CM carbonaceous and (c) ordinary chondrites (Bigolsky 2017). Colored solid lines represent simple regressions. Type I and type II chondrules are represented by the blue circle and orange square, respectively. No rimmed type II chondrule was found in the sections of CR and CV chondrites. – 102 –

Figure 4.7: Schematic representation of the proposed genetic link between chondrules and FGRs. The chondrule-forming region and chondrules are not drawn to scale. The chondrule-forming region includes a zone in which solids were melted, a peripheral region (“halo”) where solids were not melted but exceeded some arbitrary processing temperature, and an outer zone where dust went unprocessed. Chondrules (probably still warm) subsequently accreted FGRs, which were composed mostly of processed dust, with a few “contaminants” from the chondrule-melting volume (e.g., microchondrules) and presolar grains which could have survived in the unmelted halo. The abundance of rimmed chondrules depends on the dust abundance in the chondrule-forming region. Before their incorporation into a parent body, chondrule fragments with noncontinuous FGRs were likely produced through collisions in a turbulent nebular environment. – 103 –

Chapter 5

Figure 5.1: Representative examples of particle selection. (A) BSE image of LoV 123. (B) X-ray compositional map of EM 463, with Mg, Al, Ca, and Fe shown in red, blue, green, and white. The colors of particle outlines indicate component type. In (A) type-I chondrules are outlined in red, type-II chondrules in blue, refractory components in green, IOGs in orange, and fine-grained rims in yellow. In (B), outline colors are as in (A), except that refractory components are distinguished between AOAs in green and CAIs in purple. – 112 –

Figure 5.2: (A) Mean chondrule diameter vs. petrologic type of CO chondrites (data from Rubin 1989, Ebel et al. 2016, and this study). (B) Probability density function of chondrule

diameters in CO chondrites. Solid lines, this study (N, number of analyzed chondrules); dashed lines, Ebel et al. (2016). – 117 –

Figure 5.3: Equation (5) normalized to the ratio $\rho_1(0)/\rho_2(0)$ at the center of the particle clump from the beginning of a gravitational contraction leading to the formation of a planetesimal. – 118 –

Chapter 6

Figure 6.1: Localization of the 34 Atacama DCAs divided by number of meteorites in the panel (a) and by the geologic setting in the panel (b). Most DCAs are localized in Neogene surfaces in the Central Depression, meanwhile, cretaceous basement dominated DCAs in the Coastal Range. According to the Meteoritical Bulletin Database, neither the Palestina nor the Agua Buena DCA yields meteorites. Thus, there is only 32 DCAs listed. – 123 –

Figure 6.2: Different meteorite types found in situ on the Atacama Desert (except for Caleta el Cobre 022). The samples of Cariquima (c), Imilac (f), and Vaca Muerta (i) are unique pieces in their respective collection areas. All other meteorites were collected in the main Atacama DCAs: (a) Pampa de Mejillones, (b) Paposo, (d) Caleta el Cobre, (e) El Médano, (g) Los Vientos, (h) Catalina, and (j) Calama. Vaca Muerta and Calama 03 display local fragmentation. Pictures were provided by the Museo del Meteorito (San Pedro de Atacama, Chile). – 124 –

Figure 6.3: Relative abundances of meteorites found in the Atacama Desert and individual groups of carbonaceous chondrites and iron meteorites based on the total number (a) and the total mass (b). There is a significant difference between the calculation by number and mass; this is because the biggest meteorite mass found at the Atacama are the stony-irons, the Imilac Pallasite (920 kg; Killgore, 1997) and the Vaca Muerta Mesosiderite (3830 kg; Peddersen et al., 1992). Non-magmatic Irons are indicated with a yellow color. The relative proportions are estimated based on the Meteoritical Bulletin Database (2022). – 129 –

Figure 6.4: Classification of 1162 equilibrated ordinary chondrites (including brecciated textures) found at the Atacama Desert (632 H; 469 L; 53 LL; 8 H/L and L/LL). The curved lines show the kernel density estimate in 2D for each chondrite type. The operational values (Grossman and Rubin, 2002) for the classification range of ordinary chondrites are shown as square dashed lines. Data extracted from Meteoritical Bulletin Database. – 130 –

Figure 6.5: Histogram of the mass distribution of OCs from the Atacama Desert by petrologic type 3-4 (a), type 5 (b) and type 6 (c). H group lead the mass distribution in petrologic type 3-4 and 5. However, L group dominated at petrologic type 6. The last bin in each histogram displays all the larger mass than 1500 g. Data extracted from Meteoritical Bulletin Database (2022). – 132 –

Figure 6.6: Distribution of weathering grade for hot desert and Antarctic chondrites. The Atacama shows peak of weathering grade at W3 with similar values in W2, supporting a low degree of terrestrial alteration compared to other hot desert meteorites. No Antarctic meteorite

show a terrestrial alteration above W4, which is common in hot desert collections. Data extracted from that is available in the Meteoritical Bulletin Database (2022). – 138 –

Figure 6.7: Backscatter electron images and compositional maps of one calcium-aluminum rich inclusion (a-b) and one chondrule (c-d) filled by gypsum ($\text{CaSO}_4 \cdot 2\text{H}_2\text{O}$). In (b), the gypsum (pink color) filled porosity in the spinel rim and the Ca-rich pyroxene at the center area of the CAI (white arrows). The chondrule mesostasis (d) is filled by gypsum (sky-blue color) as (i) massive overgrowth in a big pore of $\sim 30 \mu\text{m}$ and (ii) thing veins among contacts with the olivine bars (white arrows). A thin layer of gypsum also delimitates most of the fine-grained rim and the matrix contact. Prv = perovskite; mel = melilite; Ol = olivine; gyp = gypsum; opx = Ca-poor pyroxene; cpx = Ca-rich pyroxene; FGR = fine grained-rim – 139 –

Figure 6.8: Weathering grade of ordinary chondrites. In (a), the weathering grade according to the main morphotectonic units on the Atacama Desert. The chondrites experience a significant weathering find on the coastal range. All the DCA grouped by proximity are shown in (b). Group 1 = Vaquillas, San Juan and Taltal; Group 2 = Paposo and Catalina; Group 3 = El Médano and Los Vientos; Group 4 = Caleta el Cobre; Group 5 = Pampa de Mejillones and La Yesera; Group 6 = Calama, Coya Sur, Chug Chug and Sierra Gorda; Group 7 = Calate and Coipuno. Data extracted from that is available in the Meteoritical Bulletin Database (2022). – 141 –

Figure 6.9: (a) Map of the three morphotectonic units defined in this article and each DCA indicated by number (see Figure 6.1 for details). (b) Morphogenetic classification of Atacama DCAs using the average annual temperature and precipitation. Boundaries of arid, semi-arid and periglacial zones are from Peltier (1973). The hyper-arid zone corresponds to the boundaries defined by the United Nations Environment Programme (<https://wedocs.unep.org/20.500.11822/30300>). The dashed line shows the winter precipitation regime, which concerns to Preandean Range/Basement area. The annual temperature and precipitation average for each DCAs were estimated as a mean point from the average of the pixel values contained in each DCA square. We plot only DCAs with more than 10 meteorites. The colors of DCAs refer to the median alteration grade: blue = W1, green = W2, and orange = W4. CD: Central depression; CR: Coastal range; and PRB: Preandean Range/Basement. – 143 –

Figure 6.10: Schematic representation of meteorite residences in the Atacama Desert. (a) Meteorite felt with a fresh fusion crust in the Atacama surfaces. According to the surface properties and the meteoroid speed, extraterrestrial fragments can be buried in the ground or stay at the surface. Whatever the case, the meteorite surfaces start reacting with H_2O and salts (i.g., gypsum [$\text{CaSO}_4 \cdot 2 \text{H}_2\text{O}$]). (b) Different weathering agents modified the meteorite characteristics. The thermal stress weathering, wind abrasion, metallic phases oxidation, and salt precipitation generate enough internal pressure to promote the formation of secondary fractures and fragmentation along shock veins, preexisting fractures, and other zones of weakness. (c) Local fragmentation. A prolonged exposition to the weathering agents breaks the entire sample into pieces, which can be disintegrated by the weathering agents or broken down into smaller pieces again. – 145 –

Chapter 7

Figure 7.1: The schematic representation of the results in this Ph.D. thesis. Chapter 3 describes the formation condition of Fe-rich chondrules by recycling Fe-poor chondrules. Chapter 4 determined the abundance of rimmed chondrule among different carbonaceous chondrite reservoirs and their relationship with the fine-grained material abundances. In chapter 5, we constrain the CO parent body formation combined particle-size distribution and theoretical model of planetesimals accretion by the collapse of a clump of chondrules. Chapter 6 recapitulates and compares the distribution and preservation of meteorites in the 32 dense collection areas in the Atacama Desert (north of Chile). – 151 –

Figure 7.2: X-ray microtomography image of LoV 123 (CO3.05) shown in the XY axis. The contrast differences in the virtual images distinguish different chondritic components, such as Fe-poor chondrules (red dotted line) and Fe-rich chondrules (with a dotted line). These virtual slides could determine the chondritic components for subsequent analysis. White arrows show Mg-rich relicts in the Fe-rich chondrules. – 152 –

List of Tables

Table 1.1. Summary of petrographic properties in each chondrite group. From Scott and Krot (2014). – 19 –

Table 3.1. Mean major and minor composition of 982 spot analysis in host and relict olivine grains among the 20 studied FeO-rich chondrules. – 75 –

Table 3.2. Compilation of mean Mg#s and oxygen isotope ratios of 128 spot analysis in the 20 FeO-rich chondrules from LoV 123 (CO3.05), Cat 008 (CO3.1), EM 463 (CO3.2), Isna (CO3.7), LoV 098 (L3.1), Renazzo (CR2.4), and DaG 574 (CR2) ordinary and carbonaceous chondrites. $\delta^{17}\text{O}$ and $\delta^{18}\text{O}$ are relative to VSMOW (Vienna Standard Mean Ocean Water). – 80 –

Table 4.1. Statistics of completely rimmed chondrules in the studied classes of carbonaceous chondrites. – 96 –

Table 5.1. Chemical Compositions of Ferroan Olivine Grains in Type-II Chondrules of Three CO Carbonaceous Chondrites (EM 463, EM 216, and LoV 123). – 113 –

Table 5.2. Modal abundances (the ratio of component pixel area relative to the total pixel area of the chondrite, in %) of refractory components and chondrules in the analyzed CO3 chondrites. – 115 –

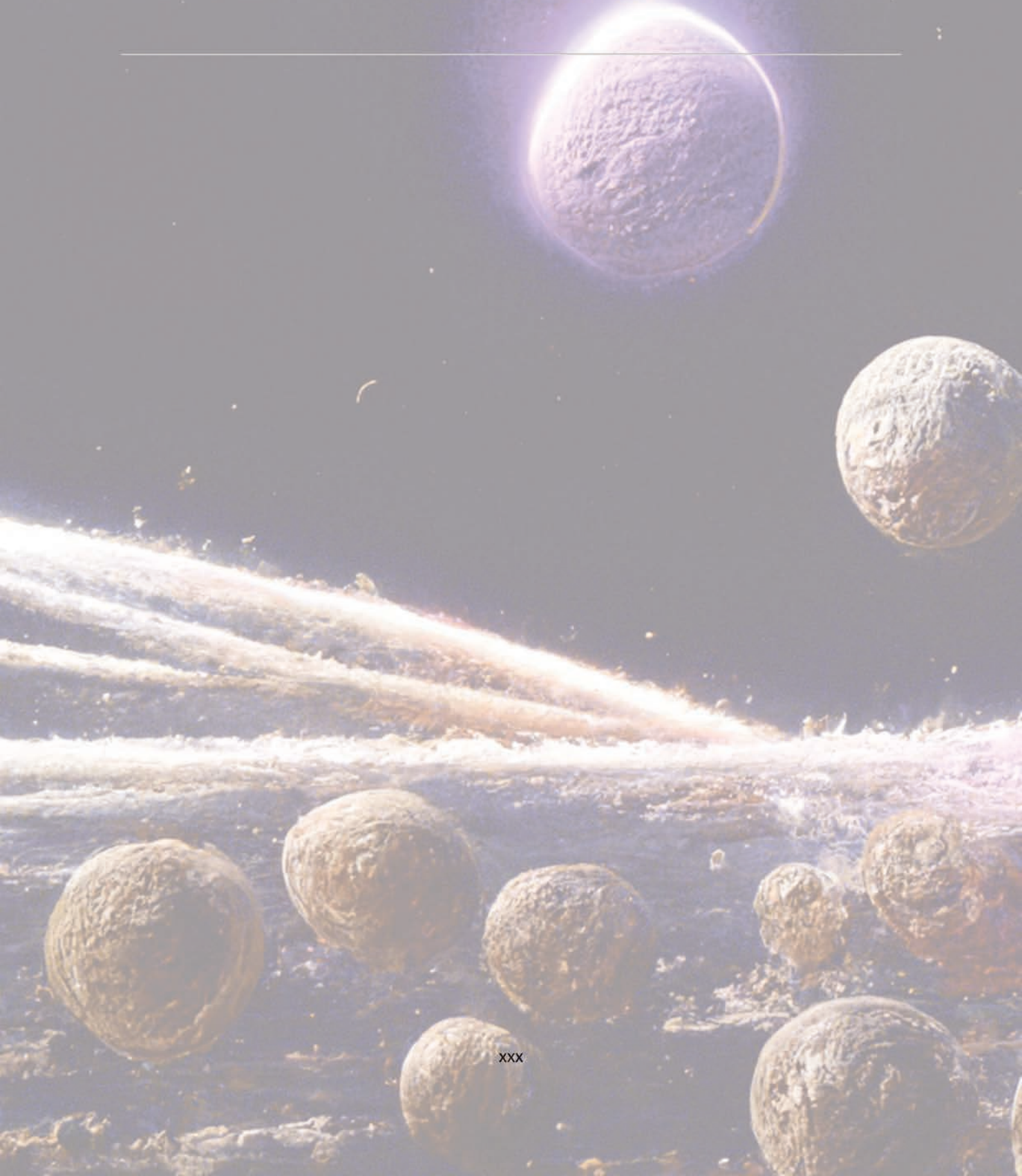
Table 5.3. The number as well as mean and median diameters (μm) of chondrules and refractory inclusions in each surveyed section. – 116 –

Table 6.1. All type of meteorite finds in the Atacama Desert. Data extracted from Meteoritical Bulletin Database. – 127 –

Table 6.2. The abundance of H and L chondrites for DCAs and petrologic type in the Atacama Desert. The OCs divided by petrologic type do not have the brecciated textures included. – 133 –

Table 6.3. The DCAs in the Atacama Desert are divided by morphotectonic units – 135 –

Résumé des travaux



I. Introduction

L'objectif principal de cette thèse est de fournir des preuves pétrographiques, chimiques et isotopiques, et astrophysiques des conditions de formation et d'agglomération de la poussière dans le système solaire primitif. Plusieurs processus astrophysiques, pétrographiques et cosmochimiques jouent un rôle dans l'agglomération des particules de poussière avant qu'elles n'atteignent l'échelle planétaire. Dans le cadre de cette thèse, nous avons analysé 14 chondrites carbonées et non carbonées non équilibrées choisies en fonction de leurs degrés d'altération limités après leur agglomération (degré pétrographique compris entre 2 et 3.8). Ce travail est centré sur trois aspects du recyclage et de l'agglomération des particules et, comme ~60% des sections étudiées sont des chondrites primitives trouvées dans le désert d'Atacama, nous résumons et comparons la distribution ainsi que la préservation des météorites sur les 32 zones de collecte dense décrites dans le désert d'Atacama (nord du Chili).

1. Système solaire et météorites

La formation du système solaire a été déclenchée par l'effondrement gravitationnel d'un nuage moléculaire. Le Soleil se forme à partir de l'effondrement d'une partie du nuage moléculaire et va produire un disque (par conservation du moment cinétique) dans lequel les premiers solides vont se former et se concentrer dans le plan médian. La structure aplatie et circulaire ainsi formée est appelée disque circum-solaire ou protoplanétaire. Dans ce contexte, les particules commencent à s'agglomérer les unes aux autres pour former des objets plus grands et finalement des planètes, dans un processus appelé accréation. Il n'y a probablement pas un seul processus d'accréation mais plusieurs, en fonction de l'échelle à laquelle l'accréation opère. La première progression est le collage de particules de μm à mm pour former des grains et des cailloux plus gros. De plus, ils sont finalement assez massifs pour être dominés par l'auto-gravité et découpler leurs mouvements du gaz, se déposant vers le plan médian du disque. Ces objets de taille km sont définis comme des planétésimaux et représentent les principaux blocs de bourgeonnement des planètes dans notre système solaire aujourd'hui.

Les météorites sont des fragments d'astéroïdes et de planètes qui tombent à travers l'atmosphère terrestre et conservent les propriétés physiques, chimiques et isotopiques héritées de leur corps parent. Elles sont divisées en chutes et découvertes selon qu'elles ont été observées (par des humains ou des appareils électroniques) avant leur atterrissage ou non. Les météorites

sont classées selon leur chimie, leurs isotopes, leur minéralogie, leurs propriétés physiques et leur pétrographie. Le schéma de classification actuel est lié à l'histoire thermique du corps parent source, qui se divise en deux grandes catégories: les météorites chondrites et les météorites différenciées (**Figure 1**). Les chondrites ou météorites indifférenciées (partie gauche de la **Figure 1**) représentent des corps parents ou des astéroïdes qui n'ont jamais été suffisamment chauffés pour fondre leurs constituants et ainsi préserver les grains primitifs des matériaux à partir desquels ils se sont agglomérés

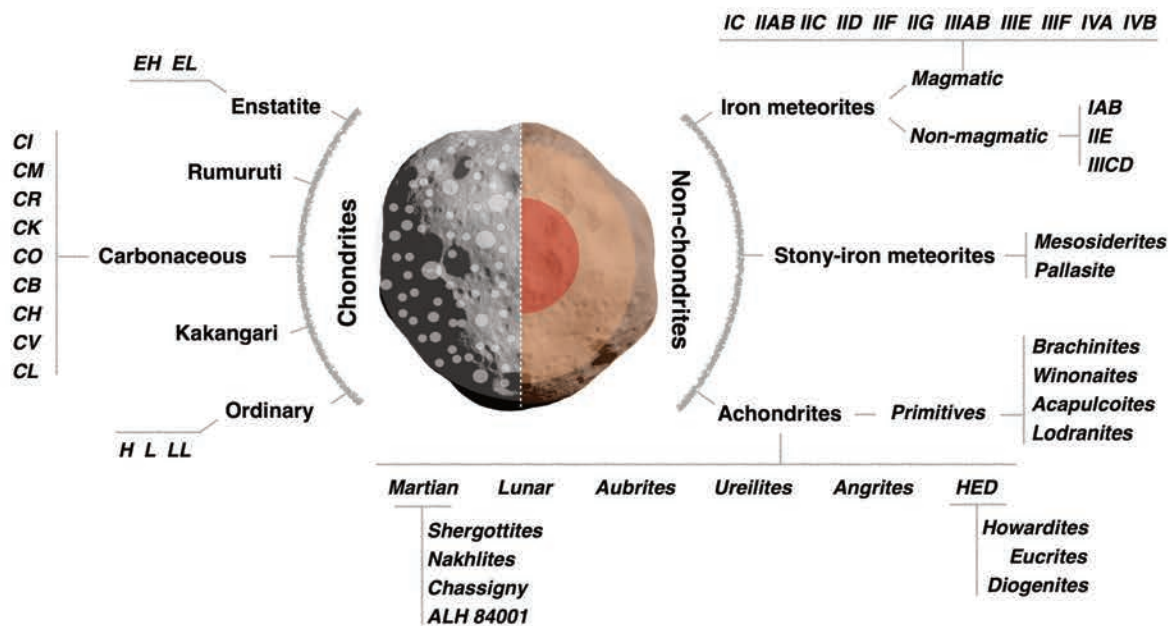


Figure 1. Schéma de classification des météorites selon leur source de corps parent. À gauche, les météorites indifférenciées (c'est-à-dire les chondrites) n'ont jamais été suffisamment chauffées pour faire fondre leurs constituants et ainsi préserver les grains primitifs des matériaux à partir desquels elles se sont agglomérées. À droite, les météorites différenciées proviennent de planétésimaux ou de planètes entièrement fondus. Elles ont réparti leurs éléments chimiques entre différentes couches, comme le noyau, le manteau et la croûte. Pas à l'échelle.

2. Chondrites et chondrules

Les chondrites représentent certains des matériaux les plus vierges pour étudier les propriétés du disque circum-solaire, la composition de la nébuleuse solaire et les conditions d'accrétion des astéroïdes et des planétésimaux. Elles conservent des composants primitifs composés de particules à gros grains ($>5 \mu\text{m}$) tels que des inclusions riches en calcium et en aluminium (CAI), des agrégats d'olivine amiboïdes (AOA), des chondres, des grains isolés et des perles métalliques (**Figure 2**). Tous ces composants sont cimentés par une matrice, un matériau à grains fins de taille $<5 \mu\text{m}$. Il est largement admis que les inclusions réfractaires, les

chondres et les métaux Fe-Ni ont subi plusieurs épisodes de formation et recyclage au cours des premiers millions d'années du système solaire par des mécanismes à haute température comprenant des processus de condensation, de cristallisation et d'évaporation (Ebel et al., 2018; Libourel & Portail, 2018; Marrocchi et al., 2018; Marrocchi et al., 2019). Les chondres sont le principal composant des chondrites; des quasi-sphéroïdes ignés de taille sub-millimétrique à millimétrique qui ont été formés par un mécanisme à haute température encore insaisissable (Connolly & Jones, 2016). Les chondres sont principalement composés d'olivine, de pyroxène, de métaux Fe-Ni, de FeS, d'une phase vitreuse et de phases minérales mineures telles que la chromite, le spinelle, l'anorthite ou la silice (Jones et al., 2018). Selon la composition chimique, les chondres peuvent être pauvres en FeO (type I) ou riches en FeO (type II). Cette classification est délimitée par le nombre de Mg ($Mg\# = 100 \times Mg / [Mg + Fe]$) dans l'olivine et le pyroxène à faible teneur en Ca; avec un $Mg\# > 90$, le chondrome est pauvre en FeO et < 90 , il est riche en FeO (**Figure 2**; Steele, 1986).

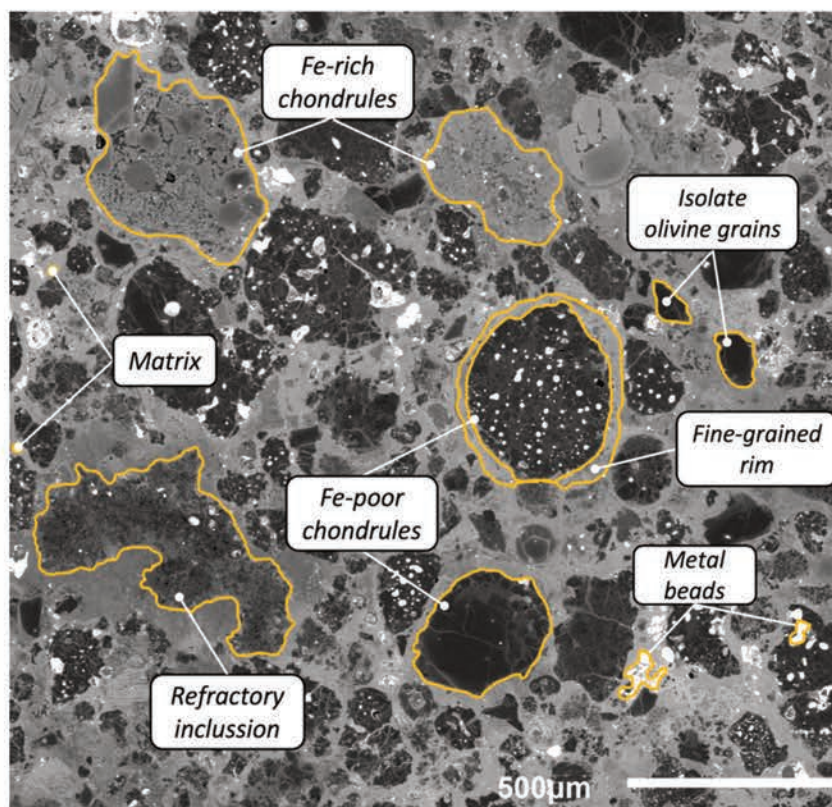


Figure 2. Image électronique rétrodiffusée de la chondrite carbonée Catalina 008 (CO3). Les composants primaires sont indiqués par des lignes orange et décrits dans le texte principal.

Les processus secondaires dans les corps parents des chondrites sont divisés en différents "types pétrologiques" (également appelés grade ou degré pétrologique) en utilisant une échelle numérique entre 1 et 6. Les types pétrologiques 2 et 1 indiquent un degré croissant

d'altération aqueuse à des températures plus basses. Seules quelques chondrites carbonées présentent un matériau à grain fin altéré omniprésent qui témoigne d'une altération aqueuse (CI, CM et CR ; figure 1). Le type pétrologique 3 à 6 définit un degré croissant d'équilibre chimique entre les composants à gros grains et à grains fins, ainsi qu'une recristallisation texturale comme résultats du métamorphisme thermique provenant de la désintégration du ^{26}Al et/ou d'événements d'impact. Les chondrites de type pétrologique 3 sont dites non équilibrées et sont divisées en une échelle de progression des sous-types de 3.00 à 3.90 qui évoluent en fonction de l'augmentation de la température dans le corps parent.

Une autre modification des chondrites est fonction de leur altération terrestre, qui est le taux d'exposition des chondrites aux agents d'altération déposés à la surface de la terre. De nombreux facteurs peuvent contrôler l'altération terrestre comme le temps de séjour dans l'environnement terrestre, la composition du sol du site de récupération, les conditions météorologiques de la région, le type de météorite, sa taille, sa forme et sa porosité. L'échelle d'altération va de W0 à W6, le classement étant déterminé par le niveau d'oxydation des métaux et des sulfures, puis des silicates (Wlotzka, 1993 ; Bland et al., 2006). Comme l'altération affecte diverses caractéristiques pétrographiques, chimiques et isotopiques des météorites, les degrés d'altération ont été étudiés par diverses méthodes comme (i) la quantité de métal, de sulfure et de silicates oxydés, (ii) l'âge de résidence terrestre, (iii) la distribution des éléments traces et (iv) la déviation de la composition isotopique.

II. Échantillons et méthodes analytiques

Les chondrites ordinaires et carbonées étudiées dans cette thèse sont présentées dans la **Figure 3**. Nous avons étudié les chondrites non équilibrées les plus primitives de la collection de météorites du Museo del Meteorito Chile (MMC). Nous avons sélectionné huit chondrites trouvées dans les zones de collection dense de Los Vientos (LoV), Catalina (Cat), et El Médano (EM) dans le désert d'Atacama. En dehors des météorites trouvées dans le désert d'Atacama, j'ai utilisé six sections (Paris, NWA 5206, Isna et Dar al Gani 574, Renazzo et Vigarano) appartenant au Muséum National d'Histoire Naturelle de Paris (MNHN, France) ou à la collection du Centre de Recherches Pétrographiques et Géochimiques (CRPG, France).

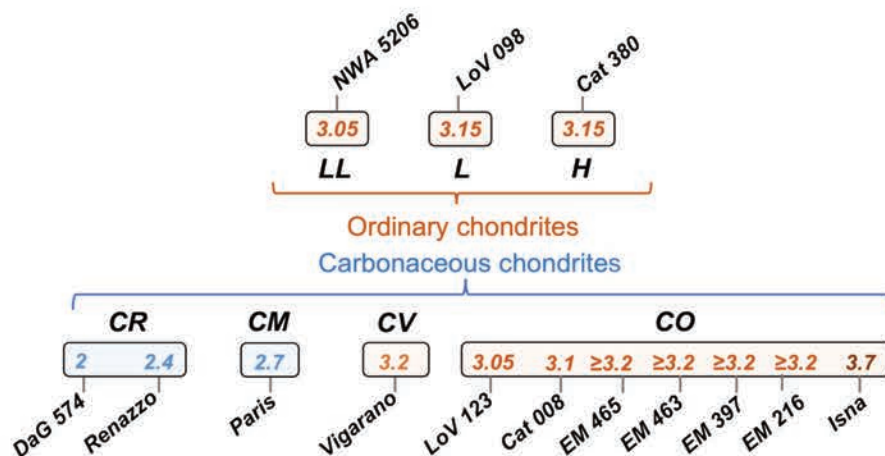


Figure 3. Toutes les chondrites étudiées dans cette thèse. Elles sont classées par classe de chondrite. Le type pétrologique estimé est indiqué pour chaque chondrite.

Cette thèse présente une approche multi-analytique de l'agglomération des dus dans le système solaire primitif. Les techniques appliquées sont présentées par échelle et par objectif dans la **Figure 4**. La pétrographie et la minéralogie de tous les échantillons ont été décrites par microscopie optique et électronique. L'analyse EMPA a été réalisée pour déterminer les compositions en éléments majeurs et mineurs de 164 grains d'olivine ferro- et magnésienne dans les chondres riches en FeO des chondrites CO, CR et ordinaires. On a également analysé quatre clastes provenant des chondrites Rennazzo (CR) et EM 463 (CO). En utilisant la teneur en Cr₂O₃ de plus de ~50 olivines riches en Fe dans les chondres de type II, nous avons classé le grade pétrographique de six chondrites non équilibrées provenant du désert d'Atacama. Des analyses des isotopes de l'oxygène ont été effectuées sur 51 reliques et 77 grains d'olivine hôtes provenant de chondres de type II dans des chondrites CO, CR et ordinaires. La microtomographie aux rayons X a été appliquée pour une chondrite carbonée et une chondrite ordinaire afin d'estimer l'abondance volumétrique des chondres de type II contenant des reliques et de caractériser leur volume. Un détail de chaque technique sera présenté dans les sections suivantes.

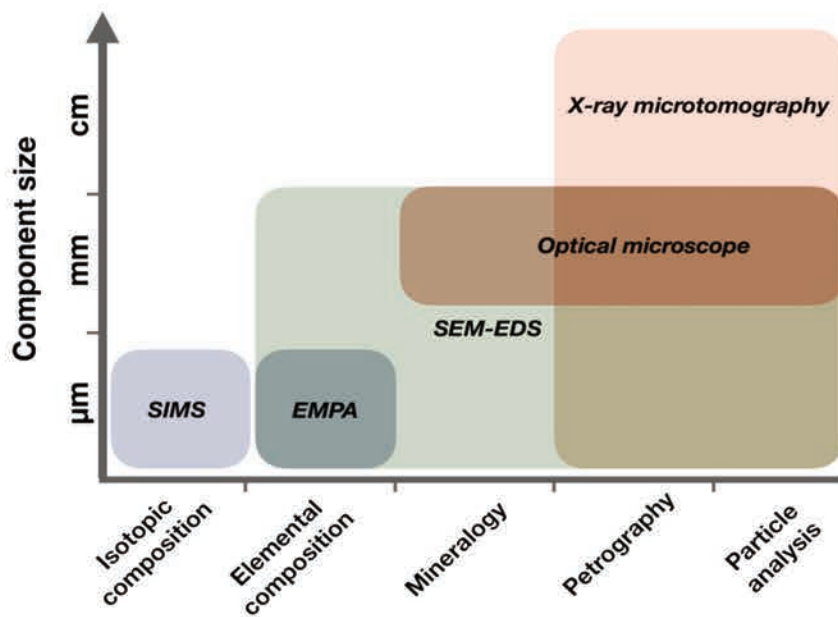


Figure 4. Diagramme des cinq techniques analytiques utilisées dans cette thèse, axées sur trois échelles différentes pour caractériser cinq paramètres différents : composition isotopique et élémentaire, minéralogie, pétrographie et analyse des particules.

III. Principaux résultats

1. Décryptage des processus de recyclage au cours de l'évolution du système solaire à partir des grains d'olivine reliques dans les chondres de type II

Il a été proposé que les chondres oxydés de type II dérivent des chondres réduits de type I par des processus de refonte et d'oxydation. Cette interprétation est soutenue par les reliques communes riches en Mg dans les chondres de type II rapportées parmi différents groupes de chondrites. Nous avons effectué des analyses chimiques mineures et majeures combinées à des mesures in situ des isotopes de l'oxygène de 51 reliques et 77 grains d'olivine hôtes sur neuf, cinq et cinq chondres de type II provenant de chondrites CO, CR et ordinaires, respectivement. Nos résultats indiquent que les grains d'olivine hôtes et reliques dans les chondrites CO, CR et ordinaires présentent des valeurs moyennes de Mg# différentes et normalement, les reliques riches en Mg sont pauvres en MnO, riches en Al₂O₃ et légèrement riches en CaO par rapport à leurs olivines hôtes. Les valeurs moyennes de $\Delta^{17}\text{O}$ des grains reliques dans les chondrites CO, CR et ordinaires sont -4.7 , -2.8 et $+0.4$ ‰, ce qui est inférieur aux valeurs moyennes de $\Delta^{17}\text{O}$ dans les olivines hôtes de type II : -2.6 , -0.5 , et $+1.1$ ‰ pour les chondrites CO, CR, et ordinaires, respectivement. Les reliques riches en Mg que nous avons signalées dans les chondres de type II se situent presque toujours dans la plage de composition isotopique en O

des olivines hôtes dans les chondres de type I ($\Delta^{17}\text{O} = -5, -2.5$ et $+2$ ‰ pour les chondrites CO, CR et ordinaires). De plus, la composition des éléments mineurs dans les reliques riches en Mg tend à être pauvre en MnO et légèrement riche en CaO, similaire aux gammes de grains hôtes dans les chondres de type I. En outre, seulement 1 des 19 (~5%) chondres de type II rapportés contenant des reliques échantillonne des grains d'olivine riches en ^{16}O similaires aux inclusions réfractaires ($\Delta^{17}\text{O} \sim -20$ ‰). Nous suggérons que la plupart des reliques forstéritiques dans les chondres de type II proviennent d'une génération précédente de chondres riches en Mg (**Figure 5a**). De plus, nous trouvons deux chondres dans la chondrite CR qui présentent des valeurs $\Delta^{17}\text{O}$ différentes dans des grains hôtes riches en Fe distincts : DaG574_Ch01 ($\Delta^{17}\text{O} = -4.7, -3.0$ et $+0.5$ ‰) et Ren_Ch01 ($\Delta^{17}\text{O} = -1.32$ et -2.97 ‰). Ces différentes valeurs de $\Delta^{17}\text{O}$ devraient indiquer un échantillon de génération précédente d'olivines riches en Fe comme récemment rapporté Kerraouch et al. (2022) dans des clastes de chondrites ordinaires. Cependant, la diffusion rapide de FeO dans les olivines riches en Mg pourrait avoir recouvert ces olivines lors du dernier événement de fusion. Quoiqu'il en soit, les grains d'olivine "hôte" riches en ^{16}O que nous avons signalé représentent des reliques isotopiques dans les chondres riches en Fe, suggérant un processus de formation au cours de plusieurs événements de chauffage.

2. Formation de bordures de chondrule à grains fins à partir de réservoirs nébulaires locaux

Les chondres sont généralement entourés de bordures à grains fins dont l'origine reste très débattue ; des origines nébulaire ou astéroïdale étant régulièrement proposées. Le décryptage de leur origine est cependant d'une importance fondamentale car il pourrait clarifier la relation matrice-chondres et ainsi contraindre les conditions de formation et de transport des chondres dans le disque circum solaire. Nous avons caractérisé les bordures à grains fins autour des chondres dans les chondrites carbonées CO, CM, CR et CV. Nos résultats ont révélé des corrélations positives entre (i) l'épaisseur du rebord et le rayon de la chondrule hôte et (ii) l'abondance des chondres rebordés et celle d'autres matériaux matriciels à grains fins. Combinées avec notre description pétrographique des bordures à grains fins, nos données suggèrent qu'elles ne se sont pas formées pendant l'évolution du corps parent, mais qu'elles résultent plutôt de processus nébulaires, la fréquence et l'épaisseur des bordures à grains fins étant directement liées à l'abondance de poussière disponible dans leurs régions respectives de formation des chondres. Puisque la migration à grande échelle dans le disque aurait détruit la

corrélation entre les abondances des bordures à grains fins et de la matrice, nos données soutiennent les modèles de formation locale de chondrule avec un transport limité, voire inexistant, dans le disque circum-solaire (**Figure 5b**). Nous supposons que les bordures à grains fins se sont accrétées dans des conditions chaudes, à des températures comprises entre le solidus des silicates (~1300 K) et la vaporisation de la glace (~170 K), à la suite des événements de formation de chondrule. Nos résultats soutiennent donc : (i) une origine nébulaire pour les bordures à grains fins, dont les abondances sont directement liées à l'abondance de la poussière disponible dans les régions d'accrétion des chondrites; et (ii) l'accrétion des chondrites à partir de chondres et de matrices formées localement, suggérant un transport radial limité dans le disque protoplanétaire.

3. Contraintes sur l'accrétion des planétésimaux déduites de la distribution de la taille des particules dans les chondrites à CO

La formation des planétésimaux a été une étape clé dans l'assemblage des corps planétaires, mais de nombreux aspects de leur formation restent mal connus. Notamment, le mécanisme par lequel les chondres –sphéroïdes sub-millimétriques qui dominent les météorites primitives– ont été incorporés dans les planétésimaux reste mal compris. Nous classons et analysons les distributions granulométriques de diverses chondrites carbonées à CO trouvées dans le désert d'Atacama. Notre analyse granulométrique des chondrites carbonées à CO a révélé que les diamètres sphériques moyens des chondres augmentent avec le degré de métamorphisme. En combinant nos résultats avec les données de la littérature, nous montrons que cette relation n'a pas été établie pendant le métamorphisme thermique post-accrétion, mais enregistre plutôt un tri aérodynamique de la taille des particules pendant l'accrétion du ou des corps parents de CO. En modélisant la contraction autogravitante des amas de chondres, nous montrons que les processus d'accrétion ont généré un changement progressif de la taille des chondres, les plus gros étant plus concentrés au centre du ou des corps parents que les plus petits. Nos résultats suggèrent également que toute croissance ultérieure des planétésimaux par accrétion de cailloux aurait dû être insignifiante. Nous concluons donc que nos observations sont cohérentes avec la formation du (des) corps parent(s) de CO via la contraction d'un amas de chondres auto-gravitant, soutenant la théorie selon laquelle la formation des planétésimaux s'est produite via un effondrement gravitationnel (**Figure 5c**).

4. Distribution et altération des météorites du désert d'Atacama : l'intacte collection dans les déserts chaud

Les conditions météorologiques et la stabilité géologique des surfaces d'Atacama favorisent l'accumulation de matériel extraterrestre sur des milliers à des millions d'années (voir par exemple Drouard et al. 2019). Il y a 20 ans, seules 64 météorites non appariées ont été trouvées sur les surfaces d'Atacama. Aujourd'hui, plus de 2141 météorites non appariées (sur un total de 2187) ont été récupérées dans 32 zones de collecte denses. Néanmoins, la plupart d'entre elles ont été collectées par des expéditions de chasseurs de météorites (c'est-à-dire que la masse principale reste en propriété privée) plutôt que par des expéditions de recherche (c'est-à-dire que la masse principale est stockée dans une collection de musée universitaire ou public). Nous examinons les données publiées et non publiées des météorites du désert d'Atacama pour (i) décrire la distribution des météorites dans le contexte des conditions géomorphologiques et climatiques des DCA d'Atacama et (ii) comparer l'altération de l'altération ainsi que leurs principales différences avec d'autres météorites de désert chaud. Les conditions climatiques et géologiques distinctives des principales unités morphotectoniques affectent l'accumulation et la conservation des météorites. Les trois principaux paramètres des DCA d'Atacama qui ont modifié le degré d'altération sont (i) la distance par rapport à l'océan Pacifique, (ii) l'altitude de surface et (iii) la lithologie de surface. Les météorites du désert d'Atacama sont principalement localisées dans la dépression centrale (47.5 %, N=1017), suivie par la chaîne côtière (31.3 %, N=671) et la chaîne/base de Preandean (21.2 %, N=453). L'abondance significative de chondrites à faible degré d'altération est située dans la dépression centrale (39.6 % avec W1), qui est protégée par la chaîne côtière à l'ouest de l'influence du brouillard côtier et des pluies saisonnières par la cordillère des Andes occidentales à l'est (**Figure 5d**). L'augmentation de l'altération est favorisée par les conditions atmosphériques, géologiques et biologiques locales de l'atterrissage de la météorite. Une comparaison avec les données d'altération rapportées par d'autres déserts froids et chauds indique que l'altération terrestre moyenne des chondrites d'Atacama (W1-2) présente moins d'altération que celle des autres déserts chauds du monde (W2-3).

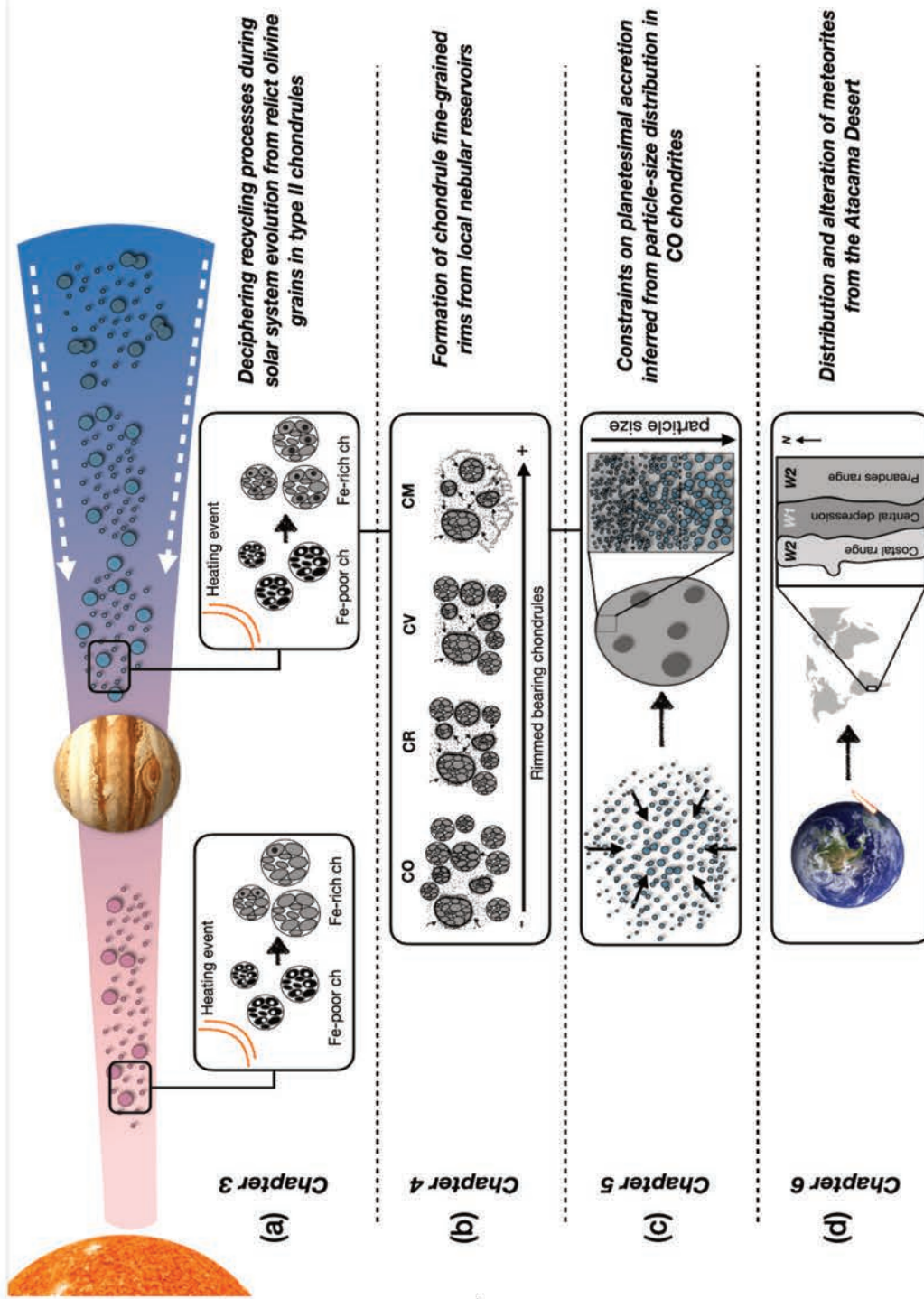
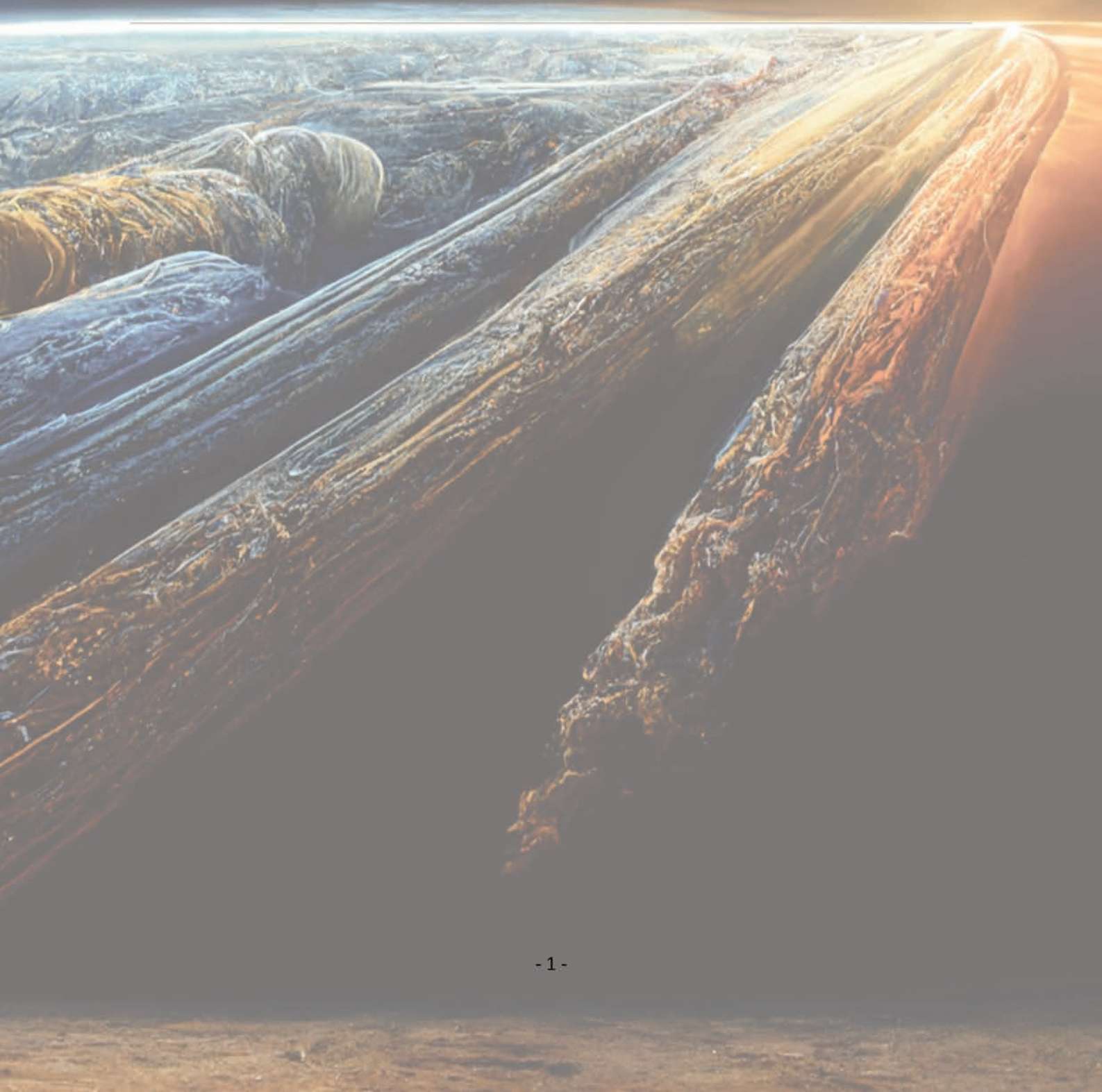


Figure 5. Représentation schématique des résultats de cette thèse de doctorat. Le chapitre 3 décrit les conditions de formation des chondres riches en Fe par recyclage des chondres pauvres en Fe. Le chapitre 4 a déterminé l'abondance des chondres bordés parmi les différents réservoirs de chondrites carbonées et leur relation avec l'abondance des matériaux à grains fins. Dans le chapitre 5, nous limitons la distribution granulométrique combinée de la formation du corps parent CO et le modèle théorique d'accrétion des planétésimaux par l'effondrement d'un amas de chondres. Le chapitre 6 récapitule et compare la distribution et la préservation des météorites dans les 32 zones de collecte dense du désert d'Atacama (nord du Chili).

Chapter 1

Introduction



I. Solar System and planetesimal formation

The formation of a planetary system is an intricate process that is still under discussion. In this section, it will be described the current suitable models for a planetary system formation focus on the Solar system.

1.1 Molecular cloud and solar nebula

According to astrophysical observations and models, the formation of stars is triggered by the gravitational collapse of local subregions inside a molecular cloud. The physical properties, such as mass and angular momentum, determined the subsequent evolution of the young stellar object (see sketch **Figure 1.1**) and their chemical/isotopic compositions. The typical elements in a molecular cloud are divided by mass into hydrogen (~74%) and helium (~24%), with just a few percent (~2%) of heavier elements (Taylor, 2001). **Figure 1.2** shows the distribution of these metals into the dusty or gaseous phase. For instance, oxygen constitutes silicates, H₂O, oxide grains and monoxide carbon in 12.6, 10.3, 68.2 and 8.9%, respectively (Taylor, 2001). The Si, Mg and Fe formed silicate grains, while Ne and N₂ are retained chiefly in the gas and ice phases.

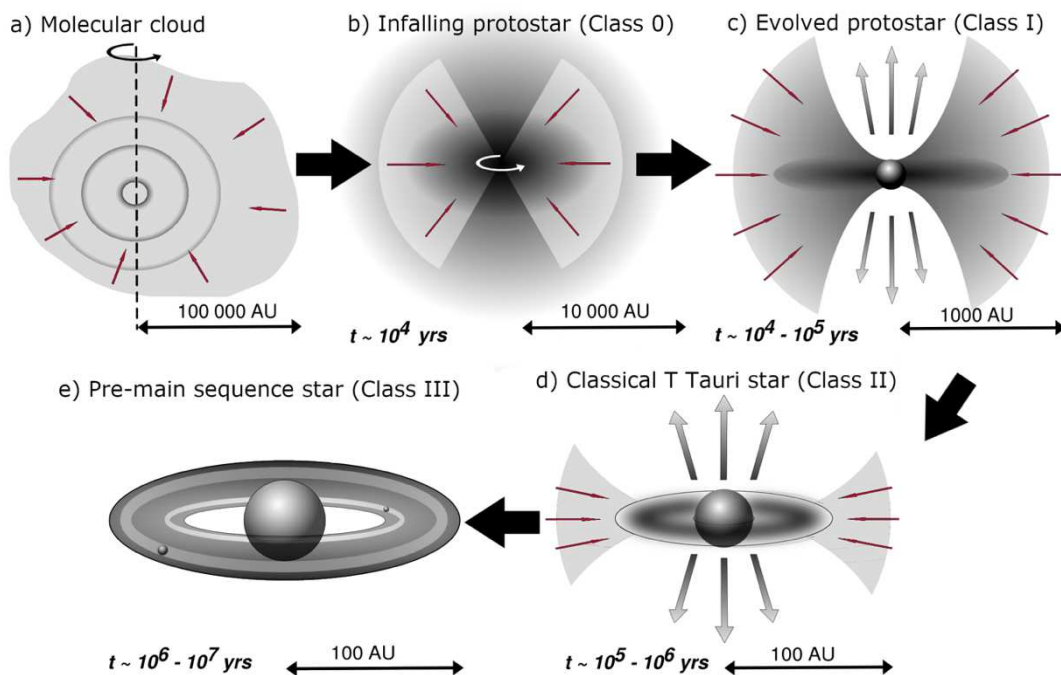


Figure 1.1. Sketch illustrating the protostellar and stellar phases of formation. Modified from Feigelson & Montmerle (1999). AU: Astronomical unit.

In the case of the Solar System, the trigger of the gravitational collapse is still unclear and remains an active field of research. It has been proposed that before the breakup of the molecular cloud, it was gravitationally supported by a combination of thermal pressure, turbulence, and possibly magnetic fields (Taylor, 2001). Shock waves are suggested to be the primary way to break up dense gas clouds. In this sense, two main scenarios could be responsible for the shock wave (i) a supernova explosion (Boss et al., 2008; Meyer et al., 2000) or (ii) strong stellar winds produced by a Wolf-Rayet or asymptotic giant branch (AGB) star (Dwarkadas et al., 2017; Gounelle & Meynet, 2012; Wasserburg et al., 2006).

Even if slowly rotating, the molecular cloud had high angular momentum for gas and dust to collapse directly into a central star. Thus, the gravitational breakup happens in cloud fragments, where a substantial fraction of the material in the collapsing core falls into a disk around the protostar. The solar nebula is a cloud fragment that became detached from the molecular cloud and generally refers to the disk of dust and gas remaining after the formation of the Sun, from which the planets, satellites and asteroids were later formed.

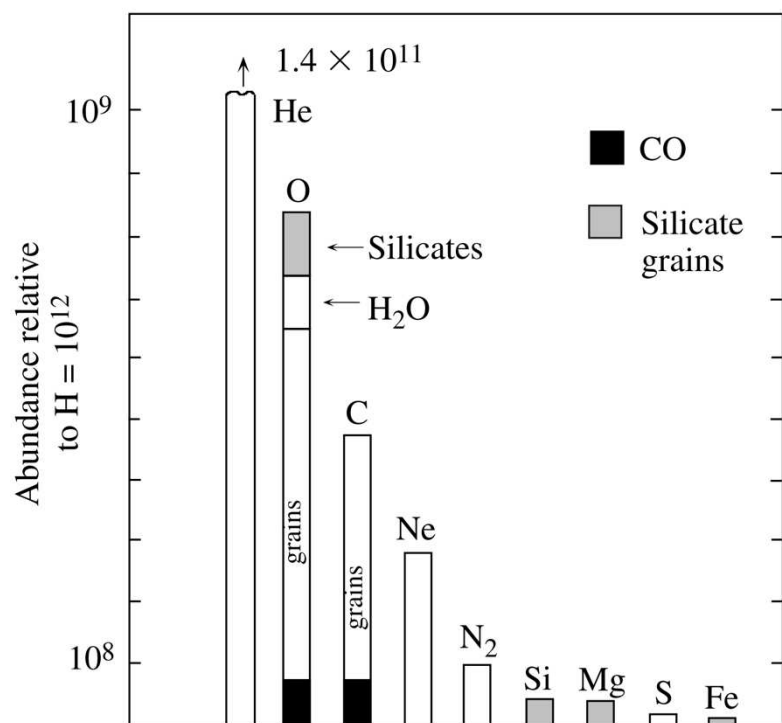


Figure 1.2. The distribution of common elements in dust and gas in molecular clouds. From (Taylor, 2001).

1.2 Protoplanetary disk evolution

The rotating solar nebula collapses into a disk, dust settles to the midplane, and the protosun begins to condense at the center. The material falling into the midplane has too much angular momentum to fall directly into the center (**Figure. 1.1c-d**). Instead, it spreads out as a rotating disk from which mass is transferred to the growing Sun and angular momentum is transferred outwards. The formed flatted and circular structure is called circumstellar or protoplanetary

disk (hereafter PPD; **Figure 1.3a**). Two main structures form the PPD: (i) the rings, that are regions of high gas and dust density, and (ii) the gaps, which indicate a low abundance of mm-sized material, suggesting the existence of a formed planet at those radii (Andrews et al., 2018). For instance, current hydrodynamical simulation of star cluster formation indicates that disks can be destroyed in dynamic encounters due to the chaotic nature of star formation (Bate, 2018). However, PPD has also been observed in binary stars, with a shorter orbital period (Czekala et al., 2019), and recently in a triple-star system (Kraus et al., 2020).

The lifetime of gas/dust dissipation in a PPD is directly related to the formation period of planetesimals (km or larger bodies that are largely decoupled from the gas), which have been estimated occurs only few Ma after the host star formation (**Figure 1.3b**; (Hernández et al., 2008)). In this sense, from a purely observational perspective, most of the gas in PPDs could be lost via accretion onto the star and by photoevaporation of the molecular gas (Armitage & Kley, 2019).

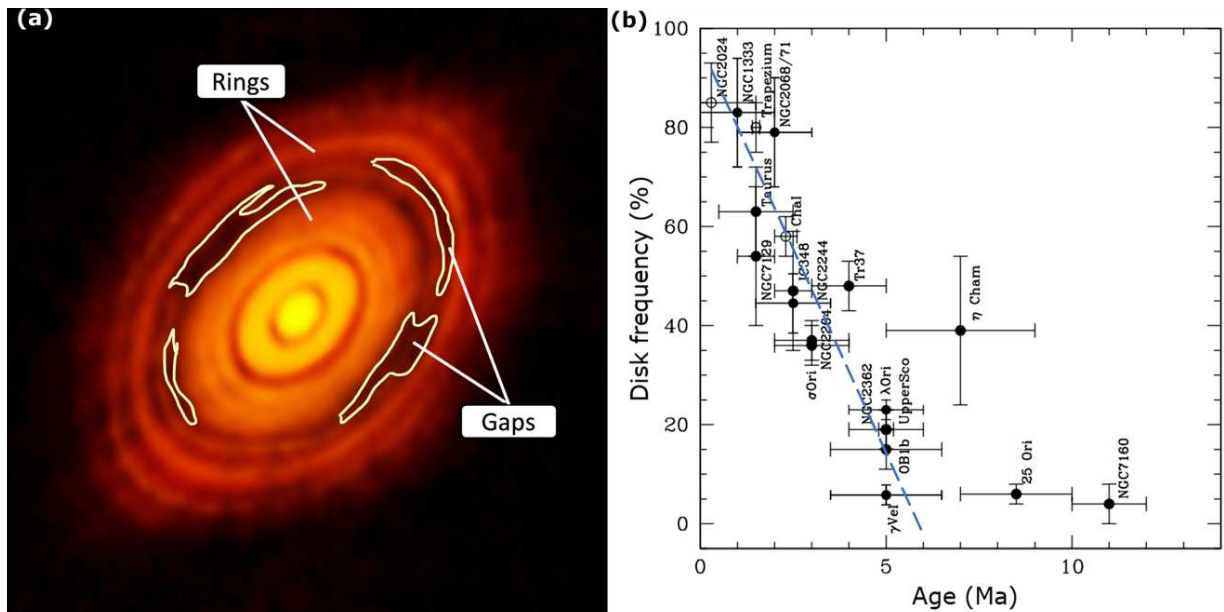


Figure 1.3. (a) circumstellar disk HL Tauri observed by ALMA telescope at a wavelength of 1.3 mm. The dark, narrow gaps between the broad red rings have low dust densities. The formation of planets and asteroids has been proposed in these regions. (b) Fraction of stars with near-infrared disk emission as a function of the age of the stellar group. The negative linear correlation (blue dotted line) between disk frequency and age of stellar clusters suggests an almost linear dissipation of the circumstellar disk over time. (b) from Hernandez et al. (2008).

1.3 Accretion processes of planetesimals and planets

Accretion is the process in which particles in the PPDs agglomerate to form larger objects and eventually planets. There is probably not one accretion process but several, depending on the scale at which accretion operates (see **Figure 1.4**). The first progression is the sticking of μm to mm particles to form larger grains and pebbles. As these grains increase in size, they are eventually massive enough to be dominated by self-gravity and decouple their motions from the gas, settling towards the midplane of the disk. These km -sized objects are defined as planetesimals and represent the second progression of material accretion. The last step is to build planets by planetesimal/protoplanet collisions and/or by the late pebble accretion model. In this sense, the dust accretion in the solar system grew by 13 orders of magnitude, from micrometers to tens of thousands of kilometers in diameter.

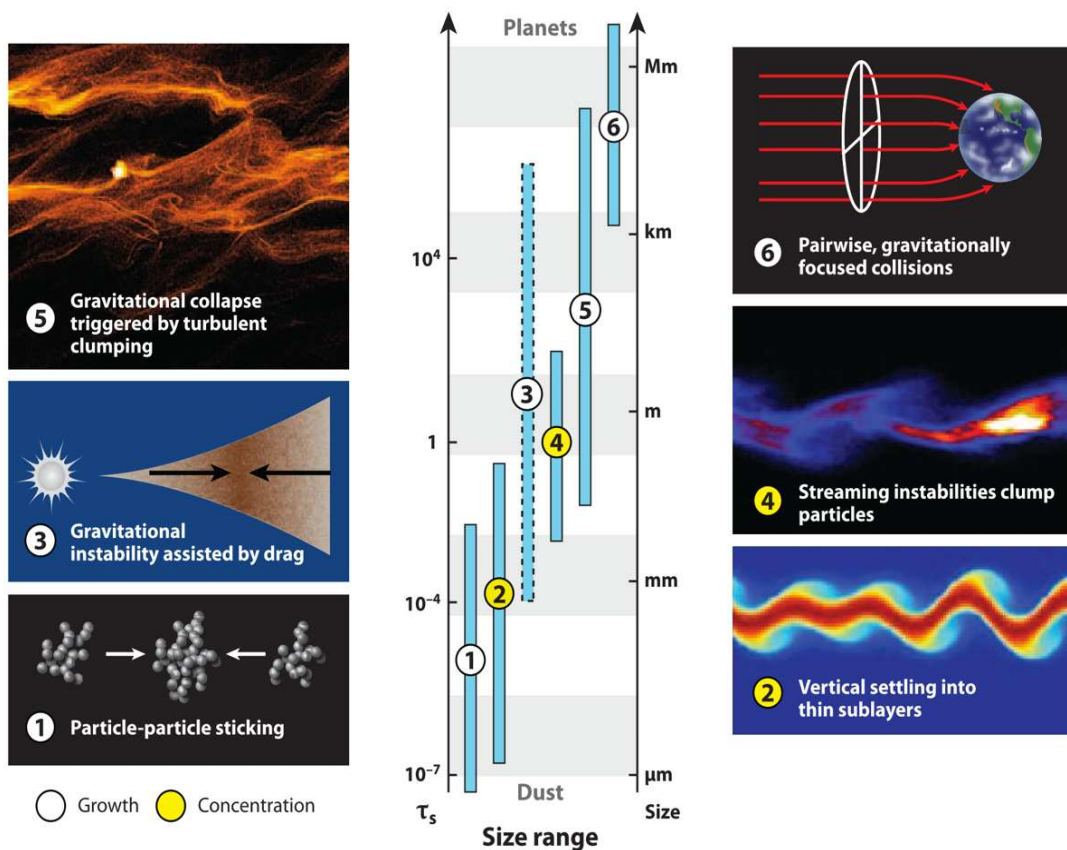


Figure 1.4. Scaling the size ladder from dust to planets. The physical processes are divided into growth (white circles) or concentration of solids (yellow). Numbers advance from the earliest to the latest stages of planet formation. The relevance of a given mechanism tends to be restricted to a certain range of particle sizes, indicated crudely by the bars on the ladder. The ranges in the figure shown are subject to debate and actively researched. Dimensionless stopping times associated with particle sizes are shown as τ_s and are defined for 1 AU. From Chiang & Youdin (2010).

The predominant evolution of a particle in a disk is dictated by the particle's stopping time τ_s (**Figure 1.4**), which is the time to eliminate any differential velocity of the particle relative to the gas drift and settle to create a particle concentration and/or growth (Morbidelli, 2018). One of the first accretion models proposed is the grains' pairwise collision and sticking. However, this growth model carries a limitation known as the “meter-sized barrier”, where agglomerate bodies larger than this scale are expected to be fragmented or bounce during high-speed collisions (Windmark et al., 2012) or develop a rapid drift migration toward the central star (Wetherill, 1990). Recent theoretical studies suggest that planetesimals formed from clumps of small particles whose common gravitational attraction outweighs the dispersive action of turbulent diffusion (Klahr & Schreiber, 2020, 2021). This model provides a physically plausible route to forming planetesimals rapidly from smaller solids. This process requires that the clumps of particles are sufficiently dense and massive, producing planetesimals of at least 100 km in diameter (Johansen et al., 2015). Many models proposed that particle clumps formed due to disk turbulences and/or streaming instabilities, i.e., hydrodynamic instabilities due to the differential velocities of particles relative to the surrounding gas (Johansen et al., 2007, 2015; Li et al., 2018, 2019; Wahlberg Jansson & Johansen, 2014, 2017; Youdin & Goodman, 2005). According to Morbidelli et al. (2022), there are two preferential usually location in the PPD to form planetesimals accretion by hydrodynamic instabilities of a cloud of particles: (i) the snowline, which is the minimum radius from the Sun at which water ice could have condensed (about 150 K at ~ 5 AU) and (ii) the silicate sublimation line, which is defined as the silicate sublimation at $1500 \text{ K} \pm 20 \text{ K}$ (~ 1 AU).

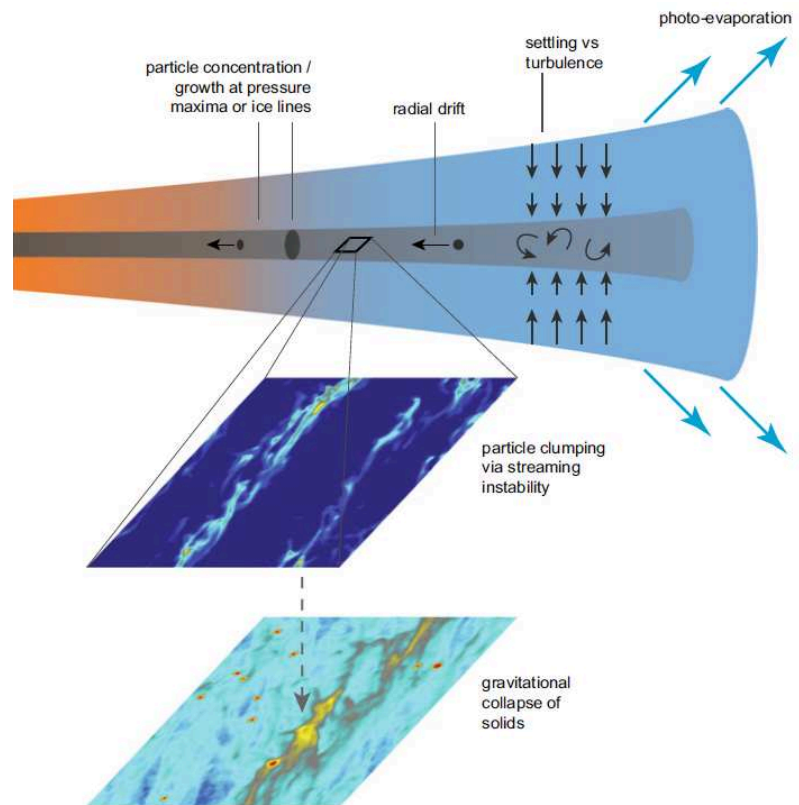
Once planetesimals have formed, they can continue growing to planets by accreting individual pebbles (if they exceed a critical size of about 1000 km diameter (Ormel & Klahr, 2010), while they drift through the disk. This process is known as pebble accretion (Johansen et al., 2015; Lambrechts & Johansen, 2012) and it is more efficient than planetesimals collisions by the larger probability for a planetesimal-pebbles encounter compared to a planetesimal-planetesimal encounter and a large number of pebbles drift from a greater distance in the disk (Morbidelli, 2018). In the following section, we described the two most promising models for planetesimals/planets accretion.

1.3.1 Streaming instability

The main variable that triggers a streaming instability in the particle-gas interaction is the differential speed of dust relative to the gas. If this differential speed causes gas-dragging onto the particles, the friction exerted from the particles back onto the gas accelerates the gas and diminishes its difference (Morbidei, 2018). Thus, if there is a small density of particles, the local gas turns to reduce the local headwind on the particles, starting to drift more slowly toward the star. Isolated particles which drift faster to the star eventually intersect the over-density region, increasing the local density of particles exponentially with time. Thus, the effectiveness of streaming instability in promoting clump formation depends on particle size, or rather on the Stokes number, which is the ratio between a particle's stopping time due to friction with the gas and its orbital period.

Figure 1.5 illustrates the main properties of theoretical models, which invoke the single particle processes as an essential element for generating streaming instabilities in PPDs. Current simulation suggests that the gravitational collapse of solids assembles a population of planetesimals with the largest radius of 100 km undergoing accretion of chondrules within ~ 3 Ma (Johansen et al., 2015). Thus, streaming instabilities suggest that planetesimals grow big in contrast to the pair-wise collision model, in which solids objects would grow progressively. However, to reach an optimal large-scale concentration, very large particles (at least decimeters in size) are needed. Moreover, primitive meteorites, which represent the interior structure of asteroids, are commonly formed by compact subspherical particles with range sizes from 0.1 to 1 mm denominated as chondrules. Such small particles are very hard to concentrate in vortices or through streaming instability (Morbidei, 2018). Using a high-resolution numerical simulation, Yang et al. (2017) suggested that chondrule-sized particles can trigger the streaming instabilities only if the solid/gas ratio is larger than 4%. However, this ratio in the solar system disk is estimated to have been only 1% (Morbidei, 2018). Another current possibility is that drifting particles first accumulate where the radial speed is lowest and trigger locally streaming instability thanks to the nearby enhancement of the particle/gas ratio. Two zones have been theoretically define to increase the surface density of solid material, (i) the snowline, due to the availability of water ice, and (ii) the silicate sublimation line, due to the outward radial motion of gas that is assisted by the sublimation and recondensation of silicates (Drażkowska et al., 2016; Morbidei et al., 2022).

Figure 1.5. Illustration of some processes that can lead to streaming instability in the aerodynamically coupled particle-gas system. The vertical settling and radial drift, operating on particles that have grown big enough to be imperfectly coupled to the gas, act to enhance the local metallicity toward the values where the streaming instability would operate. Simulations of the streaming stability and gravitational collapse by Simon et al. (2016). From Armitage & Kley (2019).



1.3.2 Pebble accretion

Once the planetesimal is formed in the circumstellar disk, it remains surrounded by gas and *pebbles*, which are added to the growing planetesimal toward their orbital movement. Even if the self-gravity of the planetesimals accreted all the pebbles in their vicinity, the local population of pebbles would be renewed by new particles drifting from large distances (Morbidelli, 2018). In this sense, one of the significant advantages of this model is that the orbital neighborhood of the growing body cannot become empty. Thus, the mass-flux of pebbles has been shown to be able to form the largest planetesimals up to multiple Earth's masses (Lambrechts & Johansen, 2012, 2014). For instance, giant planet cores have been suggested to grow by pebble accretion within the disk's lifetime (Lambrechts & Johansen, 2012, 2014). This is mainly controlled by ice pebbles that can be larger in the outer disk (a few centimeters in size) compared to pebbles in the inner disk, which are limited to sub-millimeter sizes by the bouncing silicate barrier (Morbidelli et al., 2015). **Figure 1.6** shows two initial planetesimals with a 0.5 Lunar mass growth due to a flux of pebbles on opposite sides of the snowline (assuming to be at 3.5 AU) during the first 2 Ma of the solar system formation. The

outer embryo develops a size large enough to accrete gas efficiently and eventually becomes a giant planet.

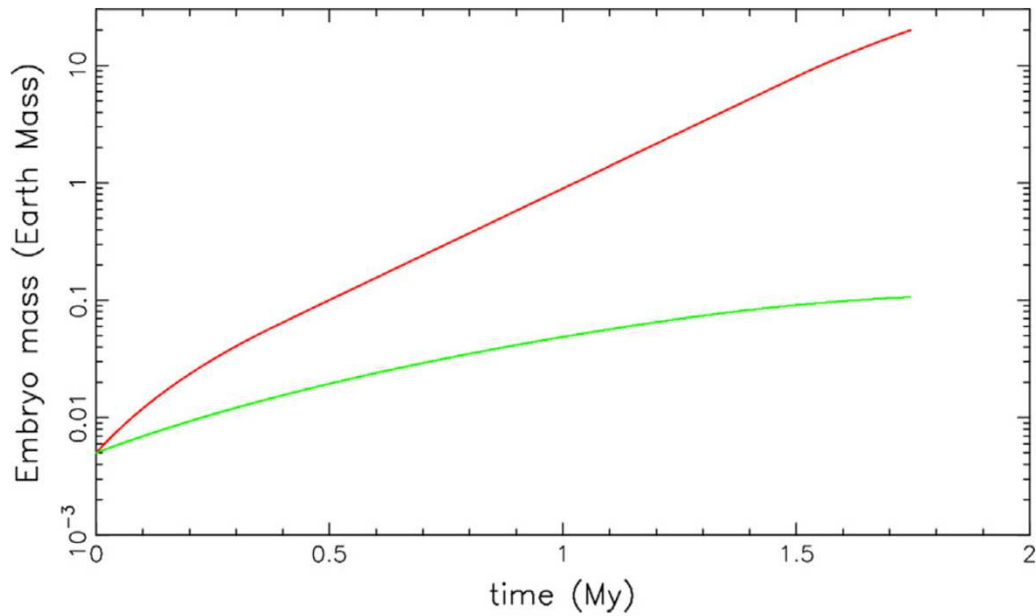


Figure 1.6. The mass growth of two planetesimals in the outer disc (red) and inner disc (green). Initially both planetesimals have 0.5 of the Lunar mass; the one in the outer disc accretes cm-size pebbles, whereas the one in the inner disc accretes mm-size pebbles, with 0.5 of the total mass flux (due to the sublimation of ice at the snowline). Thus, the planetesimal in the outer disc grows to 20 Earth masses in the time when the planetesimal in the inner disc reaches only one mass of Mars. From Morbidelli et al. (2015).

II. Cosmochemistry and meteorites

1.4 Meteorite classification

Meteorites are fragments of extraterrestrial rocks that fall through the Earth's atmosphere and retain physical, chemical, and isotopic heritage properties from their parent body. The parent body concept is defined as "a celestial body that supplies meteorites to Earth" (Greenwood et al., 2020), which can be a planet, asteroid, comet, or even a moon. Meteorites are divided into falls or finds differing in whether they were observed (by humans or electronic devices) before landing or not, respectively. Meteorites are classified using their chemistry, isotopes, mineralogy, physical properties, and petrography. The current classification scheme is related to the thermal history of the parent body source, which is divided into two major categories: chondrite and non-chondrite meteorites (**Figure 1.7**). The chondrites or undifferentiated **meteorites** (left side **Figure 1.7**) represent parent bodies that were never sufficiently heated to melt their constituent and thus preserve primitive grains of the materials from which they agglomerated. At least 16 chondrite groups have been recognized. Several other chondrites which are mineralogically, chemically and/or isotopically unique cannot be classified into the existing chondrite groups; these chondrites are commonly called ungrouped. All chondrites display chondritic texture (except for CI chondrite), which is defined by the presence of sub- to millimeter-sized igneous spheroids called chondrules (see section 1.8.2). The non-chondritic meteorites contain virtually no nebular components (e.g., chondrules) but are believed to be derived from chondritic materials by planetary melting and fractionation (Krot et al., 2014). The latter are also called **differentiated meteorites** due to their partial or complete melting, which promotes chemical and physical segregation of elements into the core, mantle, and crust that are represented by iron, stony-iron, and achondrite meteorites, respectively (right side **Figure 1.7**).

The most abundant element in rocky bodies is oxygen, which form characteristic abundances by their three stable isotopes (i.e., $^{16,17,18}\text{O}$) and are useful to assigning meteorites to classes which represents a common source materials (Clayton, 1993; 2003; Ireland et al. 2020 and reference therein). Greenwood et al. (2012) emphasize the utility of the oxygen isotope signature in matching up meteorites to parent bodies but do not specifically address the unsolved question of the origin of these signatures. The three-isotope oxygen plot is defined by

$\delta^{17}\text{O}$ versus $\delta^{18}\text{O}$, where $\delta^i\text{O} = ((^i\text{O}/^{16}\text{O})_{\text{sample}} / (^i\text{O}/^{16}\text{O}_{\text{SMOW}}) - 1) \times 1000$, and SMOW is Standard Mean Ocean Water (**Figure 1.8**). In this diagram all terrestrial samples plot along a line with a slope of 0.52, named the terrestrial fractionation line (TFL), following a mass-dependent fractionation. The vertical deviation from the TFL is defined as $\Delta^{17}\text{O} = \delta^{17}\text{O} - 0.52 \times \delta^{18}\text{O}$ (**Figure 1.8b**; see Martin, 2002) and correspond to a mass-independent fractionation. Most chondrite classes (i.e., ordinary, carbonaceous, and enstatite chondrites) plot in unique positions on this diagram. However, some of them usually show an overlapping (see **Figure 1.8a**). In the case of differentiated achondrites, the oxygen isotopic composition in each group tends to show uniform $\Delta^{17}\text{O}$ values (i.e., mass dependent fractionation), consistent with homogenization in bodies that were totally melted (**Figure 1.8b**; Greenwood et al., 2020; Ireland et al., 2020).

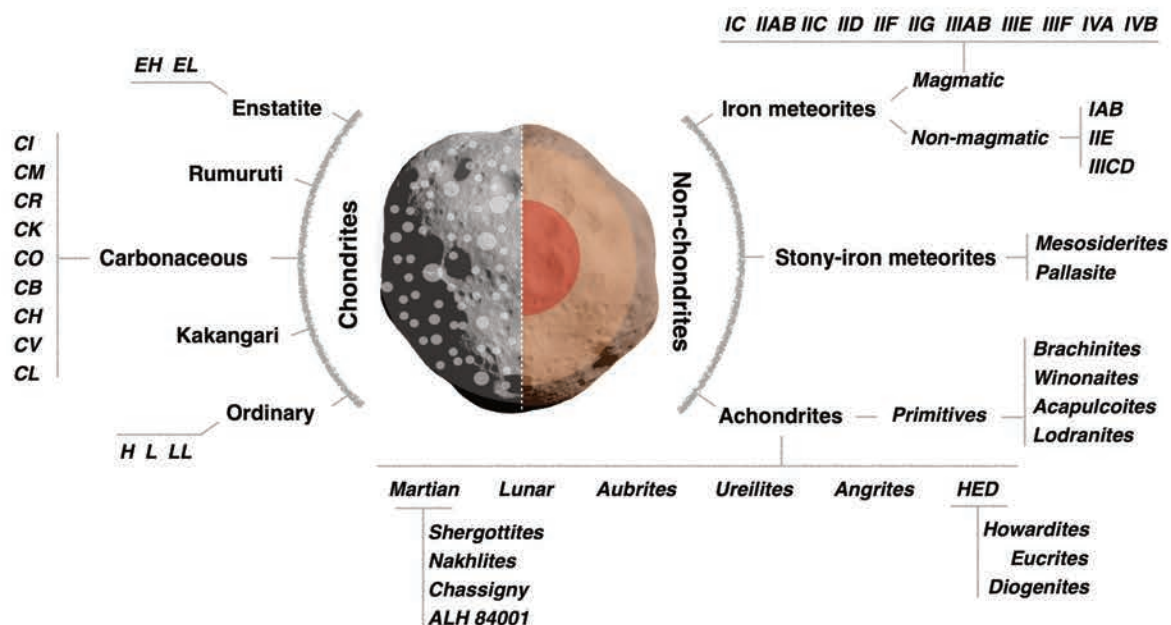


Figure 1.7 Classification scheme of meteorites by their parent bodies source. On the left side, undifferentiated meteorites (i.e., chondrites) were never sufficiently heated to melt their constituents and thus preserve primitive grains of the materials from which they agglomerated. On the right side, differentiated meteorites come from fully melted planetesimals or planets. They segregated their chemical elements among different layers, such as the core, mantle and crust. Modified from Krot et al. (2014).

1.5 The solar system dichotomy

The development of high-precision isotope measurements revealed the importance of nucleosynthetic stable-isotope anomalies in bulk meteorites and nebular components to understand genetic relationships between meteorite groups and their distribution in the solar

nebula (Trinquier et al., 2007; Trinquier et al., 2009; Warren, 2011). Nucleosynthetic isotope anomalies are defined by enrichments or depletions in nuclides formed by particular stellar nucleosynthetic processes. As the isotope variations in meteorites are typically slight, they are commonly reported in the ϵ -unit notation as parts-per-ten-thousand deviations from terrestrial standard values. For instance, Mo isotope anomalies are reported as variations in the ${}^i\text{Mo}/{}^{96}\text{Mo}$ ratio, normalized to the terrestrial ${}^{98}\text{Mo}/{}^{96}\text{Mo}$ and given as $\epsilon^i\text{Mo}$ values ($i = 92, 94, 95, 97, 100$; Burkhardt et al., 2011). **Figure 1.9** displays isotope anomalies of $\epsilon^{50}\text{Ti}$ vs. $\epsilon^{54}\text{Cr}$ and $\Delta^{17}\text{O}$ vs. $\epsilon^{54}\text{Cr}$, which reveal the dichotomy distribution of planetary materials.

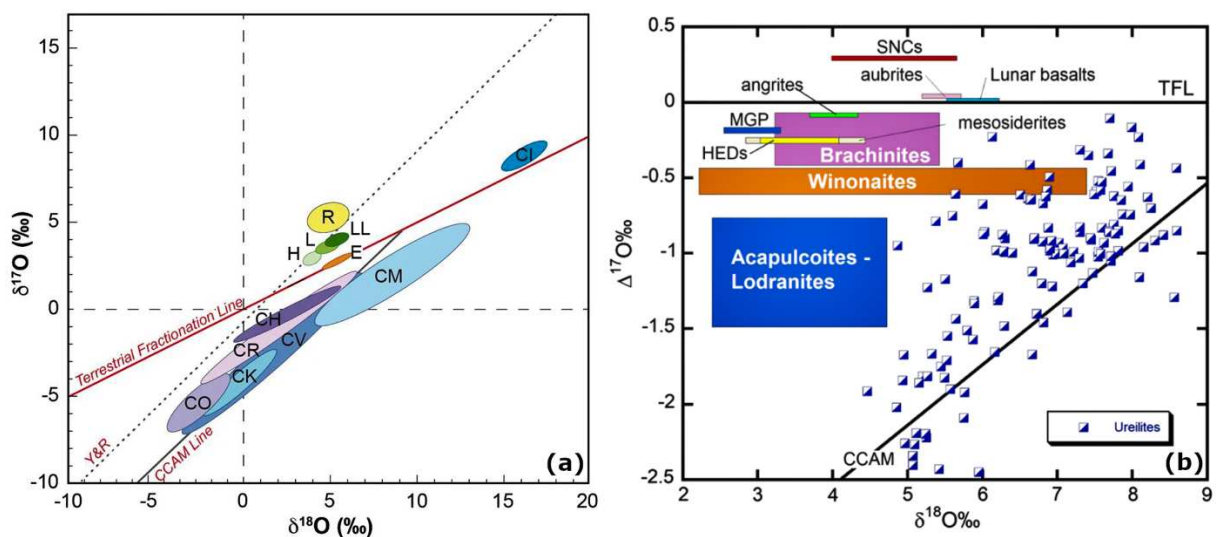


Figure 1.8. Oxygen isotopic composition for classified chondrites (a) and achondrites (b). Ordinary chondrites (H, L, LL) are enriched in $\delta^{17}\text{O}$, $\delta^{18}\text{O}$. R chondrites have the highest $\Delta^{17}\text{O}$ of any of the chondrite groups, while Estatite chondrites are not resolved from terrestrial. Carbonaceous chondrite compositions appear to be derived from a mixture of mass dependently fractionated oxygen reservoir (e.g. CI chondrites), and a ${}^{16}\text{O}$ -rich reservoir located on the CCAM mixing line. In (b) the colored boxes display $\pm 2\sigma$ variation of group mean values (see Greenwood et al. 2012 for further details). Abbreviations: MGP: main group pallasites, HEDs: Howardite-Eucrite-Diogenite suite, TFL: Terrestrial Fractionation Line, CCAM: Carbonaceous Chondrite Anhydrous Minerals line, slope = 0.95 (Clayton et al., 1977), Y&R: The ${}^{16}\text{O}$ fractionation line with slope = 1 (Young and Russell 1998). From Ireland et al. (2020).

The presence of stable isotope anomalies in meteorites provides insights into a large-scale isotopic heterogeneity resulting from the inefficient mixing of stellar-derived dust and gas after the solar nebula collapse (**Figure 1.9c**; Kruijjer et al., 2020; Kleine et al., 2020; Nanne et al., 2019). Two genetically distinct reservoirs were presumably located at the inner (non-carbonaceous reservoir, NC) and the outer (carbonaceous reservoir, CC) disk that remained isolated during the first million years of the solar system formation (Kruijjer et al., 2017; Warren, 2011). Until now, the main plausible scenario for the reservoir segregation is the early accretion

of Jupiter (Kruijer et al., 2017, 2020) or a pressure bump in the PPD near Jupiter’s orbit (Brasser & Mojzsis, 2020), whereas the drifting material from the outer solar system is blocked and prevents a complete homogenization of the disk (Figure 1.9c).

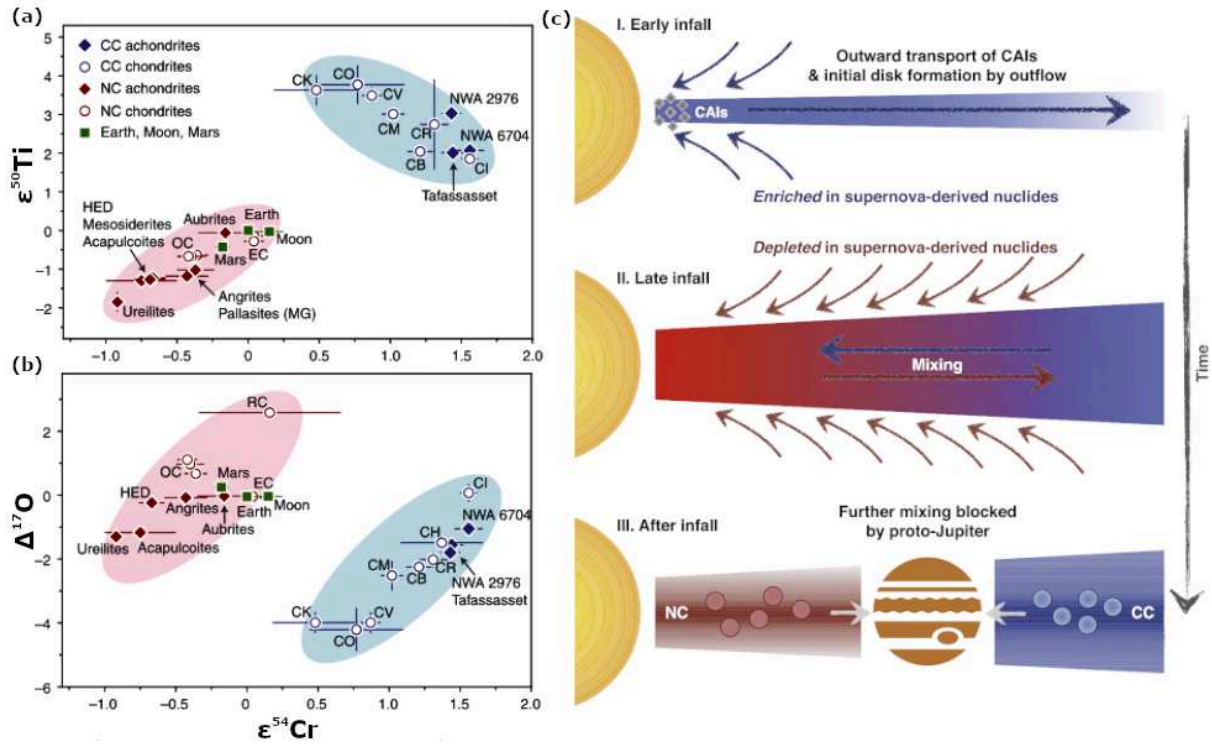


Figure 1.9. NC-CC dichotomy inferred from isotopic signatures of bulk samples: (a) ^{50}Ti vs. ^{54}Cr and (b) ^{17}O vs. ^{54}Cr . Error bars denote uncertainties ($\pm 2\sigma$). Labels depict ordinary chondrites (OC), enstatite chondrites (EC), rumuruti chondrites (RC), howardites-eucrites-diogenites (HED), and pallasite main group (MG). (c) schematic formation scenario of the NC–CC dichotomy: I. Rapid expansion of early infalling material; II. Infalling material dominates the composition of the inner disk resulting in a NC composition, i.e., depleted in neutron-rich nuclides; and III. Mixing within the disk should have reduced the initial isotopic difference between solids from the inner and outer disk, however the rapid formation of Jupiter’s core prevented a complete homogenization. (a-b) from Kruijer et al. (2020) and (c) from Nanne et al. (2019).

It is essential to consider that the nucleosynthetic isotope anomalies are not the result of isotope fractionation but instead are the results of the heterogeneous distribution of presolar grains (Kleine et al., 2020). The presolar grains are condensed nanophases identified inside the fine-grained material of chondrites and exhibit a large deviation from the solar isotopic composition (Zinner, 2014). They are mainly derived from two astrophysical environments: (i) stellar winds from evolved asymptotic giant branch AGB or red giant branch (RGB) stars (e.g., Huss & Smith, 2007; Takigawa et al., 2018) and (ii) supernovae ejects (e.g., Dauphas et al., 2010; Ott, 2017). Nevertheless, isotope anomalies in meteoritic materials are much smaller than

those found in presolar grains, attesting to the *near* complete homogenization of presolar matter in the solar nebula before dichotomy configuration (Kleine et al., 2020).

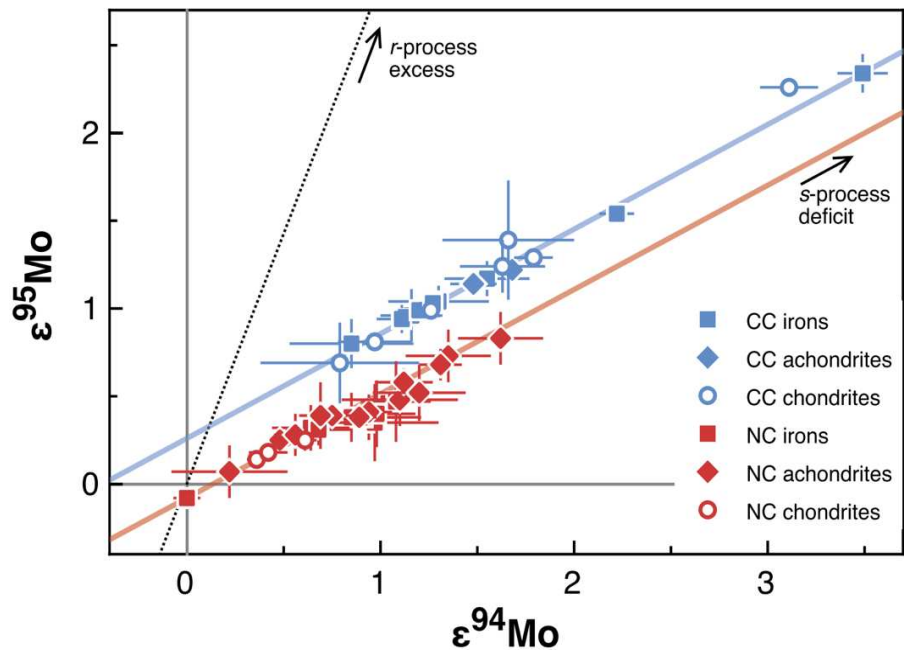
Molybdenum isotopes have a relevant role to track neutron-rich nuclides abundances among the NC and CC reservoirs. For instance, the seven Mo isotopes are associated to three different nucleosynthesis processes: the proton (p-) capture process, rapid neutron-capture (r-) process and slow neutron capture (s-) process. The first two are attributed to a high neutron-density environments such as (i) supernova explosions (Arnould et al., 2007) or (ii) neutron-star mergers (Pian et al., 2017). On the other hand, astrophysical models for s-process nucleosynthesis indicate an origin from: (i) AGB stars' atmospheres and (ii) helium-burning core of massive stars with more than 12 solar masses (D. D. Clayton, 2003). The plot of $\epsilon^{95}\text{Mo}$ (s-, r-process) vs. $\epsilon^{94}\text{Mo}$ (p-, s-process) is the best to illustrate the difference between s- and r-process isotope variations in the NC–CC dichotomy (**Figure 1.10**; Kleine et al., 2020). The linear regression calculated by Budde et al. (2019) for NC and CC planetary materials have slopes of 0.596 ± 0.008 and 0.596 ± 0.006 , respectively. These slopes are in good agreement with the slope calculated from presolar SiC grain data (0.609 ± 0.008), demonstrating that the isotopic deviations predominantly reflect s-process variations. However, Spitzer et al. (2020) recently reevaluate the NC regression line with a slope of 0.528 ± 0.045 , a slightly shallower slope compared to the CC line. The s-process mixing lines for NC and CC, demonstrating that CC achondrites and chondrites have the same characteristic r-process excess over the NC achondrites and chondrites (**Figure 1.10**). This means that the CC reservoir is enriched in neutron-rich nuclides (e.g., ^{50}Ti , ^{54}Cr , ^{48}Ca ; Schiller et al., 2015) and preserve an approximately constant r-process excess along the accretion timescale of iron, achondrite and chondrite meteorites (from 1 to 4 Ma; Kleine et al., 2020).

The dichotomy seems to arise in a heterogeneous distribution of presolar phases, or it can indicate a fluctuation of material injection from different stellar sources (Nanne et al., 2019). Trinquer (2011) indicates that it is unlikely that the ^{46}Ti - ^{50}Ti correlation line defined by solar system objects results from the simple heterogeneous distribution of presolar matter within the protoplanetary disk, given that the anomalous ^{46}Ti and ^{50}Ti reside in different carriers. It has been inferred that the presolar matter was initially homogeneously distributed but required the existence of a secondary process event (e.g., thermal episode, size- or grain-sorting, late injection of diverse nucleosynthetic components) responsible of imparting a selective loss or addition of presolar carriers before the formation of solar system solids and accretion of planetary bodies. Furthermore, calculations of the number of presolar grains that should be

dissolved (e.g., nanospinel, silicon carbide, or hibonite) to shift the bulk composition of chondrites or chondrules are inconsistent with the values observed for ^{50}Ti in bulk chondrites (Trinquier et al., 2009) or ^{54}Cr on individual chondrules (Schneider et al., 2020). In this sense, the magnitude of reported isotopic anomalies for chondrites and nebular components cannot be explained by the addition or removal of typical presolar grains; maybe it must represent the existence of additional presolar carriers and/or isotopic ratios inherited from the solar nebula.

Thus, the NC-CC dichotomy constrains diverse aspects of the early solar system architecture, such as (i) gas and dust dynamics (Budde et al., 2019; Gerber et al., 2017; Nanne et al., 2019), (ii) distribution of presolar grains and/or end-member carriers (Bryson & Brennecka, 2021; Ek et al., 2020; Elfers et al., 2018; Stephan & Davis, 2021; Trinquier et al., 2009), (iii) formation of giant planets (Kruijer et al., 2017, 2020), (iv) mechanism of terrestrial planets and planetesimals formation (Dauphas et al., 2014; Morbidelli et al., 2022; Spitzer et al., 2021) and (v) origin and nature of Earth's building blocks (Warren, 2011; Burkhardt et al., 2011, 2016; Budde et al., 2019).

Figure 1.10. s-process mixing lines using $\epsilon^{95}\text{Mo}$ versus $\epsilon^{94}\text{Mo}$ for bulk NC and CC meteorites. The Mo isotope variability along the NC- and CC-lines is predominantly governed by s-process variations, in good agreement with the calculated slope from presolar SiC grain, whereas the offset between the two lines reflects an approximately constant r-process excess in the CC over the NC reservoir. From Kleine et al. (2020).



So far, isotope anomalies have been observed for a large variety of elements, including Ti (Trinquer et al., 2009), Cr (Qin et al., 2010), Ni (Regelous et al., 2008), Mo (Dauphas et al., 2014; Burkhardt et al., 2019), Ru (Bermingham et al., 2018; Chen et al., 2010), Ba (Andreasen & Sharma, 2007), W (Budde et al., 2018), Zn (Steller et al., 2022), Sm and Nd (Andreasen & Sharma, 2006), Fe (Schiller et al., 2020) and Zr (Render et al., 2022). Most isotopic heterogeneities belong to non-volatile elements (except for Zn), which display a condensation temperature (T_c) above 1250 K (Lodders et al., 2009) conversely, the dichotomy is still not evident among other volatile elements ($T_c < 1250$ K) such as Cd (Toth et al., 2020), Se (Labidi et al., 2018), and Te (Fehr et al., 2005). Recently, Grewal et al. (2021) suggested an early distribution of nitrogen isotopes between the inner and outer disk, which has been interpreted as result of different organic matter carrier among both reservoirs.

1.6 Chondritic meteorites properties

Chondrites represent some of the most pristine materials that can be analyzed in a laboratory. They preserve primitive components from which they agglomerated and offer a unique opportunity to access the early solar system's composition. The name chondrites come from the ubiquitous presence of *chondrules* (see section 1.8.2), which are melted spherules with range sizes 0.1 – 1 mm immersed in a matrix component and originates from a still elusive high-temperature mechanism (Connolly & Jones, 2016). Although most chondrites experienced secondary processes on their parent asteroids, such as aqueous or thermal alteration (see section 1.6.1), they did not experience total melting and igneous differentiation. Chondrites that exhibit a negligible overprint by secondary processes are called unequilibrated chondrites (**Figure 1.11**). They are commonly used as a target to constrain records of nebular conditions before and during their accretion and provide essential clues about the disk properties and the local solar nebula composition.

The five classes of chondrites are divided into 16 groups by different petrographic and chemical properties (**Table 1.1**). 14 groups comprise the three major classes: ordinary, carbonaceous, and enstatite chondrites (**Figure 1.7**). The ordinary chondrites (OCs) are subdivided by their abundance of Fe-Ni metal beads, iron content in silicates and oxygen isotopic composition into three groups: high metal (H), low metal (L) and low iron-low metal

(LL) (Weisberg, 2006; Florin et al., 2020). The carbonaceous chondrites (CCs) have nine well-resolved groups: CI, CM, CR, CH, CB, CV, CK, CL, and CO. The second letters of each group are designated by the name of a recognized chondrite, which is commonly a fall meteorite (e.g., CO comes from the fall meteorite in the Ornans town, France). Enstatite chondrites (ECs) are characterized by minerals formed under extremely reducing conditions (e.g., Weisberg, 2006; Piani et al., 2020) and comprise two groups with different contents of metallic iron: EH and EL.

The chondrite oxidation state is exposed by the distribution of iron into three oxidation states: 0 (Fe-Ni metal and Fe-sulfides), +2 (silicates), and +3 (oxides). Different chondrite groups exposed a wide range of oxidation states, as seen in the “Urey-Craig” diagram. The oxidation state increases from H to L to LL in OCs, reflected by the Mg# [$Mg/(Fe+Mg)$] of olivines and pyroxenes (Krot et al., 2014). In the case of CCs, the oxidation state increases in the order CB-CH-CR-CO-CV-CK-CM-CI. The diverse oxidation state of chondrites probably was established through a combination of nebular and asteroidal processes.

The bulk chondrite composition is one of the main criteria for classifying chondrite groups (**Figure 1.12**; Weisberg, 2006) and provides insight into the parent body's processes and/or the nebular reservoir properties. To understand nebular processes is relevant to know the cosmochemical behavior of elements. In meteoritics, *cosmochemical behavior* refers to the temperature at which materials condense or evaporate within the gaseous environment in the protoplanetary disk. They are defined as refractory ($T_c > 1400$ K), main ($T_c \sim 1400-1250$ K), moderately volatile ($T_c \sim 1250-800$ K) and highly volatile ($T_c < 800$ K) elements (**Figure 1.13**; Lodders, 2010; Braukmüller et al., 2018). The CI chondritic composition is commonly used to constrain major, minor, and trace elements in meteorites. This is because the CI chondrite exhibits the same composition as the solar photosphere, excluding some volatile elements and noble gases (Lodders, 2010). As the Sun concentrates more than 99.9% of the Solar System's mass, the correlation between the solar photosphere vs. CI composition suggests that CI chondrites represent the whole solar system composition (Lodders & Fegley, 1998).

Figure 1.11. Backscattered electron maps of two unequilibrated chondrites found at Los Vientos (hereafter LoV) dense collection area in the Atacama Desert. LoV 123 (a) and LoV 098 (b) are classified as CO and ordinary chondrites, respectively. According to the Cr₂O₃ content in Fe-rich olivines, LoV 123 and 098 are classified as petrologic type 3.05 and 3.15, respectively.

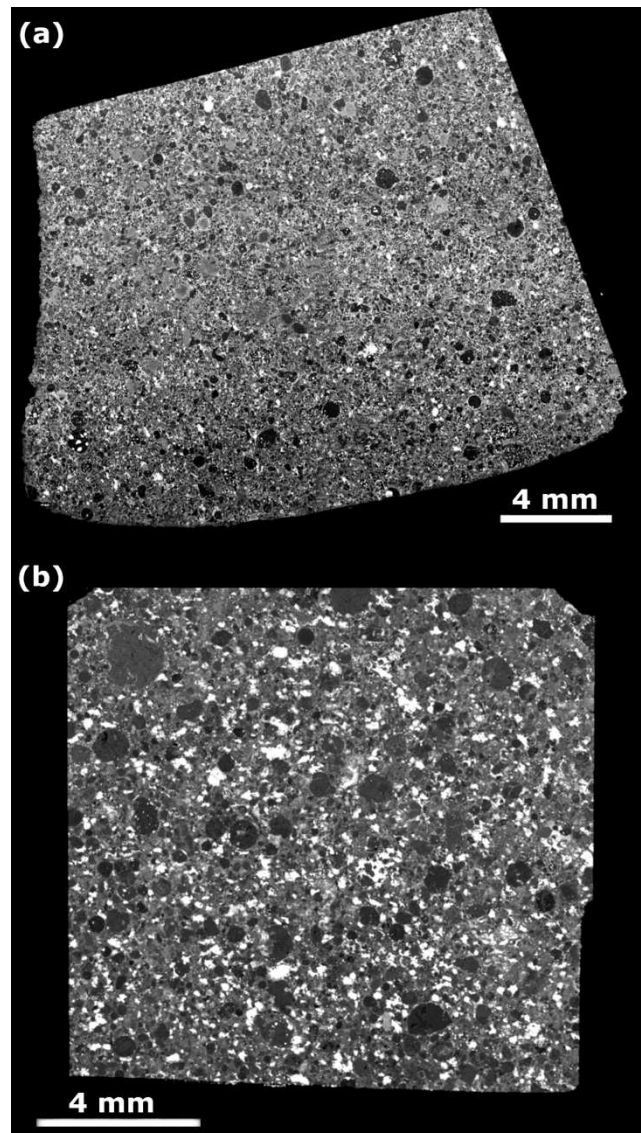


Figure 1.12 and **Table 1.1** display the main petrographic and bulk composition differences of CC and NC chondrites: (i) refractory elements abundances (Ca and Al > 1 in CC and < 1 in NC); (ii) refractory inclusion abundances (0.1 - 3 vol% in CC and ≤ 0.1 vol% in NC); (iii) chondrule modal abundance ratio (15 – 70 vol% in CC and 40 – 80 vol% in NC, except K chondrites); and (iv) moderately volatile element depletion (~0.5 in CC and ~0.8 in NC). The volatile depletion is an ongoing topic of research in chondrites. It could

result from (i) incomplete condensation of solids with subsequent migration of volatiles and/or (ii) partial evaporation of volatiles by a thermal event (McSween, Jr & Huss, 2022). Alexander (2019) reported that the chemical and isotopic composition of CC can be quantitatively recreated employing variable mixture of chondritic components. This calculation suggests that volatile elements in CC are principally acquired from CI-like matrix. The former was recently supported by Hellmann et al. (2020) using Tellurium ($T_C \approx 700$ K; Lodders, 2003) isotope composition and concentration abundance. These authors reported that not only $\delta^{128/126}\text{Te}$ values and Te concentrations are correlated with the volume fraction of matrix on each CC group (**Figure 1.13**), but also volatile elements such as S, Se, Sn, Zn, Cd, In, Pb, Ag, Tl, Cs, Rb and Ge. Furthermore, CC also show that highly volatile elements take a plateau path (Braukmüller et al., 2018), which could be generated by a subsequent addition of some CI-like material that changes the negative slope and creates a plateau distribution. The evidence of the positive

correlation between volatile elements abundances in CC and their volume fraction of matrix (Ebel et al., 2018; Hellmann et al., 2020) suggest that volatile elements concentration is originated and controlled by a very primitive and unheated CI-like material that is the carrier of highly volatile elements.

Table 1.1. Summary of petrographic properties in each chondrite group. From Scott and Krot (2014).

Group	Refract. lith./Mg rel. Cl^a	CAI (vol.%)	Chondrule avg. dia. (mm)	Chondrules (vol.%) ^b	Metal (vol.%)	Matrix (vol.%) ^c	Fall frequency (%) ^d
Carbonaceous							
CI	1.00	<0.01	None	<5	<0.01	95	0.5
CM	1.15	1.2	0.3	20	0.1	70	1.6
CO	1.13	1.0	0.15	40	1–5	30	0.5
CV	1.35	3.0	1.0	45	0–5	40	0.6
CR	1.03	0.12	0.7	50–60	5–8	30–50	0.3
CH	1.00	0.1	0.02–0.09	~70	20	5	0
CB _a	1.0	<0.1	~5	40	60	<5	0
CB _b	1.4	0.1	~0.5	30	70	<5	0
CK	1.21	0.2	0.8	15	<0.01	75	0.2
Ordinary							
H	0.93	0.01–0.2	0.3	60–80	8	10–15	34.4
L	0.94	<0.1	0.5	60–80	3	10–15	38.1
LL	0.90	<0.1	0.6	60–80	1.5	10–15	7.8
Enstatite							
EH	0.87	<0.1	0.2	60–80	8	<0.1–10	0.9
EL	0.83	<0.1	0.6	60–80	15	<0.1–10	0.8
Other							
K	0.9	<0.1	0.6	20–30	6–9	70	0.1
R	0.95	<0.1	0.4	>40	<0.1	35	0.1

Bulk oxygen isotopic composition of various chondrite groups plots in unique positions on the triple oxygen diagram (**Figure 1.8a**). The OCs plot above the TFL ($\Delta^{17}O > 0.5$ ‰) and show a progressive shift in terms of increasing $\delta^{17}O$ and $\delta^{18}O$ from H to L to LL. The CCs show a wide range in oxygen isotopic compositions for each group, but all of them fall below the TFL ($\Delta^{17}O < 0$ ‰; except for CI chondrites). CI chondrites plot close to the TFL (**Figure 1.8a**) showing a strong oxygen mass-fractionation ($\delta^{18}O \sim 16$ ‰), even their closer compositions of non-volatile elements to the solar abundances (Lodders, 2010). CM chondrites also contain strongly mass fractionated oxygen ($\delta^{18}O > 5$ ‰). These indicate that CM and CI chondrites were affected by water alteration on their parent body and/or nebular reservoir (e.g., Piralla et al., 2020). The plot area of CO chondrites displays the lowest isotopic fractionation between the CCs (-5 ‰ $< \delta^{18}O < 0$ ‰). ECs plot along the TFL, like the Earth's and Moon's oxygen composition (Irland et al., 2020; Piani et al., 2020). Furthermore, bulk oxygen isotopic composition partially or entirely overlaps between chondrite groups such as EH and EL chondrites or CO, CV, and CK chondrites (see **Figure 1.8a**). In this sense, the bulk oxygen

isotopic composition of chondrites seems to be controlled by the O-isotopes in each individual component and their abundance among chondrite groups.

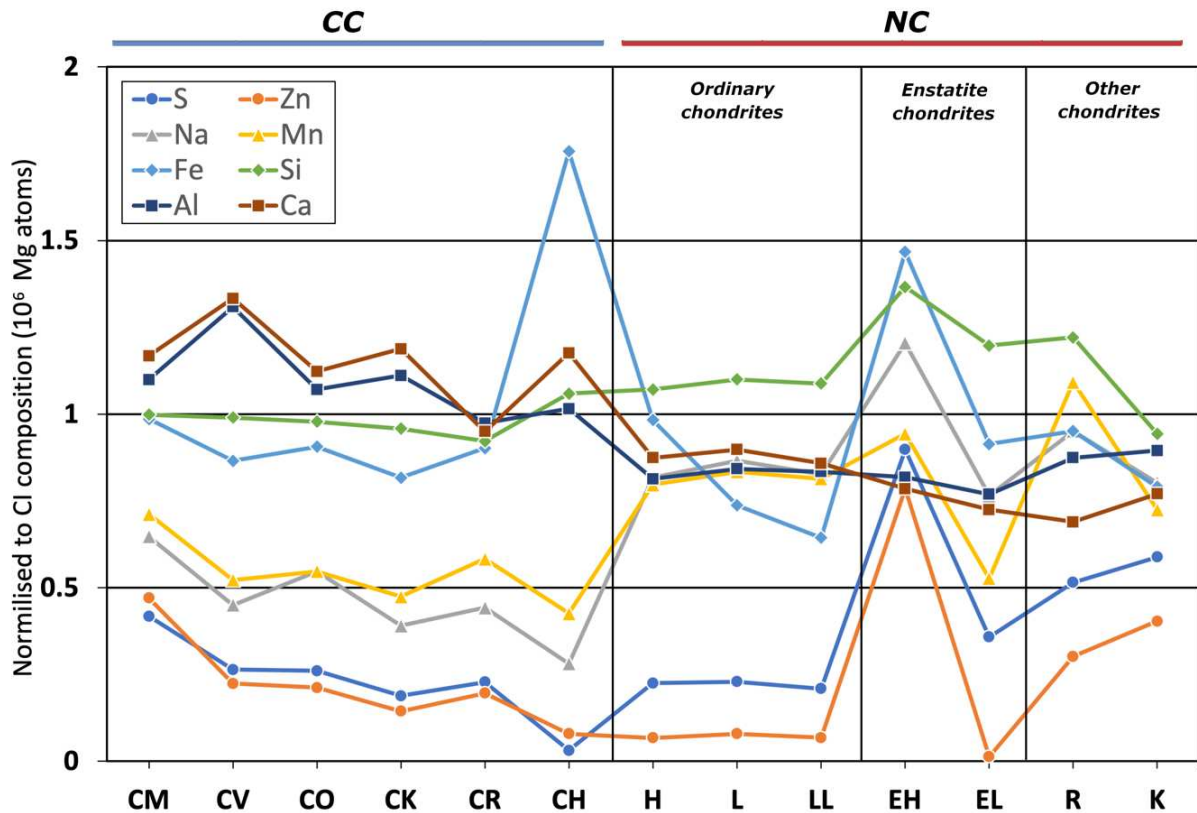


Figure 1.12. Bulk composition of chondrite groups normalized to CI composition. Major elements are represented by their “cosmochemical character” as refractory (square), main (diamond), moderately volatile (triangle), and highly volatile (circle). Data from Lodders & Fegley (1998).

1.7 Secondary processes in chondritic asteroids

The analysis of primary and secondary properties in chondrites is one of the fundamental problems for meteorite petrologists. A big challenge is to distinguish between primary properties acquired in their formation environment and the secondary modifications produced by subsequent alteration within the gas nebula, parent body and/or terrestrial environment (e.g., Barosch et al., 2019; Bonal et al., 2016; Grossman & Brearley, 2005; Pourkhorsandi et al., 2017). The main parameters to estimate the degree of thermal, aqueous, shock and subsequent terrestrial contamination will be described below.

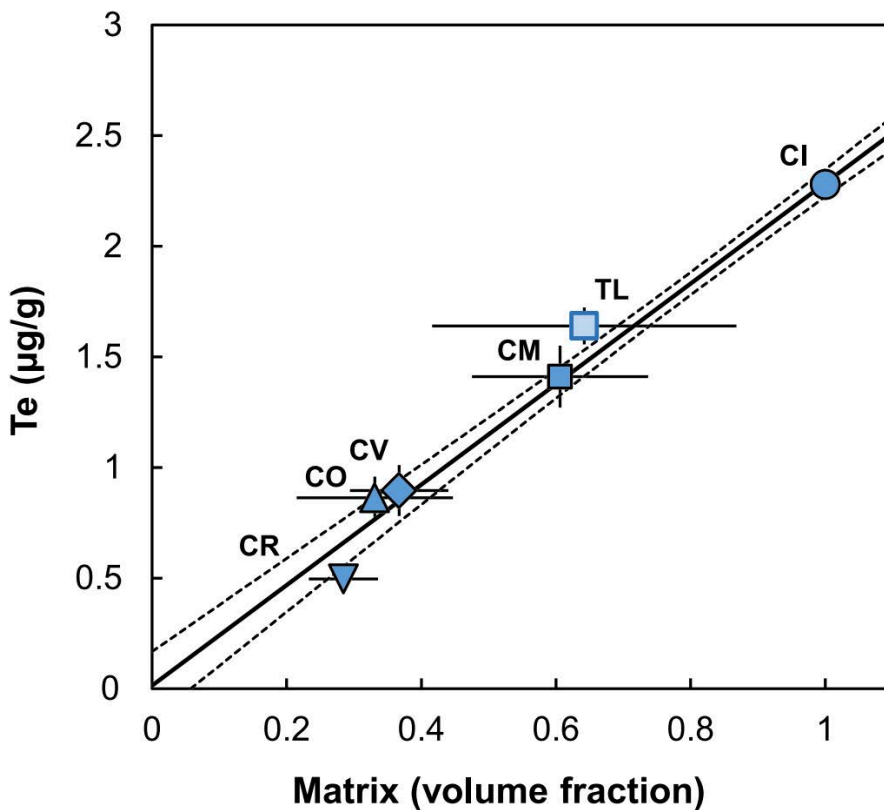


Figure 1.13. Average of Tellurium concentration of carbonaceous chondrite groups versus volume fraction of matrix. Matrix volume fractions taken from summary in Alexander (2019). Uncertainties are two times the standard deviation and dashed lines represent. TL: Tagish Lake chondrites. From Hellmann et al. (2020).

1.7.1 Petrologic type

According to the secondary processes, chondrites are divided into different “petrologic types” (also called petrologic type or degree) using a numeric scale between 1 and 6 (Figure 1.14). This scale is evidence of various degrees of thermally metamorphosed or aqueous alteration in the chondrite parent bodies. Petrologic types 1 and 2 indicate aqueous alteration at low temperatures (Brearley, 2006), where its degree increase from 2 to 1. Only some carbonaceous chondrites have evidenced of aqueous alteration (Figure 1.14) and frequently they show altered fine-grained material composed of serpentinite, phyllosilicates, sulfates, phosphates, or carbonates (e.g., Marrocchi et al., 2014; Pignatelli et al., 2017; Vacher et al., 2019). Petrologic type 3 chondrites are called unequilibrated or primitive, whereas types 4 to 6 are defined as equilibrated. The petrologic type from 4 to 6 defines an increasing degree of chemical equilibration and textural recrystallization as results of thermal metamorphism caused by ^{26}Al decay and/or impact events (Amsellem et al., 2020; Doyle et al., 2015; Keil, 2000; Vacher et al., 2018). For instance, petrologic type 6 indicates a high degree of textural and mineralogical overprint as well as compositional equilibration (Weisberg, 2006). Furthermore,

some ordinary and enstatite chondrites have been described with pervasive recrystallization and possible melting processes, which would constitute a type 7 (Sears et al., 1980).

Subdivision of petrologic type 3 chondrites was proposed by the preliminary works of Sears et al. (1980) according to the thermoluminescence characteristics of glasses mesostasis in chondrules. The properties of chondrite subtypes 3.00 to 3.90 evolved according to the progressive thermal metamorphism evidenced by (i) crystallization of glasses mesostasis into feldspar (Sears et al., 1980); (ii) a decrease of CaO concentrations in Fe-rich olivine from chondrules (Scott & Jones, 1990); (iii) FeO enrichments of chondrule borders by solid-state diffusion between chondrules and FeO-rich matrices (Scott & Jones, 1990); (iv) a decrease of the mean Cr₂O₃ abundance in Fe-rich olivine in chondrules (Grossman & Brearley, 2005); (v) change in the atomic structure of organic matter in fine-grained material (Bonal et al., 2007, 2016); and (vi) mineralogical and chemical modifications of Fe-Ni metal beads (Kimura et al., 2008). To determine the least metamorphosed unequilibrated chondrites, Grossman and Brearley (2005) propose division into 3.00 to 3.15 based on Cr₂O₃ concentrations and their standard deviation in Fe-rich olivine on type II chondrules (**Figure 1.15**). This petrologic type classification is based on the progressive loss of Cr₂O₃ from ferroan olivine grains to the matrix component, which is produced by the temperature increase in the parent body.

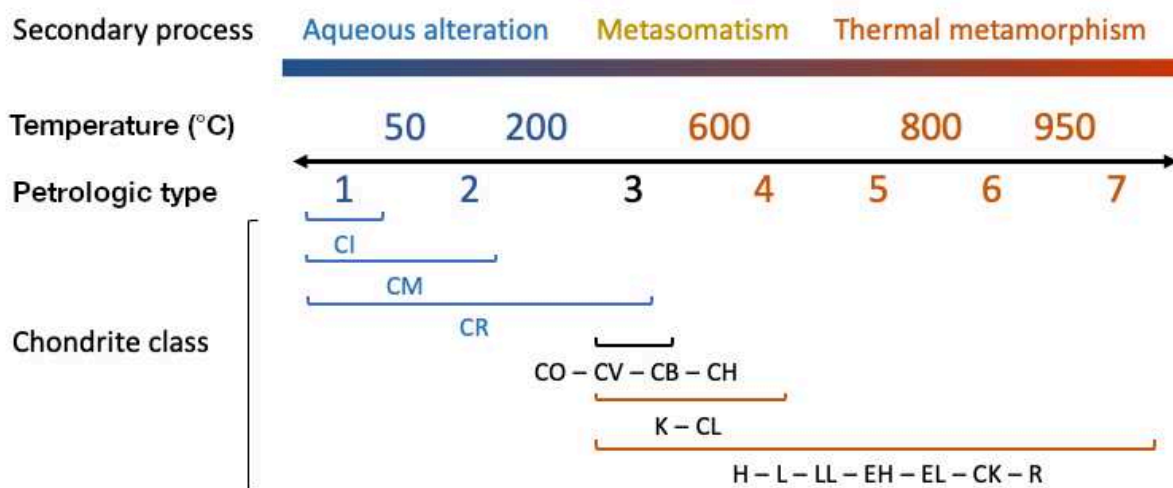


Figure 1.14. Classification system for petrologic type of chondrites by thermal and aqueous alteration. The type of secondary processes and approximate temperatures are shown at the top. The different chondrite groups are shown in the bottom. Modified from Van Schmus and Wood (1967); Sears et al. (1980) and Mccween and Huss (2022).

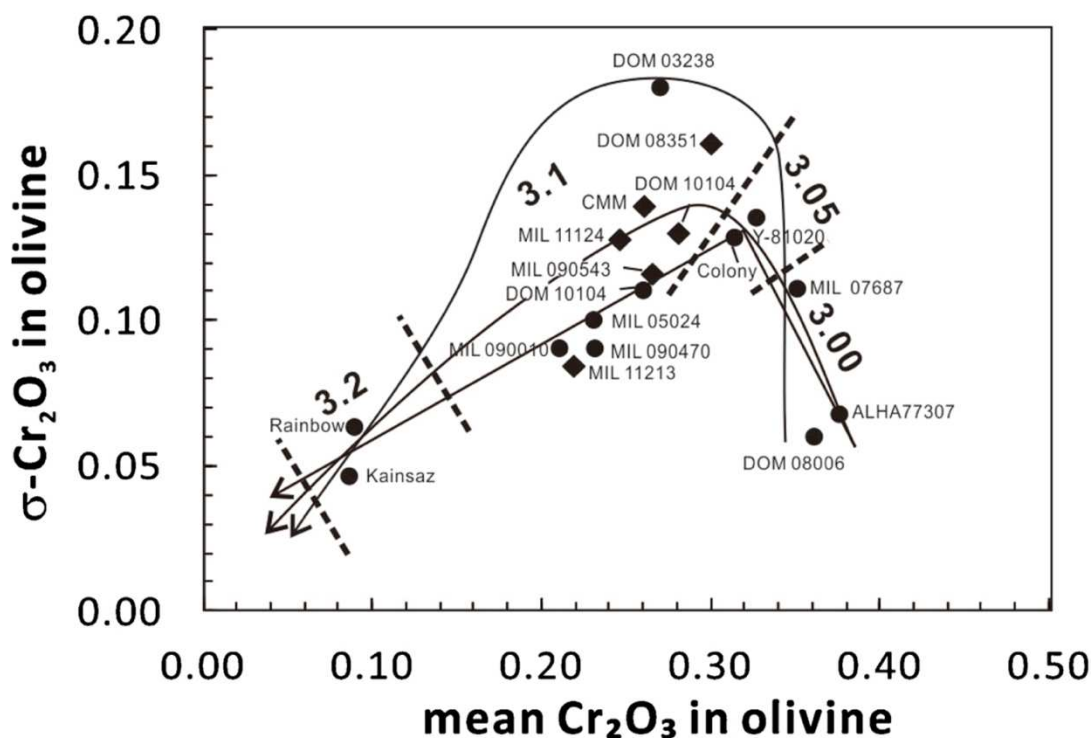
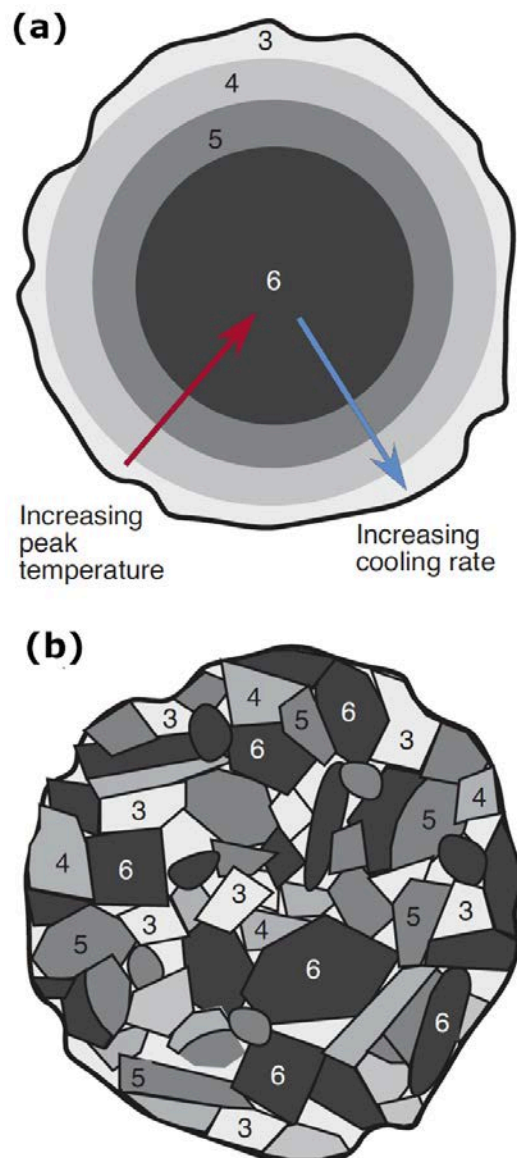


Figure 1.15. Distribution of CO3 chondrites with petrologic subtype ≤ 3.2 on the basis of $\sigma\text{-Cr}_2\text{O}_3$ vs. mean Cr_2O_3 in ferroan olivine grains. Three trends are shown: the middle trend is the original one from Grossman and Brearley (2005), the top trend is from Grossman and Rubin (2006), and the bottom trend is from Davidson et al. (2014). Diamonds are from Rubin and Li (2019) and filled circles are from Grossman and Brearley (2005); Grossman and Rubin (2006); Davidson et al. (2014). Approximate boundaries between adjacent subtypes are marked by dashed lines. From Rubin and Li (2019).

The peak temperatures of asteroids can be estimated from chemical exchange reactions between chondrite's minerals (geothermometers). In the case of asteroids, thermal models based on ^{26}Al heating have successfully reproduced the peak temperature and the cooling rate of chondrite meteorites assuming that asteroids accreted at ~ 2 Ma after the CAI formation (Keil, 2000; Kleine et al., 2008; Henke et al., 2012). These models suggest that undifferentiated asteroid interiors experienced the highest temperatures, producing highly metamorphosed (type 6) chondrites, with a peak temperature decreasing to the surfaces and resulting in a concentric petrologic-degrees structure called *onion shell* (see **Figure 1.16a**). As the heat diffusion from the deep interior is slower than near the surface, the cooling rates calculated by only radiogenic decay of ^{26}Al indicate that chondrites with a higher metamorphic grade are profound compared to lower grades (Kleine et al., 2008). For instance, Hf-W ages indicate that type 4 ordinary chondrites close the isotopic system at 3-4 Ma after CAI formation, while type 5 and 6 chondrites display close ages between ~ 6 to ~ 12 Ma after CAI formation (**Figure 1.17**; Hellmann et al., 2019). Of note, this timescale of parent body accretion is consistent with Al-Mg ages for chondrules from primitive ordinary chondrites (Kita et al., 2000; Villeneuve et al.,

2009), indicating that there was a close temporal link between chondrule formation and chondrite accretion (Kleine et al., 2018). Also, there is evidence of asteroid collisions in the early solar system, which can re-accreted debris into a new asteroid structure with lithologies of different petrological grades in direct contact (**Figure 1.16b**). These "breccia asteroids" type is called *rubble piles*. Recently, spacecraft missions have demonstrated that (101955) Bennu and (162173) Ryugu are rubble pile asteroids formed by heterogeneous mass distribution of pebbles (Michel et al., 2020).

Figure 1.16. Sketches of the internal structure of chondritic parent bodies as onion shell (a) and rubble pile (b) asteroids. The numbers identify petrologic type. Modified from McSween & Huss (2022).



1.7.2 Shock metamorphism

The degree of shock metamorphism is caused by impact or collisions between planetesimals in the early solar system. Various mineralogical and textural parameters in olivine, plagioclase, and orthopyroxene are used to determine the peak-shock pressure (Scott et al., 1992; Stöffler et al., 1991).

1.7.3 Terrestrial alteration

Terrestrial alteration is defined as the exposition rate of meteorites to the alteration agents settled on the Earth surfaces. Numerous factors can control the terrestrial alteration as standing time in the terrestrial environment, soil composition of the recovery site, meteorological condition of the area, meteorite type, size, shape and porosity (e.g., (Al-Kathiri et al., 2005; Ouknine et al., 2019; Pourkhorsandi et al.,

2021; Stephant et al., 2018; Vacher et al., 2020; Valenzuela, 2011). The method to classify the weathering degree in ordinary chondrites was initially proposed by Wlotzka (1993) and consequently adapted using intermediate steps by (Zurfluh et al., 2016). The weathering scale ranges from W0 to W6 with grading determined by the level of oxidation in metal and sulphide and subsequently silicates (Wlotzka, 1993; Bland et al., 2006). As the alteration affects diverse petrographic, chemical and isotopic characteristics of meteorites, weathering degrees have been studied by diverse methods as (i) amount of oxidized metal, sulphide and silicates (Wlotzka, 1993; Bland et al., 2006; Munayco et al., 2013), (ii) terrestrial age of residence (Drouard et al., 2019; Hezel et al., 2011; Jull et al., 1993, 2013; Stelzner et al., 1999), (iii) trace elements distribution (Crozas et al., 2003; Pourkhorsandi et al., 2017, 2021) and (iv) isotopic composition deviation (Stephan et al., 2018; Bischoff et al., 2022; Bland et al., 2000; Stephant et al., 2018; Vacher et al., 2020).

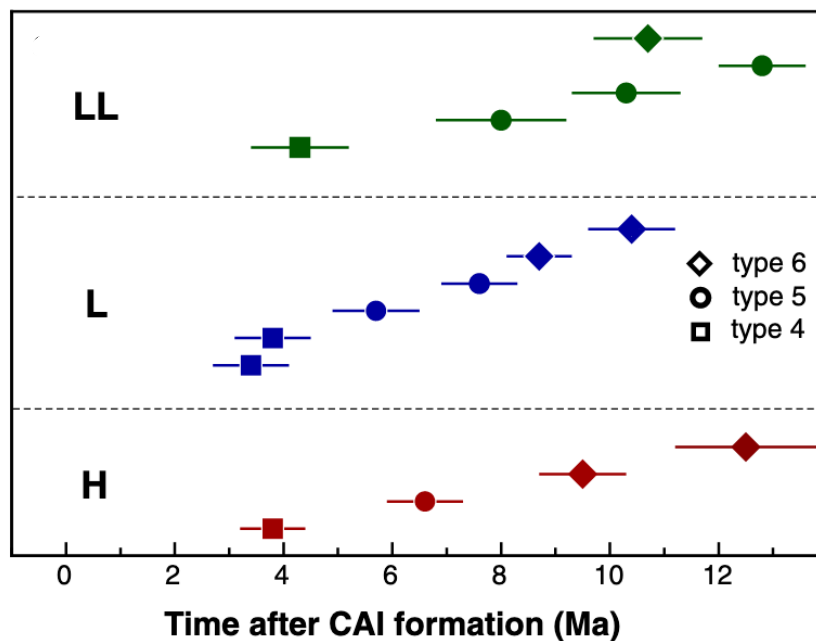


Figure 1.17. Hf-W isochron ages of ordinary chondrites. For a given petrologic type, there are no systematic Hf-W age differences between H, L and LL chondrites, and in general, the ages become younger with increasing petrologic type. From Hellmann et al. (2019).

1.8 Components in chondrites

Chondrites are primarily composed of coarse-grained particles ($>5 \mu\text{m}$ in size) that have been processed repeatedly within the PPD by high-temperature events during the first few million years of its existence. The main components in chondrites are calcium-aluminum-rich inclusions (CAIs), amoeboid olivine aggregates (AOAs), chondrules, isolate grains, presolar grains and metal beads (i.e., Fe-Ni metals and sulfide grains). All these components are cemented together by a matrix, fine-grained material with $<5 \mu\text{m}$ in size. It is generally accepted that the refractory inclusions, chondrules, and Fe-Ni metals were assembled in the solar nebula by a high-temperature mechanism that included condensation, crystallization and evaporation processes (Ebel et al., 2018; Libourel & Portail, 2018; Marrocchi et al., 2018; Marrocchi et al., 2019). The main components in chondrites are shown in **Figure 1.18**. The fine-grained material is composed mainly of residual fragments of chondrules and refractory inclusion collisions, interstellar material (i.e., presolar grains), organic matter or recondensed matter from evaporated regions close to the proto-Sun (Scott & Krot, 2014). For instance, the matrix is the main fine-grained material that cemented chondrite, nevertheless, some coarse-grained particles (i.e., chondrules, metal beads, isolated olivine grains and refractory inclusions) are surrounded by a thin-layered structure called "accretionary dust mantles" (Metzler et al., 1992) or fine-grained rims (hereafter FGRs). They are identified by textures (i.e., grain size, compaction, porosity, mineralogy; e.g., MacPherson et al., 1985; Zanetta et al., 2021) and presolar grain abundances different to the surrounding matrix (Haenecour et al., 2018; Leitner et al., 2016, 2019). Refractory inclusions and chondrules will be explained in more detail in the following subsections.

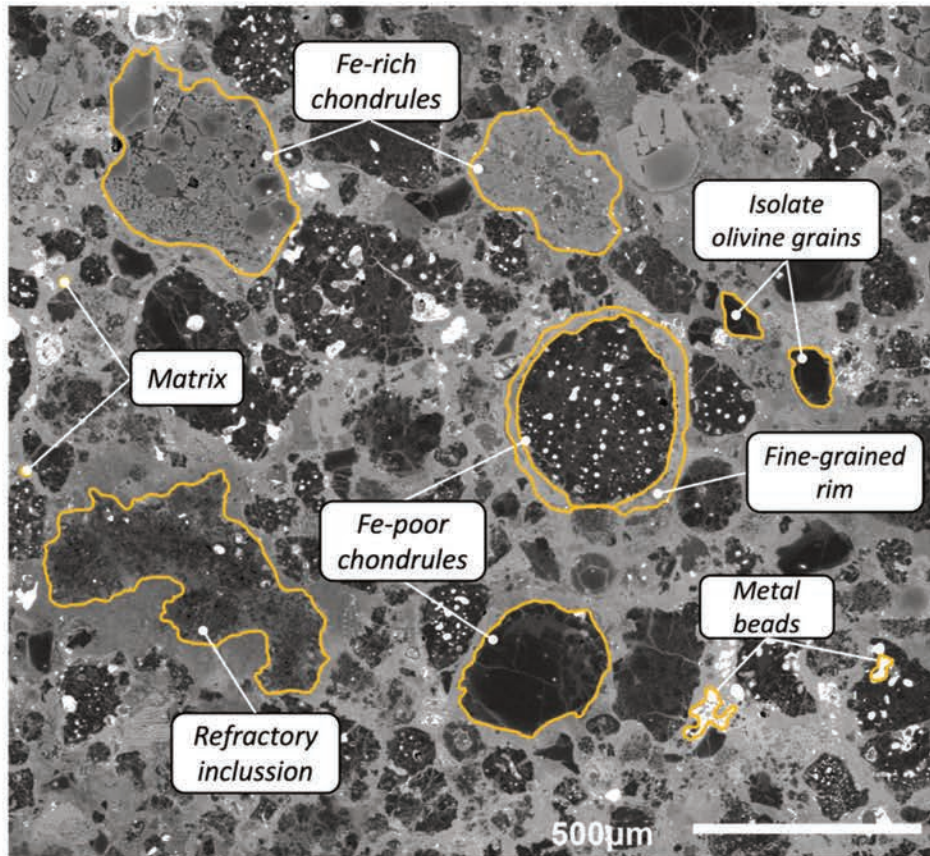


Figure 1.18. Back-scatter electron image of the carbonaceous chondrite Catalina 008 (CO3). The primary components are remarked by orange lines and describes in the main text.

1.8.1 Refractory inclusions

The CAIs are the oldest solids to have formed in the Solar System, with an estimated age of 4567.30 ± 0.16 Ma (Amelin et al., 2010; Connelly et al., 2012). Based on short-lived ^{26}Al - ^{26}Mg chronology and absolute Pb-Pb chronology, the formation of most CAIs is restricted to the first ~ 1 Ma of Solar System evolution (Connelly et al., 2012; MacPherson et al., 2012). During this epoch almost all material close to the proto-Sun was evaporated into a gas phase as a result of the high-temperature environment (>1300 K). The CAIs were condensed in a decreasing temperature and low-pressure context (~ 1600 and 10^{-4} bar; Ebel & Grosman, 2000; Lodders, 2003). Thermodynamic models are commonly used to calculate the succession of condensate phases assuming *equilibrium condensation*, which represents the equilibrium distribution of elements between coexisting phases (i.e., solids, liquid, and vapor) in a closed chemical system with vapor always present (Ebel, 2006; Ebel & Grosman, 2000). The first refractory phase condensed from a solar composition is corundum, hibonite, perovskite, spinel, melilite and diopside, the common paragenesis of CAIs (**Figure 1.19**; MacPherson, 2014).

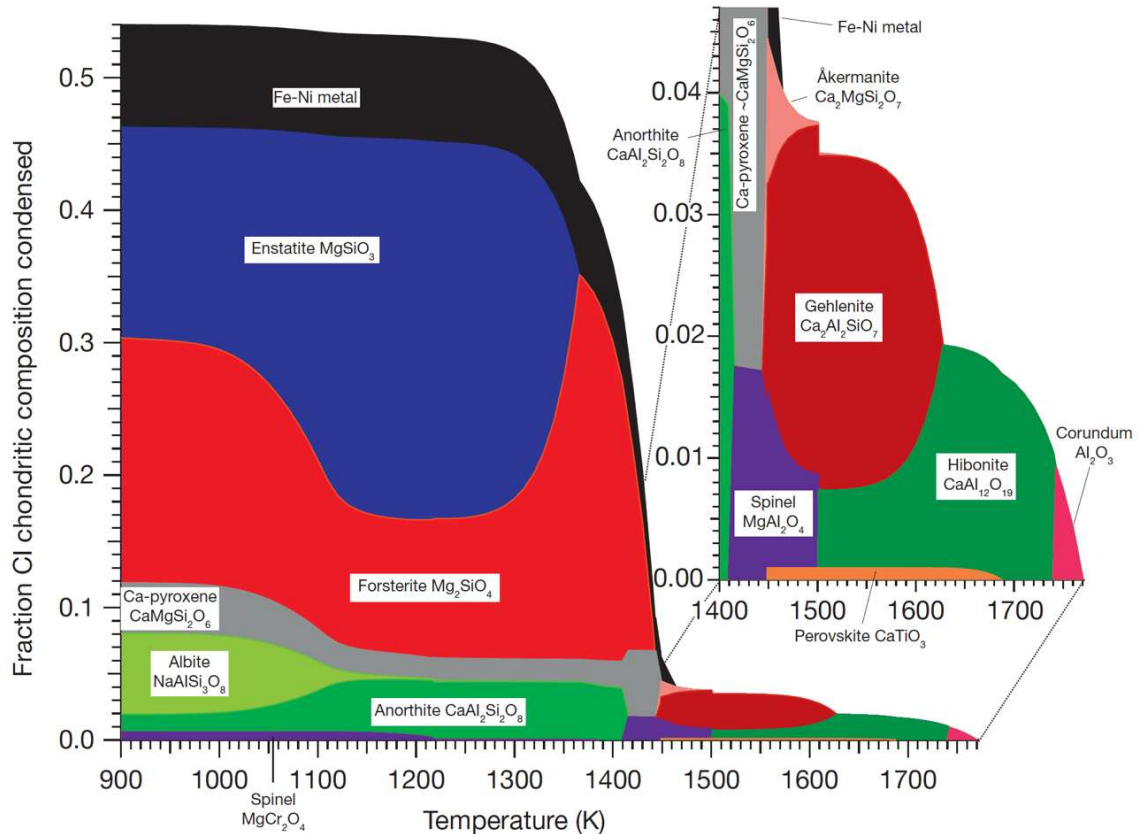


Figure 1.19. Condensation of major rock-forming phases from a gas of solar composition (Anders and Grevesse, 1989) at a total pressure of 10^3 atm. This calculation was done with the best currently available internally consistent thermodynamic data for solid and gaseous phases and includes nonideal solid solution models for melilite, Ca-rich pyroxene, feldspar, and metal. From Davis and Richter (2014).

A universal classification of CAIs is missing as a result of their broad diversity of textures, mineralogy, major and trace elements, and isotopic compositions (Krot, 2019; Macpherson et al., 2005; MacPherson, 2014; MacPherson et al., 2022). However, extensive research on CAIs from CV chondrites displays a classification into Type A, mainly Al-rich melilite and spinel-rich (**Figure 1.20a-b**); Type B, melilite, Al, Ti-pyroxene, spinel, and plagioclase (**Figure 1.20c-d**); forsterite-bearing Type B; and Type C, mainly anorthite, Al-Ti-pyroxene, melilite, and spinel (MacPherson, 2014 and reference therein). Type A CAIs are subdivided into fluffy and spheroidal compact subtypes. The last as well as Type B and Type C records petrographic and chemical features of significant melting and subsequent crystallization processes. For instance, thermal histories of Type B CAIs have been constrained by experimental analysis suggesting a peak melting temperature of ~ 1700 K, which was determined by the behavior of melilite upon crystallization. CAIs in other CC groups are often named based on their dominant minerals (e.g., Simon et al., 2019; Zhang et al., 2020).

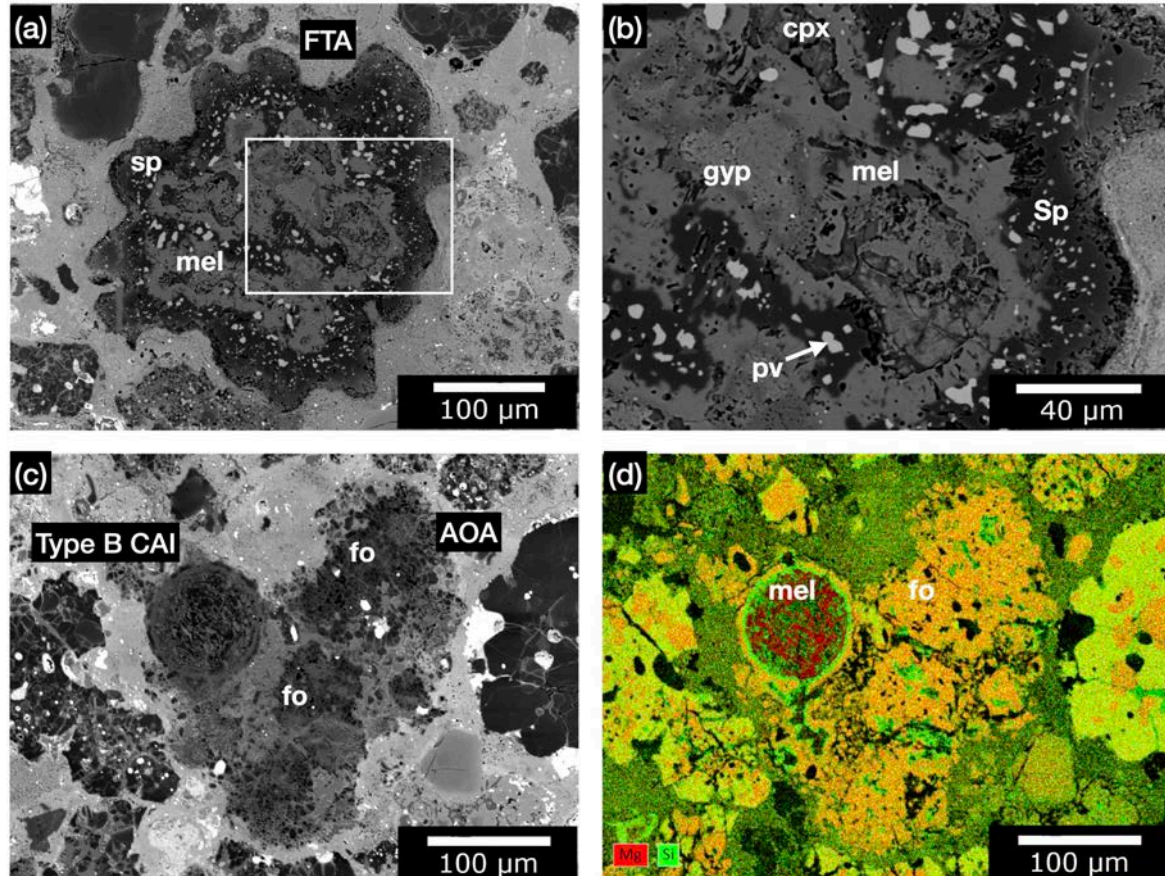


Figure 1.20. Backscattered electron images and x-ray map of refractory inclusions in the CO chondrite Catalina (Cat) 008. Fluffy Type A (FTA) CAI (a-b) composed by melilite (mel), spinel (sp), perovskite (pv), Al-diopside (cpx) and the porosity display gypsum (gyp) results of terrestrial alteration. “Compound” Type B CAI and AOA (c-d). The Type B CAI displays a forsterite (fo) rim, probably formed from the relatively melted AOA.

All CAIs may have been formed close to the Sun (~ 0.1 AU) and transported outwards by rapid radial expansion of the early infalling material (Desch et al., 2018; Jacquet et al., 2019; Krot, 2019; Macpherson et al., 2005). The transportation of CAIs within the PPD is supported by a surface layer (~ 50 μm) composed of microcrystals called Wark-Lovering rims (WLR). Yoshizaki et al. (2019) evidenced that WLR shows grain-scale oxygen isotopic disequilibrium indicating short post-formation heating that could be achieved by rapid outward transport. However, recent data on vanadium and strontium isotopic co-variations and numerical modeling of ^{50}V – ^{10}Be co-production suggest a CAIs formation at greater heliocentric distances than previously considered (~ 1 AU; Bekaert et al., 2021). Whatever the case, CAIs were subsequently melted or deformed in and outside their formation region during transient heating events (Krot, 2019; Mane et al., 2022; Richter et al., 2006).

The second type of refractory inclusions are the amoeboid olivine aggregates (AOAs; **Figure 1.20c-d**), which consists mainly of forsterite grains (>90 vol%) and rarely contain Fe-

Ni metals, anorthite or low-Ca pyroxene (Krot et al., 2004). The fine-grained and porous AOAs have never been melted and undergo only moderate thermal annealing during the evolution of the circumsolar disk, implying they might represent pristine condensates. The modal abundance of AOAs in CO and CV chondrites is always < 5 vol% (Ebel et al., 2016; G. A. Pinto et al., 2021) and display slightly chemical and petrographic modification during parent bodies processes (Chizmadia et al., 2002). Furthermore, as AOAs record the condensation of forsteritic olivine, which represented a third of CI (Ivuna-like) chondritic matter—second only to ice in terms of sheer mass—they are more representative of the protoplanetary disk than CAIs (Morin et al., 2022). Recently, Marrocchi et al. (2018; 2019) studied distribution of minor elements and O-isotopic composition in Mg-rich chondrules and describe that ¹⁶O-rich relict olivine grains are depleted in Ti, Al and Ca and enriched in Mn relative to the others olivine grains in the same chondrule. As these chemical and isotopic properties are consistent with those of olivine grains in AOAs, it has been proposed that ¹⁶O-rich relict grains in chondrules represent recycling AOA-like material, which probably was the principal precursor of Mg-rich chondrules.

1.8.2 Chondrules

Chondrules are sub- to millimeter-sized igneous quasi-spheroids (**Figure 1.21**) that were formed by a still elusive high-temperature mechanism (Connolly & Jones, 2016). The ferromagnesian chondrules are principally composed of olivine, pyroxene, Fe-Ni metals, FeS, a glass phase, and minor mineral phases (~1 vol%) such as chromite, spinel, anorthite or silica (Jones et al., 2018). As chondrules are solidified igneous droplets, they are classified according to the crystallization process using the igneous petrologic terms porphyritic and non-porphyritic. Porphyritic chondrules grow bigger crystals and are well developed, while non-porphyritic does not mature crystalline structures. This is associated with the chondrule formation processes' peak temperature and cooling rate (See **Figure 1.22**). For instance, porphyritic chondrules range from 94 to 99 vol% and 82 to 92 vol% in CCs and NCs, respectively, so they domine chondrule distribution (Jones, 2012). Conditional to the main mineral phase (commonly > 90 vol%), chondrules are divided into porphyritic olivine (PO), pyroxene (PP), and olivine-pyroxene (POP), while nonporphyritic are classified as cryptocrystalline (CC), radial or radiating pyroxene (RP), and barred olivine (BO). Furthermore, according to the chemical composition, chondrules can be FeO-poor (Type I) or

FeO-rich (Type II). This classification is delineated by the Mg-number ($Mg\# = 100 \times Mg / [Mg + Fe]$) in olivine and low-Ca pyroxene; with a $Mg\# > 90$ is FeO-poor and < 90 is FeO-rich (Figure 1.20; Jones, 1990, 1992; Steele, 1986).

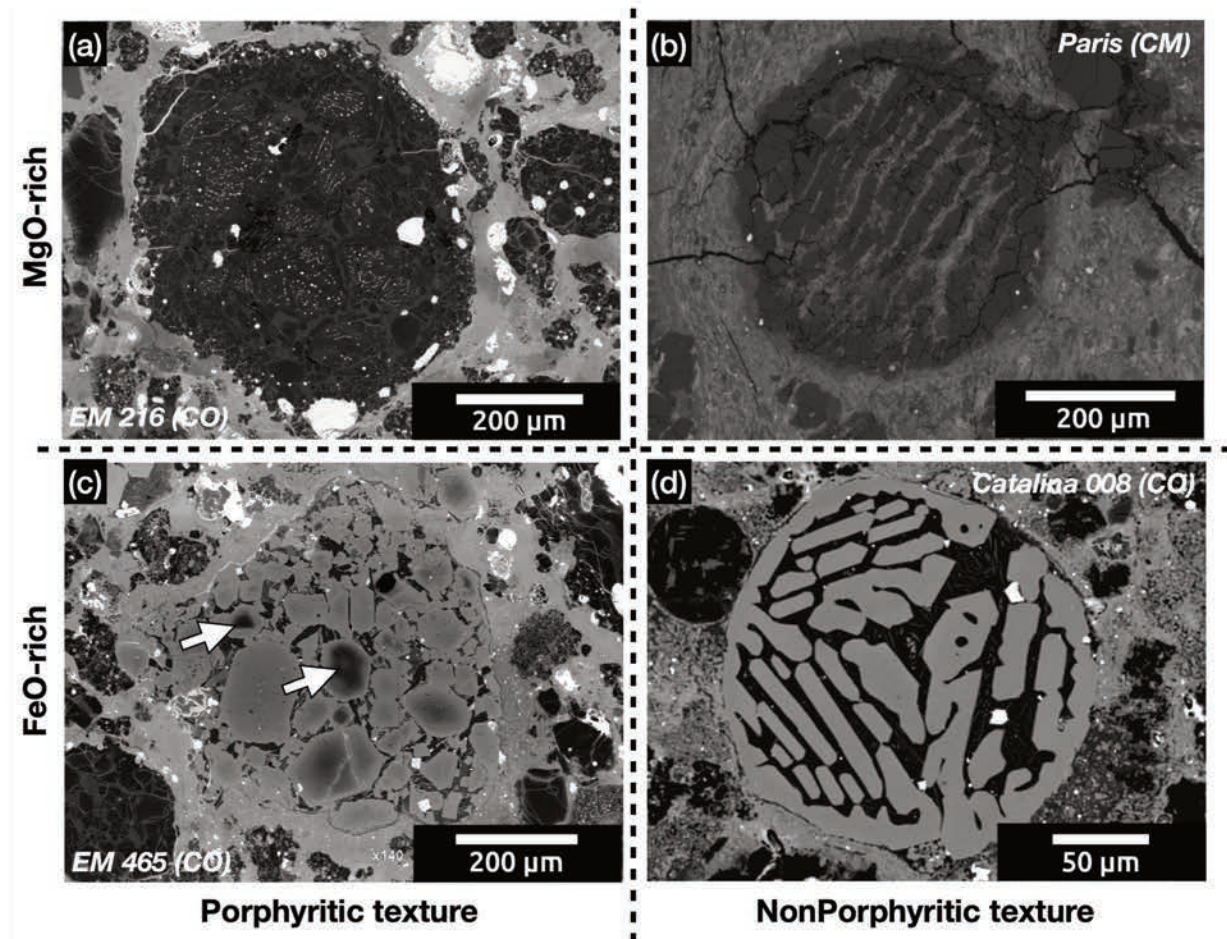


Figure 1.21. Backscattered electron image of chondrule classified by texture and chemical composition. Porphyritic chondrules (a and c) have bigger crystals well developed (euhedral to subhedral); they can have relict grains (arrows in c). On the contrary, nonporphyritic chondrules (b and d) do not develop proper crystalline structures; they are frequently composed of small grains with skeletal and/or anhedral textures. The upper and lower part represent FeO-rich and Mg-rich PO chondrules, respectively.

The chondrule thermal history has been constrained by petrographic textures, mineral chemistry as well as experimental analog studies. Chondrule textures indicates undergo an efficient high temperature event to produce substantial melting, and short enough to preserve a range of disequilibrium crystals growth at significant degrees of undercooling (i.e., at temperatures below the equilibrium crystallization of mineral phases). Their textures probably were controlled by heterogeneous nucleation, which indicate that crystals grow in the surfaces of pre-existing grains (i.e., incomplete melted precursors; Jones et al., 2018). The nucleation

sites are relevant to constrain chondrule textures and is controlled by (i) the precursor grain sizes, (ii) the peak temperature, and (iii) the cooling rate (Desch et al., 2012; Jones et al., 2018). **Figure 1.22** show a general sketch of the thermal histories of different chondrule textures crystallized by dynamic crystallization experiments using a liquidus temperature (composition dependent) around 1400-1700 °C (Radomsky & Hewins, 1990). For instance, cooling rates range from ~10 to 500 °C/h and ~2 to 500 °C/h for type I and II porphyritic chondrules, respectively (Radomsky & Hewins, 1990; Connolly et al., 1998; Jones et al., 2018). Furthermore, cooling rate of type II chondrules have been constrained by diffusion modeling of zoning olivine indicates rates ranging from 10-1000 °C/h (Miyamoto et al., 2009) and oxygen isotopic diffusion modelling between Mg-rich relict and Fe-rich overgrowth from 10^5 - 10^6 °C/h (Yurimoto & Wasson, 2002). Most of these models and experiments suggest that individual type II chondrules were form in a single melting event (Jones et al., 2018). However, some authors support a multi heating-events sustained by the iron oscillatory zoning in Fe-rich olivine and low-Ca pyroxene (Baecker et al., 2017) as well as the common two (or more) generation of crystals with different sizes in type II chondrules (Wasson & Rubin, 2003).

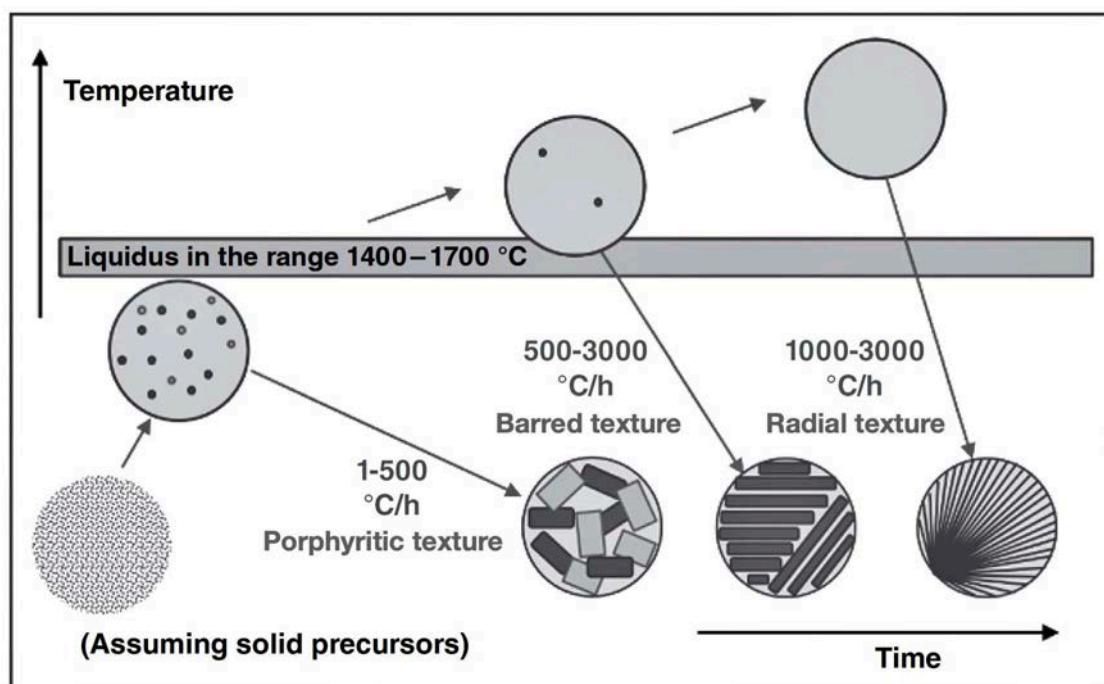


Figure 1.22. Summary of chondrule thermal history from experimental conditions. The maximum peak temperature is relative to liquidus for three different textural types, range between 1400 to 1700 °C (Hewins & Radomsky, 1990). The sketch assumes heterogeneous nucleation (solid precursor) and short exposition time to the peak temperature (maximum 2 h). The cooling rates are a range from different results of dynamics crystallization experiments. Modified from Jones et al. (2018).

The transient heating event(s) that melted chondrules is still controversial. Two great scenarios have been defined for chondrule formation: (i) as nebular products (Marrocchi et al., 2018; Marrocchi et al., 2019; Ruzicka et al., 2007) or (ii) as residues of protoplanet collisions (Johnson et al., 2015; Libourel & Krot, 2007). The last mechanism implies the accretion of planetesimals large enough to experienced partial melting and differentiation before chondrule formation (Johnson et al., 2015; Sanders & Scott, 2012). Based on numerical simulations, (Wakita et al., 2017) suggest that undifferentiated planetesimals would be more suitable for reproducing mineralogic records in chondrules than differentiated protoplanet collisions. However, the protoplanet collision model leaves dissimilar geochemical and isotopic features in chondrules, strongly constrained by oxygen isotope composition (Marrocchi et al., 2018, 2022; Marrocchi et al., 2019; Ruzicka et al., 2007, 2008). In the nebular scenario, several high-temperature events have been proposed to be responsible for chondrule formation, and current astrophysical observations play a relevant role in constraining these models. For instance, as the production of chondrules is assumed to be part of the accreted material of planetesimals, it implied that large fractions of dust in the mid-plane of the PPD were melted before asteroidal bodies were formed. With this in mind, the three most suitable mechanisms to create chondrules in a nebular environment are the (i) Shock waves model, intense flash heating wave probably produced by gravitational instabilities or density waves, however, is still elusive the source of energy (Desch et al., 2012; Morris et al., 2012); (ii) X-wind model, magnetized jets of gas created by the accretion of dust in the active Sun's corona. In this model, CAIs and chondrules are transported through the PPD (Shu et al., 1997; 2001); (iii) Lightning model, a powerful charging mechanism that is based on the differences of contact potentials between particles of different compositions (silicates and metals). The electric fields generate powerful discharges sufficiently energetic to produce chondrules (Desch & Cuzzi, 2000). Whatever the case, the energetic mechanism(s) that melted these objects operated multiple times, probably over millions of years. Various petrographic features support the latest, such as (i) igneous rims surrounding chondrules (Rubin, 1984; 2000), (ii) microchondrules-bearing spherules and amorphous silicates in fine-grained material (Bigolski et al., 2016; Pinto et al., 2022; Zanetta et al., 2021), (iii) relict grains inside chondrules (Jones, 1996; Marrocchi et al., 2018; Piralla et al., 2021; Ruzicka et al., 2007; Villeneuve et al., 2015), and (iv) non-porphyritic, compound and/or lobate chondrule abundances (e.g., Bischoff et al., 2017; Jacquet, 2021; Rubin, 2010).

1.8.3 Relicts and precursor material of chondrules

The presence of relict grains within chondrules supports a violent epoch of abrasion, fragmentation, and collisions in the solar nebula. Relict grains are identified by disequilibrium features in mineralogy, chemical and isotopic composition with their host crystal and mesostasis. As relict grains do not crystallize from the chondrule melt, they are considered as explicit precursors of chondrules (Jones et al., 2018). Various relict grains have been recognized, (i) “dusty” metal-rich olivine in type I chondrules; (ii) MgO-rich olivine grains in type II chondrules; (iii) relict olivine in pyroxene crystals; and (iv) CAI fragments in type I, type II, or Al-rich chondrules (Jones, 1996; Jones et al., 2018; Marrocchi, Euverte, et al., 2019; Piralla et al., 2021; Rambaldi, 1981; Russell et al., 2006; Schnuriger et al., 2022; Tenner et al., 2018; Wasson & Rubin, 2003). The first three kind of relict indicate derived from other nebular components as previous generation of chondrules or AOA-like grains (Jones, 1990, 1996; Marrocchi et al., 2018; Marrocchi, Euverte, et al., 2019; Ruzicka et al., 2007; Schrader et al., 2013, 2015; Villeneuve et al., 2015; Yurimoto & Wasson, 2002).

The abundance of relict grains shows heterogeneous distribution and seems to reflect different recycling grades among chondrite reservoirs. For instance, dusty olivine relicts can be determined from O-isotope ratios by a $\Delta^{17}\text{O}$ values outside 3SD of averaged homogeneous chondrule phase $\Delta^{17}\text{O}$ (Ushikubo et al., 2012). In CC chondrites, isotopic relict olivine grains represent ~32, 15, 10, and 3.5% (calculated by analyzed olivine) in CO (Tenner et al., 2018), C2-ung (Marrocchi et al., 2018), CV (Marrocchi et al., 2019a; Marrocchi et al., 2019b), and CR (Marrocchi et al., 2022; Tenner et al., 2018), respectively. In the case of NC chondrites, Miller et al. (2017) found two relict-bearing chondrule over a total of 11 chondrules on R chondrite and Piralla et al. (2021) 5 over 11 chondrules in LL chondrites. Recently, high-resolution maps and oxygen isotope composition in type I chondrules in CC reported that ^{16}O -rich relict olivine grains are Ti, Al, and Ca depleted as well as Mn enriched compared to the host and others olivines in the same chondrule (Marrocchi et al., 2018; 2019).

One of the most common relict grains is Mg-rich (olivine or pyroxene) in porphyritic type II chondrules with a relatively high abundance in CC (>50 %) compared to OC (<20 %). Typically, they show sharp transitional boundaries between the core and normally-zoned rim (**Figure 1.23**). The petrographic and geochemical constraints suggest that these relict grains are part of the precursor material of type II chondrules, which were not totally melted during the chondrule-forming event(s) (Jones et al., 2018; Ruzicka et al., 2007; Villeneuve et al., 2015). Some of them show partial reabsorption into the melt during chondrule formation, indicating a

recycling process in the environments of chondrule formation (Jones, 1996; Schrader et al., 2015). Analysis of natural chondrules and experimental analogs indicate that AOAs or type I-like chondrules could be the source of these relict grains (Schrader et al., 2013; 2015; Villeneuve et al. 2015).

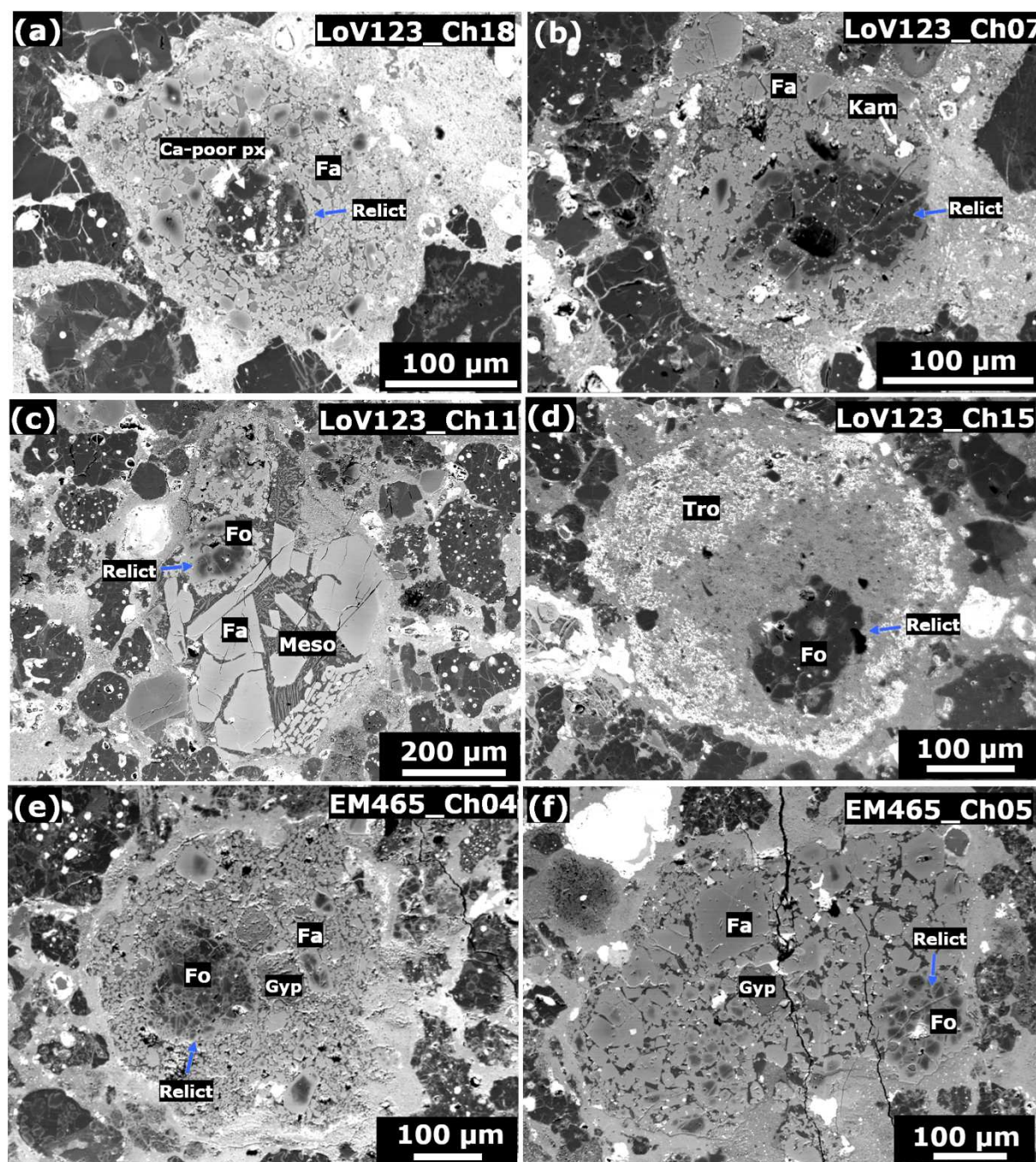


Figure 1.23. Backscattered electron image of Fe-poor relicts in type II chondrules (blue arrow) in CO3 carbonaceous chondrites: (a-d) Los Vientos 123 (CO3.1) and (e-f) El Médano 465 (CO3.2). Some chondrules display gypsum filled porosity and fractures as massive overgrowth (e-f). This secondary mineralogy is the result of terrestrial alteration in the Atacama Desert. Tro = Troilite; Kam = Kamacite; Gyp = gypsum; Fa = Fayalite; Fo = forsterite; Meso = mesostasis.

1.8.4 Oxygen composition of chondrite components

The various planetary and asteroidal bodies in the solar system contain a specific isotopic identification, which depends on the initial isotopic composition at the formation period and/or subsequently modified ratios by interior processes, such as melting, metamorphism, or aqueous alteration. Chondrites and chondrules display mass-dependent and mass-independent isotope fractionations. The first is a result from physical or chemical processes between two different phases that distributed isotopes according to their atomic mass. Isotope fractionations can also be mass-independent when they escape from the accepted mass fractionation law and are typically expressed as $\Delta^{17}\text{O}$, the deviation from the terrestrial mass fractionation line (TFL; **Figure 1.24**). For instance, carbonaceous chondrites, chondrules, CAIs and unaltered matrix minerals plot along a slope-1 line in the $\delta^{17}\text{O}$ and $\delta^{18}\text{O}$ diagram, which represents a mass-independent fractionation defined as (i) the carbonaceous chondrite anhydrous mineral (CCAM) mixing line (Clayton et al., 1977; **Figure 1.24**). The Young & Rusell (1998) is the second mixing line which denotes mass-independent fractionation with heavy isotope enrichments. It is based in oxygen isotopic composition analysis by gas-source mass spectrometry in chondrules and CAIs from Allende (CV) chondrite (Young & Rusell, 1998). The $\Delta^{18}\text{O}$ also indicates different reservoir isotopic behavior and sources (e.g., Piralla et al., 2021).

Oxygen isotope composition of refractory inclusions is diverse and strongly dependent on the mineral and/or structure analyzed (**Figure 1.24**). However, it is the most ^{16}O -poor and closer to the Sun composition in chondrite components (McKeegan et al., 2011). For instance, most CAIs in CO3 and CV3 chondrites exhibit O-isotope heterogeneity that often appears to be mineralogically controlled: anorthite, melilite, grossite, krotite, perovskite, and Zr- and Sc-rich oxides and silicates are ^{16}O -depleted relative to corundum, hibonite, spinel, Al,Ti-diopside, forsterite, and enstatite (Krot, 2019). In the case of AOAs, analyses in the CV and CO chondrites demonstrated that forsterite, spinel and diopside are ^{16}O -enriched to a level commonly observed in spinel, hibonite and fassaite of the Allende CAIs (Hiyagonand Hashimoto, 1999; Krot et al., 2004; Tenner et al., 2018).

Oxygen isotopic composition of bulk chondrules suggest diverse reservoirs that were ^{16}O -poor. However, chondrules from various CC plot closer to the TFL (smaller $\Delta^{17}\text{O}$) than the reservoir where refractory inclusions originated. Chondrules in NC chondrites plot above (OC and R) or near (E) the TFL. By contrast, CC chondrite chondrules lie slightly below along the

CCAM mixing line (**Figure 1.24**). Secondary ion mass spectrometer (SIMS) analysis of chondrules minerals such as olivine, Ca-poor pyroxene, Ca-rich pyroxene, plagioclase, and mesostasis among diverse chondrite groups (CC and NC) and ungrouped chondrites (e.g., Acfer 094, NWA 5492, and GRO 95551) show a relatively uniform composition. Different authors support that this homogeneous composition is result of exchange between the chondrule melt and nebular gas (Kita et al., 2010; Marrocchi et al., 2018, 2019a, 2019b, 2022; Piralla et al., 2021; Tenner et al., 2018). However, the nature of ^{16}O -depleted dust at the earliest stages of PPD evolution remains unclear (Krot et al., 2014).

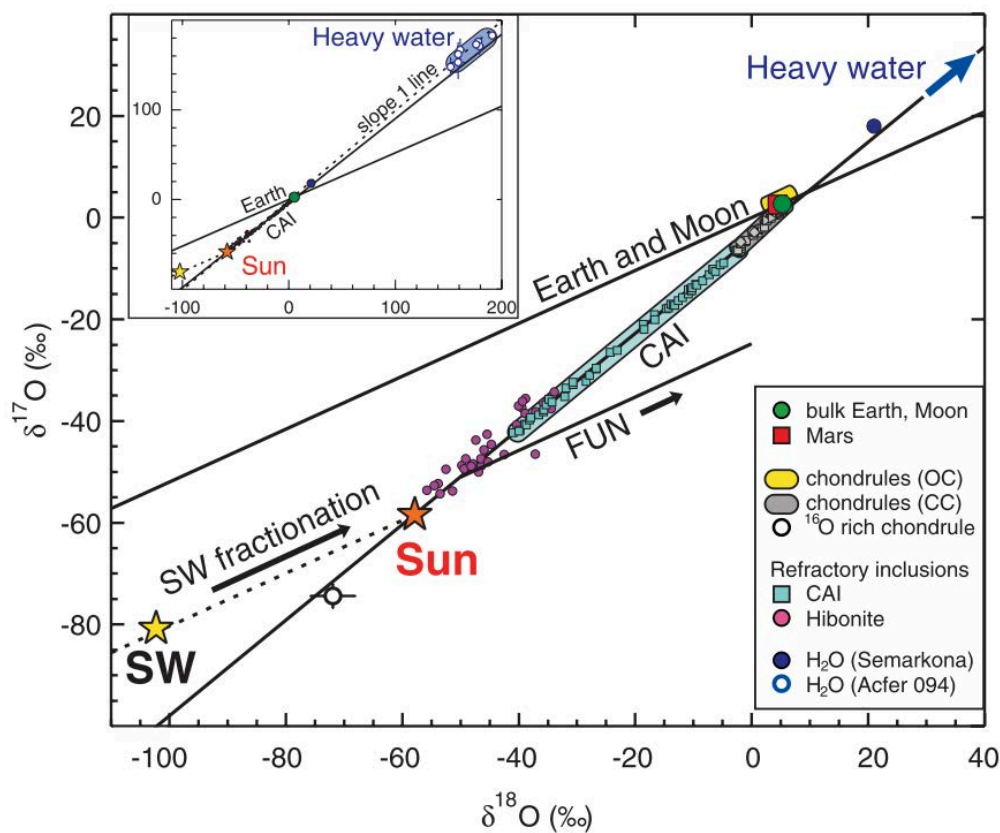


Figure 1.24. Three isotopes oxygen diagram showing representative compositions of major primary components of solar system matter, the solar wind (SW), and our preferred value for the Sun. All data fall predominantly on a single mixing line characterized by excesses (lower left) or depletions (upper right) of ^{16}O relative to all samples of the Earth and Moon. Plotted are the most ^{16}O -enriched solar system samples: an unusual chondrule (K. Kobayashi, H. Imai, H. Yurimoto, 2003); individual platy hibonite grains (Li et al., 2009), which are ultrarefractory oxides from carbonaceous chondrites (CC); water inferred to have oxidized metal to magnetite (Choi et al., 1998) ordinary chondrites (OC); very ^{16}O -depleted water from the CC Acfer 094 (Sakamoto et al., 2007), and whole CAIs from CC (Clayton, 1993); and chondrules from CC and OC (Clayton, 1993), bulk Earth (mantle), and Mars (SNC meteorites). The mass- dependent fractionation trajectory of primary minerals in FUN inclusions and the pure ^{16}O (slope1.0) line (Young & Rusell, 1998) are also shown. From McKeegan et al. (2011).

III. Thesis goals and layout

The main goal of this thesis is to provide petrographic, chemical and isotopic, and astrophysical evidence in the condition of formation and agglomeration of chondrules in the early solar system. Several astrophysical, petrographic, and cosmochemistry aspects are involved in the agglomeration of dust particles before they reach planetary scales. In this thesis's framework, we analyzed 14 unequilibrated carbonaceous and non-carbonaceous chondrites chosen by their limited alteration processes after their agglomeration (petrographic degree range from 2 to 3.8). This work is centered on three aspects of particle recycling and agglomeration, and, as ~60% of the studied sections are primitive chondrites found in the Atacama Desert, we summarize and compare the distribution as well as preservation of meteorites on the 32 dense collection areas described in the Atacama Desert (north of Chile).

The thesis is structured as follows. In chapter 1, we described the astrophysical and cosmochemical framework of the agglomeration of chondrules during the first million years of the solar system. Chapter 2 presents the meteorite samples and the technical description of the performed analytical methods. The following chapters are described below by objective, technique implemented and main results.

Chapter 3. Deciphering recycling processes during solar system evolution from relict olivine grains in type II chondrules.

Objective: The main goal of Task 1 is to determine the major and minor elements and O-isotopic composition of Fe-poor relict grains in type II chondrules from carbonaceous and non-carbonaceous chondrites. Compared with published O-isotopes data of type I chondrules we report evidence of the (i) conditions of type II chondrules formation and (ii) provenances of their Fe-poor relict grains.

Techniques involved: Optical microscope, Secondary Electron Microscope (SEM), Electron probe microanalyzer (EMPA) and Secondary Ion Mass Spectrometry (SIMS CAMECA 1280 HR).

Main results: Mg-rich relicts in type II chondrules almost always overlap in the range of O-isotopic composition of host olivines in type I chondrules ($\Delta^{17}\text{O} = -5\text{‰}$, -2.5‰ and 2‰ for CO, CR and ordinary chondrites). Besides, minor elements composition in Mg-rich relicts tend

to be MnO-poor and slightly CaO-rich similar to the ranges of host grains in type I chondrules. Combining our results with literature data, we show that most forsterite relicts in type II chondrules originate from a previous generation of Mg-rich chondrules.

Chapter 4. Formation of chondrule fine-grained rims from local nebular reservoirs

Objective: The main goal of Task 2 is deciphering the origin and relation between the rimmed bearing chondrule and the matrix abundance in carbonaceous chondrites. To this end, we selected the least aqueously and thermally altered carbonaceous chondrite groups: CO, CM, CV, and CR chondrites.

Techniques involved: Optical microscope, Secondary Electron Microscope (SEM) and image processing software.

Main results: Our systematic survey and the petrographic description of 162 rimmed bearing chondrules in CO, CM, CV, and CR chondrites were used to compare (i) the estimated thickness sizes of fine-grained rims to those of their host chondrules and (ii) the frequency of fine-grained rims to the modal abundance of the matrix in the respective host chondrite group. We show that fine-grained rims could not result from parent-body processes, whether matrix compaction or fine-grained rim fragmentation. Our results thus support: (i) a nebular origin for fine-grained rims, whose abundances are directly related to the abundance of available dust in regions of carbonaceous chondrite accretion; and (ii) rimmed bearing chondrules were accreted in the local reservoir where they agglomerate the rim, suggesting limited radial transport in the circumsolar disk.

Chapter 5. Constraints on planetesimal accretion inferred from particle-size distribution in CO chondrites

Objective: The central goal of Task 3 is the estimation of the particle-size distributions within different CO carbonaceous chondrites, suitable samples by their limited alteration processes after their agglomeration.

Techniques involved: Optical microscope, Secondary Electron Microscope (SEM), Electron probe microanalyzer (EMPA), image processing software and astrophysical models.

Main results: Our particle-size analysis of CO carbonaceous chondrites revealed that the mean spherical diameters of chondrules increase with increasing metamorphic degree. Combining our results with literature data, we show that this relationship was not established during post-accretion thermal metamorphism, but instead records aerodynamic size-sorting of particles during the accretion of the CO parent body(ies). By modeling the self-gravitating contraction of clumps of chondrules, we show that the accretion processes generated a gradual change in chondrule size, with larger chondrules being more centrally concentrated in the parent body(ies) than smaller ones.

Chapter 6. Distribution and alteration of meteorites from the Atacama Desert

Objective: Examine the published and unpublished data of meteorites found in the Atacama Desert to (i) describe the distribution and abundance of different meteorites groups, (ii) compare their terrestrial alteration degree with other hot and cold desert meteorites, and (iii) determine the more suitable DCAs for meteorite preservation according to their geomorphologic and climatic context.

Techniques involved: The information about all the meteorites found in the Atacama Desert was collected from the Atacama meteorites description in this thesis and the Meteoritical Bulletin Database¹.

Main results: The Atacama Desert displays three main morphotectonic units: the Coastal Range, Central Depression, and Preandean Range/Basement. The distinctive climatic and geological conditions of the morphotectonic units affect the accumulation and conservation of meteorites. The four main parameters involved in the alteration of meteorites in the Atacama Desert are (i) distance from the Pacific Ocean, (ii) surface altitude, (iii) surface age, and (iv) surface lithology. There are three main processes which generate chondrite disintegration in Atacama: (i) saline mineral precipitation, (ii) thermal stress weathering, and (iii) volume increase by Fe-Ni oxide and hydroxide formation. A comparison with reported weathering data from other cold and hot deserts indicates that terrestrial weathering meteorites in Atacama induces less alteration than in other hot deserts following the distribution of Antarctic meteorites.

¹ <https://www.lpi.usra.edu/meteor/>

Chapter 2

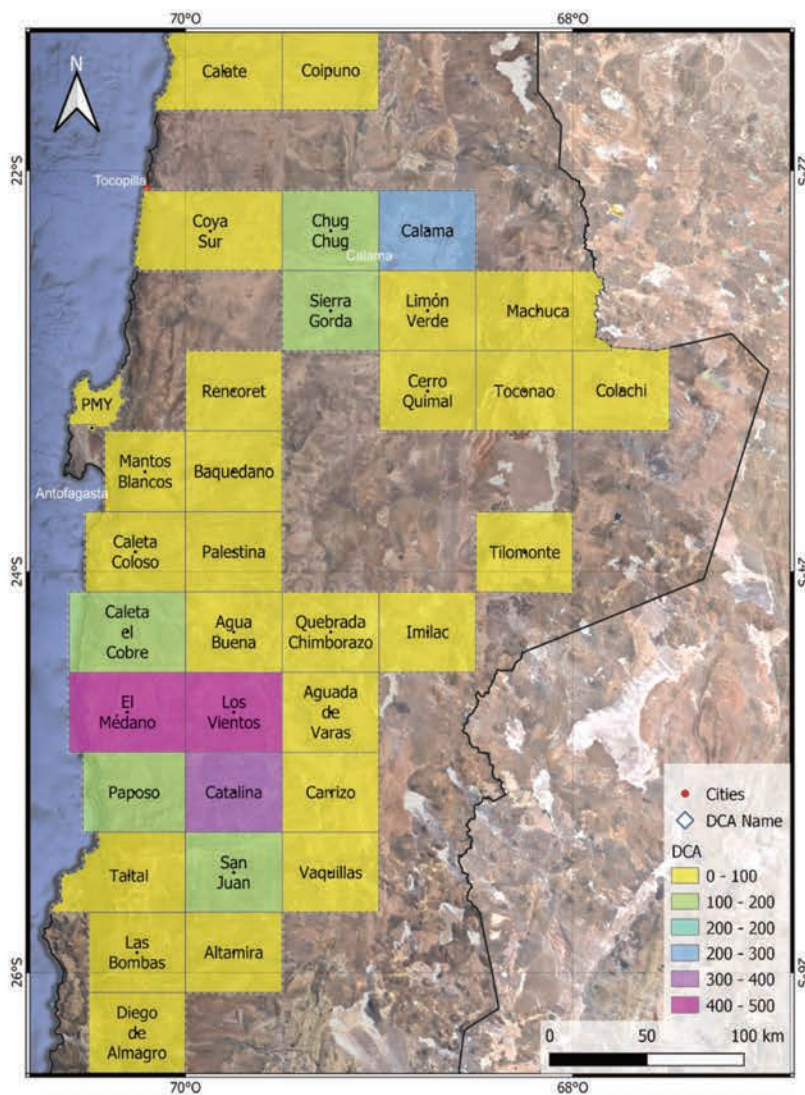
Samples and analytical techniques



I. Meteorite background and sample preparation

2.1 Sample sources

Meteorites are commonly found in cold and hot deserts around the world. The reduced abundance of water in these areas decreases weathering alteration and privileges the conservation of extraterrestrial material through thousands to millions of years in terrestrial environments (Drouard et al., 2019). In the last three decades, hot deserts such as the Sahara and Atacama, have become relevant sources for finding a large number of meteorites. Today, more than 2200 meteorites have been found among the 34 dense collection areas at the hyperarid core of the Atacama Desert (Figure 2.1; see Chapter 6).



environments (Drouard et al., 2019). In the last three decades, hot deserts such as the Sahara and Atacama, have become relevant sources for finding a large number of meteorites. Today, more than 2200 meteorites have been found among the 34 dense collection areas at the hyperarid core of the Atacama Desert (Figure 2.1; see Chapter 6).

Figure 2.1. Name and abundance of meteorites found in all dense collection areas in the Atacama Desert. The dense collection areas with a major abundance of meteorites are El Médano (EM), Los Vientos (LoV) and Catalina (Cat).

The ordinary and carbonaceous chondrites studied in this thesis are shown in **Figure 2.2**. We surveyed the most primitive chondrites, which displayed low terrestrial alteration and shock metamorphism from the whole meteorite collection at the Museo del Meteorito Chile (MMC) using the classification description as well as the chemical analysis available in the Meteoritical Bulletin database (<https://www.lpi.usra.edu/meteor/>). We selected eight ordinary and carbonaceous chondrites found in Los Vientos (LoV), Catalina (Cat), and El Médano (EM) dense collection areas from the Atacama Desert (**Figure 2.1**). These Atacama chondrites were provided by Rodrigo Martínez de Los Ríos, director of the MMC. We also selected four sections are classified as *find* (Paris, NWA 5206, Isna and Dar al Gani 574) and two as *fall* (Renazzo and Vigarano). All these four sections belong to the Muséum National d’Histoire Naturelle de Paris (MNHN, France) or to the Centre de Recherches Pétrographiques et Géochimiques (CRPG, France) collection. All samples are unequilibrated chondrites with petrologic type ranging between 2 - 3.7 and low terrestrial alteration.

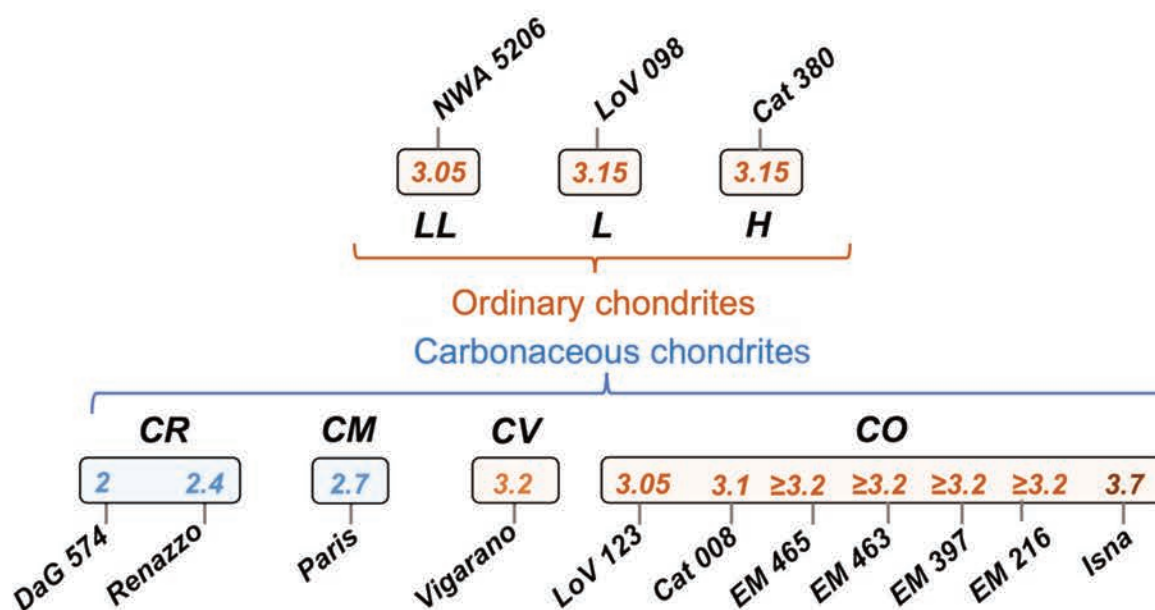


Figure 2.2. All chondrites studied in this thesis. They are classified by chondrite class. The estimated petrologic type is shown for the 14 samples found in the Atacama Desert and donated by the Museo del Meteorito (Chile) collection.

2.2 Section preparation

All the sections provided by the MMC were prepared at the CRPG or in the Department of Metallurgic Science at the University of Atacama. The homemade sections were prepared by cutting a small piece of a few millimeters size using a diamond saw and consecutively placed in a resin ring or in a resin block (**Figure 2.3**). Afterwards, the sections were polished with ethanol as lubricants to avoid water contamination and chondrite components alteration. The polishing discs are composed of silicon carbide (SiC) with different grain sizes (600, 1200, and 2400 grains/cm²). Subsequently, the polished surface is finished with a diamond paste and a granulometry particle disc of 6, 3, 1 and ¼ µm in diameter. The polished samples were covered with a thin layer of carbon coating (~20 nm) to avoid electric charge accumulation in the analyzed areas by electronic and ionic techniques.

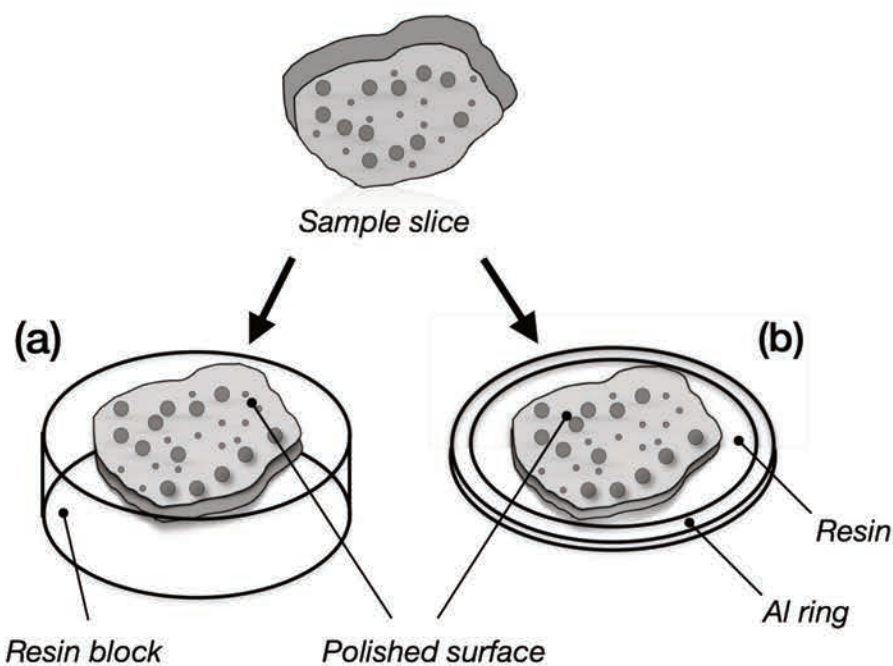


Figure 2.3. Schematic of the meteorite section preparation. After cutting the sample slice with the diamond saw, the slice is placed in (a) a resin block or (b) resin with an aluminum ring. In this study, both section types were used.

II. Analytical techniques

This thesis presents a multi-analytical approach to tackle the proposed main and specific objectives. The applied techniques are displayed by scale and objective in **Figure 2.4**. The petrography and mineralogy of all samples were described through optical and electronic microscopy. The EMPA analysis was performed to determine the major and minor element compositions of 164 ferroan and magnesian olivine grains in FeO-rich chondrules from CO, CR, and ordinary chondrites. Also, four clasts were analyzed from the Rennazzo (CR) and the EM 463 (CO) chondrites. Using the Cr_2O_3 content of more than ~ 50 Fe-rich olivines in type II chondrules, we classified the petrographic grade of 6 chondrites based on the Grossman and Brearley (2005) method. Oxygen isotope analyses were performed in 51 relicts and 77 host olivine grains from type II chondrules in CO, CR and ordinary chondrites. The X-ray microtomography was applied for one carbonaceous and one ordinary chondrite to estimate the volumetric abundance of type II chondrules with relict grains and characterize the volume of relicts and host chondrules. A detail of each technique will be presented in the following sections.

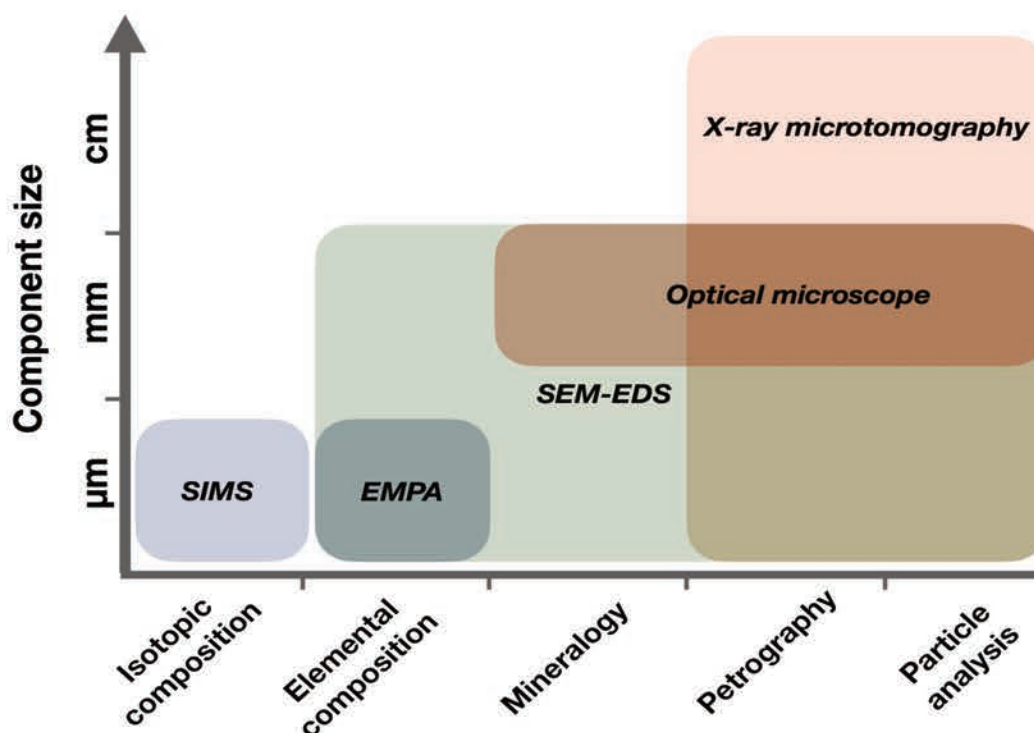


Figure 2.4. Diagram of the five analytical techniques used in this thesis focused on three different scales to characterize five different parameters: isotopic and elemental composition, mineralogy, petrography, and particle analysis.

2.3 Optical and electron microscope

Optical and electron microscopy was employed to describe the petrography and mineralogy of chondrites and chondrules. As all the samples are thick sections, only reflected light in the optical microscope was used to determine chondrule textures and opaque phases. This is because most silicates and oxides cannot be differentiated by reflected light in chondrites. Therefore, scanning electron microscope (SEM) analysis was utilized to distinguish the chemical composition of mineral phases. The SEM uses a beam of accelerated electrons for imaging. Since the wavelength of electrons is much shorter than visible light, the electron microscopy results in a much higher imaging resolution than an optical microscope. For instance, the SEM allows probing the sample surface at a very high spatial resolution (up to 1 μm or even 100 nm). In this sense, the SEM works based on the surface interaction between electrons and solid matter. The beam of primary electrons comes from a heating tungsten (W) filament, which is then accelerated by a high voltage of 2-30 kV. This beam sweeps the surface of the section and creates interactions between accelerated electrons and atoms of the sample (**Figure 2.5a**). This interaction generates emitted different signals such as X-rays (i.e., cathodoluminescence), secondary electrons (SE), backscattered electrons (BSE), and Auger electrons. BSE imaging is particularly suitable for samples in the form of a polished section and is one of the most employed emissions, in a company with X-rays, through this thesis.

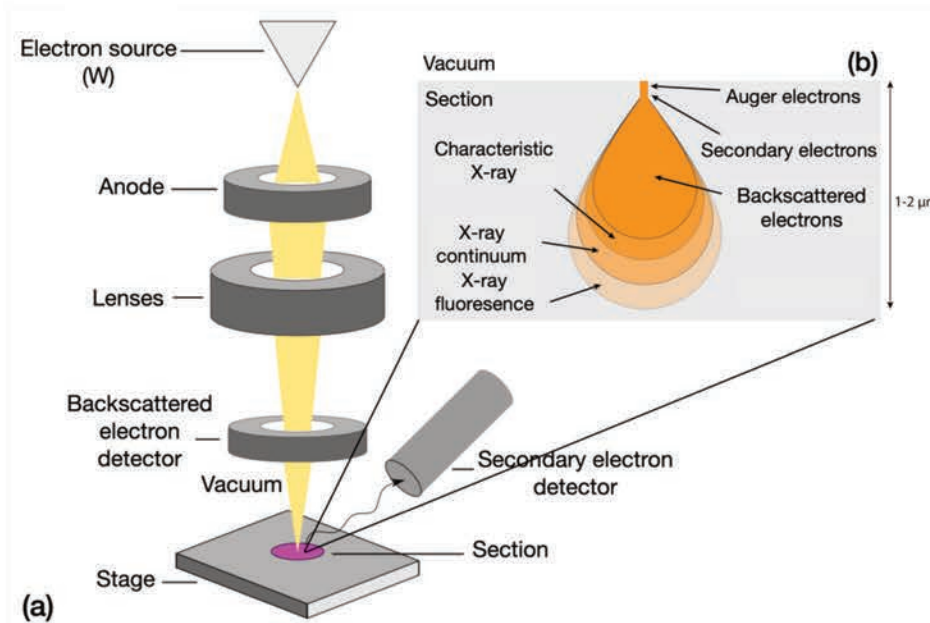


Figure 2.5. SEM components (a) and the interactions between accelerated electrons and atoms of the sample (b).

The backscattered electrons are formed by the elastic interactions of the primary electrons with nuclei of atoms. They are highly energetic (up to 30 keV) and can be emitted in depth (interaction pear: $\sim 1\mu\text{m}^3$; **Figure 2.5b**), thus showing little sensitivity to variations in topography. This imaging can be used to observe and characterize crystal microstructures at a scale of a few hundred nm. It is also highly dependent on the elements' mean atomic number (Z) in each mineral phase. Thus, it is possible to obtain qualitative chemical information from the sample by a threshold of dark and clear phases which contain light elements (low Z , e.g., Mg) and heavy elements (high Z , e.g., Fe), respectively. Analysis using X-ray spectra provide semi-quantitative analysis of the elemental composition of mineral phases. The spectrum of X-rays emitted is measured with the Energy-Dispersive X-Ray Spectroscopy (EDS). These rays are characteristic for each element and are recognized by a library within the SEM's software. As a result, the X-ray analysis highlights the element distribution of each mineral phase through a false color image (**Figure 2.10b**).

In this thesis, two scanning electron microscopes (SEM) were used to define the petrography of chondrites and determine the semi-quantitative chemical composition of minerals. The first one localized in the Department of Metallurgic Science at the University of Atacama in Copiapó (Chile). This SEM is a Zeiss Evo MA10 equipped with an Oxford X-MAX N 20 SDD energy-dispersive spectrometer, operating with a 3 nA electron beam accelerated at 15 kV. The second SEM used in this thesis is a JEOL JSM-6510 equipped with a dispersive energy detector (Bruker-AXS XFlash, silicon diffusion detector) located at the CRPG in Nancy (France).

2.4 Electron probe microanalysis (EPMA)

2.4.1. Technical description

The electron probe microanalysis (EPMA) is a non-destructive elemental analysis that operates with a similar principle to the SEM-EDS system but provides fully qualitative and quantitative results. The EPMA starts bombarding the section with a primary electron beam (typical energy between 5 to 30 keV) to collect the X-ray photons emitted by atoms in each analyzed phase. As the wavelengths of these X-rays are characteristic of the emitting element, the sample composition can be easily identified by recording the Wavelength Dispersive Spectroscopy (WDS) spectra. The WDS spectrometers operate using various moveable, shaped monocrystals as monochromators. Thus, it is possible to cover all the wavelengths and elements from B to Pu and above can be analyzed. The calibration of the X-ray emission spectra from natural or artificial mineral standards allows obtaining the concentration of various chemical elements quantitatively with a sensitivity at the level of part per millions (ppm).

2.4.2. Chemical composition of chondrules and subtype classification

The major (Si, Al, Fe, Mg, Ca, Na) and minor (Ti, Mn, Cr, K) element compositions of ferroan and magnesian olivine grains in FeO-rich chondrules from CO (EM 216, EM 463, LoV 123, EM 397, Isna and Cat 008), CR (Renazzo and Dar al Gani 574) and OC (LoV 098 and Cat 380) were quantified by EPMA. The lowest petrologic type of studied chondrites is shown in **Figure 2.6** according to the diagram classification of Grossman and Brearley (2005).

Three electron probes were employed in the course of this thesis. The CAMECA SX-Five electron microprobe at the CAMPARIS service (Sorbonne University, Paris, France). This microprobe was calibrated using the following natural and synthetic standards for silicate analyses: diopside (Si, Ca, Mg), orthoclase (Al), MnTiO₃ (Mn, Ti), Cr₂O₃ (Cr), and Fe₂O₃ (Fe). A 20 nA focused beam, accelerated to 15 kV potential difference, was used for spot analyses of olivine with 20 s analysis times. Detection limits in silicates were 0.03 wt% for SiO₂, Al₂O₃, CaO and MgO; 0.04 wt% for MnO and TiO₂, and 0.07 wt% for NiO, Cr₂O₃ and FeO. The PAP software was used for matrix corrections (Pouchou and Pichoir, 1984). The other two probe employed was a CAMECA SX100 at the Service Commun de Microscopies Electroniques et de Microanalyses X (SCMEM, Université de Lorraine, Nancy, France) operate with 12 nA

focused beam accelerated at 15 kV and the ARL-SEMQ electron microprobe at ICATE (San Juan, Argentina) operating with 15 nA electron beam accelerated at 15 kV. The minerals used as standards to calibrate the two last EPMA were olivine (Mg, Si), orthose feldspar (K, Al), hematite (Fe), Albite (Na), diopside (Ca), titanium manganese (Mn, Ti) and chromite (Cr).

The Cr_2O_3 content in ferroan olivine grains analyzed in this thesis were used to classify the petrologic subtype of five CO chondrites (Grossman and Brearley, 2005) found in the Atacama Desert (**Figure 2.6**). We determine the subtype of LoV 123 and Cat 008 as 3.05 and 3.1, respectively. Other CO3 chondrites such as EM 216, EM 463 and EM 397 plot in the area of subtype ≥ 3.2 . A classification of 3.1 is suggested for LoV 123 by the modification of organic matter on the matrix (Bonal et al., 2016).

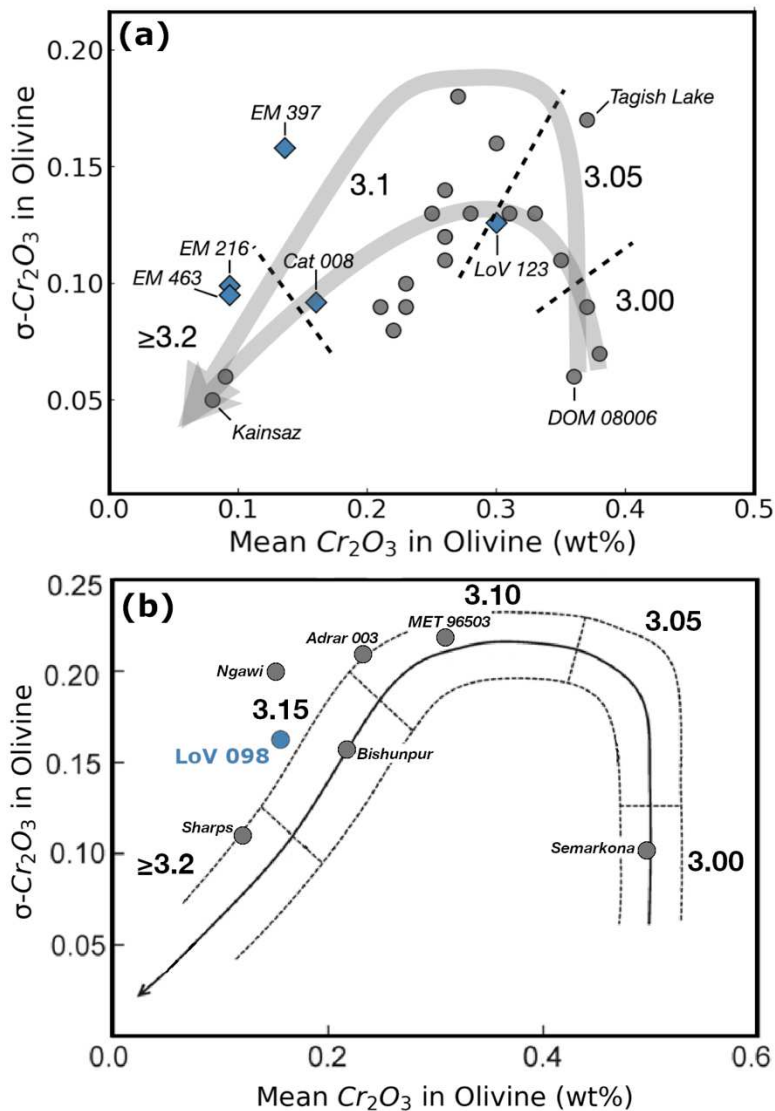


Figure 2.6. Trends of low petrologic subtype basis on $\sigma\text{-Cr}_2\text{O}_3$ vs. mean Cr_2O_3 in ferroan olivine grains for CO (a) and ordinary chondrites (b). CO chondrites displays two trends: the bottom one proposed by Grossman and Brearley (2005), and the top trend from Grossman & Rubin (2006). The approximate boundaries between adjacent subtypes (dashed lines) were modified from Rubin and Li (2019). The trend of ordinary chondrites was proposed by Grossman and Brearley (2005). LoV 098 plot above the trend defined by the other ordinary chondrites, similar to Ngawi, a breccia of type 3.1 and 3.6/3.7 material. CO chondrites analyzed in this thesis are shown as blue diamonds. LoV 098 is show as a blue circle. Literature data (filled gray circles) are from Grossman and Brearley (2005); Grossman and Rubin (2006); Davidson et al. (2014); Rubin and Li (2019); Yamanobe et al. (2018); and Ushikubo & Kimura, (2021).

2.5 Secondary Ion Mass Spectroscopy

Secondary ion mass spectroscopy (SIMS) is an instrument for *in situ* chemical analysis at a spatial resolution of micrometric scale. SIMS is one of the most sensitive techniques for surface analysis and provides information on the material's elemental, molecular, and isotopic composition. The impact area of the primary ions on the sample defines the spatial resolution of the analysis, which is typically a few tens of micrometers in diameter. The ion probe bombards the sample's surfaces with accelerated high energy (1-30 KeV) primary ions such as Cs^+ , O_2^+ , or O^- . The impact causes the expulsion of photons, electrons, and secondary ions from the sample surfaces (**Figure 2.7**). The secondary particles can be positively, negatively, or neutrally charged and can reach kinetic energy ranging from zero to several hundred of voltage in a process called sputtering (Joo and Liang, 2013). They are subsequently accelerated using an electric field and focused by an electrostatic lens before being sorted according to their mass-to-charge ratio. They will then be collected by a counting system consisting of Faraday cages or electron multipliers.

The advantage of this instrument is that virtually all chemical elements can be measured (eluding interferences) in a variety of micrometer solid phases in a quasi-non-destructive way with a detection limit of up to a few ppm to ppb. Within the framework of this thesis, we selected 20 relict-bearing and not-relict-bearing Fe-rich chondrules in COs, CRs, and ordinary chondrites to measure their triple oxygen isotopic composition.

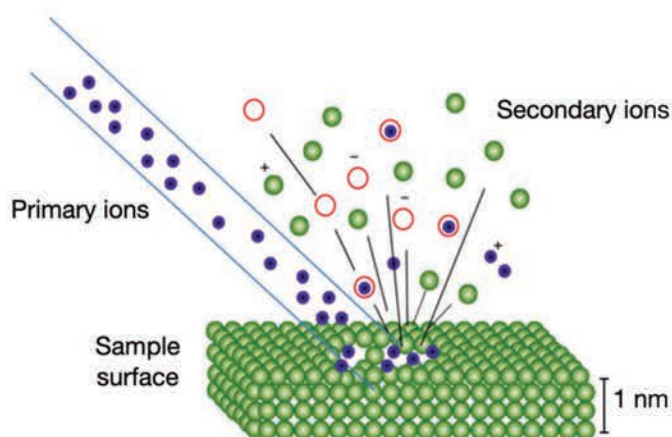


Figure 2.7. Sketch of the ionization of the surface's sample by the bombarding of ions from the primary source.

The SIMS instrumentation is distributed according to the main functional processes, such as (i) secondary ion generation and (ii) secondary ion measurement. The secondary ion generation involves several components such as the ion source, electron gun, primary ion column, and ion extraction and secondary column. The role of this part is to release secondary ions from the

sample surface to the mass spectrometer. The secondary ion measurement is done by sorting ions according to their energy and mass-to-charge ratio. This part consists of three components, an ion energy analyzer, mass analyzers, ion detectors, and collection modes. Furthermore, the methodology for the isotopic measurement analysis and the specific case of oxygen isotopic composition will be described in the last subsection.

2.5.1. Secondary ion generation

Ion sources

In the SIMS, there are two main ion sources: the duoplasmatron and the surface ionization zone, which commonly use a Cesium source. The duoplasmatron source operates with a small amount of primary gas (commonly Ar⁺ or Xe⁺) introduced into the vacuum chamber, producing atoms reacting with energetic electrons emitted from a nickel cathode filament. As atoms interact continuously with the energetic electrons, ionization proceeds to reach a critical value and forms plasma. This dense plasma is accelerated and compressed into an aperture in a planar anode and extracted as relatively high-speed ion beams. This analytical source allows the analysis of positive secondary ions such as Mg⁺, Ca⁺, or Pb⁺.

In the surface ionization operation, a cesium carbonate reservoir (Cs₂CO₃) is heated until it produces Cesium vapor. The Cesium gas is ionized on a tungsten plate's surface hot enough to produce the desorption of Cs⁺ ions. The Cs⁺ ions are extracted from the ion gun and accelerated in the primary ion column. The column usually consists of a mass filter, electrostatic lenses, apertures, and deflectors. The mass filter eliminates impurities in the beam, and electrostatic lenses and apertures control beam intensity and width. The controlled and modified beam is deflected to the desired area on the surface by a deflector. Habitually, O⁻ is used as the primary beam source for duoplasmatron and the cesium source (Cs⁺) for surface ionization.

Electron gun

The constant bombardment of Cs⁺ ions in the sample surface creates a positive charge effect, disturbing the transmission of secondary ions into the secondary column. Covering the sample surface with a nanometric layer of carbon or gold improves the conductivity. However, more is needed to equilibrate the electrical charges in the ion impacts area. To avoid excess

positive charges, the electron gun instrument "shot" electrons in the sample's surface to compensate for the charge effect and improve the transference of secondary ions to the secondary column.

The secondary column

The secondary ion products of the interaction between primary atoms and the sample surface are extracted and transferred in a high vacuum chamber called the secondary column. As these secondary ions have a wide range of trajectories and kinetic energy values (1eV-1keV), they are focused using transfer lenses (LT1 and LT3) and two diaphragms (contrast and field). The incoming particles are subjected to a high voltage (-10 keV) that allows the passing of a maximum of secondary ions toward the immersion lens, which accelerates and optimizes the ion beam. Finally, the contrast and field diaphragms eliminate ions with extreme trajectories that deviate from the optical path. The contrast diaphragm also improves the spatial resolution of the iconic image of the surface, while the field diaphragm only transmits secondary ions from a defined area of the sample surface.

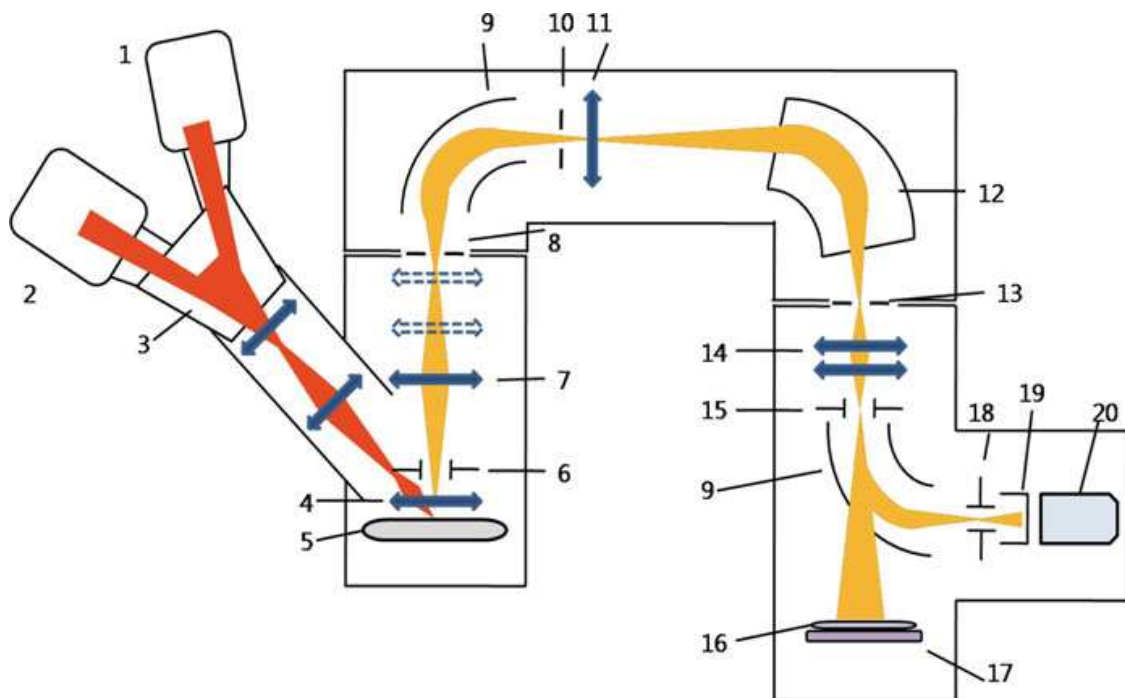


Figure 2.8. Schematic of instrument localization in the SIMS: 1. Cesium ion source; 2. Duoplasmatron ion source; 3. Primary beam mass filter; 4. Immersion lens; 5. Sample; 6. Electron gun; 7. Transfer optical system; 8. Entrance slit; 9. Electrostatic sector; 10. Energy slit; 11. Spectrometer lens; 12. Magnetic sector; 13. Exit slit; 14. Projection lenses; 15. Deflector; 16. Channel-plate; 17. Fluorescent screen; 18. Deflector; 19. Faraday cup; and 20. Electron multiplier. Adapted from Joo & Liang (2013).

2.5.2. Secondary ion measurement

Electrostatic sector

For the secondary ion measurement, the first filter is an electrostatic sector that controls the ion beam with different energy levels by bending it to different degrees. It comprises two curve plates on which direct voltage is applied to one, and the opposite voltage is applied to the other. When ions go through the space among plates, most ions follow unstable oscillation and hit the slit. However, ions with a single mass-to-charge ratio follow periodically stable oscillation and are transmitted to the following detectors (Joo and Liang, 2013).

Magnetic sector

The magnetic sector and the electrostatic sector enable a magnetic double-focusing spectrometer. The magnetic area is composed of a series of electrostatic and magnetic fields, which plays a similar role as the electrostatic sector except for the different types of field. Here, the magnetic field applies a constant force perpendicular to the trajectory of the accelerated ions. As ions have different velocities, only ions with an equivalent mass-to-charge ratio will be focused on the same place at the output slot. The ions with various energy levels are separated and controlled when they pass the slit. This method has high sensitivity compared with others and is suitable for small-area analysis and imaging.

Before the ion detector, the energy slot eludes most interference caused by molecular ions formed during the processes of ion interactions. The interference is removed by the energy difference between molecular and atomic ions. In this sense, the ions with higher initial energy will be preferentially selected.

Ion detection

After the flux of secondary ions from the spectrometer, an electrostatic sector sends ions either to a fluorescent screen or to the ion counting system (**Figure 2.8**). The fluorescent screen is used for the image mode, which allows acquiring a direct image of the element distribution on the surface of the sample. This method is mainly used for instrument alignment (e.g., primary and secondary beam adjustment).

The ion counting system depends on the secondary ion's intensity, the electron multiplier can do them, and the Faraday cup (FC) shielded room. The electron multiplier is a highly sensitive ion-counting detector with a continuous dynode structure (i.e., series of electrodes) in a vacuum tube. The procedure starts when a particle strikes one dynode and induces the emission of secondary electrons. The secondary electrons then strike the next dynode and multiply the number of secondary electrons. As a result, a cascade of electrons is generated on the metal anode to allow the detection of low count rates or low count per second (cps).

The FC shielded room directly converts each secondary ion impact into an electrical signal. The detector counts one ion when the electrical signal exceeds a certain intensity. The FC shielded room is localized in front of the electron multiplier (**Figure 2.8**) and protects it when the incoming ion signal is too high. This type of detector is principally used for low count rates such as (i) when the analyzed ions are low, (ii) when the element abundance in the sample is low, or (iii) when the spatial resolution is the priority. However, using the FC involves a major background noise associated with the amplifier's resistance that ranges from $\sim 10^2$ - 10^4 cps.

The collection modes

The SIMS has two modes of ion collection. The first is the sequential mode or monocollector, which counts ions on fixed detectors and consists of two FCs (FC1 and FC2) and one electron multiplier (axial). As the detectors are fixed, the different masses are analyzed by the value modification of the magnetic field. FC1 and FC2 are commonly equipped with a resistance of 10^{10} and 10^{11} Ω . The simultaneous or multi-collector mode allows the measurement of up to five elements using seven different detectors (L'2, L2, L1, C, H1, H2, and H'2). Opposite to the mono-collector mode, the magnetic field value is fixed, and the detectors are set into the path of ions analyzed.

2.5.3. Evaluation of isotopic analysis

Mass resolution

As spectrometers separate ions by mass, the closer masses of certain isotopes (e.g., ^{16}O , ^{17}O , and ^{18}O) must have enough mass difference to distinguish between the two measured peaks. The method to calculate the latest is the Mass Resolving Power (MRP). It is possible to separate ion masses M_1 and M_2 just if the MRP is greater or equal to:

$$MRP = \frac{M_1}{\Delta M} \quad \text{Eq. 2.1}$$

Where ΔM is the difference between two peaks, M_1 and M_2 , the MRP improves when we modify the input and output slit sizes, as shown in **Figure 2.9**. In this sense, the capacity to overcome similar peaks and achieve high mass resolution depends on the instrument properties (electrostatic and magnetic sector), the input and output slit sizes and the amount of molecular and isobaric interference of the studied isotopes.

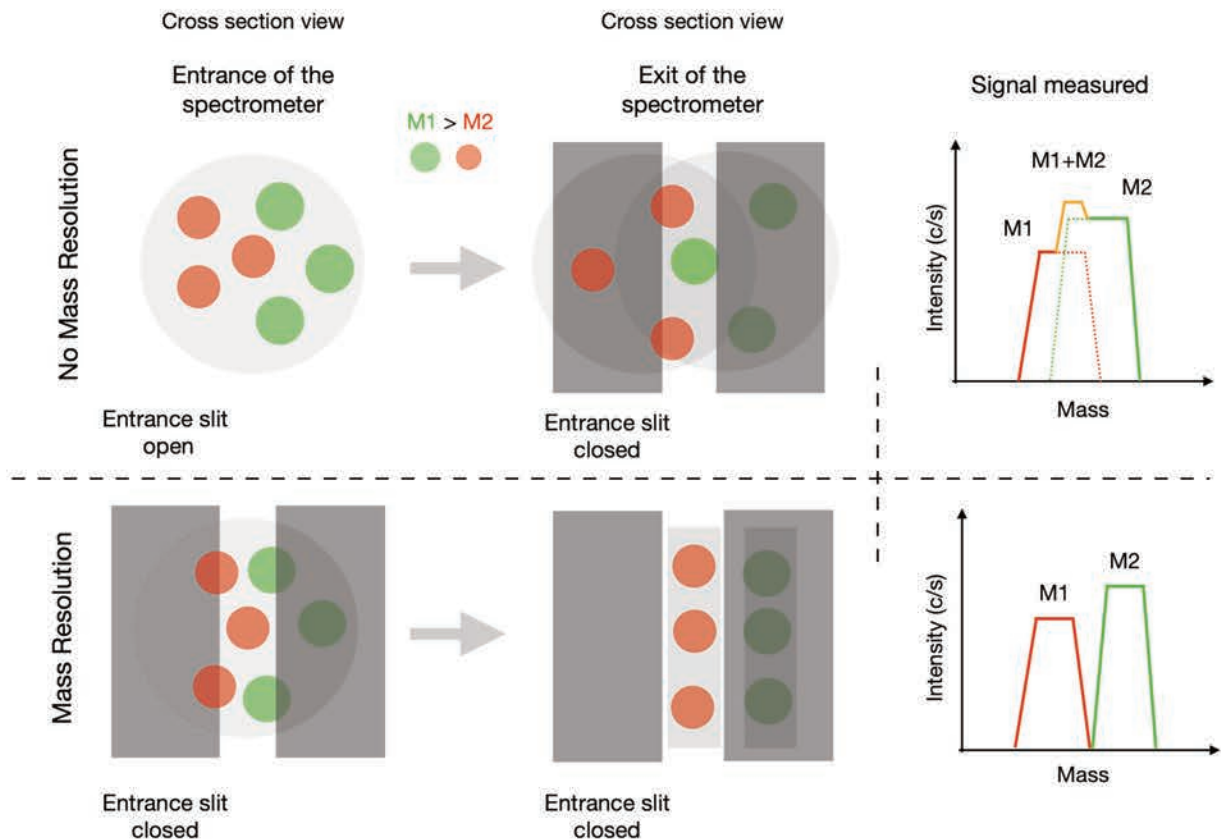


Figure 2.9. Schematic representation of spectrometer modification setting as input and output. The mass resolution setting improves the difference between the two peaks M_1 and M_2 measurements and permits overcoming isobaric and molecular interferences. Modified from Chaussidon (1998); Rollion-Bard (2001); and Villeneuve (2010).

Instrumental mass fractionation

The isotopic measurements can be compared with the analyses of other spectrometers and/or analytical sessions but require additional calibration to express themselves in an international reference method. The reference materials, or standards, help solve the difference between laboratories, instruments, and analytical sessions.

As the standard's chemical and/or isotopic composition is well known, it can be used to calibrate and track the difference between the studied sample's chemical and/or isotopic composition. To do this, it is necessary to analyze the standard, the sample, and the standard again (see **Figure 2.10**). This methodology is denominated *bracket* analysis and can provide relevant difference information about instrumental mass fractionation (IMF). The IMF expresses the difference between the measured isotope ratio (mir) and the real isotope ratio (rir). The IMF is calculated as follows:

$$IMF = \delta_{mir} - \delta_{rir} \quad \text{Eq. 2.2}$$

The slight change in the isotopic ratios results from the ionization and/or extraction of secondary ions and their transmission capacity inside the probe. It can be affected by different parameters such as (i) element mass (lighter elements display greater IMF); (ii) conditions in the analytical chamber; (iii) chemical composition of the mineral (e.g., matrix effect); (iv) crystalline structure and chemical bonds in the mineral; (v) duration of ions implantation; (vi) target position in the section (peripheric zones display different IMF); and (vii) surface of the polished section. Currently, there is no physical model to explain each ion interaction inside the ion probe, so we can assume this is a “black box” using the standard isotopic composition. It is essential that standards and samples have the same or close chemical composition and that they are measured under the same analytical conditions.

In this thesis, a relevant IMF parameter is the matrix effect associated with the O-isotopic composition of olivine grains. The typical standard for olivine grains is the San Carlos

olivine, which has Mg# (= 100 x molar ratio Mg/ [Mg + Fe]) ranging from 87 to 92 (Fournelle, 2011). As we analyzed Fe-rich olivine grains (Mg#~ 70) and the standards displayed different chemical compositions, a correction was applied using a model curve. Precision and accuracy of ~0.4‰ in $\delta^{18}\text{O}$ are achievable at the ~10–25 μm spatial scale (Isa et al., 2017).

2.5.4. Oxygen isotope composition

We measured the oxygen isotopic compositions of 20 type II chondrule olivines with different iron contents by SIMS. We used the CAMECA IMS 1270 E7 at the Centre de Recherches Pétrographiques et Géo-chimiques (CRPG-CNRS, Nancy, France) with an ion source of Cs⁺ as primary ion beam (~10 μm , ~2–2.5 nA, rastered over 5 × 5 μm^2). In the case of O-isotope composition, the analysis is performed under a multi-collection mode due to their (i) close masses (e.g., ¹⁶O, ¹⁷O, ¹⁸O), and the (ii) low mass resolution. Thus, ¹⁶O⁻, ¹⁷O⁻, and ¹⁸O⁻ were measured using three FCs, to remove the hydride peak interference of ¹⁶OH⁻ on the ¹⁷O⁻ peak and to maximize the flatness atop the ¹⁶O⁻ and ¹⁸O⁻ peaks (**Figure 2.10**). The entrance and exit slits of the FC2 were adjusted to obtain MRP (= $M/\Delta M$) of ~7,000 for ¹⁷O⁻, while ¹⁶O and ¹⁸O mass spectra were obtained with a MRP of ~2500 in L'2 and H1 FCs, respectively. As an additional safeguard against ¹⁶OH⁻ interference in the ¹⁷O⁻ peak, a liquid N₂ trap was used to reduce the pressure in the analysis chamber to <1 × 10⁻⁸ mbar. We used 10¹⁰ Ω , 10¹² Ω , and 10¹¹ Ω resistors for the L'2 (¹⁶O), central (¹⁷O), and H1 (¹⁸O) FCs, respectively (see Bouden et al., 2021, for further details). A normal-incidence electron gun was used for charge compensation. Total measurement times were 300 s, comprising 120 s of pre-sputtering and 180 s of analysis.

Two terrestrial standards, San Carlos olivine and JV1 diopside were used to define the mass-dependent fractionation line (**Figure 2.11**). The IMF and matrix effect of chondrule olivine grains was corrected using San Carlos olivine and a set of synthetic standard olivine yielding Mg# ranging from 36 to 100 (Villeneuve et al., 2019, 2020). To monitor any instrumental drift and to achieve good precision, the San Carlos olivine was analyzed after every 10–15 sample analyses. Typical count rates obtained on San Carlos olivine were 1.0 × 10⁹ cps, 4.0 × 10⁵ cps, and 2.1 × 10⁶ cps for ¹⁶O, ¹⁷O, and ¹⁸O, respectively. Oxygen isotopic compositions are expressed in δ units as $\delta^{17,18}\text{O} = [({}^{17,18}\text{O}/{}^{16}\text{O})_{\text{sample}}/({}^{17,18}\text{O}/{}^{16}\text{O})_{\text{V-SMOW}} - 1] \times 1,000 \text{ ‰}$ where V-SMOW refers to the Vienna Standard Mean Ocean Water value. The value is defined as $\Delta^{17}\text{O} = \delta^{17}\text{O} - 0.52 \times \delta^{18}\text{O}$. Typical 2 σ measurement errors, accounting for internal

errors on each measurement and the external reproducibility of the standards, were estimated to be $\sim 0.4\text{‰}$ for $\delta^{18}\text{O}$, $\sim 0.7\text{‰}$ for $\delta^{17}\text{O}$, and $\sim 0.7\text{‰}$ for $\Delta^{17}\text{O}$.

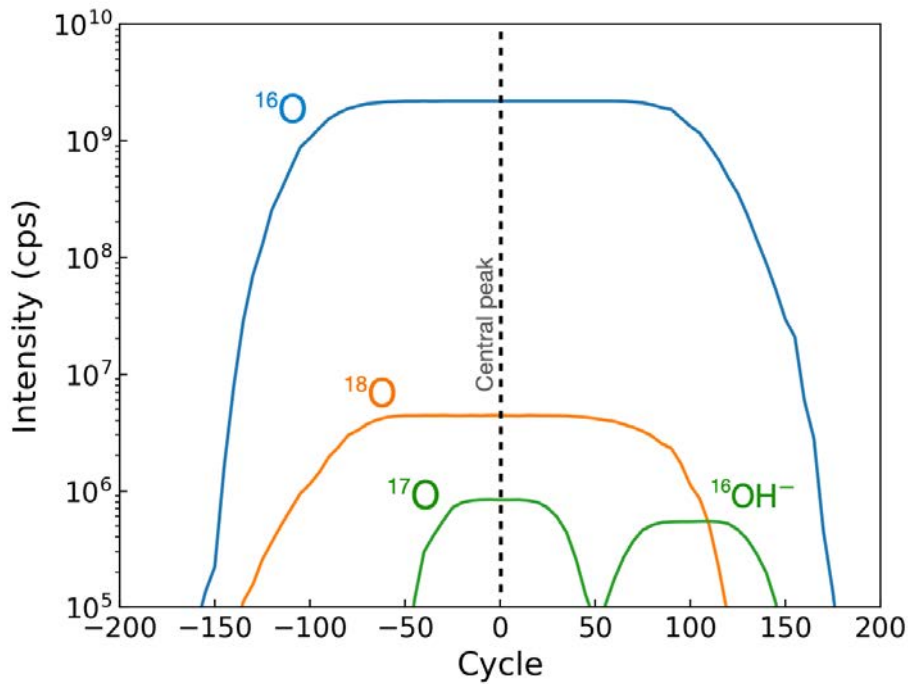


Figure 2.10. Graph of the scan of the three oxygen isotopes in the measured signal of the analysis. The separation of the ^{17}O peak from the $^{16}\text{OH}^-$ hydride was using an MRP of ~ 7000 .

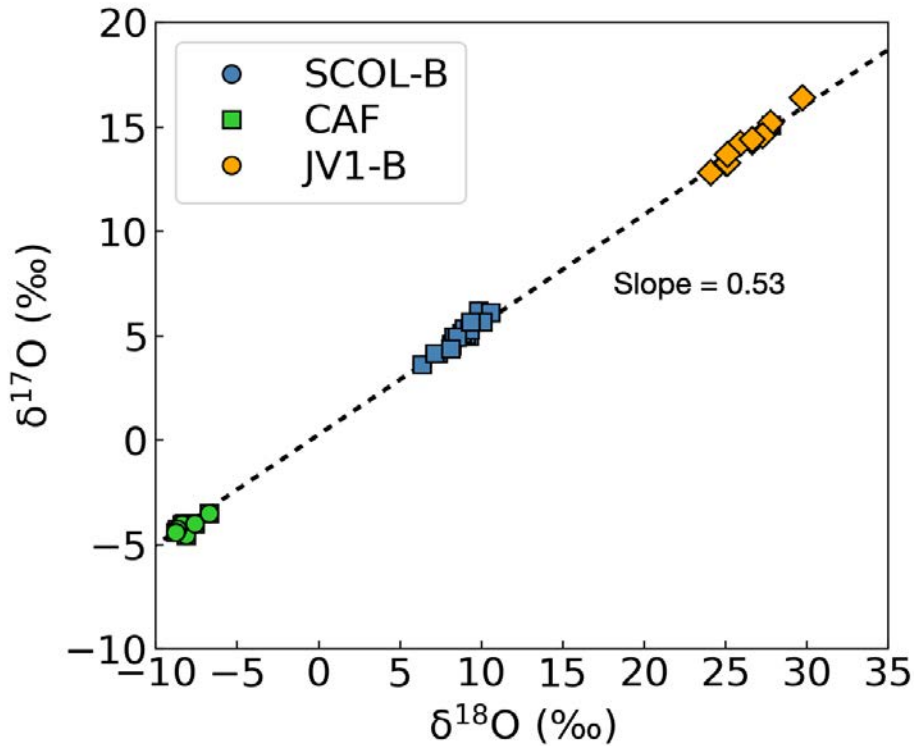


Figure 2.11. The Oxygen three-isotope diagram show the San Carlos olivine (SCOL-B), CAF and JV1 diopside (JV1-B) standards. The terrestrial standards are analyzed to calibrate the TFL of the measured samples.

The Oxygen three-isotope diagram helps determine the isotope fractionation in a nebular environment. Samples with mass dependent fractionation (i.e., kinetic isotope fractionation) follow the V-SMOW composition on a line with a slope of 0.52 (defined as Terrestrial Fractionation Line, TFL; Clayton et al., 1991). In the case of oxygen mass-independent fractionation, the sample is described as the vertical deviations from the TFL in a triple oxygen isotope diagram (**Figure 2.12**).

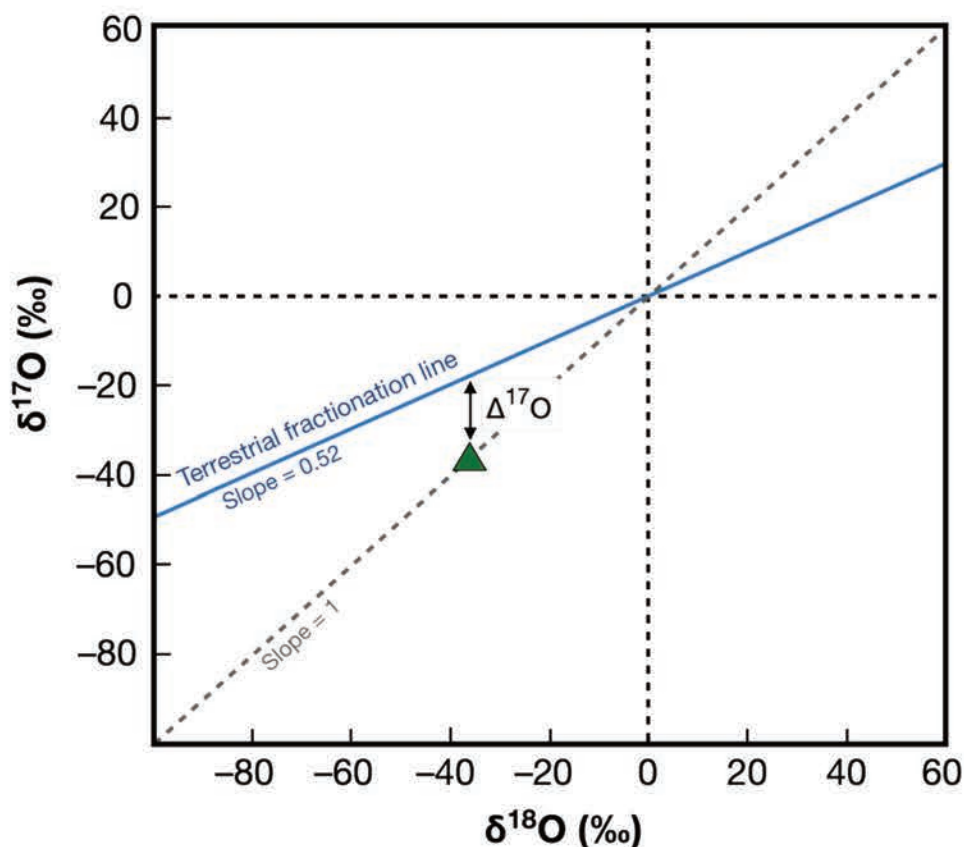


Figure 2.12. The Oxygen three-isotope diagram. Oxygen isotope ratios are referenced to deviations from Vienna Standard Mean Ocean Water (V-SMOW) to generate the delta scale. Mass dependent fractionation related to kinetic isotope mass fractionation lies on the Terrestrial Fractionation Line of slope of approximate $\frac{1}{2}$ (i.e., $\delta^{17}\text{O} = 0.5 * \delta^{18}\text{O}$). The $\Delta^{17}\text{O}$ refers to the deviation of a composition from the mass dependent fractionation line and is expressed as the distance to the Terrestrial Fractionation Line at the given $\delta^{18}\text{O}$ (i.e., $\Delta^{17}\text{O} = \delta^{17}\text{O} - 0.52 * \delta^{18}\text{O}$). For instance, the green triangle at $\delta^{18}\text{O} = -40\text{‰}$ on the slope 1 reference line, the $\Delta^{17}\text{O}$ is -19.2‰ .

2.6 X-ray microtomography

2.6.1. Technical description

X-Ray microtomography, also called micro CT, is a non-destructive technique that allows the reconstruction of the internal structure of a three-dimensional object by radiographic 3D images at a spatial resolution better than 1 micrometer. The micro CT combines information from a series of 2D X-ray images recorded while the object is rotated about a single axis (**Figure 2.13**). The main instruments required for acquiring 2D radiographs are (i) scintillation, to convert the X-rays to visible light, and (ii) photodetectors, to produce a digital image.

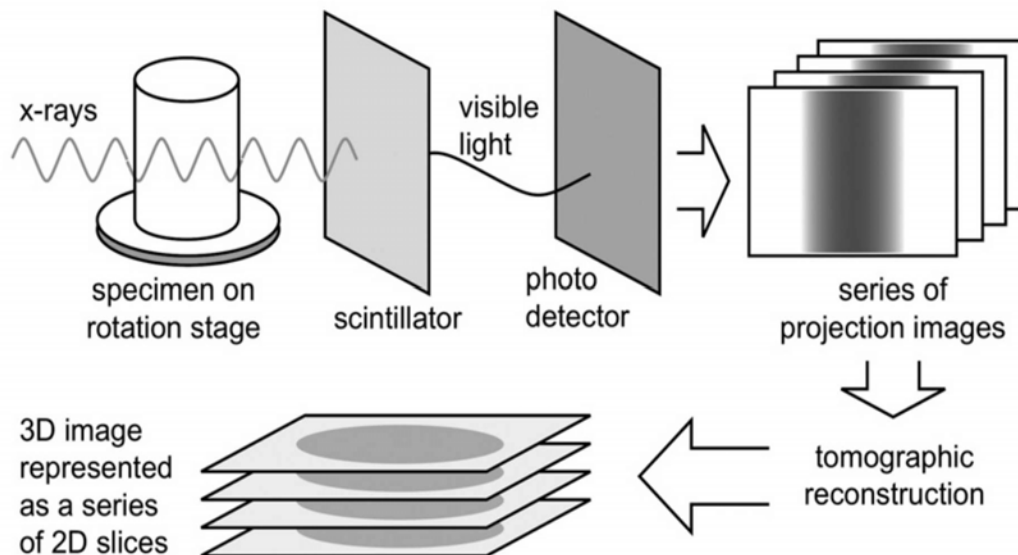


Figure 2.13. Sketch of micro CT acquisition and reconstruction data processes. A series of X-ray projection images are acquired and mathematically reconstructed to produce a 3D map of X-ray absorption in the sample volume. 3D image is commonly represented as a series of 2D slice images (virtual images). From Landis and Keane (2010).

The cross-sectional images, also called virtual slices, are reconstructed from the measurement of the X-rays attenuation passing through the sample. Thus, it depends on the attenuation (absorption) of light that passes through the material, which is a logarithmic function of each material's absorption capacity and the light's travel distance (Landis and Keane, 2010). The reconstruction of a 3D digital image from a series of 2D projections is a mathematical principle of tomography performance, which depends on each material's X-ray attenuation (Landis and Keane, 2010 for further details). The produced three-dimensional digital image consists of voxels, the volume element or 3D pixel representing each X-ray

absorption at that point. As the X-ray attenuation is proportional to the density of the local electron, it is possible to obtain qualitative information from the material composition by a threshold of black and white. For a fixed X-ray photon energy, lower-Z (fewer electrons, e.g., Si) elements absorb less than higher-Z (e.g., Fe) elements which are represented in the sample as dark and bright phases, respectively (**Figure 2.14**).

The spatial resolution of the micro CT is constrained by the geometry and size of the X-ray beam, section shape, and characteristics of the detector. For instance, a smaller spot size produces a more accurate projected image.

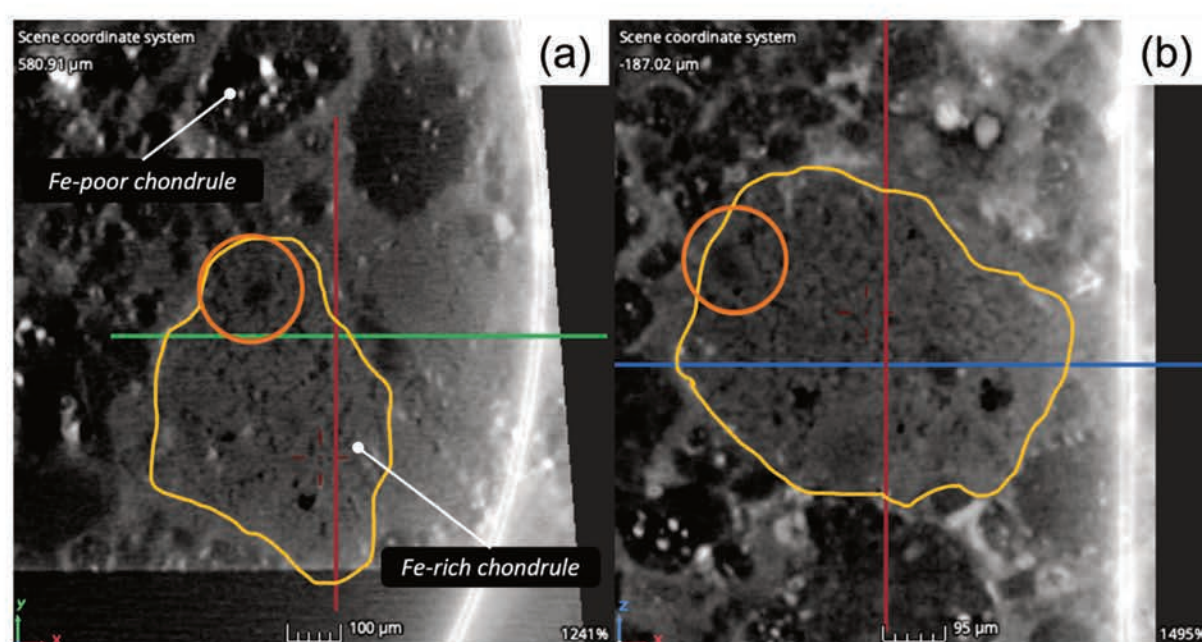


Figure 2.14. X-ray microtomography images of the relict-bearing type II chondrule in LoV 123 (CO3). Both images show a 2D slides of the chondrule Ch_20 in the xy axis (a) and the xz axis (b). The Mg-rich relict is indicated with an orange circle.

2.6.2. Chondrule analysis

We used X-Ray CT to estimate the volumetric abundance of relict-bearing type II chondrules and their volume fractions of relict and host olivine grains in one thick section of LoV 123 (CO3.05) and one fragment piece of NWA 5206 (L3.05). X-Ray images were recorded while the sample was rotating, step by step, over 360° along its vertical axis. We used a Ge-Phoenix Nanotom S 180 scanner using a nanofocus X-ray tube at the GeoRessources Laboratory (University of Lorraine, France). Virtual cross-sections from all axes were extracted from the 3D volume to observe the physical structure (e.g. inclusions and porosity) and to detect

the presence of phases with different densities. The Nanotom scanner produces files with voxel (3D pixel) resolutions between 30 and 0.6 μm as a function of sample sizes. The CT-scan settings for LOV 123 and NWA 5206 were 120 kV and 120 μA , with resolution set at 15.5 μm per Voxel. This setting was adjusted according to the material density to achieve the best resolution and contrast between the material composition in the section. After acquiring the virtual images, the first and the last images were compared by applying a displacement coefficient to correct the possible dislocation effect in the section.

The virtual images were analyzed by MyVGL and VGStudio MAX 2.2 image processing software. These software packages are employed to visualize voxel data. The result internal structure of the scanned sample is encoded in a series of 2D slices with 16 bits per pixel. The reconstruction area is defined by a region of interest (ROI), which is applied volume filters to the images to optimize the quality. We applied a "Gauss Radius" filter with an adaptive-contrast correction filter to make as large as possible the histogram of gray values. In order to distinguish the different components of the material, we used: (i) Defect detection modules to allow the measurement of distances, including a gray value profile view, surface areas, and volumes; (ii) ROI selection to create modes and modify masks of a zone of interest. We used a manual selection to extract and analyze irregular chondrule and relict shapes in 2D and 3D images; (iii) a volume analyzer to calculate the various properties of the voxels in the selected volume or ROI as sphericity and roundness (**Figure 2.15**).

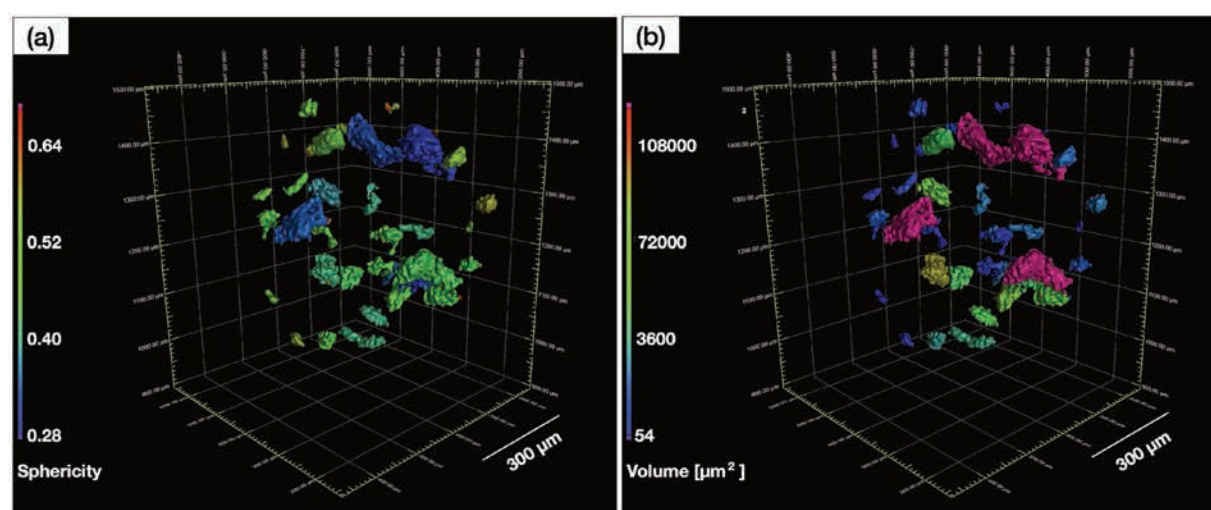


Figure 2.15. X-ray microtomography of relicts in the Ch_01 type II chondrule from LoV 123 (CO3). The sphericity (a) and volume (b) are shown for each relict in the chondrule. The relict selection starts with a black and white threshold to delimitate the Mg-rich borders, which are subsequently corrected by hand selection in each virtual image.

2.7 Particle size analysis

The particle size distribution of chondrules and their related structures (e.g., relict and accretionary rims) were performed using the *Fiji* version of ImageJ open-source software for image processing. *Fiji* introduces powerful software libraries for rapid transfer from new algorithms to practical image-analysis tools using a simple user interface (more details in Schindelin et al., 2012).

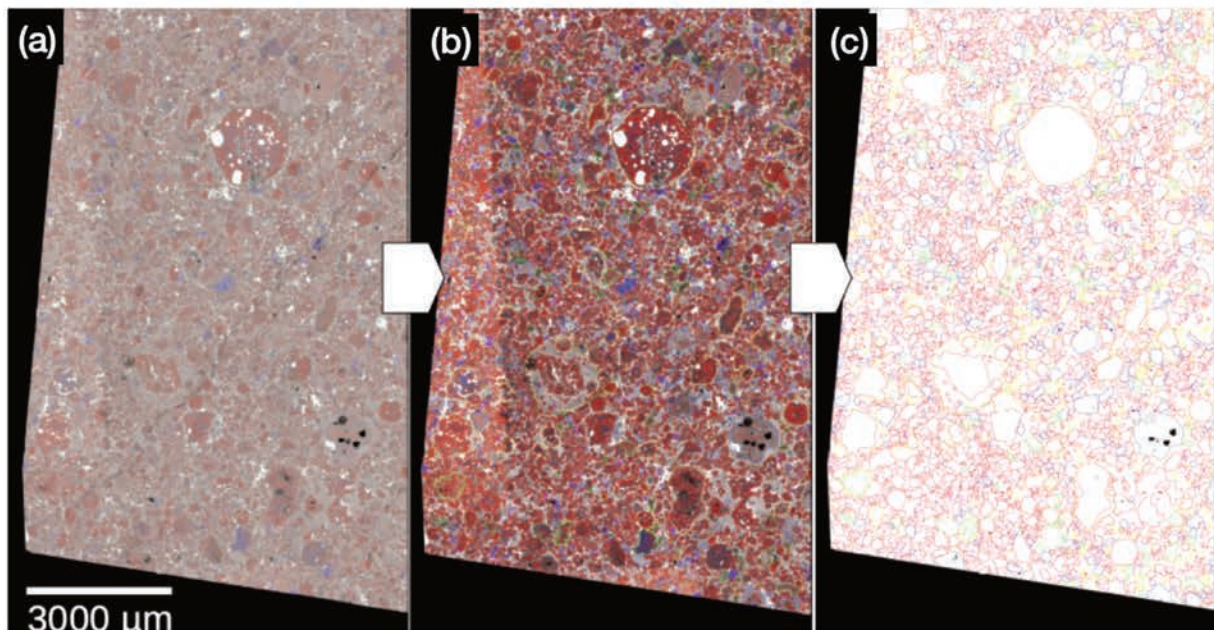


Figure 2.16. Particle analysis processes. A) X-ray compositional map of EM 463, with Mg, Al, Ca and Fe as red, blue, green and white. B) compositional map using a mean filter and enhanced contrast function in Fiji/ImageJ software. C) Mask layer of free-hand selected particles showing the colored outlines.

We analyzed all nebular components, including chondrules (types I and II being FeO-poor and rich, respectively), calcium aluminum-rich inclusions (CAIs, types A and B), amoeboid olivine aggregates (AOAs), and isolated olivine grains (IOGs) over total surface areas of 96 mm², 27 mm², 32.4 mm², and 30.6 mm² for EM 463, EM 216, LoV 123, and Isna, respectively. Also, we examined representative areas of 95.9, 134.2, 27, 32.4, and 186.9 mm² in EM 463, EM 397, EM 216, LoV 123, and Vigarano, respectively, and the total section areas of 266, 239, and 58.4 mm² in Paris, Renazzo, and DaG 574, respectively, to selected 162 rim-bearing chondrules. The Free-hand tracing recorded each particle in a mask layer (**Figure 2.16**). The sharpness and continuity of the borders in the X-ray compositional maps were improved in Fiji by first applying a mean filter at 1 pixel and then enhancing the image contrast at 0.5%. The

estimation of the uncertainty was performed by five replicate tracing iterations of 13 chondrules perimeter (more details see Chapter 4). Each particle diameter was calculated assuming that their total area was a circular cross-section using the following equation (**Figure 2.17**):

$$\text{Diameter} = \sqrt{\frac{\text{pixel area}}{\pi}} \times 2 \quad \text{Eq. 2.3}$$

As the nebular components are not perfectly circular, we determined physical parameters of each component such as roundness, circularity and aspect ratio. These three physical parameters are shown in **Figure 2.18** for type I and II chondrules in LoV 123, EM 216 and EM 463. This information indicates the shape of the chondrules that are modified for the Eq. 2.3.

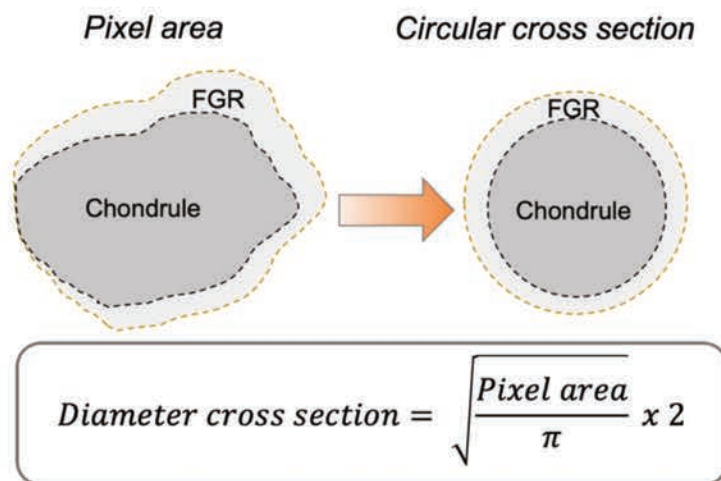


Figure 2.17. Sketch of methodology applied to determine the particle diameter and the fine-grained rim (FGR) thickness of rim-bearing chondrules.

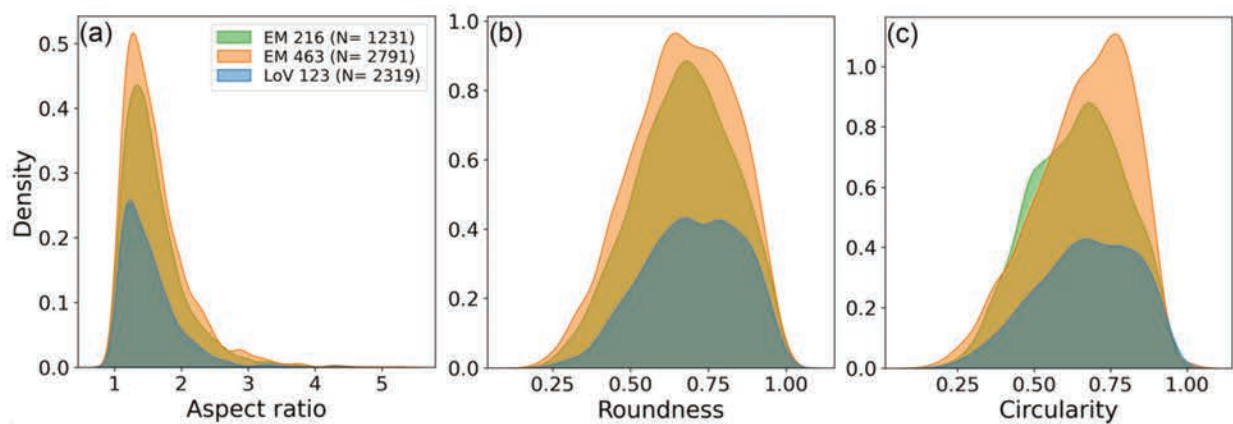


Figure 2.18. Probability density function of three physical parameters in chondrules: Aspect ratio (a); Roundness (b); and circularity (c).

Chapter 3

**Deciphering recycling
processes during solar
system evolution from
relict olivine grains in type
II chondrules**

Chapter introduction

We determine the major and minor elements and O-isotopic composition of Fe-poor relict grains in type II chondrules from CO and CR carbonaceous and one ordinary chondrites. Compared with published O-isotopes data of type I chondrules we reported evidence of the (i) conditions of type II chondrules formation and (ii) provenances of their Fe-poor relict grains. Due to the high thermal metamorphism of the ordinary chondrite (3.5 to 3.7), its data should not be directly compared to CO or CR carbonaceous chondrites. Optical microscope, Secondary Electron Microscope (SEM), electron probe microanalyzer (EMPA) and Secondary Ion Mass Spectrometry (SIMS CAMECA 1280 HR) were employed for this study. Mg-rich relicts in type II chondrules almost always plot in the range of O-isotopic composition of host olivines in type I chondrules ($\Delta^{17}\text{O} = -5\text{‰}$, -2.5‰ and 2‰ for CO, CR and ordinary chondrites). Besides, minor elements composition in Mg-rich relicts tend to be MnO-poor and slightly CaO-rich similar to the ranges of host grains in type I chondrules. Combining our results with literature data, we show that most forsterite relicts in type II chondrules originate from a previous generation of Mg-rich chondrules.

3.1 Introduction

The evolution of the circumstellar disk led to the formation of solids through a wide range of processes such as evaporation/condensation (Ebel et al., 2018; Varela & Zinner, 2018), fusion/crystallization (Connolly & Jones, 2016; Jacquet & Marrocchi, 2017) and collisional impacts (Marrocchi et al., 2021; Stöffler et al., 2018). The resulting dust provided the main building blocks of asteroids and planets (Johansen et al., 2015; G. A. Pinto et al., 2021), either in the form of refractory inclusions (i.e., CAIs = Calcium-Aluminum-rich Inclusions and AOAs = Amoeboid Olivine Aggregates), chondrules and fine-grained matrix. Thus, the mineralogical, petrographic, and isotopic features of this primordial dust represent a powerful proxy for deciphering the conditions that prevailed in the circumstellar disk.

The early stages of dust growth in the solar protoplanetary disk can be studied by surveying chondrites, primitive rocky meteorites representing fragments of asteroids that never underwent melting. Several studies have revealed a fundamental isotopic dichotomy; carbonaceous (C) chondrites are measurably enriched in many neutron-rich isotopes (e.g., ^{48}Ca ,

^{50}Ti , ^{54}Cr) compared to non-carbonaceous (NC) chondrites (Trinquier et al., 2009; Warren, 2011; Kruijer et al., 2020). This dichotomy reflects the formation of their parent bodies in two genetically distinct, probably contemporaneous (Morbidelli et al., 2022; Spitzer et al., 2021), but spatially separated disk reservoirs. In this framework, C chondrites are considered to have accreted at greater heliocentric distances than NC chondrites, consistent with their higher volatile contents (Vacher et al., 2020).

Chondrules, mm-sized igneous spheroids, are the most abundant high-temperature components of both NC and C chondrites, suggesting that the inner and outer solar system reservoirs were equally affected by chondrule production and/or redistribution. Chondrules were formed by the solidification of melt droplets interacting with the surrounding gas, although the mechanisms that first produced the droplets remain elusive: they may correspond to melted aggregates of nebular dust (Tenner et al., 2018; Marrocchi et al., 2018, 2019, 2022) or by-products of planetary collisions (Johnson et al., 2015; Wakita et al., 2017). The complexity for understanding chondrule formation stands in the fact that chondrules are complex objects whose mineralogy, textures, and chemical and isotopic compositions result from multi-step processes involving precursor recycling, melting event(s) and complex gas-melt interactions (Marrocchi et al., 2018, 2019; Libourel and Portail, 2018; Ebel et al., 2018). In addition, chondrule formation likely took place for a long period of time (i.e., 4 Ma; Bollard et al., 2017; Pape et al., 2019; Villeneuve et al., 2009), in distinct reservoirs and under different conditions during the evolution of the circumsolar disk (Jones et al., 2018).

The most abundant chondrules are ferromagnesian porphyritic chondrules that can be classified to a first order into type I and type II chondrules, depending on oxidation state (Scott & Taylor, 1983). Type I chondrules are more reduced than type II chondrules. This translates into Mg# ($\equiv 100 \times \text{molar ratio Mg}/(\text{Mg}+\text{Fe})$) higher in type I than in type II chondrules. While the limit between type I and type II is arbitrarily defined as Mg# = 90, there is a hiatus between the two types, with only few chondrules with Mg# between 90 and 97 (e.g., Hertwig et al., 2018). Abundant Fe-Ni metal beads, FeO-poor silicates and volatile element depletion characterize type I chondrules whereas their type II counterparts show FeO-rich silicates and more chondritic abundances of moderately volatile elements (e.g., Jacquet et al., 2015).

The recent characterization of the chemical and isotopic composition of relict olivine grains suggests that type I chondrules derived from AOA-like precursors (Schrader et al., 2018; Marrocchi et al., 2018, 2019), in agreement with trace element signatures (Jacquet & Marrocchi, 2017; Ruzicka et al., 2007, 2012). Gas-melt interactions with Mg- and SiO-rich gas are invoked

to account for the (i) isotopic differences observed between AOAs and the resulting chondrules (Ruzicka et al., 2007; Marrocchi et al., 2018, 2019), (ii) mineral chemical zoning in palisadic olivine in PO chondrules (Libourel and Portail, 2018; Marrocchi et al., 2018, 2019) and (iii) formation of low-Ca pyroxene shells in POP and PP chondrules (Chaussidon et al., 2008; Libourel et al., 2006; Tissandier et al., 2002). As to type II chondrules, their oxidized nature compared to their reduced counterparts could result from formation in regions with either higher dust to gas ratios (Schrader et al., 2013) or lower carbon content (Connolly et al., 1994). Recent experiments also proposed a genetic link between both types of chondrules; type II being derived from type I by remelting and oxidation (Villeneuve et al., 2015), which is supported by the Mg-rich relicts reported in type II chondrules among different chondrite groups (Jones, 1996, 2012; Kunihiro et al., 2004, 2005; Schrader et al., 2015; Wasson & Rubin, 2003; Yurimoto & Wasson, 2002).

Oxygen isotopes may provide insights into the formation conditions of both type I and type II chondrules and their potential relationship. First, chondrule isotopic compositions are widely separated from those of (very ^{16}O -rich) AOAs and CAIs, with $\Delta^{17}\text{O}$ ($= \delta^{17}\text{O} - 0.52 \times \delta^{18}\text{O}$) around -30 to -20 ‰ (e.g., Krot et al., 2004). This allows potential relicts from those populations of objects to be recognized, as already done for type I chondrules (e.g., Marrocchi et al. 2018, 2019; Piralla et al. 2021). There is some systematic difference among chondrules themselves depending on the superclan or clan: within C chondrites, type I chondrules, plotting along the Primitive Chondrule Mineral (PCM) line (Ushikubo et al., 2012), commonly show negative $\Delta^{17}\text{O}$ values (typically from -8 to -1 ‰; Tenner et al. 2018; Ushikubo & Kimura, 2020), where $\Delta^{17}\text{O} = \delta^{17}\text{O} - 0.52 \times \delta^{18}\text{O}$ represents vertical deviations from the Terrestrial Fractionation Line (TFL; Clayton et al., 1991) in a triple oxygen isotope diagram. Most chondrules in CO–CM–CV chondrites have $\Delta^{17}\text{O} < -4$ ‰ (Tenner et al., 2018; Ushikubo and Kimura, 2020), i.e., are “type I-CO chondrules” in the terminology of Marrocchi et al. (2022) while most CR chondrules have $\Delta^{17}\text{O} > -4$ ‰ (“type I-CR chondrules” of Marrocchi et al. 2022; see also Schrader et al., 2014; Tenner et al., 2013, 2015). Conversely, type I chondrules of ordinary chondrites show positive $\Delta^{17}\text{O}$ and are generally shifted to the left of the PCM (Kita et al., 2010; Piralla et al., 2021). The oxygen isotopic composition of chondrules also show systematic differences between type I and type II, especially in carbonaceous chondrites, where the former is ^{16}O -richer than the latter (Schrader et al., 2013; Tenner et al., 2015; 2018; Ushikubo and Kimura, 2020).

^{16}O -rich forsteritic olivine grains have been occasionally reported in type II chondrules (Kunihiro et al., 2004; Tenner et al., 2018). The proximity of many such grains with type I chondrules in the same chondrites have suggested that these were relicts of type I chondrules, hence a potential link between type I and type II chondrules. This was also proposed based on the similar large silicon isotopic variations observed within type I chondrules and in Mg-rich olivine relict grains in type II chondrules (Villeneuve et al., 2020). Other relicts have AOA-like compositions (Jones et al., 2002; Schrader et al., 2018; Yurimoto & Wasson, 2002). However, no systematic chemical and oxygen isotopic characterization of Mg-rich relict olivine grains in type II chondrules has been performed. In this study, we report a comprehensive survey of the oxygen isotopic compositions of relict-bearing type II chondrules in CO and CR carbonaceous chondrites as well as in one L ordinary chondrite. We use our data to quantify the conditions of formation of type II chondrules and the origins of Mg-rich olivine grain relicts.

3.2 Material and Methods

We surveyed all chondrules within (i) five thick sections of CO carbonaceous chondrites (three home-made sections: Los Vientos 123 (CO3.05), Catalina 008 (CO3.1) and El Médano 463 (CO \geq 3.2) and one thick section of Isna, section no. 3239sp1, from the Muséum national d'Histoire naturelle, Paris, France), (ii) two thick sections of CR2 carbonaceous chondrites (Renazzo and Dar al Gani 574, sections no. 719sp3 and 3681sp2, respectively; from the Muséum national d'Histoire naturelle, Paris, France) and (iii) one home-made thick section of L3 ordinary chondrites (Los Vientos 098). The petrography and mineralogy of type II chondrules were determined by optical microscopy, backscattered electron (BSE) imaging, and X-ray compositional mapping. For the latter two, we used (i) a Zeiss Evo MA10 equipped with an Oxford X-MAX N 20 SDD energy dispersive spectrometer and operating with a 3 nA electron beam accelerated at 15 kV (Universidad de Atacama) and (ii) a JEOL JSM-6510 scanning electron microscope equipped with a Genesis EDX detector using a 3 nA electron beam accelerated at 15 kV (CRPG-CNRS, Nancy, France).

Twenty type II chondrules were selected with and without apparent Mg-rich relicts: 9 in COs, 5 in CRs and 6 in the ordinary chondrites. Quantitative analyses of Al, Ti, Ca, Cr, Mn, Ni, Mg, Fe, and Si in all olivine grains large enough to be isotopically characterized by SIMS were performed using a CAMECA SX-Five electron microprobe at the CAMPARIS service

(Sorbonne University, Paris, France). The microprobe was calibrated using the following natural and synthetic standards for silicate analyses: diopside (Si, Ca, Mg), orthoclase (Al), MnTiO₃ (Mn, Ti), Cr₂O₃ (Cr), and Fe₂O₃ (Fe). A 20 nA focused beam, accelerated to 15 kV potential difference, was used for spot analyses of olivine with 20 s analysis time. Detection limits in silicates were 0.03 wt% for SiO₂, Al₂O₃, CaO and MgO; 0.04 wt% for MnO and TiO₂, and 0.07 wt% for NiO, Cr₂O₃ and FeO. The PAP software was used for matrix corrections (Pouchou and Pichoir, 1984).

We measured the oxygen isotopic compositions of type II chondrule olivines with different iron contents by SIMS. We used the CAMECA IMS 1270 E7 at the *Centre de Recherches Pétrographiques et Géochimiques* (CRPG-CNRS, Nancy, France). ¹⁶O⁻, ¹⁷O⁻, and ¹⁸O⁻ ions produced by a Cs⁺ primary ion beam (~10 μm, ~2–2.5 nA, rastered over 5 × 5 μm²) were measured in multi-collection mode using three Faraday cups (FCs). To remove the interference of ¹⁶OH⁻ on the ¹⁷O⁻ peak and to maximize the flatness atop the ¹⁶O⁻ and ¹⁸O⁻ peaks, the entrance and exit slits of the central FC were adjusted to obtain mass resolution power (MRP = $M/\Delta M$) of ~7,000 for ¹⁷O⁻. As an additional safeguard against ¹⁶OH⁻ interference, a liquid N₂ trap was used to reduce the pressure in the analysis chamber to <1 × 10⁻⁸ mbar. The two off-axis multicollection FCs, L'2 and H1, were respectively used to measure ¹⁶O⁻ and ¹⁸O⁻ and were set on exit slit 1 (MRP = 2,500). We used 10¹⁰ Ω, 10¹² Ω, and 10¹¹ Ω resistors for the L'2 (¹⁶O), central (¹⁷O), and H1 (¹⁸O) FCs, respectively (see Bouden et al. 2021 for further details). A normal-incidence electron gun was used for charge compensation. Total measurement times were 300 s, comprising 120 s of pre-sputtering and 180 s of analysis. Two terrestrial standards, San Carlos olivine and JV1 diopside, were used to define the mass-dependent fractionation line. The instrumental mass fractionation (IMF) and matrix effect of chondrule olivine grains was corrected using San Carlos olivine and a set of synthetic standard olivine yielding Mg# ranging from 36 to 100 (Villeneuve et al., 2019; 2020). To monitor any instrumental drift and to achieve good precision, the San Carlos olivine was analyzed after every 10–15 sample analyses. Typical count rates obtained on San Carlos olivine were 1.0 × 10⁹ cps, 4.0 × 10⁵ cps, and 2.1 × 10⁶ cps for ¹⁶O, ¹⁷O, and ¹⁸O, respectively. All SIMS analytical spots were checked thoroughly by scanning electron microscopy, and any spot near fractures, in the mesostasis, or not completely within olivine grains was excluded from the dataset. Oxygen isotopic compositions are expressed in δ units as $\delta^{17,18}\text{O} = [({}^{17,18}\text{O}/{}^{16}\text{O})_{\text{sample}}/({}^{17,18}\text{O}/{}^{16}\text{O})_{\text{V-SMOW}} - 1] \times 1,000 \text{ ‰}$ where V-SMOW refers to the Vienna Standard Mean Ocean Water value. Samples related by mass fractionation to the composition

of V-SMOW fall on a line with a slope of 0.52 (defining the Terrestrial Fractionation Line, TFL; Clayton et al., 1991) whereas mass-independent variations are described $\Delta^{17}\text{O} = \delta^{17}\text{O} - 0.52 \times \delta^{18}\text{O}$ (representing vertical deviations from the TFL in a triple oxygen isotope diagram). Typical 2σ measurement errors, accounting for internal errors on each measurement and the external reproducibility of the standards, were estimated to be ~ 0.4 ‰ for $\delta^{18}\text{O}$, ~ 0.7 ‰ for $\delta^{17}\text{O}$, and ~ 0.7 ‰ for $\Delta^{17}\text{O}$.

3.3 Results

3.3.1. Petrography and chemistry

We examined all type II chondrules in the seven thick sections (N = 490) and selected 20 chondrules with minimum evidence of secondary processes to perform detailed chemical and isotopic analysis. Fe-rich chondrules were selected by contrast in the backscatter electron image and Fe-poor relict grains were defined by sharper borders and abrupt FeO and/or Al₂O₃ variation in the chemical profiles. The chondrules are fairly rounded but not, in general, perfectly circular in cross-section. They all display porphyritic texture (except EM463_Ch05), with several subhedral to euhedral Fe-rich olivine grains immersed in a glassy mesostasis (**Figure 3.1**). The maximum apparent diameter of chondrules ranges from 250 to 740 μm , 400 to 750 μm , and 250 to 820 μm in CO, CR, and ordinary chondrites, respectively. Among the 20 Fe-rich chondrules, 15 exhibit Mg-Fe zoning with sharply defined Mg-rich cores (**Figure 3.1**), similar to the relict-bearing chondrules described by Jones et al. (2018). Some relict-bearing chondrule (e.g., LoV123_Ch02) display several relict grains showing Mg diffusion and sharper border inside either larger or smaller Fe-rich olivine grains.

Chondrules in ordinary chondrites display several pre-accretionary fractures, which do not cross to the matrix or another chondrite component (**Figure 3.1c-d**). However, some chondrules (Ch02p and Ch01) evidence a Fe-Mg zoning more consistent with a Fe diffusion via thermal metamorphism than a primary type II feature. In particular, Ch02p is surrounded by Fe-poor pyroxene with Fe zoning along fractures, suggesting a higher petrologic subtype. Although LoV098 is close to subtype 3.1 in the Cr diagram (**Figure 2.6**), it is slightly above the trend defined by other ordinary chondrites (Grossman & Brearley, 2005). Similar Cr abundance has been determined by Ngawi, a breccia of type 3.1 and 3.6/3.7 material.

Furthermore, LoV098 ranges between 3.5 to 3.7 subtypes based on the ordinary chondrite's classification through mafic silicates' mean and standard deviation (Grossman, 2011). Thus, as LoV098 displays chondritic components with higher thermal metamorphism overprints, we cannot consider the oxygen isotopes and chemical composition as primary features.

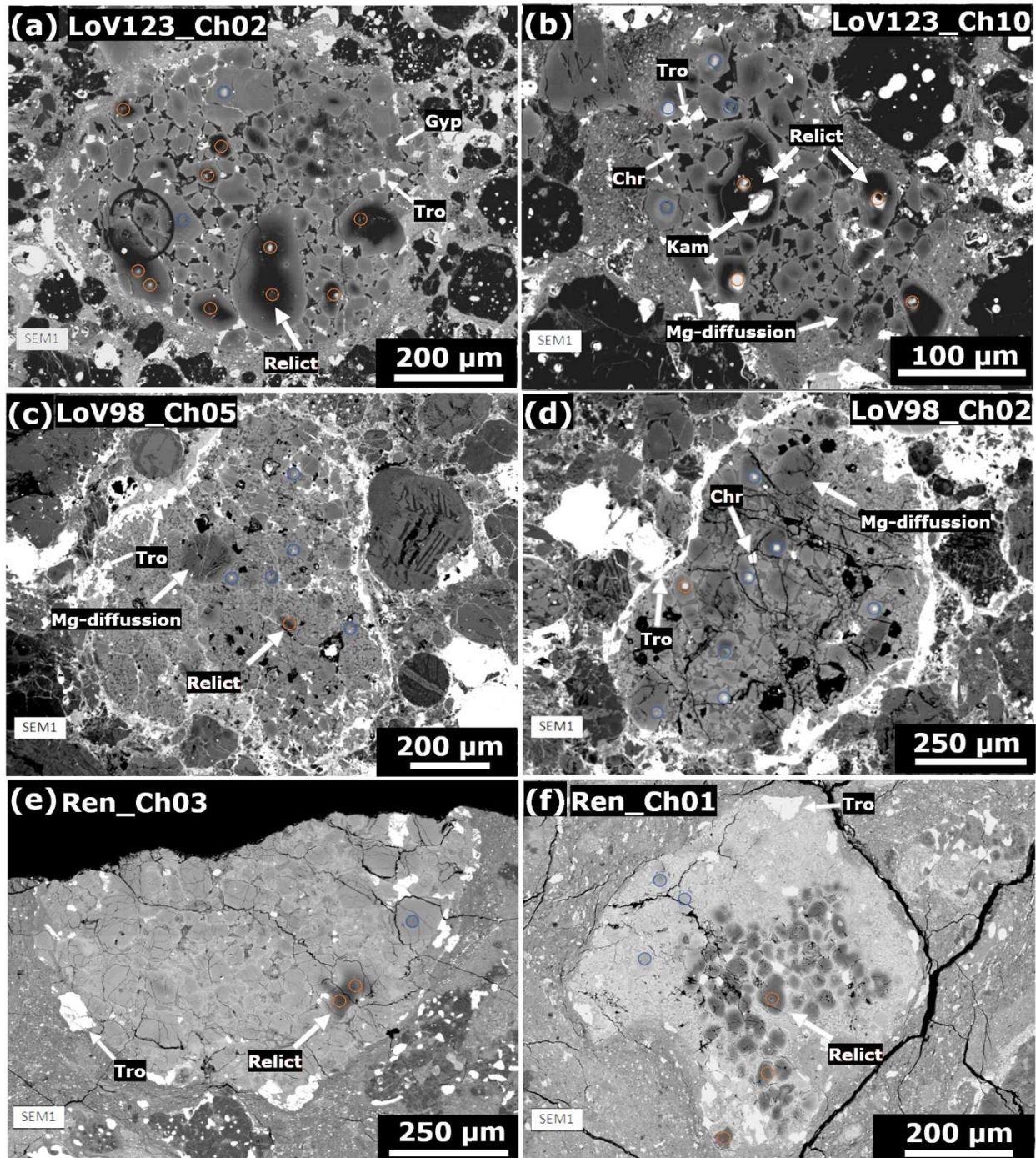


Figure 3.1. Backscattered electron images of relic-bearing type II chondrules from (a-b and g-j) LoV 123 (CO3.05), (c-d) LoV98 (L3.05) and (e-f) Renazzo (CR2.4). LoV123_Ch02 (a) is a relict-bearing chondrule with at least ~12 relict grains showing Mg diffusion and sharper border inside either larger or

smaller Fe-rich olivine grains. LoV123_Ch10 (b) show abundant metal beads in the mesostasis and inside host as well as relict olivines. The central Mg-rich relict crystal contains three metal beads with a roundness shape probably related to their reduced condition of formation. LoV98_Ch05 and LoV98_Ch02 (c-d) are classic agglomerated Fe-rich chondrules in ordinary chondrites. Both are surrounded by a relatively thin layer (~20 μm) of sulfides and metals. (e) Ren_Ch03 is a relatively large porphyritic chondrule with the most ^{16}O -rich relict grain at $\Delta^{17}\text{O} = -7.5$ ‰. (f) Ren_Ch02 display a clusters of Mg-rich olivine phenocrysts whereas each one is surrounded by thin layer of Fe diffusion. Spot analysis in SIMS is indicated as orange and blue circles for relict and host olivines. Tro = Troilite; Kam = Kamacite; Chr = Chromite; Gyp = gypsum.

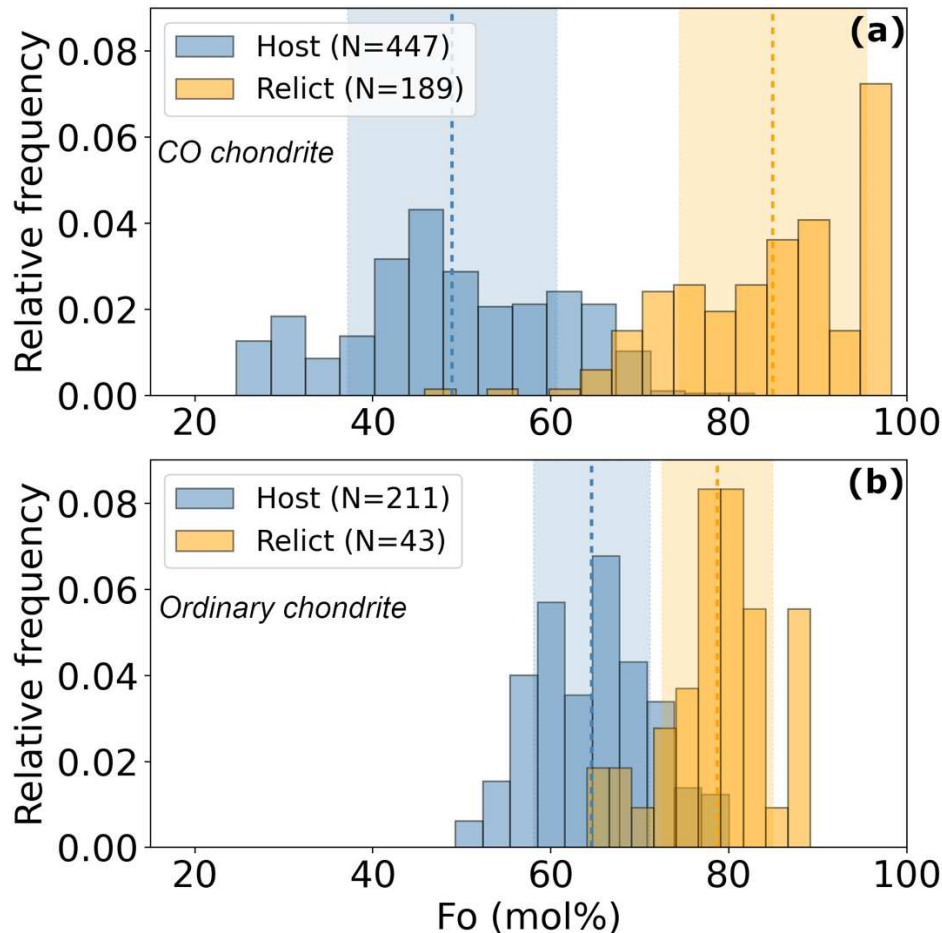


Figure 3.2. Frequency plot of olivine Fo content ($=100 \times \text{Mg}/[\text{Mg} + \text{Fe}]$) for CO carbonaceous (a) and ordinary (b) chondrites. The mean Fo composition of relict and host olivine grains is shown as dotted orange and blue lines, respectively. One sigma of each mean value is shown for reference.

The position of relict grains is random inside the chondrules, and most of them were found as (i) isolated phenocrysts with Fe-rich rims or (ii) clusters of 3 or more phenocrysts, where each grain is surrounded by a Fe-rich mantle (**Figure 3.1a-f**). Troilite and chromite are the main opaque and accessory phases in all described Fe-rich chondrules. They are contained in the mesostasis and display sizes up to 90 μm , except for CR, whose troilite reaches up to 200 μm . Chondrules in ordinary chondrite frequently are surrounded by a thin layer of sulphides

(**Figure 3.1c-d**). Metal beads are also contained into some Mg-rich relict crystal which evidenced a previous formation in reduced conditions (e.g., **Figure 3.1b**).

The mean chemical composition of relicts and host olivine grains among the 20 chondrules is shown in Table 1. The Mg# of olivine grains varies widely in the selected chondrules, from 24.6 to 98.5. It depends on whether the olivine is a relict or host grains (**Figure 3.2**). Host olivine grains in CO, CR, and ordinary chondrites display mean Mg# (\pm standard deviation) of 48.9 ± 11.8 (N = 447), 51.8 ± 6.1 (N = 22), and 64.6 ± 6.5 (N = 211), respectively. Literature values are somewhat higher (~66, 71, and 80 for CO, CR, and ordinary chondrites respectively; Berlin et al., 2011), but this may hinge on our chondrule selection, biased in favor of relict-bearing chondrules, where large phenocrysts are occupied by relicts and host analyses thus confined to (more ferroan) overgrowths of large phenocrysts or small phenocrysts. As expected, relict olivine grains are more forsteritic, with mean Mg# of 85.0 ± 10.6 (N = 189), 84.3 ± 12.9 (N = 15), and 78.7 ± 6.2 (N = 43) for CO, CR, and ordinary chondrites.

Commonly, Mg-rich relicts in type II chondrules are MnO-poor, Al₂O₃-rich and slightly CaO-rich compared to their host olivines (**Table 3.1**). Also, host olivines in type II chondrules from CR and ordinary chondrites show the highest MnO contents (0.5 and 0.4 wt%, respectively) compared to all the olivine phases in type I and II chondrules. Normally, relicts in CO and ordinary chondrites exhibit a wider range of Cr₂O₃ content (from 0.1 to 0.7) compared to the relicts in CR chondrites (from 0.2 to 0.6). Also, host olivine grains among carbonaceous and non-carbonaceous chondrites track a different path in the diagram of FeO/MnO vs. FeO/MgO (**Figure 3.3**).

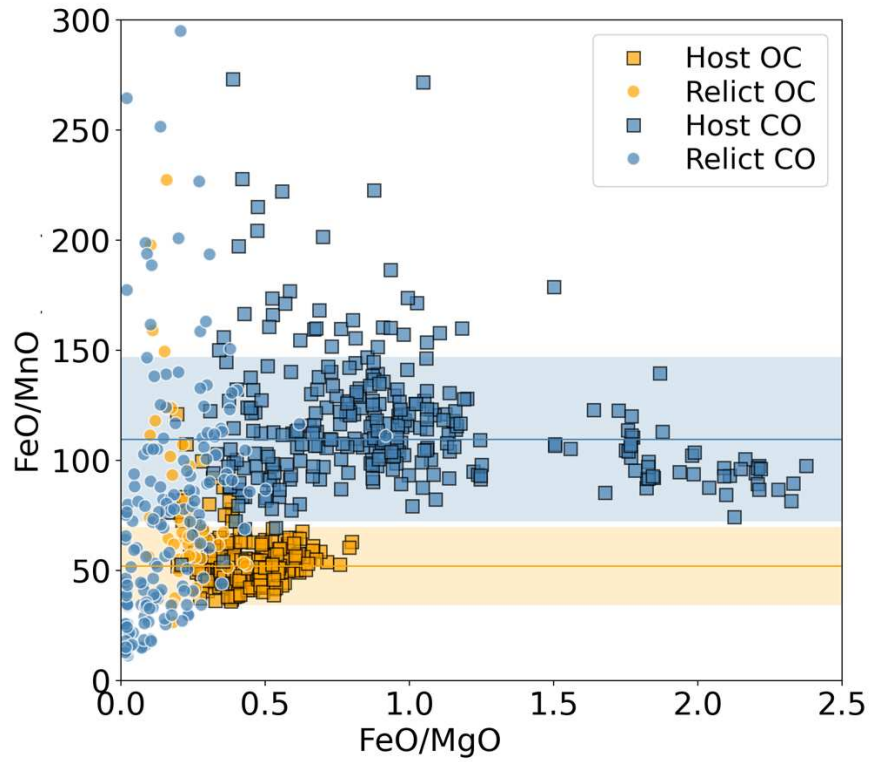


Figure 3.3. Difference trends of relicts and host olivine grains in CO, CR, and ordinary type II chondrules by FeO/MgO versus FeO/MnO ratios (b). The mean composition of host grains (\pm one sigma) in ordinary and carbonaceous chondrites is indicated by an orange and blue lines, respectively.

Table 3.1. Mean major and minor composition of 982 spot analysis in host and relict olivine grains among the 20 studied FeO-rich chondrules.

Class	Meteorite	Chondrule	Grain type	N	Mg# (mol%)	MgO	Al ₂ O ₃	SiO ₂	CaO	TiO ₂	Cr ₂ O ₃	MnO	FeO		
CO	<i>LoV123</i>	<i>Ch_02</i>	Host	82	51.66	35.52	0.08	37.64	0.35	0.01	0.34	0.23	26.00		
			Relict	53	82.78	50.29	0.07	41.34	0.25	0.04	0.37	0.16	8.27		
		<i>Ch_12</i>	Host	44	49.40	33.93	0.14	37.03	0.47	0.01	0.30	0.24	27.40		
			Relict	20	87.83	52.17	0.09	41.59	0.41	0.03	0.33	0.09	5.92		
		<i>Ch_03</i>	Host	72	45.09	31.63	0.15	36.56	0.50	0.02	0.26	0.27	30.04		
			Relict	23	72.86	46.04	0.03	39.72	0.34	0.02	0.27	0.14	13.40		
		<i>Ch_10</i>	Host	22	42.87	30.00	0.28	36.00	0.45	0.02	0.37	0.23	31.22		
			Relict	14	90.20	52.33	0.11	41.74	0.33	0.04	0.49	0.04	4.49		
		<i>Ch_11</i>	Host	49	29.54	22.05	0.01	34.34	0.18	b.d.	0.27	0.42	40.98		
			Relict	7	84.77	50.41	0.07	40.69	0.23	0.04	0.29	0.14	7.32		
		CO	<i>Cat 008</i>	<i>Ch_02</i>	Host	108	51.32	34.98	0.07	37.49	0.22	0.01	0.18	0.28	26.40
					Host	50	48.16	33.62	0.06	37.21	0.17	0.01	0.14	0.23	28.57
					Relict	20	84.62	51.20	0.10	41.63	0.37	0.05	0.13	0.08	7.47
		CO	<i>EM463</i>	<i>Ch_05</i>	Host	41	52.77	35.85	0.13	37.95	0.17	0.01	0.16	0.25	25.33
					Relict	52	88.64	52.40	0.17	41.67	0.39	0.05	0.14	0.07	5.36
		CO	<i>Isna</i>	<i>Ch_01</i>	Host	22	55.40	38.04	0.22	38.96	0.33	0.07	0.11	0.17	23.93
					Relict	12	84.37	51.51	0.34	42.20	0.42	0.09	0.09	0.05	7.50
		OC	<i>LoV 098b</i>	<i>Ch_02</i>	Host	54	59.35	38.79	0.03	37.92	0.20	b.d.	0.32	0.37	20.71

		Relict	13	72.26	44.80	0.04	39.21	0.16	0.01	0.41	0.26	13.42
	<i>Ch_01</i>	Host	27	68.66	43.47	0.09	38.97	0.26	0.03	0.11	0.27	15.44
		Relict	15	79.94	48.74	0.08	40.26	0.30	0.03	0.10	0.11	9.50
	<i>Ch_02p</i>	Host	42	70.52	44.15	0.10	39.01	0.20	0.04	0.12	0.30	14.37
		Relict	10	78.47	47.74	0.10	39.93	0.30	0.04	0.11	0.18	10.18
	<i>Ch_01p</i>	Host	49	62.83	40.89	0.02	38.40	0.06	b.d.	0.08	0.40	18.81
	<i>Ch_05</i>	Host	38	64.78	41.39	0.04	38.75	0.18	b.d.	0.41	0.32	17.60
		Relict	6	88.21	52.03	0.16	41.02	0.41	0.02	0.50	0.05	5.39
CR	<i>Renazzo</i>											
	<i>Ch_01</i>	Host	4	52.17	35.76	0.01	37.50	0.26	0.02	0.41	0.31	25.52
		Relict	3	93.94	54.93	0.02	41.96	0.32	0.03	0.35	0.11	2.75
	<i>Ch_02</i>	Host	3	53.29	36.07	0.02	37.44	0.19	0.04	0.46	0.37	24.54
		Relict	4	81.57	49.41	0.03	41.02	0.23	0.01	0.55	0.27	8.77
	<i>Ch_03</i>	Host	3	46.16	32.38	0.02	36.86	0.26	0.01	0.38	0.43	29.30
		Relict	3	83.45	49.82	0.08	41.41	0.36	0.06	0.30	0.13	8.28
	<i>DaG 574</i>											
	<i>Ch_01</i>	Host	4	55.97	37.99	0.05	38.25	0.23	0.01	0.44	0.24	23.24
		Relict	2	69.09	44.43	0.08	39.39	0.23	0.07	0.39	0.11	15.42
	<i>Ch_02</i>	Host	5	54.17	37.16	0.04	38.11	0.17	b.d.	0.42	0.40	24.58

b.d.: below detection limit

3.3.2. Oxygen isotopes

We performed a total of 128 O-isotopic measurements of relicts and host grains in which 36, 26, and 66 spots were made in ordinary, CR, and CO chondrites, respectively (**Table 3.2**). The olivine O-isotopic composition in CO, CR, and ordinary chondrites ranges respectively from -13.1 to $+15.2$ ‰, -11.3 to $+8.1$ ‰, and -0.9 to $+10.6$ ‰ for $\delta^{18}\text{O}$; and from -14.2 ‰ to $+5.8$ ‰, -13.1 ‰ to $+4.4$ ‰, and -1.21 ‰ to $+7.5$ ‰ for $\delta^{17}\text{O}$. $\Delta^{17}\text{O}$ ranges from -7.7 ‰ to $+2.3$ ‰. In the three-isotope diagram (**Figures 3.5**), our data show a good correlation with the PCM line proposed by Ushikubo et al. (2012).

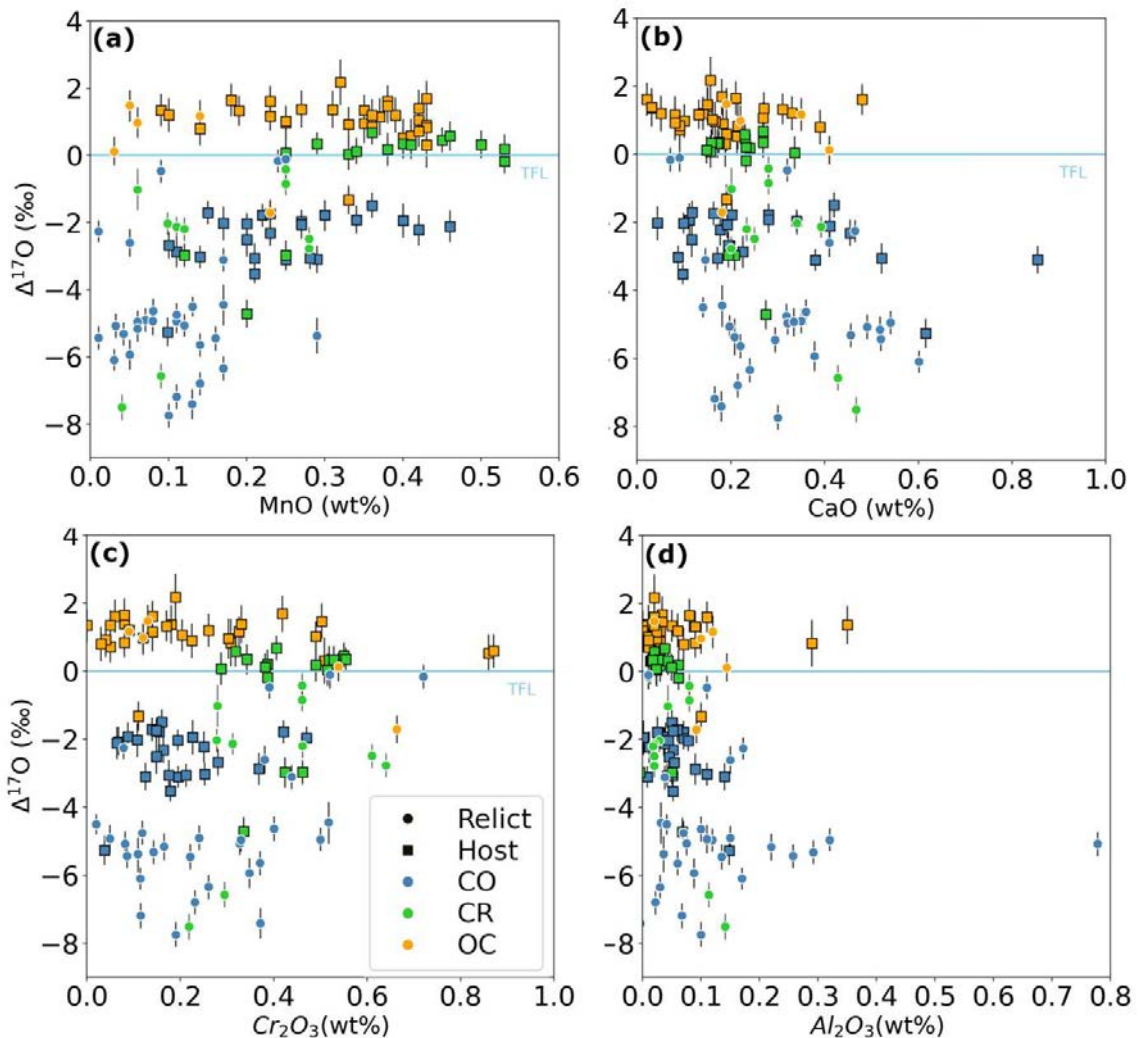


Figure 3.4 Elemental compositions of the studied olivine grains. The plots show $\Delta^{17}\text{O}$ values vs. MnO (a), CaO (b), Cr_2O_3 (c), and Al_2O_3 (d). The circle and square symbols indicate relict and host olivine grains in the type II chondrules. Reference lines are Terrestrial Fractionation (TFL; Clayton et al., 1991).

Only relict grains in Fe-rich chondrules from CO ($\Delta^{17}\text{O} = -6 \text{ ‰}$) show wide distribution of Fa content (Fa = 1.8 to 41.8 mol%). Most relicts in CR chondrites and significant data on CO chondrites display Fa values < 10 mol%, that is, in type I compositional territory (**Figures 3.3 and 3.4**). In the case of ordinary chondrite, no relict grains showed Fa composition in that range.

Several relict olivine grains are ^{16}O -rich compared to those in their Fe-rich host phenocrysts (**Figure 3.6**). However, 43.8% of them (7 over 16 relict bearing chondrules) show an overlap or similar O-isotopes signature. Only one relict grain in the biggest phenocryst of LoV123_Ch02 (**Figure 3.1a**) shows the opposite relation to its host. There are some tendencies for host grains to be isotopically uniform within each chondrule, but there are three exceptions, LoV098-Ch02p, Ren_Ch01 and DaG574_Ch01 (**Figure 3.6**). In the former two, the exception is restricted to one outlying ^{16}O -rich grain ($\Delta^{17}\text{O} = -1.32$ and -2.97 ‰ , respectively). In the latter, three Fe-rich “host” grains show three distinct $\Delta^{17}\text{O}$ values (-4.7 , -3.0 and 0.5 ‰ ; **Figure 3.6**). Two of them may thus be isotopic relicts in the sense of Ushikubo et al. (2012) but no longer recognizable in Mg# owing to the more rapid diffusion of Fe compared to O in olivine (Chakraborty, 2010).

Generally, Mg-rich relicts among CO, CR, and ordinary chondrites overlap the oxygen isotopic composition of relict and host olivine grains in type I chondrules (**Figure 3.7**; Marrocchi et al., 2018, 2019, 2022; Tenner et al., 2013, 2015; Chaumard et al., 2018). In particular, all relicts in CR chondrites plot at about -6 ‰ or -2 ‰ for $\Delta^{17}\text{O}$ values similar to the two generations of type I CR chondrules (“type I-CO” and “type I-CR”) described by Marrocchi et al. (2022), with the most ^{16}O -rich grain found in chondrule Ren_Ch03 with a mean $\Delta^{17}\text{O}$ value of $-7.5 \pm 0.4 \text{ ‰}$. The isotopic compositions do not show any correlation with size or location within chondrules.

We found five relict grains in LoV 098 (L3.1), with one Mg-rich olivine below the TFL ($\Delta^{17}\text{O} = -1.71 \pm 0.4 \text{ ‰}$) and a host olivine with negative values ($\Delta^{17}\text{O} = 1.32 \pm 0.42 \text{ ‰}$). The relict and host olivine grains in the ordinary chondrites display little $\Delta^{17}\text{O}$ variation (standard deviation = 0.8 ‰), similar to data by Kita et al. (2010) for OC chondrules at large, and to the host olivine grains in type I chondrules previously described by Piralla et al. (2021).

The mean $\Delta^{17}\text{O}$ values of relict grains in CO, CR, and ordinary chondrites are -4.7 , -2.8 , and $+0.4 \text{ ‰}$, which are lower than the mean $\Delta^{17}\text{O}$ values in type II olivine hosts: -2.6 , -0.5 , and $+1.1 \text{ ‰}$ for CO, CR, and ordinary chondrites, respectively. Analogous difference of

the mean $\Delta^{17}\text{O}$ values have been reported between relict and host grains in type I chondrules for CR (-5.2 and -3.4 ‰; Marrochi et al., 2022) and ordinary chondrites (-7.7 and +0.8‰; Piralla et al., 2021). The latest indicate a larger $\Delta^{17}\text{O}$ difference between relict and host grains from type II chondrules (**Figure 3.7, 3.8 and 3.9**). However, Tenner et al. (2013) reported similar mean $\Delta^{17}\text{O}$ values in relicts (-4.6 ‰) and host (-4.8 ‰) in CO chondrites.

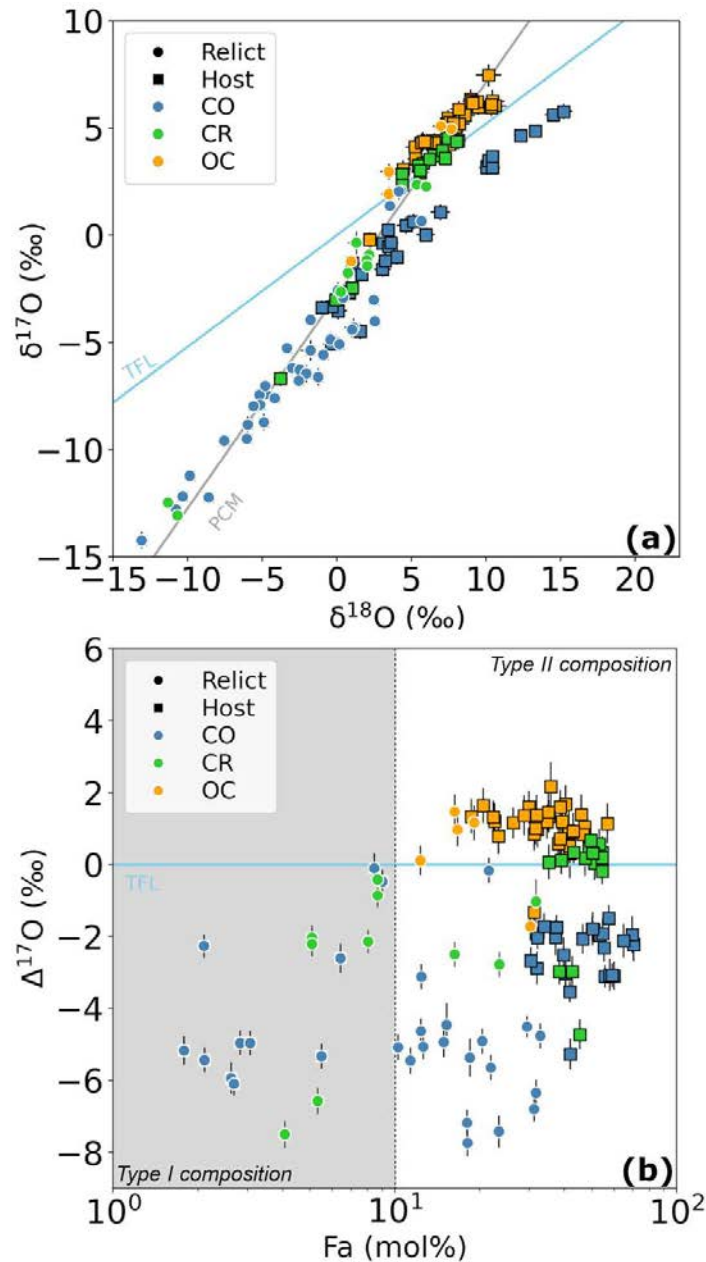


Figure 3.5. (a) Triple oxygen isotope plot of the olivine crystals in the twenty analyzed Fe-rich chondrules. Relict grains show mass-independent variations plotting along the Primary Chondrule Mineral (PCM) line. The host olivine grains in Cat08_Ch02 (CO chondrites) show mass-dependent variation indicated by a parallel slope to the Terrestrial Fractionation Line (TFL; Clayton et al., 1991). (b) Olivine Fa content ($=100 \times \text{Fe}/[\text{Mg} + \text{Fe}]$) is plotted in log scale against $\Delta^{17}\text{O}$ values ($= \delta^{17}\text{O} - 0.52 \times \delta^{18}\text{O}$). The estimated composition of type I and type II chondrules is shown for reference.

Table 3.2. Compilation of mean Mg#s and oxygen isotope ratios of 128 spot analysis in the 20 FeO-rich chondrules from LoV 123 (CO3.05), Cat 008 (CO3.1), EM 463 (CO3.2), Isna (CO3.7), LoV 098 (L3.1), Renazzo (CR2.4), and DaG 574 (CR2) ordinary and carbonaceous chondrites. $\delta^{17}\text{O}$ and $\delta^{18}\text{O}$ are relative to VSMOW (Vienna Standard Mean Ocean Water).

Class	Chondrite	Chondrule	Olivine grain	N analyses	$\delta^{18}\text{O}$ (‰)	2σ	$\delta^{17}\text{O}$ (‰)	2σ	$\Delta^{17}\text{O}$ (‰)	2σ	Mg# (mol%)		
CO	LoV123	Ch02	Relict	10	-2.27	0.31	-4.94	0.33	-3.75	0.37	84.74		
			Host	2	2.03	0.33	-0.81	0.29	-1.87	0.33	48.29		
		Ch03	Relict	5	-7.96	0.37	-10.12	0.32	-5.98	0.38	69.62		
			Host	3	2.56	0.39	-0.97	0.29	-2.30	0.35	43.91		
		Ch10	Relict	5	1.48	0.43	-3.14	0.35	-3.91	0.42	94.61		
			Host	3	2.17	0.60	-2.53	0.35	-3.66	0.47	45.09		
		Ch11	Relict	2	-5.26	0.40	-8.34	0.34	-5.61	0.40	87.39		
			Host	2	4.12	0.58	0.06	0.38	-2.08	0.49	30.16		
		Ch12	Relict	7	-1.13	0.36	-5.25	0.33	-4.67	0.38	93.97		
			Host	1	1.50	0.41	-2.14	0.34	-2.92	0.40	61.91		
		Cat008	Ch02	Host	8	12.04	0.49	4.31	0.30	-1.95	0.40	53.85	
				Ch04	Relict	3	-8.50	0.31	-10.34	0.29	-5.92	0.33	83.31
					Host	3	-1.44	0.32	-3.95	0.27	-3.20	0.32	53.06
		EM463	Ch05	Relict	6	-2.04	0.45	-6.37	0.34	-5.31	0.41	89.51	
				Host	2	6.02	0.67	0.87	0.36	-2.26	0.50	61.63	
		Isna	Ch01	Relict	3	1.69	0.38	-4.29	0.35	-5.17	0.40	79.28	
Host	1			-0.93	0.40	-5.56	0.29	-5.07	0.36	89.74			
CR	Renazzo	Ch01	Relict	3	1.61	0.35	-1.28	0.28	-2.12	0.34	93.94		
			Host	3	3.75	0.55	1.10	0.35	-0.85	0.45	50.71		
		Ch02	Relict	4	3.40	0.36	0.14	0.29	-1.63	0.35	85.73		
			Host	2	6.78	0.47	3.85	0.41	0.32	0.43	52.03		
		Ch03	Relict	2	-11.02	0.36	-12.76	0.32	-7.03	0.37	95.31		

		Host	1	4.36	0.49	2.85	0.36	0.58	0.44	46.87
	<i>DaG574</i>	<i>Ch01</i>	Relict	1	1.30	0.61	-0.35	0.53	-1.02	68.32
			Host	4	2.79	0.43	-0.21	0.30	-1.66	55.97
		<i>Ch02</i>	Host	6	6.41	0.47	3.48	0.34	0.15	52.74
<i>OC</i>	<i>LoV098</i>	Host	3	7.72	0.56	5.55	0.37	1.54	0.47	76.95
		<i>Ch02</i>	Relict	1	0.96	0.45	-1.21	0.32	-1.71	69.76
			Host	7	8.17	0.51	5.46	0.40	1.22	63.05
		<i>Ch03</i>	Host	5	6.35	0.65	4.55	0.43	1.24	58.84
		<i>Ch05</i>	Relict	1	3.47	0.50	1.93	0.33	0.12	87.72
			Host	5	9.38	0.80	5.84	0.49	0.97	58.07
		<i>Ch01p</i>	Host	6	9.02	0.56	5.77	0.39	1.08	63.08
		<i>Ch02p</i>	Relict	1	3.48	0.59	2.97	0.37	1.17	80.88
			Host	5	4.74	0.51	3.04	0.38	0.57	73.44

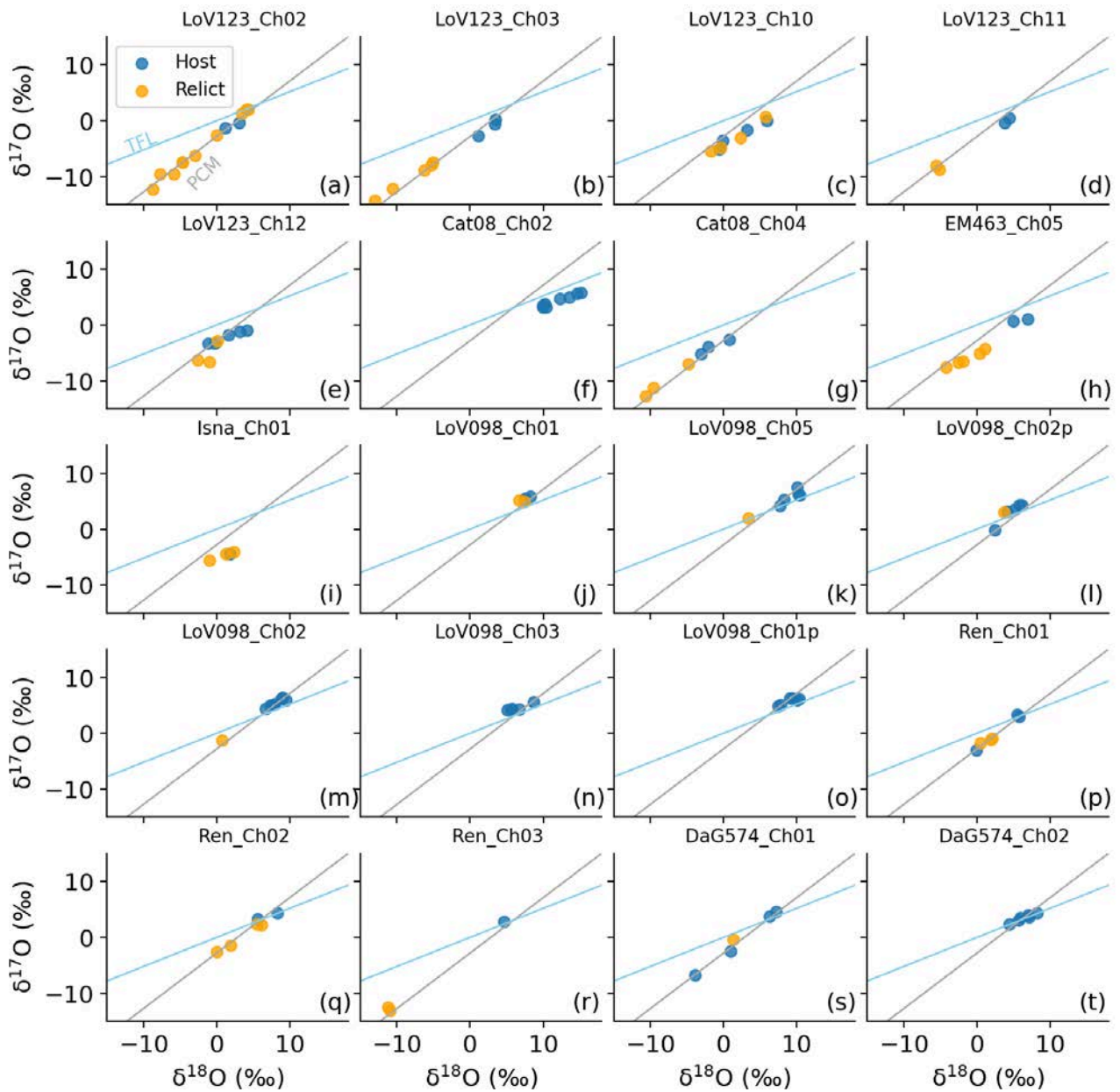


Figure 3.6. Oxygen three-isotope diagrams for type II chondrules from (a–i) CO, (j–o) ordinary, and (p–t) CR chondrites. Reference lines are Terrestrial Fractionation (TFL; Clayton et al., 1991), and the Primitive Chondrule Minerals (PCM; Ushikubo et al., 2012). The error bars are smaller than marker size.

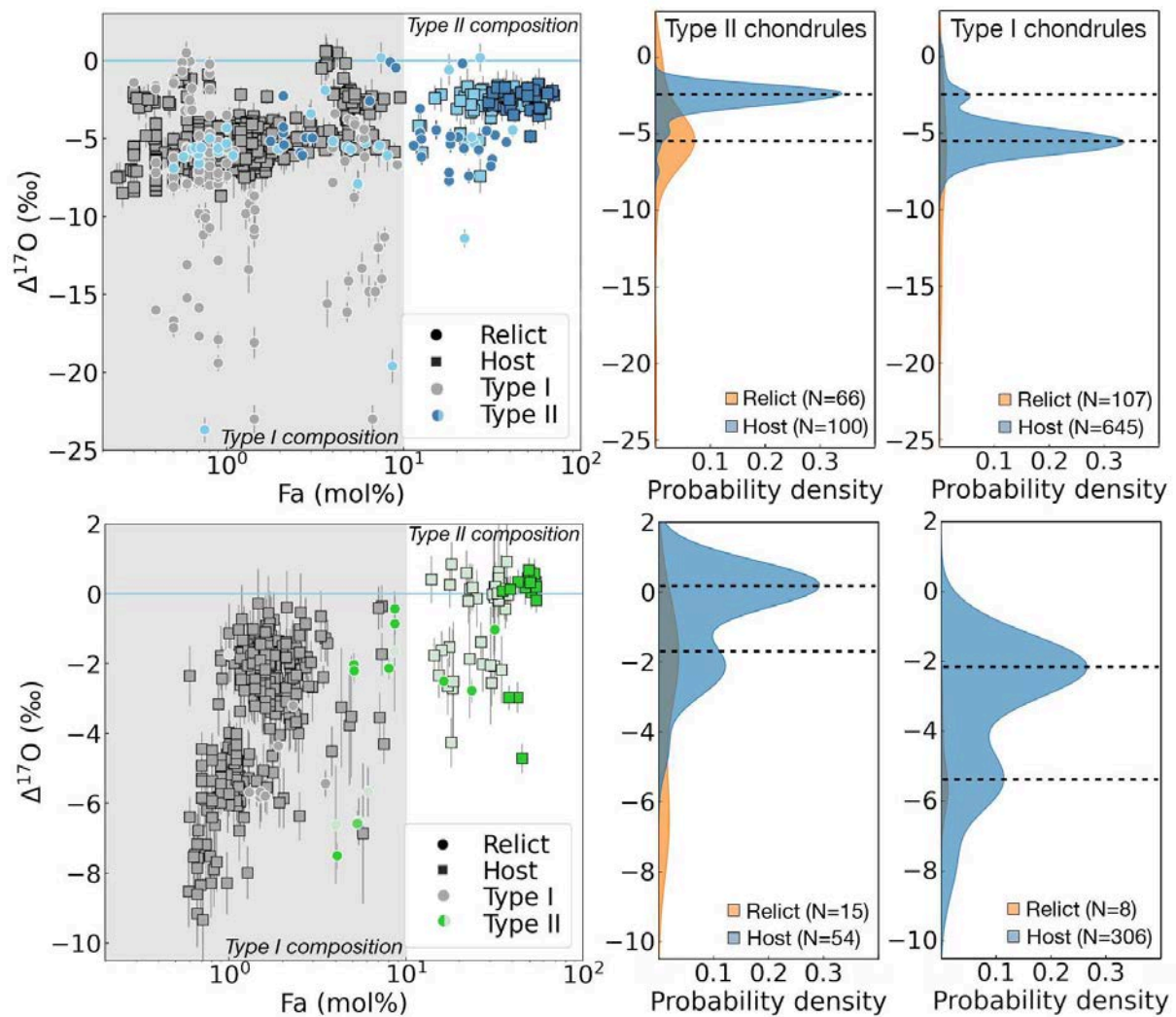


Figure 3.7. The Mg# - $\Delta^{17}\text{O}$ value of relict and host olivines in type I and type II chondrules from CO (a) and CR (b) chondrites. Fa content ($=100 \times \text{Fe}/[\text{Mg} + \text{Fe}]$) is plotted in log scale revealing a transition and overlapping between olivine grains in type I chondrules and relict grains in type II chondrules for carbonaceous chondrites. The probability density function of relict and host grains in type I and II chondrules are shown to the right of each chondrite group. Errors are 2σ . Data of type I chondrules in carbonaceous chondrites are from Schrader et al. (2013); Kunihiro et al. (2004); Tenner et al. (2013); Hertwig et al. (2016); Chaumard et al. (2018); Marrocchi et al. (2018, 2019, 2022); and Libourel et al. (2022, 2023). The TFL is shown as blue line for reference.

3.4 Discussion

3.4.1. The source of forsteritic relict grains in type II chondrules

Several of our relict olivine grains are ^{16}O -rich compared to those in their Fe-rich host phenocrysts (**Figure 3.6**). The isotopic difference between the ^{16}O -rich relicts and ^{16}O -poor hosts has been interpreted as a temporal evolution of the oxygen isotopic composition in the nebular reservoirs, implying a possible early generation of reduced Fe-poor olivines with a subsequent modification to oxidizing conditions (Jones et al., 2000; Kunihiro et al., 2004; Tenner et al., 2018). Some authors (Jones et al., 2002; Yurimoto & Wasson, 2002) have reported $\Delta^{17}\text{O}$ values $< -15\text{‰}$ in some Fe-poor relict grains in type II chondrules from CO and CV chondrites, thus advising a possible genetic link with refractory inclusions compositions ($\Delta^{17}\text{O} \sim -30$ to -10‰ ; Krot, 2019; Scott and Krot, 2014). However, all our relict grains in CO chondrites display mean $\Delta^{17}\text{O}$ values ranging from -7.7 to -0.1‰ (N=8), similar to those reported in the pristine CO3.0 Yamato 81020 ($-11.4\text{‰} < \Delta^{17}\text{O} < 0.2\text{‰}$, N = 11; Kunihiro et al., 2004; Tenner et al., 2013). The latest indicates that only 1 out 19 (~5%) relict-bearing type II chondrules sample ^{16}O -rich dust similar to refractory inclusions (this study; Yurimoto and Wasson, 2002; Kunihiro et al., 2004; Tenner et al., 2013).

Several chondrules postdate CAIs by 1-3 Ma (Villeneuve et al., 2009; Kita and Ushikubo, 2012; Bollard et al., 2016; Pape et al., 2019), which indicates that energetic mechanism(s) melted chondrules multiple times at the inner and outer regions of Jupiter's orbit to conserve the reported isotopic anomalies of meteorites (Warren, 2011; Kleine et al., 2020; Schneider et al., 2021; Piralla et al., 2021). Various petrographic features support this long timescale of chondrule formation and/or reprocessing of material, such as (i) igneous rims surrounding chondrules (Rubin, 1984; Rubin & Krot, 1996), (ii) microchondrules and amorphous silicates in fine-grained material (Zanetta et al., 2021; Bigolski et al., 2016; Pinto et al., 2022), although (Jacquet et al., 2013, 2015) have igneous rims and microchondrules formed in the same heating event as the host chondrules. Relict grains inside type I and II chondrules (Jones et al., 2018; Marrocchi et al., 2018, 2019; Ruzicka et al., 2007; Piralla et al., 2021) may thus sample earlier generations of chondrules. **Figure 3.8** show a relict type I chondrule inside a type II. The type I chondrule is mainly constituted by Ca-poor pyroxene the Indeed, Mg-rich relicts in type II chondrules always plot in the range of O-isotopic composition of host olivines in type I chondrules (**Figure 3.9** and **3.10**). Some outlying Fe-rich “host” grains also do as well

(for the CR chondrules Ren_Ch01 and DaG574_Ch01) and may have been of the same nature, but their Mg# was likely overprinted by diffusion during chondrule melting. Recently, Si isotopic and experimental chondrule analogs (Villeneuve et al., 2015; 2020) support that Fe-poor relict grains originated as an early generation of type I chondrules with subsequent recycled processes to form type II chondrules. For instance, the range of Cr₂O₃ is larger in host olivine of type II chondrules compared to the relict olivine grains in type II chondrules. Besides, other minor elements composition in Mg-rich relicts of type II chondrules tend to be MnO-poor and slightly CaO-rich, similar to the ranges of host grains in type I chondrules (**Figure 3.9a-b**).

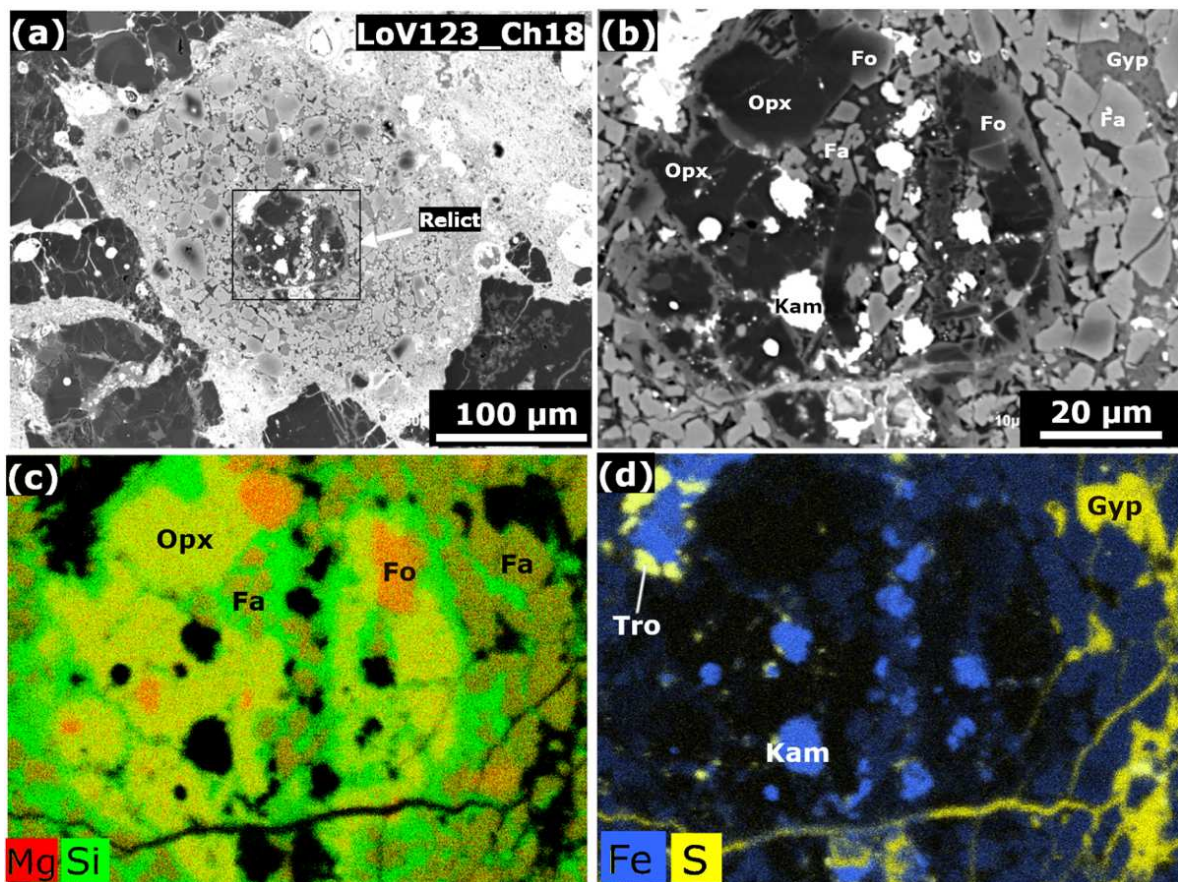


Figure 3.8. Relict bearing chondrule Ch_18 in LoV 123 (CO3.1). (a) Chondrule constituted by various small relicts in the borders and one larger Mg-rich relict chondrule in the center. (b) Zoom to the rectangle in (a) showing the larger Mg-rich relict. (c-d) Compositional maps of Mg-Si and Fe-S indicate Fe-rich olivine crystals inside the relict chondrule which is mainly constituted by Ca-poor pyroxene. Tro = Troilite; Kam = Kamacite; Chr = Chromite; Gyp = gypsum; Fa = Fayalite; Fo = forsterite; Opx = Ca-poor pyroxene

We conclude that most forsteritic relicts in type II chondrules originate mainly from Mg-rich type I chondrules. However, as the bulk chemistry of type II chondrules is less devolatilized than type I chondrules (e.g., Jacquet et al., 2015), the latter cannot be the sole precursors of the former. We may envision type I chondrules, whole or fragmented mixed with more chondritic (matrix-like) dust (not unlike the type I to type I CR chondrule recycling scenario of Marrochi et al., 2022) which would have been too fine-grained to survive as relicts. We now compare more closely the precursors of type I and type II chondrules.

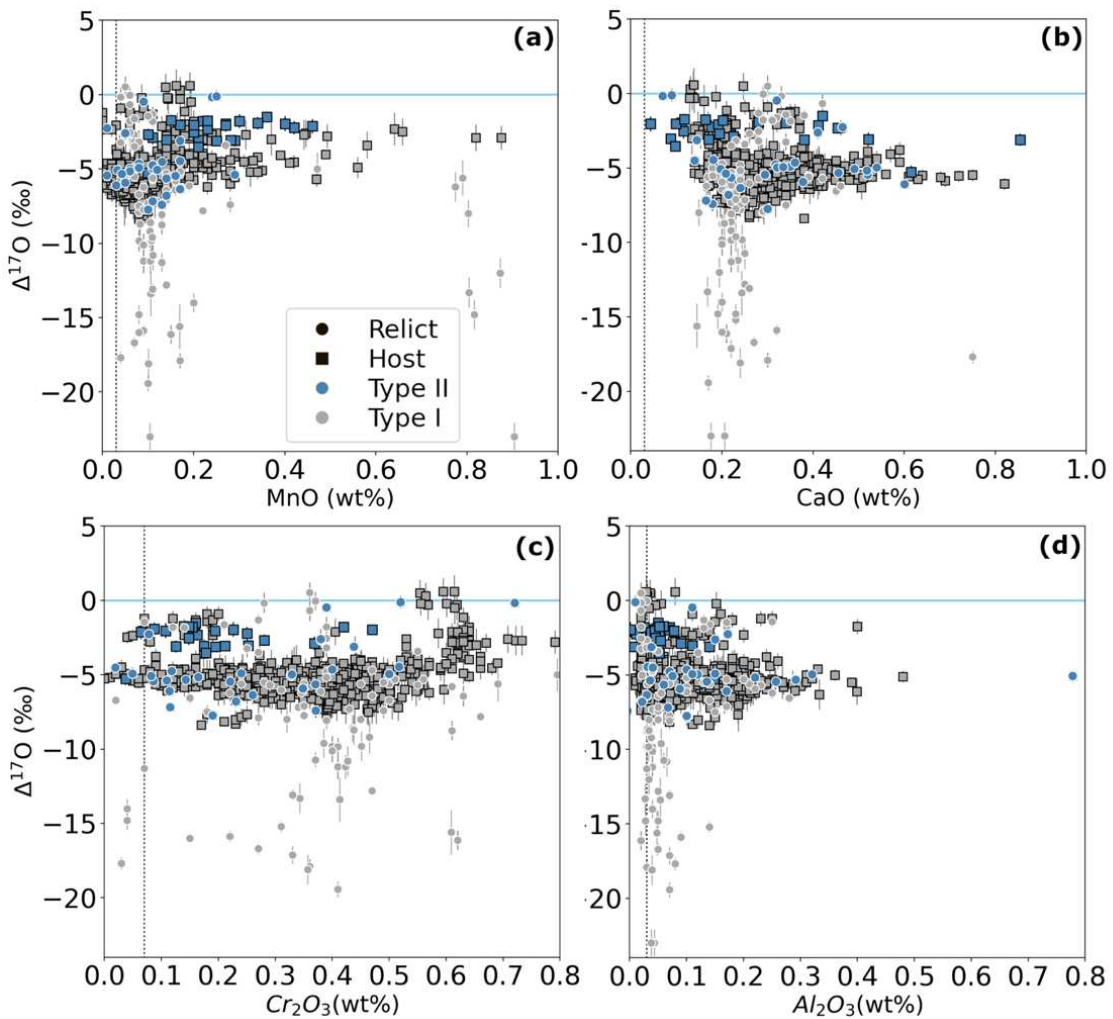


Figure 3.9. The $\Delta^{17}\text{O}$ value plotted against MnO (a), CaO (b), Cr_2O_3 (c), and Al_2O_3 (d) for relict and host olivines in type I and II chondrules from CO, CV, CM and C2 ungrouped carbonaceous chondrites. The TFL is shown as blue line for reference. Detection limit of minor elements in type II chondrules are shown as gray dashed line. Errors are 2σ . Data of type I chondrules in CV, CM and C2-an carbonaceous chondrites from Hertwig et al. (2016); Chaumard et al. (2018); Marrochi et al. (2018, 2019).

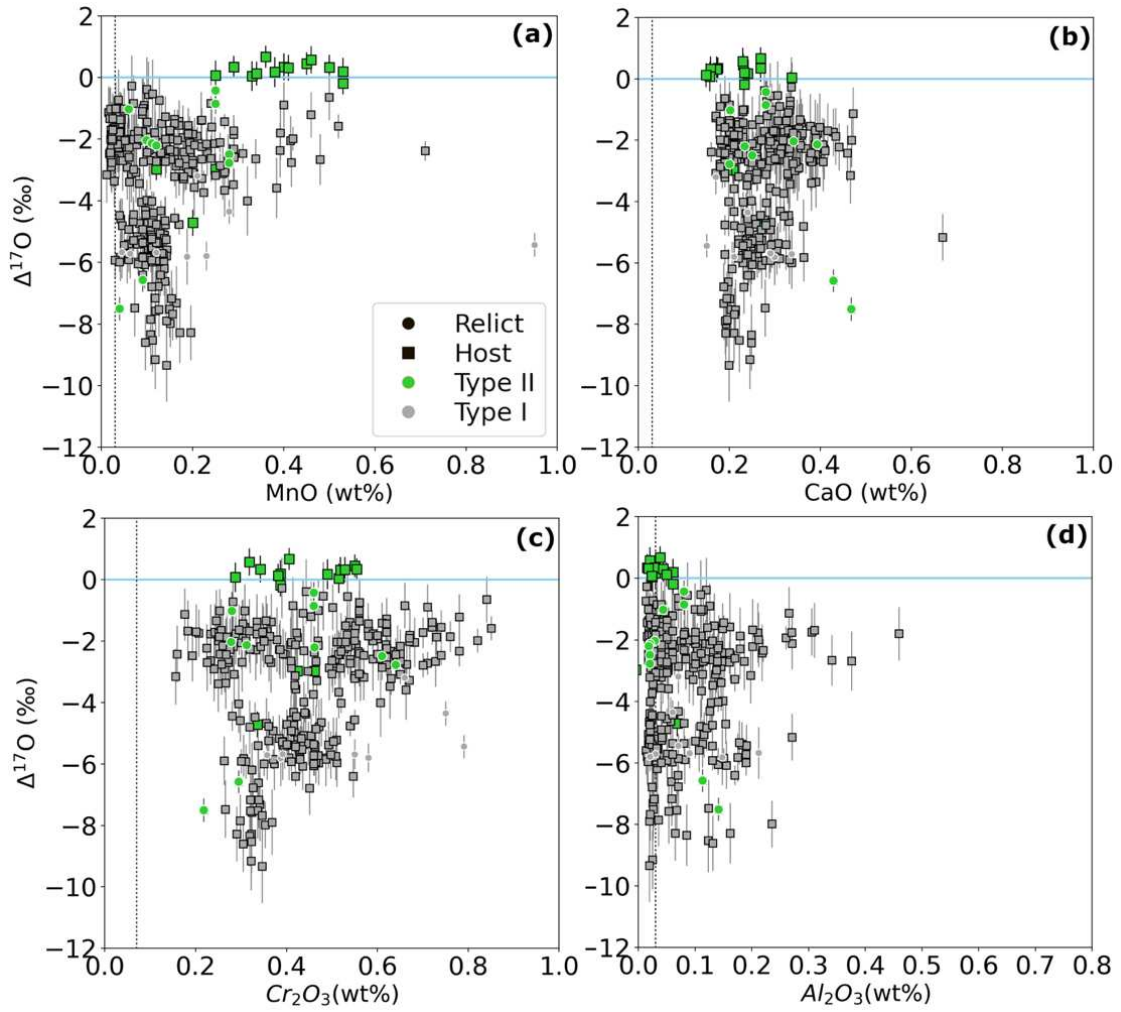


Figure 3.10. The $\Delta^{17}\text{O}$ value plotted against MnO (a), CaO (b), Cr_2O_3 (c), and Al_2O_3 (d) for relict and host olivines in type I and II chondrules from CR chondrites. The TFL is shown as blue line for reference. Errors are 2σ . Detection limit of minor elements in type II chondrules are show as gray dashed line. Data of type I chondrules from Marrocchi et al. (2022).

3.4.2. Comparison between type I and type II chondrule precursors

At first, forsteritic relict grains in type I chondrules seem very different from their counterparts in type I chondrules (e.g. Marrocchi et al., 2018; 2019; Piralla et al., 2021; Regnault et al., 2022), in that the former are analogous to type I chondrule host grains whereas the latter tend to be ^{16}O -richer than those, with 10 relict grains with $\Delta^{17}\text{O} < -10$ ‰ out of 19 in Kaba (CV3; Marrocchi et al. 2019) and 3 out 15 in NWA 5958 (C2-an; Marrocchi et al. 2018). This could suggest a chronology where type I chondrules are melted out of (partly) AOA-like precursor material and were later remelted as type II chondrules (e.g., Villeneuve et al. 2015,

2020). However, any relict of a preexisting type I chondrule would be hardly *isotopically* identifiable in a new type I chondrule if both formation reservoirs had similar $\Delta^{17}\text{O}$ (which indeed varies little for host grains of type I chondrules within each chondrite) as pointed out by Regnault et al. (2022). This bias does not exist for forsteritic relicts within type II chondrules, which are identified *chemically* (that is, from their appearance in BSE). Marrocchi et al. (2019) had noted the presence of many Al-Ti-poor olivine grains isotopically indistinguishable from the host, which could be such “cryptorelicts”. They had not upheld such an interpretation for carbonaceous chondrites because the limited proportion of chondrules suggested limited chondrule-to-chondrule recycling. Yet the fact that chondrule matter recycled from preexisting chondrules must make a small fraction of chondrules does not mean that such recycled chondrule material should be minor *among the relicts*. Indeed, survival of precursor material during chondrule melting should be essentially confined to the coarsest crystals. These are essentially found in (preexisting) chondrules and refractory inclusions (e.g., AOAs) and their debris. Since the former outnumber the latter (except for the first generations of chondrules), one may expect chondrule relicts (that is relicts from preexisting chondrules) to be a majority.

In the case of LoV 123 (CO3.05), Mg-rich relicts in type II chondrules displays larger mean spherical diameter (25.7 μm , N= 83) than isolate olivine grains (10.4 μm , N=278; this thesis). The latest endorses that most precursor material in chondrules were coarsest crystals which survived the transient melting event, and probably isolate olivine grains represents mainly fragmentation of chondrules with subsequent gas-melt interaction (Jacquet et al., 2021). Additionally, Wasson and Rubin (2003) calculated that Mg-rich precursor in Fe-rich chondrules must have experienced a low degree of melting ($\sim 10\%$) and a short heating duration above solidus temperature (~ 36 to 3600 $^{\circ}\text{C}/\text{h}$). Other authors (Yurimoto & Wasson, 2002; Miyamoto et al., 2009) calculated similar to larger cooling rate of type II chondrules crystallization (~ 500 to 10^6 $^{\circ}\text{C}/\text{h}$) using diffusion of zoning olivine and oxygen isotope diffusion models. However, most of these thermodynamical models suggest that individual type II chondrules were formed in a single melting event (Jones et al., 2018). As our data indicate, host grains of type II chondrules in carbonaceous chondrites indicate a bimodal $\Delta^{17}\text{O}$ values distribution with one large population crystallized at ~ -2 ‰ and one small at ~ -5 ‰ (**Fig. 3.7a**). Also, we found three different $\Delta^{17}\text{O}$ values at -4.7 , -3.0 , and 0.5 ‰ (**Fig. 3.6s**) in three different Fe-rich host grains in DaG574_Ch01. As olivine has a slow O-diffusion rate in silicate melts (diffusivities below 1 $\mu\text{m}^2/\text{d}$, below 1600 $^{\circ}\text{C}$; Chakraborty, 2010), this isotopic signature should have remained largely intact during the last chondrule-forming event of DaG574_Ch01. Even if the

initial Mg# have been overprinted by diffusion during chondrule melting, ^{16}O -rich “host” olivine grains represent isotopic relicts ($\Delta^{17}\text{O} > 3\sigma$, Ushikubo et al., 2012) in Fe-rich chondrules. Different authors suggest that type II chondrules must have experience multi heating-events reveals by the oscillatory iron zoning in Fe-rich olivine and low-Ca pyroxene (Baecker et al., 2017) and the diverse generations of crystal nucleation in the same Fe-rich chondrule (Wasson and Rubin, 2003). Our ^{16}O -rich “host” suggest a multi heating-events in the same Fe-rich chondrule.

Relict and host grains in type II chondrules from ordinary chondrites generally plot above the TFL ($\Delta^{17}\text{O} \sim 1 \text{ ‰}$; **Figure 3.7c**). There are only two exceptions, one host olivine from LoV98_Ch02p ($\Delta^{17}\text{O} = -1.32 \text{ ‰}$), and one relict olivine from LoV98_Ch02 ($\Delta^{17}\text{O} = -1.71 \text{ ‰}$). In comparison, reported host olivine grains in type I chondrules from three LL chondrites display comparable mean $\Delta^{17}\text{O}$ values of 0.8 ‰ (Piralla et al., 2021). These could indicate that type II chondrules must suffer efficient oxygen isotopic exchange with the surrounding gas in a melted stage via evaporation and recondensation of elements similar to the proposed for type I chondrules in ordinary chondrites (Kita et al., 2010; Piralla et al., 2021).

3.5 Conclusions

We performed minor and major chemical analysis combined with in situ oxygen isotope measurements of relicts and host grains on 9, 5 and 5 type II chondrules from CO, CR, and ordinary chondrites, respectively. Our results indicate:

- 1- Host olivine grains in CO, CR, and ordinary chondrites display mean Mg# (\pm standard deviation) of 48.9 ± 11.8 (N = 447), 51.8 ± 6.1 (N = 22), and 64.6 ± 6.5 (N = 211), respectively. In the case of relict olivine grains, they show mean Mg# of 85.0 ± 10.6 (N = 189), 84.3 ± 12.9 (N = 15), and 78.7 ± 6.2 (N = 43) for CO, CR, and ordinary chondrites. Commonly, Mg-rich relicts in type II chondrules are MnO-poor, Al₂O₃-rich and slightly CaO-rich compared to their host olivines.
- 2- The mean $\Delta^{17}\text{O}$ values of relict grains in CO, CR, and ordinary chondrites are -4.7 , -2.8 , and $+0.4$ ‰, which are lower than the mean $\Delta^{17}\text{O}$ values in type II olivine hosts: -2.6 , -0.5 , and $+1.1$ ‰ for CO, CR, and ordinary chondrites, respectively.
- 3- Two chondrules in CR chondrite displays different $\Delta^{17}\text{O}$ values in distinct Fe-rich host grains: DaG574_Ch01 ($\Delta^{17}\text{O} = -4.7$, -3.0 and 0.5 ‰) and Ren_Ch01 ($\Delta^{17}\text{O} = -1.32$ and -2.97 ‰).

From these data, we drew the following conclusions:

- 1- Our reported Mg-rich relicts in type II chondrules almost always plot in the range of O-isotopic composition of host olivines in type I chondrules ($\Delta^{17}\text{O} = -5$ ‰, -2.5 ‰ and 2 ‰ for CO, CR and ordinary chondrites). Besides, minor elements composition in Mg-rich relicts tend to be MnO-poor and slightly CaO-rich similar to the ranges of host grains in type I chondrules. Furthermore, only 1 out of 19 (~5%) reported relict-bearing type II chondrules sample ¹⁶O-rich olivine grains similar to refractory inclusions ($\Delta^{17}\text{O} \sim -20$ ‰). We suggest that most forsteritic relicts in type II chondrules originate from a previous generation of Mg-rich chondrules.
- 2- Different $\Delta^{17}\text{O}$ values in Fe-rich “host” grains of DaG574_Ch01 and Ren_Ch01 should sample previous generation of Fe-rich olivines as recently reported Kerraouch et al. (2022) in clasts from two ordinary chondrites (NWA 5206 [LL3] and NWA 6925

[L3]). However, the fast diffusion of Fe in Mg-rich olivines could have overprinted these chondrules in the last melting event. Whatever the case, our reported ^{16}O -rich “host” olivine grains represent isotopic relict in Fe-rich chondrules suggesting a formation processes in a multi heating-events.

Chapter 4

The fine-grained rim of chondrules in carbonaceous chondrites

Published research paper as Pinto et al. (2022), *Meteoritics and Planetary Science Journal*

Chapter introduction

We selected the least aqueously and thermally altered carbonaceous chondrite groups: CO, CM, CV, and CR chondrites to describe the origin and relation between the rimmed bearing chondrule and the matrix abundance in carbonaceous chondrites. An optical microscope, secondary electron microscope (SEM) and processing software were employed for this study. Our systematic survey and the petrographic description of 162 rimmed bearing chondrules in CO, CM, CV, and CR chondrites were used to compare (i) the estimated thickness sizes of fine-grained rims to those of their host chondrules and (ii) the frequency of fine-grained rims to the modal abundance of the matrix in the respective host chondrite group. We show that fine-grained rims could not result from parent-body processes, whether matrix compaction or fine-grained rim fragmentation. Our results thus support: (i) a nebular origin for fine-grained rims, whose abundances are directly related to the abundance of available dust in regions of carbonaceous chondrite accretion; and (ii) rimmed bearing chondrules were accreted in the local reservoir where they agglomerate the rim, suggesting limited radial transport in the circumsolar disk.

Formation of chondrule fine-grained rims from local nebular reservoirs

Gabriel A. PINTO ^{*1,2}, Yves MARROCCHI ², Emmanuel JACQUET ³, and Felipe OLIVARES ¹

¹Instituto de Astronomía y Ciencias Planetarias, Universidad de Atacama, Copayapu 485, Copiapó, Chile

²Université de Lorraine, CNRS, CRPG, UMR 7358, Vandœuvre-lès-Nancy 54501, France

³Institut de Minéralogie, de Physique des Matériaux et de Cosmochimie (IMPMC), Muséum national d'Histoire naturelle, Sorbonne Université, CNRS, CP52, 57 rue Cuvier, Paris 75005, France

*Corresponding author. E-mail: gabriel.pinto@univ-lorraine.fr

(Received 14 September 2021; revision accepted 08 March 2022)

Abstract—Chondrules are commonly surrounded by fine-grained rims (FGRs) whose origin remains highly debated; both nebular and parent body settings are generally proposed. Deciphering their origin, however, is of fundamental importance as they could clarify the matrix–chondrule relationship and thus constrain the formation and transport conditions of chondrules in the circumstellar disk. Here, we report a systematic survey of FGRs in CO, CM, CV, and CR chondrites; we compare (i) the thickness of FGRs to the size of their host chondrules and (ii) the frequency of FGRs to the modal abundance of matrix in the respective host chondrites. Although FGRs show textural variations depending on the petrologic type of the considered chondrites, our data show a positive correlation between apparent rim thickness and the radius of the host chondrule in all chondrite groups. We also found a positive correlation between the evaluated percentages of rimmed chondrules and the modal abundance of matrix material in the chondrites. We show that this relationship could not result from parent body processes, whether matrix compaction or FGR fragmentation. Therefore, we propose that FGRs were accreted under warm conditions at the end of chondrule-forming events. Our results thus support (i) a nebular origin for FGR, whose abundances are directly related to the abundance of available dust in regions of chondrite accretion; and (ii) the accretion of chondrites from locally formed chondrules and matrix, suggesting limited radial transport in the protoplanetary disk.

INTRODUCTION

Chondritic meteorites are fragments of asteroids that escaped melting and differentiation, and have thus remained largely unchanged since their formation in the early solar system (e.g., Piani et al., 2020; Scott & Krot, 2014). They comprise particles formed at high temperatures during the early evolution of the protoplanetary disk, such as refractory inclusions and chondrules, within a fine-grained matrix formed at low temperatures. Chondrules are ferromagnesian quasi-spheroids formed by the crystallization of magma droplets through a still-elusive high-temperature event (Connolly & Jones, 2016). To explain their formation, chondrules are considered to represent either (i) nebular products arising from the melting of early condensates (Marrocchi, Villeneuve, et al., 2018; Marrocchi et al.,

2019; Ruzicka et al., 2007), for example, during the passage of bow shocks produced by planetesimals on eccentric orbits (Morris et al., 2012), or (ii) residues of protoplanet collisions (Johnson et al., 2015; Libourel & Krot, 2007). To constrain these models, it is critical to understand the relationship between chondrules and matrix. For instance, all chondrites, except the CI group, experienced chemical fractionation involving refractory (e.g., chondrules) and volatile (e.g., matrix) elements. This might reflect spatial or temporal heterogeneities of chondrite components' formation into different reservoirs. One possible scenario is the two-component model (e.g., Anders, 1964; Zanda et al., 2006, 2018), which considers that chondrules and matrix are unrelated, for example, they formed in outer and inner regions of the disk, respectively (or, in impact scenarios, by collisions of planetary bodies at different

heliocentric distance and were subsequently mixed in varying proportions within the disk). Other researchers favor a common origin for chondrules and matrix in a closed reservoir, with elemental exchanges between the coarse- and fine-grained components leading to a complementary relationship between matrix and chondrule compositions (e.g., Goldberg et al., 2015; Hezel et al., 2018; Palme et al., 2015); this model considers that localized heating events produced chondrules from nebular dust.

To solve this enigma, further insights into the matrix–chondrule relationship could be gleaned from an additional petrographic component, intermediate between chondrules and matrix: chondrule fine-grained rims (FGRs). In various chondrite groups, chondrules are armored by FGRs, which are distinguished from the surrounding matrix (which will be called “intercomponent matrix,” or ICM) by their texture (i.e., grain size, compaction, porosity; e.g., MacPherson et al., 1985; Zanetta et al., 2021), mineralogy (Brearley, 1993; Zanetta et al., 2021), and/or presolar grain abundance (Leitner et al., 2016, 2019). FGRs are also observed around refractory inclusions, isolated olivine grains, and Fe-Ni metal beads (Brearley, 1993; Hanna & Ketcham, 2018; Jacquet et al., 2021; Lauretta et al., 2000; Simon et al., 2018; Zanetta et al., 2021). Although numerous studies have focused on the mineralogical, chemical, and isotopic characteristics of FGRs (Brearley, 1993; Cosarinsky et al., 2008; Friend et al., 2018; Huss et al., 2005; Lauretta & Buseck, 2003; MacPherson et al., 1985; Wasson & Rubin, 2014), their origin remains poorly constrained and no consensus has yet arisen. One hypothesis is that FGRs formed early in a nebular environment through the accretion of dust around free-floating chondrules before their incorporation into planetesimals (e.g., Cuzzi, 2004; Hanna & Ketcham, 2018; Liffman, 2019; Liffman & Toscano, 2000; Metzler et al., 1992; Zanetta et al., 2021). Alternatively, FGRs may have formed during parent body evolution through compaction or secondary processes such as fluid and/or thermal alteration, which would have induced pervasive modification at the chondrule–matrix boundary (e.g., Brearley & Krot, 2012; Sears et al., 1993; Takayama & Tomeoka, 2012; Tomeoka & Ohnishi, 2010, 2014, 2015; Trigo-Rodríguez et al., 2006). Either way, it must be kept in mind that chondrules and FGRs may have been lithified together *before* the final lithification of the host meteorite where they may have been incorporated as clasts (e.g., Metzler et al., 1992; Takayama & Tomeoka, 2012; Tomeoka & Ohnishi, 2014, 2015).

Most studies of FGRs have focused on the aqueously altered CM carbonaceous chondrites due to the high abundances of FGRs in these meteorites. Deciphering the

broader origin of FGRs thus requires that they be studied in other chondrite groups, particularly the least aqueously and thermally altered CO carbonaceous chondrites (Bonall et al., 2007, 2016; Marrocchi, Bekaert, et al., 2018; McSween, 1977; Pinto et al., 2021; Scott & Jones, 1990; Zolensky et al., 1993). To this end, we here report a systematic survey of FGRs in CO, CM, CV, and CR chondrites; we compare (i) the estimated sizes of FGRs to those of their host chondrules and (ii) the frequency of FGRs to the modal abundance of the matrix in the respective host chondrite group. Based on our results, we discuss the implications on the parent body versus nebular origin of FGRs and the one-reservoir versus two-reservoir origin of chondrules and matrix.

SAMPLES AND ANALYTICAL METHODS

We studied four polished sections of CO3 chondrites collected in the dense collection areas of El Médano (EM 397, EM 463, and EM 216) and Los Vientos (LoV 123), provided by the Museo del Meteorito (San Pedro de Atacama, Chile), and prepared at Universidad de Atacama (Copiapó, Chile). We also surveyed sections of CM (Paris, section 4029sp1), CV (Vigarano, section Vigarano-P), and CR carbonaceous chondrites (Dar al Gani [DaG] 574, section 3681sp2; Renazzo, section 719sp3) provided by the Muséum national d’Histoire naturelle of Paris. The petrography and mineralogy of chondrules and FGRs were determined by optical microscopy, backscattered electron (BSE) imaging, and X-ray compositional mapping. For the latter two, we used (i) a Zeiss Evo MA10 equipped with an Oxford X-MAX N 20 SDD energy-dispersive spectrometer and operating with a 3 nA electron beam accelerated at 15 kV (Universidad de Atacama) and (ii) a JEOL JSM-6510 scanning electron microscope equipped with a Genesis EDX detector using a 3 nA electron beam accelerated at 15 kV (CRPG-CNRS, Nancy, France).

The modal abundances of coarse- and fine-grained components were determined by manual point counting using JMicrovision software (3000 random points). We examined representative areas of 95.9, 134.2, 27, 32.4, and 186.9 mm² in EM 463, EM 397, EM 216, LoV 123, and Vigarano, respectively, and the total section areas of 266, 239, and 58.4 mm² in Paris, Renazzo, and DaG 574, respectively, to calculate the modal abundances and statistics of rimmed chondrules (Table 1). The perimeter of all rimmed chondrules was traced by eye using the open-source software ImageJ (Schindelin et al., 2012). We determined the sizes of individual chondrules without (i.e., particle) and with their surrounding FGRs (i.e., particle + rim) as circle-equivalent diameter (i.e., $d = \sqrt{\frac{\text{pixel area}}{\pi}} \times 2$). The

Table 1. Statistics of completely rimmed chondrules in the studied classes of carbonaceous chondrite.

Class	Meteorite	Fine-grained particles (%)	Number of chondrules ^a	Rimmed chondrules (%)
CO	LoV 123	28 ± 1	1671	0.2 ± 0.1
	EM 216	32 ± 1	966	1.9 ± 0.4
	EM 463	29 ± 1	2092	2.0 ± 0.3
	EM 397	34 ± 1	868	2.6 ± 0.5
	Mean	30.6		1.7
	STD	2.9		1.0
CR	DaG 574	34 ± 1	66	10.6 ± 4
	Renazzo	38 ± 1	177	12.4 ± 2.7
	Mean	36.1		11.5
	STD	2.7		1.3
CM	Paris ^b	66	78	80.8
	Paris section 4029sp1	64 ± 1	288	54.9 ± 2.8
	Mean	65		67.8
	STD	1.5		18.3
CV	Allende ^c	50	413	15
	Vigarano	39 ± 1	84	16.7 ± 4.4
	Mean	45		15.8
	STD	8.0		1.2

In our data, the statistical error of fine-grained material and the percentage of rimmed chondrules were calculated according to the number of counts, assuming a Poisson distribution. STD, standard deviation.

^aMinimum numbers of chondrules in the samples.

^bZanetta et al. (2021).

^cSimon et al. (2018).

apparent rim thickness was calculated as half of the difference between the two diameters. The FGR–matrix boundaries were identified after their sharpness, the change in tonality (FGR looks darker), and some imbricated minerals oriented parallel to them. To estimate the uncertainty of these free-hand measurements, we performed five replicate tracing iterations for chondrule–matrix and matrix–FGR boundary in 13 chondrules. This uncertainty shows a positive correlation between the average chondrule diameter and the standard deviation ($R^2 = 0.72$), that is, at larger chondrule diameter, the standard deviation of the five free-hand measurements increases (Table S1 in supporting information). Moreover, the linear regression of the chondrule diameter + FGR versus standard deviation displays a low value in the coefficient of determination ($R^2 = 0.43$; Table S1). We use these models to calculate the uncertainties of the 162 measured chondrules. The FGR thickness was calculated by quadratic error using the values of chondrule diameter and chondrule diameter + FGR. The porosity of the FGRs and ICM was calculated using the threshold tool in the software ImageJ.

RESULTS

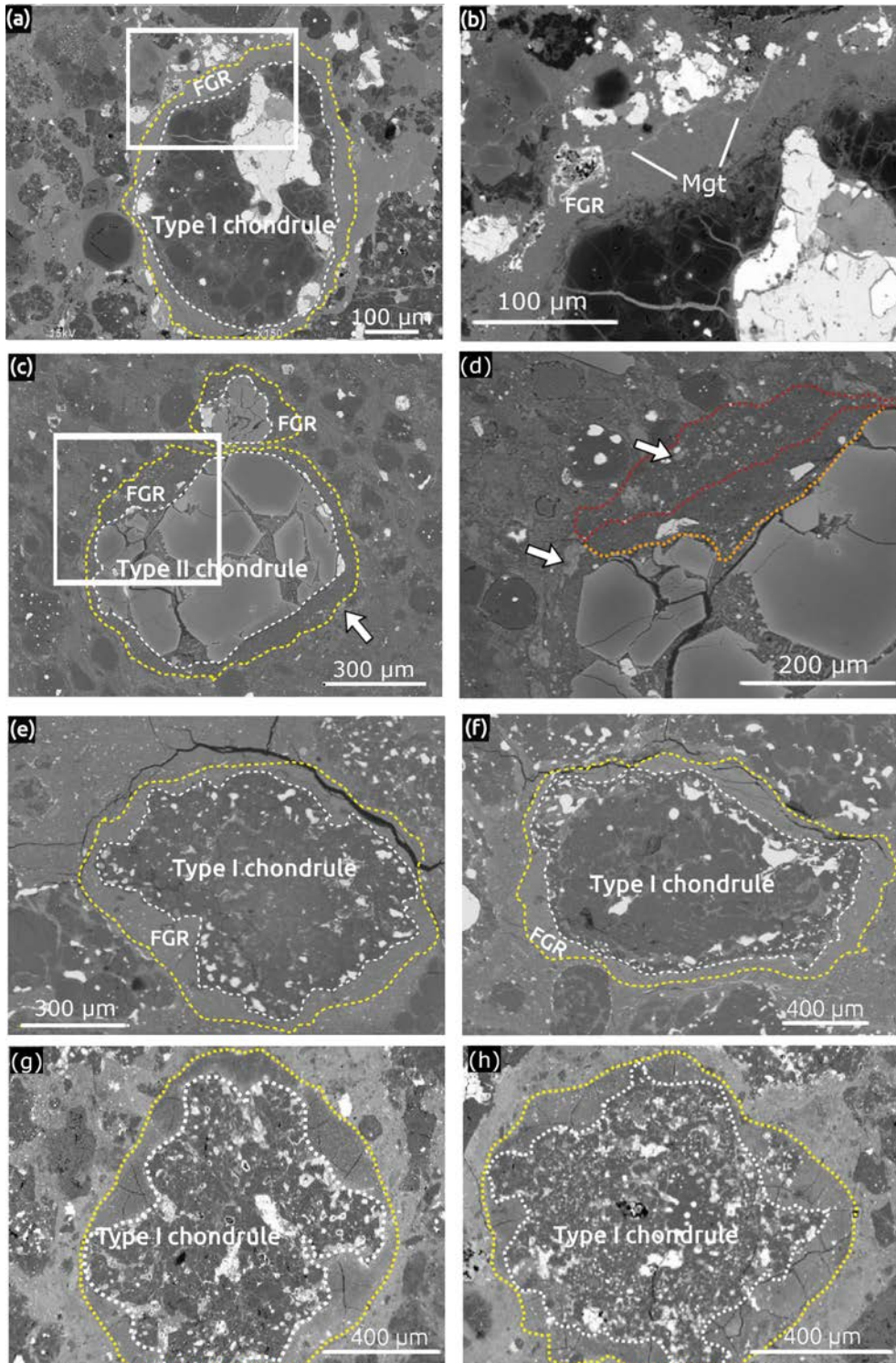
Petrographic Characteristics of FGRs Around Chondrules

Among all types of chondrules (porphyritic olivine, porphyritic pyroxene, porphyritic olivine-pyroxene, and nonporphyritic), well-defined FGRs were found (Fig. 1). Rimmed chondrules exceed 100 μm in diameter (Table S2 in supporting information). The FGRs show distinctive petrographic features compared to the ICM such as higher porosity (mean \pm standard deviation of 24 ± 11 vol%, $N = 9$, compared to 15 ± 7 vol%, $N = 9$), as previously seen by Zanetta et al. (2021) in the Paris chondrite and (ii) size of smaller opaque phases (mean circular size \pm standard deviation of 7 ± 4 μm , $N = 50$, compared to 28 ± 27 μm , $N = 52$). The FGR–matrix interface is frequently delineated by a thin layer of oriented iron oxide, sulfides, or tochilinite–cronstedtite intergrowths (TCI, Figs. 1b and 1d) (Pignatelli et al., 2016, 2017; Vacher et al., 2019) that is brighter than adjacent areas in BSE images. Several FGRs in petrologic type 2 chondrites (CM, CR) have multilayered structures comprising (i) compacted material at the chondrule–FGR interface and (ii) a porous outer layer regularly containing imbricated minerals and metal beads oriented parallel to the chondrule perimeter (Fig. 1d). In contrast, most chondrule rims in petrologic type 3 chondrites (CV, CO) show no evidence of textural or compositional layering, and the chondrule–FGR and FGR–matrix interfaces commonly include a discontinuous thin film (~ 3 μm) of iron oxide (Figs. 1a and 1b). In addition, most FGRs ($>75\%$) observed in the CO3 chondrites recovered from the Atacama Desert include calcium sulfates that fill porosity and fractures.

Most rims are continuous with round edges and sharp FGR–matrix transition. However, fractions of the FGRs are absent in the cases of (i) fragmented chondrules with angular or irregular borders (Fig. 2) (Metzler et al., 1992; Zanetta et al., 2021) or (ii) local regions where coarse-grained components impinge upon chondrule exteriors (Fig. 1c).

FGR Statistics: Frequency and Thickness

Our point counting analysis revealed coarse-grained (>5 μm , i.e., chondrules, refractory inclusions, Fe-Ni metal beads, isolated olivine grains) to fine-grained (<5 μm , i.e., ICM and FGRs) ratios of $\sim 69/31$, $\sim 64/36$, $\sim 61/39$, and $34/66$ in CO, CR, CV, and CM chondrites, respectively. The mean percentage of complete rimmed chondrules (excluding fragments) ranges from $1.6 \pm 1.0\%$ in CO chondrites to $11.8 \pm 1.3\%$, $16.4 \pm 0.4\%$, and $67.8 \pm 18.3\%$ in CR, CV, and CM chondrites, respectively (Table 1). The estimated percentages of



Origin of fine-grained rims

Fig. 1. Representative examples of rimmed chondrules in backscattered electron images of (a, b) EM 397, (c, d) Paris, (e, f) Renazzo, and (g, h) Vigarano; CO, CM, CR, and CV carbonaceous chondrites, respectively. Dashed white lines mark chondrule borders and dashed yellow lines the FGR–matrix interface. b, d) Details of FGR–matrix boundary. b) A discontinuous thin film ($\sim 3 \mu\text{m}$) of iron oxide. c) The FGRs are narrower at the contact between the two rimmed type II chondrules, which may have collided and agglomerated before the end of dust accretion onto chondrules (so that the thickness at the contact was deprived of further increase). Collision of the two rimmed type II chondrules shortly after their formation is statistically more likely than later coagulation given the rarity of type II chondrules in carbonaceous chondrites. d) Multilayered structures observed in the FGRs. Dashed orange lines indicate compacted material at the chondrule–FGR interface and dashed red line indicates the porous outer layer containing imbricated minerals and metal beads oriented parallel to the chondrule perimeter. The white arrows indicate TCI.

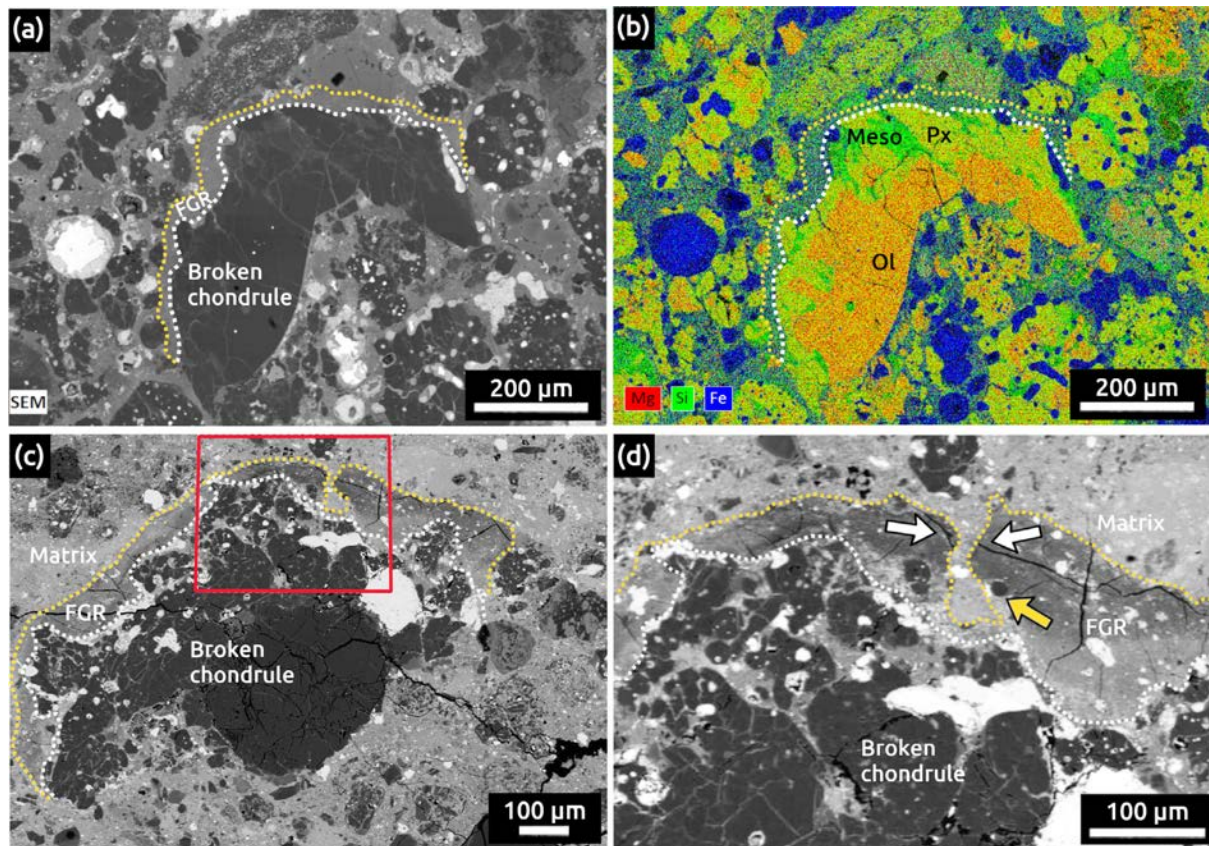


Fig. 2. Broken chondrules in (a, b) CO and (c, d) CV chondrites have FGRs mantling only their intact edges. In (d), the white arrows mark a discontinuous radial crack in the FGR of the broken CV chondrule that does not affect the matrix, and the yellow arrow indicates a microchondrule within the FGR. Dashed white lines mark the exterior borders of chondrules and dashed yellow lines the FGR–matrix interface.

FGR-bearing chondrules in CO, CR, CV, and CM chondrites are positively correlated with the modal abundances of fine-grained materials in those chondrites.

We determined the apparent thicknesses of FGRs around 97, 13, 44, and 8 continuously rimmed chondrules in CO, CR, CM, and CV chondrites, respectively (Table S2). The average (\pm standard

deviation [STD]) apparent diameters of chondrules (not including FGRs) in CO, CM, CR, and CV chondrites are $397 (\pm 210)$, $338 (\pm 229)$, $668 (\pm 337)$, and $1552 (\pm 923) \mu\text{m}$, respectively. FGR thicknesses vary greatly, but are generally within the range of 8–140 μm , with a median of $\sim 34 \mu\text{m}$ (Fig. 3). Simple linear regressions on our results show positive correlations between FGR thickness and chondrule radius (dashed lines in Fig. 3),

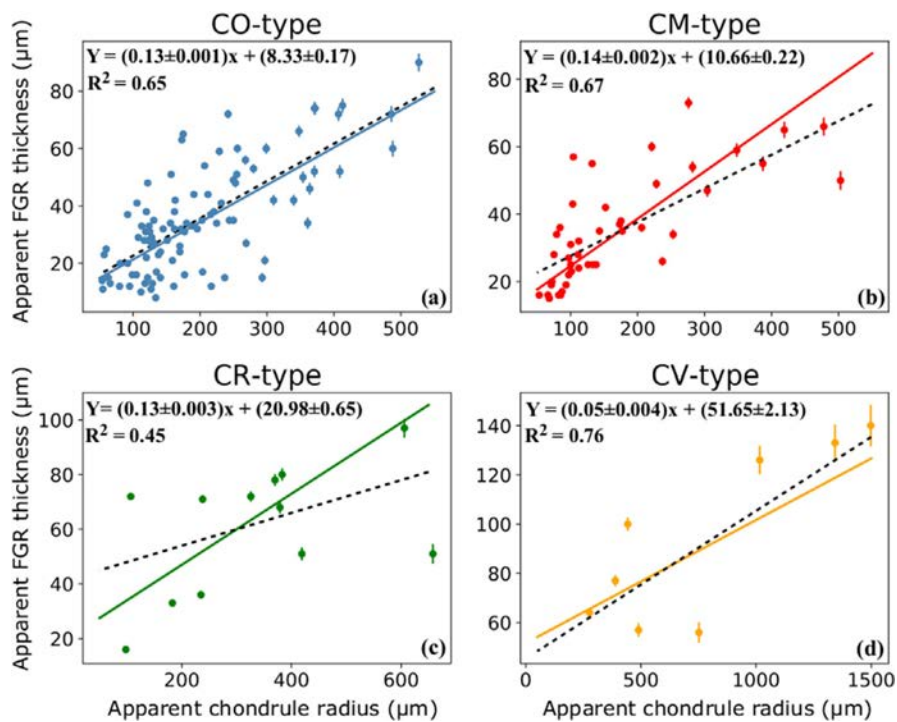


Fig. 3. Positive correlations between apparent chondrule radius and apparent FGR thickness among the studied (a) CO, (b) CM, (c) CR, and (d) CV carbonaceous chondrites. Colored solid lines and black dashed lines represent weighted and simple regressions, respectively (Thirumalai et al., 2011); fitting parameters are shown for the weighted regressions only.

if with lower R^2 for CR chondrites but the number of data points (12) may be too low for the difference to be significant. The slopes of weighted linear regressions increase from 0.05 in CV chondrites to 0.13, 0.13, and 0.14 in CR, CO, and CM chondrites, respectively, indicating that FGR thickness increases with increasing matrix abundance. The slope of the weighted regression for CMs is comparable to the range of 0.16–0.21 reported by Metzler et al. (1992) but steeper than the slope of 0.1 reported in the X-ray computed tomography study of Murchison by Hanna and Ketcham (2018). This latter difference results from the 2-D nature of our measurements, which are known to systematically overestimate true (3-D) rim thicknesses (e.g., Cuzzi & Olson, 2017). In all studied chondrites, the weighted regressions have positive y -intercepts that increase with mean chondrule size, consistent with literature data (e.g., Liffman, 2019).

The frequency of occurrence and the thickness of FGRs differ slightly between type I and type II chondrules. For instance, the percentage of rimmed type I ($n = 311$) with respect to all type I chondrules ($n = 5754$) is 5.4% with an average FGR thickness of 41 μm ($n = 140$). In comparison, the percentage of

rimmed type II ($n = 40$) with respect to all type II chondrules ($n = 536$) is 7.5% with an average FGR thickness of 36 μm ($n = 21$). In CM2 chondrites, 62% and 49% of the counted type I and II chondrules are rimmed, respectively, whereas in CO3 chondrites, 1.4% and 3.1% are rimmed, respectively (Table S3 in supporting information). In Murchison, Sears et al. (1993) reported that their “group A” chondrules (essentially type I) had thicker FGRs than their “group B” chondrules (essentially type II); the slope of their thickness versus size correlation for type I chondrules was twice as steep as that for type II chondrules. We see little difference between type II and type I FGR thickness/chondrule size correlations in our CM (Paris) and CO data, although the data are sparse.

Microchondrules in FGRs and the Intercomponent Matrix

We observed nine microchondrules (<40 μm in diameter; Krot & Rubin, 1996; Krot et al., 1997) in the fine-grained materials (FGR and ICM) of LoV 123 and Vigarano. All four microchondrules observed in Vigarano occur within the FGRs of type I chondrules;

Origin of fine-grained rims

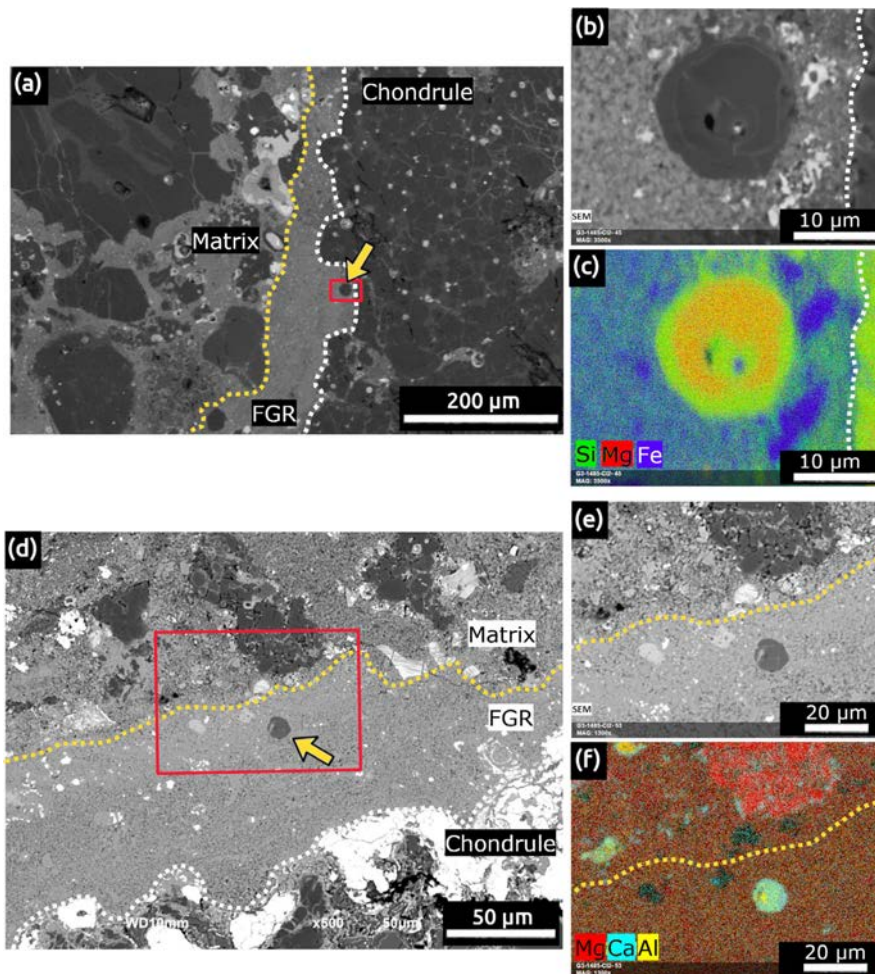


Fig. 4. Backscattered electron images and compositional maps of two microchondrules within rimmed type I chondrules in (a–c) CO and (d–f) CV chondrites. The CO chondrite microchondrule shows sharp contact with the fine-grained material and is composed of an olivine core surrounded by Ca-poor pyroxene (c) as well as a small metal bead inside (b). These petrographic features are similar to their host chondrule. The CV chondrite microchondrule shows sharp contact with the fine-grained material and is Ca- and Al-rich (f, Mg-Al-Ca compositional map), different from their host chondrule (Mg-rich). It could represent melted mesostasis expelled from some parent chondrule. Yellow arrows mark the microchondrules, and red boxes indicate the areas shown in the compositional maps. Dashed white lines mark chondrule borders and dashed yellow lines the FGR–matrix interface.

meanwhile, among the five observed microchondrules in LoV 123, two were found in the matrix and three within the FGRs of type I chondrules (Fig. 4). Most observed microchondrules are isolated, nonporous, and have sharp boundaries. The apparent diameters range from 3.2 to 37.9 μm (average $17.4 \pm 12.2 \mu\text{m}$), and some show internal zoning, with olivine cores surrounded by low-Ca pyroxene margins (Fig. 4c) and can display metal beads inside (Fig. 4b). This composition and texture are similar to type I chondrules, thus, similar to their host chondrules.

However, one microchondrule has a Ca-Al-rich composition, similar to mesostasis but different from the Mg-rich mineral in the host chondrule (Figs. 4d–f). The thickness of microchondrule-bearing FGR is comparable to that of microchondrule-free ones ($57 \pm 33 \mu\text{m}$ and $40 \pm 24 \mu\text{m}$, respectively).

Previously, microchondrules (<40 μm in diameter; Krot & Rubin, 1996; Krot et al., 1997) have been mostly reported in unequilibrated ordinary chondrites (UOC), and mostly within FGR of chondrules/inclusions and occasionally isolated or clustered in the

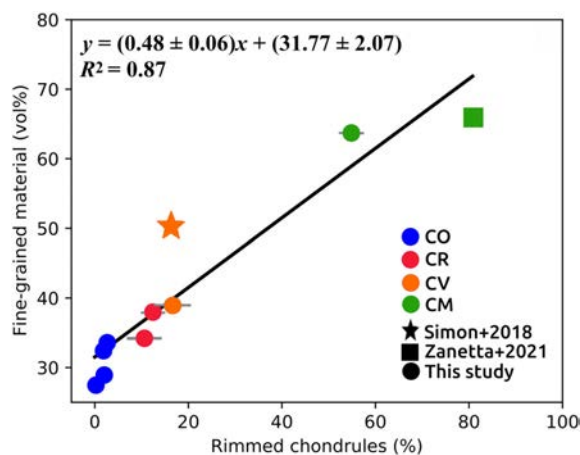


Fig. 5. Correlation between the modal abundance of ICM+FGR and the percentage of rimmed chondrules in CO, CM, CR, and CV chondrites. The black solid line represents the simple linear regression for all measurements, and the fit parameters are reported at top left. Reference data do not report errors associated with the modal abundance or percentage of rimmed chondrule. Error bars are smaller than symbol sizes in most cases of our reported data.

fine-grained matrix (Bigolski et al., 2016; Dobrică & Brearley, 2016; Rubin et al., 1982). Yet a few microchondrules were also observable around chondrule Ch4 in the CR2 chondrite Elephant Moraine 92042 (Connolly et al., 2001) and three microchondrules have also been found in the FGR of one calcium–aluminum-rich inclusion, one chondrule, and one compound chondrule in two CM chondrites, Murchison and Elephant Moraine 96029 (Suttle et al., 2019).

DISCUSSION

A Nebular Formation of FGR

The estimated percentages of FGR-bearing chondrules in CO, CR, CV, and CM chondrites are positively correlated with the modal abundances of fine-grained materials in those chondrites (Fig. 5), particularly the ICM because FGRs account for only a minority of the fine-grained materials present (Hanna & Ketcham, 2018). To explain this correlation solely through parent body processes would require that either (i) FGRs were derived from the ICM by compaction (e.g., Trigo-Rodriguez et al., 2006; Wasson & Rubin, 2014) or (ii) the ICM was derived from FGRs by attrition (e.g., Metzler et al., 1992). However, FGRs are more porous than the ICM (this work; Zanetta et al., 2021), excluding their origin by compaction of the matrix. Similar to (ii), even in those

CM lithologies deemed by Metzler et al. (1992) to be “primary accretionary rocks,” FGRs are outnumbered in modal abundance by ICM (recognizable by its larger abundance of TCI; contrast to their figs. 5, 7, 8 and their cartoon in fig. 19; see also Trigo-Rodriguez et al., 2006), so ICM must have predated the primary accretion and is thus unlikely to be derived from FGR in the parent body. More generally, FGRs are distinguished from the ICM based on the mineralogy, bulk composition (Bigolski, 2017; Friend et al., 2018; Zanetta et al., 2021), and presolar grain abundance (Haenecour et al., 2018; Leitner et al., 2016). Thus, it is unlikely that either one derived from the other within the parent body, although they may ultimately share similar pre-accretionary descent. Although some portion of the FGRs may have been incorporated into the ICM during lithification, as suggested by instances of rim fragmentation (Fig. 2) (see also Bigolski, 2017) or rare isolated microchondrules (if originally hosted in FGRs), the correlation between the frequency of FGRs and ICM abundance requires another explanation.

In fact, the very broken chondrules just mentioned, in having rims interrupted where they were fragmented, provide strong evidence for FGR formation prior to accretion. Incidentally, the FGR around a broken chondrule in Vigarano (Figs. 2c and 2d) also displays a discontinuous radial crack in the FGR that does not affect the matrix, suggesting a fragmentation before agglomeration with the ICM.

FGR thickness is positively correlated to host chondrule size (Fig. 3) (see also Cuzzi, 2004; Hanna & Ketcham, 2018). This correlation between FGR thickness and chondrule size has also been interpreted as evidence of FGR formation within the protoplanetary disk via (i) a weakly turbulent nebula (Cuzzi, 2004; Hanna & Ketcham, 2018) or (ii) supersonic interactions between chondrules and a mixture of gas and dust (Liffman, 2019; Liffman & Toscano, 2000). Indeed, in either case, the frequency of interactions between chondrules and dust should have increased with increasing chondrule size; that is, larger chondrules would have accreted more dust (see Fig. 3). This scenario is supported by the observed correlation between the abundance of FGR-bearing chondrules and matrix (Fig. 5), provided that ICM modal abundance is the representative of dust abundances in the chondrite formation regions. We note that Rubin (2010) also found matrix abundance to be anticorrelated with the porphyritic/nonporphyritic chondrule ratio among different chondrite groups (CO, CK, CR, CM, CV, R, EL, and EH), which he considered a proxy of dust abundance during chondrule-forming events.

FGR and Chondrule Formation

When exactly did FGRs accrete onto the chondrules—in particular how long after chondrule formation? What do the textural differences between FGR and ICM teach us? Mounting evidence suggests that FGRs, or their immediate precursors, formed in relatively warm environments. Indeed, Zanetta et al. (2021) reported that, despite their porosity, FGRs in Paris show low degree of aqueous alteration, which they attributed to low water/rock ratios, as expected if water was mostly gaseous at the time of FGR formation (and if water mobility was limited to a few tens of micrometers on the parent body after accretion; Brearley, 2014). Bigolski (2017) has found that most FGRs around UOC chondrules exhibit sintered textures and estimated a range of 350–800 °C for their formation. Bigolski et al. (2016) have described numerous microchondrules (which testify to temperatures reaching the point of melting) in them, which we also found in carbonaceous chondrites' FGRs, if at lower abundances (Fig. 6). The lower abundance of presolar silicate grains in FGRs compared to the ICM in CO3 chondrites (Haenecour et al., 2018) may indicate their partial destruction during a heating event, whereas the opposite trend in aqueously altered CR2 chondrites may be traced to the more efficient aqueous alteration of the ICM (Haenecour et al., 2018). One may also note that the particles or aggregates which accreted to form FGRs (Matsumoto et al., 2021) were necessarily smaller than the FGR thickness and thus did not exceed a few tens of microns. However, the few Ma elapsed since the formation of the disk would allow sufficient time for reaching the sticking barrier of the order of a millimeter (e.g., Brauer et al., 2008; Jacquet, 2014). Perhaps then, some thermal or mechanical effects, such as ice volatilization or ram pressure, had temporarily disaggregated local millimeter-sized dust aggregates.

Most available literature ascribes the warm conditions of FGR formation to reheating episodes that occurred after the formation of rimmed chondrules (e.g., Bigolski, 2017; Bigolski et al., 2014; Krot et al., 1997). In this view, coarse-grained (or “igneous”) chondrule rims could represent melted FGRs (e.g., Rubin, 2010) from which microchondrules might have originated (Krot et al., 1997). However, no igneous chondrule rims were associated with the FGRs of chondrules in our sections. Furthermore, this can explain neither the larger thicknesses of igneous rims compared to FGRs (Matsumoto et al., 2021) nor the similar oxygen isotopic compositions of igneous rims and the host chondrules (Jacquet et al., 2015). Alternatively, microchondrules could have formed

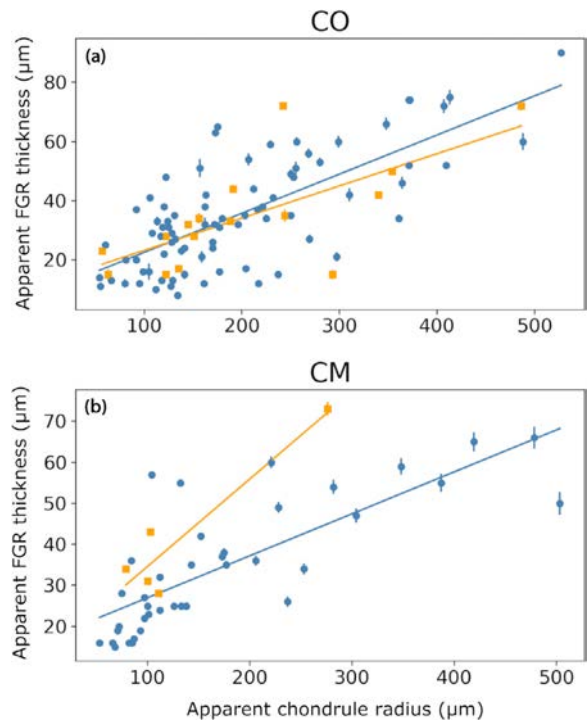


Fig. 6. Positive correlations between apparent chondrule radius and apparent FGR thickness between type I and type II chondrules in (a) CO and (b) CM carbonaceous chondrites. Colored solid lines represent simple regressions. Type I and type II chondrules are represented by the blue circle and orange square, respectively. No rimmed type II chondrule was found in the sections of CR and CV chondrites studied.

during collisions between partially molten chondrules (Dobrică & Brearley, 2016), and coarse-grained rims could have resulted from the accretion of microchondrules near the end of crystallization (Jacquet, 2021). In this view, early accreted (and “digested”) droplets would have merely increased the size of the chondrule, perhaps accounting for the correlation between average chondrule size and igneous rim thickness (Rubin, 2010).

FGRs may merely represent the tail end of this “hot dust accretion”; that is, FGRs may comprise material that was heated (but not molten) in the vicinity of the chondrule-forming region, in some “halo” around the volume where solids experienced melting (e.g., Hubbard & Ebel, 2014), as sketched in Fig. 7. Indeed, some (though perhaps not all; e.g., Hubbard & Ebel, 2014) presolar grains could have survived in such a peripheral environment, ultimately being preserved in FGRs. FGR may have incorporated some materials processed in the chondrule-forming region such as microchondrules or fine condensates (Wasson, 2008).

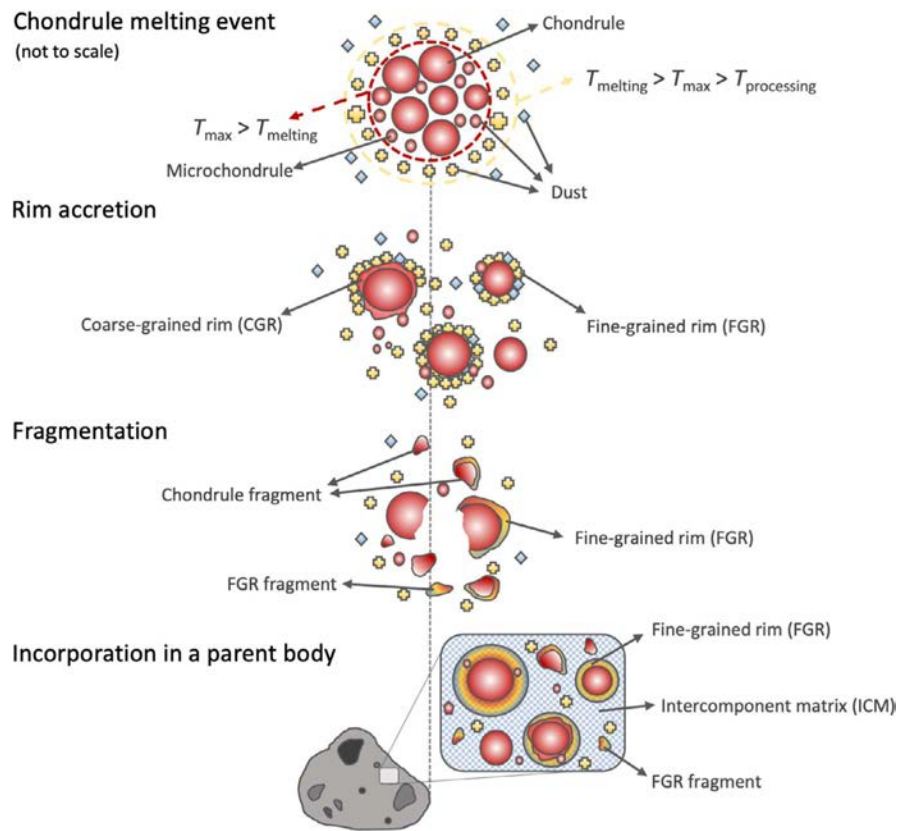


Fig. 7. Schematic representation of the proposed genetic link between chondrules and FGRs. The chondrule-forming region and chondrules are not drawn to scale. The chondrule-forming region includes a zone in which solids were melted, a peripheral region (“halo”) where solids were not melted but exceeded some arbitrary processing temperature, and an outer zone where dust went unprocessed. Chondrules (probably still warm) subsequently accreted FGRs, which were composed mostly of processed dust, with a few “contaminants” from the chondrule-melting volume (e.g., microchondrules) and presolar grains that could have survived in the unmelted halo. The abundance of rimmed chondrules depends on the dust abundance in the chondrule-forming region. Before their incorporation into a parent body, chondrule fragments with noncontinuous FGRs were likely produced through collisions in a turbulent nebular environment.

The FGR could have also accreted some unheated material but before it efficiently diluted the aforementioned higher temperature components. Rapid dust accretion would have been promoted by the higher dust densities estimated during chondrule formation (e.g., Alexander et al., 2008; Jacquet, 2021; Schrader et al., 2013). Chondrules may have essentially accreted all the “halo” material. The lack of significant differences in the FGR thickness/chondrule size relationships between type I and type II chondrules may suggest that the halo/chondrule-melting region mass ratio did not vary much. The exact properties of FGRs would depend on how the dust accretion rate compared with the cooling rate and/or the background temperature (inside or outside the snow line).

It is thus both possible and simpler to invoke the very formation of chondrules as the origin of the warm conditions recorded by FGRs, rather than a subsequent heating episode. In this scenario, the fine-grained materials produced during chondrule formation might be largely restricted to FGRs. If this is the case, matrix-chondrule complementarity (e.g., Goldberg et al., 2015; Hezel et al., 2018; Palme et al., 2015), on the matrix side, would be largely carried by FGR (and their fragments detached in the ICM; see Friend et al., 2018), with later co-accretion of unprocessed ICM not affecting the overall solar bulk elemental ratios (Braukmüller et al., 2018; Jacquet et al., 2016). Since large-scale migration within the disk would have destroyed any correlation between the frequency of

occurrence of FGRs (reflecting the conditions of chondrule formation) and ICM abundance (reflecting dust abundance during accretion), chondrules and matrix incorporated in a given chondrite must have formed locally (e.g., Piralla et al., 2021; Schneider et al., 2020).

CONCLUDING REMARKS

We characterized FGR around chondrules in CO, CM, CR, and CV carbonaceous chondrites. Our results revealed positive correlations between (i) rim thickness and host chondrule radius and (ii) the abundance of rimmed chondrules and that of other fine-grained matrix material. Combined with our petrographic description of FGR, our data suggest that they did not form during parent body evolution, but rather result from nebular processes, with the frequency and thickness of FGR being directly related to the abundance of available dust in their respective chondrule formation regions. Since large-scale migration within the disk would have destroyed the correlation between FGR and matrix abundances, our data support models of local chondrule formation with limited, if any, transport in the circumsolar disk. We hypothesize that FGR accreted under warm conditions at temperatures between silicate solidus (~1300 K) and ice vaporization (~170 K), in the aftermath of the chondrule-forming events. The matrix contribution to matrix–chondrule complementarity must then be dominated by FGR (and isolated fragments of rim within the matrix), with the later co-accretion of the unprocessed matrix not affecting the overall solar bulk composition.

Acknowledgments—We are grateful to Museo del Meteorito de San Pedro de Atacama for loaning the samples of CO chondrites. We thank the Muséum national d'Histoire naturelle de Paris for the loan of the CM, CV, and CR sections. G.A.P and F.O.E. acknowledge support from FONDECYT project 1201223. G.A.P. was supported by an Eiffel Excellence Scholarship (grant 968045D). We thank the anonymous reviewers for helpful comments that improved the manuscript. This is CRPG contribution #2794.

Data Availability Statement—The data that support the findings of this study are openly available at <https://doi.org/10.24396/ORDAR-82>.

Editorial Handling—Dr. A. J. Timothy Jull

REFERENCES

- Alexander, C. M. O'D., Grossman, J. N., Ebel, D. S., and Ciesla, F. J. 2008. The Formation Conditions of Chondrules and Chondrites. *Science* 320: 1617–9.
- Anders, E. 1964. Origin, Age, and Composition of Meteorites. *Space Science Reviews* 3: 583–714.
- Bigolski, J. N. 2017. The Formation of Fine-Grained Chondrule Rims in Unequilibrated Ordinary Chondrites. PhD thesis, The City University of New York, New York, USA.
- Bigolski, J. N., Weisberg, M. K., Connolly, H. C., and Ebel, D. S. 2016. Microchondrules in Three Unequilibrated Ordinary Chondrites. *Meteoritics & Planetary Science* 51: 235–60.
- Bigolski, J., Weisberg, M. K., Ebel, D. S., and Connolly, H. C. 2014. Microchondrules: Records of Multiple Heating Events in the Solar Nebula and Implications for Type II Chondrule Formation (Abstract #1879). 45th Lunar and Planetary Science Conference. CD-ROM.
- Bonal, L., Bourot-Denise, M., Quirico, E., Montagnac, G., and Lewin, E. 2007. Organic Matter and Metamorphic History of CO Chondrites. *Geochimica et Cosmochimica Acta* 71: 1605–23.
- Bonal, L., Quirico, E., Flandinet, L., and Montagnac, G. 2016. Thermal History of Type 3 Chondrites from the Antarctic Meteorite Collection Determined by Raman Spectroscopy of Their Polyaromatic Carbonaceous Matter. *Geochimica et Cosmochimica Acta* 189: 312–37.
- Brauer, F., Henning, T., and Dullemond, C. P. 2008. Planetesimal Formation Near the Snow Line in MRI-Driven Turbulent Protoplanetary Disks. *Astronomy and Astrophysics* 487: 1–4.
- Braukmüller, N., Wombacher, F., Hezel, D. C., Escoube, R., and Münker, C. 2018. The Chemical Composition of Carbonaceous Chondrites: Implications for Volatile Element Depletion, Complementarity and Alteration. *Geochimica et Cosmochimica Acta* 239: 17–48.
- Brearley, A. J. 1993. Matrix and Fine-Grained Rims in the Unequilibrated CO3 Chondrite, ALHA77307: Origins and Evidence for Diverse, Primitive Nebular Dust Components. *Geochimica et Cosmochimica Acta* 57: 1521–50.
- Brearley, A. J. 2014. Nebular Versus Parent Body Processing. In *Meteorites and Cosmochemical Processes*, edited by A. M. Davis, 309–34. Treatise on Geochemistry, vol. 1, 2nd ed. Oxford: Elsevier.
- Brearley, A. J., and Krot, A. N. 2012. Metasomatism in the Early Solar System: The Record from Chondritic Meteorites. In *Metasomatism and the Chemical Transformation of Rock—Lecture Notes in Earth System Sciences*, edited by D. E. Harlov and H. Austrheim, 659–789. Berlin: Springer.
- Connolly, H. C., Huss, G. R., and Wasserburg, G. J. 2001. On the Formation of Fe-Ni Metal in Renazzo-Like Carbonaceous Chondrites. *Geochimica et Cosmochimica Acta* 65: 4567–88.
- Connolly, H. C., and Jones, R. H. 2016. Chondrules: The Canonical and Noncanonical Views: A Review of Chondrule Formation. *Journal of Geophysical Research Planets* 121: 1885–99.
- Cosarinsky, M., Leshin, L. A., MacPherson, G. J., Guan, Y., and Krot, A. N. 2008. Chemical and Oxygen Isotopic Compositions of Accretionary Rim and Matrix Olivine in

- CV Chondrites: Constraints on the Evolution of Nebular Dust. *Geochimica et Cosmochimica Acta* 72: 1887–913.
- Cuzzi, J. N. 2004. Blowing in the Wind: III. Accretion of Dust Rims by Chondrule-Sized Particles in a Turbulent Protoplanetary Nebula. *Icarus* 168: 484–97.
- Cuzzi, J. N., and Olson, D. M. 2017. Recovering 3D Particle Size Distributions from 2D Sections. *Meteoritics & Planetary Science* 52: 532–45.
- Dobrică, E., and Brearley, A. J. 2016. Microchondrules in Two Unequilibrated Ordinary Chondrites: Evidence for Formation by Splattering from Chondrules During Stochastic Collisions in the Solar Nebula. *Meteoritics & Planetary Science* 51: 884–905.
- Friend, P., Hezel, D. C., Barrat, J. A., Zipfel, J., Palme, H., and Metzler, K. 2018. Composition, Petrology, and Chondrule-Matrix Complementarity of the Recently Discovered Jbilet Winselwan CM2 Chondrite. *Meteoritics & Planetary Science* 53: 2470–91.
- Goldberg, A. Z., Owen, J. E., and Jacquet, E. 2015. Chondrule Transport in Protoplanetary Discs. *Monthly Notices of the Royal Astronomical Society* 452: 4054–69.
- Haenecour, P., Floss, C., Zega, T. J., Croat, T. K., Wang, A., Jolliff, B. L., and Carpenter, P. 2018. Presolar Silicates in the Matrix and Fine-Grained Rims Around Chondrules in Primitive CO3.0 Chondrites: Evidence for Pre-Accretionary Aqueous Alteration of the Rims in the Solar Nebula. *Geochimica et Cosmochimica Acta* 221: 379–405.
- Hanna, R. D., and Ketcham, R. A. 2018. Evidence for Accretion of Fine-Grained Rims in a Turbulent Nebula for CM Murchison. *Earth and Planetary Science Letters* 481: 201–11.
- Hezel, D. C., Harak, M., and Libourel, G. 2018. What We Know About Elemental Bulk Chondrule and Matrix Compositions: Presenting the ChondriteDB Database. *Chemie der Erde* 78: 1–14.
- Hubbard, A., and Ebel, D. S. 2014. Protoplanetary Dust Porosity and FU Orionis Outbursts: Solving the Mystery of Earth's Missing Volatiles. *Icarus* 237: 84–96.
- Huss, G. R., Alexander, C. M. O'D., Palme, H., Bland, P. A., and Wasson, J. T. 2005. Genetic Relationships Between Chondrules, Fine-Grained Rims, and Interchondrule Matrix. In *Chondrites and the Protoplanetary Disk—ASP Conference Series 341*, edited by A. N. Krot, E. R. D. Scott, and B. Reipurth, 701–31. San Francisco: Astronomical Society of the Pacific.
- Jacquet, E. 2014. The Quasi-Universality of Chondrule Size as a Constraint for Chondrule Formation Models. *Icarus* 232: 176–86.
- Jacquet, E. 2021. Collisions and Compositional Variability in Chondrule-Forming Events. *Geochimica et Cosmochimica Acta* 296: 18–37.
- Jacquet, E., Alard, O., and Gounelle, M. 2015. Trace Element Geochemistry of Ordinary Chondrite Chondrules: The Type I/Type II Chondrule Dichotomy. *Geochimica et Cosmochimica Acta* 155: 47–67.
- Jacquet, E., Barrat, J. A., Beck, P., Caste, F., Gattacceca, J., Sonzogni, C., and Gounelle, M. 2016. Northwest Africa 5958: A Weakly Altered CM-Related Ungrouped Chondrite, not a C13. *Meteoritics & Planetary Science* 51: 851–69.
- Jacquet, E., Piralla, M., Kersaho, P., and Marrocchi, Y. 2021. Origin of Isolated Olivine Grains in Carbonaceous Chondrites. *Meteoritics & Planetary Science* 56: 13–33.
- Johnson, B. C., Minton, D. A., Melosh, H. J., and Zuber, M. T. 2015. Impact Jetting as the Origin of Chondrules. *Nature* 517: 339–41.
- Krot, A. N., and Rubin, A. E. 1996. Microchondrule-Bearing Chondrule Rims: Constraints on Chondrule Formation. In *Chondrules and the Protoplanetary Disk*, edited by R. H. Hewins, R. H. Jones, and E. R. D. Scott, 181–4. Cambridge, UK: Cambridge University Press.
- Krot, A. N., Rubin, A. E., Keil, K., and Wasson, J. T. 1997. Microchondrules in Ordinary Chondrites: Implications for Chondrule Formation. *Geochimica et Cosmochimica Acta* 61: 463–73.
- Lauretta, D. S., and Buseck, P. R. 2003. Opaque Minerals in Chondrules and Fine-Grained Chondrule Rims in the Bishunpur (LL3.1) Chondrite. *Meteoritics & Planetary Science* 38: 59–79.
- Lauretta, D. S., Hua, X., and Buseck, P. R. 2000. Mineralogy of Fine-Grained Rims in the ALH 81002 CM Chondrite. *Geochimica et Cosmochimica Acta* 64: 3263–73.
- Leitner, J., Metzler, K., Vollmer, C., Floss, C., Harries, D., Hoppe, P., and Haenecour, P. 2019. The Presolar Grain Inventory of Fine-Grained Chondrule Rims in the Mighei-Type (CM) Chondrites. *Meteoritics & Planetary Science* 55: 1176–206.
- Leitner, J., Vollmer, C., Floss, C., Zipfel, J., and Hoppe, P. 2016. Ancient Stardust in Fine-Grained Chondrule Dust Rims from Carbonaceous Chondrites. *Earth and Planetary Science Letters* 434: 117–28.
- Libourel, G., and Krot, A. N. 2007. Evidence for the Presence of Planetesimal Material Among the Precursors of Magnesian Chondrules of Nebular Origin. *Earth and Planetary Science Letters* 254: 1–8.
- Liffman, K. 2019. Fine-Grained Rim Formation—High Speed, Kinetic Dust Aggregation in the Early Solar System. *Geochimica et Cosmochimica Acta* 264: 118–29.
- Liffman, K., and Toscano, M. 2000. Chondrule Fine-Grained Mantle Formation by Hypervelocity Impact of Chondrules with a Dusty Gas. *Icarus* 143: 106–25.
- MacPherson, G. J., Hashimoto, A., and Grossman, L. 1985. Accretionary Rims on Inclusions in the Allende Meteorite. *Geochimica et Cosmochimica Acta* 49: 2267–79.
- Marrocchi, Y., Bekaert, D. V., and Piani L. 2018. Origin and Abundance of Water in Carbonaceous Asteroids. *Earth and Planetary Science Letters* 482: 23–32. <https://doi.org/10.1016/j.epsl.2017.10.060>.
- Marrocchi, Y., Euverte, R., Villeneuve, J., Batanova, V., Welsch, B., Ferrière, L., and Jacquet, E. 2019. Formation of CV Chondrules by Recycling of Amoeboid Olivine Aggregate-Like Precursors. *Geochimica et Cosmochimica Acta* 247: 121–41.
- Marrocchi, Y., Villeneuve, J., Batanova, V., Piani, L., and Jacquet, E. 2018. Oxygen Isotopic Diversity of Chondrule Precursors and the Nebular Origin of Chondrules. *Earth and Planetary Science Letters* 496: 132–41. <https://doi.org/10.1016/j.epsl.2018.05.042>.
- Matsumoto, Y., Hasegawa, Y., Matsuda, N., and Liu, M.-C. 2021. Formation of Rims Around Chondrules via Porous Aggregate Accretion. *Icarus* 367: 114538.
- McSween Jr., H. Y. 1977. Carbonaceous Chondrites of the Ornans Type: A Metamorphic Sequence. *Geochimica et Cosmochimica Acta* 41: 477–91.
- Metzler, K., Bischoff, A., and Stöffler, D. 1992. Accretionary Dust Mantles in CM Chondrites: Evidence for Solar

Origin of fine-grained rims

- Nebula Processes. *Geochimica et Cosmochimica Acta* 56: 2873–97.
- Morris, M. A., Boley, A. C., Desch, S. J., and Athanassiadou, T. 2012. Chondrule Formation in Bow Shocks Around Eccentric Planetary Embryos. *The Astrophysical Journal* 752: 27.
- Palme, H., Hezel, D. C., and Ebel, D. S. 2015. The Origin of Chondrules: Constraints from Matrix Composition and Matrix-Chondrule Complementarity. *Earth and Planetary Science Letters* 411: 11–9.
- Piani, L., Marrocchi, Y., Rigaudier, T., Vacher, L. G., Thomassin, D., and Marty, B. 2020. Earth's Water May Have Been Inherited from Material Similar to Enstatite Chondrite Meteorites. *Science* 369: 1110–3.
- Pignatelli, I., Marrocchi, Y., Mugnaioli, E., Bourdelle, F., and Gounelle, M. 2017. Mineralogical, Crystallographic and Redox Features of the Earliest Stages of Fluid Alteration in CM Chondrites. *Geochimica et Cosmochimica Acta* 209: 106–22.
- Pignatelli, I., Marrocchi, Y., Vacher, L. G., Delon, R., and Gounelle, M. 2016. Multiple Precursors of Secondary Mineralogical Assemblages in CM Chondrites. *Meteoritics & Planetary Science* 51: 785–805.
- Pinto, G. A., Marrocchi, Y., Morbidelli, A., Charnoz, S., Varela, M. E., Soto, K., Martínez, R., and Olivares, F. 2021. Constraints on Planetesimal Accretion Inferred from Particle-Size Distribution in CO Chondrites. *The Astrophysical Journal Letters* 917: L25.
- Piralla, M., Villeneuve, J., Batanova, V., Jacquet, E., and Marrocchi, Y. 2021. Conditions of Chondrule Formation in Ordinary Chondrites. *Geochimica et Cosmochimica Acta* 313: 295–312.
- Rubin, A. E. 2010. Physical Properties of Chondrules in Different Chondrite Groups: Implications for Multiple Melting Events in Dusty Environments. *Geochimica et Cosmochimica Acta* 74: 4807–28.
- Rubin, A. E., Scott, E. R. D., and Keil, K. 1982. Microchondrule-Bearing Clast in the Piancaldoli LL3 Meteorite: A New Kind of Type 3 Chondrite and Its Relevance to the History of Chondrules. *Geochimica et Cosmochimica Acta* 46: 1763–76.
- Ruzicka, A., Hiyagon, H., Hutson, M., and Floss, C. 2007. Relict Olivine, Chondrule Recycling, and the Evolution of Nebular Oxygen Reservoirs. *Earth and Planetary Science Letters* 257: 274–89.
- Schindelin, J., Arganda-Carreras, I., Frise, E., Kaynig, V., Longair, M., Pietzsch, T., Preibisch, S. et al. 2012. Fiji: An Open-Source Platform for Biological-Image Analysis. *Nature Methods* 9: 676–82.
- Schneider, J. M., Burkhardt, C., Marrocchi, Y., Brenneka, G. A., and Kleine, T. 2020. Early Evolution of the Solar Accretion Disk Inferred from Cr-Ti-O Isotopes in Individual Chondrules. *Earth and Planetary Science Letters* 551: 116585.
- Schrader, D. L., Connolly Jr., H. C., Lauretta, D. S., Nagashima, K., Huss, G. R., Davidson, J., and Domanik, K. J. 2013. The Formation and Alteration of the Renazzo-Like Carbonaceous Chondrites II: Linking O-Isotope Composition and Oxidation State of Chondrule Olivine. *Geochimica et Cosmochimica Acta* 101: 302–27.
- Scott, E. R. D., and Jones, R. H. 1990. Disentangling Nebular and Asteroidal Features of C03 Carbonaceous Chondrite Meteorites. *Geochimica et Cosmochimica Acta* 54: 2485–502.
- Scott, E. R. D., and Krot, A. N. 2014. Chondrites and Their Components. In *Treatise on Geochemistry*, 2nd ed., edited by H. D. Holland and K. K. Turekian, 65–137. Oxford: Elsevier.
- Sears, D. W. G., Benoit, P. H., and Jie, L. U. 1993. Two Chondrule Groups Each with Distinctive Rims in Murchison Recognized by Cathodoluminescence. *Meteoritics* 28: 669–75.
- Simon, J. I., Cuzzi, J. N., McCain, K. A., Cato, M. J., Christoffersen, P. A., Fisher, K. R., Srinivasan, P., Tait, A. W., Olson, D. M., and Scargle, J. D. 2018. Particle Size Distributions in Chondritic Meteorites: Evidence for Pre-Planetesimal Histories. *Earth and Planetary Science Letters* 494: 69–82.
- Suttle, M. D., Genge, M. J., Salge, T., Lee, M. R., Folco, L., Góral, T., Russell, S. S., and Lindgren, P. 2019. A Microchondrule-Bearing Micrometeorite and Comparison with Microchondrules in CM Chondrites. *Meteoritics & Planetary Science* 54: 1303–24.
- Takayama, A., and Tomeoka, K. 2012. Fine-Grained Rims Surrounding Chondrules in the Tagish Lake Carbonaceous Chondrite: Verification of Their Formation Through Parent-Body Processes. *Geochimica et Cosmochimica Acta* 98: 1–18.
- Thirumalai, K., Singh, A., and Ramesh, R. 2011. A MATLAB™ Code to Perform Weighted Linear Regression with (Correlated or Uncorrelated) Errors in Bivariate Data. *Journal of the Geological Society of India* 77: 377–80.
- Tomeoka, K., and Ohnishi, I. 2010. Indicators of Parent-Body Processes: Hydrated Chondrules and Fine-Grained Rims in the Mokoia CV3 Carbonaceous Chondrite. *Geochimica et Cosmochimica Acta* 74: 4438–53.
- Tomeoka, K., and Ohnishi, I. 2014. Olivine-Rich Rims Surrounding Chondrules in the Mokoia CV3 Carbonaceous Chondrite: Further Evidence for Parent-Body Processes. *Geochimica et Cosmochimica Acta* 137: 18–34.
- Tomeoka, K., and Ohnishi, I. 2015. Redistribution of Chondrules in a Carbonaceous Chondrite Parent Body: A Model. *Geochimica et Cosmochimica Acta* 164: 543–55.
- Trigo-Rodríguez, J. M., Rubin, A. E., and Wasson, J. T. 2006. Non-Nebular Origin of Dark Mantles Around Chondrules and Inclusions in CM Chondrites. *Geochimica et Cosmochimica Acta* 70: 1271–90.
- Vacher, L. G., Truche, L., Faure, F., Tissandier, L., Mosser-Ruck, R., and Marrocchi, Y. 2019. Deciphering the Conditions of Tochilinite and Cronstedtite Formation in CM Chondrites from Low Temperature Hydrothermal Experiments. *Meteoritics & Planetary Science* 54: 1870–89.
- Wasson, J. T. 2008. Evaporation of Nebular Fines During Chondrule Formation. *Icarus* 195: 895–907.
- Wasson, J. T., and Rubin, A. E. 2014. Absence of Matrix-Like Chondrule Rims in CR2 LAP 02342. *Meteoritics & Planetary Science* 49: 245–60.
- Zanda, B., Hewins, R. H., Bourot-Denise, M., Bland, P. A., and Albarède, F. 2006. Formation of Solar Nebula Reservoirs by Mixing Chondritic Components. *Earth and Planetary Science Letters* 248: 650–60.
- Zanda, B., Lewin, E., and Humayun, M. 2018. The Chondritic Assemblage: Complementarity Is Not a Required Hypothesis. In *Chondrules: Records of Protoplanetary Disk Processes*, edited by S. Russell, H. C. Connolly Jr., and A. Krot, 122–50. Cambridge, UK: Cambridge University Press.

Zanetta, P. M., Leroux, H., le Guillou, C., Zanda, B., and Hewins, R. H. 2021. Nebular Thermal Processing of Accretionary Fine-Grained Rims in the Paris CM Chondrite. *Geochimica et Cosmochimica Acta* 295: 135–54.

Zolensky, M., Barrett, R., and Browning, L. 1993. Mineralogy and Composition of Matrix and Chondrule Rims in Carbonaceous Chondrites. *Geochimica et Cosmochimica Acta* 57: 3123–48.

SUPPORTING INFORMATION

Additional supporting information may be found in the online version of this article.

Table S1. Uncertainty of free-hand measurements

Table S2. Rimmed chondrules measurements

Table S3. Abundance of rimmed chondrules

Chapter 5

Constraints on planetesimal accretion inferred from particle-size distribution in CO chondrites

Published research paper as Pinto et al. (2021), *Astrophysical Journal Letters*

Chapter introduction

We estimated the particle-size distributions of more than 6000 chondrite components within different CO carbonaceous chondrites. We used Secondary Electron Microscope (SEM) maps, electron probe microanalyzer (EMPA) to classify the petrologic degree of chondrites, image processing software for the image analysis and astrophysical models to constrain the accretion of particles in the circumsolar disk. Our particle-size analysis revealed that the mean spherical diameters of chondrules increase with increasing metamorphic degree. Combining our results with literature data, we show that this relationship was not established during post-accretion thermal metamorphism, but instead records aerodynamic size-sorting of particles during the accretion of the CO parent body(ies). By modeling the self-gravitating contraction of clumps of chondrules, we show that the accretion processes generated a gradual change in chondrule size, with larger chondrules being more centrally concentrated in the parent body(ies) than smaller ones.

Considerations: The CO chondrites EM 216 and EM 463 are classified in the zone of subtype ≥ 3.2 according to the Cr diagram (**Figure 2.6**, chapter 2). Although these chondrites can be 3.2, as shown in **Figure 2** (this chapter), further analysis through other criteria (Raman spectroscopy or metal composition) is recommended to clarify these subtypes. The second observation is the large abundance of type II chondrules in Isna (95%), shown in **Table 1** (this chapter). Maybe some of them were incorrectly classified based chiefly on the FeO content rather than texture. This consideration is not important for the aim of the paper/chapter. However, it can be misleading if someone searches for the relative abundances of different types of chondrules among CO chondrites.



Constraints on Planetesimal Accretion Inferred from Particle-size Distribution in CO Chondrites

Gabriel A. Pinto^{1,2}, Yves Marrocchi¹, Alessandro Morbidelli³, Sébastien Charnoz⁴, Maria Eugenia Varela⁵,
Kevin Soto⁶, Rodrigo Martínez⁷, and Felipe Olivares²

¹ Université de Lorraine, CNRS, CRPG, UMR 7358, Vandœuvre-lès-Nancy, F-54501, France; gabriel.pinto@univ-lorraine.fr

² Instituto de Astronomía y Ciencias Planetarias, Universidad de Atacama, Copayapu 485, Copiapó, Chile

³ Laboratoire Lagrange, UMR7293, Université de Nice Sophia-Antipolis, CNRS, Observatoire de la Côte d'Azur, Boulevard de l'Observatoire, F-06304 Nice Cedex4, France

⁴ Université de Paris, Institut de physique du globe de Paris, CNRS, F-75005 Paris, France

⁵ Instituto de Ciencias Astronómicas, de la Tierra y el Espacio, ICATE-CONICET, San Juan, Argentina

⁶ Facultad de Ciencias, Instituto de Ciencias de la Tierra, Universidad Austral de Chile, Valdivia, Chile
Museo del Meteorito, San Pedro de Atacama, Chile

Received 2021 May 20; revised 2021 July 6; accepted 2021 July 22; published 2021 August 19

Abstract

The formation of planetesimals was a key step in the assemblage of planetary bodies, yet many aspects of their formation remain poorly constrained. Notably, the mechanism by which chondrules—submillimetric spheroids that dominate primitive meteorites—were incorporated into planetesimals remains poorly understood. Here we classify and analyze particle-size distributions in various CO carbonaceous chondrites found in the Atacama Desert. Our results show that the average circle-equivalent diameters of chondrules define a positive trend with the petrographic grade, which reflects the progressive role of thermal metamorphism within the CO parent body. We show that this relationship could not have been established by thermal metamorphism alone but rather by aerodynamic sorting during accretion. By modeling the self-gravitational contraction of clumps of chondrules, we show that (i) the accretion of the CO parent body(ies) would have generated a gradual change of chondrule size with depth in the parent body, with larger chondrules being more centrally concentrated than smaller ones, and (ii) any subsequent growth by pebble accretion would have been insignificant. These findings give substantial support to the view that planetesimals formed via gravitational collapse.

Unified Astronomy Thesaurus concepts: Asteroids (72); Chondrites (228); Accretion (14); Protoplanetary disks (1300); Planetesimals (1259)

Supporting material: machine-readable table

1. Introduction

Planetesimals are solid objects larger than 1 km in diameter that formed by the accumulation of orbiting bodies in the protoplanetary disk and whose internal strengths are dominated by self-gravity; they represent the main building blocks of the planets orbiting the Sun today. Chondrites are fragments of asteroids that were never sufficiently heated to melt their constituent silicates and thus preserve primitive grains of the materials from which they agglomerated, including refractory inclusions and chondrules, cemented together by a complex fine-grained matrix. Refractory inclusions are millimeter- to centimeter-sized particles that represent the oldest dated objects in the solar system (Connelly et al. 2012). Chondrules are (sub)millimeter-sized igneous spherules that formed by a still elusive high-temperature mechanism linked to either nebular or planetary processes (e.g., Johnson et al. 2015; Marrocchi et al. 2018, 2019). Although chondrules are the main constituents of chondrites and their accretion thus represents a key step in the formation of planetesimals, the mechanism by which they assembled into planetesimals remains poorly constrained.

Recent theoretical advances suggest that planetesimals formed from clumps of small particles (mostly chondrules in the case of chondrites) whose common gravitational attraction outweighed the dispersive action of turbulent diffusion (Klahr & Schreiber 2020, 2021). This process requires that clumps of particles be sufficiently dense and massive and would produce planetesimals of typically ~10–100 km in diameter depending on the remaining gas

mass in the solar nebula at the time of planetesimal formation. However, the formation of such particle clumps remains debated.

For instance, it was proposed that particles were concentrated into large vortices (Barge & Sommeria 1995) or in regions between small vortices that developed in the disk at the dissipation scale (Cuzzi et al. 2001, 2008). More recently, it was proposed that particle clumps formed due to *streaming instabilities*, hydrodynamic instabilities due to the differential velocities of particles relative to the surrounding gas (Youdin & Goodman 2005; Johansen et al. 2009; Simon & Armitage 2014; Wahlberg Jansson & Johansen 2014, 2017; Johansen et al. 2015; Li et al. 2018, 2019).

For all these scenarios, the effectiveness of streaming instabilities in promoting clump formation depends on particle size, or rather the Stokes number, which here is the ratio between a particle's stopping time due to friction with the gas and the orbital period. For chondrule-sized particles, triggering the gravitational collapse of a pebble cloud in streaming instability (Gerbig et al. 2020) requires particles to be radially concentrated in an annulus (Drażkowska et al. 2016) to achieve a sufficiently large solid/gas ratio (Carrera et al. 2015; Yang et al. 2017). One of the strengths of the gravitational collapse scenarios is that it predicts the formation of binary planetesimals, which are observed in large numbers in the relatively pristine trans-Neptunian belt, and reproduces the observed statistics of their orbital orientations (Nesvorný et al. 2019).

Once planetesimals have formed, they can continue growing by accreting individual particles (if they exceed a critical size of about 1000 km diameter; Ormel & Klahr 2010) as they drift through the disk. This process is known as pebble accretion (Lambrechts & Johansen 2012; Johansen et al. 2015). The initial gravitational contraction of a clump of particles and later pebble accretion should produce characteristic variations of particle size with depth inside the resulting planetesimal. Here we report estimated particle-size distributions within different CO carbonaceous chondrites, chosen because they experienced limited alteration processes after their agglomeration, which could have affected the sizes of their constituent particles. We use our data to model the conditions of planetesimal accretion within the protoplanetary disk and the possible layered structure of the CO parent body(ies).

2. Material and Method

We surveyed all particles in sections of three CO₃ carbonaceous chondrites recovered in the Atacama Desert and provided by the Museo del Meteorito (San Pedro de Atacama, Chile): El Médano 216 (EM 216), El Médano 463 (EM 463), and Los Vientos 123 (LoV 123). We also determined the particle-size distribution in Isna (thick Section 3239 from the Muséum national d'Histoire naturelle, Paris, France). Backscattered electron (BSE) mosaics and X-ray compositional maps (Fe, Ni, Al, Mg, Ca, Si, S, and Cr) were acquired using (i) a JEOL JSM-6510 scanning electron microscope (SEM) equipped with a Genesis EDX detector and operating with a 3 nA electron beam accelerated at 20 kV (CRPG, Nancy, France) and (ii) a JEOL 6400 SEM operating with a 1 nA electron beam accelerated at 15 kV (Naturhistorisches Museum, Vienna, Austria). The chemical compositions of ferroan olivine grains in FeO-rich chondrules of EM 216 and EM 463 were quantified using a Cameca SX100 electron microprobe at the Service Commun de Microscopies Electroniques et de Microanalyses X (SCMEM, Université de Lorraine, Nancy, France) using a 12 nA focused beam accelerated at 15 kV. LoV 123 was analyzed by wavelength dispersive spectroscopy with an ARL-SEMQ electron microprobe at ICATE (San Juan, Argentina) operating with a 15 nA electron beam accelerated at 15 kV. Natural and synthetic standards were used for both instrument calibrations.

Mosaics of all samples were prepared using the GNU image manipulation program. Particle-size measurements were performed using the Fiji distribution of the ImageJ open-source image processing software (Schindelin et al. 2012). We analyzed all nebular components, including chondrules (types I and II being FeO-poor and -rich, respectively), calcium aluminum-rich inclusions (CAIs, types A and B), amoeboid olivine aggregates (AOAs), and isolated olivine grains (IOGs) over total surface areas of 96 mm², 27 mm², 32.4 mm², and 30.6 mm² for EM 463, EM 216, LoV 123, and Isna, respectively. The sharpness and continuity of the borders in the X-ray compositional maps was improved in Fiji by first applying mean filter at 1 pixel and then enhancing the image contrast at 0.5%. Each particle was recorded in a mask layer by free-hand tracing (Figure 1). We did not distinguish between AOAs or type-A or -B CAIs for refractory components in EM 216 and LoV 123. Each particle's diameter (d) was calculated assuming that its total area was circular in cross section (i.e., as $d = \sqrt{\text{pixel area}/\pi \times 2}$).

3. Results

The Cr₂O₃ contents of subhedral FeO-rich olivine crystals were determined for 43, 49, and 62 type-II porphyritic chondrules in EM 216, EM 463, and LoV 123, respectively. Chondrule olivine grains appear heterogeneous in both texture (Figure 1) and composition (Fa_{21.3–88.2}, mean Fa_{50.2±10.7}; Table 1). Ferroan olivines in type-II chondrules of EM 463 contain 0.04–0.57 wt% Cr₂O₃ (average 0.09 ± 0.10 wt.%, 1σ ; Table 1); those of EM 216 and LoV 123 contain 0.09 ± 0.10 and 0.30 ± 0.13 wt% Cr₂O₃, respectively.

EM 216, EM 463, and LoV 123 show high modal abundances of FeO-poor type-I chondrules (41.59, 33.15, and 46.74%, respectively; Table 2) surrounded by fine-grained Fe-rich matrix (Figure 1). Isna is dominated by type-II chondrules (33.26%) with occasional type-I chondrules (1.85%; Table 2). The modal abundances of refractory inclusion (CAIs + AOAs) range from 1.59% in Isna to 8.60% in LoV 123 (Table 1). We also observe a large variation in the modal abundances of type-II chondrules, from 5.22% in EM 216 to 33.26% in Isna (Table 2).

Our results show a significant difference between the mean spherical diameters of type-I and type-II chondrules: 92.78 and 162.52 μm , respectively (Table 3). The mean spherical diameters (1σ) of type-I chondrules vary among the different COs: those in LoV 123, EM 216, EM 463, and Isna have average sizes of 71.6 (56.51), 90.91 (65.61), 111.37 (89.44), and 170.81 μm (54.90), respectively (Figure 2(A); Table 3). Similarly, type-II chondrules and refractory inclusions (CAIs + AOAs) show variable average sizes among the different COs (Table 3): in LoV 123, EM 216, EM 463, and Isna, type-II chondrules have mean diameters of 141.64 (112.92), 103.84 (95.26), 164.10 (100.38), and 184.85 μm (80.14), respectively, and refractory inclusions have mean diameters of 62.63 (39.06), 75.32 (52.80), 109.76 (71.24), and 67.11 μm (47.81), respectively. The circularity and the mean aspect ratio of chondrules in our studied CO chondrites is 0.67 ± 0.15 and 1.60 ± 0.45 , respectively.

4. Discussion

4.1. Correlation between Chondrule-size Distribution and Degree of Metamorphism

The degree of thermal alteration (i.e., petrographic grades) experienced by the carbonaceous chondrites can be estimated based on the mean and standard deviation of Cr₂O₃ content of FeO-rich olivines in type-II chondrules (Grossman & Brearley 2005; Table 1). We determined a petrographic grade of LoV 123, EM 216, and EM 463 to be 3.05, 3.2, and 3.2, respectively. The petrographic grade of Isna has been determined to be 3.75 ± 0.05 based on the Cr₂O₃ content of Fe-rich olivines (Rubin & Li 2019) and detailed petrographic and mineralogical studies of AOAs (Chizmadia et al. 2002). Incorporating recent literature data for CO chondrites (Ebel et al. 2016), average chondrule diameters define a positive relationship with the petrographic grade of their parent chondrite (Figure 2). Such a correlation was first noticed by Rubin (1989), although they reported a dissimilar relationship (Figure 2(A)), likely due to their different estimation method and limited number of analyzed particles (<1000). Because we used a similar method to Ebel et al. (2016), here we compare our results to their data set.

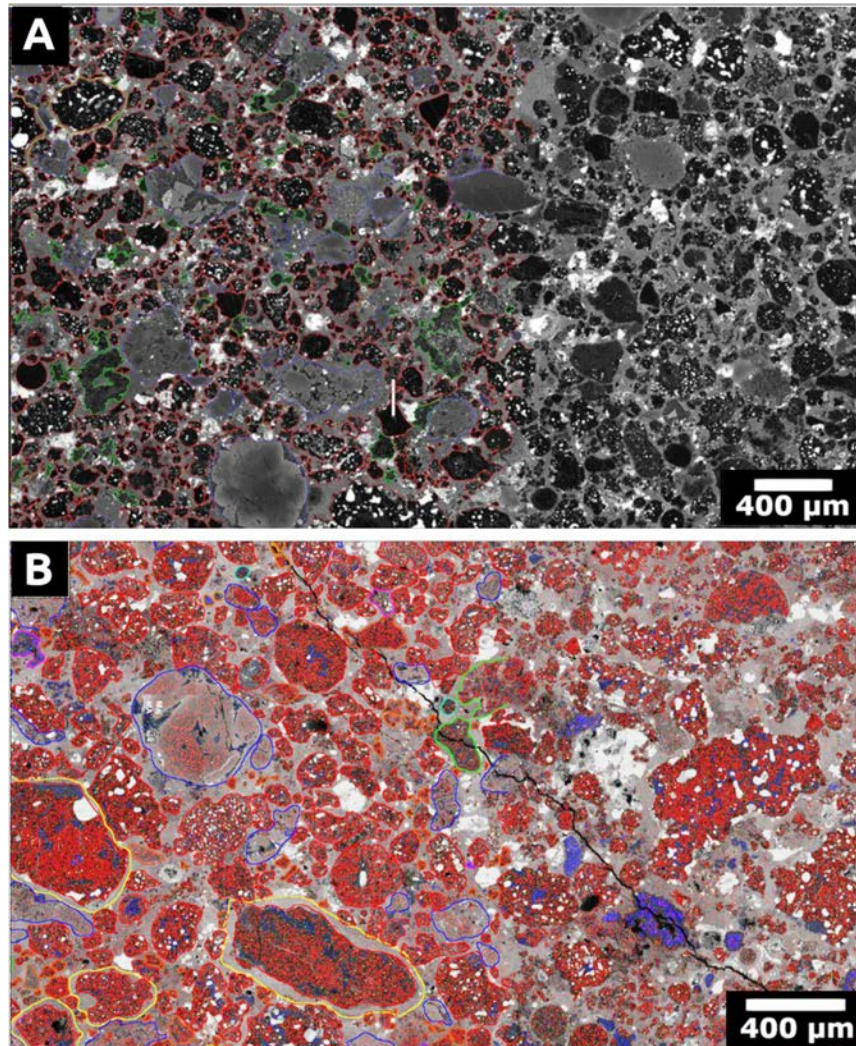


Figure 1. Representative examples of particle selection. (A) BSE image of LoV 123. (B) X-ray compositional map of EM 463, with Mg, Al, Ca, and Fe shown in red, blue, green, and white, respectively. The colors of particle outlines indicate component type. In (A) type-I chondrules are outlined in red, type-II chondrules in blue, refractory components in green, IOGs in orange, and fine-grained rims in yellow. In (B), outline colors are as in (A), except that refractory components are distinguished between AOs in green and CAIs in purple.

The deformation of chondrules (Figure 1) could have either occurred during the evolution of the protoplanetary disk or within chondritic parent bodies. As lobate chondrules are commonly observed in carbonaceous chondrites that experienced minimal secondary deformation (Jacquet 2021) and CO carbonaceous chondrites show low impact-generated metamorphism transformation (Scott et al. 1992), we thus favor a nebular origin for the nonspherical chondrules.

The observed correlation between chondrule diameter and petrographic grade in CO chondrites could result from (i) the conditions of planetesimal accretion (Scott & Jones 1990) and/or (ii) postaccretion thermal metamorphism processes resulting from impacts and/or ^{26}Al decay (Doyle et al. 2015; Vacher et al. 2018; Amsellem et al. 2020; Turner et al. 2021). Although thermal metamorphism could result in mineral coarsening (Huss et al. 2006), this would mainly affect Fe–Ni metal beads and sulfides and would require temperatures >800 °C,

significantly hotter than those estimated for CO chondrites (i.e., 300–600 °C; Jones & Rubie 1991; Keil 2000; Bonal et al. 2007). This is consistent with the fact that CV chondrules were only affected by Fe–Mg diffusion without any significant size increase, despite having undergone thermal metamorphism at temperatures higher than in CO chondrites (i.e., ≥ 600 °C; Ganino & Libourel 2017). Furthermore, type-I chondrule boundaries are well defined in CO chondrites, even in the most metamorphosed sample investigated here (i.e., CO3.8 Isna). Taken together, these lines of evidence indicate that (i) the size characteristics of chondrules result from their formation processes during the evolution of the disk and (ii) aerodynamic sorting played a key role during the accretion of the CO parent body(ies).

Rubin (1989) suggested that the relationship between chondrule size and the degree of metamorphism is related to monotonic changes in the aggregation of materials in the nebular CO

Table 1
Chemical Compositions of Ferroan Olivine Grains in Type-II Chondrules of Three CO Carbonaceous Chondrites (EM 463, EM 216, and LoV 123)

CO3	#	SiO ₂	FeO	Al ₂ O ₃	CaO	MnO	MgO	Cr ₂ O ₃	TiO ₂	Total
EM 463	49	38.34	27.85	0	0.09	0.31	34.58	0	0	101.2
		36.05	39.18	0.03	0.11	0.28	24.89	0.15	0	100.7
		37.41	30.69	0.05	0.09	0.25	31.50	0.05	0	100.0
		36.48	33.55	0.16	0.08	0.28	30.73	0.09	0	101.4
		38.51	23.92	0.03	0.01	0.31	38.32	0.01	0	101.1
		38.27	26.49	0.10	0.02	0.30	36.47	0.01	0.01	101.6
		37.83	28.32	0.10	0.14	0.34	35.69	0.14	0.01	102.6
		38.53	24.64	0.04	0.11	0.35	37.80	0	0	101.5
		37.00	31.29	0.05	0.14	0.40	31.79	0.06	0.01	100.7
		39.12	23.16	0.04	0.13	0.26	39.32	0.06	0	102.1
		35.92	35.52	0	0.11	0.36	28.72	0.03	0	100.7
		37.92	26.29	0.01	0.15	0.38	36.24	0.08	0	101.1
		37.91	30.51	0.06	0.09	0.17	32.96	0.08	0.01	101.8
		36.94	34.02	0.09	0.02	0.38	29.42	0.18	0	101.0
		39.29	23.36	0	0.18	0.25	38.18	0.19	0.04	101.5
		40.21	17.47	0.10	0.10	0.22	42.78	0.11	0	101.0
		37.97	24.12	0.23	0.30	0.26	36.13	0.57	0.01	99.6
		38.61	26.09	0.02	0.12	0.37	35.62	0.08	0.01	100.9
		38.40	24.24	0.09	0.09	0.16	36.61	0.08	0	99.7
		38.40	26.45	0.03	0	0.22	35.04	0.05	0	100.2
		37.89	30.34	0.04	0.09	0.38	33.23	0.09	0	102.1
		38.34	25.83	0	0.04	0.20	35.77	0	0.02	100.2
		39.23	21.67	0.01	0.03	0.27	39.77	0.12	0	101.1
		38.30	28.82	0.08	0.13	0.43	33.43	0.16	0	101.4
		37.41	31.61	0	0.18	0.31	31.75	0.04	0.03	101.3
		38.65	23.64	0.03	0.02	0.12	38.09	0.12	0	100.6
		38.63	24.94	0.10	0.06	0.16	37.24	0.19	0.01	101.3
		38.24	27.19	0.08	0	0.30	35.15	0.38	0	101.3
		38.28	27.97	0.10	0.01	0.26	33.84	0.05	0	100.5
		40.41	17.10	0.03	0.07	0.22	44.05	0.03	0.03	101.9
		37.81	29.89	0.06	0.17	0.28	32.57	0.10	0	100.9
		36.27	37.11	0.02	0.10	0.48	27.79	0.07	0	101.8
		36.66	33.88	0.07	0.14	0.24	30.13	0.06	0	101.2
		37.74	21.68	0.10	0.06	0.20	40.56	0.10	0	100.4
		37.55	30.09	0.01	0.11	0.22	33.38	0.04	0	101.4
		37.26	32.46	0.08	0.21	0.44	31.28	0	0.05	101.8
		36.82	34.74	0	0.08	0.53	29.35	0.05	0.04	101.6
		35.60	37.13	0.03	0.37	0.19	27.65	0.02	0	100.9
		35.32	40.69	0.02	0.27	0.46	23.44	0.07	0	100.3
		36.00	38.28	0.01	0.18	0.40	26.07	0.07	0	101.0
		37.63	31.64	0.05	0.14	0.43	31.66	0.13	0	101.7
		37.12	34.90	0.04	0.16	0.45	29.55	0.08	0.01	102.3
		38.95	23.89	0.01	0.03	0.16	38.35	0.07	0	101.4
		36.14	37.74	0.04	0.24	0.43	26.92	0.08	0	101.6
		38.19	27.40	0.03	0.14	0.32	35.56	0.15	0	101.8
		36.79	35.39	0.01	0.22	0.39	28.60	0.08	0	101.5
		38.26	28.99	0.01	0.06	0.42	34.50	0.06	0	102.3
		36.28	35.30	0.02	0.24	0.36	28.41	0.06	0.01	100.7
		37.04	29.66	0.03	0.18	0.35	33.41	0.06	0.02	100.7
	<i>Mean</i>	37.71	29.33	0.05	0.12	0.31	33.56	0.09	0.01	
	<i>STD</i>	1.13	5.57	0.05	0.08	0.10	4.57	0.10	0.01	
EM 216	43	37.04	35.98	0.04	0.08	0.41	28.47	0.02	0	102.0
		37.47	33.21	0.03	0.14	0.42	30.91	0.11	0.04	102.3
		36.13	38.93	0.09	0.28	0.39	26.55	0.10	0.01	102.5
		37.49	28.17	0.10	0.22	0.33	35.20	0.08	0	101.6
		38.52	26.03	0.01	0.06	0.30	36.89	0.11	0	101.9
		37.41	31.21	0.03	0.01	0.39	31.99	0.08	0	101.1
		35.96	39.55	0.04	0.25	0.45	24.97	0	0	101.2
		38.79	24.12	0.03	0.02	0.27	37.98	0.41	0	101.6
		37.53	33.13	0	0.15	0.27	32.12	0.09	0	103.3
		37.46	30.82	0.27	0.05	0.24	31.97	0.40	0	101.2
		36.11	39.77	0	0.14	0.22	25.86	0.03	0	102.1
		38.41	28.06	0	0.08	0.29	34.43	0.13	0	101.4
		37.11	34.77	0	0.08	0.47	29.28	0.05	0	101.8

Table 1
(Continued)

CO3	#	SiO ₂	FeO	Al ₂ O ₃	CaO	MnO	MgO	Cr ₂ O ₃	TiO ₂	Total
		38.43	25.50	0.03	0.10	0.25	36.57	0	0.02	100.9
		35.91	38.17	0.08	0.19	0.48	25.92	0.19	0	100.9
		37.73	32.52	0.02	0.02	0.22	31.88	0.02	0	102.4
		35.51	41.54	0.06	0.34	0.42	23.33	0.12	0.03	101.3
		36.01	37.16	0.03	0.15	0.46	27.34	0.06	0.02	101.2
		38.80	25.71	0.02	0.11	0.47	37.31	0.04	0	102.4
		36.89	37.57	0.02	0.06	0.37	26.87	0.11	0	101.9
		38.56	26.92	0	0.00	0.13	35.91	0.07	0	101.6
		36.18	38.87	0	0.15	0.35	26.31	0.04	0	101.9
		36.91	31.87	0.08	0.17	0.24	31.28	0.16	0	100.7
		35.93	40.76	0.02	0.22	0.55	24.52	0.05	0.04	102.1
		37.44	32.88	0.06	0.05	0.47	31.49	0.02	0.00	102.4
		35.80	40.93	0.01	0.28	0.38	24.63	0.08	0	102.1
		36.68	37.19	0.02	0.11	0.46	26.80	0.09	0.03	101.3
		37.16	34.65	0.03	0.07	0.32	30.04	0.03	0	102.3
		35.96	39.53	0	0.07	0.19	25.62	0.06	0	101.4
		36.82	36.62	0	0.12	0.32	28.42	0.06	0	102.4
		38.34	28.48	0.04	0.02	0.32	35.09	0.09	0.02	102.4
		36.15	37.60	0.03	0.07	0.32	27.12	0	0.02	101.3
		37.88	30.32	0.01	0.06	0.22	32.70	0.05	0.02	101.2
		38.28	27.78	0	0.05	0.28	35.41	0.17	0	102.0
		34.40	48.35	0.01	0.14	0.45	18.21	0.07	0	101.6
		37.04	34.55	0.04	0.09	0.32	30.23	0.01	0	102.3
		35.51	41.70	0	0.15	0.31	24.15	0.07	0	101.9
		36.93	36.28	0.01	0.13	0.27	28.88	0	0.02	102.5
		36.77	35.47	0.06	0.08	0.29	29.26	0.07	0	102.0
		36.56	35.44	0.06	0.24	0.14	28.97	0.06	0	101.5
		34.61	41.14	0.21	0.25	0.36	23.82	0.40	0	100.8
		37.98	29.72	0	0.10	0.22	33.24	0	0	101.3
		37.46	31.18	0.06	0.10	0.28	33.48	0.18	0.01	102.7
	<i>Mean</i>	36.98	34.42	0.04	0.12	0.33	29.80	0.09	0.01	
	<i>STD</i>	1.09	5.44	0.05	0.08	0.10	4.51	0.10	0.01	
<i>LoV 123</i>	62	35.67	31.03	0.31	32.75	0.24	0	100.0
		35.54	33.42	0.31	30.54	0.23	0	100.0
		35.62	32.24	0.31	32.20	0.27	0.04	100.7
		35.69	33.58	0.20	31.47	0.27	0	101.2
		33.56	42.69	0.43	23.09	0.27	0	100.0
		37.40	21.97	0.25	40.04	0.31	0	100.0
		33.61	41.06	0.33	25.03	0.32	0.03	100.4
		34.18	36.98	0.26	28.02	0.40	0	99.8
		36.65	27.88	0.22	34.58	0.13	0.04	99.5
		35.73	27.90	0.15	36.32	0.27	0.01	100.4
		35.92	31.78	0.32	33.20	0.22	0	101.4
		33.28	38.93	0.59	25.75	0.13	0.01	98.7
		33.17	42.60	0.34	23.95	0.15	0	100.2
		33.48	42.07	0.52	24.00	0.13	0.03	100.2
		33.39	41.49	0.45	24.46	0.36	0.01	100.2
		32.97	42.15	0.46	24.82	0.25	0	100.6
		37.30	26.38	0.30	35.92	0.22	0.05	100.2
		40.68	20.79	0.23	31.63	0.33	0.12	93.8
		34.73	39.52	0.43	24.90	0.27	0.02	99.8
		34.63	39.66	0.44	24.74	0.32	0	99.8
		34.68	39.59	0.43	24.82	0.29	0.01	99.8
		33.82	43.32	0.49	22.21	0.50	0.02	100.3
		35.19	38.42	0.46	25.68	0.30	0	100.1
		35.78	29.81	0.26	33.91	0.32	0.03	100.1
		35.00	34.25	0.32	29.95	0.21	0.01	99.7
		38.25	18.43	0.15	42.55	0.75	0	100.1
		34.12	38.47	0.52	26.47	0.36	0.01	100.0
		34.13	37.41	0.41	27.88	0.32	0.01	100.1
		34.97	40.21	0.53	24.48	0.27	0.04	100.5
		34.17	42.01	0.62	22.93	0.10	0	99.8
		32.64	48.74	0.53	18.20	0.32	0.02	100.4
		32.33	52.22	0.61	14.18	0.25	0.03	99.6

Table 1
(Continued)

CO3	#	SiO ₂	FeO	Al ₂ O ₃	CaO	MnO	MgO	Cr ₂ O ₃	TiO ₂	Total
		35.88	28.68	0.25	35.17	0.28	0.03	100.3
		35.78	30.47	0.39	33.34	0.31	0	100.3
		36.19	30.39	0.35	32.38	0.59	0	99.9
		36.64	30.31	0.21	33.17	0.24	0.02	100.6
		37.65	22.20	0.25	39.53	0.28	0	99.9
		37.27	27.96	0.39	34.91	0.21	0.07	100.8
		36.62	28.41	0.44	34.30	0.22	0	100.0
		37.66	23.47	0.37	38.07	0.38	0.05	100.0
		35.49	36.77	0.32	27.34	0.21	0.04	100.2
		35.86	33.14	0.25	30.56	0.51	0	100.3
		36.80	25.71	0.25	36.44	0.55	0.01	99.7
		38.40	17.55	0.18	43.11	0.23	0.04	99.5
		36.00	30.58	0.36	32.64	0.22	0	99.8
		37.61	24.04	0.22	37.69	0.45	0	100.0
		37.93	24.38	0.30	36.94	0.34	0	99.9
		36.08	31.88	0.34	31.55	0.16	0.03	100.0
		33.24	49.31	0.53	16.72	0.18	0.02	100.0
		37.14	24.45	0.26	37.49	0.23	0.01	99.6
		40.74	6.99	0.11	52.25	0.25	0.02	100.3
		36.96	28.77	0.37	33.99	0.19	0.01	100.3
		37.19	25.44	0.29	37.01	0.29	0	100.2
		35.33	38.88	0.30	25.30	0.26	0.01	100.1
		38.64	15.59	0.35	45.25	0.66	0.03	100.5
		38.82	17.52	0.15	43.18	0.19	0	99.9
		39.06	15.93	0.26	44.54	0.39	0	100.2
		38.61	20.66	0.15	40.72	0.23	0	100.4
		35.17	35.55	0.32	28.56	0.18	0	99.8
		34.18	42.09	0.36	22.67	0.32	0.01	99.6
		37.36	21.05	0.19	40.44	0.49	0.04	99.6
		36.10	29.09	0.23	34.65	0.26	0.05	100.4
	<i>Mean</i>	35.88	31.84			0.34	31.62	0.30	0.02	
	<i>STD</i>	1.92	9.27			0.12	7.50	0.13	0.02	

Note. The # symbol denotes the number of analyzed chondrules. In bold is shown the mean and STD of all chondrules per section.
(This table is available in its entirety in machine-readable form.)

Table 2

Modal Abundances (the Ratio of Component Pixel Area Relative to the Total Pixel Area of the Chondrite, in %) of Refractory Components and Chondrules in the Analyzed CO3 Chondrites

Component	LoV 123	EM 216	EM 463	Isna
Type-I chondrule	46.74	41.59	33.15	1.85
Type-II chondrule	8.64	5.22	7.75	33.26
<i>All chondrules</i>	55.37	46.81	40.90	35.11
CAI A	0.58	0.66
CAI B	0.55	0.93
AOA	2.37	...
<i>All refractory inclusions (RI)</i>	8.60	6.82	3.49	1.59
RI/chondrules ratio	0.16	0.15	0.09	0.05

reservoir. In this framework, larger chondrules would have been more centrally concentrated in the CO parent body(ies) than smaller chondrules, which could be explained by either simultaneous or sequential accretion of the two chondrule populations (Scott & Jones 1990). Larger chondrules located closer to the center of the CO parent body(ies) would have

experienced more protracted thermal metamorphism than smaller chondrules closer to the surface, where heat generated by ²⁶Al decay was more readily evacuated. Aerodynamic sorting during accretion could thus have produced the covariation of mean chondrule size with both depth and subsequently with metamorphic grade, as observed for CO chondrites. As CO refractory inclusions are smaller than chondrules (Table 3), this process would also have generated positive relationships between CO metamorphic grade and their (i) bulk oxygen isotopic compositions and (ii) refractory inclusion/chondrule (RI/C) ratios. Interestingly, the former has been reported in previous studies (Clayton & Mayeda 1999; Greenwood & Franchi 2004), and our data confirm that COs with lower metamorphic grades show higher RI/C ratios than more metamorphosed ones (Table 3). These results confirm that aerodynamic sorting during accretion concentrated larger chondrules toward the center of the CO parent body(ies), but smaller chondrules and CAIs were less concentrated at the core. Based on this conclusion, in the following section we model and discuss which accretion process best matches these peculiar features of CO chondrites.

4.2. Size Sorting during Planetesimal Formation

In this section we attempt to provide a qualitative explanation of the interpretation discussed above, in which larger chondrules

Table 3The Number as Well as Mean and Median Diameters (μm) of Chondrules and Refractory Inclusions in Each Surveyed Section

Component	LoV 123	EM 216	EM 463	Isna	All CO
<i>Type-I chondrule</i>					
<i>n</i>	2210	1140	2539	25	5914
Mean diameter	71.60	90.91	111.37	170.81	92.78
1σ	56.51	65.61	89.44	54.90	74.92
Median diameter	55.68	71.73	88.56	158.10	72.77
<i>Type-II chondrule</i>					
<i>n</i>	109	91	253	318	771
Mean diameter	141.64	103.84	164.10	184.85	162.52
1σ	112.92	95.26	100.38	80.14	97.33
Median diameter	108.01	73.56	138.00	164.99	138.34
<i>All chondrules</i>					
Mean diameter	74.89	91.86	116.15	183.82	100.47
1σ	62.11	68.28	89.48	71.62	80.27
Median diameter	57.16	71.80	92.60	164.03	79.00
<i>CAIs+AOAs</i>					
<i>n</i>	221	278	252	92	843
Mean diameter	62.63	75.32	109.76	67.11	81.35
1σ	39.06	52.80	71.24	47.81	43.08
Median diameter	53.11	61.47	88.63	49.03	64.54

are more abundant than smaller chondrules at greater depths within the parent planetesimal, and vice versa. We first consider the case of planetesimal formation due to the self-gravitational contraction of a clump of particles. Before they collapse into each other, the radial density distribution of particles in the group, $\rho(r)$, is dictated by the equilibrium between gravity and turbulent diffusion of the gas within the group, resulting in (Klahr & Schreiber 2020a, Klahr & Schreiber 2020b)

$$\rho(r) = \rho(0)\exp[-r^2/(2l_c^2)], \quad (1)$$

where

$$l_c = 1/3(\delta/\text{St})^{1/2}H, \quad (2)$$

where St is the particle's Stokes number, r is the distance to the center, H is the pressure-scaled height of the gas in the disk, and δ is the nondimensional coefficient relating the turbulent diffusion coefficient D to the disk's scale height and orbital frequency Ω :

$$D = \delta H^2\Omega. \quad (3)$$

For particles smaller than the mean free path of gas molecules, St is proportional to particle size (i.e., the Epstein regime). In the Stokes regime, St is proportional to the square of particle size, although this case is rarely considered (nor would it change the considerations below). If there are particles of multiple sizes in the clump, even if the gravitational potential is set by one dominant particle size, each will follow a radial

distribution like (1), with its own value of l_c . Thus, combining Equations (1) and (2), smaller particles have a more distended radial distribution in the clump, whereas larger particles are more concentrated toward the center. This is because, for larger and smaller particle species 1 and 2, respectively, if $\text{St}_1 > \text{St}_2$, then $l_{c1} < l_{c2}$.

We now consider the settling of particles toward the center of the clump, forming a solid planetesimal. Particles are accelerated toward the center, but undergo more and more friction as their sedimentation rate increases; the two forces cancel when a particle attains its terminal velocity (v_t). Particles accelerated in a gas medium rapidly attain the so-called terminal velocity (v_t). The value of the terminal velocity increases approaching the center of gravitational attraction, but the slowest velocity defines the time that the pebble needs to reach the center, and that velocity is set by initial terminal velocity v_t . Thus, in the following we assume, without introducing much error and to simplify the final formulae, that v_t is constant (but is particle-size dependent) during the whole contraction of the clump.

The planetesimal grows over time as more and more particles reach its surface during the sedimentation process. Thus, we can use the accretion timescale T as a proxy for planetesimal radius (not necessarily a linear relationship). In a time interval dT at time T , the planetesimal receives the particles that were originally in the clump at a distance between r and $r + dr$ where $r = v_t T$ and $dr = v_t dT$ (here is where the assumption of constant v_t is handy). At time T all particles from specie i ($i = 1$ or 2) come from a spherical shell with radius $r_i = v_{ti} T$ and thickness $dr = v_{ti} dT$, so the total mass accumulated in planetesimals between time T and $T + dT$ is $dM_i(T) = 4\pi r_i^2 \rho_i(r_i) dr = 4\pi v_{ti}^3 T^2 \rho_i(r_i) dT$. So, the mass ratio of the particles with index 1 and 2 accumulated in the time interval T to $T + dT$ is

$$\rho_1/\rho_2(T) = (v_{t1}/v_{t2})^3 \cdot [\rho_1(v_{t1}T)/\rho_2(v_{t2}T)], \quad (4)$$

where the first term $(v_{t1}/v_{t2})^3$ comes from the ratio of the volumes occupied at time 0 (i.e., at the beginning of the contraction of the clump) by the particles that sediment onto the planetesimal surface between T and $T + dT$. Let us now define $x = v_{t1}T/(2l_{c1}^2)$. Recall that $v_{t1}/v_{t2} = \text{St}_1/\text{St}_2$ and $l_{c1}/l_{c2} = (\text{St}_2/\text{St}_1)^{1/2}$. Thus, $(v_{t2}T)^2/(2l_{c2}^2) = (\text{St}_2/\text{St}_1)^3 x^2$. By applying the definition (1) into (4) and substituting for x , the mass ratio of the two population of particles landing on the planetesimal at time $T = x(2l_{c1}^2)^{1/2}/v_{t1}$ is

$$\begin{aligned} \rho_1/\rho_2(x) &= \rho_1(0)/\rho_2(0) \\ &\cdot (\text{St}_1/\text{St}_2)^3 \cdot \exp[-x^2]/\exp[-(\text{St}_2/\text{St}_1)^3 x^2]. \end{aligned} \quad (5)$$

As an example, Figure 3 shows this function for $\text{St}_2 = 0.6\text{St}_1$, which is appropriate for comparing chondrules with diameters of ~ 80 – $130 \mu\text{m}$, i.e., in the Epstein regime.

Our model shows that ρ_1/ρ_2 decreases monotonically as time progresses (i.e., when the timescale increases). This is in qualitative agreement with our interpretation that average chondrule size increases with depth in the parent body. Of note, chondrules are small compared to pebbles (i.e., 80 – $130 \mu\text{m}$; Table 3) and would have Stokes number of 1×10^{-4} at 2 au for $100 \mu\text{m}$ particle size (considering a minimum mass solar nebula). This is smaller than what is typically considered in gravitational collapse models of planetesimal formation (e.g., Yang et al. 2017). To have $\text{St} = 1e-3$, as is more traditionally

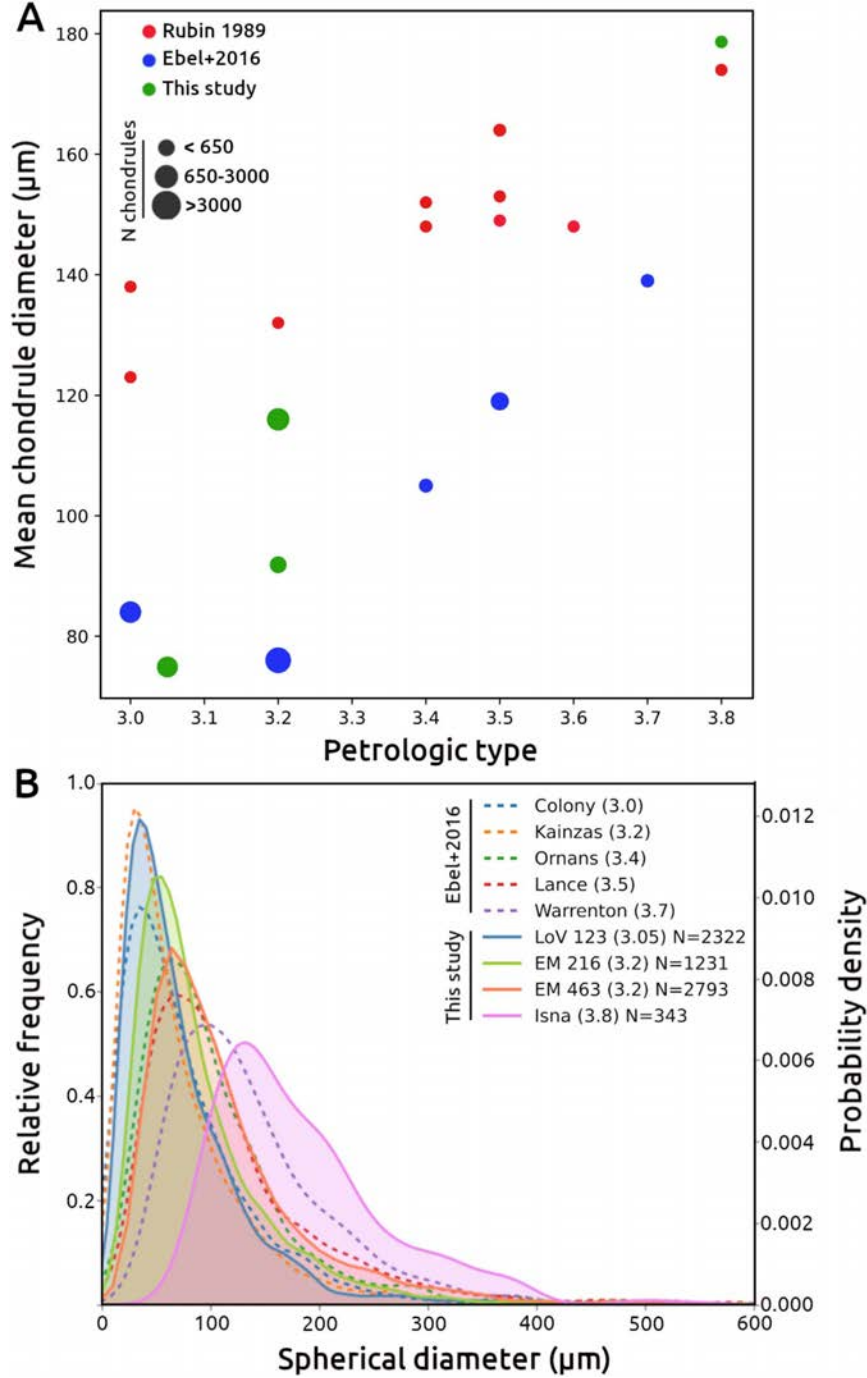


Figure 2. (A) Mean chondrule diameter vs. petrologic type of CO chondrites (data from Rubin 1989, Ebel et al. 2016, and this study). (B) Probability density function of chondrule diameters in CO chondrites. Solid lines, this study (N , number of analyzed chondrules); dashed lines, Ebel et al. (2016).

considered, the gas should have been depleted by a factor of 10. This may well be possible, because chondrites formed at a late time (2–3 Myr) in the disk’s chronology, well after the formation of Jupiter (Kruijer et al. 2017); cavity opening by Jupiter and photoevaporation may well have reduced the density of gas by one order of magnitude.

Above, we considered the case of a gravitationally contracting planetesimal, but it is well accepted that after their contraction, planetesimals may have grown through pebble accretion, as discussed by Johansen et al. (2015). If a planetesimal accreted particles in the Bondi regime, the Stokes number of the preferentially accreted pebbles increases with the

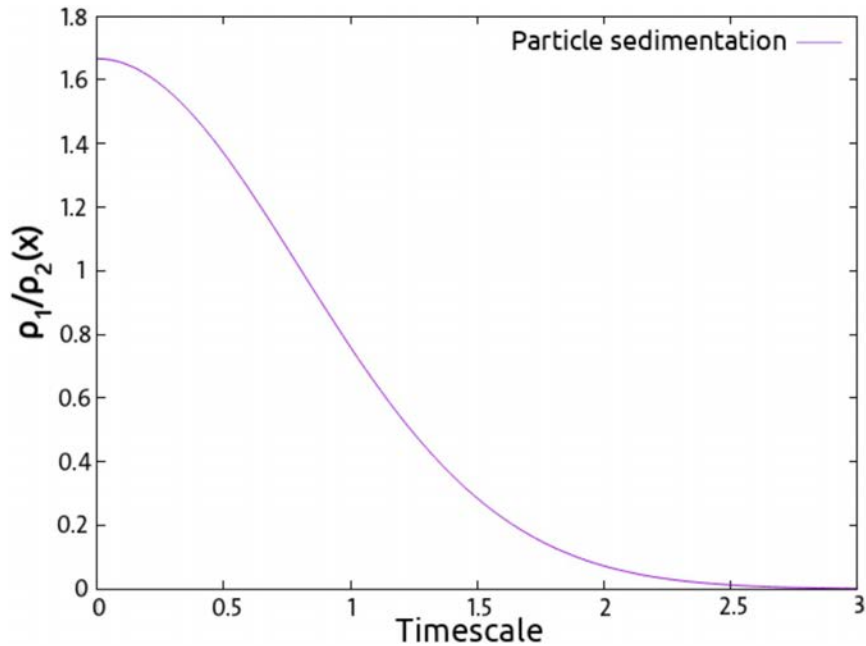


Figure 3. Equation (5) normalized to the ratio $\rho_1(0)/\rho_2(0)$ at the center of the particle clump from the beginning of a gravitational contraction leading to the formation of a planetesimal.

planetesimal’s Bondi time, which is proportional to the planetesimal’s mass (Lambrechts & Johansen 2012). This predicts that larger chondrules should have been predominant at shallower depths in their parent planetesimal, opposite to our observations. In the case that a larger protoplanet scattered a planetesimal into an orbit of greater inclination, the size of particles accreted by the planetesimal would have suddenly decreased because only small particles were available away from the disk’s midplane. However, the mass accreted should have also declined, such that small particles would dominate only in a very thin surface layer (Johansen et al. 2015). We do not observe such a drastic change in chondrule size among the studied meteorites of different petrologic types, but rather a gradual trend. Thus, we conclude that our observations are consistent with the formation of the CO parent body(ies) via the contraction of a self-gravitating clump of chondrules of various sizes, and that the subsequent growth of the parent body(ies) due to pebble accretion was insignificant.



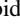

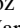
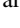


5. Conclusions

Our particle-size analysis of CO carbonaceous chondrites revealed that the mean spherical diameters of chondrules increase with increasing metamorphic degree. Combining our results with literature data, we show that this relationship was not established during postaccretion thermal metamorphism, but instead records aerodynamic size-sorting of particles during the accretion of the CO parent body(ies). By modeling the self-gravitating contraction of clumps of chondrules, we show that the accretion processes generated a gradual change in chondrule size, with larger chondrules being more centrally concentrated in the parent body(ies) than smaller ones. Our results also suggest that any subsequent planetesimal growth by pebble accretion should have been insignificant. We thus conclude that our observations are consistent with the formation of the CO parent

body(ies) via the contraction of a self-gravitating clump of chondrules, supporting the theory that the formation of planetesimals occurred via gravitational collapse.

We thank Johan Villeneuve, Nicolas Schnuriger, and Laurette Piani for helpful discussion. G.A.P and F.O.E. acknowledge support from FONDECYT project 1201223. G.A.P. was supported by an Eiffel excellence scholarship (grant 968045D). We thank the anonymous review for helpful comments and Frederic Rasio for editorial handling. This is CRPG contribution #2777.

ORCID iDs

Gabriel A. Pinto  <https://orcid.org/0000-0003-4761-9137>
 Yves Marrocchi  <https://orcid.org/0000-0001-7075-3698>
 Alessandro Morbidelli  <https://orcid.org/0000-0001-8476-7687>
 Sébastien Charnoz  <https://orcid.org/0000-0002-7442-491X>
 Maria Eugenia Varela  <https://orcid.org/0000-0002-3004-1183>
 Kevin Soto  <https://orcid.org/0000-0001-9927-2572>
 Rodrigo Martínez  <https://orcid.org/0000-0003-4161-479X>
 Felipe Olivares  <https://orcid.org/0000-0002-5115-6377>

References

- Amsellem, E., Moynier, F., Mahan, B., & Beck, P. 2020, *Icar*, **339**, 113593
 Barge, P., & Sommeria, J. 1995, arXiv:[astro-ph/9501050](https://arxiv.org/abs/astro-ph/9501050)
 Bonal, L., Bourrot-Denise, M., Quirico, E., Montagnac, G., & Lewin, E. 2007, *GeCoA*, **71**, 1605
 Carrera, D., Johansen, A., & Davies, M. B. 2015, *A&A*, **579**, A43
 Chizmadia, L. J., Rubin, A. E., & Wasson, J. T. 2002, *MAPS*, **37**, 1781
 Clayton, R. N., & Mayeda, T. K. 1999, *GeCoA*, **63**, 2089
 Connelly, J. N., Bizzarro, M., Krot, A. N., et al. 2012, *Sci*, **338**, 651
 Cuzzi, J. N., Hogan, R. C., Paque, J. M., & Dobrovolskis, A. R. 2001, *ApJ*, **546**, 496

- Cuzzi, J. N., Hogan, R. C., & Shariff, K. 2008, *ApJ*, **687**, 1432
- Doyle, P. M., Jogo, K., Nagashima, K., et al. 2015, *NatCo*, **6**, 7444
- Drażkowska, J., Alibert, Y., & Moore, B. 2016, *A&A*, **594**, A105
- Ebel, D. S., Brunner, C., Konrad, K., et al. 2016, *GeCoA*, **172**, 322
- Ganino, C., & Libourel, G. 2017, *NatCo*, **8**, 261
- Gerbig, K., Murray-Clay, R. A., Klahr, H., & Baehr, H. 2020, *ApJ*, **895**, 91
- Greenwood, R. C., & Franchi, I. A. 2004, *M&PS*, **39**, 1823
- Grossman, J. N., & Brearley, A. J. 2005, *M&PS*, **40**, 87
- Huss, G. R., Rubin, A. E., & Grossman, J. N. 2006, in *Meteorites and the Early Solar System II*, ed. D. S. Laurett & H. Y. McSween, Jr. (Tucson, AZ: Univ. Arizona Press), 567
- Jacquet, E. 2021, *GeCo*, **296**, 18
- Johansen, A., Low, M. M. M., Lacerda, P., & Bizzarro, M. 2015, *SciAdv*, **1**, 1500109
- Johansen, A., Youdin, A., & MacLow, M. M. 2009, *ApJL*, **704**, L75
- Johnson, B. C., Minton, D. A., Melosh, H. J., & Zuber, M. T. 2015, *Nat*, **517**, 339
- Jones, R. H., & Rubie, D. C. 1991, *EPSL*, **106**, 73
- Keil, K. 2000, *P&SS*, **48**, 887
- Klahr, H., & Schreiber, A. 2020, *ApJ*, **901**, 54
- Klahr, H., & Schreiber, A. 2021, *ApJ*, **911**, 9
- Kruijer, T. S., Burkhardt, C., Budde, G., & Kleine, T. 2017, *PNAS*, **114**, 6712
- Lambrechts, M., & Johansen, A. 2012, *A&A*, **544**, A32
- Li, R., Youdin, A. N., & Simon, J. B. 2018, *ApJ*, **862**, 14
- Li, R., Youdin, A. N., & Simon, J. B. 2019, *ApJ*, **885**, 69
- Marrocchi, Y., Euvette, R., Villeneuve, J., et al. 2019, *GeCoA*, **247**, 121
- Marrocchi, Y., Villeneuve, J., Batanova, V., Piani, L., & Jacquet, E. 2018, *EPSL*, **496**, 132
- Nesvorný, D., Li, R., Youdin, A. N., Simon, J. B., & Grundy, W. M. 2019, *NatAs*, **3**, 808
- Ormel, C. W., & Klahr, H. H. 2010, *A&A*, **520**, A43
- Rubin, A. E. 1989, *Metic*, **24**, 179
- Rubin, A. E., & Li, Y. 2019, *ChEG*, **79**, 125528
- Schindelin, J., Arganda-Carreras, I., Frise, E., et al. 2012, *NatMe*, **9**, 676
- Scott, E. R., Keil, K., & Stöffler, D. 1992, *GeCoA*, **56**, 4281
- Scott, E. R. D., & Jones, R. H. 1990, *GeCoA*, **54**, 2485
- Simon, J. B., & Armitage, P. J. 2014, *ApJ*, **784**, 1
- Turner, S., McGee, L., Humayun, M., Creech, J., & Zanda, B. 2021, *Sci*, **371**, 164
- Vacher, L. G., Marrocchi, Y., Villeneuve, J., Verdier-Paoletti, M. J., & Gounelle, M. 2018, *GeCoA*, **239**, 213
- Wahlberg Jansson, K., & Johansen, A. 2014, in *Proc. Asteroids, Comets, Meteors 2014*, ed. K. Muinone et al. (Cambridge: Cambridge Univ. Press), 573
- Wahlberg Jansson, K., & Johansen, A. 2017, *MNRAS*, **469**, S149
- Yang, C. C., Johansen, A., & Carrera, D. 2017, *A&A*, **606**, A80
- Youdin, A. N., & Goodman, J. 2005, *ApJ*, **620**, 459

Chapter 6

Distribution and alteration of meteorite in the dense collection areas of the Atacama Desert, northern Chile

In preparation for submission to the Meteoritics and Planetary Science Journal

Chapter introduction

We examined the published and unpublished data of meteorites found in the Atacama Desert to (i) describe the distribution and abundance of different meteorites groups, (ii) compare their terrestrial alteration degree with other hot and cold desert meteorites, and (iii) determine the more suitable DCAs for meteorite preservation according to their geomorphologic and climatic context. The information about all the meteorites found in the Atacama Desert was collected from the Atacama meteorites description in this thesis and the Meteoritical Bulletin Database². Ours results support that distinctive climatic and geological conditions of the main morphotectonic units in the Atacama Desert defined the accumulation and conservation of meteorites. The four main parameters involved in the alteration of meteorites in the Atacama Desert are (i) distance from the Pacific Ocean, (ii) surface altitude, (iii) surface age, and (iv) surface lithology. In this context, there are three main processes which generate chondrite disintegration: (i) saline mineral precipitation, (ii) thermal stress weathering, and (iii) volume increase by Fe-Ni oxide and hydroxide formation. A comparison with reported weathering data from other cold and hot deserts indicates that terrestrial weathering meteorites in Atacama induces less alteration than in other hot deserts following the distribution of Antarctic meteorites.

6.1 Introduction

Meteorites are pieces of rocks that fall through the Earth's atmosphere and retain physical, chemical, and isotopic heritage properties from asteroids, moons, and planets orbiting the Sun. They are divided into falls or finds differing in whether they were observed (by humans or electronic devices) before landing or not. Meteorite “finds” are preferentially accumulated in cold and hot desert areas, where the chemical weathering is slow enough to preserve samples over hundreds to millions of years (Bland et al., 1998, 2006; Drouard et al. 2019; Nishiizumi et al., 1989). These local regions where meteorites are preserved in large numbers over time are defined as dense collection areas (hereafter DCAs).

Although ~60% of all meteorites finds comes from the Antarctic (Meteoritical Bulletin Database, 2022), thousands of them have been recollected from hot desert DCAs. These

² <https://www.lpi.usra.edu/meteor/>

suitable surfaces display preferential conditions compared to Antarctic areas, such as (i) lower expedition costs, (ii) ease of access, and (iii) *in situ* information of meteorite showers (i.e., strewn fields characterization; Gnos et al., 2009; Kring et al., 2001; Pedersen et al., 1992; Zeng et al., 2018). However, the pervasive terrestrial alteration of hot desert meteorites leads to a preferential selection of the less weathering Antarctic meteorites (Lee and Bland, 2004) to perform petrographic, chemical, and isotopic analysis of their pre-terrestrial phases. Three decades ago, hot desert meteorites derived mainly from Australia (Bevan & Binns, 1989; Citron et al., 2021), Northern Africa (Aboulahris et al., 2019; Bischoff & Geiger, 1995; Ouazaa et al., 2009; Schlüter et al., 2002) and the Southwestern United States (Hutson et al., 2013; Kring et al., 2001; Rubin et al., 2000; Zolensky et al., 1990). However, several recent expeditions in the Arabian Peninsula (Hezel et al., 2011; Hofmann et al., 2018), Northern and Western China (Fan et al., 2022), Lut Desert (Pourkhorsandi et al., 2019) and the Atacama Desert (Gattacceca et al., 2011; Hutzler et al., 2016; Valenzuela, 2011), allowed the characterization of an extensive set of new DCAs with unique properties. Furthermore, hot desert collections have extended our knowledge concerning to (i) extraterrestrial material flux to Earth over time, (ii) statistics of number and mass of meteorites on Earth and (iii) palaeoclimatic studies of the areas from which meteorites have been recovered.

The Atacama Desert, located between Southern Peru (15°S) and Northern Chile (30°S), is one of the driest environments in the world (precipitation <10 mm yr⁻¹, Goudie et al., 2002; Houston & Hartley, 2003; Pfeiffer et al., 2021). This arid to hyper-arid conditions result from the reduced pluviosity and the evapotranspiration capabilities of its surfaces (Boy et al., 2022; Dunai et al., 2005; Houston & Hartley, 2003; Pfeiffer et al., 2021). The meteorological conditions and geological stability of Atacama surfaces promote a maximum accumulation of ~150 meteorites/ km² (Hutzler et al., 2016) with a mean terrestrial age of 710 ky (Drouard et al., 2019). Twenty years ago, only 64 non-paired meteorites were found on Atacama surfaces (Muñoz et al., 2007). Today, more than 2141 non-paired meteorites (over a total of 2187) have been recovered from 32 DCAs (**Figure 6.1**, panel (a)). Nevertheless, there is no further analysis of the climatic and geological conditions of the new and old Atacama DCAs. In this review, we examine the published and unpublished data of meteorites found in the Atacama Desert to (i) describe the distribution and abundance of different meteorites groups, (ii) compare their terrestrial alteration degree with other hot and cold desert meteorites, and (iii) determine the more suitable DCAs for meteorite preservation according to their geomorphologic and climatic

context. We survey all the meteorites found in the Atacama Desert from the Meteoritical Bulletin Database³, summarized in **Table 6.1**.

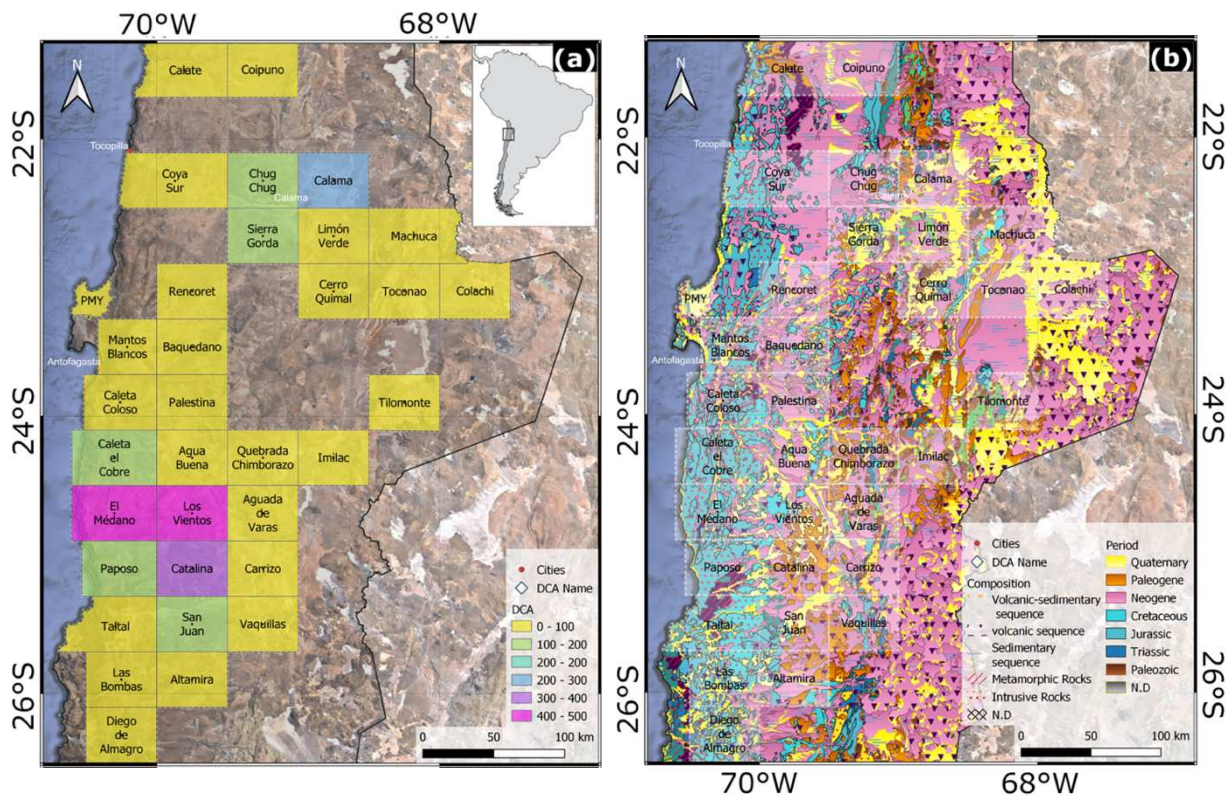


Figure 6.1. Localization of the 34 Atacama DCAs divided by number of meteorites in the panel (a) and by the geologic setting in the panel (b). Most DCAs are localized in Neogene surfaces in the Central Depression, meanwhile, cretaceous basement dominated DCAs in the Coastal Range. According to the Meteoritical Bulletin Database, neither the Palestina nor the Agua Buena DCA yields meteorites. Thus, there is only 32 DCAs listed.

6.2 Distribution of meteorites in the Atacama Desert

A set of different meteorite classes are shown *in situ* among the main DCAs in the Atacama Desert (**Figure 6.2**). The different properties of the meteorite class, local soil, and atmospheric conditions control the subsequent alteration and conservation of Atacama meteorites. For instance, the relative abundance of meteorites changed if we considered it by number or mass (**Figure 6.3**). By number, chondrites comprise the most significant proportion (~96%), slightly higher than the worldwide abundance of chondrites (~85%; Meteoritical Bulletin Database, 2022). They are followed by irons (2%), achondrites (1%), stony-irons (0.4%), and ungrouped meteorites (0.2%). However, the percentage values by the total mass are 31.1, 11.2, 0.2, and 57.5% for chondrites, irons, achondrites, and stony-irons meteorites,

³ <https://www.lpi.usra.edu/meteor/>

respectively (**Figure 6.3b**). In the next section, we detailed the statistics by types of meteorites compared to the world collection.

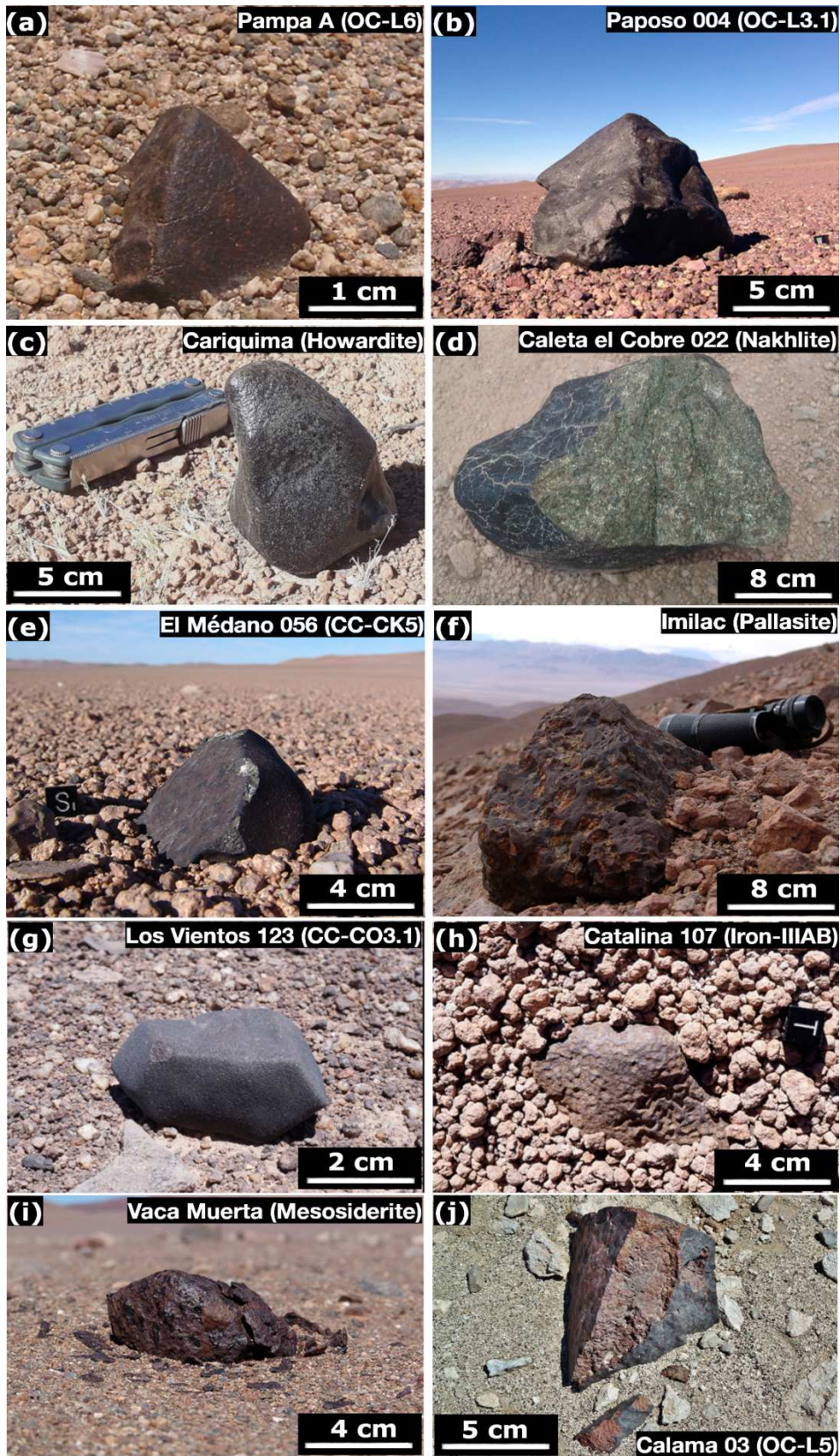


Figure 6.2. Different meteorite types found *in situ* on the Atacama Desert (except for Caleta el Cobre 022). The samples of Cariquima (c), Imilac (f), and Vaca Muerta (i) are unique pieces in their respective collection areas. All other meteorites were collected in the main Atacama DCAs: (a) Pampa de Mejillones, (b) Paposo, (d) Caleta el Cobre, (e) El Médano, (g) Los Vientos, (h) Catalina, and (j) Calama. Vaca Muerta and Calama 03 display local fragmentation. Pictures were provided by the *Museo del Meteorito* (San Pedro de Atacama, Chile).

6.2.1 Non-chondrite meteorites

The non-chondrite meteorites are characterized by having undergone total melting and differentiation processes on their parent body. It is possible to differentiate magmatic irons that represents proxies of planetesimals core, and non-magmatic irons (IAB and IIE) that are formed by impact on subsurface of planetesimals. They are classified by chemical groups using the Gallium and Germanium signatures, helpful because both are the most volatile siderophile elements (Krot et al., 2014). The iron and stony-iron meteorites found in the Atacama show small relative abundance by number (2.0 and 0.4%, respectively) compared to their abundance per mass (11.2 and 57.5%, respectively). In the case of stony-irons, the proportion by number is represented only by seven mesosiderites and two pallasites. Nevertheless, the two biggest meteorite strewnfields found in the Atacama Desert belong to this group: Imilac pallasite (920 kg; Killgore, 1997) and Vaca Muerta mesosiderite (3830 kg; Peddersen et al., 1992). The abundance variation between number and mass is also displayed for the iron meteorites (2 and 11.2%, respectively); of the 50 irons, 26 had a total mass ≥ 5 kg. Valenzuela & Benado (2018) point out that miners looking for ore deposits in the Atacama Desert discovered many iron meteorites in the 19th and 20th centuries. As a result, there is a decreasing abundance of iron meteorites found through the 19th, 20th, and 21th centuries from 41, to 30 to 26%, respectively. The most common iron meteorite found in the Atacama Desert is the IIIAB magmatic irons (31% by number and 30% by mass, **Figure 6.3**). Preliminary analysis of the Atacama iron meteorites by Wasson and Canut de Bon (1997) rules out the possible pairing of the IIIAB irons, which is consistent with their similar values in the world collection (~26% by number, Meteoritical Bulletin Database, 2022).

The Howardite-Eucrite-Diogenite (HED) is a group of achondrite meteorites with chemical and mineralogic characteristics related to the surfaces of the asteroid (4) Vesta (McSween et al., 2013; Mittlefehldt, 2015, and reference therein). The HEDs are the most common achondrite group (Krot et al., 2014), representing 75% of the world collection (Meteoritical Bulletin Database, 2022) and 55% of the Atacama collection. The recent howardite found at Cariquima exhibit a fresh fusion crust (**Figure 6.2c**), negligible rims

alteration of metals, and lack of evaporated minerals, which are classical features of hot desert meteorites (Bland et al., 2006). Probably, the Cariquima howardite is one of the least altered meteorites from the Atacama Desert. The only Martian meteorites found in the Atacama Desert is Caleta el Cobre 022 (**Figure 6.2d**), which belongs to the nakhlite group and displays characteristics of pervasive aqueous alteration products (i.e., iddingsite; Krämer Ruggiu et al., 2020). The minimal alteration products and lack of evaporated minerals on the fractures support the olivine alteration at the Mars surfaces instead of a product of terrestrial alteration (Krämer Ruggiu et al., 2020).

6.2.2 Chondrite meteorites

Ordinary chondrites (OCs) are subdivided by their abundance and siderophile elements in Fe-Ni metal beads, iron content in silicates and oxygen isotopic composition into three groups: high metal (H), low metal (L) and low iron-low metal (LL) (Weisberg et al., 2006; Florin et al., 2020). The classification 1162 equilibrated OCs from the Atacama Desert are show in **Figure 6.4**. Most Atacama OCs are classified as H and L groups, both with a 2.4% plotting outside the operational values (Grossman and Rubin, 2002). The relative abundance for H, L and LL group is 56.2, 39.2 and 4.2%, respectively. According to the mass abundance, similar values of 56.4, 40.7 and 2.5% are estimated for H, L and LL group. These probably reflect the absence of large samples which could dominate certain mass distribution of OC types. Also, isotopic and petrographic observations suggest the existence of two more independent groups with intermediate characteristics between H/L and L/LL (Kellemeyn et al., 1989; Greenwood et al., 2020). Although these groups are not abundant in the world-wide collection ($\sim 0.0006\%$ for H/L, Pourkhorsandi et al., 2022) or neither in the Atacama collection (**Figure 6.4**; $< 0.2\%$ for H/L and $< 0.3\%$ for L/LL, by mass or number), they are defined as fundamental samples to understand the different reservoirs and/or mixing of planetesimals in the inner solar system (e.g., Pourkhorsandi et al., 2022; Wittmann et al., 2011). Furthermore, El Médano 301, one of the few ungrouped reduced chondrites, exhibits petrographic textures as well as olivine and pyroxene composition intermediate between ordinary and enstatite chondrites, suggesting a formation in a nebular region with lower fO_2 than all the others OC groups (Pourkhorsandi et al., 2017).

Table 6.1. All type of meteorite finds in the Atacama Desert. Data extracted from Meteoritical Bulletin Database.

Meteorite classification	Catalina	Calama	Calate	Caleta el Cobre	Chug Chug	El Médano	Los Vientos	Machuca	Pampa de Mejillones	Paposo	San Juan	Sierra Gorda	Limón Verde	Others	Total
<i>Ordinary chondrites</i>															
H	237	113	11	24	64	277	247	4	8	49	67	19	7	24	1151
H-L	1				1	1					1	1			5
L	130	81	15	31	45	160	179	20	16	25	37	35	7	22	803
L-LL						1		1	1	1					4
LL	19	7	2	4	5	27	12			1	4			5	86
<i>Carbonaceous chondrites</i>															
CO	1	5		1		13	4			1	1				26
CK		1	1			1					1		1		5
CR	1	1					1			1					4
CH							1								1
CB												1		1	2
CL							1								1
CV	1														1
C2-ungrouped						1									1
C3/C3-ungrouped						1									1
<i>Chondrite-ungrouped</i>					1	1						1			3
<i>Rumuruti</i>															
												1			1
<i>Enstatite chondrites</i>															
EL				2		2									4
EH	1			1											2
<i>Achondrites</i>															
HEDs		3				1	9							2	15
Martian (Nakhlite)				1											1

Urelites	1	2					3			1	1				8	
Ungrouped				1											1	
Acapulcoite							1								1	
Brachinite							1								1	
<hr/>																
<i>Irons</i>																
IIIAB	1														14	15
IVB	1														2	3
IAB															6	6
IIAB		1					1					1			5	8
IAB-ungrouped						1									2	3
IVA															5	5
IIE											1					1
IIE-ungrouped															1	1
III E															1	1
IID															1	1
IID-ungrouped							1									1
IIIF															1	1
IIG															2	2
Ungrouped						1									1	2
<hr/>																
<i>Rocky iron</i>																
Mesosiderite	4						1				1				1	7
Pallasite							1								1	2
Total	398	214	29	66	116	489	461	25	25	79	114	59	15	97	2187	

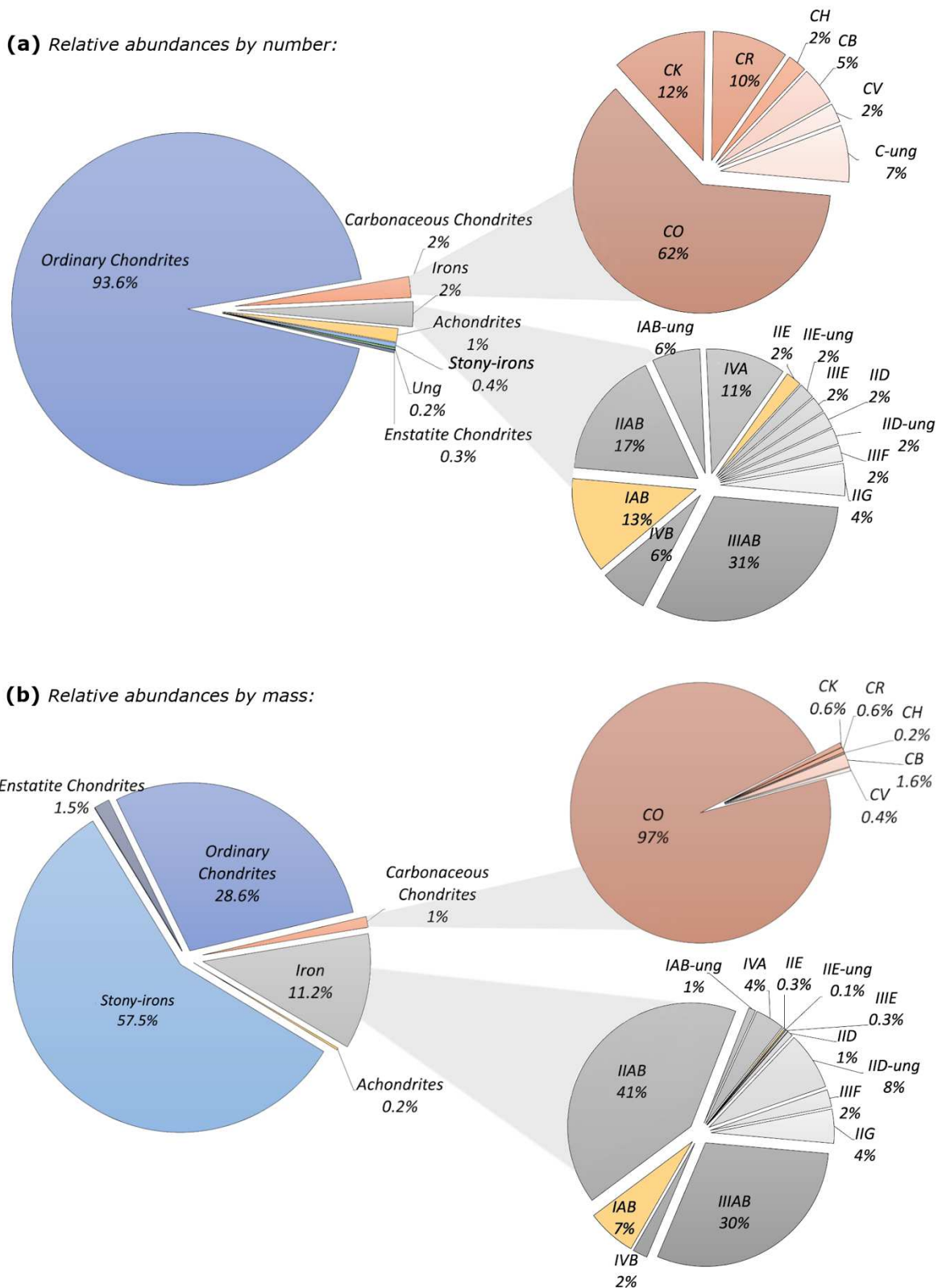


Figure 6.3. Relative abundances of meteorites found in the Atacama Desert and individual groups of carbonaceous chondrites and iron meteorites based on the total number (a) and the total mass (b). There is a significant difference between the calculation by number and mass; this is because the biggest meteorite mass found at the Atacama are the stony-irons, the Imilac Pallasite (920 kg; Killgore, 1997) and the Vaca Muerta Mesosiderite (3830 kg; Peddersen et al., 1992). Non-magmatic Irons are indicated with a yellow color. The relative proportions are estimated based on the Meteoritical Bulletin Database (2022).

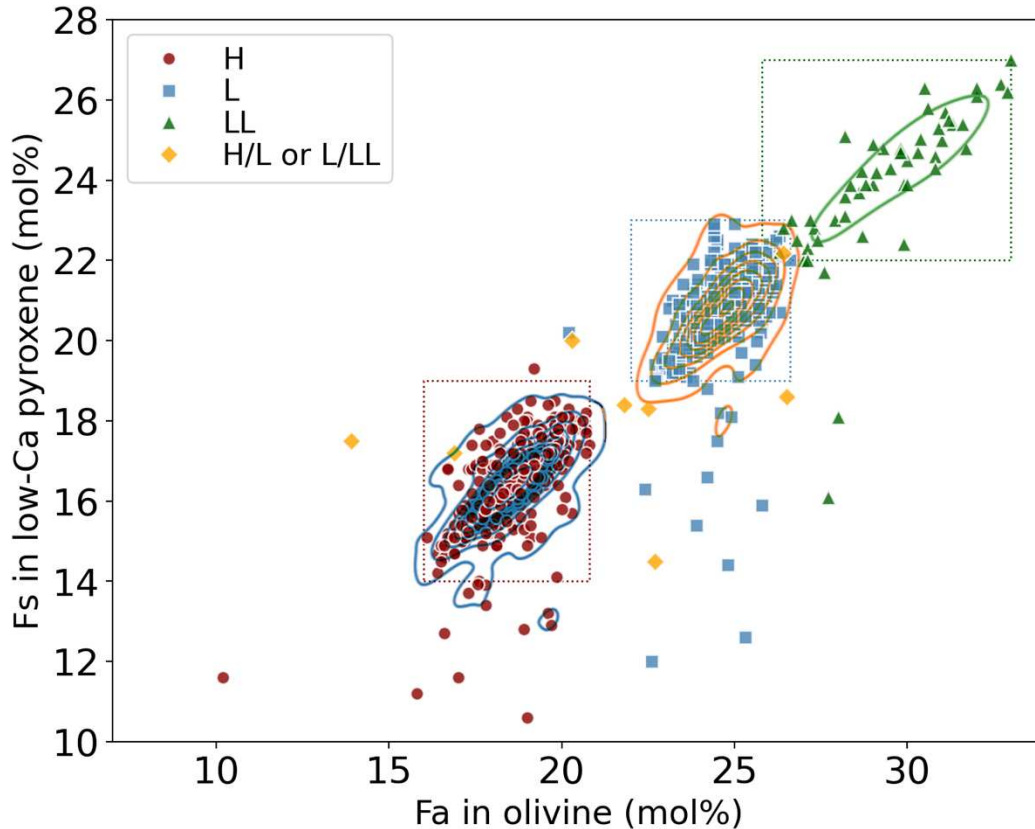


Figure 6.4. Classification of 1162 equilibrated ordinary chondrites (including brecciated textures) found at the Atacama Desert (632 H; 469 L; 53 LL; 8 H/L and L/LL). The curved lines show the kernel density estimate in 2D for each chondrite type. The operational values (Grossman and Rubin, 2002) for the classification range of ordinary chondrites are shown as square dashed lines. Data extracted from Meteoritical Bulletin Database.

The mass distribution of OCs according to the petrologic type (i.e., degree of thermal metamorphism during the planetesimal evolution; Weisberg et al., 2006) is shown in the histogram of **Figure 6.5**. For instance, H group lead the mass abundance in almost every petrologic types 3 to 5. By contrast, petrologic type 6 displays larger proportion of L group compared to the H group (**Figure 6.5**). As H- and L-chondrites are the most abundant meteorites in all collections, different studies used the H/L ratios to compare fragmentation and/or change in the extraterrestrial flux material to the Earth over geologic scales (Benoit & Sears, 1996; Gattacceca et al., 2011; Kouvatsis & Hofmann, 2020). In the Atacama Desert, this ratio changes according to the collection area and the petrologic type (see **Table 6.2**). For instance, the extreme values of the H/L ratio are 4.2 and 0.4 in grades 5 and 6, respectively. It is apparent from **Table 6.2** that among Atacama DCAs that have less than ~60 meteorites (H+L chondrites), the H/L ratios are recurrently lower than 1. In comparison, Atacama DCAs with more than ~60 meteorites display H/L ratios higher than 1. In this sense, the H/L parameter could be strongly biased by (i) the pairing processes of meteorite showers and (ii) local

fragmentation during weathering processes (Ashley and Velvel, 2000; Kouvatsis and Hofmann, 2019), which is commonly described for Atacama meteorites (Valenzuela, 2011).

Crystallographic volume calculation of Fe-Ni phases altered to goethite [$\text{Fe}^{3+}\text{O}(\text{OH})$], showed an increase of volume greater than three-fold compared to their kamacite and taenite precursors (Ashley and Velvel, 2000). Thus, the production of internal pressure in chondrites is directly correlated with the initial abundance of reduced Fe-Ni metal. For instance, the metal volume in Baszkówka (L5) has been estimated to range between 2.1-2.7 % (Friedrich et al., 2008b); assuming a 99% corrosion of the reduced Fe-Ni metal, less than half of the porosity volume will be filled (19 % of porosity; Friedrich et al., 2008a). Opposite, X-ray tomography in EET 96031 (H4-an) shows 7.4 % metal volume (Troiano et al., 2011). Similar values to the 8 % average porosity calculated for H group using the gas pycnometer method (Wilkison et al., 2003). Only a few percentages of Fe-Ni alteration in H group chondrites would increase internal pressure to encourage fragmentation along shock veins, preexisting fractures, and other zones of weakness. The effective mechanism of fragmentation may account for the three times less abundance of OCs by mass compared to number (**Figure 6.3**). Further mathematical models of Fe-Ni alteration among different meteorite and climatic parameters could reinforce the H/L ratio variation among different DCAs in Atacama as result of fragmentation process.

Among the 42 carbonaceous chondrites (CCs) found at the Atacama surfaces, the CO group is the most abundant by number and mass (62 and 97%, respectively; **Figure 6.3**). For comparison, the CO abundance in the world-wide collection is only 24 and 15% by number and mass, respectively (Meteoritical Bulletin Database, 2022). The overabundance of CO chondrites in the Atacama Desert may be related to the deficit of pairing processes of individual fragments belonging to the same fall event. For instance, petrographic description and physical parameters (i.e., magnetic susceptibility and density) of 8 CO chondrites found at El Médano DCA (El Médano 216, 390, 397, 398, 389, 463, 464, 465 and 481) indicate a likely meteorite shower related to the same CO fall event. From all Atacama CCs, the ungrouped carbonaceous reaches 7% (**Figure 6.3a**), corresponding to a more significant value than the world collection (~3%; Meteoritical Bulletin Database, 2022). This larger proportion has allowed diverse analysis using meteorites from the Atacama Desert to classify new groups of carbonaceous chondrites. For instance, Ivanova et al. (2020) demonstrated that the metal-rich chondrite Sierra Gorda 009 displays different bulk oxygen, nitrogen, and carbon isotopic compositions compared to the CH-CB chondrites. They suggest that Sierra Gorda 009 is related to the G chondrite group, which contains primitive and fractionated components from the inner solar system (Weisberg et al., 2015). Furthermore, a recent analysis of the ungrouped CC Los

Vientos 051 has been essential to defining the primary petrographic, geochemist, and isotopic composition of the new Loongana (CL) group in view of its low weathering degree (Metzler et al., 2021).

The reduced enstatite chondrites (ECs) represent only 0.3 % by number in the Atacama Desert, which is three times less than the worldwide collection of ECs (~1%; Meteoritical Bulletin Database, 2022). The only six Atacama ECs are divided into four low-iron and two high-iron (**Table 6.1**), with five of them presenting equilibrated ferrosilite composition (between 0.3 ± 0 to 1.1 ± 0.4 mol%) and just one unequilibrated ($Fs = 2.7\pm 2.1$ mol%). Today, only few analyses of Atacama ECs have been performed.

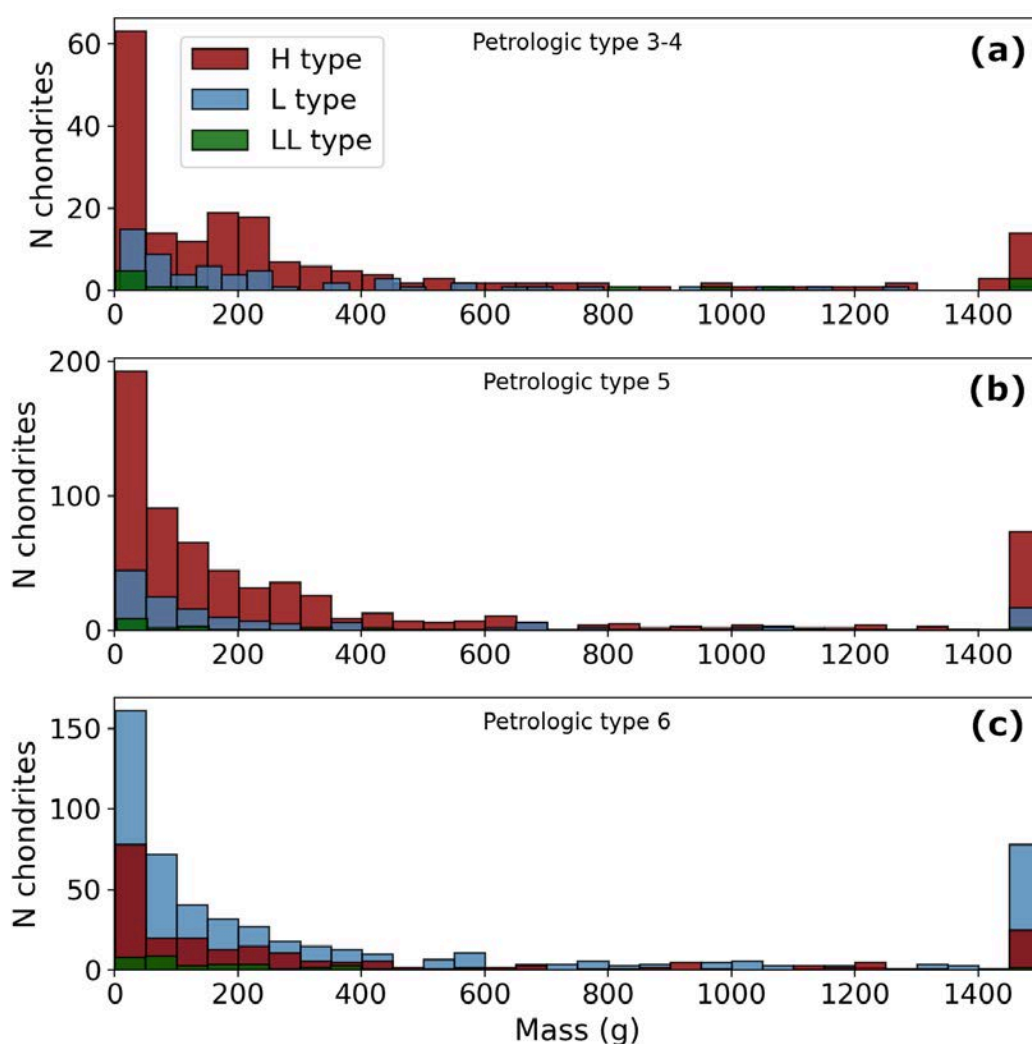


Figure 6.5. Histogram of the mass distribution of OCs from the Atacama Desert by petrologic type 3-4 (a), type 5 (b) and type 6 (c). H group lead the mass distribution in petrologic type 3-4 and 5. However, L group dominated at petrologic type 6. The last bin in each histogram display all the larger mass than 1500 g. Data extracted from Meteoritical Bulletin Database (2022).

Table 6.2. The abundance of H and L chondrites for DCAs and petrologic type in the Atacama Desert. The OCs divided by petrologic type do not have the brecciated textures included.

	H	L	H/L
<i>by DCA</i>			
Catalina	237	130	1.82
Calama	113	81	1.40
Calate	11	15	0.73
Caleta el Cobre	24	31	0.77
Chug Chug	64	45	1.42
El Médano	277	161	1.72
Los Vientos	247	179	1.38
Machuca	4	20	0.20
Pampa de Mejillones	8	16	0.50
Paposo	49	25	1.96
San Juan	67	37	1.81
Sierra Gorda	19	35	0.54
Limón Verde	7	7	1.00
Others	24	22	1.09
All Atacama	1151	803	1.43
Falls	389	449	0.87
<i>by petrologic type</i>			
3	51	37	1.38
4	139	35	3.97
5	660	156	4.23
6	232	537	0.43

6.3 Climatic and geomorphology conditions of Atacama DCAs

There is 34 DCAs defined by the Meteoritical Bulletin Database, but only 13 of them yield more than 10 non-paired meteorites (**Table 6.1**). Atacama DCAs are flat extended plains (slope $< 2^\circ$) developed mainly on Tertiary and Quaternary colluvium and alluvium with very little (if any) exposed rock outcrops. The surfaces display gravels with granular (2–4 mm) to pebble (4–64 mm) particle sizes (see **Figure 6.2**), consisting primarily of igneous and sedimentary rock fragments such as andesite, dacite, ignimbrite, gabbro, granodiorite, diorite, conglomerate, and sandstone (**Figure 6.1**, panel (b); Marinovic et al., 1995; Espinoza et al., 2011). Commonly, these areas display evidence of rocky deflation surfaces (i.e., presence of ventifacts and well-developed desert pavements; **Figure 6.2**), with a mm up to cm subsurface layer of precipitated saline minerals (e.g., sulphates, halides, chromates, borates; Ericksen, 1981).

All the Atacama DCAs are located between 21°15' to 26°30' S latitude and 70°30' to 67°30' W longitude (i.e., concentrated in the Antofagasta region) and in between four parallel (N-S) morphotectonic units: the Coastal Range (CR), the Central Depression (CD), the Preandean Range and the Preandean Basement. The CR has a width of ~50 km and altitude peaks lower than 2000 m. Its meteorological conditions are defined as semiarid, because of the direct influence of a coastal fog (locally known as *camanchaca*), which, under topographic favorable conditions, penetrates up to 50-90 km inland (e.g., Goudie et al., 2002; Rech et al., 2003). The CD is a large hyper-arid subregion almost completely devoid of plants, protected by the CR at the west from the coastal fog influence and from the seasonal rainfall by the Western Andes Cordillera at the east. Surfaces are filled with Tertiary and Quaternary alluvial, fluvial and evaporitic deposits mainly derived from the preandean range and Western Andean Cordillera. Considering the extent of the Preandean Range and Preandean Basement and in order to simplify the climatic description and their link to meteorite alteration, we combine both in a single unit: Preandean Range/Basement (PRB). The PRB comprises the (i) Cordillera de Domeyko, a N-S mountain range extended by 600 km with a maximum altitude peak of ~4000 m, and (ii) intermontane basins and salt flats, a series of Cenozoic depocenters created by reverse faulting of kilometer-scale bounded by the Domeyko Cordillera and the current Western Andean Cordillera (Amilibia et al., 2008; Arriagada et al., 2006; Martínez et al., 2021 and reference therein). According to the morphotectonic units, 9, 9 and 14 Atacama DCAs belong to the CR, CD and PRB, respectively (**Table 6.3**). The percentage of meteorites is larger in the CD (47.5%, N=1017) followed by the CR (31.3%, N=671) and the PRB (21.2%, N=453). The dominant percentage of meteorites at the CD indicates the preferential local climatic conditions to preserve extraterrestrial material and/or the likelihood of expeditions to these areas.

Table 6.3. The DCAs in the Atacama Desert are divided by morphotectonic unit.

Geomorphologic unit	DCAs	Meteorite group			
		Chondrite	Achondrite	Iron	Rocky-iron
Coastal range	Pampa de Mejillones	25			
	La Yesera	4		1	
	Caleta el Cobre	63	2	1	
	El Médano	485	3	1	
	Paposo	78	1		
	Mantos Blancos	1		1	
	Las Bombas	2			
	Diego de Almagro	2			
	Taltal	1			
	<i>Total</i>	<i>661</i>	<i>6</i>	<i>4</i>	<i>0</i>
Central depression	Altamira	2			
	San Juan	111	1	1	1
	Catalina	391	1	2	4
	Los Vientos	445	12	2	2
	Baquedano	1		1	
	Rencoret	1			
	Coya Sur	7			
	Calate	29			
	Coipuno	3			
	<i>Total</i>	<i>990</i>	<i>14</i>	<i>6</i>	<i>7</i>
Preandean range/basin	Vaquillas	6			
	Carrizo	1			
	Agua de Varas	1			
	Quebrada	1			
	Chimborazo	1			
	Imilac	4			1
	Cerro Quimal	1			
	Limon Verde	15			
	Calama	208	5	1	
	Machuca	25			
	Toconao	7			
	Colachi	1			
	Tilomonte	1			
Chug Chug	116				
Sierra Gorda	58		1		
	<i>Total</i>	<i>445</i>	<i>5</i>	<i>2</i>	<i>1</i>

6.4 Terrestrial weathering of Atacama meteorites

6.4.1 Meteorites in Atacama and other collections

Terrestrial weathering is defined as the exposition rate of meteorites to the alteration agents settled on the earth's surfaces. Numerous factors can control the terrestrial alteration as standing time in the terrestrial environment, soil composition of the recovery site, meteorological condition of the area, meteorite type, size, shape and porosity (e.g., Pourkhorsandi et al., 2021; Valenzuela, 2011; Ouknine et al., 2019; Al-Kathiti et al., 2005; Stephan et al., 2018). Opposite, stony-irons and iron meteorites weathering is controlled mainly primary along fractures and mineral phase boundaries (Leclerc, 2016).

As the chondrites represent the ~94% of meteorites in the Atacama Desert (Figure 6.3), the following discussions will be focus on this type of meteorite. The method to classify the weathering degree in ordinary chondrites was initially proposed by Wlotzka (1993) and consequently adapted using intermediate steps by Zurfluh et al. (2016). The weathering scale ranges from W0 to W6, with grading determined by the oxidation level in metal and sulfide and, subsequently, silicates (Wlotzka, 1993; Bland et al., 2006). As the alteration affects diverse petrographic, chemical, and isotopic characteristics of meteorites, weathering degrees have been studied by diverse methods as (i) amount of oxidized metal, sulphide, and silicates (Wlotzka, 1993; Bland et al., 2006; Munayco et al., 2013), (ii) terrestrial age of residence (Jull et al., 1993; Stelzner et al., 1999; Drouard et al., 2019; Hezel et al., 2011; Jull et al., 2013), (iii) trace elements distribution (Pourkhorsandi et al., 2017, 2021; Crozaz et al., 2003) and (iv) isotopic composition deviation (Stephan et al., 2018; Bland et al., 2000; Vacher et al., 2020; Bischoff et al., 2022). There are several benefits in gaining more knowledge about weathering processes among different dense collection areas, (i) describe regional and local parameters associated with terrestrial rock weathering, (ii) define environment or microenvironment variation among different climatic conditions on Earth, (iii) explore processes of asteroids alteration by not-atmospherically conditions.

Chondrites finds have different weathering trends dependent on the location areas. The distribution of weathering grades for Atacama, hot desert and Antarctic chondrites is shown in **Figure 6.6**. The peak of weathering for the Antarctic chondrites is W1 followed by W2 with 54.6 and 38.2%, respectively. For instance, the Atacama Desert is the only one with a

distribution close to Antarctic chondrites, with 35.5 and 36.2% for W1 and W2, respectively. However, evaporite minerals have been observed only in approximately 5% of all Antarctic meteorites (Losiak & Velbel, 2011). This contrasts with the often-reported calcium sulfate [$\text{CaSO}_4 \cdot 2\text{H}_2\text{O}$] filling veins and/or porosity in Atacama meteorites (**Figure 6.7**; Valenzuela, 2011; Pinto et al., 2022). Likewise, the difficulty in comparing meteorite preservation between hot and cold deserts is the variable classification of weathering degrees considered in the Meteoritical Bulletin Database. For instance, Antarctic chondrites involve a visual inspection of the specimens given a letter classification of A, B or C, indicating minor, moderate, and severe rusting, respectively (Wlotzka 1993). Considering the high number of ordinary chondrites found in Antarctica (~33700, Meteoritical Bulletin Database, 2022), only 18.9% of them display weathering scale ranges from W0 to W6. The remaining 81.1% have (i) mixing of W degree (e.g., W0/4), (ii) different classification scales or (iii) directly not information. By contrast, the percentage of classified chondrites using the weathering scale (W0-W6) is more common among hot deserts with a 96, 80 and 83% for Atacama, Sahara, and Oman Desert, respectively. Recently, Ouknine et al. (2019) analyzed the weathering of the African meteorites, showing the dominance of W1 (32%) and W2 (34%). Nevertheless, African chondrites exhibit a certain difference in the alteration degree between samples collected in the north, tropic, and south areas. As the continental scale can bias these results, we selected meteorites found in the Sahara Desert using North African countries (i.e., Algeria, Libya, Tunisia, Morocco, and Egypt; **Figure 6.6**). Compared to the Atacama, the values of the Sahara are similar for W2 (33.1%) but considerably different for W1 (19.3%). The China chondrites have similar values to the Sahara Desert. On the other hand, the most altered collection belongs to Oman and Iran (**Figure 6.6**). This agrees with the petrographic and chemical analysis done by Zurfluh et al. (2016) and Pourkhorsandi et al. (2019) on Oman and Iran chondrites, respectively.

Recurrent evidence makes hot desert meteorites suspect samples for cosmochemical studies due to their multifactor terrestrial weathering products (Pourkhorsandi et al., 2021). However, the Atacama Desert displays advantageous conservation characteristics compared to other locations (see **Figure 6.6**). Commonly, the bulk oxygen isotopic composition of meteorite finds displays large terrestrial contamination, shifts away from the primary compositional fields (Greenwood et al. 2012). According to the few reported bulk oxygen composition of Atacama OCs, they display minor shift compared to other environments where the oxygen composition suggests a pervasive contamination by ^{18}O -rich precipitated phases (Bischoff et al., 2022). Note that the incorporation of significant terrestrial oxygen is dominated by the

terrestrial weathered of iron and sulfide into hydroxides and oxyhydroxides (Lee & Bland, 2004). In the case of silicates and oxides, oxygen diffuses very slowly at atmospheric conditions (Chakraborty, 2010), so their contamination should be negligible compared to metallic beads oxidation. Thus, chondrules and calcium aluminum rich-inclusions on Atacama chondrites should preserve their O isotopic composition it had upon crystallization. The formed have a remarkable importance to precise the pre-terrestrial history of chondritic components in the nebular or asteroid conditions (e.g., Tenner et al., 2018; Marrocchi et al., 2018; 2019; Piralla et al., 2021; Schnuriger et al., 2022). Recently, Metzler et al. (2021) determined that Los Vientos 051 is the most ^{16}O -rich chondrite associated with the recently proposed CL group. Also, performed *in situ* O-isotopes analysis of olivine and pyroxene crystals in Sierra Gorda 009 and GRO 95551, indicated negligible difference even they difference provenance from Atacama and Antarctic, respectively (Ivanova et al., 2020).

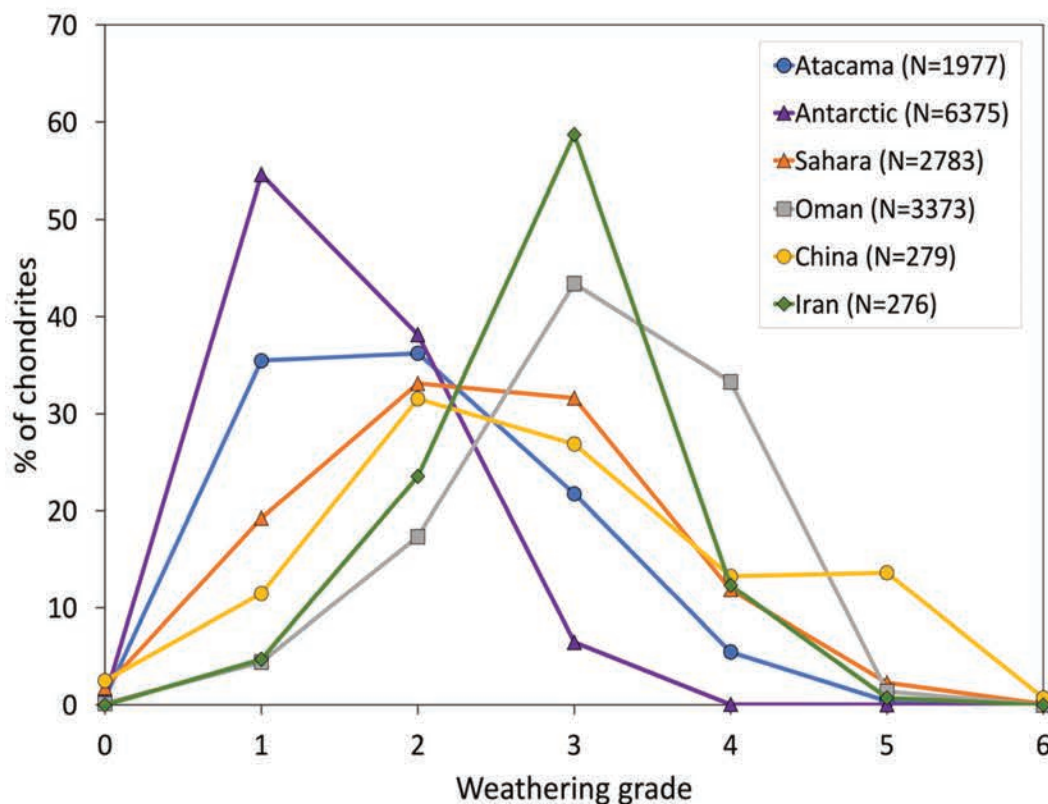


Figure 6.6. Distribution of weathering grade for hot desert and Antarctic chondrites. The Atacama chondrites shows peak of weathering grade at W2 with similar values in W1, supporting a low degree of terrestrial alteration compared to other hot desert chondrites. No Antarctic chondrites show always a small fraction of terrestrial alteration above W4. Data extracted from that is available in the Meteoritical Bulletin Database (2022).

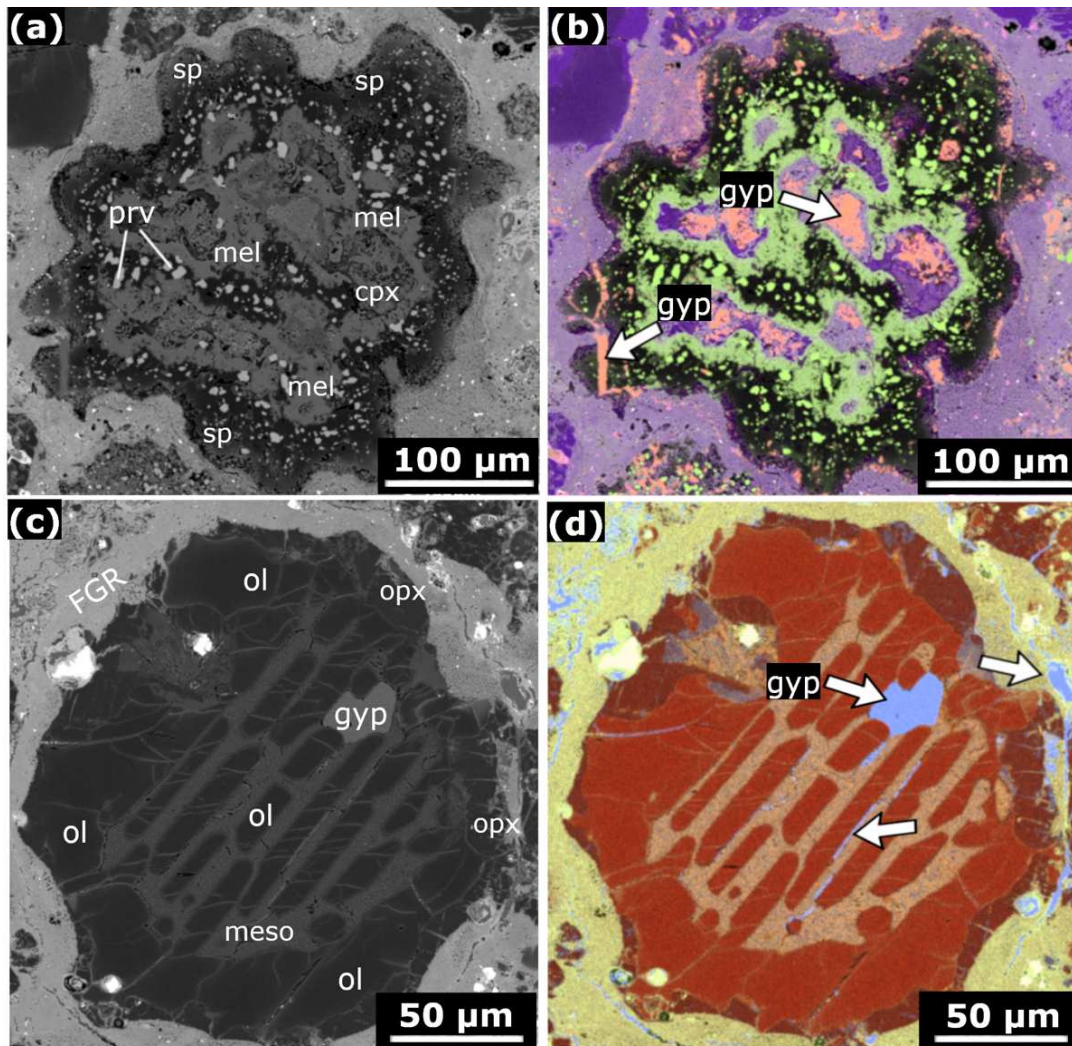


Figure 6.7. Backscatter electron images and compositional maps of one calcium-aluminum rich inclusion (a-b) and one chondrule (c-d) filled by gypsum ($\text{CaSO}_4 \cdot 2\text{H}_2\text{O}$). In (b), the gypsum (pink color) filled porosity in the spinel rim and the Ca-rich pyroxene at the center area of the CAI (white arrows). The chondrule mesostasis (d) is filled by gypsum (sky-blue color) as (i) massive overgrowth in a big pore of $\sim 30 \mu\text{m}$ and (ii) thing veins among contacts with the olivine bars (white arrows). A thin layer of gypsum also delimitates most of the fine-grained rim and the matrix contact. Prv = perovskite; mel = melilite; Ol = olivine; gyp = gypsum; opx = Ca-poor pyroxene; cpx = Ca-rich pyroxene; FGR = fine grained-rim

The higher alteration of some Atacama meteorites should be related to their extensive average time of residence on Earth's surfaces. According to Drouard et al. (2019), meteorites from the Atacama show fifty times older cosmogenic exposure ages compared to other hot desert meteorites (~ 700 and ~ 12 ky, respectively). This longer average of terrestrial residence could be responsible for their higher concentration of Sr, Ba and LREE-enriched (Sm, Nd, Ce, La), that is evidence of terrestrial soil contamination (Pourkhorsandi et al., 2017). In other words, fractionated REE, rusty percentage of metals, and precipitated secondary minerals are

parameters associated with the regional/sub-regional climatic condition of each DCAs in the Atacama Desert and the time of residence which the meteorites remain in these surfaces.

6.4.2 Suitable areas in the Atacama Desert for meteorite preservation

Three main factors that modulate the precipitation deficit in the Atacama Desert are: (i) a constant temperature inversion generated by the cool north-flowing Peruvian Current in the Pacific Ocean, (ii) the rain shadow effect produced by the proximity of the high Andes upwind, and (iii) its location in the subtropical high-pressure belt (Marquet et al., 1998; Clark, 2006; Rundel et al., 1991; Houston & Hartley, 2003; Latorre et al., 2003; Grosjean et al., 2003). These factors influence at different degree the morphotectonic units where DCAs are placed. As reported Boy et al. (2022), transects perpendicular to the Andes displayed multiple drivers of aridity while gradients parallel are more stable. These west - east gradients depend principally on (i) the distance from the Pacific Ocean, affected or not by a dense coastal fog, and (ii) the topographic elevations of the surfaces which control the precipitation rate among the different morphotectonic units. The major abundance of weathering OCs are at the CR surfaces (30.1% with W3; **Figure 6.8a**). In comparison, the CD yields a large abundance of lower weathering OCs (39.6% with W1). As the oldest surfaces are distributed from W to E (see **Figure 6.1b**), highly weathered OCs are no correlated with the surface age, but with the regional/sub-regional climatic condition (Munayco et al., 2013). The OCs found at the southern surfaces of Atacama show less alteration even if there are closer to the coastal area.

According to the proximity groups, Catalina and Paposo DCAs (Group 2; **Figure 6.8b**) shows the high proportion of lower weathering grade with a 44.6 % of chondrites with W1. Only three DCAs located in the CR displays OCs with a W5 degree of weathering: Pampa de Mejillones, Paposo and Calate. Moreover, Pampa de Mejillones + La Yesera are the closer DCAs to the Pacific Ocean and display the most altered meteorites (Group 5; **Figure 6.8b**); evidenced also by the higher fractionated REEs (e.g., Pourkhorsandi et al., 2017). Experimental analysis had demonstrated that thermal stress weathering, produced by temperature fluctuations during day/night, and the high humidity are fundamental parameters for metal corrosion in OCs (Goderis et al., 2022). Furthermore, interaction of H₂O and the salty soil had been described as cause of pervasive saline obliteration in the meteorites from Atacama Desert (Muñoz et al., 2007; Valenzuela, 2011) and had also been previously reported for volcanic rocks (Searl and Rankin, 1993). Moreover, various petrographic studies of Atacama chondrites

have shown evidence of veins and/or porosity filled by nitrate or sulfate precipitations (**Figure 6.7**; Valenzuela, 2011; Pinto et al., 2022; Pourkhorsandi et al., 2017). Thus, the three main processes of chondrites fragmentation in the Atacama Desert are results of (i) saline mineral precipitation, (ii) thermal stress weathering, and (iii) volume increase by Fe-Ni oxide and hydroxide formation. The efficient mechanism of Atacama rocks disintegration is evidenced by the recurrent local fragmentation of chondrites in Calama, Catalina and Los Vientos DCAs. Although terrestrial colonization of microorganisms has been demonstrated by an important promoter of chondrite obliteration through increasing the production of sulfate, carbonate, Fe-oxide and smectite minerals (Lee et al., 2017; Tait et al., 2017), no analysis of microorganism colonization had been performance in Atacama chondrites.

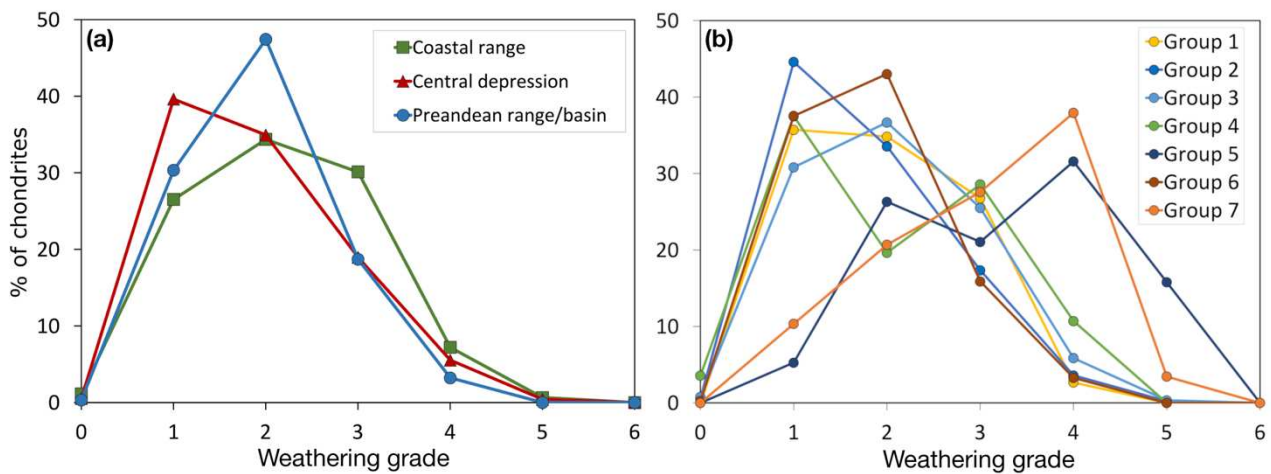


Figure 6.8. Weathering grade of ordinary chondrites. In (a), the weathering grade according to the main morphotectonic units on the Atacama Desert. The chondrites experience a significant weathering find on the coastal range. All the DCA grouped by proximity are shown in (b). Group 1 = Vaquillas, San Juan and Taltal; Group 2 = Paposo and Catalina; Group 3 = El Médano and Los Vientos; Group 4 = Caleta el Cobre; Group 5 = Pampa de Mejillones and La Yesera; Group 6 = Calama, Coya Sur, Chug Chug and Sierra Gorda; Group 7 = Calate and Coipuno. Data extracted from that is available in the Meteoritical Bulletin Database (2022).

In order to construct a morphogenetic classification (Peltier, 1950) of DCAs in the Atacama Desert, we extracted climatic information from TerraClimate (Abatzoglou et al., 2018) using the Google Earth Engine platform (Gorelick et al., 2017). A posterior verification of TerraClimate data were performed using meteorological stations of the *Dirección General de Aguas* (<https://www.cr2.cl/>). The morphogenetic classification of CR, CD and PRB as well as the main DCAs are shown in **Figure 6.9**. The annual temperature and precipitation for each DCAs were estimated as a mean of all pixel values contained in the DCAs extension, which is defined by the Meteoritical Society.

In order to determine a hyper-arid zone within the morphogenetic classification, we followed the recommendations of the UNEP (1997). This corresponds to a ratio of annual precipitation to potential annual evaporation of less than 0.05. We used the potential evapotranspiration approximation via the Koppen classification for arid areas which distinguishes two regimes of interest for the study area considered in this article: a winter precipitation regime and a summer precipitation regime (Peel et al., 2007). Thus, it is possible to define two borderline cases, characterized by linear or affine relationships between temperature and precipitation. To determine the hyper-arid zone, we used the potential evapotranspiration via the Koppen relation for precipitation regimes occurring mainly during winter (Peel et al., 2007):

$$P \text{ [mm]} = T \text{ [}^\circ\text{C]} \quad (1)$$

Where P is precipitation and T is temperature. To estimate a summer precipitation context (i.e., Bolivian rain phenomenon) we modified the relationship to:

$$T \text{ [}^\circ\text{C]} = P \text{ [mm]} - 14 \quad (2)$$

In general, the three morphotectonic units (CR, CD and PRB) evolve from hyper-arid zones to arid or cold semi-arid and even periglacial zones (**Figure 6.9**). This trend follows the altitudinal gradient from west to east, leading from the coast to the cordillera and causing topographic effects that accentuate precipitation and decrease temperatures. In the case of DCAs, 69.2% are concentrated in the hyper-arid zone, while 30.7% plot in the arid range. If we considered the winter precipitation regime (i.e., Bolivian rain phenomenon), which concerns most of the areas close to the Andes Mountain (PRB), the DCAs on hyper-arid regions increase to 84.6%. This result agrees with the climatic description performed in early meteorite accumulation areas in Pampa de Mejillones, San Juan and El Médano (Muñoz et al., 2007; Valenzuela, 2011; Hutzler et al., 2017). Overall, all DCAs with more than 10 meteorites have an annual mean air temperature range from 7 – 19°C and annual cumulative precipitation between 1 – 30 mm. We attribute the extreme limits (i.e., 7°C and 30 mm) to fast erosion and freezing processes, which can accelerate the weathering of meteorites. The predominant degree of weathering of DCAs does not show a clear relationship with the precipitation and temperature variables. However, there is subregional variation at DCAs scale which does not correspond to the morphotectonic unit localization. For instance, four DCAs plot in the climatic

range defined for the PRB, but only Calama (5) belongs to this morphotectonic unit; San Juan (22) and Los Vientos (33) belong to the CD and Paposo (34) to CR. Similar mismatch are evidenced by El Médano (29) from CR but in the range of CD. All these DCAs have more than 100 meteorites classified in their surfaces. Thus, DCAs are defined by microenvironments, which diverge from the regional climatic context.

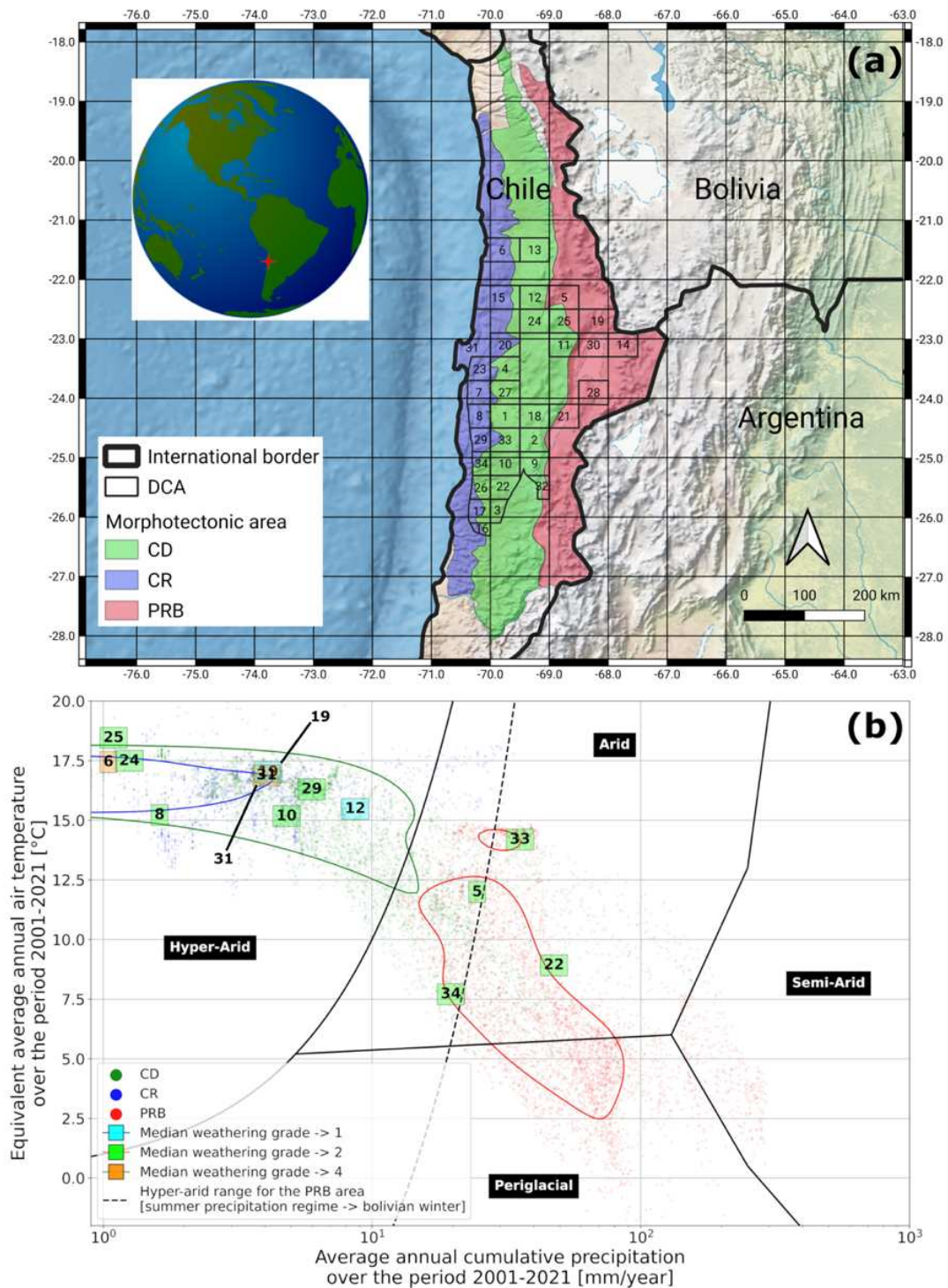


Figure 6.9. (a) Map of the three morphotectonic units defined in this article and each DCA indicated by number (see Figure 6.1 for details). (b) Morphogenetic classification of Atacama DCAs using the average reconstructed annual temperature and precipitation. Boundaries of arid, semi-arid and periglacial zones are from Peltier (1973). The hyper-arid zone corresponds to the boundaries defined by the United Nations Environment Programme (<https://wedocs.unep.org/20.500.11822/30300>). The dashed line shows the winter precipitation regime calculated from equation 2. The last concerns to Preandean Range/Basement area. The annual temperature and precipitation average for each DCAs were estimated as a mean point from the average of the pixel values contained in each DCA square. We plot only DCAs with more than 10 meteorites. The colors of DCAs refer to the median alteration grade: blue = W1, green = W2, and orange = W4. CD: Central depression; CR: Coastal range; and PRB: Preandean Range/Basement.

All things considered indicate that terrestrial weathering of the Atacama Desert meteorites shows less alteration than other hot deserts and their modifications depend on the local atmospheric and geological conditions of each DCA. Overall, three main processes generate chondrite disintegration in the Atacama surfaces: saline mineral precipitation, thermal stress weathering, and volume increase through Fe-Ni oxide and hydroxide formation. The schematic representation of alteration processes of meteorites in the Atacama surfaces is shown in **Figure 6.10**. According to the morphogenetic diagram, DCAs with a high meteorite yield mismatch with the mean precipitation and temperature of the host morphotectonic unit. These could be the results of microclimate environments controlled by parameter(s) that are not considered yet to define suitable areas of high density of meteorites in the Atacama Desert.

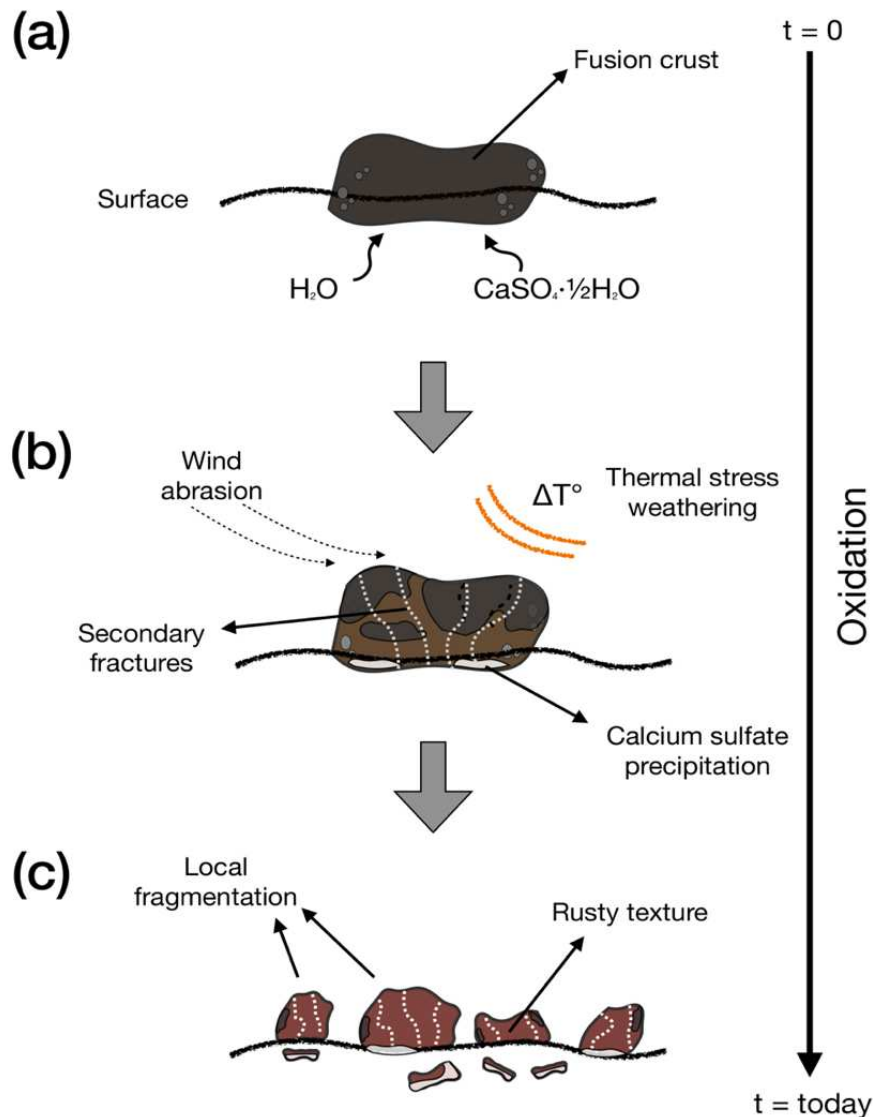


Figure 6.10. Schematic representation of meteorite residences in the Atacama Desert. (a) Meteorite felt with a fresh fusion crust in the Atacama surfaces. According to the surface properties and the meteoroid speed, extraterrestrial fragments can be buried in the ground or stay at the surface. Whatever the case, the meteorite surfaces start reacting with H_2O and salts (i.e., gypsum [$CaSO_4 \cdot 2 H_2O$]). (b) Different weathering agents modified the meteorite characteristics. The thermal stress weathering, wind abrasion, metallic phases oxidation, and salt precipitation generate enough internal pressure to promote the formation of secondary fractures and fragmentation along shock veins, preexisting fractures, and other zones of weakness. (c) Local fragmentation. A prolonged exposition to the weathering agents breaks the entire sample into pieces, which can be disintegrated by the weathering agents or broken down into smaller pieces again.

6.5 Final consideration and perspectives

The Atacama Desert displays three main morphotectonic units: the Coastal Range, Central Depression, and Preandean Range/Basement. The distinctive climatic and geological conditions of the morphotectonic units affect the accumulation and conservation of meteorites. The three main parameters of the Atacama DCAs which modified the alteration degree are (i) distance from the Pacific Ocean, (ii) surface altitude, and (iv) surface lithology. Meteorites from the Atacama Desert are mostly localized in the Central Depression (47.5%, N=1017) followed by the Coastal Range (31.3%, N=671) and the Preandean Range/Basement (21.2%, N=453). The significant abundance of lower weathering chondrites is located at the Central Depression (39.6% with W1), which is protected by the Coastal Range in the west from the coastal fog influence and the seasonal rainfall by the Western Andes Cordillera in the east. The terrestrial alteration is controlled by the original composition, time of residence, and subregional location. There are three main processes which generate chondrite disintegration in Atacama (i) saline mineral precipitation, (ii) thermal stress weathering, and (iii) volume increase by Fe-Ni oxide and hydroxide formation. The role of biological alteration of Atacama meteorites had not yet been defined. A comparison with reported weathering data from other cold and hot deserts indicates that mean terrestrial weathering of Atacama chondrites (W1-2) displays less alteration than other hot deserts (W2-3) following the distribution of the Antarctic meteorites collection (W1-2).

Chapter 7

Conclusions and perspectives



7.1 Conclusions

Chondritic meteorites evidence the complex histories recorded in the formation and agglomeration of solids during the first million years of the Solar System. In this thesis, I described chondritic components such as chondrules and fine-grained material, which retain petrographic, chemical, and isotopic characteristics related to the nature of events in the early solar system. Three questions associated to specific objectives were proposed to fill some gaps in the formation and agglomeration of solids: (i) is there a genetic link between Mg-rich and Fe-rich chondrules? I used oxygen isotopic composition in Mg-rich relicts in type II chondrules to constrain this genetic relationship. My results support a hereditary connection between type I and II chondrules with a global implication in the recycling of solids in the early solar system. Previous models propose a formation of type I chondrules from ameboid olivine aggregates-like composition (Marrocchi et al., 2018, 2019). Combined with our data, this indicate that several transit-heating events occurred in the protoplanetary disk to form a total or partial melting spherules. Furthermore, both types of chondrules display an agglomerated dust mantle defined as fine-grained rim. But (ii) how was the environment and dynamics of the dust agglomeration around chondrules? My data support that fine-grained rims were formed in a nebular environment. Also, a new positive correlation between the abundance of rimmed chondrules and fine-grained matrix indicate that the dust agglomeration was linked to each carbonaceous chondrite reservoirs and the abundance of available dust in their respective chondrule formation regions before the planetesimal accretion. But (iii) Can we constrain the astrophysical models of solids accretion in the protoplanetary disk using chondrites? My morphometric analysis of chondrules among different CO carbonaceous chondrites revealed that the mean spherical diameters of chondrules increase with increasing metamorphic degree. Combining our results with literature data, we show that this relationship was not established during post-accretion thermal metamorphism, but instead it records aerodynamic size-sorting of particles during the accretion of the CO parent body(ies). I support the empirical data modeling the self-gravitating contraction of a clumps of chondrules that indicate larger chondrules are more centrally concentrated in the parent body(ies) than smaller ones.

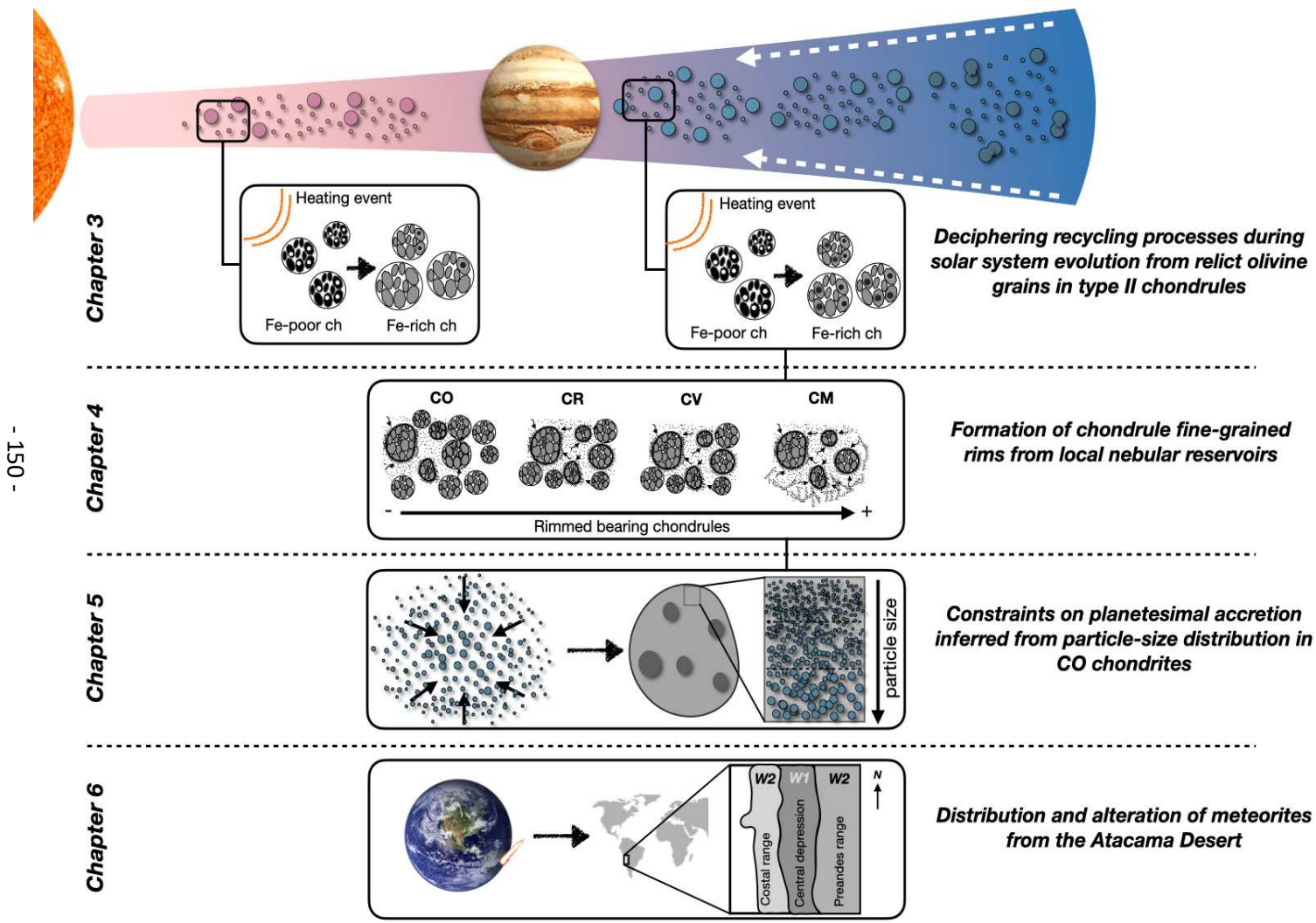


Figure 7.1. The schematic representation of the results in this Ph.D. thesis. Chapter 3 describes the formation condition of Fe-rich chondrules by recycling Fe-poor chondrules. Chapter 4 determined the abundance of rimmed chondrule among different carbonaceous chondrite reservoirs and their relationship with the fine-grained material abundances. In chapter 5, we constrain the CO parent body formation combined particle-size distribution and theoretical model of planetesimals accretion by the collapse of a clump of chondrules. Chapter 6 recapitulates and compares the distribution and preservation of meteorites in the 32 dense collection areas in the Atacama Desert (north of Chile).

7.2 Perspectives and ongoing work

According to our reported oxygen isotopic data, most of the Mg-rich relicts in type II chondrules originated as reduced type I chondrules. Moreover, two “host” olivine grains in CR chondrules display Fe-rich and ^{16}O -rich composition ($\text{Mg}\# = 50.7$ and 55.9 ; $\Delta^{17}\text{O}$ values = -2.8 and -4.7 ‰), defining isotopic relicts in type II chondrules (difference of $\Delta^{17}\text{O} > 3\sigma$, Ushikubo et al., 2012). These grains can result from a previous generation of (i) type II chondrules or (ii) type I chondrules with their Mg# overprinted by diffusion. I propose to do high-current X-ray maps using an electron probe to determine Al, P, and Ca distribution on these chondrules. These results will reveal whether or not the ^{16}O -rich were overprinted by Fe diffusion. Additionally, we will report modal abundance and volumetric analysis of bearing relict type II chondrules in ordinary and carbonaceous chondrites using the X-ray microtomography data. Furthermore, X-ray microtomography can be combined with SIMS analysis as “integrated microscopy” to determine oxygen isotopes (or Si isotopes) in the relict center and borders.

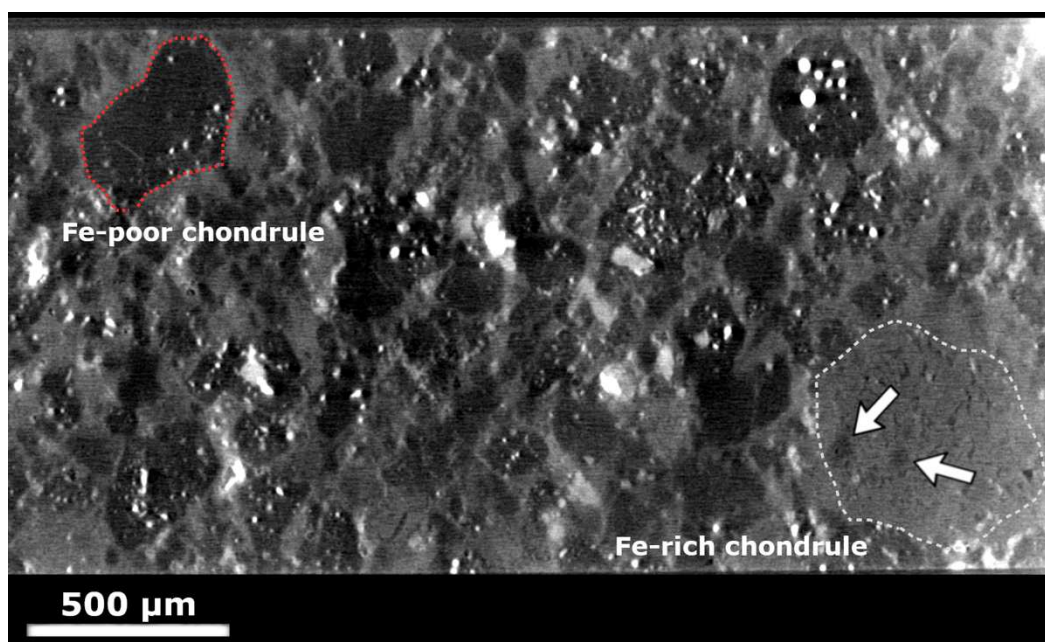


Figure 7.2. X-ray microtomography image of LoV 123 (CO3.05) shown in the XY axis. The contrast differences in the virtual images distinguish different chondritic components, such as Fe-poor chondrules (red dotted line) and Fe-rich chondrules (with a dotted line). These virtual slides could determine the chondritic components for subsequent analysis. White arrows show Mg-rich relicts in the Fe-rich chondrules.

According to our fine-grained rim data from different carbonaceous chondrite groups, the “agglomerated mantle” probably was accreted in each local chondritic reservoir. Is there a similar correlation for the inner solar system reservoirs (ordinary, rumuruti, and enstatite chondrites)? Preliminary results of Bigolski (2017) on rimmed bearing chondrules from ordinary chondrites indicates higher temperatures of dust agglomeration by the presence of sintered texture close to the chondrule surfaces. A detail petrographic analysis by X-ray microtomography among a set of different non-carbonaceous chondrites could dilucidated not only different conditions of accretion, as well dissimilar recycling rate between the inner and outer solar system.

The particular petrographic features of the CO chondrite group make them an interesting target to determine agglomeration of chondritic components in the early solar system. They show smaller chondrules (mean <100 μm in apparent diameter), high abundance of coarse-grained particles compared to other carbonaceous chondrite groups, high modal abundance of refractory inclusions and a progressive metamorphic sequence at relative lower temperature. Recently, Jacquet (2021) interpreted early agglomeration of chondrules in a melting state using minor and trace element composition of 18 lobates chondrules in CO chondrites.

After an intensive evaluation of reported chondrule sizes data as well as discussions with others meteorite researchers, it seems that CO chondrite group is the only one that display a positive correlation between the mean chondrule sizes and the petrographic grade. However, the agglomeration of metal beads (which are denser than silicates) is still poorly understand among carbonaceous and ordinary chondrite reservoirs (Johansen et al., 2009). Distribution of metal particle sizes could be a key constrain to study the accretion of undifferentiated planetesimals in the inner and outer solar system.

Furthermore, understand how the organic material is accumulated under a framework of a collapsed clump of particles, could bring evidence about its distribution within planetesimals. Currently, the high abundance of meteorites found in the Atacama Desert have deliver also peculiar samples for the meteoritical community. As we show by our statistical analysis, the Atacama meteorites collection is the most pristine from hot deserts. However only few articles have pay attention into the terrestrial alteration of Atacama meteorites (Gattacceca et al., 2011; Pourkhorsandi et al., 2020). As the Atacama Desert is widely used as Mars analog (Azua-Bustos et al., 2020; Boy et al., 2022), understand the conservation of meteorites could evidence the processes of meteorites alteration in a Mars environment.

References

- Abatzoglou, J. T., Dobrowski, S. Z., Parks, S. A., & Hegewisch, K. C. (2018). TerraClimate, a high-resolution global dataset of monthly climate and climatic water balance from 1958–2015. *Scientific data*, 5(1), 1-12
- Aboulahris, M., Chennaoui Aoudjehane, H., Rochette, P., Gattacceca, J., Jull, A. J. T., Laridhi Ouazaa, N., Folco, L., & Buhl, S. (2019). Characteristics of the Sahara as a meteorite recovery surface. *Meteoritics and Planetary Science*, 54(12), 2908–2928. <https://doi.org/10.1111/maps.13398>
- Al-Kathiri, A., Hofmann, B. A., Jull, A. J. T., & Gnos, E. (2005). Weathering of meteorites from Oman: Correlation of chemical and mineralogical weathering proxies ¹⁴C terrestrial ages and the influence of soil chemistry. *Meteoritics and Planetary Science*, 40(8), 1215–1239. <https://doi.org/10.1111/j.1945-5100.2005.tb00185.x>
- Alexander, C. M. D. (2019). Quantitative models for the elemental and isotopic fractionations in chondrites: The carbonaceous chondrites. *Geochimica et Cosmochimica Acta*, 254, 277-309.
- Alexander, C. O. D., Grossman, J. N., Ebel, D. S., & Ciesla, F. J. (2008). The formation conditions of chondrules and chondrites. *Science* 320:1617–1619.
- Amilibia, A., Sàbat, F., McClay, K. R., Muñoz, J. A., Roca, E., & Chong, G. (2008). The role of inherited tectono-sedimentary architecture in the development of the central Andean mountain belt: Insights from the Cordillera de Domeyko. *Journal of Structural Geology*, 30(12), 1520–1539. <https://doi.org/10.1016/j.jsg.2008.08.005>
- Amsellem, E., Moynier, F., Mahan, B., & Beck, P. (2020). Timing of thermal metamorphism in CM chondrites: Implications for Ryugu and Bennu future sample return. *Icarus*, 339, 113593.
- Anders E. (1964). Origin, age, and composition of meteorites. *Space Science Reviews* 3:583–714.
- Anders, E., & Grevesse, N. (1989). Abundances of the elements: Meteoritic and solar. *Geochimica et Cosmochimica acta*, 53(1), 197-214.
- Andreasen, R., & Sharma, M. (2006). Solar nebula heterogeneity in p-process samarium and neodymium isotopes. *Science*, 314(5800), 806–809. <https://doi.org/10.1126/science.1131708>
- Andreasen, R., & Sharma, M. (2007). Mixing and Homogenization in the Early Solar System: Clues from Sr, Ba, Nd, and Sm Isotopes in Meteorites. *The Astrophysical Journal*, 665(1), 874–883. <https://doi.org/10.1086/518819>
- Andrews, S. M., Huang, J., Pérez, L. M., Isella, A., Dullemond, C. P., Kurtovic, N. T., Guzmán, V. v., Carpenter, J. M., Wilner, D. J., Zhang, S., Zhu, Z., Birnstiel, T., Bai, X.-N., Benisty, M., Hughes, A. M., Öberg, K. I., & Ricci, L. (2018). The Disk Substructures at High Angular Resolution Project (DSHARP). I. Motivation, Sample, Calibration, and Overview. *The Astrophysical Journal*, 869(2), L41. <https://doi.org/10.3847/2041-8213/aaf741>
- Armitage, P. J., & Kley, W. (2019). *From Protoplanetary Disks to Planet Formation* (Vol. 45). <http://www.springer.com/series/4284%0Ahttp://link.springer.com/10.1007/978-3-662-58687-7>
- Arnould, M., Goriely, S., & Takahashi, K. (2007). The r-process of stellar nucleosynthesis: Astrophysics and nuclear physics achievements and mysteries. *Physics Reports*, 450(4–6), 97–213. <https://doi.org/10.1016/j.physrep.2007.06.002>
- Arriagada, C., Cobbold, P. R., & Roperch, P. (2006). Salar de Atacama basin: A record of compressional tectonics in the central Andes since the mid-Cretaceous. *Tectonics*, 25(1), 1–19. <https://doi.org/10.1029/2004TC001770>
- Ashley, J. W., & Velbel, M. A. (2000). Weathering-induced differences in fragmentation rates between H and L ordinary chondrites as an explanation for observed differences in Antarctic/non-Antarctic H/L ratios. *Meteoritics and Planetary Science Supplement*, 35, A22.
- Azua-Bustos, A., Fairén, A. G., Silva, C. G., Carrizo, D., Fernández-Martínez, M. Á., Arenas-Fajardo, C., Fernández-Sampedro, M., Gil-Lozano, C., Sánchez-García, L., Ascaso, C., Wierzchos, J., & Rampe, E. B. (2020). Inhabited subsurface wet smectites in the hyperarid core of the Atacama Desert as an analog for the search for life on Mars. *Scientific Reports*, 10(1), 1–17. <https://doi.org/10.1038/s41598-020-76302-z>

- Baecker, B., Rubin, A. E., & Wasson, J. T. (2017). Secondary melting events in Semarkona chondrules revealed by compositional zoning in low-Ca pyroxene. *Geochimica et Cosmochimica Acta*, 211, 256–279. <https://doi.org/10.1016/j.gca.2017.05.013>
- Barge, P., & Sommeria, J. (1995). Did planet formation begin inside persistent gaseous vortices?. *arXiv preprint astro-ph/9501050*.
- Barosch, J., Hezel, D. C., Ebel, D. S., & Friend, P. (2019). Mineralogically zoned chondrules in ordinary chondrites as evidence for open system chondrule behaviour. *Geochimica et Cosmochimica Acta*, 249, 1–16. <https://doi.org/10.1016/j.gca.2019.01.018>
- Bate, M. R. (2018). On the diversity and statistical properties of protostellar discs. *Monthly Notices of the Royal Astronomical Society*, 475(4), 5618–5658. <https://doi.org/10.1093/mnras/sty169>
- Bekaert, D. v., Auro, M., Shollenberger, Q. R., Liu, M. C., Marschall, H., Burton, K. W., Jacobsen, B., Brennecke, G. A., McPherson, G. J., von Mutius, R., Sarafian, A., & Nielsen, S. G. (2021). Fossil records of early solar irradiation and cosmolocation of the CAI factory: A reappraisal. *Science Advances*, 7(40). <https://doi.org/10.1126/sciadv.abg8329>
- Benoit, P. H., & Sears, D. W. G. (1996). Rapid changes in the nature of the H chondrites falling to Earth. *Meteoritics & Planetary Science*, 31(1996), 81–86.
- Berlin, J., Jones, R. H., & Brearley, A. J. (2011). Fe-Mn systematics of type IIA chondrules in unequilibrated CO, CR, and ordinary chondrites. *Meteoritics and Planetary Science*, 46(4), 513–533. <https://doi.org/10.1111/j.1945-5100.2011.01171.x>
- Birmingham, K. R., Worsham, E. A., & Walker, R. J. (2018). New insights into Mo and Ru isotope variation in the nebula and terrestrial planet accretionary genetics. *Earth and Planetary Science Letters*, 487, 221–229. <https://doi.org/10.1016/j.epsl.2018.01.017>
- Bevan, A. W. R., & Binns, R. A. (1989). Meteorites from the Nullarbor Region, Western Australia: I. A review of past recoveries and a procedure for naming new finds. *Meteoritics*, 24(3), 127–133. <https://doi.org/10.1111/j.1945-5100.1989.tb00954.x>
- Bigolski J. N. (2017). The Formation of Fine-Grained Chondrule Rims in Unequilibrated Ordinary Chondrites. Ph.D. thesis, The City University of New York, New York, USA.
- Bigolski J., Weisberg M. K., Ebel D. S., and Connolly H. C. (2014). Microchondrules; records of multiple heating events in the solar nebula and implications for type II chondrule formation. In *Lunar and Planetary Science Conference*. p. 1879
- Bigolski, J. N., Weisberg, M. K., Connolly, H. C., & Ebel, D. S. (2016). Microchondrules in three unequilibrated ordinary chondrites. *Meteoritics and Planetary Science*, 51(2), 235–260. <https://doi.org/10.1111/maps.12585>
- Bischoff, A., & Geiger, T. (1995). Meteorites from the Sahara: find locations, shock classification, degree of weathering and pairing. *Meteoritics*, 30(1), 113–122. <https://doi.org/10.1111/j.1945-5100.1995.tb01219.x>
- Bischoff, A., Storz, J., Barrat, J. A., Heinlein, D., Jull, A. J. T., Merchel, S., Pack, A., & Rugel, G. (2022). Blaubeuren, Cloppenburg, and Machtenstein—Three recently recognized H-group chondrite finds in Germany with distinct terrestrial ages and weathering effects. *Meteoritics and Planetary Science*, 57(1), 136–153. <https://doi.org/10.1111/maps.13779>
- Bischoff, A., Wurm, G., Chaussidon, M., Horstmann, M., Metzler, K., Weyrauch, M., & Weinauer, J. (2017). The Allende multicomponent chondrule (ACC)—Chondrule formation in a local superdense region of the early solar system. *Meteoritics and Planetary Science*, 52(5), 906–924. <https://doi.org/10.1111/maps.12833>
- Bland, P. A., Lee, M. R., Sexton, A. S., Franchi, I. A., Fallick, A. E. T., Miller, M. F., Cadogan, J. M., Berry, F. J., & Pillinger, C. T. (2000). Aqueous alteration without a pronounced oxygen-isotopic shift: Implications for the asteroidal processing of chondritic materials. *Meteoritics and Planetary Science*, 35(6), 1387–1395. <https://doi.org/10.1111/j.1945-5100.2000.tb01523.x>
- Bland, P. A., Sexton, A. S., Jull, A. J. T., Bevan, A. W. R., Berry, F. J., Thornley, D. M., Astin, T. R., Britt, D. T., & Pillinger, C. T. (1998). Climate and rock weathering: A study of terrestrial age dated ordinary chondritic meteorites from hot desert regions. *Geochimica et Cosmochimica Acta*, 62(18), 3169–3184. [https://doi.org/10.1016/S0016-7037\(98\)00199-9](https://doi.org/10.1016/S0016-7037(98)00199-9)
- Bland, P. A., Zolensky, M. E., Benedix, G. K., & Sephton, M. A. (2006). Weathering of Chondritic Meteorites. In D. S. Laretta, L. A. Leshin, & H. Y. McSween (Eds.), *Meteorites and the Early Solar System II* (The Univer, pp. 853–867). <https://doi.org/10.2307/j.ctv1v7zdmm.45>

- Bollard, J., Connelly, J. N., Whitehouse, M. J., Pringle, E. A., Bonal, L., Jørgensen, J. K., Nordlund, Å., Moynier, F., & Bizzarro, M. (2017). Early formation of planetary building blocks inferred from Pb isotopic ages of chondrules. *Science Advances*, 3(8), 1–23. <https://doi.org/10.1126/sciadv.1700407>
- Bonal, L., Bourot-Denise, M., Quirico, E., Montagnac, G., & Lewin, E. (2007). Organic matter and metamorphic history of CO chondrites. *Geochimica et Cosmochimica Acta*, 71(6), 1605–1623. <https://doi.org/10.1016/j.gca.2006.12.014>
- Bonal, L., Quirico, E., Flandinet, L., & Montagnac, G. (2016). Thermal history of type 3 chondrites from the Antarctic meteorite collection determined by Raman spectroscopy of their polyaromatic carbonaceous matter. *Geochimica et Cosmochimica Acta*, 189, 312–337. <https://doi.org/10.1016/j.gca.2016.06.017>
- Boss, A. P., Ipatov, S. I., Keiser, S. A., Myhill, E. A., & Vanhala, H. A. T. (2008). Simultaneous Triggered Collapse of the Presolar Dense Cloud Core and Injection of Short-Lived Radioisotopes by a Supernova Shock Wave. *The Astrophysical Journal*, 686(2), L119–L122. <https://doi.org/10.1086/593057>
- Bouden, N., Villeneuve, J., Marrocchi, Y., Deloule, E., Füre, E., Gurenko, A., Piani, L., Thomassot, E., Peres, P., & Fernandes, F. (2021). Triple Oxygen Isotope Measurements by Multi-Collector Secondary Ion Mass Spectrometry. *Frontiers in Earth Science*, 8, 1–9. <https://doi.org/10.3389/feart.2020.601169>
- Boy, D., Moeller, R., Sauheilt, L., Schaarschmidt, F., Rapp, S., Brink, L., Gschwendtner, S., Borquez, R. G., Matus, F. J., Horn, M. A., Guggenberger, G., & Boy, J. (2022). Gradient Studies Reveal the True Drivers of Extreme Life in the Atacama Desert. *Journal of Geophysical Research: Biogeosciences*, 127(3), 1–18. <https://doi.org/10.1029/2021jg006714>
- Brauer F., Henning T., and Dullemond C. P. 2008. Planetesimal formation near the snow line in MRI-driven turbulent protoplanetary disks. *Astronomy and Astrophysics* 487:1–4.
- Braukmüller N., Wombacher F., Hezel D. C., Escoube R., and Münker C. 2018. The chemical composition of carbonaceous chondrites: Implications for volatile element depletion, complementarity and alteration. *Geochimica et Cosmochimica Acta* 239:17–48.
- Brasser, R., & Mojzsis, S. J. (2020). The partitioning of the inner and outer Solar System by a structured protoplanetary disk. *Nature Astronomy*, 4(5), 492–499. <https://doi.org/10.1038/s41550-019-0978-6>
- Brearley A. J. (1993). Matrix and fine-grained rims in the unequilibrated CO3 chondrite, ALHA77307: Origins and evidence for diverse, primitive nebular dust components. *Geochimica et Cosmochimica Acta* 57:1521–1550.
- Brearley, A. J. (2014). Nebular Versus Parent Body Processing. In *Meteorites and Cosmochemical Processes, Treatise on Geochemistry* (Second Edition). Edited by A. M. Davis. Elsevier-Pergamon: Oxford, Vol. 2. p. 309-334.
- Brearley, A. J. (2006). The action of water. *Meteorites and the Early Solar System II, September*, 587–624.
- Brearley, A.J. & Krot A. N. (2012) Metasomatism in the early solar system: The record from chondritic meteorites. In *Metasomatism and the chemical transformation of rock— Lecture notes in Earth system sciences*, edited by Harlov D. E. and Austrheim H. Berlin: Springer. pp. 659–789.
- Bryson, J. F. J., & Brennecka, G. A. (2021). Constraints on Chondrule Generation, Disk Dynamics, and Asteroid Accretion from the Compositions of Carbonaceous Meteorites. *The Astrophysical Journal*, 912(2), 163. <https://doi.org/10.3847/1538-4357/abea12>
- Budde, G., Burkhardt, C., & Kleine, T. (2019). Molybdenum isotopic evidence for the late accretion of outer Solar System material to Earth. *Nature Astronomy*, 3(8), 736–741. <https://doi.org/10.1038/s41550-019-0779-y>
- Budde, G., Kleine, T., Kruijjer, T. S., Burkhardt, C., & Metzler, K. (2016). Tungsten isotopic constraints on the age and origin of chondrules. *Proceedings of the National Academy of Sciences of the United States of America*, 113(11), 2886–2891. <https://doi.org/10.1073/pnas.1524980113>
- Burkhardt, C., Kleine, T., Oberli, F., Pack, A., Bourdon, B., & Wieler, R. (2011). Molybdenum isotope anomalies in meteorites: Constraints on solar nebula evolution and origin of the Earth. *Earth and Planetary Science Letters*, 312(3–4), 390–400. <https://doi.org/10.1016/j.epsl.2011.10.010>

- Carrera, D., Johansen, A., & Davies, M. B. (2015). How to form planetesimals from mm-sized chondrules and chondrule aggregates. *Astronomy & Astrophysics*, 579, A43.
- Chakraborty, S. (2010). Diffusion coefficients in olivine, wadsleyite and ringwoodite. *Reviews in Mineralogy and Geochemistry*, 72, 603–639. <https://doi.org/10.2138/rmg.2010.72.13>
- Chaumard, N., Defouilloy, C., & Kita, N. T. (2018). Oxygen isotope systematics of chondrules in the Murchison CM2 chondrite and implications for the CO-CM relationship. *Geochimica et Cosmochimica Acta*, 228, 220–242. <https://doi.org/10.1016/j.gca.2018.02.040>
- Chaussidon M. (1988) Géochimie du soufre dans le manteau et la croûte océanique: apports de l'analyse isotopique in situ par sonde ionique. Ph.D. thesis, Université de Lorraine, Vandoeuvre-les-Nancy, France.
- Chaussidon, M., Libourel, G., & Krot, A. N. (2008). Oxygen isotopic constraints on the origin of magnesian chondrules and on the gaseous reservoirs in the early Solar System. *Geochimica et Cosmochimica Acta*, 72(7), 1924–1938. <https://doi.org/10.1016/j.gca.2008.01.015>
- Chen, J. H., Papanastassiou, D. A., & Wasserburg, G. J. (2010). Ruthenium endemic isotope effects in chondrites and differentiated meteorites. *Geochimica et Cosmochimica Acta*, 74(13), 3851–3862. <https://doi.org/10.1016/j.gca.2010.04.013>
- Chiang, E., & Youdin, A. N. (2010). Forming planetesimals in solar and extrasolar nebulae. In *Annual Review of Earth and Planetary Sciences* (Vol. 38). <https://doi.org/10.1146/annurev-earth-040809-152513>
- Chizmadia, L. J., Rubin, A. E., & Wasson, J. T. (2002). Mineralogy and petrology of amoeboid olivine inclusions in CO3 chondrites: Relationship to parent-body aqueous alteration. *Meteoritics and Planetary Science*, 37(12), 1781–1796. <https://doi.org/10.1111/j.1945-5100.2002.tb01163.x>
- Choi, B. G., McKeegan, K. D., Krot, A. N., & Wasson, J. T. (1998). Extreme oxygen-isotope compositions in magnetite from unequilibrated ordinary chondrites. *Nature*, 392(6676), 577–579.
- Citron, R. I., Jenniskens, P., Watkins, C., Sinha, S., Shah, A., Raissi, C., Devillepoix, H., & Albers, J. (2021). Recovery of meteorites using an autonomous drone and machine learning. *Meteoritics and Planetary Science*, 56(6), 1073–1085. <https://doi.org/10.1111/maps.13663>
- Clarke, J. D. A. (2006). Antiquity of aridity in the Chilean Atacama Desert. *Geomorphology*, 73(1–2), 101–114. <https://doi.org/10.1016/j.geomorph.2005.06.008>
- Clayton, D. D. (2003). *Handbook of Isotopes in the Cosmos: Hydrogen to Gallium*. Cambridge, UK: Cambridge University Press. Vol. 1, p. 326.
- Clayton, R. N. (1993). Oxygen isotopes in meteorites. *Annual Review of Earth and Planetary Sciences*, 21, 115–149.
- Clayton, R. N. (2003). Oxygen isotopes in meteorites. H.D. Holland, K.K. Turekian (Eds.), *Meteorites, Comets, and Planets. Treatise on Geochemistry*, vol. 1, Elsevier, Oxford (2003), pp. 129–142.
- Clayton, R. N., & Mayeda, T. K. (1999). Oxygen isotope studies of carbonaceous chondrites. *Geochimica et Cosmochimica Acta*, 63(13–14), 2089–2104.
- Clayton, R. N., Mayeda, T. K., Goswami, J. N., & Olsen, E. J. (1991). Oxygen isotope studies of ordinary chondrites. *Geochimica et Cosmochimica Acta*, 55(8), 2317–2337. [https://doi.org/10.1016/0016-7037\(91\)90107-G](https://doi.org/10.1016/0016-7037(91)90107-G)
- Clayton, R. N., Onuma, N., Grossman, L., & Mayeda, T. K. (1977). Distribution of the pre-solar component in Allende and other carbonaceous chondrites. *Earth and Planetary Science Letters*, 34(2), 209–224. [https://doi.org/10.1016/0012-821X\(77\)90005-X](https://doi.org/10.1016/0012-821X(77)90005-X)
- Connolly, H. C., Hewins, R. H., Ash, R. D., Zanda, B., Lofgren, G. E., & Bourot-Denise, M. (1994). Carbon and the formation of reduced chondrules. *Nature*, 371(6493), 136–139. <https://doi.org/10.1038/371136a0>
- Connolly Jr, Harold C., and Rhian H. Jones (2016). Chondrules: The canonical and noncanonical views. *Journal of Geophysical Research: Planets* 121(10). P. 1885–1899. <https://doi.org/10.1002/2016JE005113>
- Connolly H. C., Huss G. R., and Wasserburg G. J. (2001). On the formation of Fe-Ni metal in renazzo-like carbonaceous chondrites. *Geochimica et Cosmochimica Acta* 65:4567–4588.
- Connolly Jr, H. C., Jones, B. D., & Hewins, R. H. (1998). The flash melting of chondrules: An experimental investigation into the melting history and physical nature of chondrule precursors. *Geochimica et Cosmochimica Acta*, 62(15), 2725–2735.

- Cosarinsky M., Leshin L. A., MacPherson G. J., Guan Y., and Krot A. N. (2008). Chemical and oxygen isotopic compositions of accretionary rim and matrix olivine in CV chondrites: Constraints on the evolution of nebular dust. *Geochimica et Cosmochimica Acta* 72:1887–1913.
- Crozaz, G., Floss, C., & Wadhwa, M. (2003). Chemical alteration and REE mobilization in meteorites from hot and cold deserts. *Geochimica et Cosmochimica Acta*, 67(24), 4727–4741. <https://doi.org/10.1016/j.gca.2003.08.008>
- Cuzzi J. N. (2004). Blowing in the wind: III. Accretion of dust rims by chondrule-sized particles in a turbulent protoplanetary nebula. *Icarus* 168:484–497.
- Cuzzi, J. N., Hogan, R. C., Paque, J. M., & Dobrovolskis, A. R. (2001). Size-selective concentration of chondrules and other small particles in protoplanetary nebula turbulence. *The Astrophysical Journal*, 546(1), 496.
- Cuzzi, J. N., Hogan, R. C., & Shariff, K. (2008). Toward planetesimals: Dense chondrule clumps in the protoplanetary nebula. *The Astrophysical Journal*, 687(2), 1432.
- Cuzzi J. N., and Olson D. M. (2017). Recovering 3D particle size distributions from 2D sections. *Meteoritics and Planetary Science* 52:532–545
- Czekala, I., Chiang, E., Andrews, S. M., Jensen, E. L. N., Torres, G., Wilner, D. J., Stassun, K. G., & Macintosh, B. (2019). The Degree of Alignment between Circumbinary Disks and Their Binary Hosts. *The Astrophysical Journal*, 883(1), 22. <https://doi.org/10.3847/1538-4357/ab287b>
- Dauphas, N., Chen, J. H., Zhang, J., Papanastassiou, D. A., Davis, A. M., & Travaglio, C. (2014). Calcium-48 isotopic anomalies in bulk chondrites and achondrites: Evidence for a uniform isotopic reservoir in the inner protoplanetary disk. *Earth and Planetary Science Letters*, 407, 96–108. <https://doi.org/10.1016/j.epsl.2014.09.015>
- Dauphas, N., Remusat, L., Chen, J. H., Roskosz, M., Papanastassiou, D. A., Stodolna, J., Guan, Y., Ma, C., & Eiler, J. M. (2010). Neutron-rich chromium isotope anomalies in supernova nanoparticles. *Astrophysical Journal*, 720(2), 1577–1591. <https://doi.org/10.1088/0004-637X/720/2/1577>
- Davidson, J., Nittler, L. R., Alexander, C. M. O., & Stroud, R. M. (2014). Petrography of very primitive CO3 chondrites: dominion range 08006, miller range 07687, and four others. *Lunar and Planetary Science Conference*, 9–10.
- Davis, A. M., & Richter, F. M. (2014). Condensation and evaporation of solar system materials. In *Meteorites and Cosmochemical Processes, Treatise on Geochemistry* (Second Edition). Edited by A. M. Davis. Elsevier-Pergamon: Oxford, Vol. 2. pp 335-360.
- Desch, S. J., & Cuzzi, J. N. (2000). The Generation of Lightning in the Solar Nebula. *Icarus*, 143(1), 87–105. <https://doi.org/10.1006/icar.1999.6245>
- Desch, S. J., Kalyaan, A., & Alexander, C. M. O. (2018). The Effect of Jupiter’s Formation on the Distribution of Refractory Elements and Inclusions in Meteorites. *The Astrophysical Journal Supplement Series*, 238(1), 11. <https://doi.org/10.3847/1538-4365/aad95f>
- Desch, S. J., Morris, M. A., Connolly, H. C., & Boss, A. P. (2012). The importance of experiments: Constraints on chondrule formation models. *Meteoritics and Planetary Science*, 47(7), 1139–1156. <https://doi.org/10.1111/j.1945-5100.2012.01357.x>
- Dobrică E., and Brearley A. J. 2016. Microchondrules in two unequilibrated ordinary chondrites: Evidence for formation by splattering from chondrules during stochastic collisions in the solar nebula. *Meteoritics and Planetary Science* 51:884–905.
- Doyle, P. M., Jogo, K., Nagashima, K., Krot, A. N., Wakita, S., Ciesla, F. J., & Hutcheon, I. D. (2015). Early aqueous activity on the ordinary and carbonaceous chondrite parent bodies recorded by fayalite. *Nature Communications*, 6(1), 1-10.
- Drażkowska, J., Alibert, Y., & Moore, B. (2016). Close-in planetesimal formation by pile-up of drifting pebbles. *Astronomy and Astrophysics*, 594, 1–12. <https://doi.org/10.1051/0004-6361/201628983>
- Drouard, A., Gattacceca, J., Hutzler, A., Rochette, P., Braucher, R., Bourlès, D., Gounelle, M., Morbidelli, A., Debaille, V., van Ginneken, M., Valenzuela, M., Quesnel, Y., Martinez, R., Aumaitre, G., & Keddadouche, K. (2019). The meteorite flux of the past 2 m.y. Recorded in the Atacama Desert. *Geology*, 47(7), 673–676. <https://doi.org/10.1130/G45831.1>
- Dunai, T. J., González López, G. A., & Juez-Larré, J. (2005). Oligocene-Miocene age of aridity in the Atacama Desert revealed by exposure dating of erosion-sensitive landforms. *Geology*, 33(4), 321–324. <https://doi.org/10.1130/G21184.1>

- Dwarkadas, V. v., Dauphas, N., Meyer, B., Boyajian, P., & Bojazi, M. (2017). Triggered Star Formation inside the Shell of a Wolf–Rayet Bubble as the Origin of the Solar System. *The Astrophysical Journal*, 851(2), 147. <https://doi.org/10.3847/1538-4357/aa992e>
- Ebel, D. S., Alexander, C. M. O., & Libourel, G. (2018). Vapor – Melt Exchange Constraints on Chondrite Formation Conditions. *Chondrules. Records of Protoplanetary Disk Processes*, 151–174.
- Ebel, D. S., Brunner, C., Konrad, K., Leftwich, K., Erb, I., Lu, M., Rodriguez, H., Crapster-Pregont, E. J., Friedrich, J. M., & Weisberg, M. K. (2016). Abundance, major element composition and size of components and matrix in CV, CO and Acfer 094 chondrites. *Geochimica et Cosmochimica Acta*, 172, 322–356. <https://doi.org/10.1016/j.gca.2015.10.007>
- Ek, M., Hunt, A. C., Lugaro, M., & Schönabächler, M. (2020). The origin of s-process isotope heterogeneity in the solar protoplanetary disk. *Nature Astronomy*, 4(3), 273–281. <https://doi.org/10.1038/s41550-019-0948-z>
- Elfers, B. M., Sprung, P., Pfeifer, M., Wombacher, F., Peters, S. T. M., & Münker, C. (2018). Variable distribution of s-process Hf and W isotope carriers in chondritic meteorites – Evidence from 174Hf and 180W. *Geochimica et Cosmochimica Acta*, 239, 346–362. <https://doi.org/10.1016/j.gca.2018.08.009>
- Ericksen, G. E. (1981). Geology and origin of the Chilean nitrate deposits. *US Geological Survey, Professional Paper*, 1188.
- Espinoza, F.; Matthews, S.; Cornejo, P.; Venegas, C. (2011). Carta Catalina, Región de Antofagasta. Servicio Nacional de Geología y Minería, Carta Geológica de Chile, Serie Geología Básica 129: 63 p., 1 mapa escala 1:100.000. Santiago.
- Fan, Y., Li, S., Liu, S., Peng, H., Song, G., & Smith, T. (2022). The distribution of the desert meteorites in China and their classification. *Meteoritics & Planetary Science* 57.3 (2022): 683-701.. <https://doi.org/10.1111/maps.13789>
- Fehr, M. A., Rehkämper, M., Halliday, A. N., Wiechert, U., Hattendorf, B., Günther, D., Ono, S., Eigenbrode, J. L., & Rumble, D. (2005). Tellurium isotopic composition of the early solar system - A search for effects resulting from stellar nucleosynthesis, 126Sn decay, and mass-independent fractionation. *Geochimica et Cosmochimica Acta*, 69(21), 5099–5112. <https://doi.org/10.1016/j.gca.2005.04.020>
- Feigelson, E. D., & Montmerle, T. (1999). High-energy processes in young stellar objects. *Annual Review of Astronomy and Astrophysics*, 37(1), 363-408.
- Florin G., Luais B., Rushmer T., Alard O. (2020) Influence of redox processes on the germanium isotopic composition of ordinary chondrites. *Geochim Cosmochim Acta* 269, 270-291.
- Fournelle, J. (2011). An investigation of “San Carlos Olivine”: comparing USNM-distributed material with commercially available material. *Microscopy and Microanalysis*, 17 (Supplement 2), 842-8
- Friend P., Hezel D. C., Barrat J. A., Zipfel J., Palme H., and Metzler K. (2018). Composition, petrology, and chondrule-matrix complementarity of the recently discovered Jbilet Winselwan CM2 chondrite. *Meteoritics and Planetary Science* 53:2470–2491.
- Ganino, C., & Libourel, G. (2017). Reduced and unstratified crust in CV chondrite parent body. *Nature communications*, 8(1), 1-10.
- Gattacceca, J., Valenzuela, M., Uehara, M., Jull, A. J. T., Giscard, M., Rochette, P., Braucher, R., Suavet, C., Gounelle, M., Morata, D., Munayco, P., Bourot-Denise, M., Bourles, D., & Demory, F. (2011). The densest meteorite collection area in hot deserts: The San Juan meteorite field (Atacama Desert, Chile). *Meteoritics and Planetary Science*, 46(9), 1276–1287. <https://doi.org/10.1111/j.1945-5100.2011.01229.x>
- Gerber, S., Burkhardt, C., Budde, G., Metzler, K., & Kleine, T. (2017). Mixing and transport of dust in the early solar nebula as inferred from titanium isotope variations among chondrules. *ArXiv*, 841(1), L17. <https://doi.org/10.3847/2041-8213/aa72a2>
- Gerbig, K., Murray-Clay, R. A., Klahr, H., & Baehr, H. (2020). Requirements for Gravitational Collapse in Planetesimal Formation—The Impact of Scales Set by Kelvin–Helmholtz and Nonlinear Streaming Instability. *The Astrophysical Journal*, 895(2), 91.
- Gnos, E., Silvio, L., Otto, E., Timothy Jull, A. J., Hofmann, B. A., Al-Kathiri, A., & Eggimann, M. (2009). The Jiddat al Harasis 073 strewn field, Sultanate of Oman. *Meteoritics and Planetary Science*, 44(3), 375–387. <https://doi.org/10.1111/j.1945-5100.2009.tb00739.x>

- Goderis, S., Ginneken, M. van, Debaille, V., Ee, S. D., Woodland, A. B., Wozniakiewicz, P., Ceukelaire, M. de, Leduc, T., & Claeys, P. (2022). *Artificial weathering of an ordinary chondrite : Recommendations for the curation of Antarctic meteorites*. 20, 1–20. <https://doi.org/10.1111/maps.13818>
- Goldberg A. Z., Owen J. E., and Jacquet E. (2015). Chondrule transport in protoplanetary discs. *Monthly Notices of the Royal Astronomical Society* 452:4054–4069.
- Gorelick, N., Hancher, M., Dixon, M., Ilyushchenko, S., Thau, D., & Moore, R. (2017). Google Earth Engine: Planetary-scale geospatial analysis for everyone. *Remote sensing of Environment*, 202, 18–27.
- Goudie, A. S., Wright, E., & Viles, H. A. (2002). The roles of salt (sodium nitrate) and fog in weathering: a laboratory simulation of conditions in the northern Atacama Desert, Chile. *Catena*, 48(4), 255–266.
- Gounelle, M., & Meynet, G. (2012). Solar system genealogy revealed by extinct short-lived radionuclides in meteorites. *Astronomy and Astrophysics*, 545, 1–9. <https://doi.org/10.1051/0004-6361/201219031>
- Greenwood, R. C., Burbine, T. H., & Franchi, I. A. (2020). Linking asteroids and meteorites to the primordial planetesimal population. *Geochimica et Cosmochimica Acta*, 277, 377–406. <https://doi.org/10.1016/j.gca.2020.02.004>
- Greenwood, R. C., & Franchi, I. A. (2004). Alteration and metamorphism of CO₃ chondrites: Evidence from oxygen and carbon isotopes. *Meteoritics & Planetary Science*, 39(11), 1823–1838.
- Greenwood, R. C., Franchi, I. A., Gibson, J. M., & Benedix, G. K. (2012). Oxygen isotope variation in primitive achondrites: The influence of primordial, asteroidal and terrestrial processes. *Geochimica et Cosmochimica Acta*, 94, 146–163. <https://doi.org/10.1016/j.gca.2012.06.025>
- Grewal, D. S., Dasgupta, R., & Marty, B. (2021). A very early origin of isotopically distinct nitrogen in inner Solar System protoplanets. *Nature Astronomy*, 1–9. <http://www.nature.com/articles/s41550-020-01283-y>
- Grosjean, M., Cartajena, I., Geyh, M. A., & Nuñez, L. (2003). From proxy data to paleoclimate interpretation: The mid-Holocene paradox of the Atacama Desert, northern Chile. *Palaeogeography, Palaeoclimatology, Palaeoecology*, 194(1–3), 247–258. [https://doi.org/10.1016/S0031-0182\(03\)00280-3](https://doi.org/10.1016/S0031-0182(03)00280-3)
- Grossman, J. N., & Brearley, A. J. (2005). The onset of metamorphism in ordinary and carbonaceous chondrites. *Meteoritics and Planetary Science*, 40(1), 87–122. <https://doi.org/10.1111/j.1945-5100.2005.tb00366.x>
- Grossman, J. N., & Rubin, A. E. (2006). Dominion range 03238: a possible missing link in the metamorphic sequence of CO₃ chondrites. *Lunar and Planetary Science Conference*, 2(06), 6–9.
- Haenecour, P., Floss, C., Zega, T. J., Croat, T. K., Wang, A., Jolliff, B. L., & Carpenter, P. (2018). Presolar silicates in the matrix and fine-grained rims around chondrules in primitive CO₃.0 chondrites: Evidence for pre-accretionary aqueous alteration of the rims in the solar nebula. *Geochimica et Cosmochimica Acta*, 221, 379–405. <https://doi.org/10.1016/j.gca.2017.06.004>
- Hanna R. D., and Ketcham R. A. (2018). Evidence for accretion of fine-grained rims in a turbulent nebula for CM Murchison. *Earth and Planetary Science Letters* 481:201–211.
- Hellmann, J. L., Hopp, T., Burkhardt, C., & Kleine, T. (2020). Origin of volatile element depletion among carbonaceous chondrites. *Earth and Planetary Science Letters*, 549, 116508. <https://doi.org/10.1016/j.epsl.2020.116508>
- Hellmann, J. L., Kruijjer, T. S., Van Orman, J. A., Metzler, K., & Kleine, T. (2019). Hf-W chronology of ordinary chondrites. *Geochimica et Cosmochimica Acta*, 258, 290–309.
- Henke, S., Gail, H. P., Trieloff, M., Schwarz, W. H., & Kleine, T. (2012). Thermal history modelling of the H chondrite parent body. *Astronomy & Astrophysics*, 545, A135.
- Hernández, J., Hartmann, L., Calvet, N., Jeffries, R. D., Gutermuth, R., Muzerolle, J., & Stauffer, J. (2008). A Spitzer View of Protoplanetary Disks in the γ Velorum Cluster. *The Astrophysical Journal*, 686(2), 1195–1208. <https://doi.org/10.1086/591224>
- Hertwig, A. T., Defouilloy, C., & Kita, N. T. (2018). Formation of chondrules in a moderately high dust enriched disk: Evidence from oxygen isotopes of chondrules from the Kaba CV3 chondrite. *Geochimica et Cosmochimica Acta*, 224, 116–131. <https://doi.org/10.1016/j.gca.2017.12.013>

- Hewins, R. H., & Radomsky, P. M. (1990). Temperature conditions for chondrule formation. *Meteoritics*, 25(4), 309–318. <https://doi.org/10.1111/j.1945-5100.1990.tb00715.x>
- Hezel D. C., Harak M., and Libourel G. (2018). What we know about elemental bulk chondrule and matrix compositions: Presenting the ChondriteDB Database. *Chemie der Erde* 78:1–14.
- Hezel, D. C., Schlüter, J., Kallweit, H., Jull, A. J. T., al Fakeer, O. Y., al Shamsi, M., & Strekopytov, S. (2011). Meteorites from the United Arab Emirates: Description, weathering, and terrestrial ages. *Meteoritics and Planetary Science*, 46(2), 327–336. <https://doi.org/10.1111/j.1945-5100.2010.01165.x>
- Hofmann, B. A., Gnos, E., Jull, A. J. T., Szidat, S., Majoub, A., al Wagdani, K., Habibullah, S. N., Halawani, M., Hakeem, M., al Shanti, M., & al Solami, A. (2018). Meteorite reconnaissance in Saudi Arabia. *Meteoritics and Planetary Science*, 53(11), 2372–2394. <https://doi.org/10.1111/maps.13132>
- Houston, J., & Hartley, A. J. (2003). The central andean west-slope rainshadow and its potential contribution to the origin of hyper-aridity in the Atacama Desert. *International Journal of Climatology*, 23(12), 1453–1464. <https://doi.org/10.1002/joc.938>
- Hubbard A., and Ebel D. S. (2014). Protoplanetary dust porosity and FU Orionis outbursts: Solving the mystery of Earth’s missing volatiles. *Icarus* 237:84–96.
- Huss G. R., Alexander C. M. O., Palme H., Bland P. A., and Wasson J. T. (2005). Genetic relationships between chondrules, fine-grained rims, and interchondrule matrix. In *Chondrites and the protoplanetary disk - ASP Conference Series* 341:701–731
- Huss, G. R., Rubin, A. E., & Grossman, J. N. (2006). Thermal metamorphism in chondrites. *Meteorites and the early solar system II*, 943, 567–586.
- Huss, G. R., & Smith, J. B. (2007). Titanium isotopic compositions of well-characterized silicon carbide grains from Orgueil (CI): Implications for s-process nucleosynthesis. *Meteoritics & Planetary Science*, 42(7–8), 1055–1075. <https://doi.org/10.1111/j.1945-5100.2007.tb00561.x>
- Hutson, M., Ruzicka, A., Timothy Jull, A. J., Smaller, J. E., & Brown, R. (2013). Stones from mohave county, arizona: Multiple falls in the “franconia strewn field.” *Meteoritics and Planetary Science*, 48(3), 365–389. <https://doi.org/10.1111/maps.12062>
- Hutzler, A., Gattacceca, J., Rochette, P., Braucher, R., Carro, B., Christensen, E. J., Cournede, C., Gounelle, M., Laridhi Ouazaa, N., Martinez, R., Valenzuela, M., Warner, M., & Bourles, D. (2016). Description of a very dense meteorite collection area in western Atacama: Insight into the long-term composition of the meteorite flux to Earth. *Meteoritics and Planetary Science*, 51(3), 468–482. <https://doi.org/10.1111/maps.12607>
- Ireland, T. R., Avila, J., Greenwood, R. C., Hicks, L. J., & Bridges, J. C. (2020). Oxygen Isotopes and Sampling of the Solar System. *Space Science Reviews*, 216(2), 25. <https://doi.org/10.1007/s11214-020-0645-3>
- Isa, J., Kohl, I. E., Liu, M. C., Wasson, J. T., Young, E. D., & McKeegan, K. D. (2017). Quantification of oxygen isotope SIMS matrix effects in olivine samples: Correlation with sputter rate. *Chemical Geology*, 458(October 2016), 14–21. <https://doi.org/10.1016/j.chemgeo.2017.03.020>
- Ivanova, M. A., Lorenz, C. A., Humayun, M., Corrigan, C. M., Ludwig, T., Trierloff, M., ... & Grokhovsky, V. I. (2020). Sierra Gorda 009: A new member of the metal-rich G chondrites grouplet. *Meteoritics & Planetary Science*, 55(8). <https://doi.org/10.1111/maps.13546>
- Jacquet E. (2014). The quasi-universality of chondrule size as a constraint for chondrule formation models. *Icarus* 232:176–186.
- Jacquet, E. (2021). Collisions and compositional variability in chondrule-forming events. *Geochimica et Cosmochimica Acta*, 296, 18–37. <https://doi.org/10.1016/j.gca.2020.12.025>
- Jacquet, E., Alard, O., & Gounelle, M. (2015). Trace element geochemistry of ordinary chondrite chondrules: The type I/type II chondrule dichotomy. *Geochimica et Cosmochimica Acta*, 155, 47–67. <https://doi.org/10.1016/j.gca.2015.02.005>
- Jacquet E., Barrat J. A., Beck P., Caste F., Gattacceca J., Sonzogni C., and Gounelle M. (2016). Northwest Africa 5958: A weakly altered CM-related ungrouped chondrite, not a CI3. *Meteoritics and Planetary Science* 51:851–869.
- Jacquet, E., & Marrocchi, Y. (2017). Chondrule heritage and thermal histories from trace element and oxygen isotope analyses of chondrules and amoeboid olivine aggregates. *Meteoritics and Planetary Science*, 52(12), 2672–2694. <https://doi.org/10.1111/maps.12985>

- Jacquet, E., Paulhiac-Pison, M., Alard, O., Kearsley, A. T., & Gounelle, M. (2013). Trace element geochemistry of CR chondrite metal. *Meteoritics and Planetary Science*, 48(10), 1981–1999. <https://doi.org/10.1111/maps.12212>
- Jacquet, E., Pignatale, F. C., Chaussidon, M., & Charnoz, S. (2019). Fingerprints of the Protosolar Cloud Collapse in the Solar System. II. Nucleosynthetic Anomalies in Meteorites. *The Astrophysical Journal*, 884(1), 32. <https://doi.org/10.3847/1538-4357/ab38c1>
- Jacquet E., Piralla M., Kersaho P., and Marrocchi Y. (2021). Origin of isolated olivine grains in carbonaceous chondrites. *Meteoritics & Planetary Science* 56:13-33.
- Johansen, A., Low, M. M. mac, Lacerda, P., & Bizzarro, M. (2015). Growth of asteroids, planetary embryos, and Kuiper belt objects by chondrule accretion. *Science Advances*, 1(3). <https://doi.org/10.1126/sciadv.1500109>
- Johansen, A., Oishi, J. S., Low, M. M. mac, Klahr, H., Henning, T., & Youdin, A. (2007). Rapid planetesimal formation in turbulent circumstellar disks. *Nature*, 448(7157), 1022–1025. <https://doi.org/10.1038/nature06086>
- Johansen, A., Youdin, A. N. D. R. E. W., & MacLow, M. M. (2009). Particle Clumping in Protoplanetary Disks Depends Strongly on Metallicity. *ArXiv e-prints*.
- Johnson, B. C., Minton, D. A., Melosh, H. J., & Zuber, M. T. (2015). Impact jetting as the origin of chondrules. *Nature*, 517(7534), 339–341. <https://doi.org/10.1038/nature14105>
- Jones, R. H. (1990). Petrology and mineralogy of Type II, FeO-rich chondrules in Semarkona (LL3.0): Origin by closed-system fractional crystallization, with evidence for supercooling. *Geochimica et Cosmochimica Acta*, 54(6), 1785–1802. [https://doi.org/10.1016/0016-7037\(90\)90408-D](https://doi.org/10.1016/0016-7037(90)90408-D)
- Jones, R. H. (1992). On the relationship between isolated and chondrule olivine grains in the carbonaceous chondrite ALHA 77307. *Geochimica et Cosmochimica Acta*, 56(9), 3593. [https://doi.org/10.1016/0016-7037\(92\)90403-6](https://doi.org/10.1016/0016-7037(92)90403-6)
- Jones, R. H. (1996). Relict Grains in Chondrules: Evidence for Chondrule Recycling. In *Chondrules and the Protoplanetary Disk*, edited by R. H. Hewins, R. H. Jones, & Scott. Cambridge, UK: Cambridge University Press, Vol. 1, pp. 163–172.
- Jones, R. H. (2012). Petrographic constraints on the diversity of chondrule reservoirs in the protoplanetary disk. *Meteoritics and Planetary Science*, 47(7), 1176–1190. <https://doi.org/10.1111/j.1945-5100.2011.01327.x>
- Jones, R. H., Leshin, L. A., & Guan, Y. (2002). Heterogeneity and ¹⁶O-enrichments in oxygen isotope ratios of olivine from chondrules in the mokoia CV3 chondrite. *Lunar and Planetary Conference*, 1571.
- Jones, R. H., & Rubie, D. C. (1991). Thermal histories of CO3 chondrites: application of olivine diffusion modelling to parent body metamorphism. *Earth and Planetary Science Letters*, 106(1-4), 73-86.
- Jones, R. H., Saxton, J. M., Lyon, I. C., & Turner, G. (2000). Oxygen isotopes in chondrule olivine and isolated olivine grains from the CO3 chondrite Allan Hills A77307. *Meteoritics and Planetary Science*, 35(4), 849–857. <https://doi.org/10.1111/j.1945-5100.2000.tb01468.x>
- Jones, R. H., Villeneuve, J., & Libourel, G. (2018). Thermal Histories of Chondrules: Petrologic Observations and Experimental Constraints. *Chondrules and the Protoplanetary Disk*, edited by Russell, S. S., Connolly Jr, H. C., & Krot, A. N: Cambridge, UK: Cambridge University Press, Vol. 1, 57–90.
- Joo, S., & Liang, H. (2013). Secondary ion mass spectroscopy (SIMS). *Encyclopedia of Tribology; Springer US: Boston, MA, USA*, 2989-2994
- Jull, A. J. T., Donahue, D. J., Cielaszyk, E., & Wlotzka, F. (1993). Carbon-14 terrestrial ages and weathering of 27 meteorites from the southern High Plains and adjacent areas (USA). *Meteoritics*, 28(2), 188–195. <https://doi.org/10.1111/j.1945-5100.1993.tb00756.x>
- Jull, A. J. T., Giscard, M. D., Hutzler, A., Schnitzer, C. J., Zahn, D., Burr, G. S., McHargue, L. R., & Hill, D. (2013). Radionuclide Studies of Stony Meteorites from Hot Deserts. *Radiocarbon*, 55(3), 1779–1789. <https://doi.org/10.1017/s0033822200048682>
- Keil, K. (2000). Thermal alteration of asteroids: evidence from meteorites. *Planetary and Space Science*, 48(10), 887-903.
- Kerraouch, I., Bischoff, A., Zolensky, M. E., Trieloff, M., Krot, A. N., Nagashima, K., ... & Rubin, A. E. (2022). Discovery of hydrated clasts with very high abundance of ferromagnesian ¹⁶O-rich

- olivine: inner or outer solar system origin?. in *Meteoritics & planetary science Conference* (vol. 57).
- Killgore, B. M. (1997). Imilac strewnfield, Chile, revisited. In *Lunar and Planetary Science Conference* (p. 725).
- Kita, N. T., Nagahara, H., Tachibana, S., Tomomura, S., Spicuzza, M. J., Fournelle, J. H., & Valley, J. W. (2010). High precision SIMS oxygen three isotope study of chondrules in LL3 chondrites: Role of ambient gas during chondrule formation. *Geochimica et Cosmochimica Acta*, 74(22), 6610–6635. <https://doi.org/10.1016/j.gca.2010.08.011>
- Klahr, H., & Schreiber, A. (2020). Turbulence sets the length scale for planetesimal formation: Local 2D simulations of streaming instability and planetesimal formation. *ArXiv*, 2019. <https://doi.org/10.3847/1538-4357/abac58>
- Klahr, H., & Schreiber, A. (2021). Testing the Jeans, Toomre, and Bonnor–Ebert Concepts for Planetesimal Formation: 3D Streaming-instability Simulations of Diffusion-regulated Formation of Planetesimals. *The Astrophysical Journal*, 911(1), 9. <https://doi.org/10.3847/1538-4357/abca9b>
- Kleine, T., Touboul, M., Van Orman, J. A., Bourdon, B., Maden, C., Mezger, K., & Halliday, A. N. (2008). Hf–W thermochronometry: closure temperature and constraints on the accretion and cooling history of the H chondrite parent body. *Earth and Planetary Science Letters*, 270(1-2), 106–118.
- Kleine, T., Budde, G., Hellmann, J., Kruijjer, T. S., & Burkhardt, C. (2018). Tungsten isotopes and the origin of chondrules and chondrites. *Chondrules and the Protoplanetary Disk*; edited by Russell, S. S., Connolly Jr, H. C., & Krot, A. N. Cambridge, UK: Cambridge University Press, Vol. 1, 276–299.
- Kleine, T., Budde, G., Burkhardt, C., Kruijjer, T. S., Worsham, E. A., Morbidelli, A., & Nimmo, F. (2020). The Non-carbonaceous–Carbonaceous Meteorite Dichotomy. *Space Science Reviews*, 216(4). <https://doi.org/10.1007/s11214-020-00675-w>
- Kouvatsis, I., & Hofmann, B. A. (2020). A statistical analysis of the H/L ratio of ordinary chondrite finds and falls: A comparison of Oman finds with other populations. *Meteoritics and Planetary Science*, 55(1), 67–76. <https://doi.org/10.1111/maps.13410>
- Krämer Ruggiu, L., Gattacceca, J., Devouard, B., Udry, A., Debaille, V., Rochette, P., Lorand, J. P., Bonal, L., Beck, P., Sautter, V., Busemann, H., Meier, M. M. M., Maden, C., Hublet, G., & Martinez, R. (2020). Caleta el Cobre 022 Martian meteorite: Increasing nakhlite diversity. *Meteoritics and Planetary Science*, 55(7), 1539–1563. <https://doi.org/10.1111/maps.13534>
- Kraus, S., Kreplin, A., Young, A. K., Bate, M. R., Monnier, J. D., Harries, T. J., Avenhaus, H., Kluska, J., Laws, A. S. E., Rich, E. A., Willson, M., Aarnio, A. N., Adams, F. C., Andrews, S. M., Anugu, N., Bae, J., ten Brummelaar, T., Calvet, N., Curé, M., ... Zhu, Z. (2020). A triple-star system with a misaligned and warped circumstellar disk shaped by disk tearing. *Science*, 369(6508), 1233–1238. <https://doi.org/10.1126/SCIENCE.ABA4633>
- Kring, D. A., Jull, A. J. T., McHargue, L. R., Bland, P. A., Hill, D. H., & Berry, F. J. (2001). Gold basin meteorite strewn field, Mojave desert, Northwestern Arizona: Relic of a small late pleistocene impact event. *Meteoritics and Planetary Science*, 36(8), 1057–1066. <https://doi.org/10.1111/j.1945-5100.2001.tb01944.x>
- Krot A. N. and Rubin A. E. (1996). Microchondrule-bearing chondrule rims: constraints on chondrule formation. In *Chondrules and the protoplanetary disk*, edited by Hewins R. H., Jones R. H., and Scott E. R. D. Cambridge, UK: Cambridge University Press. pp. 181–184.
- Krot, A. N. (2019). Refractory inclusions in carbonaceous chondrites: Records of early solar system processes. *Meteoritics and Planetary Science*, 54(8), 1647–1691. <https://doi.org/10.1111/maps.13350>
- Krot, A. N., Keil, K., Scott, E. R. D., Goodrich, C. A., Weisberg, M. K. (2014). Classification of Meteorites and Their Genetic Relationships. In *Meteorites and Cosmochemical Processes, Treatise on Geochemistry* (Second Edition). Edited by A. M. Davis. Elsevier-Pergamon: Oxford, Vol. 2. pp 1– 63.
- Krot, A. N., Petaev, M. I., Russell, S. S., Itoh, S., Fagan, T. J., Yurimoto, H., Chizmadia, L., Weisberg, M. K., Komatsu, M., Ulyanov, A. A., & Keil, K. (2004). Amoeboid olivine aggregates and related objects in carbonaceous chondrites: Records of nebular and asteroid processes. *Chemie Der Erde*, 64(3), 185–239. <https://doi.org/10.1016/j.chemer.2004.05.001>

- Krot A. N., Rubin A. E., Keil K., and Wasson J. T. (1997). Microchondrules in ordinary chondrites: Implications for chondrule formation. *Geochimica et Cosmochimica Acta* 61:463–473.
- Kruijjer, T. S., Burkhardt, C., Budde, G., & Kleine, T. (2017). Age of Jupiter inferred from the distinct genetics and formation times of meteorites. *Proceedings of the National Academy of Sciences of the United States of America*, 114(26), 6712–6716. <https://doi.org/10.1073/pnas.1704461114>
- Kruijjer, T. S., Kleine, T., & Borg, L. E. (2020). The great isotopic dichotomy of the early Solar System. *Nature Astronomy*, 4(1), 32–40. <https://doi.org/10.1038/s41550-019-0959-9>
- Kunihiro, T., Rubin, A. E., McKeegan, K. D., & Wasson, J. T. (2004). Oxygen-isotopic compositions of relict and host grains in chondrules in the Yamato 81020 CO3.0 chondrite. *Geochimica et Cosmochimica Acta*, 68(17), 3599–3606. <https://doi.org/10.1016/j.gca.2004.02.011>
- Kunihiro, T., Rubin, A. E., & Wasson, J. T. (2005). Oxygen-isotopic compositions of low-FeO relicts in high-FeO host chondrules in Acfer 094, a type 3.0 carbonaceous chondrite closely related to CM. *Geochimica et Cosmochimica Acta*, 69(15), 3831–3840. <https://doi.org/10.1016/j.gca.2005.01.031>
- Labidi, J., König, S., Kurzawa, T., Yierpan, A., & Schoenberg, R. (2018). The selenium isotopic variations in chondrites are mass-dependent ; Implications for sulfide formation in the early solar system. *Earth and Planetary Science Letters*, 481, 212–222. <https://doi.org/10.1016/j.epsl.2017.10.032>
- Lambrechts, M., & Johansen, A. (2012). Rapid growth of gas-giant cores by pebble accretion. *Astronomy and Astrophysics*, 544, 1–13. <https://doi.org/10.1051/0004-6361/201219127>
- Lambrechts, M., & Johansen, A. (2014). Forming the cores of giant planets from the radial pebble flux in protoplanetary discs. *Astronomy and Astrophysics*, 572. <https://doi.org/10.1051/0004-6361/201424343>
- Latorre, C., Betancourt, J. L., Rylander, K. A., Quade, J., & Matthei, O. (2003). A vegetation history from the arid prepuna of northern Chile (22–23°S) over the last 13 500 years. *Palaeogeography, Palaeoclimatology, Palaeoecology*, 194(1–3), 223–246. [https://doi.org/10.1016/S0031-0182\(03\)00279-7](https://doi.org/10.1016/S0031-0182(03)00279-7)
- Lauretta D. S., Hua X., and Buseck P. R. (2000). Mineralogy of fine-grained rims in the ALH 81002 CM chondrite. *Geochimica et Cosmochimica Acta* 64:3263–3273.
- Lauretta D. S., and Buseck P. R. (2003). Opaque minerals in chondrules and fine-grained chondrule rims in the Bishunpur (LL3.1) chondrite. *Meteoritics and Planetary Science* 38:59–79.
- Leclerc, M. D. (2016). Cosmochemistry of iron meteorites: trace element composition of metal and sulfide phases. PhD thesis, Imperial College London, London, England, p. 308
- Lee, M. R., & Bland, P. A. (2004). Mechanisms of weathering of meteorites recovered from hot and cold deserts and the formation of phyllosilicates. *Geochimica et Cosmochimica Acta*, 68(4), 893–916. [https://doi.org/10.1016/S0016-7037\(03\)00486-1](https://doi.org/10.1016/S0016-7037(03)00486-1)
- Lee, N. N., Fritz, J., Fries, M. D., Gil, J. F., Beck, A., Pellinen-Wannberg, A., ... & Hofmann, B. A. (2017). The extreme biology of meteorites: their role in understanding the origin and distribution of life on Earth and in the Universe. In *Adaption of microbial life to environmental extremes* (pp. 283-325). Springer, Cham.
- Leitner, J., Metzler, K., Vollmer, C., Floss, C., Harries, D., Hoppe, P., & Haenecour, P. (2019). The presolar grain inventory of fine-grained chondrule rims in the Mighei-type (CM) chondrites. *Meteoritics & Planetary Science*, 31(1). <https://doi.org/10.1111/maps.13412>
- Leitner, J., Vollmer, C., Floss, C., Zipfel, J., & Hoppe, P. (2016). Ancient stardust in fine-grained chondrule dust rims from carbonaceous chondrites. *Earth and Planetary Science Letters*, 434, 117–128. <https://doi.org/10.1016/j.epsl.2015.11.028>
- Li, R., Youdin, A. N., & Simon, J. B. (2018). On the Numerical Robustness of the Streaming Instability: Particle Concentration and Gas Dynamics in Protoplanetary Disks. *The Astrophysical Journal*, 862(1), 14. <https://doi.org/10.3847/1538-4357/aaca99>
- Li, R., Youdin, A. N., & Simon, J. B. (2019). Demographics of Planetesimals Formed by the Streaming Instability. *The Astrophysical Journal*, 885(1), 69. <https://doi.org/10.3847/1538-4357/ab480d>
- Libourel, G., & Krot, A. N. (2007). Evidence for the presence of planetesimal material among the precursors of magnesian chondrules of nebular origin. *Earth and Planetary Science Letters*, 254(1–2), 1–8. <https://doi.org/10.1016/j.epsl.2006.11.013>

- Libourel, G., Krot, A. N., & Tissandier, L. (2006). Role of gas-melt interaction during chondrule formation. *Earth and Planetary Science Letters*, 251(3–4), 232–240. <https://doi.org/10.1016/j.epsl.2006.09.011>
- Libourel, G., & Portail, M. (2018). Chondrules as direct thermochemical sensors of solar protoplanetary disk gas. *Science Advances*, 4(7). <https://doi.org/10.1126/sciadv.aar3321>
- Liffman K. (2019). Fine-grained rim formation – High speed, kinetic dust aggregation in the early Solar System. *Geochimica et Cosmochimica Acta* 264:118–129.
- Liffman K., and Toscano M. (2000). Chondrule Fine-Grained Mantle Formation by Hypervelocity Impact of Chondrules with a Dusty Gas. *Icarus* 143:106–125.
- Lodders, K., & Fegley, B. (1998). *The planetary scientist's companion*. Oxford University Press on Demand.
- Lodders, K. (2010). Solar system abundances of the elements. In *Astrophysics and Space Science Proceedings* (Issue 202579). https://doi.org/10.1007/978-3-642-10352-0_8
- Lodders, K., Palme, H., & Gail, H. P. (2009). *Abundances of the elements in the solar system: Vol. VI/4B* (Issue 13, pp. 560–630). <https://doi.org/10.1001/jama.1884.02390620026012>
- Losiak, A., & Velbel, M. A. (2011). Evaporite formation during weathering of Antarctic meteorites--A weathering census analysis based on the ANSMET database. *Meteoritics and Planetary Science*, 46(3), 443–458. <https://doi.org/10.1111/j.1945-5100.2010.01166.x>
- MacPherson, G. J. (2014). Calcium-aluminum-rich inclusions in chondritic meteorites. In *Meteorites and Cosmochemical Processes, Treatise on Geochemistry* (Second Edition). Edited by A. M. Davis. Elsevier-Pergamon: Oxford, Vol. 2. pp 139-179.
- MacPherson, G. J., Hashimoto, A., & Grossman, L. (1985). Accretionary rims on inclusions in the Allende meteorite. *Geochimica et Cosmochimica Acta*, 49(11), 2267–2279. [https://doi.org/10.1016/0016-7037\(85\)90227-3](https://doi.org/10.1016/0016-7037(85)90227-3)
- MacPherson, G. J., Krot, A. N., Kita, N. T., Bullock, E. S., Nagashima, K., Ushikubo, T., & Ivanova, M. A. (2022). The formation of Type B CAIs: Evolution from Type A CAIs. *Geochimica et Cosmochimica Acta*, 321, 343–374. <https://doi.org/10.1016/j.gca.2021.12.033>
- Macpherson, G. J., Simon, S. B., Davis, a M., Grossman, L., & Krot, A. N. (2005). Calcium-Aluminum-rich Inclusions : Major Unanswered Questions. *Chondrites and the Protoplanetary Disk, Vol. 341*, 341(1), 225–251.
- Michel, P., Ballouz, R. L., Barnouin, O. S., Jutzi, M., Walsh, K. J., May, B. H., ... & Lauretta, D. S. (2020). Collisional formation of top-shaped asteroids and implications for the origins of Ryugu and Bennu. *Nature Communications*, 11(1), 1-11.
- Mane, P., Wallace, S., Bose, M., Wallace, P., Wadhwa, M., Weber, J., & Zega, T. J. (2022). Earliest evidence of nebular shock waves recorded in a calcium-aluminum-rich Inclusion. *Geochimica et Cosmochimica Acta*, 332, 369–388. <https://doi.org/10.1016/j.gca.2022.06.006>
- Marinovic, N.; Smoje, I.; Maksaev, V.; Hervé, M.; Mpodozis, C. (1995). Hoja Aguas Blancas. Servicio Nacional de Geología y Minería, Carta Geológica de Chile No. 70, Región de Antofagasta: 150 p. Santiago.
- Marquet, P., Bozinovic, F., Bradshaw, G. a, Cornelius, C., Gonzalez, H., Gutierrez, J. R., Hajek, E. R., Lagos, J. a, Lopez-Cortes, F., Nunez, L., Rosello, E. F., Santoro, C., Samaniego, H., Standen, V. G., Torres-Mura, F. M., & Jaksic, J. C. (1998). Los ecosistemas del Desierto de Atacama y área Andina adyacente. *Revista Chilena de Historia Natural*, 71, 593–617.
- Marrocchi Y., Bekaert D., and Piani L. (2018b). Origin and abundance of water in carbonaceous asteroids. *Earth and Planetary Science Letters* 482:23–32. <https://doi.org/10.1016/j.epsl.2017.10.060>.
- Marrocchi, Y., Delbo, M., & Gounelle, M. (2021). The astrophysical context of collision processes in meteorites. *Meteoritics and Planetary Science*, 56(7), 1406–1421. <https://doi.org/10.1111/maps.13716>
- Marrocchi, Y., Euverte, R., Villeneuve, J., Batanova, V., Welsch, B., Ferrière, L., & Jacquet, E. (2019a). Formation of CV chondrules by recycling of amoeboid olivine aggregate-like precursors. *Geochimica et Cosmochimica Acta*, 247, 121–141. <https://doi.org/10.1016/j.gca.2018.12.038>
- Marrocchi, Y., Gounelle, M., Blanchard, I., Caste, F., & Kearsley, A. T. (2014). The Paris CM chondrite: Secondary minerals and asteroidal processing. *Meteoritics and Planetary Science*, 49(7), 1232–1249. <https://doi.org/10.1111/maps.12329>

- Marrocchi, Y., Piralla, M., Regnault, M., Batanova, V., Villeneuve, J., & Jacquet, E. (2022). Isotopic evidence for two chondrule generations in CR chondrites and their relationships to other carbonaceous chondrites. *Earth and Planetary Science Letters*, 593, 117683. <https://doi.org/10.1016/j.epsl.2022.117683>
- Marrocchi, Y., Villeneuve, J., Batanova, V., Piani, L., & Jacquet, E. (2018a). Oxygen isotopic diversity of chondrule precursors and the nebular origin of chondrules. *Earth and Planetary Science Letters*, 496, 132–141. <https://doi.org/10.1016/j.epsl.2018.05.042>
- Marrocchi, Y., Villeneuve, J., Jacquet, E., Piralla, M., & Chaussidon, M. (2019b). Rapid condensation of the first Solar System solids. *Proceedings of the National Academy of Sciences of the United States of America*, 116(47), 23461–23466. <https://doi.org/10.1073/pnas.1912479116>
- Martin, F. M. (2002). Isotopic fractionation and the quantification of ^{17}O anomalies in the oxygen three-isotope system: an appraisal and geochemical significance. *Geochimica et Cosmochimica Acta*, 66(11), 1881–1889. <http://www.sciencedirect.com/science/article/pii/S0016703702008323>
- Martínez, F., Muñoz, B., López, C., González, R., Parra, M., & Riquelme, R. (2021). Complex Basement-Involved Contractual Structures in the Pre-Andean Basins of Northern Chile: A Review From Seismic Data. *Tectonics*, 40(2), 1–23. <https://doi.org/10.1029/2020TC006433>
- Matsumoto Y., Hasegawa Y., Matsuda N., and Liu M.-C. (2021). Formation of rims around chondrules via porous aggregate accretion. *Icarus* 367, 114538
- McKeegan, K. D., Kallio, A. P. A., Heber, V. S., Jarzebinski, G., Mao, P. H., Coath, C. D., Kunihiro, T., Wiens, R. C., Nordholt, J. E., Moses Jr., R. W., Reisenfeld, D. B., Jurewicz, J. G., & Burnett, D. S. (2011). The Oxygen Isotopic Composition of the Sun Inferred from Captured Solar Wind. *Science*, 332(6037), 1528–1532.
- McSween H. Y. Jr. (1977). Carbonaceous chondrites of the Ornans type: A metamorphic sequence. *Geochimica et Cosmochimica Acta* 41:477–491.
- McSween, H. Y., Binzel, R. P., de Sanctis, M. C., Ammannito, E., Prettyman, T. H., Beck, A. W., Reddy, V., le Corre, L., Gaffey, M. J., Mccord, T. B., Raymond, C. A., & Russell, C. T. (2013). Dawn; the Vesta-HED connection; and the geologic context for eucrites, diogenites, and howardites. *Meteoritics and Planetary Science*, 48(11), 2090–2104. <https://doi.org/10.1111/maps.12108>
- McSween, Jr, H., & Huss, G. (2022). Meteorites, Interplanetary Dust, and Lunar Samples. In *Cosmochemistry*. Cambridge: Cambridge University Press. Vol 2, pp. 110-138. doi:10.1017/9781108885263.007
- Metzler, K., Bischoff, A., & Stöffler, D. (1992). Accretionary dust mantles in CM chondrites: Evidence for solar nebula processes. *Geochimica et Cosmochimica Acta*, 56(7), 2873–2897. [https://doi.org/10.1016/0016-7037\(92\)90365-P](https://doi.org/10.1016/0016-7037(92)90365-P)
- Metzler, K., Hezel, D. C., Barosch, J., Wölfer, E., Schneider, J. M., Hellmann, J. L., Berndt, J., Stracke, A., Gattacceca, J., Greenwood, R. C., Franchi, I. A., Burkhardt, C., & Kleine, T. (2021). The Loongana (CL) group of carbonaceous chondrites. *Geochimica et Cosmochimica Acta*, 304, 1–31. <https://doi.org/10.1016/j.gca.2021.04.007>
- Meyer, B. S., Clayton, D. D., & The, L.-S. (2000). Molybdenum and Zirconium Isotopes from a Supernova Neutron Burst. *The Astrophysical Journal*. <https://doi.org/10.1086/312865>
- Miller, K. E., Lauretta, D. S., Connolly, H. C., Berger, E. L., Nagashima, K., & Domanik, K. (2017). Formation of unequilibrated R chondrite chondrules and opaque phases. *Geochimica et Cosmochimica Acta*, 209, 24–50. <https://doi.org/10.1016/j.gca.2017.04.009>
- Mittlefehldt, D. W. (2015). Asteroid (4) Vesta: I. The howardite-eucrite-diogenite (HED) clan of meteorites. *Chemie Der Erde*, 75(2), 155–183. <https://doi.org/10.1016/j.chemer.2014.08.002>
- Miyamoto, M., Mikouchi, T., & Jones, R. H. (2009). Cooling rates of porphyritic olivine chondrules in the Semarkona (LL3.00) ordinary chondrite: A model for diffusional equilibration of olivine during fractional crystallization. *Meteoritics and Planetary Science*, 44(4), 521–530. <https://doi.org/10.1111/j.1945-5100.2009.tb00748.x>
- Morbidelli, A. (2018). Accretion processes. In *Oxford Encyclopedia* (p. 19).
- Morbidelli, A., Baillié, K., Batygin, K., Charnoz, S., Guillot, T., Rubie, D. C., & Kleine, T. (2022). Contemporary formation of early Solar System planetesimals at two distinct radial locations. *Nature Astronomy*, 6(1), 72–79. <https://doi.org/10.1038/s41550-021-01517-7>

- Morbidelli, A., Lambrechts, M., Jacobson, S., & Bitsch, B. (2015). The great dichotomy of the Solar System: Small terrestrial embryos and massive giant planet cores. *Icarus*, 258, 418–429. <https://doi.org/10.1016/j.icarus.2015.06.003>
- Morin, G. L. F., Marrocchi, Y., Villeneuve, J., & Jacquet, E. (2022). anhydrous silicates in CI chondrites: Implications for the nature and dynamics of dust in the solar accretion disk. *Geochimica et Cosmochimica Acta*. <https://doi.org/10.1016/j.gca.2022.06.017>
- Morris, M. A., Boley, A. C., Desch, S. J., & Athanassiadou, T. (2012). Chondrule formation in bow shocks around eccentric planetary embryos. *Astrophysical Journal*, 752(1). <https://doi.org/10.1088/0004-637X/752/1/27>
- Munayco, P., Munayco, J., de Avillez, R. R., Valenzuela, M., Rochette, P., Gattacceca, J., & Scorzelli, R. B. (2013). Weathering of ordinary chondrites from the Atacama Desert, Chile, by Mössbauer spectroscopy and synchrotron radiation X-ray diffraction. *Meteoritics and Planetary Science*, 48(3), 457–473. <https://doi.org/10.1111/maps.12067>
- Muñoz, C., Guerra, N., Martínez-Frías, J., Lunar, R., & Cerda, J. (2007). The Atacama Desert: A preferential arid region for the recovery of meteorites-Find location features and strewnfield distribution patterns. *Journal of Arid Environments*, 71(2), 188–200. <https://doi.org/10.1016/j.jaridenv.2007.03.007>
- Nanne, J. A. M., Nimmo, F., Cuzzi, J. N., & Kleine, T. (2019). Origin of the non-carbonaceous–carbonaceous meteorite dichotomy. *Earth and Planetary Science Letters*, 511, 44–54. <https://doi.org/10.1016/j.epsl.2019.01.027>
- Nesvorný, D., Li, R., Youdin, A. N., Simon, J. B., & Grundy, W. M. (2019). Trans-Neptunian binaries as evidence for planetesimal formation by the streaming instability. *Nature Astronomy*, 3(9), 808–812.
- Nishiizumi, K., D. Elmore, and P. W. Kubik. "Update on terrestrial ages of Antarctic meteorites." *Earth and Planetary Science Letters* 93.3-4 (1989): 299-313.
- Ormel, C. W., & Klahr, H. H. (2010). The effect of gas drag on the growth of protoplanets. *Astronomy and Astrophysics*, 520, A43. <https://doi.org/10.1051/0004-6361/201014903>
- Ott, U. (2017). Isotope Variations in the Solar System: Supernova Fingerprints. In *Handbook of Supernovae* (pp. 2331–2357). Springer International Publishing. https://doi.org/10.1007/978-3-319-21846-5_17
- Ouazaa, N. L., Perchiazzi, N., Kassaa, S., Zeoli, A., Ghanmi, M., & Folco, L. (2009). Meteorite finds from southern Tunisia. *Meteoritics and Planetary Science*, 44(7), 955–960. <https://doi.org/10.1111/j.1945-5100.2009.tb00780.x>
- Ouknine, L., Khiri, F., Ibhi, A., Heikal, M. T. S., Saint-Gerant, T., & Medjkane, M. (2019). Insight into African meteorite finds: Typology, mass distribution and weathering process. *Journal of African Earth Sciences*, 158(June), 103551. <https://doi.org/10.1016/j.jafrearsci.2019.103551>
- Palme H., Hezel D. C., and Ebel D. S. (2015). The origin of chondrules: Constraints from matrix composition and matrix-chondrule complementarity. *Earth and Planetary Science Letters* 411:11–19.
- Pape, J., Mezger, K., Bouvier, A. S., & Baumgartner, L. P. (2019). Time and duration of chondrule formation: Constraints from ²⁶Al-²⁶Mg ages of individual chondrules. *Geochimica et Cosmochimica Acta*, 244, 416–436. <https://doi.org/10.1016/j.gca.2018.10.017>
- Pedersen, H., Bon, C. C., & Lindgren, H. (1992). Vaca Muerta mesosiderite strewnfield. *Meteoritics*, 27(2), 126–135. <https://doi.org/10.1111/j.1945-5100.1992.tb00739.x>
- Peel, Murray C., Brian L. Finlayson, and Thomas A. McMahon. "Updated world map of the Köppen-Geiger climate classification." *Hydrology and earth system sciences* 11.5 (2007): 1633-1644.
- Peltier, L. C. (1950). The geographic cycle in periglacial regions as it is related to climatic geomorphology. *Annals of the association of American Geographers*, 40(3), 214-236.
- Pfeiffer, M., Morgan, A., Heimsath, A., Jordan, T., Howard, A., & Amundson, R. (2021). Century scale rainfall in the absolute Atacama Desert: Landscape response and implications for past and future rainfall. *Quaternary Science Reviews*, 254, 106797. <https://doi.org/10.1016/j.quascirev.2021.106797>
- Piani, L., Marrocchi, Y., Rigaudier, T., Vacher, L. G., Thomassin, D., & Marty, B. (2020). Earth's water may have been inherited from material similar to enstatite chondrite meteorites. *Science*, 369(6507), 1110–1113. <https://doi.org/10.1126/science.aba1948>

- Pignatelli, I., Marrocchi, Y., Mugnaioli, E., Bourdelle, F., & Gounelle, M. (2017). Mineralogical, crystallographic and redox features of the earliest stages of fluid alteration in CM chondrites. *Geochimica et Cosmochimica Acta*, 209, 106–122. <https://doi.org/10.1016/j.gca.2017.04.017>
- Pignatelli I., Marrocchi Y., Vacher L. G., Delon R., and Gounelle M. (2016). Multiple precursors of secondary mineralogical assemblages in CM chondrites. *Meteoritics and Planetary Science* 51:785–805.
- Pinto, G. A., Marrocchi, Y., Jacquet, E., & Olivares, F. (2022). Formation of chondrule fine-grained rims from local nebular reservoirs. *Meteoritics & Planetary Science*, 14, 1–14. <https://doi.org/10.1111/maps.13812>
- Pinto, G. A., Marrocchi, Y., Morbidelli, A., Charnoz, S., Eugenia Varela, M., Soto, K., Martínez, R., & Olivares, F. (2021). Constraints on Planetesimal Accretion Inferred from Particle-size Distribution in CO Chondrites. *The Astrophysical Journal Letters*, 917(2), L25. <https://doi.org/10.3847/2041-8213/ac17f2>
- Pinto, G. A., Marrocchi, Y., Villeneuve, J., Olivares, F., Soto, K., Corgne, A., & Luis, B. (2022). The Frequency of Fe-Poor Relicts in Type II Chondrules of Carbonaceous and Ordinary Chondrites. *LPI Contributions*, 2678.
- Piralla, M., Marrocchi, Y., Verdier-Paoletti, M. J., Vacher, L. G., Villeneuve, J., Piani, L., ... & Gounelle, M. (2020). Primordial water and dust of the Solar System: Insights from in situ oxygen measurements of CI chondrites. *Geochimica et Cosmochimica Acta*, 269, 451-464.
- Piralla, M., Villeneuve, J., Batanova, V., Jacquet, E., & Marrocchi, Y. (2021). Conditions of chondrule formation in ordinary chondrites. *Geochimica et Cosmochimica Acta*, 313, 295–312. <https://doi.org/10.1016/j.gca.2021.08.007>
- Pourkhorsandi, H., Debaille, V., Armytage, R. M. G., van Ginneken, M., Rochette, P., & Gattacceca, J. (2021). The effects of terrestrial weathering on samarium-neodymium isotopic composition of ordinary chondrites. *Chemical Geology*, 562, p. 120056 <https://doi.org/10.1016/j.chemgeo.2020.120056>
- Pourkhorsandi, H., D’Orazio, M., Rochette, P., Valenzuela, M., Gattacceca, J., Mirnejad, H., Sutter, B., Hutzler, A., & Aboulahris, M. (2017). Modification of REE distribution of ordinary chondrites from Atacama (Chile) and Lut (Iran) hot deserts: Insights into the chemical weathering of meteorites. *Meteoritics and Planetary Science*, 52(9), 1843–1858. <https://doi.org/10.1111/maps.12894>
- Pourkhorsandi, H., Gattacceca, J., Devouard, B., D’Orazio, M., Rochette, P., Beck, P., Sonzogni, C., & Valenzuela, M. (2017). The ungrouped chondrite El Médano 301 and its comparison with other reduced ordinary chondrites. *Geochimica et Cosmochimica Acta*, 218, 98–113. <https://doi.org/10.1016/j.gca.2017.09.013>
- Pourkhorsandi, H., Gattacceca, J., Rochette, P., D’Orazio, M., Kamali, H., de Avillez, R., Letichevsky, S., Djamali, M., Mirnejad, H., Debaille, V., & Jull, A. J. T. (2019). Meteorites from the Lut Desert (Iran). *Meteoritics and Planetary Science*, 54(8), 1737–1763. <https://doi.org/10.1111/maps.13311>
- Pourkhorsandi, H., Gattacceca, J., Rochette, P., Smith, T., Bonal, L., D’Orazio, M., Devouard, B., Sonzogni, C., & Debaille, V. (2022). The Famenin fall and other ordinary chondrites intermediate between H and L groups. *Meteoritics & Planetary Science*, 22. <https://doi.org/10.1111/maps.13801>
- Qin, L., Alexander, C. M. O. D., Carlson, R. W., Horan, M. F., & Yokoyama, T. (2010). Contributors to chromium isotope variation of meteorites. *Geochimica et Cosmochimica Acta*, 74(3), 1122–1145. <https://doi.org/10.1016/j.gca.2009.11.005>
- Radomsky, P. M., & Hewins, R. H. (1990). Formation conditions of pyroxene-olivine and magnesian olivine chondrules. *Geochimica et Cosmochimica Acta*, 54(12), 3475-3490.
- Rambaldi, E. R. (1981). Relict grains in chondrules. *Nature*, 293(5833), 558–561. <https://doi.org/10.1038/293558a0>
- Rech, J. A., Quade, J., & Hart, W. S. (2003). Isotopic evidence for the source of Ca and S in soil gypsum, anhydrite and calcite in the Atacama Desert, Chile. *Geochimica et Cosmochimica Acta*, 67(4), 575–586. [https://doi.org/10.1016/S0016-7037\(02\)01175-4](https://doi.org/10.1016/S0016-7037(02)01175-4)
- Regelous, M., Elliott, T., & Coath, C. D. (2008). Nickel isotope heterogeneity in the early Solar System. *Earth and Planetary Science Letters*, 272(1–2), 330–338. <https://doi.org/10.1016/j.epsl.2008.05.001>

- Regnault, M., Marrocchi, Y., Piralla, M., Villeneuve, J., Batanova, V., Schnuriger, N., & Jacquet, E. (2022). Oxygen isotope systematics of chondrules in Rumuruti chondrites: Formation conditions and genetic link with ordinary chondrites. *Meteoritics and Planetary Science*, 57(1), 122–135. <https://doi.org/10.1111/maps.13778>
- Render, J., Brennecke, G. A., Burkhardt, C., & Kleine, T. (2022). Solar System evolution and terrestrial planet accretion determined by Zr isotopic signatures of meteorites. *Earth and Planetary Science Letters*, 595, 117748.
- Richter, F. M., Mendybaev, R. A., & Davis, A. M. (2006). Conditions in the protoplanetary disk as seen by the type B CAIs. *Meteoritics and Planetary Science*, 41(1), 83–93. <https://doi.org/10.1111/j.1945-5100.2006.tb00194.x>
- Rollion-Bard C. (2001) Variabilité des isotopes de l'oxygène dans les coraux Porites: développement et implications des microanalyses d'isotopes stables (B, C et O) par sonde ionique. Nancy 1.
- Rubin, A. E. (1984). Coarse-grained chondrule rims in type 3 chondrites. *Geochimica et Cosmochimica Acta*, 48(9), 1779–1789. [https://doi.org/10.1016/0016-7037\(84\)90032-2](https://doi.org/10.1016/0016-7037(84)90032-2)
- Rubin, A. E. (2000). Petrologic, geochemical and experimental constraints on models of chondrule formation. *Earth Science Reviews*, 50(1–2), 3–27. [https://doi.org/10.1016/S0012-8252\(99\)00067-7](https://doi.org/10.1016/S0012-8252(99)00067-7)
- Rubin, A. E. (2010). Physical properties of chondrules in different chondrite groups: Implications for multiple melting events in dusty environments. *Geochimica et Cosmochimica Acta*, 74(16), 4807–4828. <https://doi.org/10.1016/j.gca.2010.05.018>
- Rubin, A. E. (1989). Size-frequency distributions of chondrules in CO3 chondrites. *Meteoritics*, 24(3), 179–189.
- Rubin, A. E., & Krot, A. N. (1996). Multiple heating of chondrules. *Chondrules and the protoplanetary disk*, 173–180.
- Rubin, A. E., & Li, Y. (2019). Formation and destruction of magnetite in CO3 chondrites and other chondrite groups. *Chemie Der Erde*, 79(4). <https://doi.org/10.1016/j.chemer.2019.07.009>
- Rubin A. E., Scott E. R. D., and Keil K. (1982). Microchondrule-bearing clast in the Piancaldoli LL3 meteorite: a new kind of type 3 chondrite and its relevance to the history of chondrules. *Geochimica et Cosmochimica Acta* 46:1763–1776.
- Rubin, A. E., Verish, R. S., Moore, C. B., & Oriti, R. A. (2000). Numerous unpaired meteorites exposed on a deflating playa lake at Lucerne Valley, California. *Meteoritics & Planetary Science*, 35(S5), A181–A183. <https://doi.org/10.1111/j.1945-5100.2000.tb01793.x>
- Rundel, P. W., Dillon, M. O., Palma, B., Mooney, H. A., Gulmon, S. L., & Ehleringer, J. R. (1991). The phytogeography and ecology of the coastal Atacama and Peruvian Deserts. *Aliso*, 13(1), 1–49. <https://doi.org/10.5642/aliso.19911301.02>
- Russell, S. S., Hartmann, L., Cuzzi, J., Krot, A. N., Gounelle, M., & Weidenschilling, S. (2006). Timescales of the Solar Protoplanetary Disk. *Meteorites and the Early Solar System II*, 233–252. <https://doi.org/10.2307/j.ctv1v7zdm.17>
- Ruzicka, A., Floss, C., & Hutson, M. (2008). Relict olivine grains, chondrule recycling, and implications for the chemical, thermal, and mechanical processing of nebular materials. *Geochimica et Cosmochimica Acta*, 72(22), 5530–5557. <https://doi.org/10.1016/j.gca.2008.08.017>
- Ruzicka, A., Floss, C., & Hutson, M. (2012). Amoeboid olivine aggregates (AOAs) in the Efremovka, Leoville and Vigarano (CV3) chondrites: A record of condensate evolution in the solar nebula. *Geochimica et Cosmochimica Acta*, 79, 79–105. <https://doi.org/10.1016/j.gca.2011.11.043>
- Ruzicka, A., Hiyagon, H., Hutson, M., & Floss, C. (2007). Relict olivine, chondrule recycling, and the evolution of nebular oxygen reservoirs. *Earth and Planetary Science Letters*, 257(1–2), 274–289. <https://doi.org/10.1016/j.epsl.2007.02.037>
- Sakamoto, N., Seto, Y., Itoh, S., Kuramoto, K., Fujino, K., Nagashima, K., ... & Yurimoto, H. (2007). Remnants of the early solar system water enriched in heavy oxygen isotopes. *Science*, 317(5835), 231–233.
- Sanders, I. S., & Scott, E. R. D. (2012). The origin of chondrules and chondrites: Debris from low-velocity impacts between molten planetesimals? *Meteoritics and Planetary Science*, 47(12), 2170–2192. <https://doi.org/10.1111/maps.12002>

- Schiller, M., Bizzarro, M., & Siebert, J. (2020). Iron isotope evidence for very rapid accretion and differentiation of the proto-Earth. *Science advances*, 6(7), eaay7604.
- Schiller, M., Paton, C., & Bizzarro, M. (2015). Evidence for nucleosynthetic enrichment of the protosolar molecular cloud core by multiple supernova events. *Geochimica et Cosmochimica Acta*, 149, 88–102. <https://doi.org/10.1016/j.gca.2014.11.005>
- Schindelin, J., Arganda-Carreras, I., Frise, E., Kaynig, V., Longair, M., Pietzsch, T., Preibisch, S., Rueden, C., Saalfeld, S., Schmid, B., Tinevez, J. Y., White, D. J., Hartenstein, V., Eliceiri, K., Tomancak, P., & Cardona, A. (2012). Fiji: An open-source platform for biological-image analysis. *Nature Methods*, 9(7), 676–682. <https://doi.org/10.1038/nmeth.2019>
- Schlüter, J., Schultz, L., Thiedig, F., Al-Mahdi, B. O., & Aghreb, A. E. A. (2002). The Dar al Gani meteorite field (Libyan Sahara): Geological setting, pairing of meteorites, and recovery density. *Meteoritics and Planetary Science*, 37(8), 1079–1093. <https://doi.org/10.1111/j.1945-5100.2002.tb00879.x>
- Schneider, J. M., Burkhardt, C., Marrocchi, Y., Brennecka, G. A., & Kleine, T. (2020). Early evolution of the solar accretion disk inferred from Cr-Ti-O isotopes in individual chondrules. *Earth and Planetary Science Letters*, 551, 116585. <https://doi.org/10.1016/j.epsl.2020.116585>
- Schnuriger, N., Cartier, C., Villeneuve, J., Batanova, V., Regnault, M., & Marrocchi, Y. (2022). Spinels in CV chondrules: Investigating precursor legacy and chondrule thermal histories. *Meteoritics and Planetary Science*, 20, 1–20. <https://doi.org/10.1111/maps.13802>
- Schrader, D. L., Connolly, H. C., Lauretta, D. S., Nagashima, K., Huss, G. R., Davidson, J., & Domanik, K. J. (2013). The formation and alteration of the Renazzo-like carbonaceous chondrites II: Linking O-isotope composition and oxidation state of chondrule olivine. *Geochimica et Cosmochimica Acta*, 101, 302–327. <https://doi.org/10.1016/j.gca.2012.09.045>
- Schrader, D. L., Connolly, H. C., Lauretta, D. S., Zega, T. J., Davidson, J., & Domanik, K. J. (2015). The formation and alteration of the Renazzo-like carbonaceous chondrites III: Toward understanding the genesis of ferromagnesian chondrules. *Meteoritics and Planetary Science*, 50(1), 15–50. <https://doi.org/10.1111/maps.12402>
- Schrader, D. L., Nagashima, K., Krot, A. N., Oglione, R. C., & Hellebrand, E. (2014). Variations in the O-isotope composition of gas during the formation of chondrules from the CR chondrites. *Geochimica et Cosmochimica Acta*, 132, 50–74. <https://doi.org/10.1016/j.gca.2014.01.034>
- Schrader, D. L., Nagashima, K., Waitukaitis, S. R., Davidson, J., McCoy, T. J., Connolly, H. C., & Lauretta, D. S. (2018). The retention of dust in protoplanetary disks: Evidence from agglomeratic olivine chondrules from the outer Solar System. *Geochimica et Cosmochimica Acta*, 223, 405–421. <https://doi.org/10.1016/j.gca.2017.12.014>
- Scott, E. R. D., & Jones, R. H. (1990). Disentangling nebular and asteroidal features of CO3 carbonaceous chondrite meteorites. *Geochimica et Cosmochimica Acta*, 54(9), 2485–2502. [https://doi.org/10.1016/0016-7037\(90\)90235-D](https://doi.org/10.1016/0016-7037(90)90235-D)
- Scott, E. R. D., Keil, K., & Stöffler, D. (1992). Shock metamorphism of carbonaceous chondrites. *Geochimica et Cosmochimica Acta*, 56(12), 4281–4293. [https://doi.org/10.1016/0016-7037\(92\)90268-N](https://doi.org/10.1016/0016-7037(92)90268-N)
- Scott, E. R. D., & Krot, A. N. (2014). Chondrites and Their Components. In *Meteorites and Cosmochemical Processes, Treatise on Geochemistry* (Second Edition). Edited by A. M. Davis. Elsevier-Pergamon: Oxford, Vol. 2. pp 65–137. <https://doi.org/https://doi.org/10.1016/B978-0-08-095975-7.00104-2>
- Scott, E. R. D., & Taylor, G. J. (1983). Chondrules and Other Components in C, O, and E Chondrites: Similarities in Their Properties and Origins. *Journal of Geophysical Research*, 88 Suppl, 275–286. <https://doi.org/10.1029/jb088is01p0b275>
- Searl, A., & Rankin, S. (1993). A preliminary petrographic study of the Chilean nitrates. *Geological Magazine*, 130(3), 319–333.
- Sears D. W. G., Benoit P. H., and Lu Jie. (1993). Two chondrule groups each with distinctive rims in Murchison recognized by cathodoluminescence. *Meteoritics* 28:669–675.
- Sears, D. W., Grossman, J. . N., Melcher, C. L., Ross, L. M., & Mills, A. A. (1980). Measuring the metamorphic history of unequilibrated ordinary chondrites. *Nature*, 791–795
- Shu, F. H., Shang, H., Glassgold, A. E., & Lee, T. (1997). X-rays and fluctuating X-winds from protostars. *Science*, 277(5331), 1475–1479.

- Simon, J. B., & Armitage, P. J. (2014). Efficiency of particle trapping in the outer regions of protoplanetary disks. *The Astrophysical Journal*, 784(1), 15.
- Simon, J. B., Armitage, P. J., Li, R., & Youdin, A. N. (2016). The mass and size distribution of planetesimals formed by the streaming instability. I. The role of self-gravity. *The Astrophysical Journal*, 822(1), 55. <https://doi.org/10.3847/0004-637x/822/1/55>
- Simon, J. I., Cuzzi, J. N., McCain, K. A., Cato, M. J., Christoffersen, P. A., Fisher, K. R., ... & Scargle, J. D. (2018). Particle size distributions in chondritic meteorites: Evidence for pre-planetesimal histories. *Earth and Planetary Science Letters*, 494, 69-82.
- Simon, S. B., Krot, A. N., Nagashima, K., Kööp, L., & Davis, A. M. (2019). Condensate refractory inclusions from the CO3.00 chondrite Dominion Range 08006: Petrography, mineral chemistry, and isotopic compositions. *Geochimica et Cosmochimica Acta*, 246, 109–122. <https://doi.org/10.1016/j.gca.2018.11.029>
- Spitzer, F., Burkhardt, C., Budde, G., Kruijjer, T. S., Morbidelli, A., & Kleine, T. (2020). Isotopic Evolution of the Inner Solar System Inferred from Molybdenum Isotopes in Meteorites. *The Astrophysical Journal*, 898(1), L2. <https://doi.org/10.3847/2041-8213/ab9e6a>
- Spitzer, F., Burkhardt, C., Nimmo, F., & Kleine, T. (2021). *Nucleosynthetic Pt isotope anomalies and the Hf-W chronology of core formation in inner and outer solar system planetesimals*. 1–40. <http://arxiv.org/abs/2109.15250>
- Steele, I. M. (1986). Compositions and textures of relic forsterite in carbonaceous and unequilibrated ordinary chondrites. *Geochimica et Cosmochimica Acta*, 50(7), 1379–1395. [https://doi.org/10.1016/0016-7037\(86\)90312-1](https://doi.org/10.1016/0016-7037(86)90312-1)
- Steller, T., Burkhardt, C., Yang, C., & Kleine, T. (2022). Nucleosynthetic zinc isotope anomalies reveal a dual origin of terrestrial volatiles. *Icarus*, 386(May), 115171. <https://doi.org/10.1016/j.icarus.2022.115171>
- Stelzner, T., Heide, K., Bischoff, A., Weber, D., Scherer, P., Schultz, L., Happel, M., Schrön, W., Neupert, U., Michel, R., Clayton, R. N., Mayeda, T. K., Bonani, G., Haidas, I., Ivy-Ochs, S., & Suter, M. (1999). An interdisciplinary study of weathering effects in ordinary chondrites from the Acfer region, Algeria. *Meteoritics and Planetary Science*, 34(5), 787–794. <https://doi.org/10.1111/j.1945-5100.1999.tb01391.x>
- Stephan, T., & Davis, A. M. (2021). Molybdenum Isotope Dichotomy in Meteorites Caused by s-Process Variability. *The Astrophysical Journal*, 909(1), 8. <https://doi.org/10.3847/1538-4357/abd725>
- Stephant, A., Garvie, L. A. J., Mane, P., Hervig, R., & Wadhwa, M. (2018). Terrestrial exposure of a fresh Martian meteorite causes rapid changes in hydrogen isotopes and water concentrations. *Scientific Reports*, 8(1), 6–12. <https://doi.org/10.1038/s41598-018-30807-w>
- Stöffler, D., Hamann, C., & Metzler, K. (2018). Shock metamorphism of planetary silicate rocks and sediments: Proposal for an updated classification system. *Meteoritics and Planetary Science*, 53(1), 5–49. <https://doi.org/10.1111/maps.12912>
- Stöffler, D., Keil, K., & Edward R.D, S. (1991). Shock metamorphism of ordinary chondrites. *Geochimica et Cosmochimica Acta*, 55(12), 3845–3867. [https://doi.org/10.1016/0016-7037\(91\)90078-J](https://doi.org/10.1016/0016-7037(91)90078-J)
- Suttle M. D., Genge M. J., Salge T., Lee M. R., Folco L., Góral T., Russell S. S., and Lindgren P. (2019). A microchondrule-bearing micrometeorite and comparison with microchondrules in CM chondrites. *Meteoritics and Planetary Science* 54:1303–1324.
- Tait, A. W., Wilson, S. A., Tomkins, A. G., Gagen, E. J., Fallon, S. J., & Southam, G. (2017). Evaluation of meteorites as habitats for terrestrial microorganisms: results from the Nullarbor Plain, Australia, a Mars analogue site. *Geochimica et Cosmochimica Acta*, 215, 1-16.
- Takayama A., and Tomeoka K. (2012). Fine-grained rims surrounding chondrules in the Tagish Lake carbonaceous chondrite: Verification of their formation through parent-body processes. *Geochimica et Cosmochimica Acta* 98:1–18
- Takigawa, A., Stroud, R. M., Nittler, L. R., Alexander, C. M. O., & Miyake, A. (2018). High-temperature Dust Condensation around an AGB Star: Evidence from a Highly Pristine Presolar Corundum. *The Astrophysical Journal*, 862(1), L13. <https://doi.org/10.3847/2041-8213/aad1f5>
- Taylor, S. R. (2001). The Solar Nebula. In *Solar System Evolution A New Perspective* (Vol. 1, pp. 47–72). <https://doi.org/10.1016/B0-08-043751-6/01061-6>

- Tenner, T. J., Nakashima, D., Ushikubo, T., Kita, N. T., & Weisberg, M. K. (2015). Oxygen isotope ratios of FeO-poor chondrules in CR3 chondrites: Influence of dust enrichment and H₂O during chondrule formation. *Geochimica et Cosmochimica Acta*, 148, 228–250. <https://doi.org/10.1016/j.gca.2014.09.025>
- Tenner, T. J., Ushikubo, T., Kurahashi, E., Kita, N. T., & Nagahara, H. (2013). Oxygen isotope systematics of chondrule phenocrysts from the CO3.0 chondrite Yamato 81020: Evidence for two distinct oxygen isotope reservoirs. *Geochimica et Cosmochimica Acta*, 102, 226–245. <https://doi.org/10.1016/j.gca.2012.10.034>
- Tenner, T. J., Ushikubo, T., Nakashima, D., Schrader, D. L., Weisberg, M. K., Kimura, M., & Kita, N. T. (2018). Oxygen Isotope Characteristics of Chondrules from Recent Studies by Secondary Ion Mass Spectrometry. *Chondrules: Records of Protoplanetary Disk Processes*, 196–246. <https://doi.org/10.1017/9781108284073.008>
- Thirumalai, K., Singh, A., & Ramesh, R. (2011). A MATLAB™ code to perform weighted linear regression with (correlated or uncorrelated) errors in bivariate data. *Journal of the Geological Society of India*, 77(4), 377–380.
- Tissandier, L., Libourel, G., & Robert, F. (2002). Gas-melt interactions and their bearing on chondrule formation. *Meteoritics & Planetary Science*, 37, 1377–1389.
- Tomeoka K., and Ohnishi I. (2010). Indicators of parent-body processes: Hydrated chondrules and fine-grained rims in the Mokoia CV3 carbonaceous chondrite. *Geochimica et Cosmochimica Acta* 74:4438–4453.
- Tomeoka K., and Ohnishi I. (2014). Olivine-rich rims surrounding chondrules in the Mokoia CV3 carbonaceous chondrite: Further evidence for parent-body processes. *Geochimica et Cosmochimica Acta* 137:18–34.
- Tomeoka K., and Ohnishi I. (2015). Redistribution of chondrules in a carbonaceous chondrite parent body: A model. *Geochimica et Cosmochimica Acta* 164:543–555.
- Toth, E. R., Fehr, M. A., Friebel, M., & Schönbächler, M. (2020). Cadmium isotopes in chondrites and acid leachates: Nucleosynthetic homogeneity and a monitor for thermal neutron capture effects. *Geochimica et Cosmochimica Acta*, 274, 286–301. <https://doi.org/10.1016/j.gca.2020.01.059>
- Trigo-Rodríguez J. M., Rubin A. E., and Wasson J. T. (2006). Non-nebular origin of dark mantles around chondrules and inclusions in CM chondrites. *Geochimica et Cosmochimica Acta* 70:1271–1290.
- Trinquier, A., Elliott, T., Ulfbeck, D., Coath, C., Krot, A. N., & Bizzarro, M. (2009). Origin of nucleosynthetic isotope heterogeneity in the solar protoplanetary disk. *Science*, 324(5925), 374–376. <https://doi.org/10.1126/science.1168221>
- Troiano, J., Rumble III, D., Rivers, M. L., & Friedrich, J. M. (2011). Compositions of three low-FeO ordinary chondrites: Indications of a common origin with the H chondrites. *Geochimica et Cosmochimica Acta*, 75(21), 6511–6519.
- Turner, S., McGee, L., Humayun, M., Creech, J., & Zanda, B. (2021). Carbonaceous chondrite meteorites experienced fluid flow within the past million years. *Science*, 371(6525), 164–167.
- United Nations Environment Programme (1997). *World Atlas of Desertification: Second Edition*. <https://wedocs.unep.org/20.500.11822/30300>.
- Ushikubo, T., & Kimura, M. (2020). Oxygen-isotope systematics of chondrules and olivine fragments from Tagish Lake C2 chondrite: Implications of chondrule-forming regions in protoplanetary disk. In *Geochimica et Cosmochimica Acta*. The Author(s). <https://doi.org/10.1016/j.gca.2020.11.003>
- Ushikubo, T., & Kimura, M. (2021). Oxygen-isotope systematics of chondrules and olivine fragments from Tagish Lake C2 chondrite: Implications of chondrule-forming regions in protoplanetary disk. *Geochimica et Cosmochimica Acta*, 293, 328–343. <https://doi.org/10.1016/j.gca.2020.11.003>
- Ushikubo, T., Kimura, M., Kita, N. T., & Valley, J. W. (2012). Primordial oxygen isotope reservoirs of the solar nebula recorded in chondrules in Acfer 094 carbonaceous chondrite. *Geochimica et Cosmochimica Acta*, 90, 242–264. <https://doi.org/10.1016/j.gca.2012.05.010>
- Vacher, L. G., Piani, L., Rigaudier, T., Thomassin, D., Florin, G., Piralla, M., & Marrocchi, Y. (2020). Hydrogen in chondrites: Influence of parent body alteration and atmospheric contamination on primordial components. *Geochimica et Cosmochimica Acta*, 281, 53–66. <https://doi.org/10.1016/j.gca.2020.05.007>

- Vacher, L. G., Truche, L., Faure, F., Tissandier, L., Mosser-Ruck, R., & Marrocchi, Y. (2019). Deciphering the conditions of tochilinite and cronstedtite formation in CM chondrites from low temperature hydrothermal experiments. *Meteoritics and Planetary Science*, 54(8), 1870–1889. <https://doi.org/10.1111/maps.13317>
- Vacher, L. G., Marrocchi, Y., Villeneuve, J., Verdier-Paoletti, M. J., & Gounelle, M. (2018). Collisional and alteration history of the CM parent body. *Geochimica et Cosmochimica Acta*, 239, 213–234.
- Valenzuela E. M. (2011). Procesos de Meteorización en Condritos Ordinarios del Desierto de Atacama, Norte de Chile: Nuevos Antecedentes sobre Meteorización de Material Extraterrestre en Ambientes Desérticos. Universidad de Chile.
- Valenzuela, M., & Benado, J. (2018). *Meteorites and Craters Found in Chile: A Bridge to Introduce the First Attempt for Geoheritage Legal Protection in the Country*. 103–115. https://doi.org/10.1007/978-3-319-75373-7_7
- Van Schmus, W. R., & Wood, J. A. (1967). A chemical-petrologic classification for the chondritic meteorites. *Geochimica et Cosmochimica Acta*, 31(5), 747–765.
- Varela, M. E., & Zinner, E. (2018). Unraveling the role of liquids during chondrule formation processes. *Geochimica et Cosmochimica Acta*, 221, 358–378. <https://doi.org/10.1016/j.gca.2017.03.038>
- Villeneuve J. (2010) Formation des chondres: Précurseurs et chronologie. Vandoeuvres-Nancy, INPL.
- Villeneuve, J., Chaussidon, M., & Libourel, G. (2009). Homogeneous distribution of ²⁶Al in the solar system from the Mg isotopic composition of chondrules. *Science*, 325(5943), 985–988
- Villeneuve, J., Chaussidon, M., Marrocchi, Y., Deng, Z., & Watson, E. B. (2019). High-precision in situ silicon isotopic analyses by multi-collector secondary ion mass spectrometry in olivine and low-calcium pyroxene. *Rapid Communications in Mass Spectrometry*, 33(20), 1589–1597. <https://doi.org/10.1002/rcm.8508>
- Villeneuve, J., Libourel, G., & Soulié, C. (2015). Relationships between type I and type II chondrules: Implications on chondrule formation processes. *Geochimica et Cosmochimica Acta*, 160, 277–305. <https://doi.org/10.1016/j.gca.2015.03.033>
- Villeneuve, J., Marrocchi, Y., & Jacquet, E. (2020). Silicon isotopic compositions of chondrule silicates in carbonaceous chondrites and the formation of primordial solids in the accretion disk. *Earth and Planetary Science Letters*, 542, 116318. <https://doi.org/10.1016/j.epsl.2020.116318>
- Wahlberg Jansson, K., & Johansen, A. (2014). Formation of planetesimals in collapsing pebble clouds. *Asteroids, Comets, Meteors 2014*, 573.
- Wahlberg Jansson, K., & Johansen, A. (2017). Radially resolved simulations of collapsing pebble clouds in protoplanetary discs. *Monthly Notices of the Royal Astronomical Society*, 469, S149–S157. <https://doi.org/10.1093/mnras/stx1470>
- Wakita, S., Matsumoto, Y., Oshino, S., & Hasegawa, Y. (2017). Planetesimal Collisions As a Chondrule Forming Event. *The Astrophysical Journal*, 834(2), 125. <https://doi.org/10.3847/1538-4357/834/2/125>
- Warren, P. H. (2011). Stable-isotopic anomalies and the accretionary assemblage of the Earth and Mars: A subordinate role for carbonaceous chondrites. *Earth and Planetary Science Letters*, 311(1–2), 93–100. <https://doi.org/10.1016/j.epsl.2011.08.047>
- Wasserburg, G. J., Busso, M., Gallino, R., & Nollett, K. M. (2006). Short-lived nuclei in the early Solar System: Possible AGB sources. *Nuclear Physics A*, 777, 5–69. <https://doi.org/10.1016/j.nuclphysa.2005.07.015>
- Wasson J. T. (2008). Evaporation of nebular fines during chondrule formation. *Icarus* 195:895–907.
- Wasson, J. T., & Rubin, A. E. (2003). Ubiquitous low-FeO relict grains in type II chondrules and limited overgrowths on phenocrysts following the final melting event. *Geochimica et Cosmochimica Acta*, 67(12), 2239–2250. [https://doi.org/10.1016/S0016-7037\(03\)00023-1](https://doi.org/10.1016/S0016-7037(03)00023-1)
- Wasson J. T., and Rubin A. E. (2014). Absence of matrix-like chondrule rims in CR2 LAP 02342. *Meteoritics and Planetary Science* 49:245–260.
- Wasson, J. T., & DE BON, C. C. (1998). New Chilean iron meteorites: Medium octahedrites from Northern Chile are unique. *Meteoritics & Planetary Science*, 33(2), 175–179.
- Weisberg, M. K., Ebel, D. S., Nakashima, D., Kita, N. T., & Humayun, M. (2015). Petrology and geochemistry of chondrules and metal in NWA 5492 and GRO 95551: A new type of metal-rich

- chondrite. *Geochimica et Cosmochimica Acta*, 167, 269–285. <https://doi.org/10.1016/j.gca.2015.07.021>
- Weisberg, M. K., McCoy, T. J., & Krot, A. N. (2006). Systematics and evaluation of meteorite classification. *Meteorites and the early solar system II*, 19, 19–52.
- Wetherill, G. (1990). Formation of the Earth. *Annual Review of Earth and Planetary Sciences*, 18(205), 56.
- Windmark, F., Birnstiel, T., Ormel, C. W., & Dullemond, C. P. (2012). Breaking through: The effects of a velocity distribution on barriers to dust growth. *Astronomy and Astrophysics*, 544, 1–4. <https://doi.org/10.1051/0004-6361/201220004>
- Wittmann, A., Friedrich, J. M., Troiano, J., Macke, R. J., Britt, D. T., Swindle, T. D., Weirich, J. R., Rumble, D., Lasue, J., & Kring, D. A. (2011). H/L chondrite LaPaz Icefield 031047 - A feather of Icarus? *Geochimica et Cosmochimica Acta*, 75(20), 6140–6159. <https://doi.org/10.1016/j.gca.2011.07.037>
- Wlotzka, F. (1993). A weathering scale for the ordinary chondrites. *Meteoritics*, 28.
- Yamanobe, M., Nakamura, T., & Nakashima, D. (2018). Oxygen isotope reservoirs in the outer asteroid belt inferred from oxygen isotope systematics of chondrule olivines and isolated forsterite and olivine grains in Tagish Lake-type carbonaceous chondrites, WIS 91600 and MET 00432. *Polar Science*, 15(October 2017), 29–38. <https://doi.org/10.1016/j.polar.2017.12.002>
- Yang, C. C., Johansen, A., & Carrera, D. (2017). Concentrating small particles in protoplanetary disks through the streaming instability. *Astronomy and Astrophysics*, 606. <https://doi.org/10.1051/0004-6361/201630106>
- Yoshizaki, T., Nakashima, D., Nakamura, T., Park, C., Sakamoto, N., Ishida, H., & Itoh, S. (2019). Nebular history of an ultrarefractory phase bearing CAI from a reduced type CV chondrite. *Geochimica et Cosmochimica Acta*, 252, 39–60. <https://doi.org/10.1016/j.gca.2019.02.034>
- Youdin, A. N., & Goodman, J. (2005). Streaming Instabilities in Protoplanetary Disks. *The Astrophysical Journal*, 620(1), 459–469. <https://doi.org/10.1086/426895>
- Young, E. D., & Russell, S. S. (1998). Oxygen reservoirs in the early solar nebula inferred from an Allende CAI. *Science*, 282(5388), 452–455.
- Yurimoto, H., & Wasson, J. T. (2002). Extremely rapid cooling of a carbonaceous-chondrite chondrule containing very ¹⁶O-rich olivine and a ²⁶Mg-excess. *Geochimica et Cosmochimica Acta*, 66(24), 4355–4363. [https://doi.org/10.1016/S0016-7037\(02\)01218-8](https://doi.org/10.1016/S0016-7037(02)01218-8)
- Zanda, B. (2004). Chondrules. *Earth and Planetary Science Letters* 224:1–17.
- Zanda B., Hewins R. H., Bourot-Denise M., Bland P. A., and Albarède F. (2006). Formation of solar nebula reservoirs by mixing chondritic components. *Earth and Planetary Science Letters* 248:650–660.
- Zanda B., Lewin E., and Humayun M. (2018). The Chondritic Assemblage: Complementarity Is Not a Required Hypothesis. In *Chondrules: Records of Protoplanetary Disk Processes (Cambridge Planetary Science)*, edited by Russell S., Jr. H. C., and A. K. Cambridge Planetary Science. pp. 122–150.
- Zanetta, P., Guillou, C. le, Leroux, H., Zanda, B., Hewins, R., & Bellino, G. (2021a). Processes and temperatures of FGR formation in chondrites. *Geochimica et Cosmochimica Acta*. <https://doi.org/10.1016/j.gca.2021.11.019>
- Zanetta, P. M., Leroux, H., le Guillou, C., Zanda, B., & Hewins, R. H. (2021b). Nebular thermal processing of accretionary fine-grained rims in the Paris CM chondrite. *Geochimica et Cosmochimica Acta*, 295, 135–154. <https://doi.org/10.1016/j.gca.2020.12.015>
- Zeng, X., Li, S., Leya, I., Wang, S., Smith, T., Li, Y., & Wang, P. (2018). The Kumtag 016 L5 strewn field, Xinjiang Province, China. *Meteoritics and Planetary Science*, 53(6), 1113–1130. <https://doi.org/10.1111/maps.13073>
- Zhang, M., Bonato, E., King, A. J., Russell, S. S., Tang, G., & Lin, Y. (2020). Petrology and oxygen isotopic compositions of calcium-aluminum-rich inclusions in primitive CO3.0-3.1 chondrites. *Meteoritics and Planetary Science*, 55(4), 911–935. <https://doi.org/10.1111/maps.13473>
- Zinner, E. (2014). Presolar Grains. In *Meteorites and Cosmochemical Processes, Treatise on Geochemistry (Second Edition)*. Edited by A. M. Davis. Elsevier-Pergamon: Oxford, Vol. 2. pp. 181–213. <https://doi.org/10.1016/B978-0-08-095975-7.00101-7>

- Zolensky M., Barrett R., and Browning L. (1993). Mineralogy and composition of matrix and chondrule rims in carbonaceous chondrites. *Geochimica et Cosmochimica Acta* 57:3123–3148.
- Zolensky, M. E., Wells, G. L., & Rendell, H. M. (1990). The accumulation rate of meteorite falls at the Earth's surface: The view from Roosevelt County, New Mexico. *Meteoritics*, 25(1), 11–17. <https://doi.org/10.1111/j.1945-5100.1990.tb00965.x>
- Zurfluh, F. J., Hofmann, B. A., Gnos, E., Eggenberger, U., & Jull, A. J. T. (2016). Weathering of ordinary chondrites from Oman: Correlation of weathering parameters with ¹⁴C terrestrial ages and a refined weathering scale. *Meteoritics and Planetary Science*, 51(9), 685–1700. <https://doi.org/10.1111/maps.12690>

Appendix A

Supplementary material Chapter 3

Table A1-1. Individual EPMA analysis of major and minor elements of all the olivine grains studied in type II chondrules from CO, CR and ordinary chondrites. The profile (Pr) indicate the change between relict and host olivine grains.

Meteorite	Chondrule	Profile	DataSet/Point	Olivine	Fo	Distance (μm)	MgO	Al ₂ O ₃	SiO ₂	CaO	TiO ₂	Cr ₂ O ₃	MnO	FeO	NiO	Total
LoV123	Ch_02	Pr1	93 / 1 .	Host	49.7	0.0	35.1	0.1	38.0	0.3	0.0	0.3	0.2	27.5	0.0	101.5
			93 / 2 .	Host	50.4	9.5	35.6	0.1	37.9	0.3	0.0	0.4	0.3	27.1	0.0	101.6
			93 / 3 .	Host	53.0	19.0	36.8	0.1	38.2	0.3	0.0	0.4	0.3	25.3	-0.1	101.4
			93 / 4 .	Host	58.7	28.5	38.9	0.1	38.2	0.3	0.0	0.5	0.3	21.2	-0.1	99.5
			93 / 5 .	Host	64.4	38.0	42.3	0.0	39.5	0.2	0.0	0.3	0.3	18.1	0.1	100.9
			93 / 6 .	Host	68.9	47.5	44.3	0.0	40.1	0.2	0.0	0.3	0.3	15.5	0.0	100.7
			93 / 7 .	Relict	73.1	57.0	46.2	0.0	40.5	0.1	0.0	0.4	0.3	13.1	0.0	100.7
			93 / 8 .	Relict	76.9	66.5	47.9	0.0	40.8	0.1	0.0	0.3	0.4	11.1	-0.1	100.6
			93 / 9 .	Relict	78.6	76.0	48.8	0.0	40.7	0.1	0.0	0.3	0.4	10.3	-0.1	100.6
			93 / 10 .	Relict	78.4	85.5	48.3	0.0	41.0	0.1	0.0	0.7	0.2	10.3	0.0	100.7
			93 / 11 .	Relict	75.7	95.0	47.2	0.0	41.0	0.1	0.0	0.5	0.3	11.8	-0.1	100.9
			93 / 12 .	Relict	73.6	104.5	46.0	0.0	40.7	0.2	0.0	0.6	0.4	12.8	0.0	100.7
			93 / 13 .	Relict	77.3	114.0	48.0	0.0	41.2	0.1	0.0	0.4	0.3	10.9	0.0	100.9
			93 / 14 .	Relict	83.5	123.5	50.4	0.0	41.8	0.1	0.0	0.5	0.3	7.7	-0.1	100.9
			93 / 15 .	Relict	88.4	133.0	52.7	0.0	42.1	0.1	0.0	0.5	0.3	5.3	-0.1	101.0
			93 / 16 .	Relict	90.3	142.5	53.5	0.0	42.1	0.1	0.0	0.4	0.3	4.4	0.0	100.8
			93 / 17 .	Relict	91.8	152.0	53.8	0.0	42.1	0.1	0.0	0.4	0.2	3.7	-0.1	100.4
			93 / 18 .	Relict	91.6	161.5	53.7	0.0	42.0	0.1	0.0	0.5	0.3	3.8	0.2	100.6
			93 / 19 .	Relict	90.9	171.0	53.4	0.0	42.8	0.1	0.0	0.5	0.2	4.2	0.0	101.1
			93 / 20 .	Relict	88.2	180.5	52.5	0.0	41.8	0.1	0.0	0.3	0.3	5.5	0.0	100.5
			93 / 21 .	Relict	83.7	190.0	50.7	0.0	41.9	0.1	0.0	0.4	0.3	7.6	0.1	101.1
			93 / 22 .	Relict	77.1	199.5	47.6	0.0	40.8	0.1	0.0	0.3	0.4	11.0	-0.1	100.2
			93 / 23 .	Host	68.8	209.0	44.2	0.0	39.9	0.2	0.0	0.7	0.3	15.6	0.2	101.0
			93 / 24 .	Host	59.1	218.5	39.4	0.0	38.8	0.3	0.0	0.5	0.3	21.1	0.2	100.7

	93 / 25 .	Host	53.2	228.0	36.5	0.1	38.0	0.3	0.0	0.3	0.2	24.9	0.0	100.5
Pr2	94 / 1 .	Host	49.0	0.0	34.6	0.0	37.7	0.3	0.0	0.3	0.2	27.9	0.2	101.3
	94 / 2 .	Host	56.0	6.3	37.8	0.0	38.6	0.3	0.0	0.3	0.2	23.0	0.1	100.4
	94 / 3 .	Host	64.5	12.6	42.0	0.0	39.1	0.4	0.0	0.4	0.2	17.9	0.1	100.1
	94 / 4 .	Relict	83.2	18.9	50.4	0.1	41.3	0.4	0.1	0.4	0.1	7.9	-0.1	100.5
	94 / 5 .	Relict	91.0	25.2	53.5	0.1	41.6	0.3	0.1	0.4	0.1	4.1	0.0	100.2
	94 / 6 .	Relict	90.3	31.5	53.4	0.1	42.4	0.3	0.1	0.5	0.0	4.5	0.1	101.5
	94 / 7 .	Relict	84.3	37.8	51.0	0.2	41.6	0.3	0.1	0.5	0.1	7.4	0.0	101.2
	94 / 8 .	Relict	73.9	44.1	46.6	0.1	40.2	0.3	0.1	0.3	0.1	12.8	0.0	100.4
	94 / 9 .	Host	60.7	50.4	40.3	0.1	39.0	0.3	0.0	0.2	0.2	20.3	0.0	100.4
	94 / 10 .	Host	51.5	56.7	35.4	0.1	38.0	0.4	0.0	0.3	0.2	25.9	0.1	100.3
Pr3	95 / 1 .	Host	59.6	0.0	39.8	0.0	39.1	0.2	0.0	0.3	0.2	21.0	0.1	100.7
	95 / 2 .	Host	62.6	8.2	41.3	0.0	38.8	0.2	0.0	0.3	0.2	19.1	0.1	100.1
	95 / 3 .	Host	64.3	16.4	42.0	0.0	39.4	0.3	0.1	0.4	0.2	18.1	0.0	100.4
	95 / 4 .	Relict	67.9	24.6	44.0	0.0	39.5	0.3	0.0	0.3	0.2	16.1	0.0	100.4
	95 / 5 .	Relict	68.4	32.8	44.2	0.0	40.4	0.2	0.0	0.3	0.2	15.9	0.1	101.3
	95 / 6 .	Relict	69.2	41.0	44.3	0.0	39.7	0.2	0.0	0.4	0.1	15.3	0.0	100.2
	95 / 7 .	Relict	72.3	49.2	45.9	0.0	40.0	0.2	0.0	0.4	0.2	13.6	0.0	100.4
	95 / 8 .	Relict	75.5	57.4	47.4	0.0	40.9	0.2	0.0	0.2	0.1	11.9	0.2	101.0
	95 / 9 .	Relict	78.1	65.6	48.5	0.1	41.0	0.2	0.0	0.4	0.1	10.5	0.0	100.8
	95 / 10 .	Relict	75.8	73.8	47.7	0.0	40.8	0.2	0.1	0.4	0.1	11.8	0.1	101.1
	95 / 11 .	Relict	71.7	82.0	45.7	0.0	40.3	0.2	0.0	0.3	0.1	14.0	0.0	100.7
	95 / 12 .	Host	66.6	90.2	43.5	0.0	39.1	0.3	0.0	0.4	0.2	16.9	-0.2	100.3
	95 / 13 .	Host	62.5	98.4	41.2	0.1	38.8	0.3	0.0	0.4	0.2	19.2	0.0	100.1
	95 / 14 .	Host	60.5	106.6	40.2	0.0	38.6	0.3	0.0	0.4	0.1	20.4	0.1	100.1
	95 / 15 .	Host	60.4	114.8	40.2	0.1	38.9	0.3	0.0	0.3	0.2	20.5	0.2	100.8
	95 / 16 .	Host	59.8	123.0	39.7	0.0	38.7	0.3	0.0	0.3	0.2	20.7	0.0	100.0
	95 / 17 .	Host	56.7	131.2	38.1	0.1	38.4	0.3	0.0	0.4	0.2	22.6	0.1	100.2

	95 / 18 .	Host	52.6	139.4	36.0	0.1	37.7	0.3	0.0	0.4	0.3	25.2	0.1	100.0
	95 / 19 .	Host	48.9	147.6	34.3	0.1	37.1	0.3	0.0	0.3	0.2	27.8	-0.1	100.2
	95 / 20 .	Host	42.0	155.8	30.0	0.0	36.4	0.4	0.0	0.2	0.3	32.2	0.2	99.9
Pr4	96 / 1 .	Host	46.9	0.0	33.5	0.0	37.2	0.4	0.0	0.4	0.2	29.4	-0.1	101.1
	96 / 2 .	Host	46.6	8.8	32.6	0.0	36.6	0.4	0.0	0.2	0.2	29.0	0.1	99.2
	96 / 3 .	Host	46.8	17.6	32.8	0.0	36.9	0.4	0.0	0.1	0.3	29.0	0.0	99.5
	96 / 4 .	Host	46.5	26.4	32.5	0.1	36.7	0.4	0.0	0.2	0.3	29.1	-0.1	99.3
	96 / 5 .	Host	46.4	0.0	33.2	0.0	37.2	0.3	0.0	0.3	0.3	29.8	0.1	101.2
	96 / 6 .	Host	48.1	8.8	34.1	0.0	37.5	0.3	0.0	0.3	0.3	28.6	-0.1	101.1
	96 / 7 .	Host	48.3	17.6	33.8	0.0	37.4	0.3	0.0	0.2	0.2	28.1	-0.1	100.0
	96 / 8 .	Host	47.1	26.4	32.9	0.1	37.0	0.4	0.0	0.2	0.2	28.6	0.2	99.5
	96 / 9 .	Host	42.3	35.2	30.0	0.1	36.4	0.5	0.0	0.4	0.3	31.8	0.3	99.7
	96 / 10 .	Host	46.7	0.0	32.8	0.0	37.2	0.4	0.0	0.3	0.3	29.1	0.0	100.1
	96 / 11 .	Host	46.4	8.8	32.7	0.1	37.1	0.4	0.0	0.4	0.3	29.3	0.1	100.5
	96 / 12 .	Host	44.2	17.6	31.2	0.1	35.4	0.8	0.0	0.6	0.2	30.5	0.7	99.4
	96 / 13 .	Host	49.7	26.4	34.3	0.1	37.4	0.3	0.0	0.3	0.2	27.0	0.1	99.7
	96 / 14 .	Host	50.4	35.2	34.9	0.1	37.6	0.3	0.0	0.2	0.3	26.6	-0.1	99.9
	96 / 15 .	Host	50.5	44.0	34.9	0.1	37.2	0.3	0.0	0.4	0.2	26.5	0.1	99.6
	96 / 16 .	Host	49.9	52.8	34.6	0.1	37.5	0.3	0.0	0.4	0.2	27.0	0.1	100.2
	96 / 17 .	Host	49.5	61.6	34.3	0.1	37.5	0.3	0.0	0.4	0.2	27.2	0.1	100.2
	96 / 18 .	Host	48.4	70.4	33.8	0.1	36.7	0.3	0.0	0.4	0.2	28.0	0.2	99.8
	96 / 19 .	Host	47.1	79.2	33.7	0.1	37.2	0.4	0.0	0.3	0.3	29.4	0.2	101.5
	96 / 20 .	Host	40.5	88.0	29.7	0.2	35.9	0.5	0.0	0.8	0.3	33.8	0.0	101.0
Pr5	97 / 1 .	Host	45.0	0.0	32.1	0.0	36.1	0.4	0.1	0.3	0.2	30.4	0.1	99.7
	97 / 2 .	Host	46.5	7.6	32.8	0.1	36.9	0.3	0.0	0.3	0.2	29.3	0.2	100.2
	97 / 3 .	Host	46.8	15.2	32.8	0.1	37.4	0.3	0.0	0.5	0.3	28.9	0.1	100.3
	97 / 4 .	Host	46.1	22.8	32.4	0.0	37.0	0.3	0.0	0.2	0.2	29.3	0.1	99.6
	97 / 5 .	Host	46.2	30.4	32.2	0.0	38.1	0.4	0.0	0.3	0.3	29.1	-0.2	100.4

	97 / 6 .	Host	47.1	38.0	33.5	0.1	36.5	0.4	0.0	0.3	0.2	29.1	0.2	100.3
	97 / 7 .	Host	47.0	45.6	33.4	0.1	37.3	0.3	0.0	0.2	0.2	29.3	0.0	100.9
	97 / 8 .	Host	47.2	53.2	33.6	0.1	37.4	0.4	0.0	0.3	0.3	29.2	0.0	101.2
	97 / 9 .	Host	47.5	60.8	33.2	0.1	36.8	0.4	0.0	0.3	0.3	28.5	-0.1	99.6
	97 / 10 .	Host	47.3	68.4	33.2	0.1	37.1	0.3	0.0	0.2	0.3	28.7	-0.1	99.9
	97 / 11 .	Host	47.1	76.0	33.0	0.0	37.0	0.4	0.0	0.2	0.3	28.7	0.1	99.7
	97 / 12 .	Host	46.4	83.6	32.6	0.0	37.0	0.3	0.0	0.3	0.3	29.2	0.1	99.9
	97 / 13 .	Host	46.5	91.2	32.9	0.0	37.6	0.3	0.0	0.3	0.3	29.4	0.0	100.7
	97 / 14 .	Host	47.3	98.8	33.1	0.1	37.0	0.4	0.0	0.3	0.2	28.6	-0.1	99.7
	97 / 15 .	Host	47.6	114.0	33.2	0.1	37.2	0.4	0.0	0.4	0.2	28.4	0.2	100.0
Pr6	98 / 1 .	Host	45.4	0.0	32.0	0.0	36.5	0.3	0.0	0.3	0.2	29.9	-0.1	99.1
	98 / 2 .	Host	52.2	7.3	35.6	0.3	37.6	0.3	0.0	0.4	0.2	25.3	0.0	99.8
	98 / 3 .	Host	63.4	14.6	41.6	0.2	39.1	0.3	0.0	0.2	0.1	18.6	0.1	100.2
	98 / 5 .	Relict	97.2	21.9	56.4	0.2	42.4	0.5	0.1	0.1	0.0	1.3	0.1	101.1
	98 / 6 .	Relict	79.6	29.2	48.4	0.1	40.8	0.3	0.0	0.2	0.1	9.6	0.0	99.7
	98 / 7 .	Host	60.6	36.5	40.1	0.2	38.5	0.3	0.0	0.3	0.2	20.2	0.2	100.0
	98 / 8 .	Host	52.1	43.8	36.1	0.1	36.8	0.8	0.0	0.2	0.2	25.7	0.1	100.0
Pr7	99 / 2 .	Host	45.6	7.9	32.2	0.0	36.5	0.4	0.0	0.2	0.3	29.8	0.1	99.5
	99 / 3 .	Host	40.0	15.7	29.0	0.1	35.9	0.5	0.0	0.1	0.3	33.7	0.1	99.7
	99 / 4 .	Relict	71.6	0.0	45.3	0.1	40.4	0.3	0.1	0.4	0.2	13.9	0.0	100.6
	99 / 5 .	Relict	97.2	7.9	56.1	0.1	42.6	0.3	0.1	0.3	0.1	1.3	0.0	101.0
	99 / 6 .	Relict	97.2	15.7	56.2	0.3	43.0	0.5	0.2	0.5	0.1	1.3	0.0	102.2
	99 / 7 .	Relict	84.0	23.6	51.8	0.1	41.4	0.3	0.1	0.4	0.1	7.6	0.2	102.0
	99 / 8 .	Relict	66.9	31.4	44.0	0.1	39.9	0.3	0.0	0.3	0.2	16.9	0.0	101.8
	99 / 9 .	Relict	86.9	39.3	52.7	0.1	42.1	0.3	0.1	0.4	0.1	6.2	0.1	102.0
	99 / 10 .	Host	50.6	47.2	34.9	0.1	37.8	0.4	0.0	0.4	0.2	26.5	0.0	100.4
Pr8	100 / 1 .	Host	44.4	0.0	32.2	0.0	36.8	0.3	0.0	0.2	0.3	31.2	0.1	101.3
	100 / 2 .	Host	47.1	6.9	32.8	0.3	37.0	0.6	0.0	0.5	0.2	28.5	0.2	100.3

		100 / 5 .	Relict	95.2	27.5	56.3	0.1	42.2	0.4	0.1	0.3	0.0	2.2	0.0	101.7
		100 / 6 .	Relict	93.6	34.4	55.8	0.2	42.2	0.4	0.1	0.4	0.0	3.0	0.1	102.2
		100 / 7 .	Host	58.8	41.3	39.6	0.1	38.7	0.3	0.0	0.3	0.2	21.6	0.0	100.8
	Pr9	101 / 2 .	Host	57.0	7.0	38.1	0.4	37.9	0.3	0.1	1.0	0.1	22.3	0.0	100.3
		101 / 3 .	Relict	81.9	14.0	50.0	0.1	41.4	0.3	0.0	0.2	0.1	8.6	-0.1	100.6
		101 / 4 .	Relict	91.8	21.0	54.2	0.0	42.5	0.2	0.0	0.3	0.1	3.7	0.0	101.2
		101 / 5 .	Relict	90.2	28.0	53.4	0.0	41.9	0.2	0.0	0.3	0.1	4.5	0.0	100.5
		101 / 6 .	Relict	86.0	35.0	51.8	0.0	41.1	0.2	0.0	0.3	0.2	6.6	0.1	100.3
		101 / 7 .	Relict	70.5	42.0	44.4	0.1	40.0	0.3	0.0	0.3	0.1	14.4	0.0	99.6
		101 / 8 .	Host	47.0	49.0	33.1	0.1	36.6	0.3	0.0	0.2	0.3	29.0	-0.1	99.5
		101 / 9 .	Host	46.6	56.0	32.6	0.2	36.5	0.3	0.0	0.7	0.2	28.9	0.1	99.5
		101 / 10 .	Host	49.2	63.0	33.9	0.2	37.3	0.3	0.1	0.3	0.2	27.2	0.0	99.6
	Pr10	102 / 1 .	Host	46.0	0.0	32.5	0.1	36.7	0.3	0.0	0.2	0.3	29.6	0.1	99.7
		102 / 2 .	Host	53.5	7.5	36.5	0.2	37.6	0.4	0.0	0.4	0.2	24.6	0.0	99.9
		102 / 3 .	Relict	76.4	15.0	47.7	0.1	40.5	0.3	0.1	0.4	0.1	11.4	0.1	100.7
		102 / 4 .	Relict	87.7	22.5	52.5	0.1	41.7	0.4	0.0	0.4	0.1	5.7	0.0	100.9
		102 / 5 .	Relict	83.6	30.0	50.7	0.1	41.2	0.3	0.1	0.3	0.1	7.7	0.0	100.5
		102 / 6 .	Relict	81.0	37.5	49.7	0.1	41.3	0.3	0.0	0.3	0.1	9.1	-0.1	100.9
		102 / 7 .	Relict	81.7	45.0	49.7	0.1	41.1	0.3	0.1	0.3	0.1	8.6	0.0	100.4
		102 / 8 .	Relict	90.8	52.5	53.4	0.1	41.8	0.4	0.1	0.4	0.1	4.2	0.1	100.6
		102 / 9 .	Relict	95.0	60.0	55.2	0.1	42.4	0.4	0.1	0.4	0.1	2.2	-0.1	100.9
		102 / 10 .	Relict	92.0	67.5	53.9	0.1	42.0	0.4	0.1	0.3	0.1	3.7	-0.1	100.6
		102 / 11 .	Relict	88.4	75.0	52.7	0.1	42.0	0.4	0.1	0.4	0.1	5.4	0.1	101.2
		102 / 12 .	Host	71.6	82.5	45.3	0.1	40.0	0.2	0.0	0.3	0.1	14.0	-0.1	100.0
		102 / 13 .	Host	57.0	90.0	38.9	0.0	38.6	0.3	0.0	0.3	0.2	22.7	0.2	101.4
		102 / 14 .	Host	51.0	97.5	35.6	0.0	38.2	0.4	0.0	0.4	0.2	26.6	0.1	101.4
		102 / 15 .	Host	49.0	105.0	34.3	0.0	37.3	0.4	0.0	0.3	0.3	27.7	-0.1	100.3
Ch_12	Pr1	103 / 2 .	Host	42.6	7.2	29.6	0.5	33.5	0.4	0.0	2.0	0.1	30.9	0.6	97.8

		103 / 3 .	Host	59.6	14.4	39.4	0.1	37.8	0.3	0.0	0.3	0.1	20.7	0.0	98.9
		103 / 5 .	Host	70.1	28.8	44.8	0.2	39.7	0.2	0.0	0.4	0.1	14.8	0.1	100.3
		103 / 6 .	Host	68.6	36.0	44.8	0.1	40.2	0.2	0.0	0.3	0.1	15.9	0.2	101.7
		103 / 8 .	Host	68.1	50.4	44.4	0.1	39.8	0.2	0.0	0.4	0.1	16.2	-0.1	101.2
		103 / 9 .	Host	67.4	57.6	44.0	0.1	39.8	0.2	0.0	0.3	0.2	16.5	-0.1	101.1
		103 / 10 .	Host	66.2	64.8	43.3	0.1	39.7	0.4	0.0	0.2	0.2	17.2	0.1	101.2
		103 / 11 .	Host	64.6	72.0	42.1	0.2	38.6	0.6	0.0	0.4	0.2	17.9	0.1	100.0
		103 / 12 .	Host	66.0	79.2	41.1	0.1	38.0	2.0	0.0	0.3	0.2	16.4	0.1	98.4
		103 / 15 .	Host	65.6	100.8	42.4	0.2	39.0	0.2	0.0	0.4	0.1	17.3	0.2	99.8
		103 / 16 .	Host	64.9	108.0	42.3	0.2	39.1	0.2	0.0	0.5	0.2	17.7	-0.1	100.2
		103 / 17 .	Host	64.5	115.2	41.9	0.2	38.9	0.2	0.0	0.4	0.1	17.9	0.1	99.9
		103 / 18 .	Host	63.2	122.4	41.2	0.2	38.6	0.2	0.0	0.5	0.2	18.6	0.0	99.5
		103 / 19 .	Host	57.7	129.6	38.6	0.2	38.7	0.3	0.0	0.4	0.1	22.0	0.1	100.4
		103 / 20 .	Host	47.1	136.8	33.0	0.1	36.6	0.4	0.0	0.2	0.2	28.7	0.1	99.3
	Pr2	104 / 1 .	Host	49.7	0.0	34.6	0.1	37.2	0.3	0.0	0.2	0.3	27.2	0.2	100.1
		104 / 2 .	Relict	78.1	5.1	47.3	0.1	39.1	1.8	0.0	0.3	0.1	10.3	0.2	99.1
		104 / 3 .	Relict	96.9	10.2	56.3	0.1	43.0	0.4	0.0	0.3	0.1	1.4	-0.1	101.6
		104 / 5 .	Relict	97.6	20.4	56.1	0.1	42.3	0.4	0.1	0.3	0.1	1.1	0.1	100.5
		104 / 6 .	Relict	97.6	25.5	56.3	0.1	42.7	0.4	0.0	0.4	0.1	1.1	-0.1	101.0
		104 / 7 .	Relict	97.7	30.6	56.3	0.1	42.7	0.4	0.0	0.3	0.1	1.0	0.0	100.9
		104 / 8 .	Relict	97.5	35.7	56.2	0.1	42.4	0.4	0.0	0.3	0.0	1.1	-0.1	100.5
		104 / 9 .	Relict	97.4	40.8	56.1	0.1	42.5	0.4	0.0	0.3	0.0	1.2	0.0	100.6
		104 / 11 .	Relict	97.2	51.0	56.2	0.1	42.3	0.3	0.0	0.4	0.1	1.3	-0.1	100.6
		104 / 12 .	Relict	90.0	56.1	53.3	0.1	42.3	0.3	0.0	0.2	0.1	4.6	0.1	100.9
		104 / 13 .	Relict	60.8	61.2	39.9	0.2	38.0	0.3	0.0	0.7	0.2	19.9	0.0	99.3
		104 / 14 .	Host	45.0	66.3	31.6	0.3	36.6	0.4	0.0	0.7	0.3	30.0	0.1	100.1
		104 / 15 .	Host	40.9	71.4	29.6	0.3	34.7	0.5	0.0	0.5	0.2	33.3	0.2	99.4
	Pr3	105 / 1 .	Host	54.1	0.0	37.0	0.0	37.6	0.2	0.0	0.3	0.2	24.3	0.0	99.7

		105 / 2 .	Host	67.5	7.6	43.5	0.1	39.3	0.2	0.0	0.4	0.1	16.2	0.0	99.8
		105 / 3 .	Host	60.2	15.2	40.3	0.4	37.5	0.2	0.0	0.4	0.1	20.6	0.6	100.1
		105 / 5 .	Host	69.7	30.3	44.4	0.1	39.9	0.2	0.0	0.3	0.1	15.0	0.0	100.0
		105 / 6 .	Host	66.0	0.0	42.8	0.1	38.9	0.2	0.0	0.4	0.1	17.1	0.1	99.9
		105 / 7 .	Host	65.7	7.6	42.7	0.0	39.2	0.2	0.0	0.3	0.2	17.3	0.0	99.9
		105 / 8 .	Host	54.3	15.2	37.0	0.1	37.8	0.2	0.0	0.2	0.2	24.1	0.0	99.6
		105 / 11 .	Host	53.4	37.9	37.0	0.1	38.0	0.3	0.0	0.3	0.2	25.1	0.0	100.9
		105 / 12 .	Host	61.6	45.5	41.4	0.1	39.4	0.2	0.0	0.3	0.2	20.0	0.2	101.8
		105 / 13 .	Host	62.1	53.1	41.5	0.1	39.0	0.2	0.0	0.3	0.1	19.6	0.0	100.8
		105 / 14 .	Host	56.9	60.6	38.2	0.0	38.5	0.3	0.0	0.3	0.2	22.5	0.1	100.1
		105 / 15 .	Host	38.4	68.2	27.0	0.1	35.9	1.1	0.0	0.3	0.4	33.5	0.1	98.3
	Pr4	106 / 2 .	Host	35.8	5.4	26.2	0.0	35.5	0.5	0.0	0.2	0.3	36.5	0.1	99.3
		106 / 3 .	Host	44.6	10.9	31.8	0.0	36.6	0.3	0.0	0.2	0.3	30.6	-0.2	99.8
		106 / 5 .	Host	40.1	21.8	28.4	0.1	35.1	0.9	0.0	0.1	0.3	32.9	0.2	98.0
		106 / 8 .	Host	37.4	38.1	27.3	0.1	35.3	0.5	0.0	0.2	0.3	35.5	0.2	99.3
	Pr5	107 / 1 .	Host	28.6	0.0	21.8	0.1	33.9	0.7	0.0	0.2	0.4	42.4	0.0	99.6
		107 / 5 .	Host	66.8	33.6	42.3	0.1	37.3	1.5	0.0	0.4	0.1	16.3	0.1	98.0
		107 / 6 .	Relict	82.2	42.0	50.0	0.0	41.3	0.2	0.0	0.4	0.1	8.4	0.0	100.5
		107 / 7 .	Relict	77.4	50.4	46.6	0.0	41.5	0.6	0.0	0.1	0.1	10.6	0.1	99.6
		107 / 8 .	Relict	87.6	58.8	52.7	0.0	41.9	0.1	0.0	0.4	0.2	5.8	0.0	101.1
		107 / 9 .	Relict	72.3	67.2	46.1	0.1	39.9	0.2	0.0	0.3	0.1	13.7	0.1	100.4
		107 / 10 .	Relict	55.7	75.6	37.9	0.0	38.4	0.4	0.0	0.3	0.2	23.4	0.0	100.5
	Pr6	108 / 1 .	Host	28.4	0.0	21.4	0.3	33.3	1.2	0.1	0.2	0.4	41.9	0.4	99.2
		108 / 3 .	Relict	94.4	12.0	54.8	0.2	42.6	0.4	0.1	0.4	0.0	2.5	0.1	101.2
		108 / 4 .	Relict	96.8	18.0	56.1	0.1	42.7	0.4	0.1	0.3	0.0	1.4	0.1	101.1
		108 / 5 .	Relict	96.9	24.0	56.2	0.1	42.5	0.3	0.1	0.3	0.1	1.4	0.0	101.0
		108 / 6 .	Relict	96.5	30.0	56.1	0.1	42.3	0.3	0.1	0.3	0.1	1.6	0.1	100.9
		108 / 8 .	Relict	85.9	42.0	53.3	0.1	41.6	0.3	0.0	0.3	0.0	6.8	0.0	102.4

	Pr7	109 / 1 .	Host	40.6	0.0	29.1	0.1	36.0	0.4	0.0	0.2	0.3	33.0	0.2	99.1
		109 / 2 .	Host	43.9	6.0	31.3	0.1	36.5	0.3	0.0	0.2	0.3	31.0	0.1	99.8
		109 / 3 .	Host	44.7	12.0	31.6	0.1	37.2	0.3	0.0	0.2	0.3	30.3	0.1	100.0
		109 / 4 .	Host	48.5	18.0	33.9	0.1	37.0	0.3	0.0	0.3	0.2	27.9	0.0	99.7
		109 / 5 .	Host	48.7	24.0	33.1	0.6	37.4	0.6	0.0	0.2	0.3	27.0	0.2	99.4
		109 / 6 .	Host	49.7	30.0	34.4	0.1	36.8	0.2	0.0	0.2	0.3	26.9	0.0	98.9
		109 / 7 .	Host	49.5	36.0	34.2	0.1	37.0	0.3	0.0	0.3	0.2	27.1	0.0	99.1
Ch_03	Pr1	110 / 2 .	Host	40.5	7.3	29.1	0.0	35.7	0.5	0.0	0.2	0.3	33.1	-0.1	99.0
		110 / 3 .	Host	42.6	14.6	30.4	0.1	36.7	0.4	0.0	0.2	0.4	31.7	0.0	99.8
		110 / 4 .	Host	44.8	21.9	31.9	0.1	36.6	0.4	0.0	0.3	0.3	30.5	0.2	100.2
		110 / 5 .	Host	42.5	29.2	29.3	0.5	35.5	0.4	0.0	1.6	0.2	30.7	0.4	98.7
		110 / 6 .	Host	46.1	36.5	32.3	0.0	37.2	0.4	0.0	0.3	0.2	29.3	0.0	99.8
		110 / 7 .	Host	43.8	43.8	31.2	0.1	36.1	0.4	0.0	0.2	0.3	31.1	-0.1	99.4
		110 / 8 .	Host	40.7	51.1	29.1	0.1	35.5	0.6	0.0	0.2	0.3	32.9	0.0	98.7
	Pr2	111 / 1 .	Host	55.7	0.0	38.1	0.0	37.5	0.3	0.0	0.2	0.3	23.5	0.1	100.1
		111 / 2 .	Relict	76.6	5.9	47.8	0.0	40.8	0.2	0.0	0.4	0.1	11.3	-0.1	100.6
		111 / 3 .	Relict	85.6	11.8	51.3	0.0	40.8	0.2	0.0	0.4	0.2	6.7	0.0	99.6
		111 / 4 .	Host	53.6	17.7	36.1	0.1	37.8	0.4	0.0	0.4	0.2	24.3	0.0	99.3
		111 / 6 .	Host	42.3	23.6	30.2	0.0	36.0	0.4	0.0	0.2	0.3	32.0	0.1	99.3
		111 / 7 .	Host	43.5	29.5	30.9	0.0	36.1	0.4	0.0	0.1	0.4	31.2	0.2	99.3
		111 / 8 .	Host	44.7	0.0	31.3	0.0	36.3	0.4	0.0	0.1	0.2	30.1	0.1	98.6
		111 / 10 .	Host	44.4	5.9	31.5	0.0	36.3	0.4	0.0	0.2	0.3	30.6	-0.1	99.3
		111 / 11 .	Host	42.8	11.8	30.5	0.0	35.7	0.5	0.0	0.2	0.3	31.6	0.1	98.8
		111 / 12 .	Host	36.8	17.7	26.3	0.5	36.2	1.7	0.2	0.1	0.3	35.0	0.1	100.4
	Pr3	112 / 2 .	Host	59.5	6.8	39.4	0.0	38.5	0.3	0.0	0.2	0.2	20.8	0.2	99.7
		112 / 3 .	Relict	68.9	13.6	45.1	0.0	39.2	0.2	0.0	0.2	0.1	15.8	0.2	100.9
		112 / 5 .	Relict	71.8	20.4	44.5	0.0	38.5	1.0	0.0	0.3	0.2	13.6	0.2	98.3
		112 / 7 .	Host	55.6	27.2	37.4	0.0	38.0	0.3	0.0	0.2	0.2	23.2	0.1	99.4

	112 / 8 .	Host	44.4	34.0	31.5	0.0	36.7	0.5	0.0	0.1	0.3	30.6	0.1	99.7
Pr4	113 / 1 .	Host	36.8	0.0	27.2	0.0	34.7	0.5	0.0	0.1	0.4	36.2	0.1	99.4
	113 / 2 .	Host	42.7	5.9	30.4	0.0	36.2	0.6	0.0	0.2	0.3	31.6	0.0	99.4
	113 / 3 .	Host	50.3	11.8	34.6	0.0	36.8	0.5	0.0	0.2	0.2	26.5	-0.1	99.0
	113 / 4 .	Relict	73.3	17.7	46.2	0.1	40.0	0.3	0.0	0.3	0.1	13.0	0.2	100.2
	113 / 5 .	Relict	67.3	23.6	43.7	0.0	39.4	0.3	0.0	0.2	0.1	16.5	0.1	100.3
	113 / 6 .	Relict	67.2	29.5	43.6	0.1	39.3	0.3	0.0	0.1	0.1	16.5	0.0	100.1
	113 / 7 .	Relict	72.2	35.4	46.0	0.0	39.8	0.2	0.0	0.2	0.1	13.8	-0.1	100.2
	113 / 8 .	Host	64.0	41.3	42.3	0.0	38.5	0.4	0.0	0.3	0.1	18.5	-0.1	100.2
	113 / 9 .	Host	53.9	47.2	36.8	0.0	37.8	0.5	0.0	0.2	0.3	24.4	0.0	100.2
	113 / 10 .	Host	47.0	53.1	32.1	1.9	35.6	0.5	0.1	1.9	0.1	28.1	0.0	100.3
Pr5	114 / 2 .	Host	40.8	5.3	29.3	0.0	36.1	0.4	0.0	0.1	0.3	32.9	0.0	99.1
	114 / 3 .	Host	43.2	10.6	30.8	0.0	36.5	0.4	0.0	0.1	0.2	31.4	0.2	99.7
	114 / 4 .	Host	44.2	15.9	31.4	0.0	36.4	0.4	0.0	0.2	0.3	30.8	0.0	99.6
	114 / 5 .	Host	44.5	21.2	31.5	0.0	36.7	0.4	0.0	0.2	0.3	30.5	0.1	99.7
	114 / 6 .	Host	44.1	26.5	31.2	0.0	36.4	0.4	0.0	0.1	0.3	30.7	0.0	99.2
	114 / 7 .	Host	44.7	31.8	31.6	0.0	36.7	0.4	0.0	0.2	0.3	30.3	0.2	99.8
	114 / 8 .	Host	44.8	37.1	31.8	0.0	36.4	0.4	0.0	0.2	0.3	30.4	0.2	99.7
Pr6	115 / 2 .	Host	43.8	5.7	31.1	0.1	36.5	0.4	0.0	0.2	0.3	31.0	0.0	99.6
	115 / 3 .	Host	44.9	11.4	31.8	0.0	36.2	0.4	0.0	0.2	0.3	30.3	0.0	99.3
	115 / 5 .	Host	45.1	22.8	31.6	0.1	36.9	0.5	0.0	0.4	0.3	29.9	0.1	99.9
	115 / 6 .	Host	45.2	28.5	32.1	0.0	36.6	0.4	0.0	0.2	0.3	30.2	0.1	99.9
	115 / 7 .	Host	44.8	34.2	31.6	0.1	36.3	0.5	0.0	0.2	0.2	30.3	0.0	99.1
	115 / 8 .	Host	43.9	39.9	30.9	0.1	36.5	0.7	0.0	0.4	0.2	30.6	0.0	99.7
	115 / 9 .	Host	44.6	45.6	31.5	0.1	36.7	0.4	0.0	0.2	0.2	30.4	0.0	99.6
	115 / 10 .	Host	43.2	51.3	31.0	0.0	36.6	0.4	0.0	0.2	0.3	31.6	0.2	100.2
Pr7	116 / 1 .	Host	45.3	0.0	31.9	0.0	36.9	0.6	0.0	0.2	0.3	29.8	0.0	99.7
	116 / 2 .	Host	62.1	5.2	40.8	0.1	38.7	0.3	0.0	0.2	0.2	19.3	0.0	99.7

		116 / 3 .	Host	46.7	10.3	32.7	0.0	37.0	0.6	0.0	0.2	0.2	28.9	0.1	99.7
		116 / 4 .	Host	37.2	15.5	26.7	1.0	36.1	0.9	0.0	0.1	0.3	35.0	0.0	100.1
	Pr8	117 / 1 .	Host	36.3		25.4	1.3	37.5	1.2	0.1	0.1	0.3	34.6	0.3	100.9
		117 / 5 .	Host	45.8		31.4	0.0	36.2	0.5	0.0	0.2	0.3	28.9	0.2	97.8
		117 / 6 .	Host	41.6		29.1	0.0	35.9	0.5	0.0	0.2	0.4	31.7	0.1	97.9
	Pr9	118 / 1 .	Host	41.7	0.0	29.7	0.0	36.5	0.5	0.0	0.1	0.3	32.3	0.2	99.7
		118 / 2 .	Host	41.9	4.0	30.0	0.0	36.0	0.6	0.0	0.2	0.3	32.3	0.0	99.3
		118 / 3 .	Host	40.0	8.0	28.9	0.1	36.1	0.6	0.0	0.2	0.3	33.6	0.0	99.7
		118 / 4 .	Host	35.4	12.0	25.8	0.3	35.4	0.7	0.0	0.1	0.3	36.6	0.0	99.5
Ch_10	Pr1	119 / 1 .	Relict	95.0	0.0	53.9	0.0	42.1	0.2	0.0	1.0	0.0	2.2	0.1	99.5
		119 / 2 .	Relict	78.0	5.2	46.3	0.1	40.3	0.2	0.0	1.9	0.0	10.1	0.0	99.1
		119 / 3 .	Relict	82.1	10.5	47.8	0.2	41.0	0.3	0.1	1.4	0.0	8.1	0.0	98.8
		119 / 4 .	Relict	96.7	15.7	55.6	0.2	42.8	0.4	0.0	0.6	0.0	1.5	0.1	101.2
		119 / 5 .	Relict	97.6	21.0	55.8	0.2	42.7	0.5	0.1	0.1	0.0	1.1	0.2	100.6
		119 / 6 .	Relict	97.9	26.2	55.8	0.2	42.6	0.5	0.1	0.1	0.0	0.9	0.2	100.3
		119 / 7 .	Relict	98.1	31.4	55.8	0.2	42.3	0.5	0.1	0.1	0.0	0.8	-0.1	99.8
		119 / 8 .	Relict	97.9	36.7	55.9	0.2	42.4	0.5	0.1	0.1	0.1	0.9	0.1	100.3
		119 / 9 .	Relict	97.3	41.9	55.3	0.1	42.6	0.3	0.0	0.2	0.0	1.2	0.1	99.8
		119 / 10 .	Relict	87.0	47.2	50.9	0.0	41.2	0.2	0.0	0.2	0.0	5.9	0.0	98.6
	Pr2	120 / 2 .	Host	42.3	6.2	29.9	0.0	35.4	0.5	0.0	0.2	0.2	31.7	0.1	98.1
		120 / 3 .	Host	42.3	12.4	29.9	0.1	35.7	0.5	0.0	0.2	0.2	31.6	0.1	98.3
		120 / 4 .	Host	42.3	18.6	29.9	0.0	35.7	0.5	0.0	0.2	0.3	31.6	0.0	98.2
		120 / 5 .	Host	42.3	24.8	29.8	0.0	35.9	0.5	0.0	0.2	0.3	31.6	0.0	98.3
	Pr3	121 / 3 .	Host	38.4	11.8	28.2	0.1	35.2	0.5	0.0	0.2	0.3	35.1	0.0	99.6
		121 / 5 .	Host	42.3	23.6	29.8	0.1	36.0	0.3	0.0	0.3	0.2	31.5	0.2	98.4
		121 / 6 .	Host	42.3	29.5	29.8	0.1	36.0	0.3	0.0	0.3	0.3	31.5	0.1	98.3
		121 / 7 .	Host	38.2	35.4	27.5	0.0	35.5	0.4	0.0	0.2	0.2	34.5	0.2	98.6
		121 / 8 .	Host	33.2	41.3	23.4	1.3	35.7	0.9	0.1	0.3	0.3	36.5	0.2	98.6

	Pr4	122 / 2 .	Host	41.3	6.8	29.1	0.1	36.2	0.4	0.0	0.3	0.2	32.1	0.1	98.5
		122 / 3 .	Host	53.9	13.6	35.5	0.2	37.2	0.3	0.0	1.1	0.2	23.6	0.2	98.4
		122 / 4 .	Relict	84.8	20.4	50.3	0.0	41.3	0.2	0.0	0.5	0.2	7.0	0.1	99.7
		122 / 5 .	Relict	86.6	27.2	50.8	0.0	41.0	0.2	0.0	0.5	0.2	6.1	0.0	98.7
		122 / 6 .	Host	63.3	34.0	41.4	0.0	39.1	0.2	0.0	0.2	0.1	18.6	0.0	99.7
	Pr5	123 / 1 .	Host	43.1	0.0	30.3	0.1	36.1	0.3	0.0	0.3	0.2	31.0	0.0	98.2
		123 / 2 .	Host	47.0	5.2	32.3	0.1	37.3	0.3	0.0	0.4	0.2	28.3	0.1	98.8
		123 / 3 .	Host	40.3	10.4	28.9	0.0	35.9	0.3	0.0	0.2	0.3	33.3	0.1	99.1
	Pr6	124 / 2 .	Host	33.8	2.5	24.4	1.5	33.7	0.5	0.0	1.3	0.3	37.2	-0.1	98.9
		124 / 3 .	Host	39.7	5.0	28.3	0.0	36.1	0.5	0.0	0.1	0.2	33.4	0.0	98.7
		124 / 4 .	Host	44.5	0.0	31.2	0.0	36.4	0.5	0.0	0.1	0.2	30.2	0.1	98.7
		124 / 5 .	Relict	73.0	2.5	44.9	0.1	40.1	0.3	0.0	0.1	0.1	12.9	0.0	98.5
		124 / 6 .	Relict	90.9	5.0	53.4	0.1	41.9	0.4	0.1	0.1	0.0	4.2	0.0	100.1
		124 / 7 .	Host	55.6	7.5	37.5	0.1	38.0	0.4	0.0	0.2	0.2	23.3	0.0	99.7
		124 / 8 .	Host	43.9	10.0	30.7	0.6	35.3	0.4	0.1	0.7	0.2	30.4	0.1	98.5
		124 / 9 .	Host	39.3	12.5	27.9	0.6	35.2	0.6	0.0	0.8	0.3	33.4	0.0	98.8
		124 / 10 .	Host	34.1	15.0	24.3	1.1	34.6	0.9	0.0	0.2	0.2	36.4	0.1	97.7
Ch_11	Pr1	126 / 2 .	Host	38.9	5.6	27.7	0.0	35.2	0.3	0.0	0.3	0.4	33.8	0.0	97.8
		126 / 3 .	Host	55.9	11.1	37.4	0.0	38.4	0.2	0.0	0.2	0.2	22.9	0.2	99.5
		126 / 4 .	Relict	70.3	16.7	44.8	0.1	38.8	0.2	0.1	0.2	0.1	14.7	0.2	99.1
		126 / 5 .	Relict	90.7	22.2	53.3	0.1	41.6	0.3	0.1	0.3	0.1	4.3	0.0	100.0
		126 / 6 .	Relict	90.2	27.8	53.0	0.1	41.6	0.3	0.1	0.3	0.1	4.5	0.1	100.1
		126 / 7 .	Relict	96.0	33.4	54.9	0.1	41.4	0.3	0.1	0.3	0.1	1.8	0.0	98.9
		126 / 8 .	Relict	95.4	38.9	54.7	0.1	41.7	0.2	0.0	0.4	0.1	2.1	0.0	99.4
		126 / 9 .	Relict	87.4	44.5	51.2	0.1	41.3	0.2	0.0	0.3	0.1	5.7	0.1	99.1
		126 / 12 .	Relict	63.5	61.2	40.9	0.0	38.5	0.2	0.0	0.1	0.2	18.3	0.0	98.3
	Pr2	127 / 1 .	Host	24.6	0.0	18.8	0.0	33.8	0.3	0.0	0.2	0.5	44.7	0.1	98.3
		127 / 2 .	Host	25.0	10.8	19.2	0.0	33.8	0.2	0.0	0.2	0.5	44.8	0.1	98.9

	127 / 3 .	Host	25.4	21.6	19.4	0.0	33.9	0.2	0.0	0.2	0.5	44.1	0.1	98.4
	127 / 4 .	Host	26.0	32.4	19.7	0.0	33.8	0.2	0.0	0.3	0.4	43.5	0.0	98.0
	127 / 7 .	Host	26.1	64.8	19.8	0.0	33.6	0.2	0.0	0.3	0.5	43.6	0.0	98.0
	127 / 8 .	Host	26.0	75.6	19.7	0.0	34.1	0.3	0.0	0.3	0.4	43.5	-0.1	98.3
	127 / 9 .	Host	26.0	86.4	19.8	0.0	34.1	0.2	0.0	0.2	0.5	43.7	0.0	98.6
	127 / 10 .	Host	26.7	97.2	20.2	0.0	34.2	0.3	0.0	0.2	0.6	42.8	0.1	98.2
	127 / 11 .	Host	26.4	108.0	20.0	0.0	34.3	0.3	0.0	0.2	0.4	43.3	0.1	98.6
	127 / 12 .	Host	27.0	118.8	20.5	0.0	34.0	0.2	0.0	0.1	0.5	42.9	0.0	98.4
	127 / 13 .	Host	26.9	129.6	20.5	0.0	33.9	0.2	0.0	0.2	0.5	43.2	0.2	98.6
	127 / 14 .	Host	26.5	140.4	20.1	0.0	33.8	0.3	0.0	0.1	0.4	43.3	-0.2	98.1
	127 / 15 .	Host	25.9	151.2	19.7	0.0	33.8	0.3	0.0	0.1	0.5	43.6	0.1	98.0
Pr3	128 / 1 .	Host	26.0	0.0	19.8	0.0	33.9	0.2	0.0	0.1	0.5	43.8	0.0	98.4
	128 / 2 .	Host	27.1	8.4	20.6	0.0	33.7	0.2	0.0	0.0	0.4	43.0	0.0	97.9
	128 / 3 .	Host	28.2	16.8	21.2	0.0	34.0	0.1	0.0	0.1	0.4	41.9	0.1	97.9
	128 / 4 .	Host	28.1	25.2	21.2	0.0	33.8	0.1	0.0	0.1	0.4	42.1	0.1	97.8
	128 / 5 .	Host	29.6	33.6	22.2	0.0	34.1	0.1	0.0	0.3	0.4	40.9	0.0	98.0
	128 / 6 .	Host	29.9	42.0	22.3	0.0	34.2	0.1	0.0	0.2	0.5	40.5	0.0	97.8
	128 / 7 .	Host	29.9	50.4	22.4	0.0	34.4	0.1	0.0	0.2	0.4	40.8	0.0	98.3
	128 / 8 .	Host	30.5	58.8	22.8	0.0	34.5	0.1	0.0	0.2	0.4	40.3	-0.1	98.4
	128 / 9 .	Host	30.7	67.2	23.1	0.0	34.7	0.1	0.0	0.2	0.4	40.3	-0.1	98.8
	128 / 10 .	Host	32.1	75.6	23.7	0.0	34.7	0.1	0.0	0.4	0.3	38.8	0.2	98.2
	128 / 12 .	Host	34.0	92.4	24.9	0.0	34.7	0.1	0.0	0.5	0.3	37.4	0.2	98.2
	128 / 13 .	Host	34.0	100.8	24.9	0.0	35.5	0.1	0.0	0.6	0.4	37.5	0.1	99.0
	128 / 14 .	Host	33.3	109.2	24.6	0.0	35.3	0.1	0.0	0.2	0.4	38.3	-0.2	98.9
	128 / 15 .	Host	31.6	117.6	23.3	0.0	34.6	0.1	0.0	0.5	0.5	39.0	0.0	98.0
Pr4	129 / 1 .	Host	27.1	0.0	20.4	0.0	33.9	0.3	0.0	0.2	0.5	42.7	0.2	98.1
	129 / 2 .	Host	27.6	10.2	20.7	0.0	33.8	0.2	0.0	0.3	0.5	42.1	0.2	97.9
	129 / 3 .	Host	28.6	20.4	21.7	0.0	34.5	0.2	0.0	0.4	0.4	42.0	0.0	99.3

			129 / 4 .	Host	29.8	30.6	22.3	0.0	34.4	0.1	0.0	0.5	0.4	40.8	0.2	98.9
			129 / 5 .	Host	30.6	40.8	22.8	0.0	34.6	0.1	0.0	0.5	0.4	40.1	0.1	98.6
			129 / 6 .	Host	31.0	51.0	23.2	0.0	34.7	0.1	0.0	0.2	0.3	40.0	0.0	98.7
			129 / 7 .	Host	30.6	61.2	22.8	0.0	33.9	0.1	0.0	1.2	0.4	40.0	0.2	98.7
			129 / 8 .	Host	30.4	71.4	22.6	0.0	34.5	0.1	0.0	0.2	0.4	40.2	0.1	98.1
			129 / 9 .	Host	29.8	81.6	22.4	0.0	34.4	0.2	0.0	0.2	0.4	40.9	0.0	98.6
			129 / 11 .	Host	29.8	102.0	22.3	0.0	34.7	0.2	0.0	0.3	0.4	40.8	0.0	98.7
			129 / 12 .	Host	30.3	112.2	22.6	0.0	34.1	0.2	0.0	0.2	0.4	40.3	0.1	98.0
			129 / 13 .	Host	30.5	122.4	22.7	0.0	34.2	0.1	0.0	0.3	0.4	40.1	-0.1	97.7
			129 / 14 .	Host	30.5	132.6	22.6	0.0	34.7	0.1	0.0	0.6	0.4	39.9	0.1	98.4
			129 / 15 .	Host	30.5	142.8	22.8	0.0	35.0	0.1	0.0	0.3	0.3	40.3	0.1	99.1
		Pr5	130 / 1 .	Host	25.0	0.0	19.1	0.0	33.3	0.3	0.0	0.2	0.5	44.4	0.2	98.0
			130 / 2 .	Host	28.1	8.7	21.1	0.0	34.1	0.2	0.0	0.2	0.4	41.8	0.0	97.7
			130 / 3 .	Host	29.6	17.4	22.0	0.0	34.3	0.1	0.0	0.3	0.4	40.6	0.0	97.8
			130 / 4 .	Host	30.5	26.1	22.8	0.0	34.7	0.2	0.0	0.3	0.4	40.2	0.0	98.5
			130 / 5 .	Host	29.3	34.8	22.0	0.0	34.0	0.1	0.0	0.2	0.3	41.2	0.2	98.1
			130 / 6 .	Host	29.2	43.5	21.9	0.0	34.2	0.1	0.0	0.2	0.4	41.0	0.0	97.9
Cat008	Ch_02	Pr1	142 / 1 .	Host	57.1	0.0	38.7	0.0	38.8	0.1	0.0	0.2	0.1	22.6	0.1	100.6
			142 / 2 .	Host	61.6	9.0	40.8	0.1	39.3	0.1	0.0	0.2	0.1	19.7	0.0	100.3
			142 / 3 .	Host	63.9	18.0	42.0	0.1	39.1	0.1	0.0	0.2	0.2	18.4	0.0	100.1
			142 / 4 .	Host	65.2	27.0	42.8	0.0	39.7	0.1	0.0	0.2	0.1	17.7	0.1	100.7
			142 / 5 .	Host	66.1	36.0	43.2	0.0	39.4	0.1	0.0	0.2	0.2	17.2	0.2	100.5
			142 / 6 .	Host	66.8	45.0	43.3	0.0	40.1	0.1	0.0	0.2	0.2	16.7	0.0	100.6
			142 / 7 .	Host	67.4	54.0	43.6	0.0	39.6	0.1	0.0	0.2	0.2	16.4	0.1	100.3
			142 / 8 .	Host	67.6	63.0	43.6	0.0	39.6	0.1	0.0	0.1	0.1	16.3	0.1	99.9
			142 / 9 .	Host	66.0	72.0	43.2	0.0	40.2	0.1	0.0	0.1	0.1	17.2	-0.1	101.0
			142 / 10 .	Host	66.2	81.0	43.1	0.1	39.5	0.1	0.0	0.1	0.2	17.1	0.1	100.2
			142 / 11 .	Host	65.7	90.0	43.0	0.0	39.6	0.1	0.0	0.2	0.2	17.4	0.0	100.5

	142 / 12 .	Host	65.9	99.0	43.0	0.0	39.5	0.1	0.0	0.2	0.2	17.2	0.0	100.3
	142 / 13 .	Host	66.1	108.0	43.1	0.0	39.9	0.2	0.0	0.1	0.2	17.2	0.2	100.9
	142 / 14 .	Host	66.3	117.0	43.0	0.0	39.8	0.1	0.0	0.1	0.2	17.0	0.0	100.2
	142 / 15 .	Host	66.6	126.0	43.3	0.0	39.6	0.1	0.0	0.2	0.2	16.9	-0.1	100.2
	142 / 16 .	Host	66.5	135.0	43.3	0.0	39.9	0.1	0.0	0.1	0.2	16.9	-0.1	100.6
	142 / 17 .	Host	68.3	144.0	43.2	0.1	40.4	0.2	0.0	0.1	0.2	15.5	0.1	99.8
	142 / 18 .	Host	67.4	153.0	43.7	0.0	39.8	0.1	0.0	0.1	0.2	16.4	0.0	100.3
	142 / 19 .	Host	68.0	162.0	43.7	0.1	40.0	0.1	0.0	0.2	0.2	16.0	-0.1	100.3
	142 / 20 .	Host	68.5	171.0	44.1	0.0	39.9	0.1	0.0	0.2	0.3	15.7	0.0	100.3
	142 / 21 .	Host	68.5	180.0	44.2	0.0	40.2	0.1	0.0	0.1	0.1	15.7	0.1	100.7
	142 / 22 .	Host	67.8	189.0	43.8	0.0	39.8	0.1	0.0	0.1	0.1	16.1	0.1	100.3
	142 / 23 .	Host	65.7	198.0	42.5	0.1	39.6	0.2	0.0	0.4	0.2	17.2	0.1	100.3
	142 / 24 .	Host	62.7	207.0	41.2	0.1	40.0	0.3	0.0	0.3	0.2	19.0	0.0	101.1
	142 / 25 .	Host	58.8	216.0	39.5	0.0	38.7	0.1	0.0	0.1	0.2	21.4	0.1	100.0
Pr2	143 / 1 .	Host	28.8	0.0	21.2	1.3	34.4	0.3	0.1	0.1	0.5	40.8	0.0	98.7
	143 / 2 .	Host	31.2	7.4	23.5	0.0	34.5	0.3	0.0	0.4	0.3	40.4	0.0	99.4
	143 / 3 .	Host	42.1	14.8	30.2	0.1	36.3	0.2	0.0	0.1	0.4	32.3	0.1	99.6
	143 / 4 .	Host	45.5	22.2	31.9	0.0	36.4	0.2	0.0	0.1	0.4	29.7	0.1	98.8
	143 / 5 .	Host	44.9	29.6	31.8	0.0	36.6	0.3	0.0	0.1	0.3	30.2	0.0	99.4
	143 / 6 .	Host	45.4	37.0	32.1	0.0	36.4	0.3	0.0	0.1	0.3	30.0	0.0	99.3
	143 / 7 .	Host	46.7	44.4	33.0	0.0	37.4	0.2	0.0	0.1	0.3	29.3	0.1	100.3
	143 / 8 .	Host	47.7	51.8	33.3	0.0	37.2	0.2	0.0	0.1	0.3	28.4	0.0	99.5
	143 / 9 .	Host	46.8	59.2	32.9	0.0	36.4	0.3	0.0	0.1	0.3	29.1	0.0	99.1
	143 / 10 .	Host	45.3	66.6	32.2	0.0	36.8	0.2	0.0	0.1	0.3	30.1	0.1	99.9
Pr3	144 / 2 .	Host	29.8	6.1	22.6	0.0	34.4	0.4	0.0	0.1	0.4	41.3	0.1	99.4
	144 / 3 .	Host	33.1	12.2	24.7	0.0	34.9	0.4	0.0	0.2	0.4	38.7	0.0	99.3
	144 / 4 .	Host	31.5	18.3	23.6	0.0	34.5	0.4	0.0	0.2	0.3	39.9	0.1	99.1
	144 / 6 .	Host	28.8	30.5	21.9	0.0	34.0	0.3	0.0	0.2	0.4	42.0	0.2	99.0

	144 / 7 .	Host	32.6	36.6	24.4	0.0	35.1	0.2	0.0	0.2	0.4	39.2	0.0	99.5
	144 / 8 .	Host	35.3	42.7	26.1	0.0	35.7	0.2	0.0	0.2	0.4	37.0	0.0	99.7
	144 / 9 .	Host	32.1	48.8	24.1	0.0	34.9	0.3	0.0	0.2	0.3	39.5	-0.1	99.3
	144 / 10 .	Host	31.2	54.9	23.1	0.5	34.9	0.6	0.0	0.2	0.4	39.5	0.1	99.3
Pr4	145 / 1 .	Host	34.2	0.0	25.4	0.0	34.7	0.4	0.0	0.1	0.5	37.8	0.0	98.9
	145 / 2 .	Host	37.5	7.2	27.4	0.0	36.0	0.3	0.0	0.1	0.4	35.3	0.2	99.7
	145 / 3 .	Host	38.4	14.4	27.9	0.1	35.5	0.4	0.0	0.1	0.3	34.7	0.1	99.1
	145 / 4 .	Host	38.3	21.6	27.9	0.1	35.6	0.4	0.0	0.0	0.4	34.9	-0.1	99.3
	145 / 5 .	Host	36.6	28.8	27.0	0.0	35.7	0.4	0.0	0.0	0.4	36.3	0.0	99.8
	145 / 6 .	Host	35.3	36.0	26.1	0.0	35.2	0.4	0.0	0.1	0.5	37.0	0.1	99.3
	145 / 7 .	Host	29.2	43.2	22.1	0.0	34.3	0.5	0.0	0.1	0.4	41.5	0.1	99.1
Pr5	146 / 1 .	Host	34.8	0.0	25.8	0.1	35.2	0.3	0.0	0.9	0.4	37.5	0.0	100.1
	146 / 2 .	Host	50.0	7.8	34.6	0.0	37.5	0.2	0.0	0.1	0.3	26.8	0.0	99.5
	146 / 3 .	Host	48.2	15.5	34.3	0.1	37.7	0.2	0.0	0.1	0.2	28.5	0.2	101.2
	146 / 4 .	Host	60.9	23.3	40.4	0.0	38.6	0.1	0.0	0.1	0.2	20.2	0.1	99.8
	146 / 5 .	Host	64.7	31.0	42.3	0.0	39.2	0.1	0.0	0.1	0.2	17.9	0.0	99.9
	146 / 6 .	Host	64.2	38.8	42.0	0.1	38.9	0.2	0.0	0.1	0.2	18.2	-0.1	99.6
	146 / 7 .	Host	63.5	46.5	41.5	0.1	39.3	0.2	0.0	0.2	0.2	18.5	0.1	100.2
	146 / 8 .	Host	62.3	54.3	40.5	0.1	38.9	0.2	0.0	0.3	0.2	19.0	0.0	99.3
	146 / 9 .	Host	62.5	62.0	40.9	0.1	38.8	0.2	0.0	0.1	0.2	19.0	0.0	99.3
	146 / 10 .	Host	62.4	69.8	41.0	0.0	39.2	0.3	0.0	0.3	0.2	19.1	0.1	100.2
	146 / 11 .	Host	62.4	77.5	40.6	0.1	38.7	0.2	0.0	0.1	0.2	19.0	0.1	99.0
	146 / 12 .	Host	63.3	85.3	41.0	0.1	39.0	0.5	0.0	0.4	0.2	18.4	-0.1	99.7
	146 / 13 .	Host	63.4	93.0	41.3	0.1	39.0	0.1	0.0	0.5	0.2	18.5	0.3	100.1
	146 / 14 .	Host	64.0	100.8	41.9	0.0	39.2	0.1	0.0	0.1	0.1	18.3	0.0	99.8
	146 / 15 .	Host	63.2	108.5	41.5	0.0	38.9	0.2	0.0	0.2	0.2	18.8	0.0	99.9
	146 / 16 .	Host	61.4	116.3	40.6	0.0	38.7	0.1	0.0	0.1	0.2	19.8	0.2	99.8
	146 / 17 .	Host	56.1	124.0	37.8	0.0	37.9	0.1	0.0	0.1	0.2	23.0	0.2	99.4

		146 / 18 .	Host	43.3	131.8	30.9	0.0	36.5	0.1	0.0	0.1	0.3	31.3	0.2	99.5
		146 / 19 .	Host	36.3	139.5	26.6	0.0	35.4	0.3	0.0	0.1	0.4	36.3	-0.2	99.3
		146 / 20 .	Host	31.8	147.3	23.7	0.1	34.9	0.5	0.0	0.0	0.5	39.3	0.0	98.9
	Pr6	147 / 1 .	Host	43.9	0.0	31.2	0.0	36.8	0.3	0.0	0.1	0.3	30.9	0.0	99.7
		147 / 2 .	Host	49.0	7.8	34.1	0.0	37.1	0.2	0.0	0.1	0.4	27.5	0.1	99.5
		147 / 3 .	Host	51.7	15.6	35.6	0.0	37.4	0.2	0.0	0.1	0.2	25.8	0.0	99.3
		147 / 4 .	Host	53.7	23.3	36.7	0.0	38.2	0.2	0.0	0.1	0.3	24.5	0.1	100.0
		147 / 5 .	Host	53.9	31.1	36.7	0.0	37.8	0.2	0.0	0.1	0.3	24.4	0.1	99.7
		147 / 6 .	Host	53.1	38.9	36.2	0.0	37.9	0.2	0.0	0.1	0.2	24.8	0.0	99.5
		147 / 7 .	Host	48.7	46.7	34.0	0.0	37.2	0.2	0.0	0.1	0.3	27.7	0.0	99.5
		147 / 9 .	Host	29.5	62.2	22.3	0.0	34.5	0.4	0.0	0.0	0.4	41.4	0.1	99.2
		147 / 10 .	Host	27.6	70.0	21.2	0.1	34.0	0.3	0.0	0.1	0.5	43.2	0.1	99.3
	Pr7	148 / 1 .	Host	32.9	0.0	24.2	0.5	33.9	0.2	0.1	1.4	0.3	38.4	-0.1	98.9
		148 / 2 .	Host	38.6	7.3	28.1	0.0	35.9	0.3	0.0	0.2	0.2	34.6	0.1	99.5
		148 / 3 .	Host	46.9	14.6	33.1	0.0	36.9	0.2	0.0	0.3	0.3	29.0	0.1	100.0
		148 / 4 .	Host	57.1	21.9	38.4	0.0	38.3	0.1	0.0	0.1	0.3	22.4	0.1	99.7
		148 / 5 .	Host	57.6	29.2	38.5	0.1	38.7	0.1	0.0	0.2	0.3	21.9	0.0	99.8
		148 / 6 .	Host	52.6	36.5	35.4	0.2	36.8	0.4	0.0	1.6	0.2	24.8	0.2	99.7
		148 / 7 .	Host	57.4	43.8	38.4	0.0	38.2	0.2	0.0	0.1	0.3	22.1	0.0	99.3
		148 / 8 .	Host	56.6	51.1	38.1	0.0	38.3	0.2	0.0	0.1	0.3	22.7	0.2	99.9
		148 / 9 .	Host	55.8	58.4	37.6	0.2	37.8	0.1	0.0	0.3	0.3	23.1	0.0	99.4
		148 / 10 .	Host	55.1	65.7	36.9	0.1	37.7	0.2	0.0	0.3	0.2	23.4	0.1	99.0
		148 / 11 .	Host	54.8	73.0	36.9	0.2	37.8	0.2	0.0	0.5	0.2	23.6	0.1	99.6
		148 / 12 .	Host	55.7	80.3	37.6	0.1	38.1	0.2	0.0	0.2	0.3	23.1	0.0	99.5
		148 / 13 .	Host	56.8	87.6	38.2	0.1	38.1	0.2	0.0	0.1	0.3	22.6	0.0	99.5
		148 / 14 .	Host	55.2	94.9	37.3	0.0	37.8	0.1	0.0	0.0	0.2	23.6	0.1	99.1
		148 / 15 .	Host	48.4	102.2	33.8	0.0	37.0	0.2	0.0	0.1	0.3	27.9	0.0	99.3
	Pr8	149 / 2 .	Host	42.9	7.2	30.7	0.0	36.2	0.3	0.0	0.1	0.3	31.6	0.0	99.3

			149 / 3 .	Host	46.6	14.4	32.6	0.1	36.8	0.2	0.0	0.2	0.3	29.0	0.1	99.3
			149 / 4 .	Host	47.6	21.6	33.3	0.0	36.8	0.2	0.0	0.2	0.4	28.4	0.1	99.3
			149 / 5 .	Host	48.3	28.8	33.7	0.0	36.9	0.2	0.0	0.1	0.3	28.0	-0.1	99.2
			149 / 6 .	Host	49.0	36.0	34.2	0.0	37.1	0.2	0.0	0.1	0.3	27.6	-0.1	99.6
			149 / 7 .	Host	49.6	43.2	33.5	0.0	36.9	0.2	0.0	0.0	0.3	26.5	0.1	97.6
			149 / 8 .	Host	49.8	50.4	34.5	0.0	37.5	0.2	0.0	0.2	0.3	27.0	0.0	99.8
			149 / 9 .	Host	50.4	57.6	34.7	0.0	37.2	0.2	0.0	0.1	0.3	26.5	0.2	99.3
			149 / 10 .	Host	50.4	64.8	34.9	0.0	37.4	0.3	0.0	0.1	0.3	26.7	0.1	99.8
			149 / 11 .	Host	49.8	72.0	34.5	0.0	37.3	0.3	0.0	0.1	0.3	27.0	0.1	99.5
			149 / 12 .	Host	48.1	79.2	33.6	0.1	36.7	0.2	0.0	0.1	0.3	28.2	0.2	99.4
			149 / 13 .	Host	42.1	86.4	30.2	0.1	36.0	0.2	0.0	0.1	0.3	32.2	0.0	99.1
			149 / 14 .	Host	43.2	93.6	31.0	0.0	36.0	0.3	0.0	0.1	0.3	31.6	0.1	99.4
			149 / 15 .	Host	44.8	100.8	31.7	0.0	37.2	0.3	0.0	0.0	0.3	30.3	0.1	100.0
	Ch_04	Pr1	150 / 1 .	Host	36.9	0.0	27.2	0.0	35.8	0.2	0.0	0.2	0.2	36.1	0.1	100.0
			150 / 2 .	Host	38.8	5.4	28.5	0.0	35.8	0.2	0.0	0.2	0.3	34.8	0.2	100.0
			150 / 3 .	Host	39.9	10.7	29.2	0.0	36.3	0.2	0.0	0.2	0.2	34.1	0.1	100.3
			150 / 4 .	Host	41.1	16.1	29.9	0.0	36.4	0.2	0.0	0.2	0.3	33.2	0.0	100.2
			150 / 5 .	Host	42.2	21.4	30.4	0.0	36.3	0.1	0.0	0.1	0.3	32.4	0.2	99.8
			150 / 6 .	Host	42.5	26.8	30.8	0.0	36.5	0.2	0.0	0.1	0.3	32.3	0.2	100.4
			150 / 7 .	Host	43.0	32.1	31.0	0.0	36.6	0.1	0.0	0.1	0.3	31.9	0.2	100.2
			150 / 8 .	Host	43.2	37.5	31.1	0.0	36.6	0.2	0.0	0.1	0.3	31.8	0.0	100.1
			150 / 9 .	Host	43.8	42.8	31.3	0.1	37.1	0.2	0.0	0.1	0.2	31.3	0.2	100.5
			150 / 10 .	Host	43.9	48.2	31.5	0.0	37.1	0.2	0.0	0.1	0.3	31.3	0.2	100.7
			150 / 11 .	Host	43.8	53.5	31.5	0.0	36.4	0.2	0.0	0.1	0.3	31.4	0.2	100.1
			150 / 12 .	Host	43.3	58.9	31.2	0.0	36.6	0.1	0.0	0.1	0.3	31.7	0.2	100.3
			150 / 13 .	Host	41.9	64.2	30.4	0.0	36.2	0.2	0.0	0.2	0.2	32.7	0.0	100.0
			150 / 14 .	Host	40.1	69.6	29.3	0.0	35.8	0.2	0.0	0.1	0.3	34.0	0.1	99.8
			150 / 15 .	Host	36.9	74.9	27.4	0.0	36.1	0.2	0.0	0.1	0.3	36.4	0.1	100.6

Pr2	151 / 1 .	Host	33.4	0.0	25.1	0.1	35.3	0.2	0.0	0.2	0.3	38.8	0.2	100.3
	151 / 2 .	Host	40.9	6.2	29.8	0.0	36.3	0.1	0.0	0.2	0.4	33.4	0.0	100.3
	151 / 3 .	Host	48.9	12.4	34.1	0.2	37.9	0.1	0.0	0.2	0.2	27.6	-0.1	100.3
	151 / 4 .	Relict	65.9	18.6	42.8	0.1	39.7	0.4	0.1	0.1	0.1	17.2	0.0	100.4
	151 / 5 .	Relict	89.7	24.8	52.4	0.1	42.5	0.6	0.1	0.2	0.0	4.7	0.0	100.6
	151 / 6 .	Relict	97.0	31.0	56.2	0.2	42.8	0.6	0.0	0.1	0.0	1.3	0.1	101.2
	151 / 7 .	Relict	97.3	37.2	56.3	0.2	42.4	0.6	0.1	0.1	0.0	1.2	0.0	101.0
	151 / 8 .	Relict	97.5	43.4	56.6	0.2	42.9	0.6	0.0	0.1	0.0	1.1	0.0	101.6
	151 / 9 .	Relict	97.6	49.6	56.6	0.1	43.0	0.6	0.0	0.1	0.0	1.1	0.0	101.5
	151 / 10 .	Relict	97.5	55.8	56.6	0.1	42.9	0.6	0.0	0.1	0.0	1.1	-0.1	101.6
	151 / 11 .	Relict	97.4	62.0	56.6	0.2	43.0	0.5	0.1	0.1	0.0	1.2	0.1	101.8
	151 / 12 .	Relict	94.5	68.2	55.3	0.1	42.6	0.5	0.1	0.1	0.0	2.5	0.0	101.1
	151 / 13 .	Relict	79.0	74.4	48.7	0.1	41.4	0.4	0.0	0.2	0.0	10.0	0.1	100.9
	151 / 14 .	Host	44.4	80.6	31.6	0.1	37.0	0.2	0.0	0.2	0.2	30.7	0.1	100.0
Pr3	152 / 1 .	Host	50.3	0.0	35.2	0.0	37.8	0.1	0.0	0.2	0.2	27.0	0.1	100.6
	152 / 2 .	Host	54.4	10.3	37.4	0.0	37.9	0.1	0.0	0.1	0.2	24.3	0.1	100.1
	152 / 3 .	Host	57.1	20.6	38.5	0.1	38.3	0.1	0.0	0.1	0.2	22.5	0.0	99.8
	152 / 4 .	Host	53.3	30.9	36.9	0.1	37.8	0.1	0.0	0.2	0.2	25.0	0.1	100.4
	152 / 5 .	Host	51.3	41.2	35.7	0.0	37.9	0.1	0.0	0.1	0.2	26.3	0.1	100.5
	152 / 6 .	Host	58.4	51.5	39.2	0.1	38.4	0.1	0.0	0.1	0.2	21.7	0.0	99.8
	152 / 7 .	Host	59.8	61.8	40.1	0.1	38.5	0.1	0.0	0.3	0.1	20.9	0.1	100.2
	152 / 8 .	Host	61.0	72.1	40.7	0.1	39.1	0.1	0.0	0.2	0.2	20.2	0.1	100.6
	152 / 9 .	Host	60.5	82.4	40.3	0.1	38.7	0.1	0.0	0.2	0.2	20.4	0.0	100.1
	152 / 10 .	Host	59.2	92.7	39.9	0.0	38.6	0.1	0.0	0.1	0.2	21.3	0.1	100.3
	152 / 11 .	Host	58.2	103.0	39.1	0.1	38.8	0.1	0.0	0.2	0.2	21.8	0.0	100.3
	152 / 12 .	Host	57.8	113.3	39.0	0.1	37.9	0.1	0.0	0.1	0.2	22.1	-0.1	99.4
	152 / 13 .	Host	54.5	123.6	37.0	0.2	38.2	0.3	0.0	0.1	0.2	23.9	0.0	99.8
	152 / 14 .	Host	56.5	133.9	38.4	0.1	38.4	0.2	0.0	0.1	0.2	23.0	0.0	100.5

			152 / 15 .	Host	51.5	144.2	35.8	0.0	37.6	0.2	0.0	0.1	0.2	26.1	-0.1	100.2
	Pr4		153 / 1 .	Host	30.9	0.0	23.3	0.0	34.7	0.4	0.0	0.0	0.3	40.5	-0.1	99.3
			153 / 3 .	Host	30.9	10.0	23.5	0.1	34.8	0.3	0.0	0.1	0.4	40.8	0.2	100.1
			153 / 4 .	Host	32.4	15.0	24.3	0.1	35.1	0.3	0.1	0.2	0.3	39.3	-0.2	99.5
			153 / 5 .	Host	33.2	20.0	24.9	0.1	35.1	0.2	0.0	0.1	0.3	38.9	-0.1	99.6
			153 / 6 .	Host	33.0	25.0	24.8	0.0	34.5	0.3	0.0	0.0	0.4	39.1	-0.1	99.1
	Pr5		154 / 1 .	Host	56.8	0.0	38.7	0.0	38.8	0.1	0.0	0.1	0.1	22.8	0.1	100.9
			154 / 2 .	Host	62.5	6.4	41.7	0.1	39.1	0.2	0.0	0.1	0.1	19.4	0.2	100.9
			154 / 3 .	Relict	66.9	12.8	43.7	0.1	39.5	0.1	0.1	0.2	0.1	16.7	0.0	100.6
			154 / 4 .	Relict	74.2	19.2	47.2	0.1	40.4	0.4	0.1	0.2	0.2	12.7	0.0	101.1
			154 / 5 .	Relict	73.9	25.6	47.2	0.0	40.3	0.2	0.0	0.1	0.2	12.9	-0.1	100.9
			154 / 6 .	Relict	70.6	32.0	45.3	0.0	40.7	0.1	0.0	0.0	0.1	14.6	0.0	101.0
			154 / 7 .	Host	64.7	38.4	42.8	0.1	39.4	0.1	0.0	0.1	0.1	18.1	0.1	100.9
			154 / 8 .	Host	58.7	44.8	39.6	0.0	39.0	0.1	0.0	0.0	0.2	21.6	0.0	100.6
			154 / 9 .	Host	52.3	51.2	35.0	0.0	38.1	0.2	0.0	0.1	0.2	24.8	0.1	98.6
	Pr6		155 / 1 .	Host	46.5	0.0	33.1	0.1	37.0	0.1	0.1	0.1	0.3	29.5	0.0	100.2
			155 / 2 .	Host	54.4	4.2	37.5	0.0	38.0	0.1	0.0	0.1	0.2	24.4	0.1	100.5
			155 / 3 .	Host	67.2	8.4	43.8	0.1	39.5	0.1	0.1	0.1	0.2	16.6	-0.1	100.5
			155 / 4 .	Relict	83.1	12.7	51.1	0.1	41.7	0.2	0.1	0.2	0.1	8.1	-0.1	101.6
			155 / 5 .	Relict	87.3	16.9	52.6	0.1	41.7	0.2	0.1	0.0	0.2	5.9	-0.1	100.7
			155 / 6 .	Relict	86.1	21.1	52.3	0.0	41.6	0.2	0.0	0.1	0.1	6.5	0.0	100.9
			155 / 7 .	Relict	82.0	25.3	50.9	0.1	41.7	0.2	0.1	0.1	0.1	8.7	0.2	102.0
			155 / 8 .	Relict	73.9	29.5	47.1	0.1	40.6	0.1	0.1	0.2	0.1	12.9	0.0	101.2
			155 / 9 .	Host	53.0	33.8	36.6	0.1	37.5	0.2	0.1	0.2	0.1	25.1	0.0	100.0
			155 / 10 .	Host	36.7	0.0	27.1	0.0	35.5	0.2	0.0	0.2	0.3	36.2	0.2	99.7
			155 / 12 .	Host	62.2	8.4	40.0	0.2	38.5	0.3	0.1	0.3	0.1	18.9	0.2	98.5
			155 / 13 .	Relict	81.0	12.7	48.7	0.1	41.1	0.3	0.0	0.2	0.1	8.9	-0.1	99.5
EM463	Ch_05	Pr1	156 / 2 .	Host	40.6	7.5	29.3	0.0	36.0	0.4	0.0	0.1	0.4	33.3	0.0	99.6

	156 / 3 .	Host	40.1	15.0	28.9	0.5	36.2	0.2	0.0	0.5	0.3	33.4	0.1	100.1
	156 / 5 .	Relict	89.3	30.0	52.2	0.2	41.6	0.5	0.0	0.1	0.0	4.8	-0.1	99.5
	156 / 6 .	Relict	97.7	37.5	56.0	0.2	42.7	0.5	0.1	0.1	0.0	1.0	-0.1	100.7
	156 / 7 .	Relict	98.0	45.0	56.0	0.2	42.7	0.5	0.0	0.2	0.0	0.9	0.1	100.6
	156 / 8 .	Relict	98.2	52.5	56.0	0.2	42.4	0.5	0.0	0.2	0.1	0.8	0.0	100.2
	156 / 9 .	Relict	98.2	60.0	56.1	0.2	42.1	0.5	0.0	0.2	0.0	0.8	0.0	100.0
	156 / 10 .	Relict	97.3	67.5	55.6	0.2	42.4	0.5	0.1	0.2	0.0	1.2	0.0	100.2
	156 / 11 .	Relict	83.2	75.0	49.4	0.5	40.9	0.4	0.0	0.2	0.1	7.7	0.0	99.3
	156 / 12 .	Relict	97.4	82.5	53.8	0.3	42.6	0.5	0.1	0.2	0.0	1.1	0.1	98.7
	156 / 14 .	Relict	98.3	97.5	55.9	0.2	42.3	0.5	0.0	0.2	0.0	0.8	0.1	99.9
	156 / 15 .	Relict	98.2	105.0	55.8	0.2	42.7	0.5	0.1	0.2	0.0	0.8	0.1	100.4
	156 / 16 .	Relict	98.1	112.5	55.3	0.2	42.7	0.5	0.1	0.1	0.0	0.8	0.0	99.8
	156 / 17 .	Relict	98.2	120.0	55.8	0.2	42.1	0.5	0.1	0.2	0.0	0.8	0.1	99.7
	156 / 18 .	Relict	98.1	127.5	55.8	0.2	42.4	0.5	0.1	0.0	0.0	0.9	0.0	100.0
	156 / 19 .	Relict	97.9	135.0	56.0	0.3	42.3	0.5	0.1	0.1	0.0	0.9	0.0	100.2
	156 / 20 .	Relict	97.1	142.5	55.8	0.3	42.8	0.5	0.1	0.1	0.0	1.3	0.0	100.9
	156 / 21 .	Relict	94.5	150.0	55.1	0.3	42.2	0.5	0.1	0.1	0.0	2.5	0.1	100.8
	156 / 22 .	Relict	98.0	157.5	56.0	0.2	42.6	0.5	0.0	0.1	0.1	0.9	-0.1	100.4
	156 / 23 .	Relict	97.6	165.0	56.1	0.2	42.5	0.5	0.1	0.1	0.0	1.1	0.1	100.7
	156 / 24 .	Relict	84.1	172.5	51.3	0.4	40.9	0.4	0.0	0.1	0.1	7.5	0.2	100.9
	156 / 25 .	Host	41.8	180.0	29.8	0.1	36.3	0.1	0.0	0.1	0.3	32.2	0.0	99.0
Pr2	157 / 1 .	Relict	88.0	0.0	54.0	0.1	41.0	0.4	0.0	0.1	0.0	5.7	0.2	101.6
	157 / 2 .	Relict	90.9	5.0	53.2	0.1	41.4	0.4	0.0	0.1	0.0	4.2	-0.1	99.4
	157 / 3 .	Relict	90.6	10.0	52.6	0.1	41.5	0.4	0.1	0.1	0.0	4.2	0.1	99.2
	157 / 4 .	Relict	89.2	15.0	52.2	0.1	41.1	0.4	0.0	0.2	0.0	4.9	-0.1	98.9
	157 / 5 .	Relict	87.4	20.0	51.4	0.1	41.1	0.4	0.0	0.2	0.0	5.7	0.0	98.9
	157 / 6 .	Relict	84.9	25.0	50.5	0.1	40.7	0.3	0.0	0.1	0.1	7.0	0.1	98.9
	157 / 7 .	Relict	80.6	30.0	48.7	0.0	40.3	0.2	0.0	0.1	0.1	9.1	0.1	98.7

		157 / 8 .	Relict	72.4	35.0	45.2	0.0	39.5	0.2	0.0	0.1	0.1	13.4	-0.1	98.6
		157 / 9 .	Host	44.4	40.0	31.3	0.0	36.3	0.2	0.0	0.1	0.3	30.3	0.0	98.6
	Pr3	158 / 1 .	Host	53.7	0.0	36.1	0.4	37.9	0.2	0.1	0.1	0.2	24.1	-0.1	99.0
		158 / 2 .	Relict	76.5	5.3	47.3	0.0	40.7	0.2	0.0	0.2	0.2	11.3	-0.1	99.7
		158 / 3 .	Relict	75.9	10.5	47.0	0.0	40.0	0.2	0.0	0.1	0.2	11.6	0.0	99.1
		158 / 4 .	Relict	75.3	15.8	46.7	0.0	40.3	0.2	0.0	0.0	0.1	11.9	0.0	99.3
		158 / 5 .	Host	56.1	21.0	36.8	0.0	37.8	0.2	0.0	0.1	0.2	22.3	0.1	97.5
		158 / 6 .	Host	47.4	26.3	32.6	0.0	36.4	0.2	0.0	0.0	0.2	28.1	0.0	97.5
	Pr4	159 / 1 .	Host	56.9	0.0	39.1	0.0	39.0	0.1	0.0	0.0	0.2	23.0	0.0	101.4
		159 / 2 .	Relict	73.8	4.4	46.5	0.0	40.6	0.2	0.0	0.0	0.2	12.8	0.1	100.4
		159 / 3 .	Relict	77.2	8.9	47.6	0.1	39.7	0.1	0.0	0.1	0.2	10.9	0.1	98.7
		159 / 4 .	Relict	81.8	13.3	50.9	0.0	41.4	0.1	0.0	0.1	0.3	8.8	0.0	101.6
		159 / 5 .	Relict	81.5	17.8	50.2	0.0	41.3	0.2	0.0	0.1	0.3	8.8	0.0	100.9
		159 / 6 .	Relict	78.0	22.2	48.7	0.0	40.2	0.2	0.0	0.0	0.3	10.7	0.1	100.1
		159 / 8 .	Host	47.1	31.1	32.9	0.1	36.6	0.2	0.0	0.0	0.3	28.7	-0.1	98.8
		159 / 9 .	Host	42.5	35.5	30.2	0.2	36.5	0.2	0.0	0.4	0.3	31.7	0.0	99.5
	Pr5	160 / 2 .	Host	38.6	5.0	28.0	0.0	37.3	0.4	0.0	0.1	0.4	34.6	0.1	100.8
		160 / 3 .	Host	38.4	10.0	27.9	0.0	36.4	0.5	0.0	0.2	0.4	34.8	-0.2	100.2
		160 / 7 .	Host	38.3	30.0	28.0	0.0	35.8	0.3	0.0	0.0	0.4	35.0	0.0	99.6
		160 / 8 .	Host	38.4	35.0	28.0	0.0	35.8	0.2	0.0	0.1	0.4	34.8	0.0	99.3
		160 / 10 .	Host	39.5	45.0	28.5	0.4	36.7	0.4	0.0	0.1	0.3	33.8	0.1	100.2
	Pr6	161 / 1 .	Relict	85.1	0.0	51.9	0.1	41.9	0.6	0.1	0.2	0.0	7.0	-0.1	101.9
		161 / 2 .	Relict	97.5	6.0	56.4	0.2	42.9	0.7	0.1	0.1	0.0	1.1	0.0	101.5
		161 / 3 .	Relict	97.2	12.0	56.2	0.3	42.7	0.6	0.1	0.1	0.0	1.2	-0.1	101.1
		161 / 4 .	Relict	95.8	18.0	55.8	0.2	42.4	0.6	0.1	0.1	0.0	1.9	0.2	101.2
		161 / 5 .	Relict	93.0	24.0	53.4	0.3	42.5	0.7	0.1	0.2	0.0	3.1	0.0	100.3
		161 / 6 .	Host	46.6	30.0	32.7	0.1	37.6	0.0	0.0	0.0	0.3	29.0	0.1	99.9
	Pr7	162 / 1 .	Relict	69.7	0.0	44.8	0.1	40.7	0.2	0.1	0.1	0.0	15.1	0.0	101.1

		162 / 2 .	Relict	85.1	6.0	51.7	0.1	42.1	0.3	0.0	0.1	0.1	7.0	0.1	101.4
		162 / 3 .	Relict	85.8	12.0	52.0	0.1	42.2	0.2	0.0	0.1	0.0	6.7	-0.1	101.3
		162 / 4 .	Relict	85.6	18.0	52.0	0.1	42.1	0.3	0.0	0.1	0.1	6.8	0.1	101.5
		162 / 5 .	Relict	74.1	24.0	46.4	0.2	40.8	0.2	0.1	0.3	0.1	12.6	-0.1	100.6
		162 / 6 .	Host	40.2	30.0	28.4	1.1	35.4	1.1	0.0	0.6	0.3	32.7	0.1	99.8
		162 / 7 .	Host	41.0	36.0	30.1	0.3	36.3	0.3	0.0	0.1	0.3	33.6	0.0	101.0
		162 / 8 .	Host	39.8	42.0	28.8	0.1	36.5	0.3	0.1	0.1	0.3	33.8	0.1	100.0
	Pr8	163 / 1 .	Host	78.8	0.0	48.9	0.1	41.2	0.2	0.0	0.1	0.2	10.2	-0.1	100.8
		163 / 2 .	Relict	86.0	6.3	51.9	0.1	42.2	0.3	0.1	0.1	0.1	6.6	0.1	101.5
		163 / 4 .	Relict	89.2	18.9	53.1	0.1	41.8	0.3	0.1	0.2	0.2	5.0	0.0	100.8
		163 / 5 .	Relict	89.9	25.2	53.2	0.1	42.3	0.3	0.1	0.2	0.1	4.7	0.0	101.0
		163 / 6 .	Relict	90.6	31.5	53.6	0.1	42.0	0.3	0.0	0.1	0.2	4.3	0.0	100.7
		163 / 7 .	Relict	89.9	37.8	53.4	0.1	41.5	0.3	0.1	0.2	0.1	4.7	0.0	100.5
		163 / 8 .	Relict	88.7	44.1	53.2	0.1	42.1	0.3	0.1	0.2	0.2	5.3	0.1	101.5
		163 / 9 .	Relict	82.8	50.4	49.4	0.6	40.9	0.1	0.1	0.5	0.1	7.9	0.0	99.7
		163 / 10 .	Host	45.4	56.7	32.0	0.3	36.2	0.1	0.1	1.1	0.2	29.9	0.0	99.9
	Pr9	164 / 1 .	Host	51.8	0.0	35.7	0.0	38.0	0.1	0.0	0.1	0.2	25.8	0.1	100.0
		164 / 2 .	Host	55.4	7.6	37.6	0.1	38.4	0.0	0.0	0.1	0.2	23.5	-0.1	99.9
		164 / 3 .	Host	58.1	15.2	39.2	0.0	38.5	0.0	0.0	0.1	0.2	21.9	0.1	100.0
		164 / 4 .	Host	60.2	22.8	40.2	0.1	39.2	0.0	0.0	0.1	0.2	20.6	0.1	100.5
		164 / 5 .	Host	62.6	30.4	41.4	0.0	39.7	0.0	0.0	0.0	0.2	19.1	-0.1	100.4
		164 / 6 .	Host	65.6	38.0	42.8	0.0	39.9	0.0	0.0	0.0	0.2	17.4	-0.1	100.4
		164 / 7 .	Host	67.3	45.6	43.6	0.0	40.2	0.1	0.0	0.1	0.2	16.5	-0.2	100.7
		164 / 8 .	Host	67.6	53.2	43.8	0.0	40.0	0.0	0.0	0.1	0.2	16.3	0.1	100.6
		164 / 9 .	Host	66.6	60.8	43.2	0.0	39.9	0.1	0.0	0.0	0.1	16.9	-0.1	100.3
		164 / 10 .	Host	65.5	68.4	42.6	0.0	40.2	0.0	0.0	0.0	0.2	17.4	-0.1	100.5
		164 / 11 .	Host	62.9	76.0	41.6	0.0	39.0	0.0	0.0	0.1	0.2	19.0	0.1	100.0
		164 / 12 .	Host	56.8	83.6	38.0	0.1	37.7	0.1	0.0	0.2	0.3	22.4	0.1	98.7

164 / 13 .	Host	51.6	91.2	35.1	0.5	37.9	0.1	0.0	0.8	0.2	25.5	0.0	100.1
164 / 14 .	Host	57.5	98.8	38.9	0.0	38.8	0.1	0.0	0.1	0.2	22.3	0.1	100.5
164 / 15 .	Host	58.6	106.4	39.1	0.0	38.7	0.0	0.0	0.1	0.2	21.4	0.1	99.7
164 / 16 .	Host	59.4	114.0	39.8	0.0	38.7	0.0	0.0	0.2	0.2	21.1	-0.1	100.1
164 / 17 .	Host	59.7	121.6	39.1	0.0	39.7	0.1	0.0	0.1	0.2	20.5	0.1	99.9
164 / 18 .	Host	60.9	129.2	40.3	0.1	39.5	0.1	0.0	0.1	0.2	20.1	-0.1	100.4
164 / 19 .	Host	60.4	136.8	40.1	0.0	38.9	0.1	0.0	0.1	0.2	20.4	0.0	100.0
164 / 20 .	Host	59.8	144.4	39.9	0.0	39.1	0.0	0.0	0.2	0.3	20.8	0.1	100.3

Isna	Ch_01	Pr1	165 / 1 .	Host	49.5	0.0	35.2	0.0	38.5	0.0	0.0	0.1	0.2	27.9	0.1	102.0
			165 / 3 .	Host	62.9	12.8	42.3	0.1	40.0	0.1	0.0	0.1	0.1	19.3	-0.1	102.1
			165 / 5 .	Relict	73.0	25.6	47.2	0.0	41.2	0.2	0.0	0.0	0.1	13.5	0.1	102.4
			165 / 7 .	Relict	79.6	38.4	50.1	0.1	41.7	0.1	0.1	0.1	0.0	10.0	0.1	102.4
			165 / 9 .	Relict	87.5	51.2	53.2	0.2	42.4	0.4	0.1	0.1	0.1	5.9	0.0	102.2
			165 / 10 .	Relict	88.3	57.6	53.6	0.2	42.2	0.4	0.1	0.2	0.0	5.5	0.0	102.2
			165 / 12 .	Relict	89.7	70.4	53.1	0.8	42.9	0.5	0.1	0.1	0.0	4.7	-0.1	102.2
			165 / 13 .	Relict	90.4	76.8	54.1	0.2	42.8	0.4	0.1	0.1	0.1	4.5	0.0	102.2
			165 / 18 .	Relict	87.4	108.8	52.7	0.4	42.7	0.5	0.1	0.1	0.1	5.9	0.0	102.4
			165 / 21 .	Host	61.5	128.0	41.3	0.2	39.5	0.5	0.0	0.0	0.2	20.1	-0.1	101.8
			165 / 22 .	Relict	72.5	134.4	45.9	0.8	40.9	0.5	0.2	0.1	0.1	13.5	0.2	102.1
			165 / 23 .	Host	50.6	140.8	35.6	0.5	37.7	0.2	0.2	0.1	0.2	26.9	0.0	101.4
			165 / 24 .	Host	48.7	147.2	34.8	0.4	38.0	0.1	0.1	0.2	0.2	28.4	-0.1	102.1
			165 / 25 .	Host	53.7	153.6	37.7	0.2	38.6	0.4	0.1	0.1	0.2	25.2	0.0	102.4
			165 / 26 .	Host	51.4	160.0	36.2	0.1	38.8	0.5	0.0	0.1	0.2	26.5	0.0	102.4
			165 / 27 .	Host	48.8	166.4	33.3	0.2	36.6	0.3	0.1	0.2	0.2	27.1	0.1	98.0
			165 / 30 .	Host	49.8	185.6	34.9	0.1	38.4	0.3	0.1	0.1	0.2	27.3	-0.1	101.4
			165 / 31 .	Host	53.3	192.0	36.8	0.2	39.0	0.6	0.1	0.1	0.2	25.0	0.1	101.9
			165 / 32 .	Host	58.2	198.4	39.4	0.1	40.0	0.6	0.1	0.0	0.1	22.0	-0.1	102.3
			165 / 43 .	Host	59.7	268.8	40.5	0.2	39.7	0.3	0.1	0.2	0.1	21.2	0.0	102.4

			165 / 45 .	Host	53.1	281.6	37.2	0.0	39.1	0.2	0.0	0.0	0.2	25.5	0.1	102.3
		Pr2	166 / 1 .	Host	46.5	0.0	33.1	0.1	38.6	0.1	0.1	0.1	0.2	29.6	-0.1	101.9
			166 / 6 .	Relict	94.5	27.5	55.6	0.3	43.4	0.5	0.1	0.1	0.0	2.5	-0.1	102.5
			166 / 17 .	Host	64.9	88.0	42.4	0.3	40.6	0.6	0.1	0.1	0.1	17.8	0.0	101.9
			166 / 18 .	Host	53.9	93.5	37.5	0.3	38.6	0.2	0.1	0.2	0.2	24.9	0.0	102.0
			166 / 19 .	Host	53.5	99.0	36.9	0.3	38.7	0.2	0.1	0.1	0.2	24.9	0.1	101.5
			166 / 26 .	Host	51.6	137.5	36.3	0.1	38.5	0.5	0.1	0.1	0.2	26.4	-0.2	102.2
			166 / 27 .	Host	52.0	143.0	36.3	0.1	38.5	0.4	0.0	0.1	0.2	26.0	0.0	101.8
			166 / 28 .	Host	52.6	148.5	36.6	0.4	38.7	0.3	0.1	0.2	0.1	25.6	-0.1	102.0
			166 / 29 .	Host	71.9	154.0	46.3	0.6	40.4	0.6	0.2	0.1	0.0	14.0	0.1	102.3
			166 / 30 .	Relict	78.5	159.5	48.8	0.6	41.7	0.7	0.1	0.1	0.0	10.4	0.0	102.5
			166 / 32 .	Relict	85.8	170.5	52.2	0.4	42.1	0.7	0.1	0.0	0.0	6.7	0.0	102.2
			166 / 44 .	Relict	85.1	236.5	51.6	0.1	42.6	0.3	0.1	0.0	0.1	7.0	-0.2	101.8
			166 / 45 .	Host	70.8	242.0	46.4	0.1	40.5	0.2	0.1	0.2	0.2	14.8	0.1	102.5
LoV 098b	Ch_02	Pr1	48 / 1 .	Host	49.3	0.0	34.1	0.0	36.3	0.2	0.0	0.3	0.4	27.2	0.2	98.7
			48 / 2 .	Host	52.1	8.6	35.6	0.0	36.6	0.2	0.0	0.2	0.5	25.4	0.0	98.6
			48 / 3 .	Host	54.3	17.1	36.4	0.0	36.7	0.2	0.0	0.3	0.4	23.7	0.0	97.8
			48 / 5 .	Host	57.8	34.3	38.1	0.0	37.9	0.2	0.0	0.4	0.3	21.6	0.2	98.6
			48 / 6 .	Host	58.6	42.9	38.5	0.0	37.7	0.2	0.0	0.3	0.4	21.1	0.1	98.3
			48 / 7 .	Host	60.1	51.4	39.6	0.0	37.6	0.2	0.1	0.3	0.4	20.4	0.0	98.6
			48 / 8 .	Host	60.0	60.0	39.1	0.0	38.0	0.2	0.0	0.3	0.4	20.2	0.1	98.3
			48 / 9 .	Host	59.7	68.6	39.0	0.0	38.3	0.2	0.0	0.4	0.4	20.4	-0.1	98.7
			48 / 10 .	Host	60.9	77.1	39.2	0.0	38.1	0.2	0.0	0.6	0.3	19.5	0.1	98.0
		Pr2	49 / 2 .	Relict	64.0	8.3	41.0	0.0	38.5	0.2	0.0	0.3	0.3	17.9	0.1	98.3
			49 / 3 .	Relict	67.8	16.7	42.7	0.0	38.3	0.1	0.0	0.4	0.3	15.8	0.1	97.8
			49 / 4 .	Relict	69.8	25.0	43.2	0.1	38.6	0.2	0.0	0.7	0.2	14.5	0.1	97.6
			49 / 5 .	Relict	68.6	33.3	43.0	0.0	39.0	0.1	0.0	1.1	0.2	15.2	0.1	98.8

	49 / 6 .	Relict	64.6	41.7	41.3	0.0	38.0	0.2	0.0	0.2	0.3	17.6	0.1	97.7
	49 / 7 .	Host	59.9	50.0	38.8	0.0	37.7	0.3	0.0	0.4	0.4	20.2	0.0	97.8
	49 / 8 .	Host	56.1	58.3	37.5	0.4	37.9	0.4	0.0	0.3	0.3	22.7	0.0	99.6
Pr3	50 / 3 .	Host	67.0	15.0	42.4	0.0	38.7	0.1	0.0	0.3	0.2	16.2	-0.1	97.9
	50 / 4 .	Relict	72.3	22.5	45.4	0.0	39.5	0.1	0.0	0.3	0.2	13.5	0.0	99.0
	50 / 5 .	Relict	74.2	30.0	45.9	0.0	39.3	0.1	0.0	0.4	0.2	12.4	0.0	98.3
	50 / 6 .	Relict	75.0	37.5	46.2	0.0	39.7	0.1	0.0	0.4	0.3	11.9	0.1	98.7
	50 / 7 .	Relict	73.7	44.9	45.5	0.0	39.4	0.1	0.0	0.3	0.2	12.6	-0.1	98.2
	50 / 8 .	Host	60.5	52.4	39.3	0.0	37.8	0.1	0.0	0.4	0.4	20.0	0.2	98.2
Pr4	51 / 1 .	Host	56.3	0.0	37.3	0.0	37.2	0.2	0.0	0.2	0.4	22.4	0.1	97.8
	51 / 2 .	Host	56.9	7.5	37.8	0.0	37.6	0.2	0.0	0.2	0.4	22.2	0.1	98.6
	51 / 3 .	Host	56.4	15.0	37.2	0.0	37.4	0.3	0.0	0.4	0.4	22.3	-0.1	98.0
	51 / 4 .	Host	55.7	22.5	36.8	0.0	37.8	0.2	0.0	0.3	0.5	22.7	0.0	98.3
	51 / 5 .	Host	54.3	30.0	36.3	0.0	36.9	0.3	0.0	0.2	0.4	23.7	0.0	97.9
	51 / 6 .	Host	52.9	37.5	35.6	0.0	37.1	0.3	0.0	0.2	0.4	24.5	0.0	98.2
	51 / 7 .	Host	50.6	45.0	33.7	0.0	40.3	0.4	0.0	0.2	0.5	25.6	0.1	100.9
Pr5	52 / 1 .	Host	53.9	0.0	36.0	0.0	36.7	0.2	0.0	0.2	0.4	23.9	0.1	97.5
	52 / 2 .	Host	56.1	7.6	37.1	0.0	37.5	0.2	0.0	0.3	0.4	22.6	0.0	98.1
	52 / 3 .	Host	56.9	15.2	37.5	0.0	37.7	0.2	0.0	0.4	0.4	22.0	0.0	98.2
	52 / 4 .	Host	57.3	22.8	37.8	0.0	37.4	0.2	0.0	0.3	0.4	21.8	-0.1	97.9
	52 / 5 .	Host	57.9	30.4	38.0	0.0	37.8	0.2	0.0	0.2	0.4	21.5	0.0	98.2
	52 / 6 .	Host	57.2	38.0	37.7	0.0	37.4	0.2	0.0	0.2	0.4	21.8	0.1	97.9
	52 / 7 .	Host	53.9	45.6	36.4	0.0	37.5	0.3	0.0	0.1	0.4	24.1	0.0	98.8
Pr6	53 / 1 .	Relict	66.3	0.0	41.9	0.0	38.9	0.2	0.0	0.4	0.3	16.5	-0.1	98.3
	53 / 2 .	Host	68.9	10.0	42.8	0.0	39.0	0.1	0.0	0.6	0.3	15.0	0.0	97.9
	53 / 3 .	Host	68.5	20.0	43.0	0.0	38.5	0.2	0.0	0.5	0.3	15.3	0.0	97.7
	53 / 4 .	Host	67.0	30.0	42.4	0.0	38.9	0.1	0.0	0.3	0.4	16.2	0.1	98.4
	53 / 5 .	Host	64.3	40.0	41.1	0.0	38.0	0.1	0.0	0.3	0.3	17.7	0.1	97.7

		53 / 6 .	Host	49.5	50.0	33.5	0.1	37.1	0.2	0.0	0.3	0.4	26.5	-0.1	98.1
	Pr7	54 / 2 .	Host	63.3	8.5	40.7	0.0	38.4	0.2	0.0	0.2	0.4	18.3	-0.1	98.1
		54 / 3 .	Host	65.4	17.0	41.6	0.0	38.5	0.1	0.0	0.3	0.4	17.0	0.1	98.0
		54 / 4 .	Host	66.8	25.5	42.1	0.0	38.5	0.1	0.0	0.4	0.2	16.2	0.1	97.6
		54 / 5 .	Host	67.7	34.0	42.5	0.0	38.8	0.2	0.0	0.4	0.3	15.7	-0.1	97.9
		54 / 7 .	Host	69.1	51.0	43.1	0.0	38.9	0.2	0.0	0.3	0.3	15.0	0.0	97.8
	Pr8	55 / 1 .	Host	71.8	0.0	44.8	0.0	39.5	0.2	0.0	0.2	0.3	13.7	0.1	98.8
		55 / 2 .	Relict	80.7	6.8	48.7	0.1	40.6	0.2	0.0	0.2	0.2	9.1	0.1	99.1
		55 / 3 .	Relict	81.2	13.6	49.1	0.0	39.8	0.2	0.0	0.3	0.3	8.8	0.0	98.4
		55 / 4 .	Relict	81.2	20.4	48.6	0.1	40.2	0.2	0.0	0.4	0.3	8.7	0.0	98.6
	Pr9	56 / 1 .	Host	57.8	0.0	38.3	0.0	37.9	0.2	0.0	0.5	0.5	21.7	0.0	99.0
		56 / 2 .	Host	61.5	8.2	40.0	0.0	38.5	0.2	0.0	0.5	0.4	19.4	0.1	99.2
		56 / 3 .	Host	64.9	16.4	41.7	0.0	38.7	0.1	0.0	0.5	0.4	17.5	0.0	99.0
		56 / 4 .	Host	66.4	24.6	42.8	0.0	38.9	0.1	0.0	0.2	0.3	16.8	0.0	99.2
		56 / 5 .	Host	65.6	32.8	42.1	0.0	38.8	0.2	0.0	0.4	0.3	17.1	0.1	99.1
		56 / 6 .	Host	63.0	41.0	40.9	0.0	38.5	0.1	0.0	0.2	0.3	18.6	-0.1	98.7
		56 / 7 .	Host	61.4	49.2	40.1	0.0	38.2	0.2	0.0	0.3	0.3	19.6	-0.1	98.8
		56 / 8 .	Host	58.7	57.4	38.7	0.0	37.8	0.2	0.0	0.4	0.4	21.1	-0.1	98.6
		56 / 9 .	Host	57.0	65.6	37.6	0.0	37.6	0.2	0.0	0.3	0.4	22.0	0.2	98.3
		56 / 10 .	Host	55.1	73.8	36.8	0.0	37.5	0.3	0.0	0.3	0.4	23.3	0.0	98.7
	Pr10	57 / 1 .	Host	55.3	0.0	36.9	0.1	37.5	0.3	0.0	0.3	0.3	23.2	0.0	98.6
		57 / 2 .	Host	56.0	8.2	37.5	0.0	37.6	0.2	0.0	0.3	0.4	22.9	0.1	99.1
		57 / 3 .	Host	57.3	16.4	38.1	0.0	37.7	0.2	0.0	0.4	0.4	22.0	0.0	98.8
		57 / 4 .	Host	57.2	24.6	38.0	0.0	37.5	0.2	0.0	0.3	0.4	22.1	0.0	98.5
		57 / 5 .	Host	57.1	32.8	37.9	0.0	38.1	0.2	0.0	0.3	0.3	22.1	0.1	98.9
		57 / 6 .	Host	55.8	41.0	36.9	0.0	37.3	0.2	0.0	0.3	0.4	22.7	-0.2	97.8
Ch_01	Pr1	58 / 1 .	Host	67.5	0.0	42.9	0.1	39.2	0.3	0.1	0.0	0.3	16.0	0.2	99.0
		58 / 2 .	Relict	73.1	7.0	45.5	0.1	39.1	0.2	0.0	0.1	0.2	13.0	0.1	98.4

	58 / 3 .	Host	62.8	14.0	40.7	0.1	38.1	0.2	0.0	0.0	0.3	18.7	0.1	98.4
	58 / 5 .	Host	73.7	28.0	46.6	0.1	40.1	0.2	0.0	0.0	0.2	12.9	0.0	100.1
	58 / 6 .	Host	79.8	35.0	48.7	0.1	40.1	0.2	0.1	0.1	0.2	9.5	0.0	98.9
	58 / 7 .	Relict	83.3	42.0	50.4	0.1	41.0	0.2	0.0	0.1	0.1	7.8	0.1	99.8
	58 / 8 .	Relict	83.1	49.0	50.0	0.1	40.3	0.2	0.0	0.1	0.0	7.9	0.0	98.8
	58 / 9 .	Relict	80.3	56.0	48.7	0.1	40.5	0.4	0.0	0.1	0.0	9.3	0.1	99.3
	58 / 10 .	Host	67.4	63.0	42.9	0.0	38.7	0.4	0.0	0.1	0.2	16.1	0.0	98.4
Pr2	59 / 1 .	Host	65.5	0.0	42.0	0.1	38.4	0.3	0.1	0.1	0.3	17.2	0.0	98.6
	59 / 2 .	Relict	81.3	7.2	49.3	0.1	40.5	0.3	0.0	0.0	0.1	8.8	0.0	99.0
	59 / 3 .	Relict	81.8	14.4	49.5	0.1	40.3	0.3	0.1	0.1	0.1	8.6	-0.1	99.1
	59 / 4 .	Host	74.1	21.6	46.2	0.0	39.4	0.2	0.0	0.1	0.2	12.5	0.0	98.6
	59 / 5 .	Host	66.4	28.8	41.9	0.2	38.0	0.1	0.1	0.9	0.3	16.5	0.0	97.9
	59 / 6 .	Host	77.6	36.0	47.6	0.1	40.1	0.2	0.0	0.1	0.1	10.7	0.1	99.0
	59 / 7 .	Host	75.4	43.2	46.8	0.1	39.9	0.2	0.0	0.1	0.2	11.9	0.1	99.2
	59 / 8 .	Host	70.1	50.4	44.1	0.1	39.1	0.2	0.0	0.1	0.3	14.6	0.2	98.6
	59 / 9 .	Host	68.0	57.6	43.2	0.1	38.9	0.2	0.0	0.1	0.3	15.8	-0.1	98.6
	59 / 10 .	Host	63.6	64.8	41.1	0.1	38.2	0.4	0.1	0.1	0.4	18.3	0.0	98.5
Pr3	60 / 2 .	Host	70.1	6.3	44.1	0.1	38.9	0.5	0.0	0.1	0.2	14.6	0.0	98.6
	60 / 3 .	Host	69.5	12.6	43.9	0.1	38.8	0.3	0.0	0.1	0.2	14.9	0.0	98.4
	60 / 4 .	Host	66.2	18.9	42.5	0.0	38.8	0.2	0.0	0.0	0.3	16.8	0.1	98.8
Pr4	61 / 1 .	Host	65.4	0.0	41.8	0.1	38.7	0.3	0.0	0.1	0.3	17.2	0.1	98.5
	61 / 2 .	Host	68.7	6.4	43.6	0.0	38.9	0.1	0.0	0.0	0.2	15.4	0.0	98.3
	61 / 3 .	Host	71.0	12.8	44.7	0.1	39.1	0.2	0.0	0.1	0.2	14.2	-0.1	98.4
	61 / 4 .	Host	63.2	19.2	40.7	0.3	38.8	0.2	0.0	0.2	0.4	18.4	0.0	99.1
	61 / 5 .	Host	72.8	25.6	45.5	0.1	39.3	0.1	0.0	0.2	0.2	13.2	0.2	98.8
	61 / 6 .	Relict	79.4	32.0	48.6	0.1	40.4	0.2	0.1	0.1	0.2	9.8	0.1	99.5
	61 / 7 .	Relict	78.0	38.4	47.9	0.1	40.0	0.3	0.0	0.1	0.2	10.5	0.0	99.1
Pr5	62 / 1 .	Host	62.8	0.0	40.7	0.1	38.8	0.4	0.0	0.1	0.4	18.7	0.0	99.1

		62 / 2 .	Relict	76.9	6.5	47.5	0.1	39.9	0.5	0.0	0.2	0.2	11.1	0.0	99.4
		62 / 3 .	Relict	82.0	13.0	49.9	0.1	40.8	0.4	0.1	0.1	0.1	8.5	-0.1	99.8
		62 / 4 .	Relict	82.7	19.5	50.3	0.0	41.0	0.1	0.0	0.0	0.1	8.2	0.0	99.8
		62 / 5 .	Relict	83.7	26.0	50.5	0.0	40.9	0.2	0.0	0.1	0.1	7.6	-0.1	99.5
		62 / 6 .	Relict	78.5	32.5	48.2	0.1	39.9	0.3	0.0	0.1	0.1	10.3	0.1	99.0
		62 / 7 .	Host	62.4	39.0	40.5	0.1	38.3	0.3	0.1	0.1	0.3	18.9	-0.1	98.5
	Pr6	63 / 1 .	Host	61.6	0.0	39.8	0.1	38.0	0.4	0.0	0.1	0.5	19.2	0.0	98.1
		63 / 2 .	Host	66.4	6.5	42.4	0.1	38.6	0.5	0.0	0.1	0.3	16.6	0.0	98.7
		63 / 3 .	Relict	76.6	13.0	46.9	0.1	39.4	0.4	0.1	0.2	0.1	11.1	0.1	98.4
		63 / 4 .	Relict	78.5	19.5	47.8	0.1	39.9	0.4	0.1	0.0	0.2	10.1	0.0	98.6
		63 / 5 .	Host	72.2	26.0	45.1	0.1	39.6	0.1	0.0	0.1	0.3	13.5	0.0	98.9
		63 / 6 .	Host	69.6	32.5	43.8	0.1	39.4	0.2	0.1	0.0	0.3	14.8	0.1	98.7
Ch_03p	Pr1	86 / 1 .	Host	41.6	0.0	30.1	0.0	35.9	0.0	0.0	0.1	0.4	32.8	-0.1	99.3
		86 / 2 .	Host	42.7	8.9	30.6	0.0	36.2	0.1	0.0	0.0	0.4	31.8	0.1	99.2
		86 / 3 .	Host	45.0	17.8	31.8	0.0	36.4	0.1	0.0	0.1	0.4	30.2	-0.2	99.0
		86 / 4 .	Host	48.8	26.7	34.1	0.0	37.4	0.1	0.0	0.0	0.4	27.8	0.1	99.9
		86 / 5 .	Host	53.7	35.6	36.6	0.0	38.0	0.1	0.0	0.0	0.3	24.5	0.0	99.6
		86 / 6 .	Host	55.9	44.5	37.9	0.0	38.0	0.1	0.0	0.0	0.3	23.2	0.0	99.5
		86 / 7 .	Host	57.1	53.4	38.4	0.0	38.1	0.1	0.0	0.0	0.3	22.4	-0.1	99.4
		86 / 8 .	Host	57.4	62.3	38.5	0.0	38.5	0.1	0.0	0.0	0.3	22.1	-0.1	99.6
		86 / 9 .	Host	56.8	71.2	38.3	0.0	38.0	0.1	0.0	0.2	0.3	22.6	0.0	99.4
		86 / 10 .	Host	56.3	80.1	38.1	0.0	38.1	0.1	0.0	0.0	0.4	22.9	0.0	99.7
		86 / 11 .	Host	53.8	89.0	36.6	0.0	37.6	0.1	0.0	0.1	0.3	24.4	-0.1	99.2
		86 / 12 .	Host	51.1	97.9	35.3	0.0	37.3	0.1	0.0	0.1	0.3	26.3	-0.2	99.5
		86 / 13 .	Host	46.9	106.8	33.0	0.0	37.0	0.1	0.0	0.0	0.4	28.9	-0.2	99.5
		86 / 14 .	Host	44.0	115.7	31.3	0.0	36.7	0.1	0.0	0.1	0.4	31.0	-0.1	99.6
	Pr2	87 / 1 .	Host	41.3	0.0	29.8	0.0	35.9	0.1	0.0	0.1	0.4	32.9	0.0	99.2
		87 / 2 .	Host	41.8	6.9	30.1	0.0	35.8	0.1	0.0	0.1	0.5	32.5	0.0	99.2

	87 / 3 .	Host	41.4	13.7	29.8	0.0	36.4	0.1	0.0	0.1	0.5	32.7	0.0	99.6
	87 / 4 .	Host	41.9	20.6	30.1	0.0	36.1	0.1	0.0	0.0	0.5	32.4	0.0	99.2
	87 / 5 .	Host	42.2	27.4	30.3	0.0	36.3	0.1	0.0	0.1	0.4	32.2	-0.1	99.5
	87 / 6 .	Host	42.7	34.3	30.6	0.0	36.6	0.1	0.0	0.0	0.4	31.8	-0.1	99.5
	87 / 8 .	Host	43.3	48.0	30.8	0.0	36.3	0.1	0.0	0.1	0.4	31.3	-0.2	99.0
	87 / 9 .	Host	44.1	54.8	31.5	0.0	36.7	0.1	0.0	0.1	0.4	31.0	0.1	99.9
	87 / 10 .	Host	44.5	61.7	31.6	0.0	37.1	0.1	0.0	0.2	0.4	30.5	0.0	100.0
	87 / 11 .	Host	45.0	68.5	31.9	0.0	36.7	0.1	0.0	0.2	0.3	30.2	0.0	99.6
	87 / 12 .	Host	44.8	75.4	31.8	0.0	36.5	0.1	0.0	0.3	0.5	30.4	0.1	99.6
	87 / 13 .	Host	44.8	82.2	31.8	0.0	36.5	0.1	0.0	0.2	0.5	30.4	0.1	99.5
	87 / 14 .	Host	44.4	89.1	31.7	0.0	36.9	0.1	0.0	0.1	0.4	30.7	-0.1	99.9
Pr3	88 / 1 .	Host	53.0	0.0	36.2	0.0	37.7	0.2	0.0	0.1	0.5	24.9	0.1	99.5
	88 / 2 .	Host	55.5	6.5	37.4	0.0	38.1	0.1	0.0	0.1	0.6	23.2	0.0	99.6
	88 / 3 .	Host	56.8	13.0	38.5	0.0	38.1	0.1	0.0	0.0	0.5	22.7	0.0	100.0
	88 / 5 .	Host	57.6	26.0	38.5	0.0	38.7	0.1	0.0	0.1	0.5	22.0	0.0	99.9
	88 / 6 .	Host	57.1	32.5	38.4	0.0	37.6	0.1	0.0	0.0	0.4	22.4	-0.1	99.1
	88 / 7 .	Host	56.0	39.0	37.8	0.0	38.2	0.1	0.0	0.0	0.4	23.1	0.0	99.8
	88 / 8 .	Host	55.8	45.5	37.9	0.0	37.8	0.1	0.0	0.0	0.5	23.3	0.1	99.7
	88 / 9 .	Host	54.3	52.0	36.9	0.0	38.0	0.2	0.0	0.1	0.4	24.1	0.0	99.6
	88 / 10 .	Host	53.6	58.5	36.6	0.0	37.5	0.1	0.0	0.1	0.4	24.5	0.0	99.3
	88 / 11 .	Host	52.8	65.0	36.2	0.0	37.6	0.1	0.0	0.0	0.4	25.1	0.2	99.6
	88 / 12 .	Host	53.2	71.5	36.2	0.0	37.7	0.1	0.0	0.1	0.4	24.7	0.0	99.2
Pr4	89 / 1 .	Host	60.1	0.0	40.0	0.0	38.9	0.0	0.0	0.1	0.4	20.6	0.0	100.0
	89 / 2 .	Host	61.2	10.0	40.6	0.0	39.0	0.0	0.0	0.0	0.4	19.9	0.0	99.9
	89 / 3 .	Host	60.9	20.0	40.6	0.0	39.0	0.0	0.0	0.1	0.4	20.2	0.1	100.4
	89 / 4 .	Host	59.6	30.0	40.7	0.4	36.3	0.1	0.0	0.1	0.3	21.4	0.7	99.9
	89 / 5 .	Host	63.2	40.0	41.4	0.0	39.1	0.0	0.0	0.1	0.3	18.7	0.1	99.7
	89 / 6 .	Host	64.9	50.0	42.3	0.0	39.7	0.0	0.0	0.1	0.4	17.7	-0.1	100.2

89 / 7 .	Host	67.0	60.0	43.5	0.0	39.4	0.0	0.0	0.1	0.3	16.6	0.1	100.0
89 / 8 .	Host	67.9	70.0	43.7	0.1	39.1	0.0	0.0	0.2	0.4	16.0	0.1	99.6
89 / 9 .	Host	68.9	80.0	43.9	0.1	39.3	0.0	0.0	0.2	0.3	15.4	0.0	99.1
89 / 10 .	Host	69.7	90.0	44.6	0.0	39.6	0.0	0.0	0.1	0.3	15.0	0.0	99.7
89 / 11 .	Host	70.3	100.0	44.7	0.0	40.1	0.0	0.0	0.1	0.3	14.6	0.1	100.0
89 / 12 .	Host	71.2	110.0	46.1	0.0	39.6	0.0	0.0	0.2	0.3	14.5	0.0	100.8
89 / 13 .	Host	71.5	120.0	45.5	0.0	40.1	0.0	0.0	0.1	0.3	14.1	0.0	100.2
89 / 14 .	Host	72.5	130.0	47.2	0.1	39.4	0.0	0.0	0.1	0.3	13.9	-0.1	101.0
89 / 15 .	Host	71.5	140.0	45.6	0.0	40.2	0.1	0.0	0.1	0.3	14.1	-0.1	100.4
89 / 16 .	Host	71.5	150.0	45.3	0.0	39.7	0.0	0.0	0.1	0.4	14.0	0.0	99.5
89 / 17 .	Host	71.3	160.0	45.1	0.0	39.6	0.0	0.0	0.2	0.3	14.1	0.0	99.4
89 / 18 .	Host	70.7	170.0	44.8	0.0	40.1	0.0	0.0	0.1	0.3	14.4	0.0	99.7
89 / 19 .	Host	70.2	180.0	44.5	0.0	39.7	0.0	0.0	0.1	0.3	14.6	-0.1	99.2
89 / 20 .	Host	69.8	190.0	44.5	0.0	39.9	0.0	0.0	0.1	0.3	14.9	0.0	99.8
89 / 21 .	Host	68.2	200.0	43.2	0.3	40.0	0.0	0.0	0.3	0.3	15.6	-0.2	99.9
89 / 22 .	Host	66.9	210.0	43.1	0.0	39.4	0.0	0.0	0.1	0.3	16.5	0.1	99.4
89 / 23 .	Host	63.2	220.0	41.3	0.1	38.8	0.0	0.0	0.1	0.3	18.7	0.0	99.3
89 / 24 .	Host	58.3	230.0	39.1	0.0	38.4	0.0	0.0	0.1	0.3	21.7	-0.2	99.6
89 / 25 .	Host	50.9	240.0	35.3	0.0	37.4	0.1	0.0	0.1	0.3	26.4	0.0	99.6

Ch_02p	Pr1	66 / 1 .	Host	68.8	0.0	43.6	0.1	38.3	0.1	0.1	0.1	0.4	15.3	0.0	97.9
		66 / 2 .	Host	74.8	7.1	46.2	0.1	39.3	0.1	0.1	0.2	0.2	12.1	0.0	98.3
		66 / 3 .	Relict	79.6	14.2	48.2	0.1	39.7	0.2	0.0	0.2	0.1	9.6	0.1	98.2
		66 / 4 .	Relict	79.6	21.3	48.5	0.1	40.0	0.1	0.0	0.1	0.2	9.6	-0.1	98.7
		66 / 5 .	Host	73.3	28.4	45.6	0.1	39.1	0.1	0.0	0.1	0.3	12.9	0.1	98.3
		66 / 6 .	Host	65.7	35.5	42.0	0.1	38.1	0.0	0.1	0.1	0.4	17.0	0.0	97.8
		66 / 7 .	Host	70.8	42.6	44.2	0.1	39.5	0.2	0.0	0.2	0.3	14.1	0.1	98.8
		66 / 8 .	Relict	80.9	49.7	48.9	0.1	40.7	0.4	0.1	0.1	0.1	9.0	0.0	99.4
		66 / 9 .	Relict	85.9	56.8	50.6	0.1	40.4	0.4	0.0	0.1	0.1	6.5	0.1	98.4

	66 / 10 .	Host	76.4	63.9	47.0	0.1	39.9	0.3	0.0	0.1	0.2	11.3	0.1	98.9
Pr2	67 / 1 .	Host	67.2	0.0	42.7	0.1	38.7	0.2	0.1	0.1	0.4	16.2	0.1	98.5
	67 / 2 .	Host	70.5	7.7	44.1	0.1	38.9	0.3	0.0	0.1	0.3	14.3	0.1	98.3
	67 / 3 .	Host	72.1	15.4	45.0	0.1	38.9	0.1	0.0	0.1	0.3	13.5	0.0	98.1
	67 / 4 .	Host	71.0	23.1	44.6	0.0	38.8	0.1	0.0	0.0	0.3	14.1	0.1	98.1
	67 / 5 .	Host	69.6	30.8	44.1	0.0	39.0	0.1	0.0	0.0	0.3	14.9	0.0	98.5
	67 / 6 .	Host	68.8	38.5	43.5	0.1	38.4	0.2	0.1	0.1	0.3	15.3	-0.1	97.9
	67 / 7 .	Host	66.4	46.2	42.6	0.1	38.6	0.1	0.0	0.2	0.4	16.7	0.1	98.9
	67 / 8 .	Host	66.9	53.9	42.2	0.3	39.3	0.0	0.0	0.1	0.4	16.2	-0.1	98.6
	67 / 9 .	Host	67.2	61.6	42.8	0.1	39.0	0.1	0.1	0.2	0.4	16.2	0.2	99.0
	67 / 10 .	Host	66.6	69.3	42.1	0.2	38.3	0.0	0.1	0.6	0.4	16.4	0.0	98.1
	67 / 12 .	Host	73.5	84.7	45.5	0.1	39.3	0.4	0.0	0.2	0.1	12.7	0.1	98.5
	67 / 13 .	Relict	76.7	92.4	47.0	0.1	39.6	0.4	0.1	0.1	0.2	11.0	-0.1	98.5
	67 / 14 .	Relict	76.7	100.1	47.0	0.1	40.0	0.4	0.0	0.0	0.1	11.1	0.0	98.7
	67 / 15 .	Relict	75.7	107.8	46.6	0.1	39.6	0.4	0.0	0.0	0.3	11.6	0.1	98.6
	67 / 16 .	Host	73.5	115.5	45.5	0.1	39.7	0.3	0.1	0.1	0.3	12.7	0.0	98.8
	67 / 17 .	Host	70.4	123.2	43.9	0.1	39.1	0.2	0.1	0.1	0.3	14.4	0.0	98.1
Pr3	68 / 1 .	Host	74.7	0.0	46.0	0.1	39.4	0.3	0.0	0.1	0.2	12.1	0.1	98.3
	68 / 2 .	Host	78.6	8.3	46.9	0.1	40.1	0.4	0.0	0.1	0.1	9.9	0.1	97.7
	68 / 3 .	Host	80.0	16.6	48.3	0.1	40.0	0.3	0.0	0.1	0.1	9.4	-0.2	98.3
	68 / 4 .	Host	79.8	24.9	48.5	0.1	40.4	0.3	0.0	0.1	0.1	9.5	-0.1	99.0
	68 / 5 .	Host	79.0	33.2	47.9	0.1	40.1	0.3	0.0	0.1	0.1	9.8	-0.1	98.5
	68 / 6 .	Host	77.4	41.5	47.3	0.1	39.6	0.3	0.0	0.1	0.1	10.7	-0.2	98.1
	68 / 7 .	Host	75.1	49.8	46.3	0.1	39.8	0.3	0.0	0.1	0.2	11.9	0.0	98.7
	68 / 8 .	Host	71.8	58.1	44.6	0.1	39.0	0.3	0.0	0.1	0.2	13.6	0.0	98.0
Pr4	69 / 1 .	Host	67.8	0.0	42.7	0.3	38.7	0.1	0.0	0.5	0.4	15.7	-0.1	98.4
	69 / 2 .	Host	70.5	7.7	44.1	0.1	38.5	0.3	0.0	0.1	0.4	14.3	0.0	97.9

			69 / 3 .	Host	72.7	15.3	45.2	0.1	39.4	0.3	0.1	0.1	0.3	13.2	0.0	98.6
			69 / 4 .	Relict	75.2	23.0	46.3	0.1	39.5	0.2	0.1	0.1	0.2	11.8	0.1	98.5
			69 / 5 .	Relict	77.7	30.6	47.5	0.1	40.0	0.3	0.0	0.2	0.2	10.6	0.1	99.0
			69 / 6 .	Relict	76.7	38.3	46.8	0.1	39.8	0.3	0.0	0.1	0.2	11.1	0.1	98.5
			69 / 7 .	Host	71.9	45.9	44.6	0.1	39.2	0.3	0.0	0.1	0.2	13.5	-0.1	98.2
			69 / 8 .	Host	67.3	53.6	42.8	0.1	38.6	0.2	0.1	0.1	0.3	16.1	0.1	98.5
			69 / 9 .	Host	65.7	61.2	42.2	0.0	38.4	0.1	0.0	0.0	0.4	17.1	-0.1	98.3
			69 / 10 .	Host	65.7	68.9	42.2	0.0	38.7	0.0	0.1	0.1	0.4	17.1	-0.1	98.7
	Pr5		70 / 1 .	Host	66.4	0.0	42.2	0.0	38.6	0.0	0.1	0.0	0.4	16.5	0.1	97.9
			70 / 3 .	Host	65.0	16.4	41.7	0.1	38.7	0.0	0.0	0.1	0.4	17.4	0.0	98.4
			70 / 4 .	Host	65.7	24.6	42.0	0.0	38.6	0.1	0.0	0.1	0.4	17.0	0.0	98.3
			70 / 5 .	Host	65.7	32.8	41.8	0.0	38.9	0.3	0.0	0.0	0.3	17.0	-0.1	98.4
			70 / 6 .	Host	66.1	41.0	42.1	0.1	38.5	0.1	0.1	0.1	0.4	16.8	0.2	98.5
			70 / 7 .	Host	66.6	49.2	42.4	0.1	38.2	0.3	0.1	0.1	0.3	16.5	0.1	98.1
			70 / 8 .	Host	68.4	57.4	43.0	0.1	38.8	0.3	0.0	0.1	0.2	15.5	0.0	98.1
			70 / 9 .	Host	66.7	65.6	42.3	0.1	38.2	0.3	0.1	0.0	0.3	16.3	0.0	97.6
	Ch_01p	Pr1	71 / 5 .	Host	68.0	49.2	42.8	0.0	39.0	0.1	0.0	0.1	0.2	15.6	0.0	97.8
			71 / 6 .	Host	69.1	61.5	43.5	0.0	39.0	0.1	0.0	0.1	0.3	15.0	0.0	98.1
			71 / 7 .	Host	69.3	73.8	43.6	0.0	39.1	0.1	0.0	0.1	0.3	14.9	-0.1	98.0
			71 / 9 .	Host	69.3	98.4	43.6	0.0	38.9	0.1	0.0	0.1	0.3	15.0	0.0	98.0
			71 / 10 .	Host	69.3	110.7	43.5	0.0	39.5	0.1	0.0	0.1	0.3	14.9	0.1	98.4
			71 / 11 .	Host	68.6	123.0	43.2	0.0	38.6	0.1	0.0	0.1	0.3	15.3	0.0	97.6
			71 / 12 .	Host	67.8	135.3	42.8	0.0	39.1	0.1	0.0	0.0	0.4	15.8	0.0	98.2
			71 / 13 .	Host	66.8	147.6	42.5	0.0	38.8	0.1	0.0	0.0	0.3	16.4	0.1	98.1
			71 / 14 .	Host	66.0	159.9	42.2	0.0	38.4	0.0	0.0	0.1	0.4	16.9	0.0	97.9
			71 / 15 .	Host	64.8	172.2	41.3	0.0	38.8	0.0	0.0	0.0	0.3	17.4	0.0	97.9
			71 / 17 .	Host	61.1	196.8	39.7	0.0	38.1	0.0	0.0	0.1	0.5	19.6	0.0	98.1
		Pr2	72 / 1 .	Host	58.2	0.0	38.3	0.1	37.7	0.0	0.0	0.3	0.5	21.4	0.1	98.4

	72 / 2 .	Host	58.7	12.7	39.1	0.0	38.1	0.1	0.0	0.0	0.4	21.4	0.0	99.1
	72 / 3 .	Host	59.7	25.4	39.4	0.0	38.3	0.1	0.0	0.0	0.4	20.6	0.1	99.0
	72 / 4 .	Host	56.4	38.1	38.2	0.0	36.4	0.1	0.0	0.0	0.4	22.9	0.2	98.1
	72 / 5 .	Host	61.3	50.8	40.6	0.0	38.9	0.0	0.0	0.1	0.4	19.8	0.2	99.9
	72 / 6 .	Host	62.3	63.5	41.4	0.0	38.7	0.0	0.0	0.0	0.4	19.5	0.2	100.2
	72 / 7 .	Host	63.0	76.2	41.6	0.0	39.0	0.0	0.0	0.1	0.5	18.9	0.2	100.4
	72 / 8 .	Host	63.9	88.9	41.5	0.0	38.4	0.0	0.0	0.1	0.4	18.2	-0.2	98.6
	72 / 9 .	Host	64.7	101.6	41.7	0.0	38.6	0.0	0.0	0.1	0.4	17.7	0.0	98.7
	72 / 10 .	Host	65.3	114.3	42.2	0.0	38.9	0.1	0.0	0.1	0.4	17.4	0.0	99.0
	72 / 11 .	Host	65.5	127.0	42.1	0.0	38.8	0.0	0.0	0.0	0.4	17.2	-0.1	98.5
	72 / 12 .	Host	65.3	139.7	42.2	0.0	38.7	0.0	0.0	0.0	0.4	17.4	-0.1	98.9
	72 / 13 .	Host	65.2	152.4	42.2	0.0	38.9	0.0	0.0	0.1	0.3	17.4	0.1	99.0
	72 / 14 .	Host	65.1	165.1	42.0	0.0	39.0	0.0	0.0	0.1	0.3	17.5	-0.1	98.9
	72 / 15 .	Host	64.3	177.8	41.6	0.0	38.5	0.0	0.0	0.1	0.3	17.9	0.1	98.6
	72 / 16 .	Host	63.9	190.5	41.5	0.0	38.4	0.0	0.0	0.1	0.4	18.2	0.1	98.7
	72 / 17 .	Host	63.5	203.2	41.2	0.0	38.5	0.0	0.0	0.1	0.4	18.4	0.0	98.7
	72 / 18 .	Host	62.0	215.9	39.8	0.0	38.2	0.2	0.0	0.9	0.4	18.9	0.0	98.3
	72 / 19 .	Host	61.7	228.6	40.5	0.0	37.7	0.0	0.0	0.0	0.4	19.5	-0.1	98.1
	72 / 20 .	Host	60.9	241.3	39.9	0.0	38.2	0.0	0.0	0.1	0.4	19.9	0.0	98.6
Pr3	73 / 1 .	Host	59.4	0.0	39.3	0.0	38.1	0.1	0.0	0.0	0.5	20.9	0.2	99.1
	73 / 2 .	Host	59.7	12.8	39.5	0.0	38.4	0.1	0.0	0.1	0.5	20.7	0.0	99.2
	73 / 3 .	Host	60.6	25.6	39.9	0.0	38.2	0.0	0.0	0.0	0.5	20.2	-0.1	98.9
	73 / 4 .	Host	60.6	38.5	40.1	0.0	38.3	0.1	0.0	0.0	0.5	20.2	0.0	99.2
	73 / 5 .	Host	61.4	51.3	40.4	0.0	38.1	0.1	0.0	0.0	0.4	19.7	0.1	98.9
	73 / 6 .	Host	61.8	64.1	40.5	0.0	37.9	0.1	0.0	0.0	0.4	19.4	0.0	98.4
	73 / 7 .	Host	61.8	76.9	40.7	0.0	38.2	0.0	0.0	0.1	0.4	19.5	0.0	98.9
	73 / 8 .	Host	61.7	89.7	40.7	0.0	38.7	0.0	0.0	0.1	0.4	19.6	0.1	99.6

			73 / 9 .	Host	61.5	102.6	40.5	0.0	38.3	0.0	0.0	0.0	0.3	19.6	0.0	98.8
			73 / 10 .	Host	61.7	115.4	40.4	0.0	38.6	0.1	0.0	0.1	0.4	19.5	-0.1	99.2
			73 / 11 .	Host	61.2	128.2	40.2	0.0	38.0	0.1	0.0	0.1	0.5	19.7	0.1	98.8
			73 / 12 .	Host	60.9	141.0	39.9	0.0	38.2	0.0	0.0	0.1	0.4	19.9	0.1	98.6
			73 / 13 .	Host	59.2	153.8	39.1	0.0	37.7	0.0	0.0	0.1	0.5	21.0	0.1	98.6
			73 / 14 .	Host	59.0	166.7	39.4	0.0	37.6	0.1	0.0	0.1	0.4	21.2	-0.1	98.8
			73 / 15 .	Host	58.9	179.5	39.2	0.0	38.5	0.0	0.0	0.1	0.4	21.2	0.0	99.5
			73 / 16 .	Host	59.4	192.3	39.2	0.0	38.1	0.1	0.0	0.0	0.5	20.8	0.0	98.7
			73 / 17 .	Host	59.7	205.1	39.6	0.0	38.2	0.0	0.0	0.0	0.4	20.7	0.1	99.0
			73 / 18 .	Host	59.5	217.9	39.5	0.0	37.7	0.0	0.0	0.0	0.5	20.9	0.1	98.8
	Ch_05	Pr1	74 / 1 .	Host	65.7	0.0	42.1	0.0	38.9	0.2	0.0	0.5	0.3	17.0	0.0	99.0
			74 / 2 .	Host	70.0	6.2	44.0	0.1	40.0	0.1	0.0	0.5	0.3	14.7	-0.1	99.7
			74 / 3 .	Host	73.1	12.4	45.2	0.0	39.6	0.1	0.0	0.3	0.3	12.9	0.0	98.4
			74 / 4 .	Host	74.0	18.6	46.3	0.0	39.2	0.1	0.0	0.3	0.3	12.6	0.0	98.9
			74 / 5 .	Host	71.9	24.8	44.7	0.0	39.3	0.2	0.0	0.4	0.2	13.5	0.0	98.3
			74 / 6 .	Host	71.4	31.0	44.4	0.0	39.0	0.1	0.0	0.3	0.2	13.8	0.0	98.0
			74 / 7 .	Host	70.8	37.2	44.3	0.0	39.4	0.1	0.0	0.6	0.2	14.2	0.0	98.9
			74 / 8 .	Host	70.7	43.4	44.2	0.0	39.6	0.2	0.0	0.5	0.3	14.2	0.0	98.9
		Pr2	75 / 1 .	Host	73.0	0.0	45.2	0.0	39.6	0.1	0.0	0.6	0.3	13.0	0.1	98.8
			75 / 2 .	Host	73.6	6.6	45.6	0.0	39.8	0.1	0.0	0.3	0.3	12.7	0.0	98.9
			75 / 3 .	Host	74.2	13.2	45.9	0.0	39.7	0.1	0.0	0.2	0.2	12.4	0.1	98.8
			75 / 4 .	Host	74.2	19.8	45.9	0.0	39.8	0.1	0.0	0.3	0.2	12.4	0.0	98.8
			75 / 5 .	Host	73.5	26.4	46.0	0.0	39.6	0.1	0.0	0.3	0.2	12.8	0.1	99.1
			75 / 6 .	Host	72.2	33.0	45.0	0.0	39.6	0.1	0.0	0.4	0.3	13.4	-0.1	98.9
			75 / 7 .	Host	68.8	39.6	43.4	0.0	39.1	0.1	0.0	0.4	0.3	15.3	0.1	98.7
			75 / 8 .	Host	57.3	46.2	37.6	0.0	37.7	0.3	0.0	0.6	0.4	21.7	0.0	98.4
		Pr3	76 / 1 .	Host	67.0	0.0	42.7	0.1	39.1	0.3	0.0	0.5	0.3	16.3	0.1	99.5
			76 / 2 .	Relict	86.7	7.1	50.9	0.1	40.9	0.4	0.0	0.4	0.1	6.0	-0.1	98.8

		76 / 3 .	Relict	88.5	14.2	52.3	0.2	40.9	0.4	0.0	0.5	0.0	5.3	0.1	99.6
		76 / 4 .	Relict	88.7	21.3	52.3	0.1	41.2	0.4	0.0	0.5	0.1	5.2	0.1	99.8
		76 / 5 .	Relict	89.1	28.4	54.1	0.2	40.4	0.4	0.0	0.5	0.1	5.1	0.0	100.8
		76 / 6 .	Relict	88.4	35.5	51.8	0.2	41.1	0.4	0.0	0.5	0.0	5.3	-0.1	99.3
		76 / 7 .	Relict	87.7	42.6	50.9	0.1	41.7	0.4	0.0	0.5	0.0	5.5	-0.1	99.3
		76 / 8 .	Host	78.2	49.7	47.7	0.1	40.6	0.4	0.0	0.6	0.1	10.3	0.1	99.9
		76 / 10 .	Host	66.9	63.9	42.4	0.1	39.4	0.3	0.0	0.4	0.2	16.3	0.1	99.2
	Pr4	77 / 1 .	Host	56.3	0.0	37.4	0.0	37.5	0.3	0.0	0.4	0.4	22.5	-0.1	98.5
		77 / 2 .	Host	59.8	6.7	39.3	0.0	38.1	0.2	0.0	0.3	0.3	20.5	0.2	98.8
		77 / 3 .	Host	61.6	13.4	40.0	0.0	38.6	0.2	0.0	0.3	0.4	19.4	0.0	98.8
		77 / 4 .	Host	61.3	20.1	39.6	0.1	38.2	0.2	0.0	0.3	0.3	19.4	0.0	98.2
		77 / 5 .	Host	58.6	26.8	38.6	0.0	38.0	0.2	0.0	0.3	0.4	21.1	0.0	98.5
		77 / 6 .	Host	55.6	33.5	37.0	0.0	37.5	0.2	0.0	0.5	0.4	22.9	-0.1	98.3
	Pr5	78 / 1 .	Host	54.8	0.0	36.1	0.2	37.7	0.3	0.0	0.2	0.5	23.1	0.0	98.2
		78 / 2 .	Host	58.1	6.5	38.0	0.0	38.1	0.2	0.0	0.6	0.4	21.3	0.0	98.5
		78 / 3 .	Host	59.6	13.0	38.8	0.0	38.3	0.2	0.0	0.3	0.4	20.4	0.2	98.6
		78 / 4 .	Host	59.6	19.5	38.6	0.0	38.1	0.2	0.0	0.5	0.3	20.3	0.1	98.0
		78 / 5 .	Host	58.3	26.0	38.4	0.0	38.1	0.2	0.0	0.5	0.4	21.3	0.0	99.0
	Pr6	79 / 1 .	Host	59.2	0.0	38.9	0.0	37.5	0.2	0.0	0.4	0.4	20.8	-0.1	98.1
		79 / 2 .	Host	64.3	5.5	41.4	0.0	39.1	0.2	0.0	0.2	0.3	17.8	-0.1	99.0
		79 / 3 .	Host	66.5	11.0	42.4	0.0	38.9	0.1	0.0	0.3	0.3	16.6	0.1	98.9
		79 / 4 .	Host	58.5	16.5	38.7	0.0	38.2	0.2	0.0	0.3	0.4	21.3	0.0	99.0
	Pr7	80 / 1 .	Host	53.5	0.0	35.5	0.3	37.9	0.2	0.0	0.3	0.4	24.0	0.0	98.7
		80 / 2 .	Host	56.2	7.5	37.1	0.0	37.8	0.2	0.0	0.4	0.4	22.4	0.1	98.4
		80 / 3 .	Host	58.5	15.0	38.0	0.0	38.4	0.2	0.0	0.9	0.4	20.9	0.0	98.8
		80 / 5 .	Host	54.5	30.0	36.5	0.0	37.6	0.2	0.0	0.2	0.4	23.6	0.0	98.6
Renazzo	Ch_01	1	Relict	94.9		55.4	0.0	41.9	0.3	0.0	0.3	0.1	2.3	-0.1	100.4
		2	Relict	92.0		53.9	0.0	42.0	0.4	0.0	0.3	0.1	3.6	0.0	100.5

		3	Relict	94.9	55.5	0.0	42.0	0.2	0.0	0.5	0.1	2.3	0.0	100.6
		4	Host	57.4	38.6	0.0	38.4	0.2	0.0	0.4	0.2	22.2	0.1	100.2
		5	Host	56.6	38.3	0.0	37.9	0.2	0.0	0.3	0.3	22.9	0.1	100.1
		6	Host	45.8	32.2	0.0	36.5	0.3	0.0	0.3	0.4	29.6	0.2	99.5
		7	Host	49.0	33.9	0.0	37.2	0.3	0.0	0.5	0.3	27.4	0.0	99.7
	Ch_02	8	Relict	83.7	50.4	0.0	41.3	0.2	0.0	0.6	0.3	7.6	0.1	100.6
		9	Relict	76.5	47.3	0.0	40.5	0.2	0.0	0.6	0.3	11.2	0.3	100.5
		10	Relict	91.3	53.2	0.1	42.0	0.3	0.0	0.5	0.3	3.9	0.0	100.1
		11	Relict	74.7	46.8	0.0	40.3	0.2	0.0	0.5	0.3	12.3	-0.1	100.4
		12	Host	51.2	34.9	0.0	36.6	0.2	0.0	0.5	0.5	25.8	-0.1	98.5
		13	Host	55.8	37.5	0.0	38.2	0.1	0.1	0.3	0.3	23.0	0.0	99.4
		14	Host	52.8	35.9	0.0	37.6	0.2	0.0	0.5	0.4	24.8	0.1	99.6
	Ch_03	15	Relict	95.9	55.4	0.1	43.0	0.5	0.1	0.2	0.0	1.8	0.1	101.2
		16	Relict	59.7	39.4	0.0	38.8	0.2	0.0	0.4	0.3	20.6	-0.1	99.8
		17	Host	44.6	31.5	0.0	36.9	0.3	0.0	0.5	0.4	30.3	0.3	100.2
		18	Host	47.1	33.0	0.0	37.0	0.3	0.0	0.3	0.4	28.8	0.0	99.8
		19	Host	46.9	32.7	0.0	36.7	0.2	0.0	0.3	0.5	28.8	0.0	99.2
		20	Relict	94.7	54.6	0.1	42.4	0.4	0.1	0.3	0.1	2.4	-0.1	100.4
DaG 574	Ch_01	32	Host	56.9	38.3	0.0	38.4	0.2	0.0	0.6	0.3	22.5	0.1	100.4
		33	Relict	69.9	44.7	0.1	39.3	0.3	0.1	0.5	0.2	14.9	0.1	100.1
		34	Relict	68.3	44.2	0.0	39.5	0.2	0.0	0.3	0.1	15.9	0.0	100.2
		35	Host	54.7	37.6	0.1	37.9	0.3	0.0	0.3	0.2	24.2	0.0	100.6
		36	Host	61.8	41.0	0.0	38.8	0.2	0.0	0.5	0.1	19.7	0.0	100.3
		37	Host	50.5	35.0	0.0	37.9	0.3	0.0	0.4	0.4	26.6	0.0	100.6
	Ch_02	31	Host	45.6	32.4	0.1	36.6	0.2	0.0	0.4	0.5	30.0	0.1	100.2
		38	Host	64.9	42.9	0.0	39.6	0.2	0.0	0.3	0.2	18.0	0.0	101.1
		39	Host	49.5	35.0	0.0	37.7	0.2	0.0	0.5	0.4	27.7	-0.1	101.5
		40	Host	49.8	34.3	0.0	37.3	0.2	0.0	0.5	0.5	26.9	0.1	99.8

Table A1-2. Individual spot analysis of O isotopic compositions and mineral chemistry of all olivine grains studied in type II chondrules from CO, CR and ordinary chondrites.

Class	Chondrite	Chondrule	$\delta^{18}\text{O}$ (‰)	2σ	$\delta^{17}\text{O}$ (‰)	2σ	$\Delta^{17}\text{O}$ (‰)	2σ	MgO	Al ₂ O ₃	SiO ₂	CaO	TiO ₂	Cr ₂ O ₃	MnO	FeO	NiO	Total	Mg# (mol%)	Olivine grain		
CO	<i>LoV123</i>	<i>Ch02</i>	4.3	0.3	2.1	0.3	-0.2	0.3	48.3	0.0	41.0	0.1	0.0	0.7	0.2	10.3	0.0	100.7	78.4	Relict		
			4.1	0.3	2.0	0.4	-0.1	0.4	53.7	0.0	42.0	0.1	0.0	0.5	0.3	3.8	0.2	100.6	91.6	Relict		
			3.5	0.3	1.4	0.3	-0.5	0.3	53.5	0.1	41.6	0.3	0.1	0.4	0.1	4.1	0.0	100.2	91.0	Relict		
			0.1	0.3	-2.6	0.4	-2.6	0.4	55.8	0.2	42.2	0.4	0.1	0.4	0.0	3.0	0.1	102.2	93.6	Relict		
			-4.8	0.3	-7.4	0.3	-5.0	0.3	56.2	0.3	43.0	0.5	0.2	0.5	0.1	1.3	0.0	102.2	97.2	Relict		
			-4.8	0.3	-7.4	0.3	-4.9	0.4	48.4	0.1	40.8	0.3	0.0	0.2	0.1	9.6	0.0	99.7	79.6	Relict		
			-7.6	0.3	-9.6	0.3	-5.6	0.4	48.5	0.1	41.0	0.2	0.0	0.4	0.1	10.5	0.0	100.8	78.1	Relict		
			-6.0	0.3	-9.5	0.3	-6.3	0.4	44.2	0.0	40.4	0.2	0.0	0.3	0.2	15.9	0.1	101.3	68.4	Relict		
			-8.6	0.3	-12.2	0.3	-7.7	0.4	50.0	0.1	41.4	0.3	0.0	0.2	0.1	8.6	-0.1	100.6	81.9	Relict		
			-3.0	0.3	-6.2	0.3	-4.6	0.4	52.5	0.1	41.7	0.4	0.0	0.4	0.1	5.7	0.0	100.9	87.7	Relict		
		1.0	0.3	-1.3	0.3	-1.8	0.3	34.6	0.1	37.5	0.3	0.0	0.4	0.2	27.0	0.1	100.2	49.9	Host			
		3.1	0.3	-0.4	0.3	-2.0	0.3	32.8	0.1	37.4	0.3	0.0	0.5	0.3	28.9	0.1	100.3	46.7	Host			
				<i>Ch03</i>	3.4	0.4	0.3	0.3	-1.5	0.4	30.4	0.1	36.7	0.4	0.0	0.2	0.4	31.7	0.0	99.8	42.6	Host
					-6.0	0.4	-8.8	0.4	-5.7	0.4	n.d.	n.d.	n.d.	n.d.	n.d.	n.d.	n.d.	n.d.	n.d.	n.d.	73.3	Relict
					-10.4	0.3	-12.2	0.3	-6.8	0.4	45.1	0.0	39.2	0.2	0.0	0.2	0.1	15.8	0.2	100.9	68.9	Relict
					-5.2	0.4	-7.5	0.3	-4.7	0.4	43.6	0.1	39.3	0.3	0.0	0.1	0.1	16.5	0.0	100.1	67.2	Relict
					0.8	0.3	-2.7	0.3	-3.1	0.3	31.5	0.0	36.3	0.4	0.0	0.2	0.3	30.6	-0.1	99.3	44.4	Host
					-13.1	0.4	-14.2	0.4	-7.4	0.4	47.8	0.0	40.8	0.2	0.0	0.4	0.1	11.3	-0.1	100.6	76.6	Relict
					3.4	0.4	-0.5	0.3	-2.3	0.4	31.6	0.1	36.3	0.5	0.0	0.2	0.2	30.3	0.0	99.1	44.8	Host
					-5.2	0.4	-7.9	0.3	-5.2	0.3	n.d.	n.d.	n.d.	n.d.	n.d.	n.d.	n.d.	n.d.	n.d.	n.d.	n.d.	62.0
		<i>Ch10</i>	5.6		0.3	0.7	0.3	-2.3	0.3	55.8	0.2	42.6	0.5	0.1	0.1	0.0	0.9	0.2	100.3	97.9	Relict	
			-1.8		0.7	-5.4	0.5	-4.4	0.6	50.3	0.0	41.3	0.2	0.0	0.5	0.2	7.0	0.1	99.7	84.8	Relict	
			-0.4	0.3	-4.9	0.3	-4.6	0.4	n.d.	n.d.	n.d.	n.d.	n.d.	n.d.	n.d.	n.d.	n.d.	n.d.	n.d.	97.9	Relict	
			2.5	0.4	-3.0	0.3	-4.3	0.4	n.d.	n.d.	n.d.	n.d.	n.d.	n.d.	n.d.	n.d.	n.d.	n.d.	n.d.	97.9	Relict	
			0.0	0.6	-3.5	0.4	-3.5	0.5	n.d.	n.d.	n.d.	n.d.	n.d.	n.d.	n.d.	n.d.	n.d.	n.d.	n.d.	42.3	Host	

		5.9	0.6	0.0	0.3	-3.1	0.4	29.9	0.1	35.7	0.5	0.0	0.2	0.2	31.6	0.1	98.3	42.3	Host
		-0.4	0.6	-5.0	0.3	-4.9	0.4	n.d.	n.d.	n.d.	n.d.	n.d.	n.d.	n.d.	n.d.	n.d.	n.d.	47.9	Host
		3.0	0.6	-1.6	0.4	-3.2	0.5	n.d.	n.d.	n.d.	n.d.	n.d.	n.d.	n.d.	n.d.	n.d.	n.d.	47.9	Host
	<i>Ch11</i>	3.6	0.5	-0.3	0.4	-2.2	0.5	22.3	0.0	34.7	0.2	0.0	0.3	0.4	40.8	0.0	98.7	29.8	Host
		4.6	0.6	0.5	0.4	-1.9	0.5	22.8	0.0	34.5	0.1	0.0	0.2	0.4	40.3	-0.1	98.4	30.5	Host
		-5.6	0.3	-8.0	0.3	-5.1	0.3	51.2	0.1	41.3	0.2	0.0	0.3	0.1	5.7	0.1	99.1	87.4	Relict
		-4.9	0.5	-8.7	0.4	-6.2	0.5	n.d.	n.d.	n.d.	n.d.	n.d.	n.d.	n.d.	n.d.	n.d.	n.d.	87.4	Relict
	<i>Ch12</i>	3.2	0.5	-1.2	0.4	-2.9	0.5	44.4	0.1	39.8	0.2	0.0	0.4	0.1	16.2	-0.1	101.2	68.1	Host
		-0.4	0.4	-3.3	0.3	-3.1	0.4	n.d.	n.d.	n.d.	n.d.	n.d.	n.d.	n.d.	n.d.	n.d.	n.d.	62.1	Host
		-1.3	0.4	-6.6	0.4	-5.9	0.4	56.1	0.1	42.5	0.4	0.0	0.3	0.0	1.2	0.0	100.6	97.4	Relict
		1.6	0.4	-1.8	0.3	-2.7	0.4	44.4	0.1	39.9	0.2	0.0	0.3	0.1	15.0	0.0	100.0	69.7	Host
		-1.0	0.4	-3.4	0.3	-2.8	0.4	n.d.	n.d.	n.d.	n.d.	n.d.	n.d.	n.d.	n.d.	n.d.	n.d.	69.7	Host
		0.4	0.4	-2.9	0.3	-3.1	0.4	52.7	0.0	41.9	0.1	0.0	0.4	0.2	5.8	0.0	101.1	87.6	Relict
		4.0	0.4	-1.0	0.3	-3.1	0.4	28.4	0.1	35.1	0.9	0.0	0.1	0.3	32.9	0.2	98.0	40.1	Host
		-2.5	0.3	-6.3	0.3	-5.0	0.3	56.2	0.1	42.5	0.3	0.1	0.3	0.1	1.4	0.0	101.0	96.9	Relict
<i>Cat008</i>	<i>Ch02</i>	13.3	0.4	4.9	0.2	-2.0	0.3	43.7	0.1	40.0	0.1	0.0	0.2	0.2	16.0	-0.1	100.3	68.0	Host
		10.4	0.4	3.7	0.3	-1.7	0.4	43.1	0.1	39.5	0.1	0.0	0.1	0.2	17.1	0.1	100.2	66.2	Host
		14.5	0.6	5.6	0.3	-1.9	0.4	32.1	0.0	36.4	0.3	0.0	0.1	0.3	30.0	0.0	99.3	45.4	Host
		12.3	0.4	4.7	0.3	-1.7	0.4	40.9	0.1	38.8	0.2	0.0	0.1	0.2	19.0	0.0	99.3	62.5	Host
		10.0	0.5	3.1	0.3	-2.1	0.4	36.7	0.0	38.2	0.2	0.0	0.1	0.3	24.5	0.1	100.0	53.7	Host
		10.2	0.5	3.5	0.4	-1.8	0.5	34.5	0.0	37.5	0.2	0.0	0.2	0.3	27.0	0.0	99.8	49.8	Host
		10.4	0.5	3.2	0.3	-2.3	0.4	n.d.	n.d.	n.d.	n.d.	n.d.	n.d.	n.d.	n.d.	n.d.	n.d.	49.9	Host
		15.2	0.6	5.8	0.4	-2.1	0.5	26.1	0.0	35.2	0.4	0.0	0.1	0.5	37.0	0.1	99.3	35.3	Host
	<i>Ch04</i>	0.8	0.3	-2.6	0.3	-3.1	0.3	29.9	0.0	36.4	0.2	0.0	0.2	0.3	33.2	0.0	100.2	41.1	Host
		-9.9	0.3	-11.2	0.3	-6.1	0.3	56.3	0.2	42.4	0.6	0.1	0.1	0.0	1.2	0.0	101.0	97.3	Relict
		-1.8	0.3	-3.9	0.3	-3.0	0.3	40.1	0.1	38.5	0.1	0.0	0.3	0.1	20.9	0.1	100.2	59.8	Host
		-3.4	0.3	-5.3	0.2	-3.5	0.3	39.1	0.1	38.8	0.1	0.0	0.2	0.2	21.8	0.0	100.3	58.2	Host
		-4.8	0.3	-7.0	0.2	-4.5	0.3	45.3	0.0	40.7	0.1	0.0	0.0	0.1	14.6	0.0	101.0	70.6	Relict

			-10.8	0.3	-12.8	0.3	-7.2	0.4	50.9	0.1	41.7	0.2	0.1	0.1	0.1	8.7	0.2	102.0	82.0	Relict
	<i>EM463</i>	<i>Ch05</i>	-4.7	0.3	-8.0	0.3	-5.6	0.3	52.2	0.1	41.1	0.4	0.0	0.2	0.0	4.9	-0.1	98.9	89.2	Relict
			-2.1	0.6	-6.4	0.4	-5.4	0.5	50.2	0.0	41.3	0.2	0.0	0.1	0.3	8.8	0.0	100.9	81.5	Relict
			-4.2	0.4	-7.6	0.3	-5.4	0.4	56.0	0.3	42.3	0.5	0.1	0.1	0.0	0.9	0.0	100.2	97.9	Relict
			0.1	0.4	-5.1	0.3	-5.2	0.4	56.0	0.2	42.4	0.5	0.0	0.2	0.1	0.8	0.0	100.2	98.2	Relict
			1.1	0.6	-4.3	0.4	-4.8	0.5	n.d.	n.d.	n.d.	n.d.	n.d.	n.d.	n.d.	n.d.	n.d.	n.d.	81.5	Relict
			-2.6	0.4	-6.8	0.3	-5.5	0.4	53.2	0.1	42.1	0.3	0.1	0.2	0.2	5.3	0.1	101.5	88.7	Relict
			5.1	0.7	0.6	0.4	-2.0	0.5	41.6	0.0	39.0	0.0	0.0	0.1	0.2	19.0	0.1	100.0	62.9	Host
			6.9	0.7	1.1	0.4	-2.5	0.5	40.1	0.0	38.9	0.1	0.0	0.1	0.2	20.4	0.0	100.0	60.4	Host
	<i>Isna</i>	<i>Ch01</i>	-0.9	0.4	-5.6	0.3	-5.1	0.4	53.1	0.8	42.9	0.5	0.1	0.1	0.0	4.7	-0.1	102.2	89.7	Host
			1.0	0.4	-4.4	0.4	-4.9	0.4	51.6	0.1	42.6	0.3	0.1	0.0	0.1	7.0	-0.2	101.8	85.1	Relict
			1.5	0.4	-4.5	0.4	-5.3	0.4	39.4	0.1	40.0	0.6	0.1	0.0	0.1	22.0	-0.1	102.3	58.2	Relict
			2.5	0.3	-4.0	0.3	-5.3	0.4	55.6	0.3	43.4	0.5	0.1	0.1	0.0	2.5	-0.1	102.5	94.5	Relict
CR	<i>Renazzo</i>	<i>Ch01</i>	2.1	0.3	-0.9	0.3	-2.0	0.3	55.4	0.0	41.9	0.3	0.0	0.3	0.1	2.3	-0.1	100.4	94.9	Relict
			0.7	0.3	-1.8	0.3	-2.1	0.3	53.9	0.0	42.0	0.4	0.0	0.3	0.1	3.6	0.0	100.5	92.0	Relict
			2.0	0.4	-1.2	0.3	-2.2	0.3	55.5	0.0	42.0	0.2	0.0	0.5	0.1	2.3	0.0	100.6	94.9	Relict
			5.6	0.6	2.9	0.4	0.1	0.5	33.9	0.0	37.2	0.3	0.0	0.5	0.3	27.4	0.0	99.7	49.0	Host
			5.8	0.5	3.4	0.3	0.4	0.4	32.2	0.0	36.5	0.3	0.0	0.3	0.4	29.6	0.2	99.5	45.8	Host
			-0.1	0.5	-3.0	0.4	-3.0	0.4	38.6	0.0	38.4	0.2	0.0	0.4	0.2	22.2	0.1	100.2	57.4	Host
		<i>Ch02</i>	5.3	0.4	2.4	0.3	-0.4	0.3	53.2	0.1	42.0	0.3	0.0	0.5	0.3	3.9	0.0	100.1	91.3	Relict
			6.0	0.4	2.3	0.3	-0.8	0.3	53.2	0.1	42.0	0.3	0.0	0.5	0.3	3.9	0.0	100.1	91.3	Relict
			2.0	0.4	-1.4	0.3	-2.5	0.4	50.4	0.0	41.3	0.2	0.0	0.6	0.3	7.6	0.1	100.6	83.7	Relict
			0.2	0.3	-2.6	0.3	-2.8	0.4	47.3	0.0	40.5	0.2	0.0	0.6	0.3	11.2	0.3	100.5	76.5	Relict
			5.4	0.4	3.3		0.5	0.4	34.9	0.0	36.6	0.2	0.0	0.5	0.5	25.8	-0.1	98.5	51.2	Host
			8.1	0.5	4.4	0.4	0.2	0.5	35.9	0.0	37.6	0.2	0.0	0.5	0.4	24.8	0.1	99.6	52.8	Host
		<i>Ch03</i>	-10.7	0.4	-13.1	0.3	-7.5	0.4	55.4	0.1	43.0	0.5	0.1	0.2	0.0	1.8	0.1	101.2	95.9	Relict
			-11.3	0.4	-12.5	0.3	-6.6	0.4	54.6	0.1	42.4	0.4	0.1	0.3	0.1	2.4	-0.1	100.4	94.7	Relict

			4.4	0.5	2.8	0.4	0.6	0.4	32.7	0.0	36.7	0.2	0.0	0.3	0.5	28.8	0.0	99.2	46.9	Host
	<i>DaG574</i>	<i>Ch01</i>	6.5	0.4	3.7	0.3	0.4	0.4	38.3	0.0	38.4	0.2	0.0	0.6	0.3	22.5	0.1	100.4	56.9	Host
			1.3	0.6	-0.3	0.5	-1.0	0.6	44.2	0.0	39.5	0.2	0.0	0.3	0.1	15.9	0.0	100.2	68.3	Relict
			-3.8	0.5	-6.7	0.3	-4.7	0.4	37.6	0.1	37.9	0.3	0.0	0.3	0.2	24.2	0.0	100.6	54.7	Host
			1.0	0.4	-2.4	0.3	-3.0	0.4	41.0	0.0	38.8	0.2	0.0	0.5	0.1	19.7	0.0	100.3	61.8	Host
			7.4	0.5	4.6	0.3	0.7	0.4	35.0	0.0	37.9	0.3	0.0	0.4	0.4	26.6	0.0	100.6	50.5	Host
		<i>Ch02</i>	7.1	0.5	4.0	0.3	0.3	0.4	35.0	0.0	37.7	0.2	0.0	0.5	0.4	27.7	-0.1	101.5	49.5	Host
			8.0	0.5	4.4	0.4	0.2	0.4	32.4	0.1	36.6	0.2	0.0	0.4	0.5	30.0	0.1	100.2	45.6	Host
			6.2	0.5	3.6	0.3	0.3	0.4	34.3	0.0	37.3	0.2	0.0	0.5	0.5	26.9	0.1	99.8	49.8	Host
			4.4	0.5	2.4	0.4	0.1	0.5	42.9	0.0	39.6	0.2	0.0	0.3	0.2	18.0	0.0	101.1	64.9	Host
			5.6	0.4	3.0	0.3	0.1	0.4	41.2	0.0	39.5	0.1	0.0	0.4	0.3	20.4	-0.1	102.0	61.1	Host
			7.3	0.4	3.6	0.3	-0.2	0.4	32.4	0.1	36.6	0.2	0.0	0.4	0.5	30.0	0.1	100.2	45.6	Host
<i>OC</i>	<i>LoV098</i>	<i>Ch01</i>	7.4	0.5	5.5	0.4	1.6	0.5	44.1	0.1	38.9	0.5	0.0	0.1	0.2	14.6	0.0	98.6	70.1	Host
			7.6	0.5	5.3	0.4	1.4	0.5	49.3	0.1	40.5	0.3	0.0	0.0	0.1	8.8	0.0	99.0	81.3	Host
			7.7	0.5	5.0	0.4	1.0	0.5	50.4	0.1	41.0	0.2	0.0	0.1	0.1	7.8	0.1	99.8	83.3	Relict
			8.2	0.6	5.9	0.4	1.6	0.5	48.6	0.1	40.4	0.2	0.1	0.1	0.2	9.8	0.1	99.5	79.4	Host
			7.0	0.5	5.1	0.4	1.5	0.5	50.5	0.0	40.9	0.2	0.0	0.1	0.1	7.6	-0.1	99.5	83.7	Relict
		<i>Ch02</i>	7.8	0.5	5.2	0.4	1.2	0.5	41.6	0.0	38.5	0.1	0.0	0.3	0.4	17.0	0.1	98.0	65.4	Host
			6.5	0.5	4.4	0.4	1.0	0.4	43.0	0.0	38.5	0.2	0.0	0.5	0.3	15.3	0.0	97.7	68.5	Host
			9.1	0.5	6.2	0.4	1.5	0.5	41.7	0.0	38.7	0.1	0.0	0.5	0.4	17.5	0.0	99.0	64.9	Host
			1.0	0.5	-1.2	0.3	-1.7	0.4	43.2	0.1	38.6	0.2	0.0	0.7	0.2	14.5	0.1	97.6	69.8	Relict
			7.4	0.5	5.0	0.4	1.2	0.4	45.5	0.0	39.4	0.1	0.0	0.3	0.2	12.6	-0.1	98.2	73.7	Host
			9.5	0.5	6.0	0.4	1.1	0.5	35.6	0.0	37.1	0.3	0.0	0.2	0.4	24.5	0.0	98.2	52.9	Host
			9.0	0.5	6.4	0.5	1.7	0.5	39.0	0.0	38.3	0.2	0.0	0.4	0.4	20.4	-0.1	98.7	59.7	Host
			8.0	0.6	5.1	0.4	0.9	0.5	37.7	0.0	37.4	0.2	0.0	0.2	0.4	21.8	0.1	97.9	56.2	Host
		<i>Ch03</i>	5.8	0.6	4.4	0.4	1.4	0.6	45.1	0.0	39.6	0.0	0.0	0.2	0.3	14.1	0.0	99.4	71.3	Host
			5.7	0.6	4.3	0.4	1.4	0.6	43.2	0.3	40.0	0.0	0.0	0.3	0.3	15.6	-0.2	99.9	68.2	Host

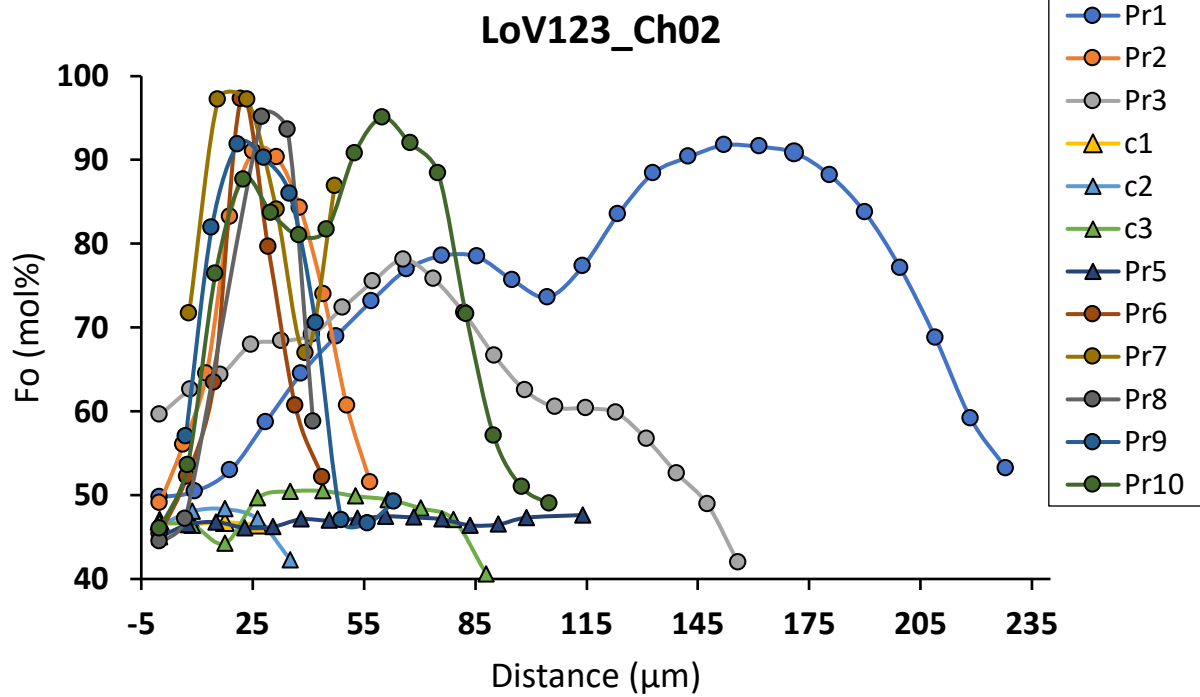
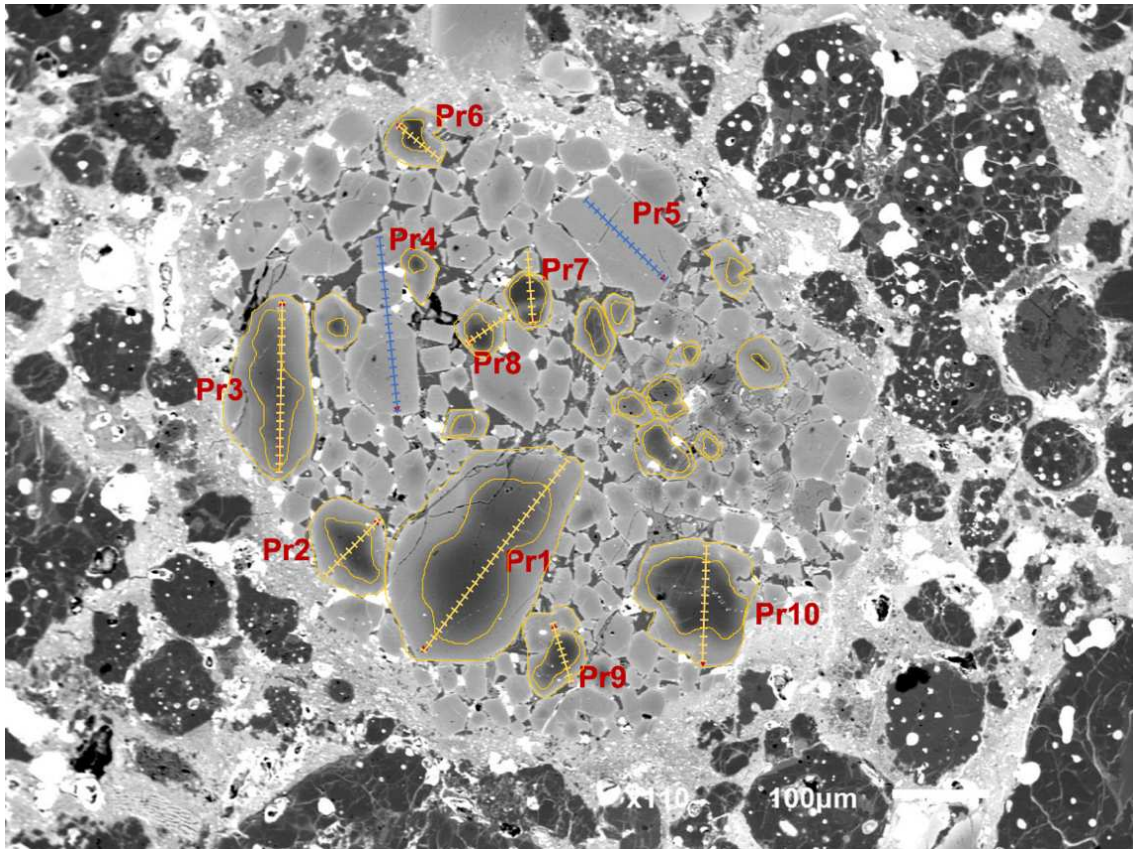
	6.5	0.7	4.3	0.4	0.9	0.5	38.4	0.0	38.1	0.1	0.0	0.0	0.3	22.4	-0.1	99.4	57.1	Host
	8.6	0.6	5.6	0.4	1.1	0.5	30.8	0.0	36.3	0.1	0.0	0.1	0.4	31.3	-0.2	99.0	43.3	Host
	5.2	0.7	4.1	0.4	1.4	0.6	36.9	0.0	38.0	0.2	0.0	0.1	0.4	24.1	0.0	99.6	54.3	Host
<i>Ch05</i>	10.4	0.8	6.3	0.5	0.8	0.7	35.5	0.3	37.9	0.2	0.0	0.3	0.4	24.0	0.0	98.7	53.5	Host
	3.5	0.5	1.9	0.3	0.1	0.4	50.9	0.1	41.7	0.4	0.0	0.5	0.0	5.5	-0.1	99.3	87.7	Relict
	10.2	0.9	7.5	0.5	2.2	0.7	41.4	0.0	39.1	0.2	0.0	0.2	0.3	17.8	-0.1	99.0	61.4	Host
	8.2	0.7	5.2	0.5	1.0	0.6	38.6	0.0	38.0	0.2	0.0	0.3	0.4	21.1	0.0	98.5	58.6	Host
	7.5	0.8	4.2	0.5	0.3	0.7	38.4	0.0	38.1	0.2	0.0	0.5	0.4	21.3	0.0	99.0	58.3	Host
	10.6	0.7	6.0	0.4	0.5	0.6	38.0	0.0	38.4	0.2	0.0	0.9	0.4	20.9	0.0	98.8	58.5	Host
<i>Ch01p</i>	9.0	0.6	6.3	0.4	1.6	0.5	40.6	0.0	38.9	0.0	0.0	0.1	0.4	19.8	0.2	99.9	61.3	Host
	10.3	0.6	6.0	0.4	0.6	0.5	39.8	0.0	38.2	0.2	0.0	0.9	0.4	18.9	0.0	98.3	62.0	Host
	9.4	0.6	6.2	0.3	1.4	0.5	41.3	0.0	38.8	0.0	0.0	0.0	0.3	17.4	0.0	97.9	64.8	Host
	7.4	0.6	4.8	0.4	1.0	0.5	42.8	0.0	39.0	0.1	0.0	0.1	0.2	15.6	0.0	97.8	68.0	Host
	10.4	0.6	6.1	0.3	0.7	0.5	40.4	0.0	38.1	0.1	0.0	0.0	0.4	19.7	0.1	98.9	61.4	Host
	7.6	0.5	5.2	0.4	1.2	0.5	39.9	0.0	38.2	0.0	0.0	0.1	0.4	19.9	0.1	98.6	60.9	Host
<i>Ch02p</i>	6.0	0.5	4.3	0.4	1.2	0.5	47.3	0.1	39.6	0.3	0.0	0.1	0.1	10.7	-0.2	98.1	77.4	Host
	3.5	0.6	3.0	0.4	1.2	0.5	48.9	0.1	40.7	0.4	0.1	0.1	0.1	9.0	0.0	99.4	80.9	Relict
	5.3	0.5	3.6	0.3	0.8	0.4	43.6	0.1	38.3	0.1	0.1	0.1	0.4	15.3	0.0	97.9	68.8	Host
	4.4	0.5	3.1	0.4	0.8	0.5	47.0	0.1	40.0	0.4	0.0	0.0	0.1	11.1	0.0	98.7	76.7	Host
	2.2	0.4	-0.2	0.4	-1.3	0.4	43.5	0.1	38.4	0.2	0.1	0.1	0.3	15.3	-0.1	97.9	68.8	Host
	5.9	0.5	4.4	0.4	1.3	0.5	47.5	0.1	40.0	0.3	0.0	0.2	0.2	10.6	0.1	99.0	75.4	Host

n.d.: not determined

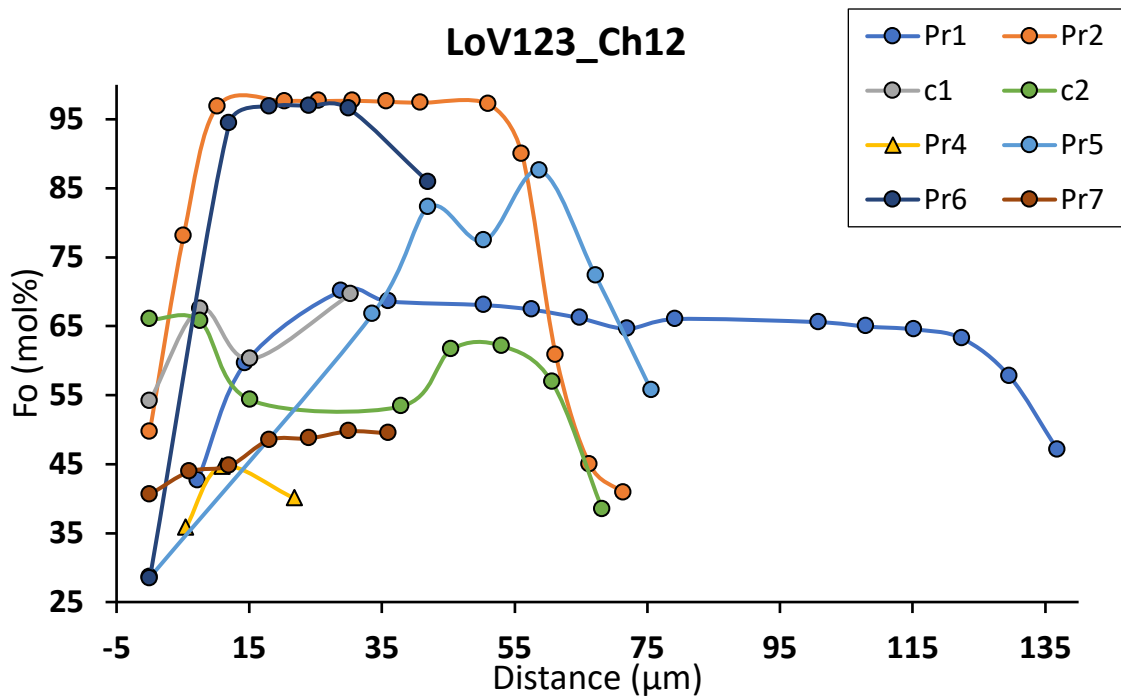
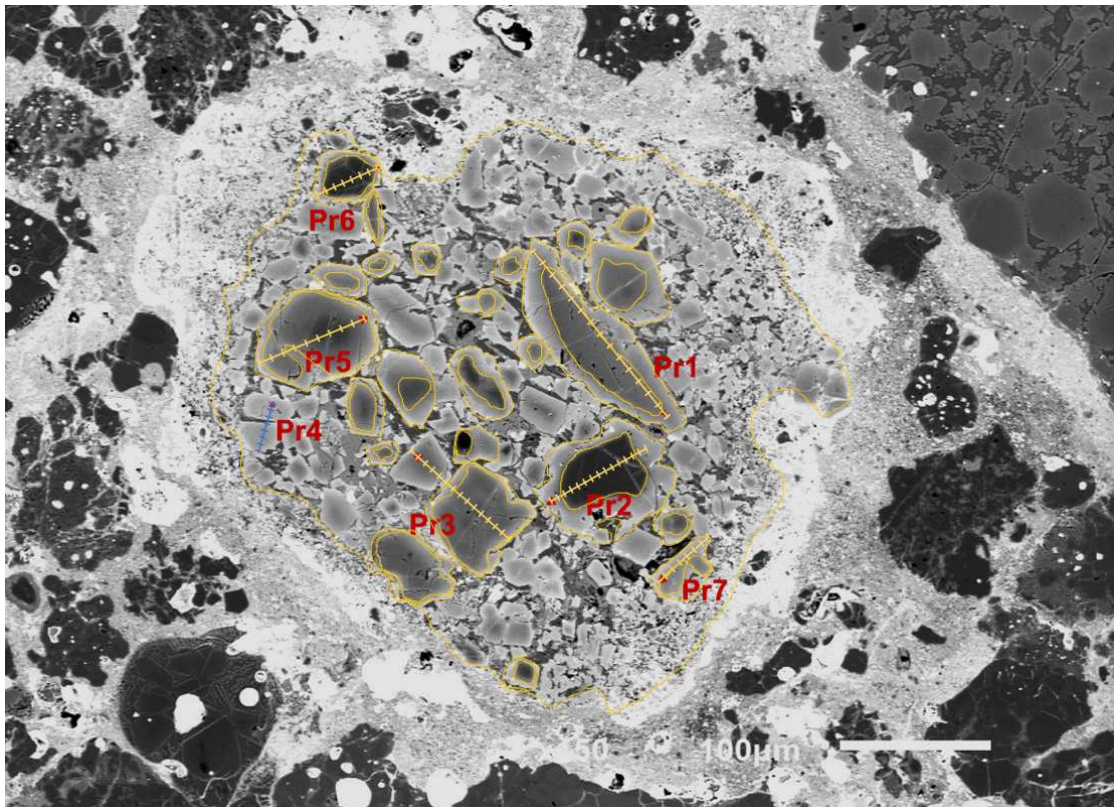
Mg# profile of Type II chondrules in COs and OC chondrites

Carbonaceous chondrite CO3

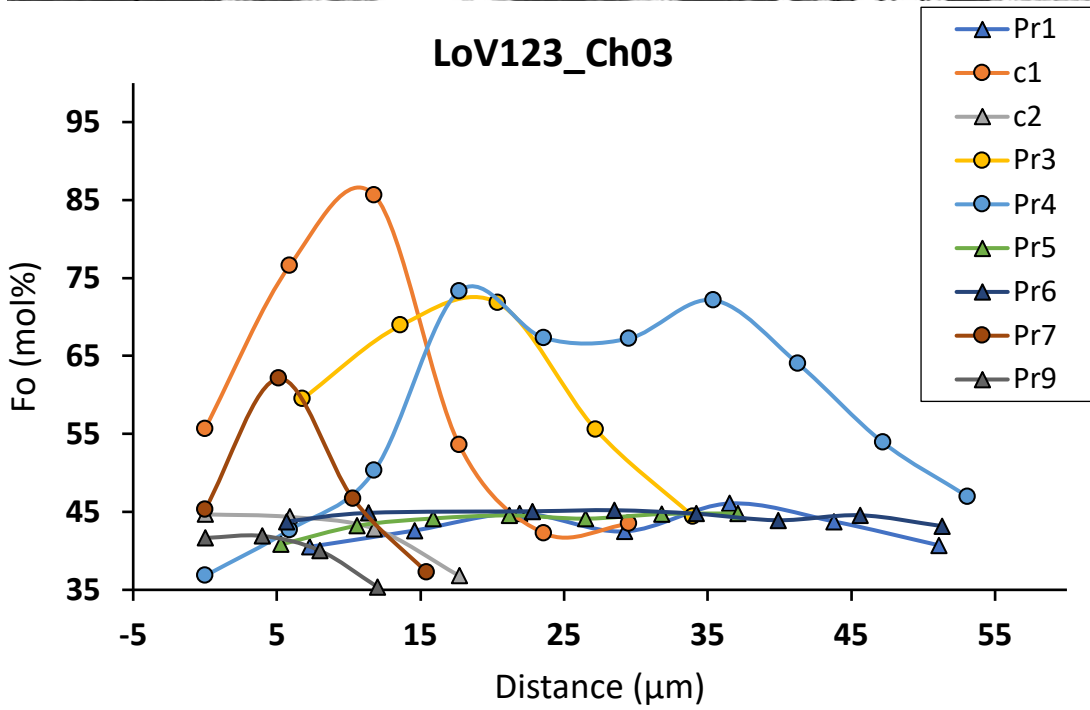
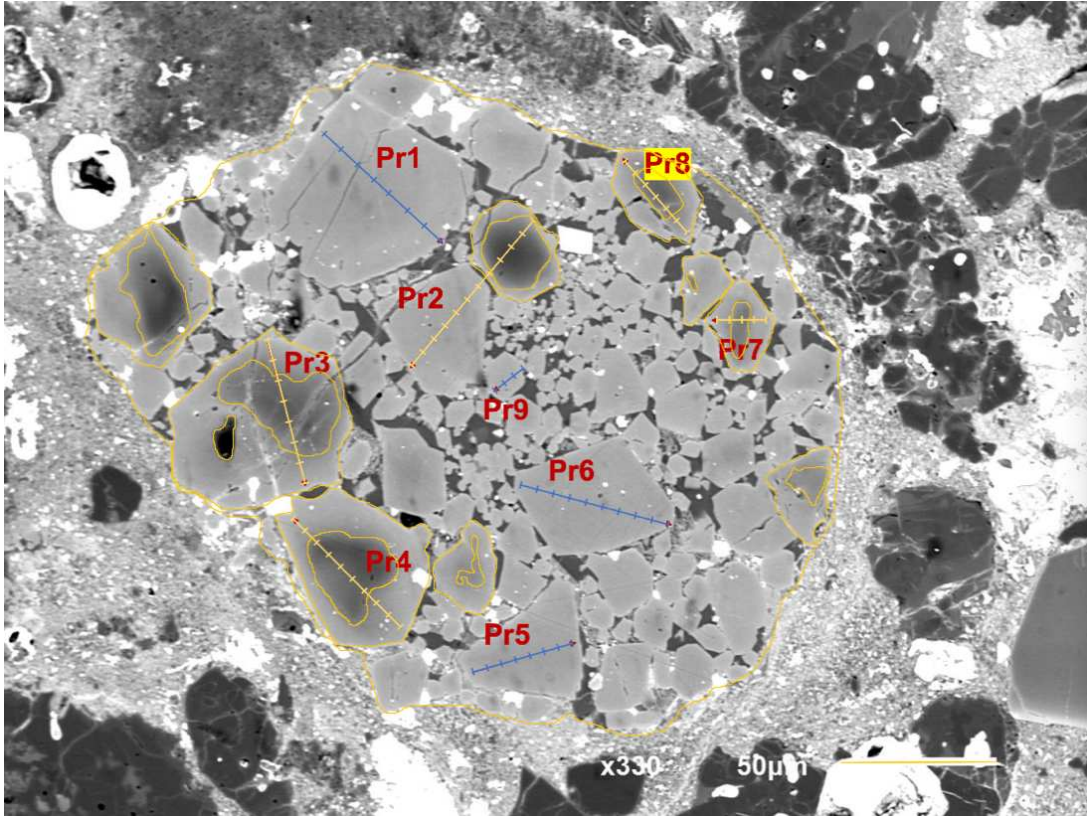
LoV123_Ch02



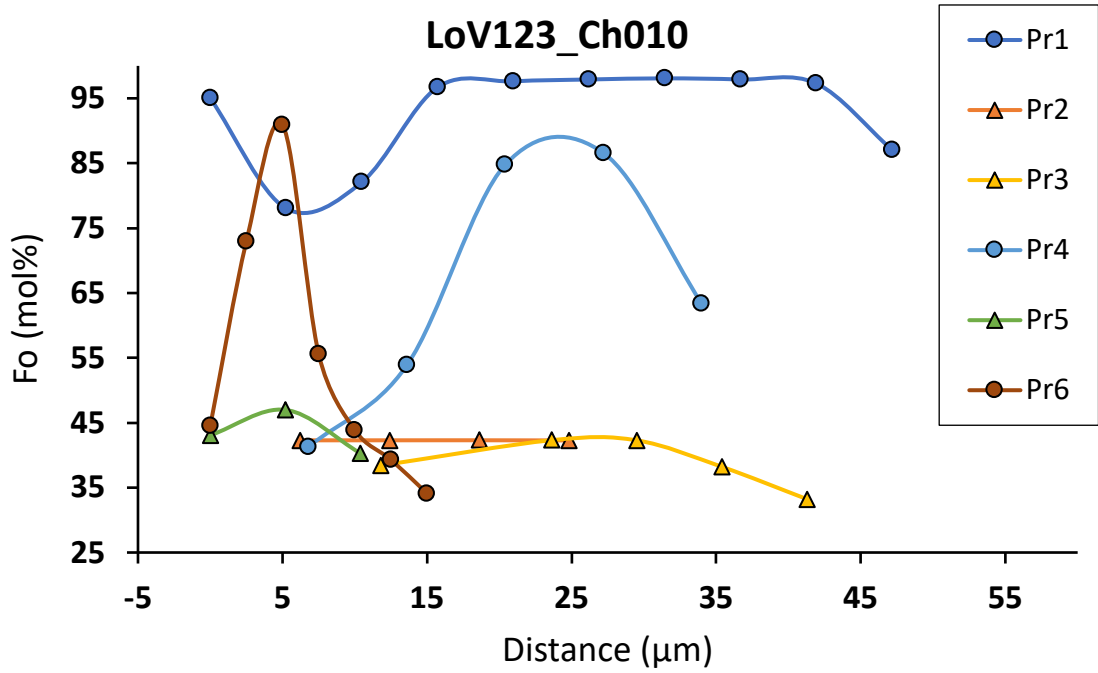
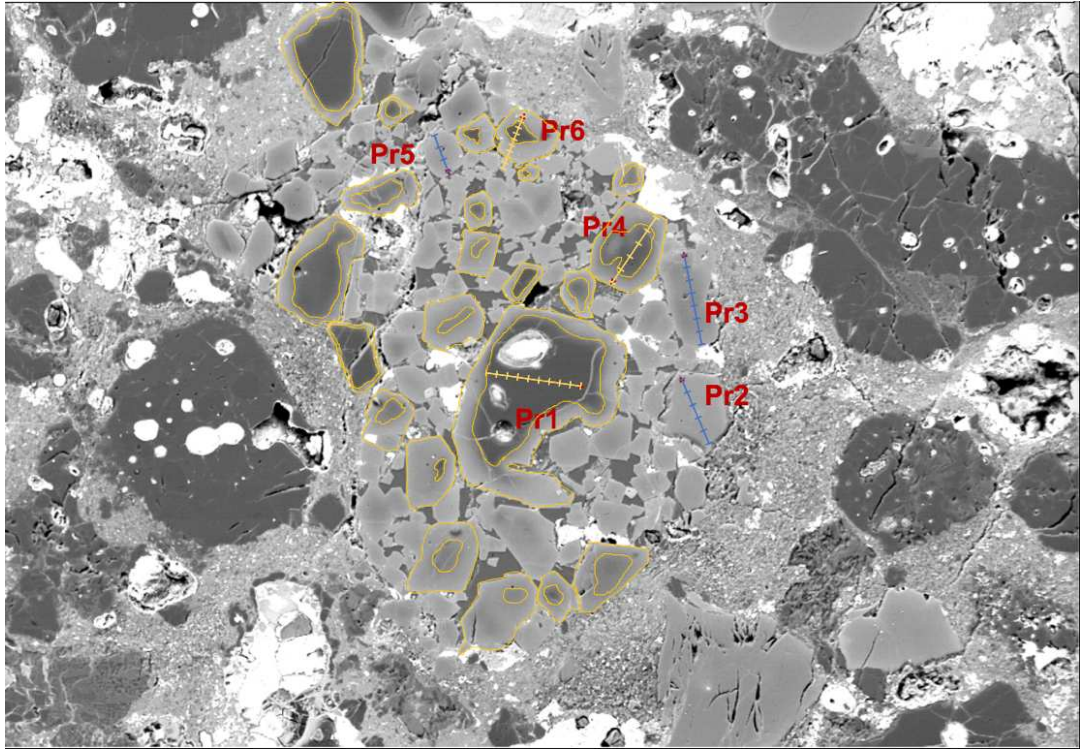
LoV123_Ch12



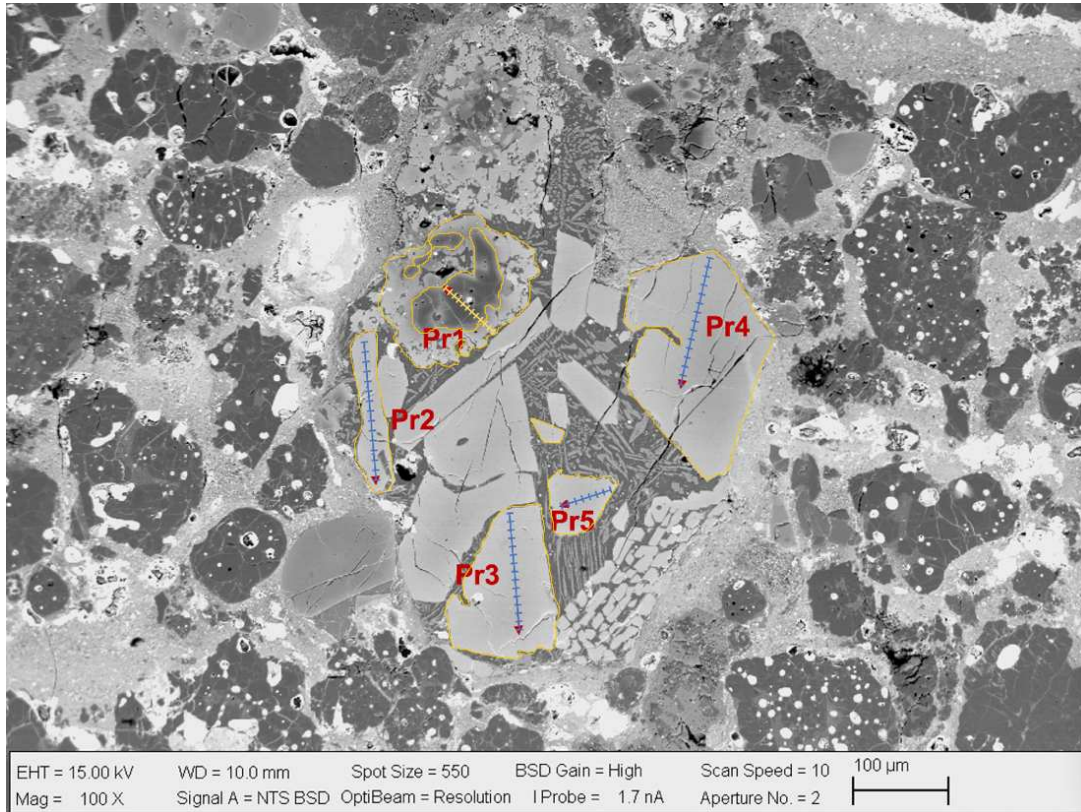
LoV123_Ch03



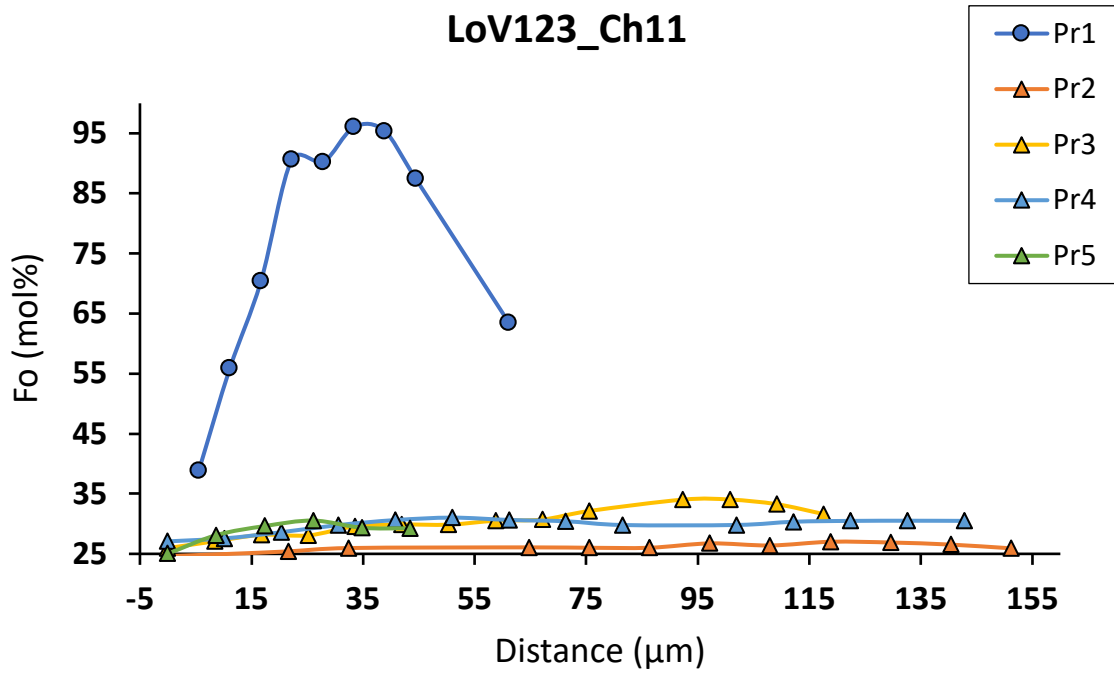
LoV123_Ch10



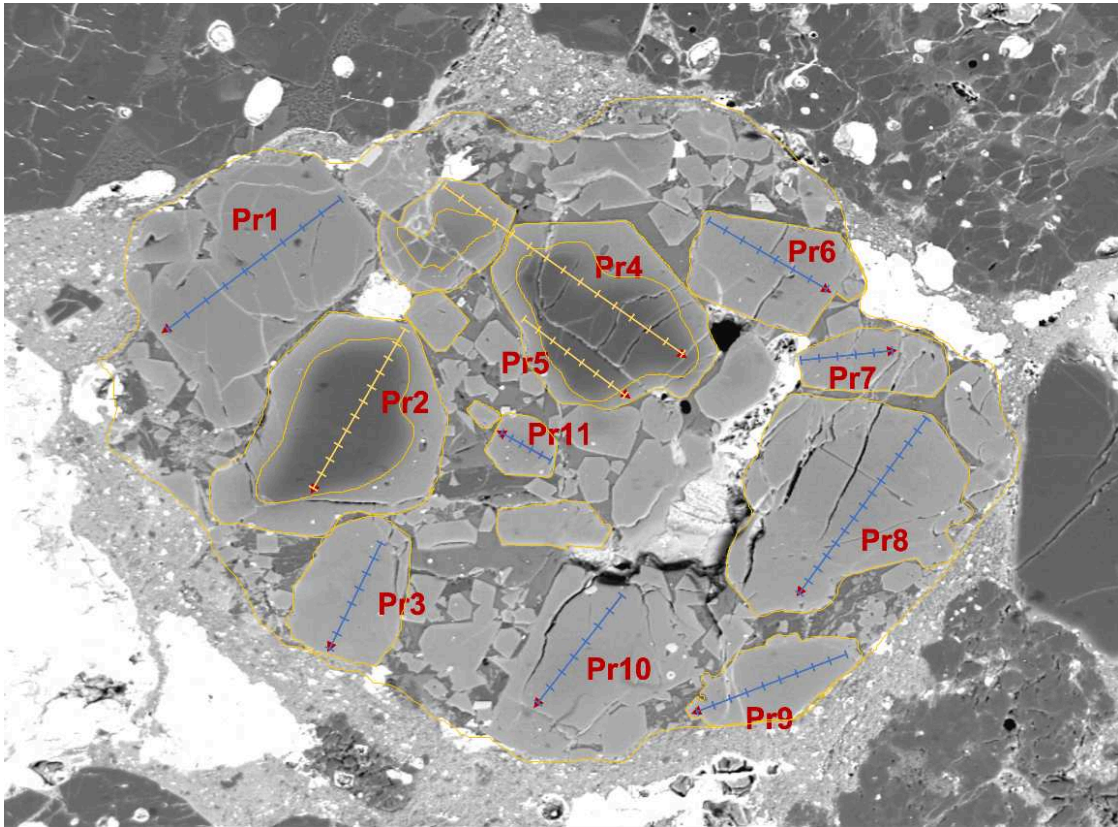
LoV123_Ch11



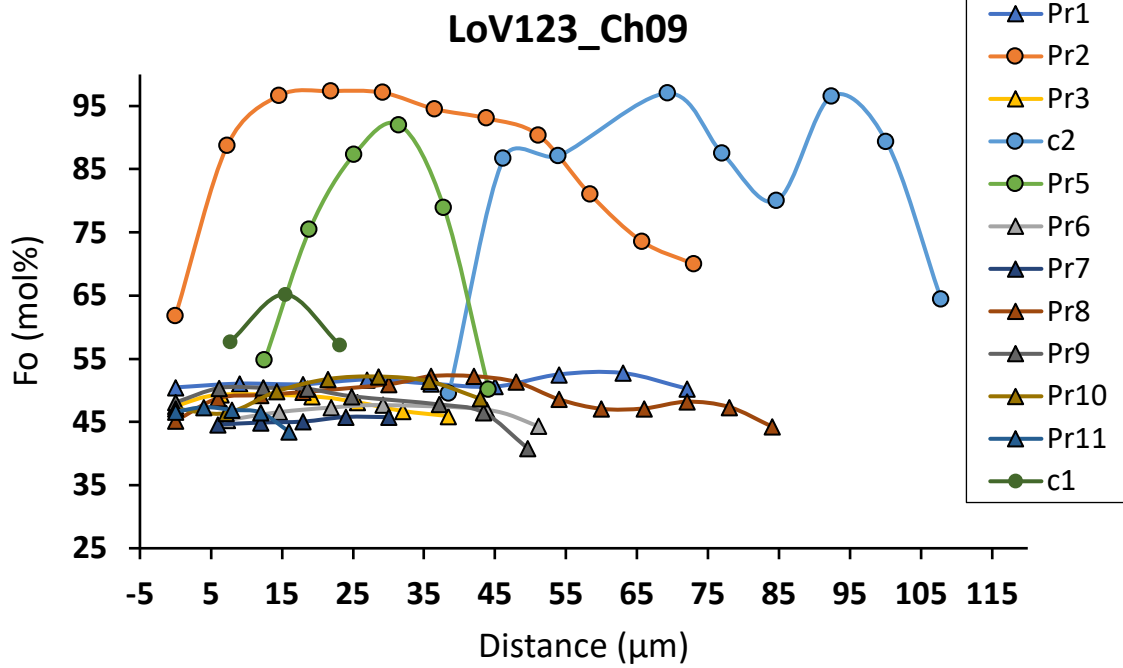
LoV123_Ch11



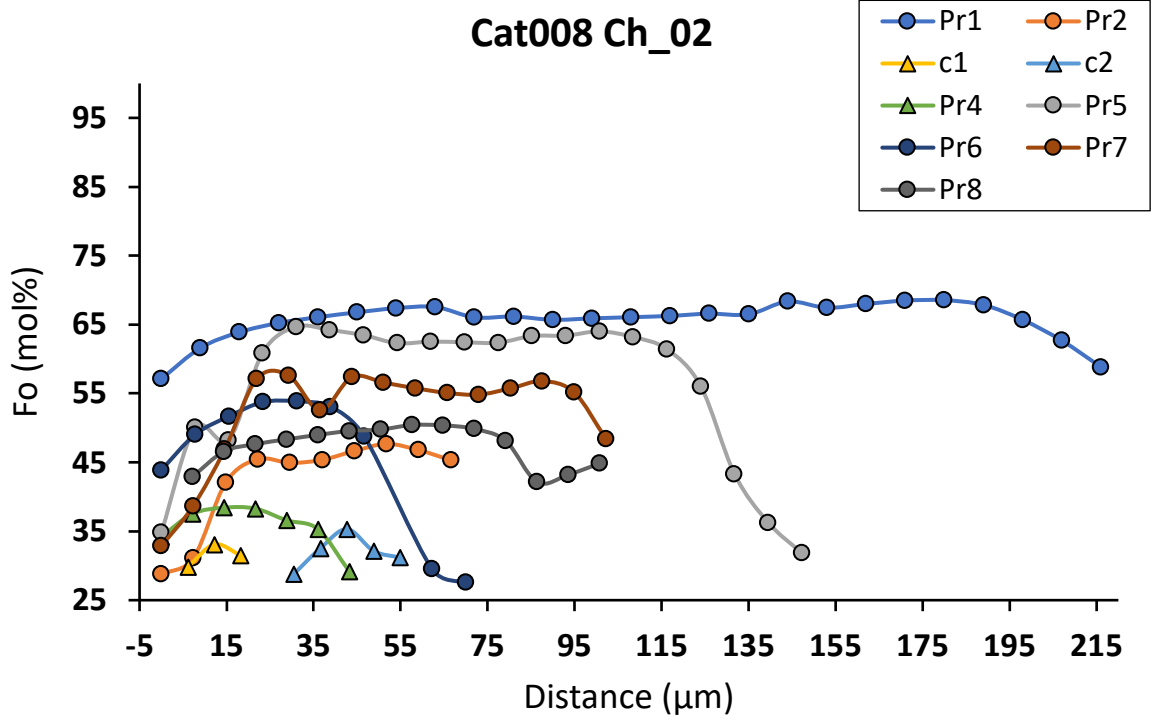
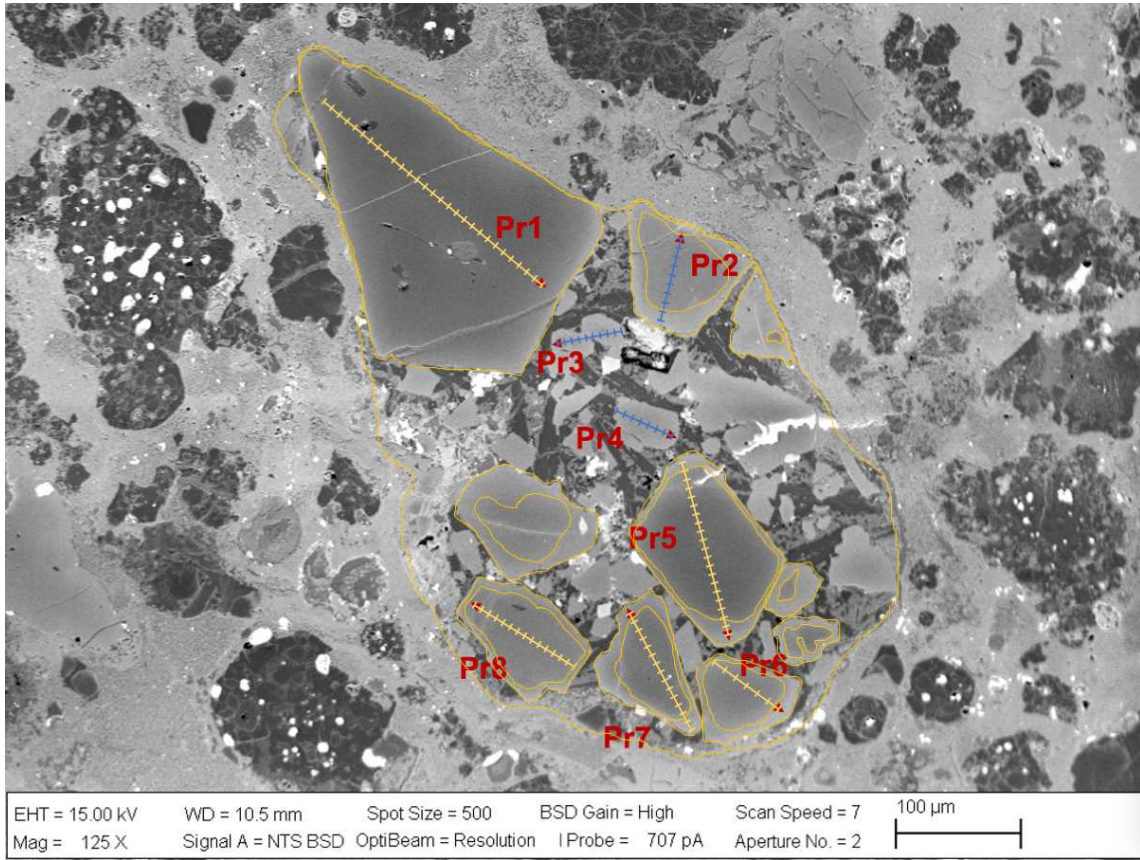
LoV123_Ch09



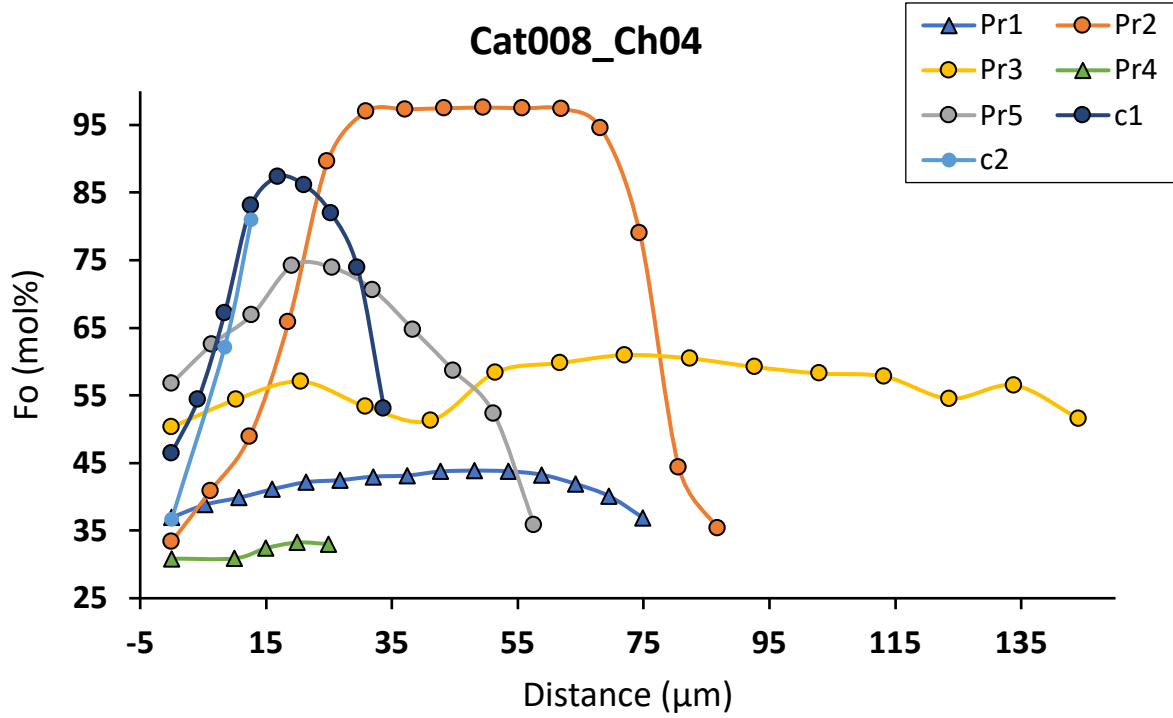
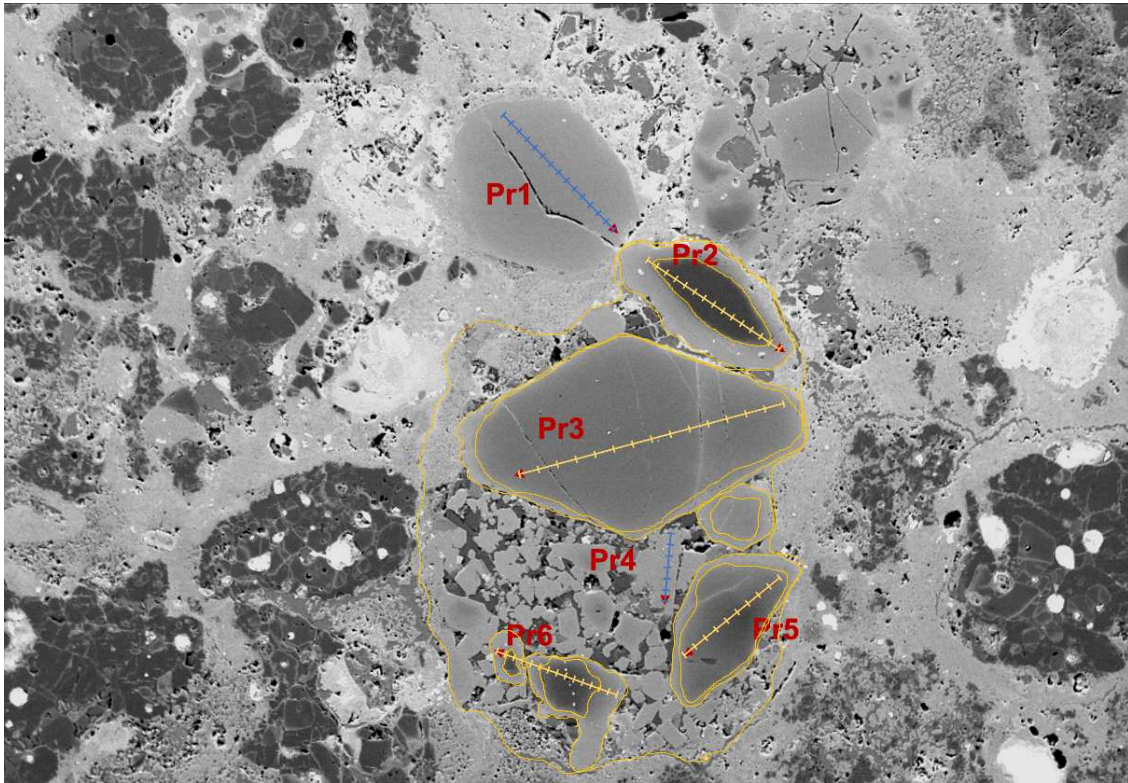
15.00 kV WD = 10.0 mm Spot Size = 550 BSD Gain = High Scan Speed = 10 20 µm
 230 X Signal A = NTS BSD OptiBeam = Resolution I Probe = 1.7 nA Aperture No. = 2



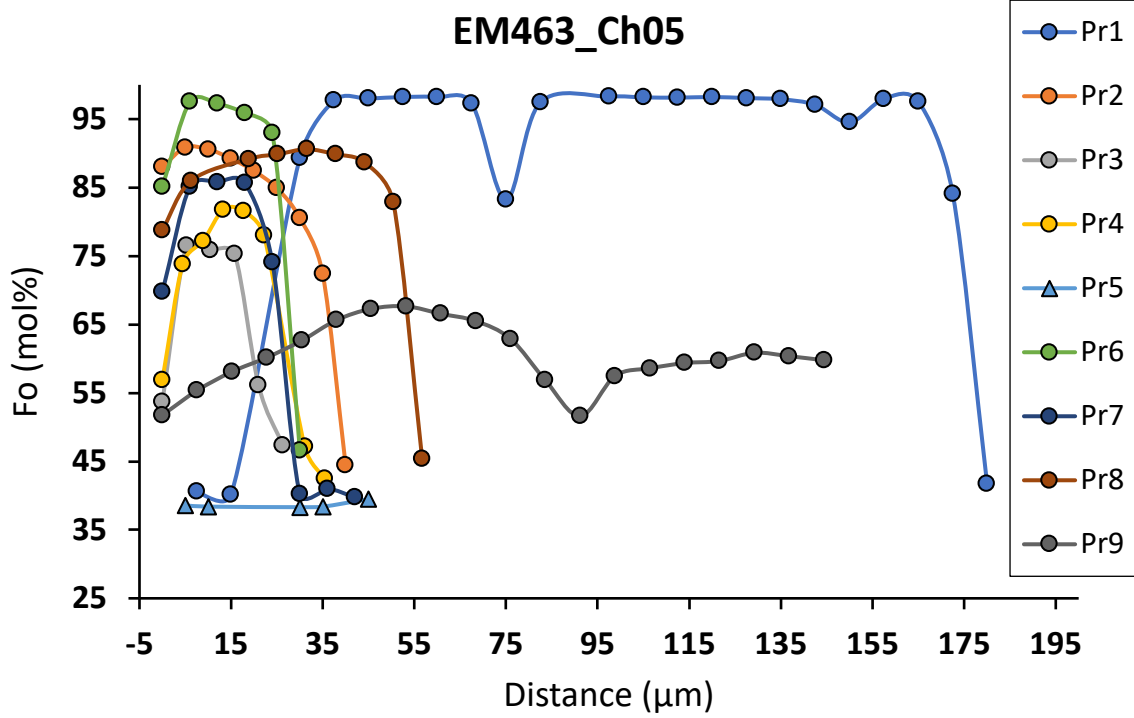
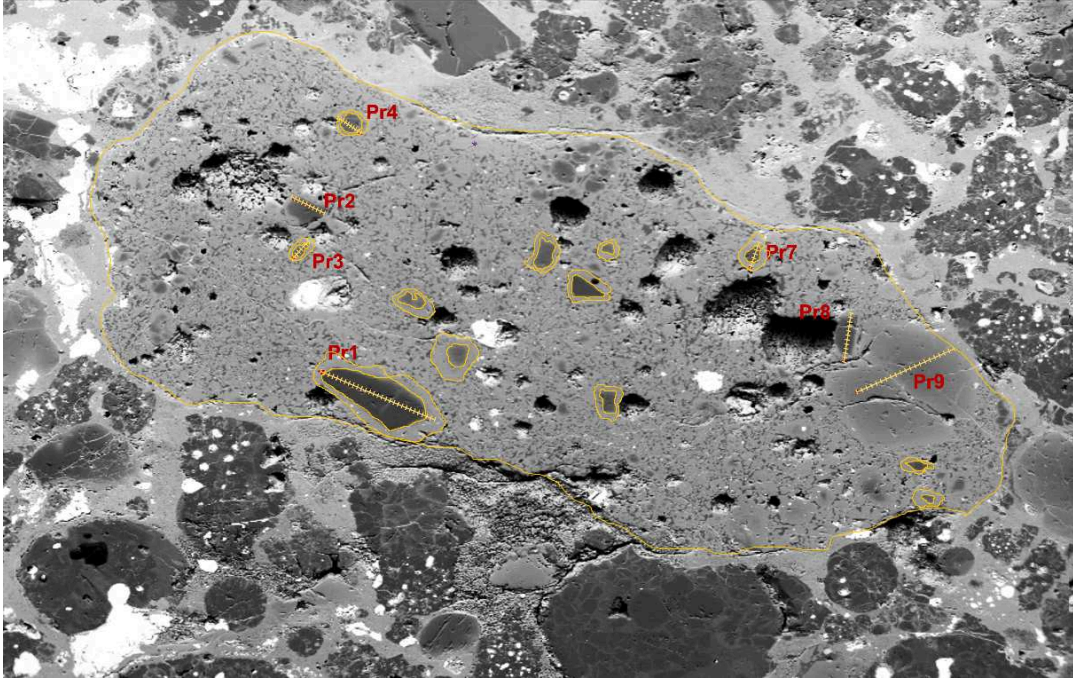
Cat008_Ch02



Cat008_Ch04

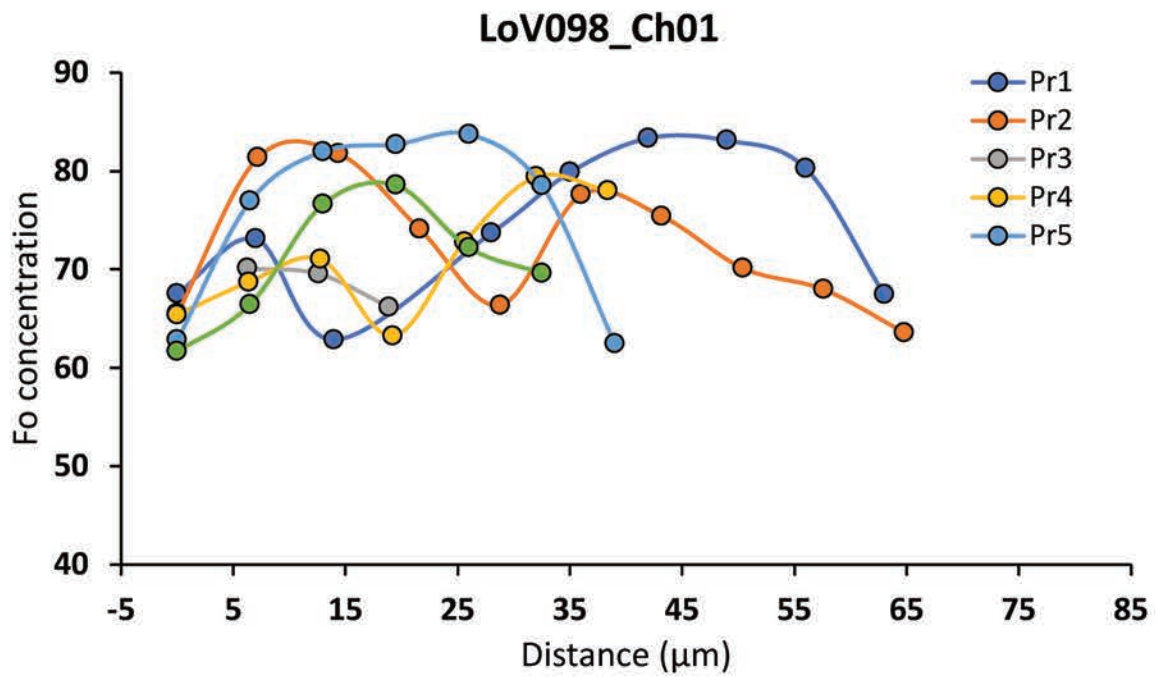
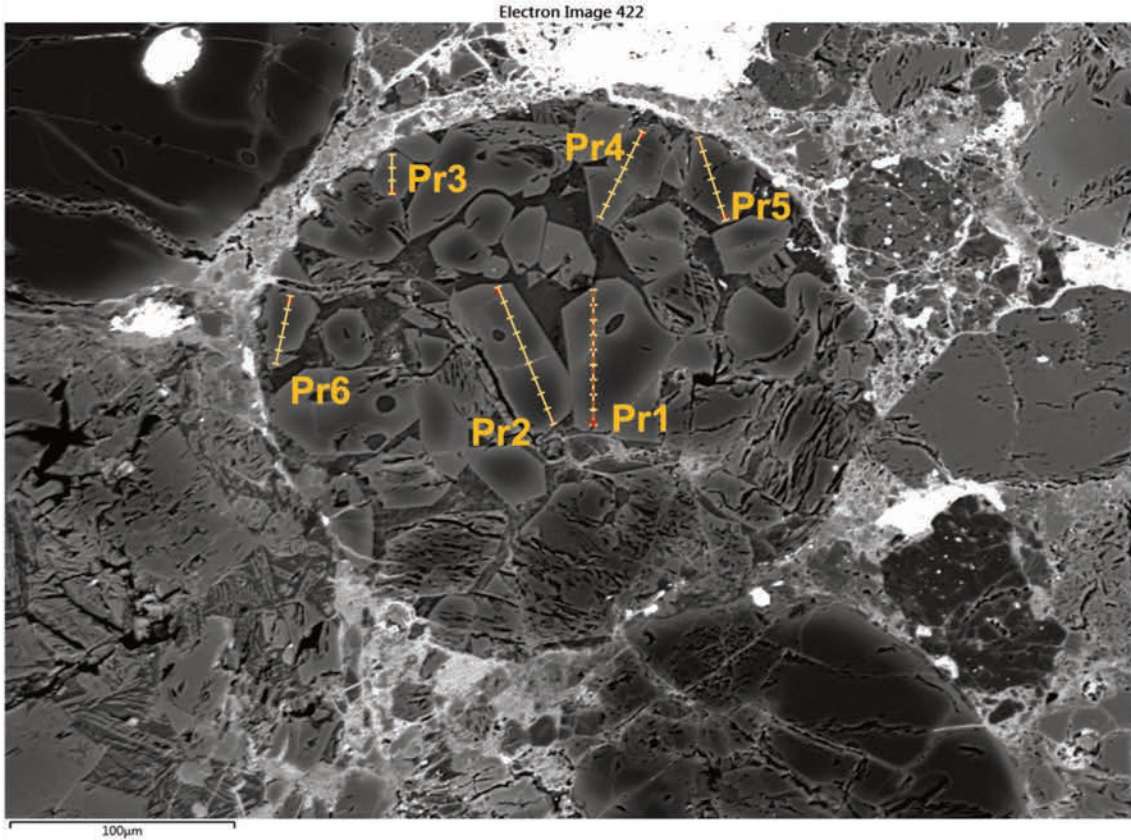


EM463_Ch05



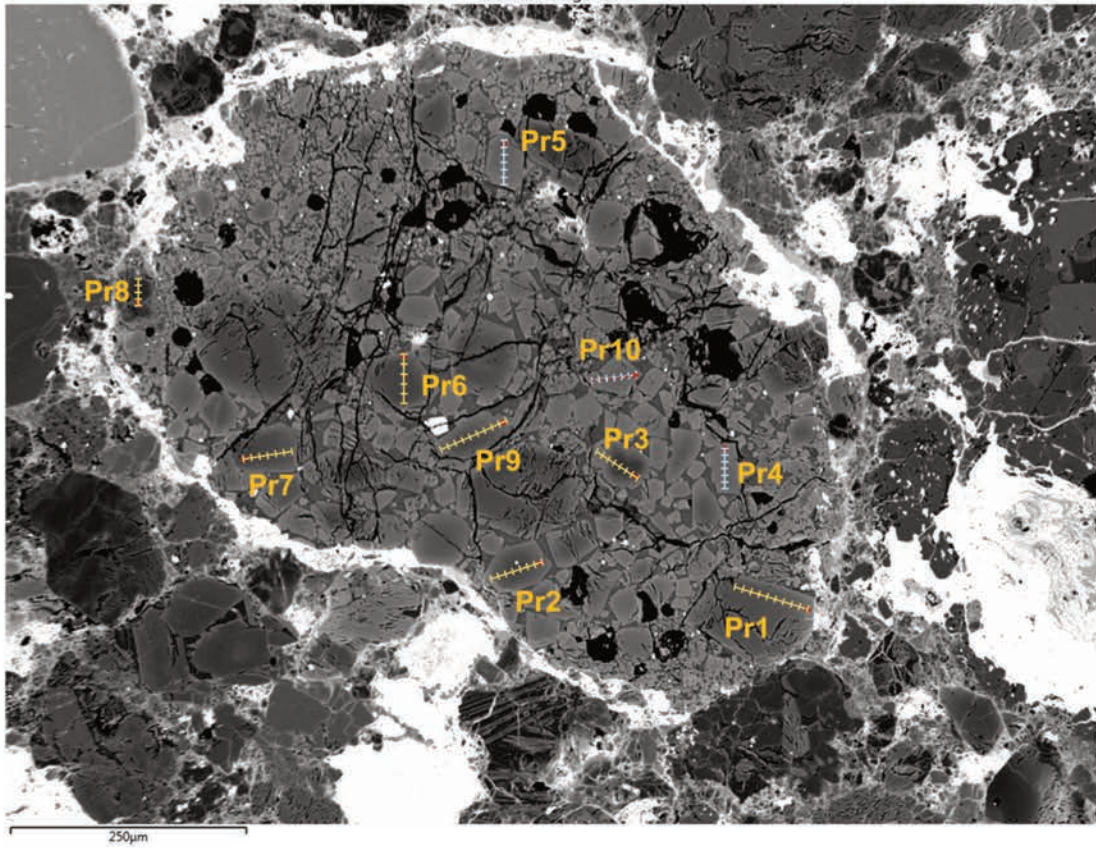
Ordinary chondrite L group

LoV098_Ch01

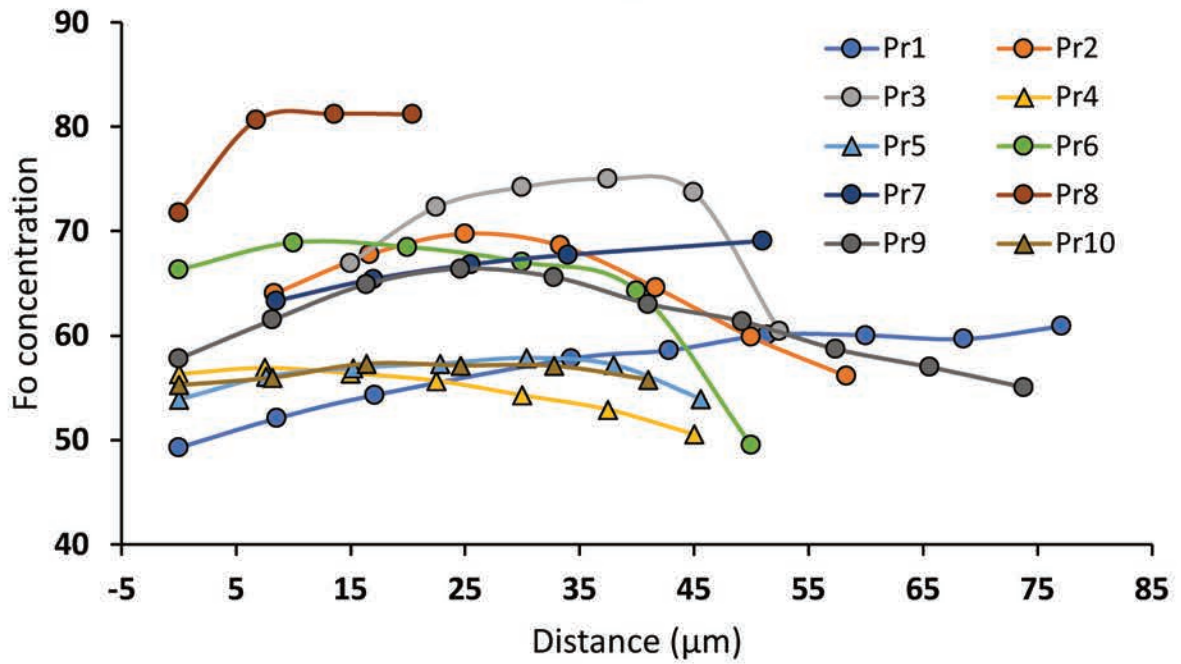


LoV098_Ch02

Electron Image 427

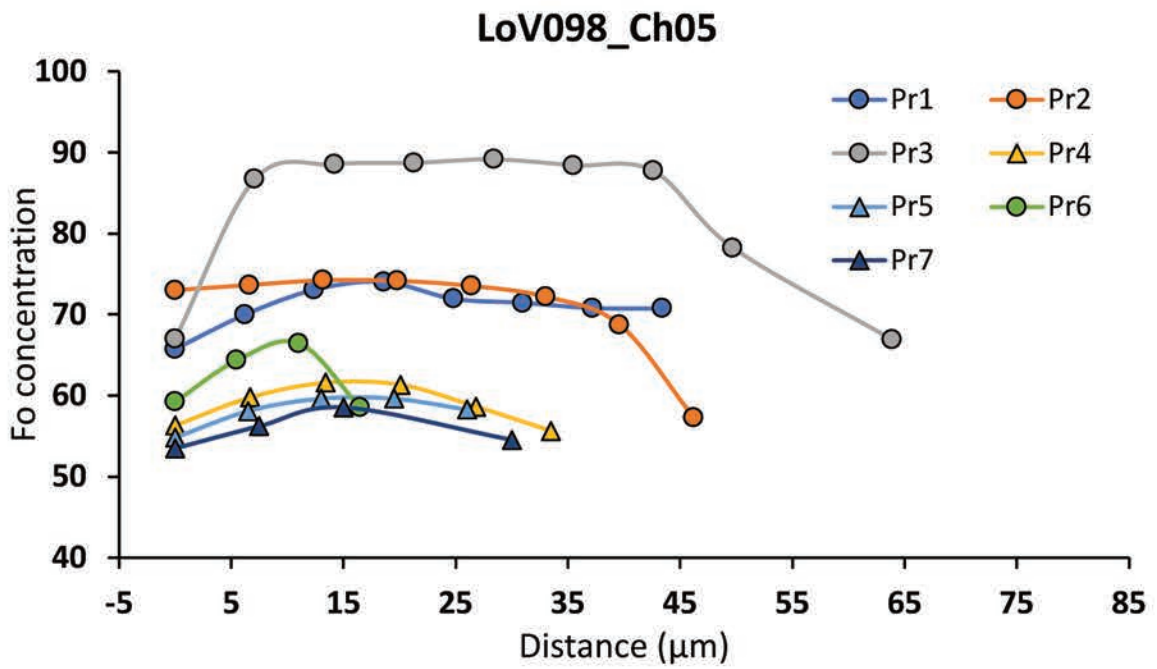
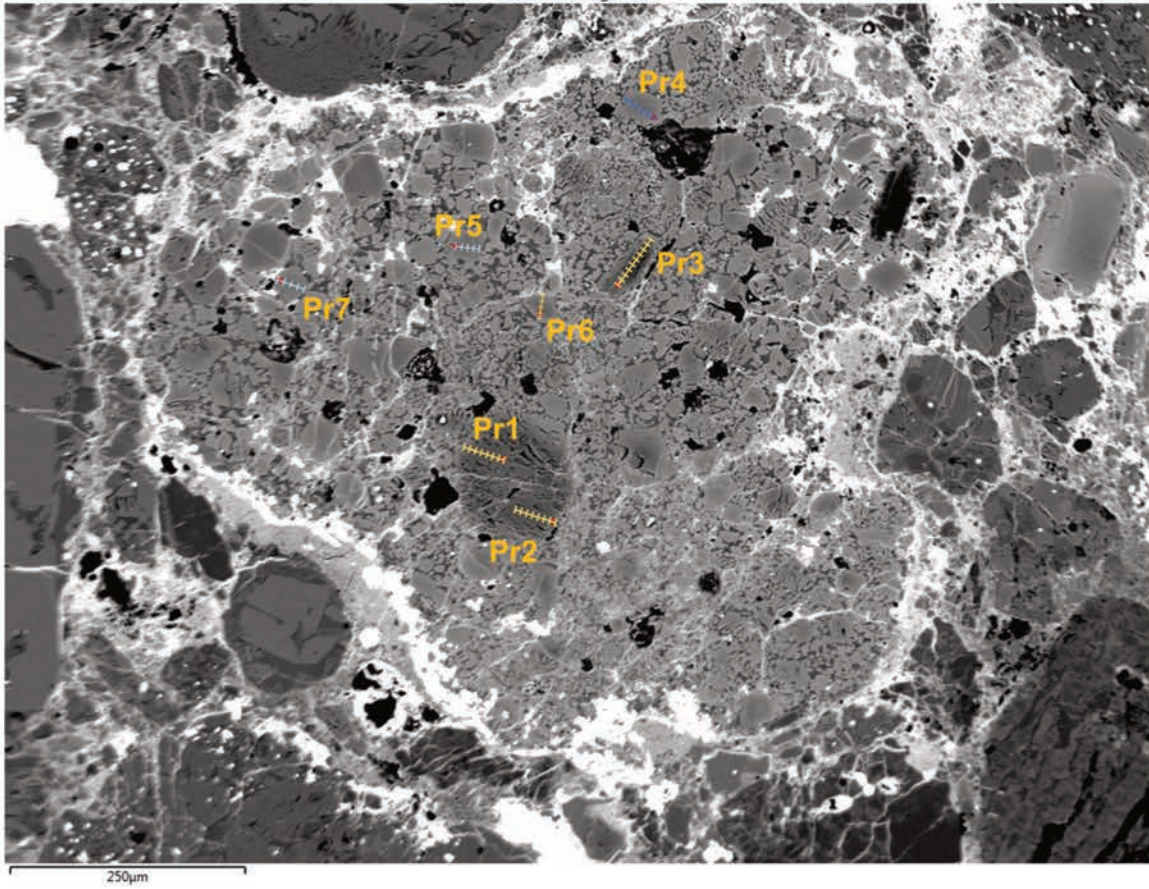


LoV098_Ch02

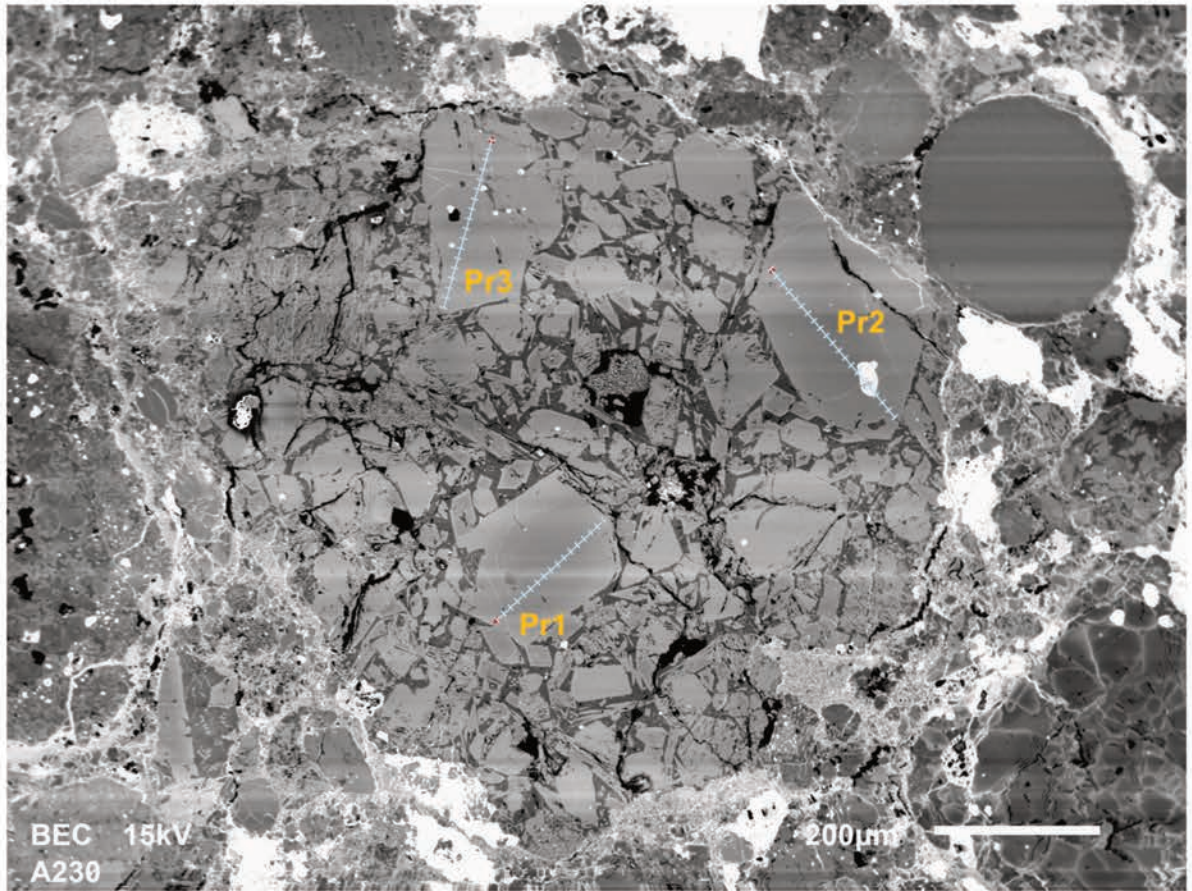


LoV098_Ch05

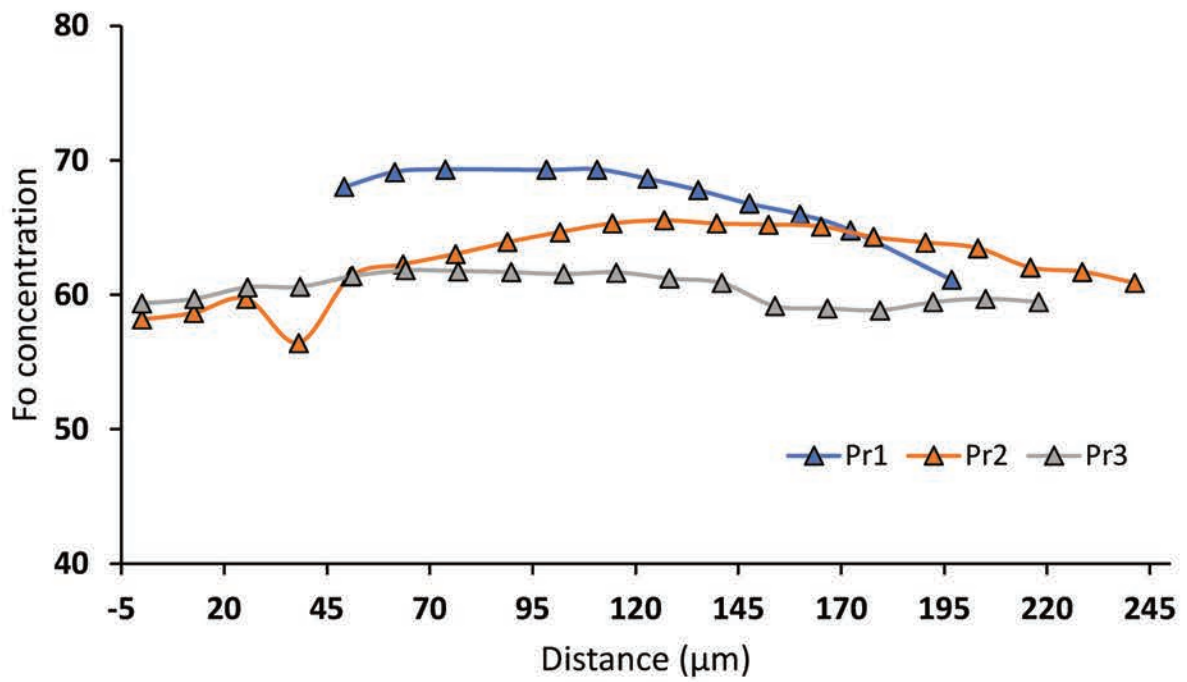
Electron Image 433



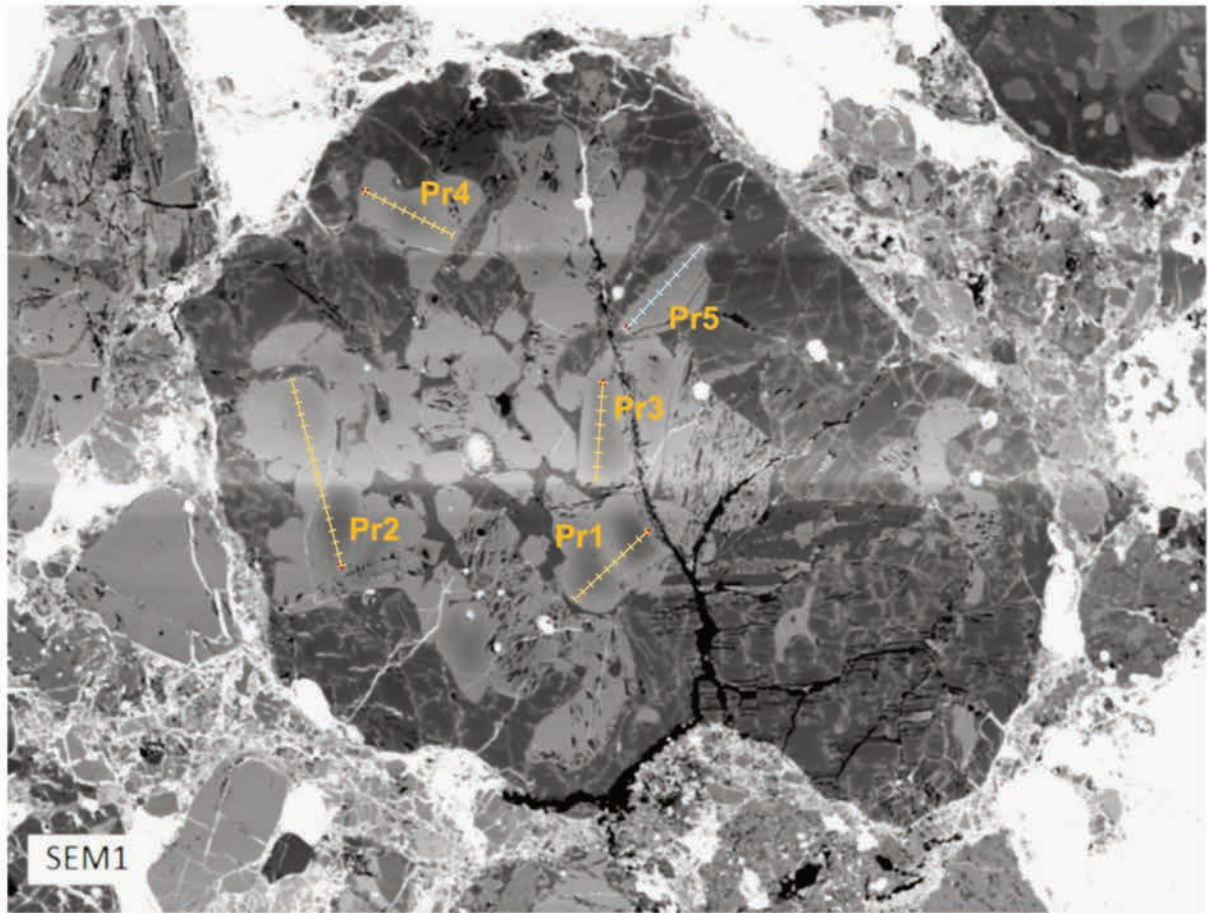
LoV098_Ch01p



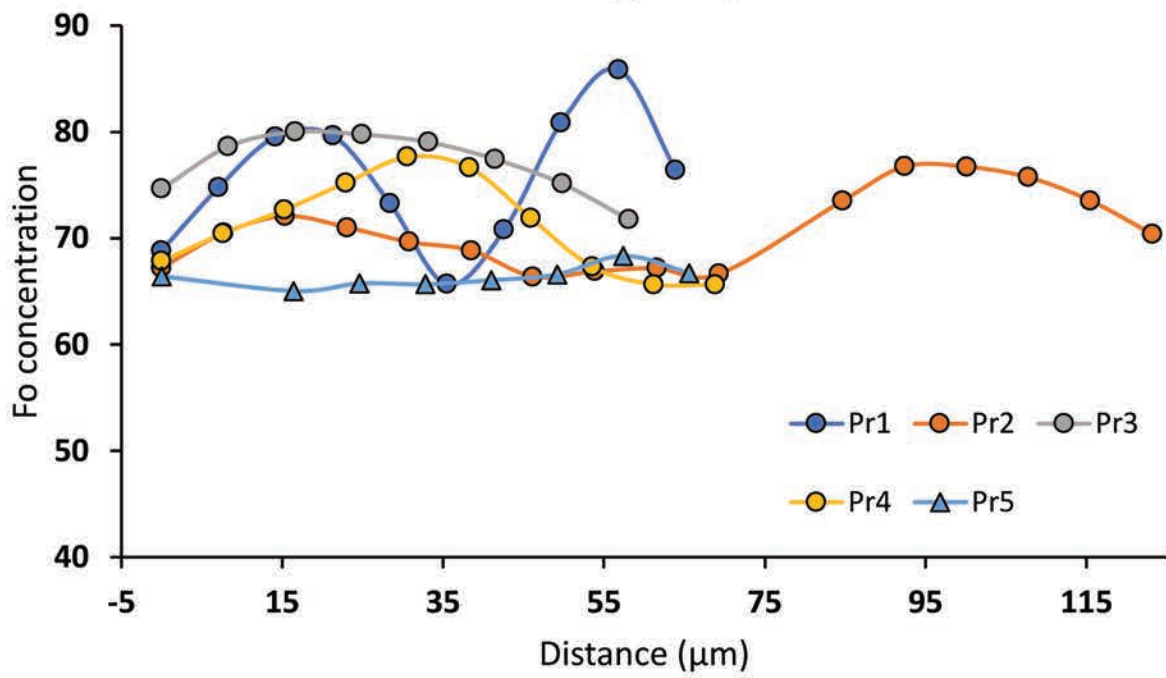
LoV098_Ch01p



LoV098_Ch02p

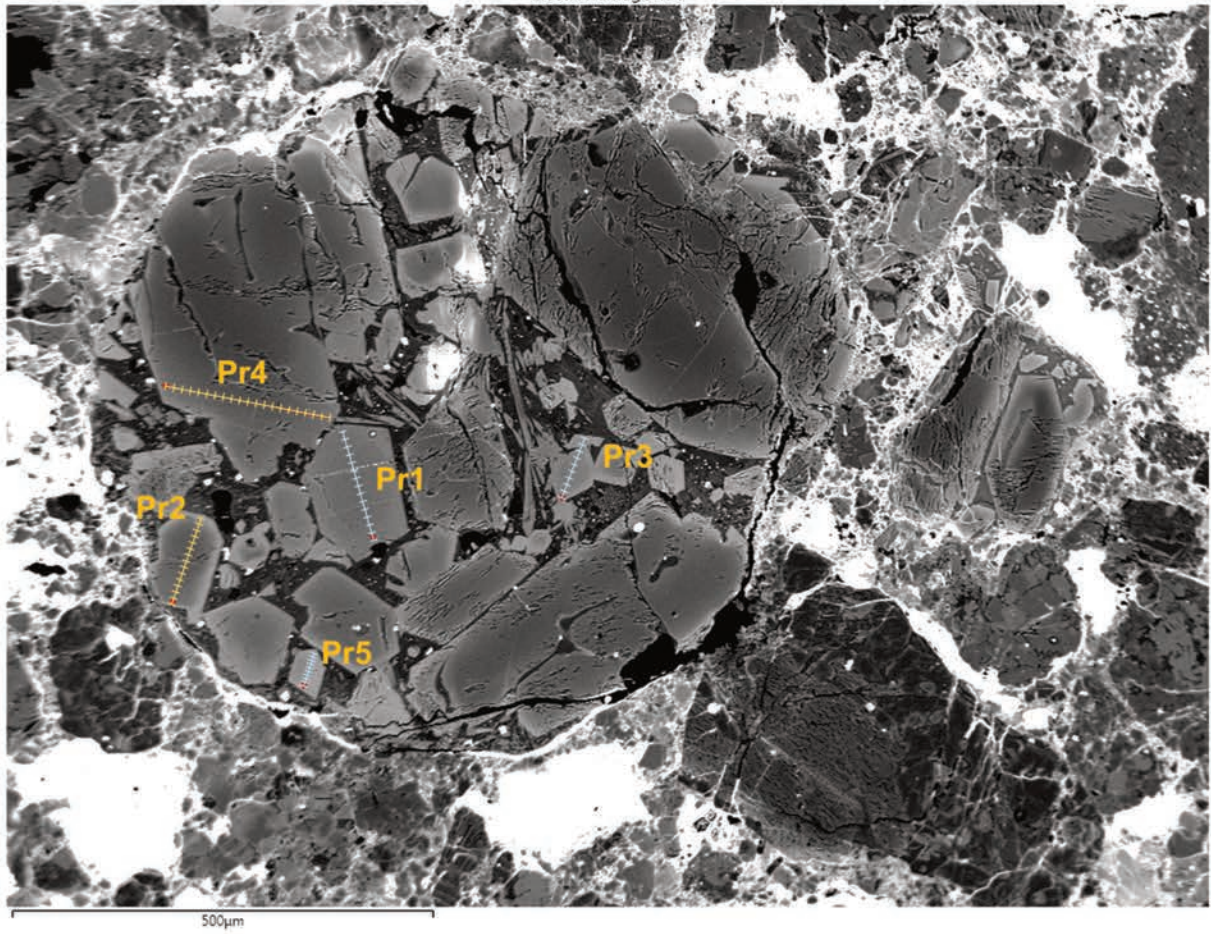


LoV098_Ch02p

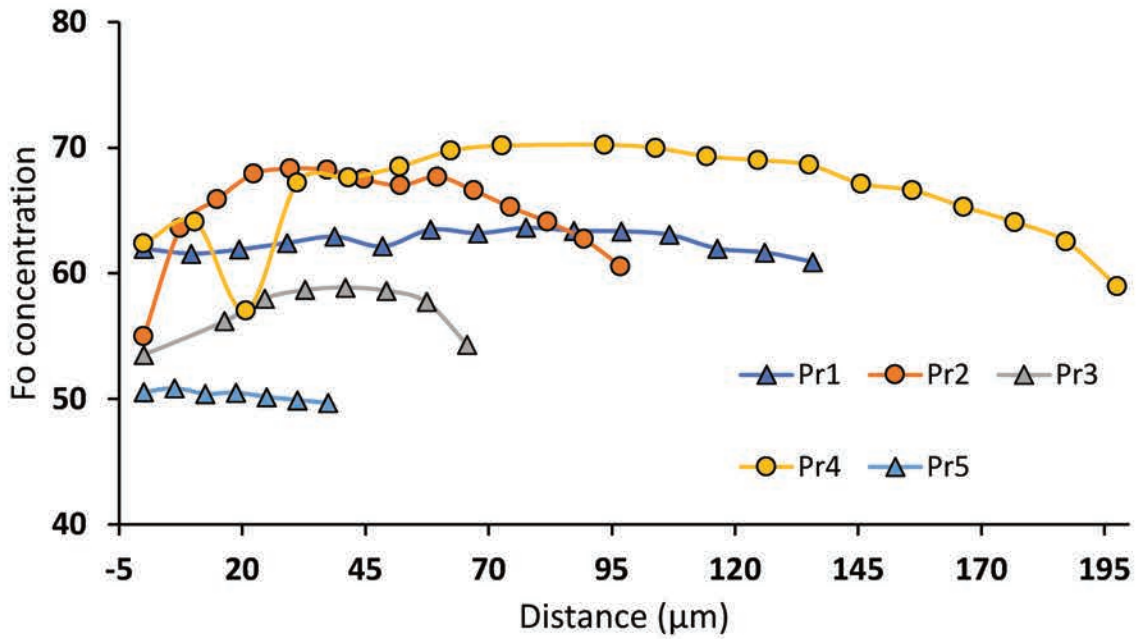


LoV098_Ch04

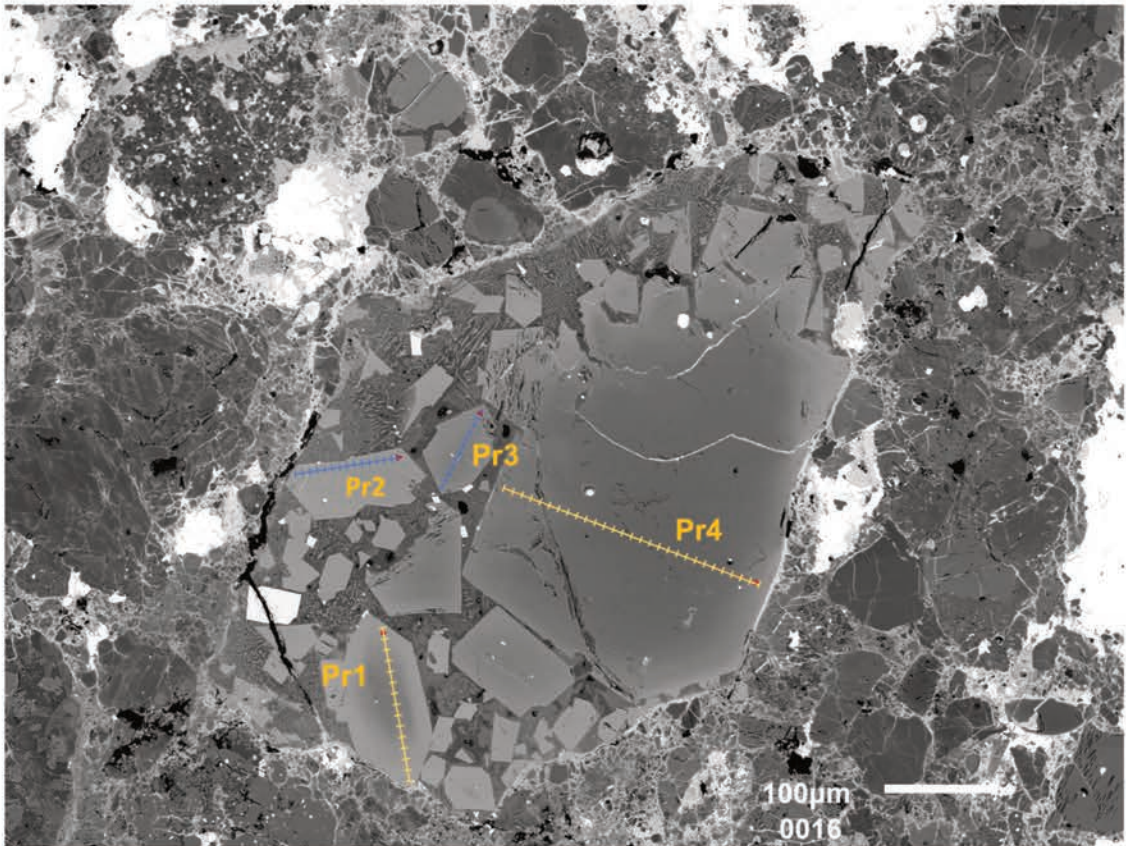
Electron Image 430



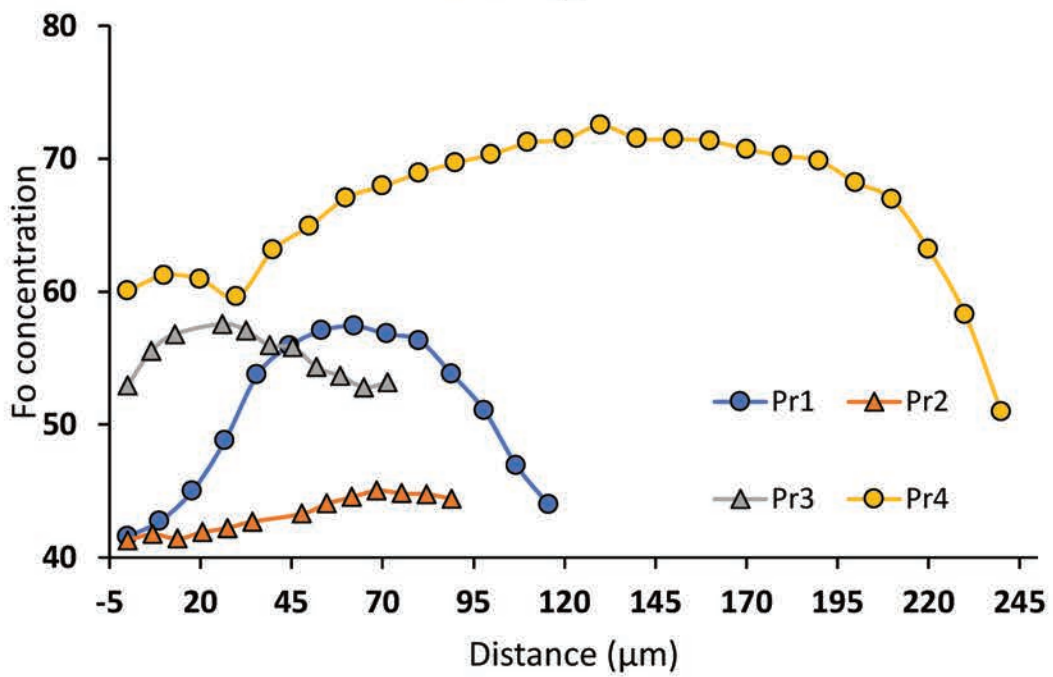
LoV098_Ch04



LoV098_Ch03



LoV098_Ch03



Appendix B

Supplementary material Chapter 4

Table A2-1. Five replicate tracing iterations for chondrule-FGR in 13 chondrules. Measure in mm.

Chondrule	Measure 1	Measure 2	Measure 3	Measure 4	Measure 5	Mean	STDV	CV
Ch#1	0.9296	0.9259	0.9236	0.9257	0.9235	0.9257	0.0025	0.27%
Ch#2	0.0741	0.0744	0.0739	0.0736	0.0733	0.0738	0.0004	0.61%
Ch#3	0.7239	0.7221	0.7180	0.7192	0.7159	0.7198	0.0032	0.45%
Ch#4	0.2605	0.2627	0.2615	0.2620	0.2590	0.2611	0.0014	0.55%
Ch#5	0.4046	0.4070	0.4049	0.4005	0.4036	0.4041	0.0024	0.59%
Ch#6	0.4271	0.4243	0.4227	0.4234	0.4209	0.4237	0.0023	0.53%
Ch#7	0.1312	0.1297	0.1292	0.1302	0.1295	0.1300	0.0008	0.61%
Ch#8	0.2000	0.2016	0.2034	0.2032	0.2030	0.2022	0.0015	0.73%
Ch#9	0.2030	0.2036	0.2040	0.2039	0.2066	0.2042	0.0014	0.69%
Ch#10	1.0055	1.0022	1.0072	1.0057	1.0006	1.0042	0.0027	0.27%
Ch#11	0.9807	0.9903	0.9952	0.9915	0.9917	0.9899	0.0054	0.55%
Ch#12	0.8858	0.8951	0.8970	0.8974	0.8974	0.8946	0.0050	0.56%
Ch#13	0.1749	0.1762	0.1768	0.1777	0.1763	0.1764	0.0010	0.59%

CV = Coefficient of variation

Table A2-2. Five replicate tracing iterations for matrix-FGR boundary in 13 chondrules. Measure in mm.

Chondrule	Measure 1	Measure 2	Measure 3	Measure 4	Measure 5	Mean	STDV	CV
Ch#1	1.1212	1.1232	1.1224	1.1220	1.1175	1.1213	0.0023	0.20%
Ch#2	0.0977	0.0998	0.1000	0.0964	0.1003	0.0988	0.0017	1.71%
Ch#3	0.8473	0.8463	0.8430	0.8447	0.8402	0.8443	0.0028	0.33%
Ch#4	0.3006	0.3041	0.3055	0.3043	0.3011	0.3031	0.0022	0.71%
Ch#5	0.4500	0.4481	0.4469	0.4461	0.4464	0.4475	0.0016	0.36%
Ch#6	0.4777	0.4770	0.4774	0.4780	0.4774	0.4775	0.0004	0.08%
Ch#7	0.1637	0.1596	0.1593	0.1612	0.1620	0.1612	0.0018	1.12%
Ch#8	0.2494	0.2409	0.2418	0.2421	0.2423	0.2433	0.0034	1.41%
Ch#9	0.2490	0.2472	0.2489	0.2477	0.2493	0.2484	0.0009	0.37%
Ch#10	1.1056	1.0867	1.0884	1.0848	1.0820	1.0895	0.0093	0.86%
Ch#11	1.0946	1.0988	1.1042	1.1085	1.1081	1.1028	0.0060	0.55%
Ch#12	1.0864	1.0835	1.0882	1.0844	1.0934	1.0872	0.0039	0.36%
Ch#13	0.2079	0.2055	0.2062	0.2044	0.2055	0.2059	0.0013	0.63%

CV = Coefficient of variation

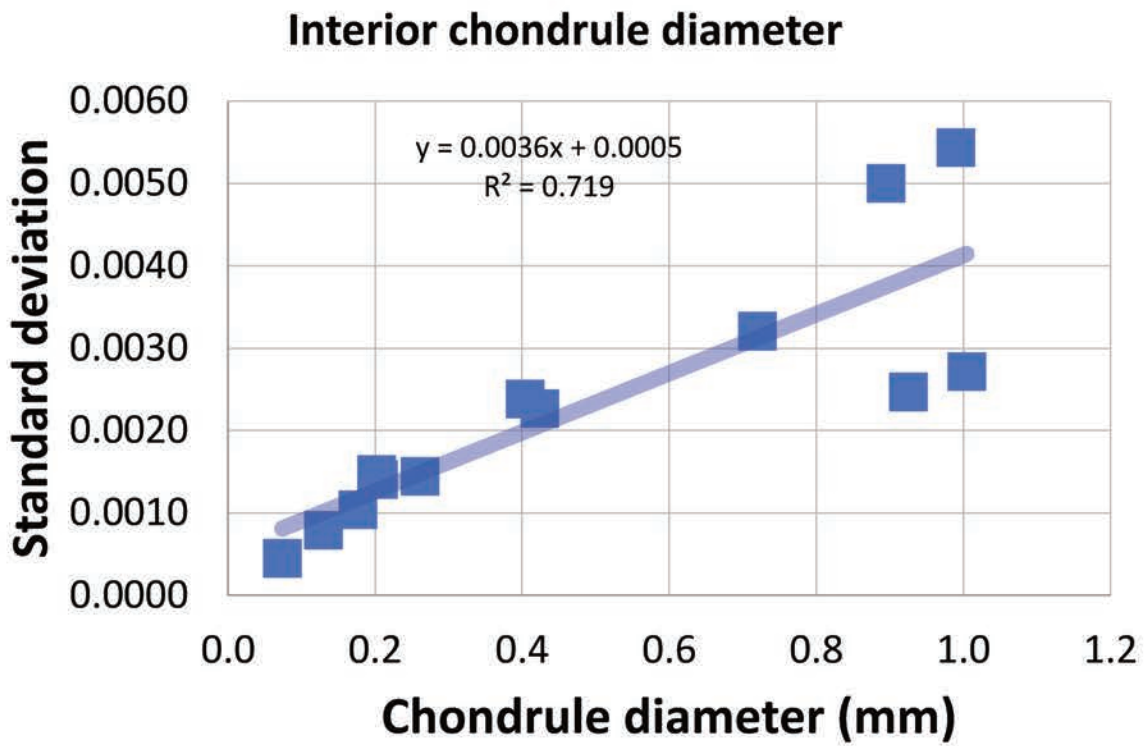


Figure A2-1. Standar deviation vs. chondrule diameter. This uncertainty shows a positive correlation between the average chondrule diameter and the standard deviation ($R^2 = 0.72$). It means that biggest chondrule

Table A2-3. Rimmed chondrules measurements in CO, CV, CM and CR.

Class	Meteorite	Chemical classification	Interior chondrule diameter (μm)	STDV (1σ)	FGR thickness (μm)	STDV (1σ)	Chondrule + FGR (μm)	STDV (1σ)
CO3	<i>EM 463</i>	Type I	537	1.9	27	1.5	564	2.3
		Type I	263	0.9	27	0.8	290	1.2
		Type I	233	0.8	28	0.7	261	1.1
		Type I	161	0.6	20	0.5	181	0.8
		Type I	244	0.9	48	0.8	292	1.3
		Type I	536	1.9	56	1.6	592	2.5
		Type I	392	1.4	32	1.1	424	1.8
		Type I	423	1.5	44	1.3	467	2.0
		Type I	408	1.5	17	1.1	425	1.7
		Type I	255	0.9	26	0.8	281	1.2
		Type I	326	1.2	42	1.0	368	1.6
		Type I	354	1.3	16	1.0	370	1.5
		Type I	240	0.9	22	0.7	262	1.1
		Type I	238	0.9	31	0.7	269	1.2
		Type I	449	1.6	34	1.3	483	2.0
		Type I	282	1.0	24	0.8	306	1.3
		Type I	239	0.9	38	0.7	277	1.2
		Type I	324	1.2	38	1.0	362	1.6
		Type I	261	0.9	35	0.8	296	1.3
		Type I	215	0.8	29	0.7	244	1.1
		Type I	250	0.9	31	0.8	281	1.2
		Type I	120	0.4	25	0.4	145	0.7
		Type I	211	0.8	41	0.7	252	1.1
		Type I	344	1.2	32	1.0	376	1.6
		Type I	108	0.4	14	0.3	122	0.5
		Type I	813	2.9	72	2.4	885	3.7
		Type I	695	2.5	66	2.0	761	3.2
		Type I	339	1.2	26	1.0	365	1.5
		Type I	727	2.6	46	2.1	773	3.2
		Type I	826	3.0	75	2.4	901	3.8
		Type I	350	1.3	65	1.1	415	1.9
		Type I	248	0.9	33	0.8	281	1.2
		Type I	345	1.2	63	1.1	408	1.8
		Type I	457	1.6	59	1.4	516	2.2
		Type I	512	1.8	60	1.5	572	2.5
Type I	559	2.0	53	1.6	612	2.6		
Type I	500	1.8	49	1.5	549	2.3		
Type I	976	3.5	60	2.8	1036	4.3		

	Type II	302	1.3	28	1.1	330	1.7
	Type II	382	1.7	44	1.3	426	2.1
	Type II	113	0.9	23	0.8	136	1.2
	Type II	312	2.2	34	1.8	346	2.8
	Type II	244	1.1	28	1.0	272	1.6
	Type II	290	1.0	32	0.8	322	1.3
	Type II	375	1.6	33	1.3	408	2.0
	Type II	125	2.2	15	1.8	140	2.7
	Type II	971	1.8	72	1.5	1043	2.4
	Type II	487	2.7	35	2.1	522	3.3
<i>EM 397</i>	Type I	359	0.7	34	0.5	393	0.9
	Type I	463	1.5	41	1.2	504	1.9
	Type I	256	0.8	29	0.7	285	1.1
	Type I	598	2.6	60	2.0	658	3.1
	Type I	314	3.8	51	3.1	365	4.8
	Type I	275	1.3	23	1.0	298	1.6
	Type I	442	0.7	38	0.6	480	1.0
	Type I	619	2.7	42	2.2	661	3.5
	Type I	509	2.7	51	2.2	560	3.5
	Type I	741	1.2	52	1.0	793	1.5
	Type I	183	1.6	20	1.3	203	2.0
	Type I	406	1.8	35	1.4	441	2.2
	Type I	226	1.8	33	1.5	259	2.3
	Type I	722	1.7	34	1.3	756	2.0
	Type I	1053	0.9	90	0.7	1143	1.1
	Type I	354	0.4	31	0.3	385	0.5
	Type I	184	1.2	37	1.0	221	1.5
	Type I	741	0.8	74	0.6	815	0.9
	Type I	744	0.7	74	0.6	818	0.9
	Type I	324	2.9	32	2.3	356	3.6
	Type I	431	1.0	37	0.7	468	1.1
	Type I	500	0.5	35	0.4	535	0.6
	Type I	505	0.7	48	0.5	553	0.8
	Type II	484	0.8	72	0.7	556	1.0
	Type II	680	0.8	42	0.6	722	0.9
	Type II	708	0.6	50	0.5	758	0.7
<i>EM 216</i>	Type I	473	1.0	15	0.8	488	1.2
	Type I	254	1.1	11	0.9	265	1.4
	Type I	109	1.5	11	1.3	120	2.0
	Type I	340	1.1	24	0.9	364	1.4
	Type I	223	1.4	10	1.1	233	1.8
	Type I	197	0.4	16	0.4	213	0.6
	Type I	818	1.1	52	0.9	870	1.5

	Type I	267	0.9	8	0.7	275	1.2
	Type I	132	1.0	13	0.9	145	1.4
	Type I	190	1.4	12	1.1	202	1.7
	Type I	235	0.5	13	0.4	248	0.6
	Type I	209	3.5	16	2.8	225	4.3
	Type I	160	1.8	12	1.4	172	2.2
	Type I	281	1.7	15	1.5	296	2.4
	Type I	317	2.4	21	1.9	338	3.0
	Type I	413	2.5	54	2.0	467	3.1
	Type II	269	1.0	17	0.8	286	1.2
	Type II	243	0.9	15	0.7	258	1.1
	Type II	585	2.1	15	1.6	600	2.4
<i>LoV 123</i>	Type I	321	1.2	12	0.9	333	1.3
	Type I	257	0.9	13	0.7	270	1.1
	Type I	433	1.6	12	1.2	445	1.8
	Type I	593	2.1	21	1.6	614	2.5
CR2 <i>Renazzo</i>	Type I	765	2.8	80	2.3	845	3.6
	Type I	366	1.3	33	1.1	399	1.7
	Type I	475	1.7	71	1.5	546	2.4
	Type I	757	2.7	68	2.2	825	3.5
	Type I	685	2.5	103	2.1	788	3.5
	Type I	214	0.8	72	0.8	286	1.4
	Type I	1211	4.4	97	3.5	1308	5.5
	Type I	740	2.7	78	2.2	818	3.5
	Type I	196	0.7	16	0.6	212	0.9
	Type I	837	3.0	51	2.4	888	3.7
	Type I	469	1.7	36	1.4	505	2.1
<i>DaG574</i>	Type I	1316	4.7	51	3.6	1367	5.5
	Type I	652	2.3	72	1.9	724	3.1
CM2 <i>Paris</i>	Type I	697	2.5	59	2.0	756	3.2
	Type I	209	0.8	57	0.7	266	1.3
	Type I	106	0.4	16	0.3	122	0.5
	Type I	175	0.6	17	0.5	191	0.8
	Type I	305	1.1	42	0.9	347	1.5
	Type II	207	0.7	43	0.7	249	1.1
	Type I	474	1.7	26	1.3	499	2.0
	Type I	165	0.6	16	0.5	180	0.8
	Type I	507	1.8	34	1.4	541	2.2
	Type I	266	1.0	25	0.8	291	1.2
	Type II	200	0.7	31	0.6	231	1.0
	Type I	137	0.5	15	0.4	152	0.7
	Type I	150	0.5	28	0.5	178	0.8
	Type II	552	2.0	73	1.7	625	2.7

Type I	186	0.7	19	0.6	205	0.9
Type I	456	1.6	49	1.4	505	2.2
Type I	265	1.0	55	0.9	320	1.5
Type I	168	0.6	36	0.6	205	0.9
Type I	773	2.8	55	2.2	828	3.4
Type I	442	1.6	60	1.4	502	2.2
Type I	957	3.4	66	2.7	1023	4.2
Type I	609	2.2	47	1.8	655	2.7
Type II	221	0.8	28	0.7	249	1.1
Type I	286	1.0	35	0.9	321	1.4
Type I	200	0.7	25	0.6	225	1.0
Type I	203	0.7	23	0.6	226	1.0
Type I	345	1.2	37	1.0	382	1.6
Type I	170	0.6	16	0.5	185	0.8
Type I	276	1.0	25	0.8	300	1.3
Type I	412	1.5	36	1.2	447	1.9
Type I	142	0.5	19	0.4	162	0.7
Type I	252	0.9	25	0.7	277	1.2
Type I	225	0.8	24	0.7	249	1.1
Type I	224	0.8	32	0.7	257	1.1
Type I	194	0.7	27	0.6	221	1.0
Type I	193	0.7	22	0.6	215	0.9
Type I	1005	3.6	50	2.8	1056	4.3
Type I	131	0.5	16	0.4	147	0.6
Type I	354	1.3	35	1.0	389	1.7
Type I	564	2.0	54	1.7	618	2.6
Type I	839	3.0	65	2.4	904	3.8
Type II	158	0.6	34	0.5	191	0.9
Type I	350	1.3	38	1.0	388	1.7
Type I	144	0.5	20	0.4	164	0.7
CV3 <i>Vigarano</i> Type I	2995	10.8	140	8.4	3135	12.8
Type I	981	3.5	57	2.8	1038	4.3
Type I	555	2.0	64	1.7	619	2.7
Type I	2686	9.7	133	7.5	2819	11.5
Type I	1505	5.4	56	4.2	1561	6.3
Type I	886	3.2	100	2.7	986	4.2
Type I	2031	7.3	126	5.8	2157	8.9
